Pageoph Topical Volumes

Tomasz Niedzielski
Krzysztof Migała
Editors

Geoinformatics and Atmospheric Science

Birkhäuser

Birkhäuser

Geoinformatics and Atmospheric Science

Edited by
Tomasz Niedzielski
Krzysztof Migała

Previously published in *Pure and Applied Geophysics* (PAGEOPH),
Volume 174, No. 2, 2017.

Birkhäuser

Editors
Tomasz Niedzielski
Department of Geoinformatics and Cartography
University of Wrocław
Wrocław
Poland

Krzysztof Migała
University of Wrocław
Wrocław
Poland

ISBN 978-3-319-66091-2

Library of Congress Control Number: 2017950286

© Springer International Publishing AG 2018
This work is subject to copyright. All rights are reserved by the Publisher, whether the whole or part of the material is concerned, specifically the rights of translation, reprinting, reuse of illustrations, recitation, broadcasting, reproduction on microfilms or in any other physical way, and transmission or information storage and retrieval, electronic adaptation, computer software, or by similar or dissimilar methodology now known or hereafter developed.
The use of general descriptive names, registered names, trademarks, service marks, etc. in this publication does not imply, even in the absence of a specific statement, that such names are exempt from the relevant protective laws and regulations and therefore free for general use.
The publisher, the authors and the editors are safe to assume that the advice and information in this book are believed to be true and accurate at the date of publication. Neither the publisher nor the authors or the editors give a warranty, express or implied, with respect to the material contained herein or for any errors or omissions that may have been made. The publisher remains neutral with regard to jurisdictional claims in published maps and institutional affiliations.

Cover illustration: Clouds with superimposed database view, Tomasz Niedzielski
Cover design: deblik, Berlin

Printed on acid-free paper

This book is published under the trade name Birkhäuser (www.birkhauser-science.com)
The registered company is Springer International Publishing AG
The registered company address is: Gewerbestrasse 11, 6330 Cham, Switzerland

Contents

Pure Appl. Geophys. 174 (2017), 459–462

DOI 10.1007/s00024-017-1478-1

Pure and Applied Geophysics

Geoinformatics and Atmospheric Science: Introduction

TOMASZ NIEDZIELSKI[1] and KRZYSZTOF MIGAŁA[1]

Numerous products of meteorological analyses are nowadays required to be available in real or near real time. For instance, this concerns: monitoring networks designed to measure weather parameters or air quality indices, numerical weather predictions or air quality forecasts. In addition, the dynamics of the atmosphere and its permanent assessment and prediction influence water management. Therefore, investigations into hydrologic phenomena or ocean dynamics have to be enhanced by rapidly available meteorological products or—e.g., in the case of ocean–atmosphere interactions—the products themselves may make use of ocean-related real- or near-real-time analyses. In particular, applications of weather forecasts go beyond meteorology and are important in environmental protection activities as well as social and economic analyses.

The aforementioned tasks cannot be efficiently carried out without the use of recent advances in geoinformatics, the scope of which is to provide broadly understood geosciences with information technologies and infrastructure. In particular, geoinformatics—a modern discipline that makes use of geographic information systems, remote sensing, computer science as well as physical and empirical modelling methods—offers computational tools which are suitable for modelling spatial- or spatio-temporal phenomena. Not only remotely sensed data but also in situ measurements can be handled by geoinformation tools, for instance to produce gridded data products. The objective of this special issue of Pure and Applied Geophysics on "Geoinformatics and Atmospheric Science" is to present recent geoinformatics-based tools to solve atmospheric and water-related problems. A particular emphasis is put on geophysical problems which are associated with physics of atmosphere, meteorology, hydrology, ocean dynamics or climatology.

Associated with the special issue was the conference, the 22nd Cartographic School "Geoinformatics and Atmospheric Science" held in Wałbrzych-Książ (Poland) on 6–9 May 2014. Several papers presented at the 22nd Cartographic School are published in the special issue, but the selection of the papers has been successfully enriched by external submissions.

Many papers published in the special issue focus on Poland, the area which represents the European transitional zone between oceanic and continental features of the mid-latitude climate. A meaningful interseasonal and weather-related variability of the features within the zone in question causes difficulties in accurate modelling of the spatial distribution of atmospheric processes and phenomena. Improving skillfulness of the spatial modelling approaches for the said area, in particular operating in real time, remains one of the most important applications of geoinformatics in the field of atmospheric science.

Two papers of the special issue focus on oceanic problems. The work of Vaid (2017) aims to present the analysis of the biweekly oscillation in sea surface temperature (SST) changes in the South China Sea, with a particular emphasis put on its relations with the Western North Pacific Summer Monsoon. The author uses SST data acquired by the microwave imager (TMI) of the Tropical Rainfall Measuring Mission (TRMM) as well as the satellite-observed rainfall measurements and heat flux data. It is found that ocean-to-atmosphere processes induced by the biweekly oscillation in SST variations in the South China Sea enhance both sea level pressure and

---

[1] Faculty of Earth Sciences and Environmental Management, Institute of Geography and Regional Development, University of Wrocław, pl. Uniwersytecki 1, 50-137 Wrocław, Poland. E-mail: tomasz.niedzielski@uwr.edu.pl; krzysztof.migala@uwr.edu.pl

surface shortwave radiation flux, during the summer monsoon. The study confirms the usefulness of geoinformatics (here, remote sensing data and geocomputation) to solve the problems of ocean–atmosphere interactions. Yet another analysis of monsoon circulation, focused on the Indian Summer Monsoon, is offered by Yadav and Singh (2017). The authors concentrate on two specific years, 2013 and 2014, in which the monsoon dynamics differed significantly (2013—timely onset and rapid progression; 2014—delayed onset and slow progression). It is found that those differences were controlled by the strength of persistent convection over the north equatorial Indian Ocean in May which implied several consequences for the atmospheric circulation over the study area. In the context of the scope of the special issue, an emphasis should be placed on geoinformatics tools which are used to carry out the analyses—among others the authors utilised the Ferret software (visualisation and analysis environment dedicated for meteorologists and oceanographers) and the NCL environment (language for research data processing and visualisation).

The special issue consists of a few papers on mesoscale numerical weather prediction, carried out using the Weather Research and Forecasting (WRF) model. The WRF model is a large, computationally efficient platform dedicated for forecasting the dynamics of various elements of the atmosphere. Wałaszek et al. (2017) use the WRF model to simulate the cloud cover over Poland in the case study for a specific period when ozone concentration was very high. Numerous microphysics parameterization schemes are used, and the authors arrive at the conclusion that the Morrison Double-Moment microphysics is recommended for the scrutinised episode. A different application of the WRF model for Poland is presented by Kryza et al. (2017) and Ojrzyńska et al. (2017) who makes use of dynamical downscaling of four meteorological variables (air temperature, relative humidity, wind speed, wind direction). The statistical assessment of modelling skills shows a particularly good agreement between air temperature simulations and measured data (Kryza et al. 2017). The calibrated model is used by Ojrzyńska et al. (2017) to classify macrotypes of atmospheric circulation in an automatic fashion. The WRF model may also be used to simulate and predict air quality, as presented by Werner et al. (2017) who utilise its version with chemistry known as WRF-Chem. The authors apply the model in question to check the impact of direct and indirect feedback effects of aerosols on simulations of PM_{10} concentration and the selected meteorological variables.

Yet another example of physically-based modelling of meteorological variables is presented by Jancewicz and Szymanowski (2017) who make use of the computational fluid dynamics (CFD) diagnostic solver Canyon, included in WindStation software, for the purpose of simulating wind field in mountainous terrain. The CFD solution is based on: mass conservation, momentum conservation and energy conservation. The authors concentrate on the Śnieżnik Massif in southwestern Poland and perform a wind field reconstruction experiment for a few specific episodes. The objective of the work is to quantify the impact of surface roughness computed on a basis of different source spatial data on the output wind field simulations. It is found that the roughness based on LIDAR (Light Detection and Ranging) data, derived from the information on the complexity of relief without considering land cover characteristics, offers the acceptable wind field reconstruction.

Apart from the above-mentioned physically-based meteorological modelling, the special issue consists of two articles that utilise data-based (or empirical) models to simulate meteorological or climatological variables. The data-based models usually omit physical fundamentals that control a given phenomenon, but they extensively use data processing methods which aim to build models that associate inputs with outputs. Many geographic information systems and environments for scientific computing have such modelling tools implemented, and therefore the methods belong to the scope of geoinformatics. Szymanowski and Kryza (2017) present an extensive study on the use of mixed deterministic–stochastic models in modelling air temperature in Poland. The authors' main objective is to check if it is justified to incorporate as many explanatory variables as possible to improve the accuracy of air temperature modelling. They arrive at the conclusion that only first 1–3 environmental variables (elevation, location, distance from the sea) are meaningful. Deterministic and stochastic modelling may also be used for simulating climatological variables, as presented by Szymanowski et al. (2017). The authors focus on the Ewert's index which quantifies the continentality of climate. On the example of Poland, which is located on the contact of continental and oceanic climate forcing, Szymanowski et al. (2017) perform spatial interpolation of the index in question. They formulate recommendations on using specific interpolators, in particular in the context of possible automation of the procedure. A different approach for predicting local-scale extreme weather phenomena is proposed by Walawender et al. (2017) who utilised the Favourable Meteorological Conditions (FMC) algorithms and several data-based statistical models. The authors aim to forecast thunderstorms, fog, glaze and rime, and their exercise uses a long time period (45 years) and concentrates on Poland. The paper serves as a methodological background for producing predictive maps, as presented in the Meteorological Hazard Atlas of Poland.

Since it is difficult to elaborate accurate prognoses of drought, which is associated with a long-term variability of the phenomenon, it is usually convenient to carry out drought risk assessment. Ruda et al. (2017) present a multi-stage approach for quantifying risk level, and illustrate it on the example area located in southeastern Czechia. A particular emphasis is put on a role of landscape complexity in drought development. It is found that even within a relatively small area, the risk level varies significantly in space.

A natural area of application of atmospheric products and reports is hydrology. Two papers published in the special issue offer case studies on applications of geoinformation methods in hydrologic analyses, in particular in flood hazard assessment. Mentzafou et al. (2017) use the geographically weighted regression to classify the Evros river basin into areas of dissimilar flood hazard categories. A different approach is explored by Rutkowska et al. (2017) who presents the L-moment-based analysis for the upper Vistula river basin. The authors claim that the approach may be used to estimate flood quantiles at ungauged sites and therefore has a considerable potential for flood risk assessment studies.

Atmospheric processes are not only associated with oceanic and hydrologic phenomena, but also may have a significant influence on solid Earth. One of such impacts is the atmospheric mass loading which remains a part of the entire signal measured at reference stations of the Global Navigation Satellite System (GNSS). Peng et al. (2017) consider the time series of vertical GNSS coordinates of the selected reference stations located in China. One of the main findings is decomposition of the seasonal non-tectonic signal into terms which correspond to atmospheric and soil moisture mass loading. The GNSS observations and their processing belong to very important areas of geoinformatics, since they provide location data for the majority of geoscientific analyses.

Acknowledgements

Guest Editors would like to express sincere thanks to a few persons and organisations. In particular, we are grateful to Dr. Renata Dmowska, the Editor-in-Chief for topical issues and book reviews of Pure and Applied Geophysics, who kindly accepted the proposal of the special issue on "Geoinformatics and Atmospheric Science". Dr. Dmowska's advice was very helpful and professional at all stages of the editorial work. We are also indebted to experts representing Birkhäuser/Springer Basel AG who kindly offered technical support. The members of Scientific Organising Committee and Local Organising Committee of the 22nd Cartographic School are also acknowledged. The conference was supported by Rector of the University of Wrocław, Section for Cartography of Polish Geographical Society and the Lower Silesian Marshal's Office. Special thanks should be given to all contributors who submitted their work to the special issue. We also wish to express our thanks to all reviewers who evaluated the manuscripts and provided the authors with valuable comments.

provide a link to the Creative Commons license, and indicate if changes were made.

References

Jancewicz, K., & Szymanowski, M. (2017). The relevance of surface roughness data qualities in diagnostic modeling of wind velocity in complex terrain: a case study from the Śnieżnik Massif (SW Poland). *Pure and Applied Geophysics*. doi:10.1007/s00024-016-1297-9.

Kryza, M., Wałaszek, K., Ojrzyńska, H., Szymanowski, M., Werner, M., & Dore, A. J. (2017). High-resolution dynamical downscaling of ERA-interim using the WRF regional climate model for the area of Poland. Part 1: model configuration and statistical evaluation for the 1981–2010 period. *Pure and Applied Geophysics*. doi:10.1007/s00024-016-1272-5.

Mentzafou, A., Markogianni, V., & Dimitriou, E. (2017). The use of geospatial technologies in flood hazard mapping and assessment: case study from River Evros. *Pure and Applied Geophysics*. doi:10.1007/s00024-016-1433-6.

Ojrzyńska, H., Kryza, M., Wałaszek, K., Szymanowski, M., Werner, M., & Dore, A. J. (2017). High-resolution dynamical downscaling of ERA-interim using the WRF regional climate model for the Area of Poland. Part 2: model performance with respect to automatically derived circulation types. *Pure and Applied Geophysics*. doi:10.1007/s00024-016-1273-4.

Peng, W., Dai, W., Santerre, R., Cai, C., & Kuang, C. (2017). GNSS vertical coordinate time series analysis using single-channel independent component analysis method. *Pure and Applied Geophysics*. doi:10.1007/s00024-016-1309-9.

Ruda, A., Kolejka, J., & Batelková, K. (2017). *Geocomputation and spatial modelling for geographical drought risk assessment: a case study of the Hustopeče Area*. Pure and Applied Geophysics: Czech Republic. doi:10.1007/s00024-016-1296-x.

Rutkowska, A., Żelazny, M., Kohnová, S., Łyp, M., & Banasik, K. (2017). *Regional L-moment-based flood frequency analysis in the upper Vistula River Basin*. Poland: Pure and Applied Geophysics. doi:10.1007/s00024-016-1298-8.

Szymanowski, M., Bednarczyk, P., Kryza, M., & Nowosad, M. (2017). Spatial interpolation of Ewert's index of continentality in Poland. *Pure and Applied Geophysics*. doi:10.1007/s00024-016-1413-x.

Szymanowski, M., & Kryza, M. (2017). The role of auxiliary variables in deterministic and deterministic-stochastic spatial models of air temperature in Poland. *Pure and Applied Geophysics*. doi:10.1007/s00024-015-1199-2.

Vaid, B. H. (2017). Biweekly Sea surface temperature over the South China Sea and its association with the Western North Pacific Summer Monsoon. *Pure and Applied Geophysics*. doi:10.1007/s00024-015-1198-3.

Wałaszek, K., Kryza, M., Szymanowski, M., Werner, M., & Ojrzyńska, H. (2017). Sensitivity study of cloud cover and ozone modeling to microphysics parameterization. *Pure and Applied Geophysics*. doi:10.1007/s00024-015-1227-2.

Walawender, E., Walawender, J. P., & Ustrnul, Z. (2017). Geospatial predictive modelling for climate mapping of selected severe weather phenomena over Poland: a methodological approach. *Pure and Applied Geophysics*. doi:10.1007/s00024-016-1250-y.

Werner, M., Kryza, M., Skjøth, C. A., Wałaszek, K., Dore, A. J., Ojrzyńska, H., et al. (2017). Aerosol-radiation feedback and PM_{10} air concentrations over Poland. *Pure and Applied Geophysics*. doi:10.1007/s00024-016-1267-2.

Yadav, R. K., & Singh, B. B. (2017). North equatorial Indian Ocean convection and Indian Summer Monsoon June progression: a case study of 2013 and 2014. *Pure and Applied Geophysics*. doi:10.1007/s00024-016-1341-9.

Pure Appl. Geophys. 174 (2017), 463–475

DOI 10.1007/s00024-015-1198-3

Pure and Applied Geophysics

Biweekly Sea Surface Temperature over the South China Sea and its association with the Western North Pacific Summer Monsoon

B. H. Vaid[1]

Abstract—The association of the biweekly intraseasonal (BWI) oscillation in the Sea Surface Temperature (SST) over the South China Sea (SCS) and the Western North Pacific Summer Monsoon is authenticated using version 4 the Tropical Rainfall Measuring Mission Microwave Imager data (SST and rain) and heat fluxes from Ocean Atmosphere Flux project data during 1998–2012. The results suggest that the SCS involves ocean–atmosphere coupling on biweekly timescales. The positive biweekly SST anomalies lead the rain anomalies over the SCS by 3 days, with a significant correlation coefficient ($r = 0.6$, at 99 % significance levels) between the SST-rain anomalies. It is evident from lead/lag correlation between biweekly SST and zonal wind shear that warm ocean surface induced by wind shear may contribute to a favorable condition of the convective activity over the SCS. The present study suggests that ocean–to-atmospheric processes induced by the BWI oscillation in the SCS SST results in enhanced sea level pressure and surface shortwave radiation flux during the summer monsoon. Besides, it is observed that the SCS BWI oscillation in the changes of SST causes a feedback in the atmosphere by modifying the atmospheric instability. This suggests that the active/break biweekly cycle of the SST over the SCS is related by sea level pressure, surface heat fluxes and atmospheric instability. The potential findings here indicate that the biweekly SST over the SCS play an important role in the eastward and the southward propagation of the biweekly anomalies in the Western North Pacific.

Key words: Biweekly Intraseasonal Oscillations, Sea surface temperature, Rain, South China Sea, Western North Pacific Summer Monsoon.

1. *Introduction*

Biweekly (also called 10–20 day mode) intraseasonal (BWI) oscillation is one of the major oscillation and most important component of the tropical variation on a time scale in between day-to-day weather together with the Madden–Julian oscillation (MJO) (Madden and Julian 1971, 1972). However, knowledge is limited concerning its propagation, especially in the South China Sea (SCS). An examination of the intraseasonal oscillations based on the data from the SCS Monsoon Experiment, showed their influence on the maintenance and break of the SCS summer monsoon (SM) (Chan *et al.* 2000, 2002; Mao and Chan 2005; Zhou and Miller 2005); consequently, the cognition of its temporal evolution is critical for improving regional intraseasonal weather and climate prediction. Intraseasonal oscillations of the SCS involve two intraseasonal time scales in the periods ranging from 10 to 20 days (Krishnamurti and Ardanuy 1980) and 30–60 days (Murakami *et al.* 1984; Krishnamurti and Subrahmanyam 1982; Lau and Peng 1987). Mao and Chan (2005), using National Centers for Environmental Prediction/National Center for Atmospheric Research (NCEP-NCAR) reanalysis data, found that for the years when both time scales are present, the SCS activities are basically controlled by the 30–60 day time scale, modified by the 10–20 day time scale. Assuming that the 30–60 days and biweekly mode have different dynamics (Chatterjee and Goswami 2004), structure and propagation (Murakami and Frydrych 1974; Krishnamurti and Ardanuy 1980; Chen and Chen 1993), it is expected that they have different impacts on the sea surface temperature (SST). While there are several studies of the 30–60 day air–sea relationship in the SCS (Zeng and Wang 2009; Roxy and Tanimoto 2011), the biweekly SST variability over the SCS has not been fully explored yet and the possible mechanism remains elusive.

The SST investigations over the SCS is very important because the SM over East Asia and the

---

[1] School of Marine Sciences, Nanjing University of Information Science and Technology (NUIST), Nanjing, China. E-mail: bakshi32@gmail.com

Western North Pacific (WNP) generally starts over the SCS (Wu and Wang 2000, 2001; Wang and Lin 2002). Since the WNP is also the most intensive among tropical monsoons, its behavior is of great scientific concern. The concept of the WNP SM was first introduced by Tao and Chen (1987) and they found that its influence on Australian High and cross-equatorial flows. The convective activity over the WNP has considerable influence on the weather and climate in the East Asia (Nitta 1987) and the WNP sea level pressure (SLP) and wind anomalies play a key role in linking El Nino Southern Oscillation (ENSO) to the East Asian climate (Wang and Fan 1999). Besides, the East Asian SM is significantly influenced by the convective activity over the WNP (Murakami and Matsumoto 1994; Ueda and Yasunari 1996; Kawamura and Murakami 1998; Lu 2001). It has also been pointed out that an atmospheric Rossby wave is generated by anomalous convective activities over the WNP and propagates in the extra tropics, and influences the interannual and intraseasonal variations of the East Asian SM. Obviously, the role of the WNP on weather and climate variability over the East Asia is noteworthy. However, the SCS SST association with the WNP has not yet been discussed so much in the literature. In this paper, we will focus on the SST over the SCS and its association with the WNP monsoons. Apart from the role of the SCS BWI SST oscillation in the WNP SM, we also provided a step by step process of the ocean-to-atmosphere interaction involved. The role of intraseasonal SST anomalies in assisting the conviction, particularly for the WNP SM was examined by analyzing satellite observations along with reanalysis data. The goal of this paper is to quantify the impact of BWI oscillations on the SST in the SCS, investigate the processes that cause its change, and examine the influence of the SCS SST on the WNP SM. Neither of these has been previously examined yet and they are important for understanding the coupled mechanisms of BWI oscillation.

The Role of the SCS SST in influencing the SCS SM has been extensively studied in the literature. For example; Wang and Wu (1997) showed that, from May to July, the intraseasonal variability (30–60 days) of the SCS SM is primarily associated with a northward propagation of the intraseasonal anomalies from the equator to 25°N. Wu (2010) indicated that the northward propagation of the SCS SM intraseasonal anomalies relates to the ocean-to-atmosphere interaction during April-June, involving the wind-evaporation and cloud-radiation effects on the SST as well as the SST impacts on lower-level convergence over the equatorial western Pacific and atmospheric instability over the Philippine Sea and the SCS. Thereafter, Roxy and Tanimoto (2011) examine the intraseasonal SCS SM variability (30–60 days) during April–July over the SCS and showed the northward propagating intraseasonal anomalies and its association with the SCS SM. However, in the present study, we presented the SCS SST influence on the WNP SM and established the first time observational evidence for the role of the SCS SST in the eastward and the southward propagation of rainfall associated with the WNP SM. The objective of this study is to examine, based on recently available high resolution satellite and observational data, the evolution and role of BWI SST oscillation in influencing the intraseasonal variability of the WNP SM. The study focuses on the biweekly timescale SST and its influence on eastward and southward propagating anomalies over the SCS. In Sect. 2, we describe the data and the basic analytic methods. In Sect. 3, we begin by demonstrating the connection between BWI SST oscillation over the SCS and the WNP monsoons, and continue by describing in more detail on the southward and eastward propagation of BWI oscillation to the WNP. We also provide a step by step process of the ocean-to-atmosphere interaction involved association of BWI oscillation on the WNP monsoons. The concluding remarks are given in Sect. 4.

2. *Datasets and Methods*

The Tropical Rainfall Measuring Mission (TRMM) Microwave Imager (TMI) provides a novel observation of tropical SST, unaffected by clouds, aerosols, and atmospheric water vapor (Wentz *et al.* 2000). The TMI reveals intraseasonal SST perturbations considerably larger than the reanalysis product (Sengupta *et al.* 2001; Vecchi and Harrison 2002; Vaid *et al.* 2011). The TMI is a multi-channel, dual polarized, conical scanning passive microwave radiometer designed to take SST measurements over a wide swath under the TRMM satellite. The design of the instrument is similar to that of other satellite radiometers but the resolution of data measurement is better due to the lower altitude of the satellite orbit. The TRMM travels in a geosynchronous orbit with an inclination of 35°. This type of orbit precesses approximately 7° per day allowing for the TMI to sample the surface at all times of day as opposed to the twice per day windows of the polar-orbiting radiometers. The TRMM is a joint program between National Aeronautics and Space Administration (NASA) and the Japan Aerospace Exploration Agency (JAXA). Version 4 TMI data of the SST and rainfall are available online through http://www.ssmi.com/. The present study uses 3-day running means that have much better spatial coverage than daily data. The original data on 0.25° × 0.25° latitude–longitude grids have been interpolated to 1° × 1° latitude–longitude grids with spatial averaging to reduce the number of missing grids. Sea surface winds, SLP, relative humidity and air temperature datasets are obtained from the NCEP-Department of Energy (NCEP-DOE) Reanalysis Version 2 data (Kanamitsu *et al.* 2002).

The surface short wave radiation flux (SSWRF), surface latent heat flux (SLHF), surface sensible heat flux (SSHF), surface net heat flux (SNHF) is obtained at the 1° grid with a temporal resolution of 1 day from the Woods Hole Oceanographic Institute's (WHOI) Objectively Analyzed Air–Sea Fluxes (OA Flux) project (Yu *et al.* 2008). The OA Flux project integrates satellite observations with surface moorings, ship reports, and atmospheric model reanalyzed surface meteorology to develop the OA flux data. Besides, the lower tropospheric air temperature and relative humidity are used to derive the equivalent potential temperature (θ_e or THETA_E), which is a useful parameter in understanding the atmospheric stability. The lower tropospheric stability is estimated as a difference in θ_e between 1000 and 700 mb,

$$\Delta\theta_e = \theta_{e1000} - \theta_{e700}$$

where θ_{e1000} and θ_{e700} are θ_e at 1000 and 700 mb, respectively.

In addition to the above, the Lanczos filtering technique has been extensively used in the study (Duchon 1979). This is a Fourier method of filtering digital data and has been successively also used in Vaid *et al.* (2011). The general purpose of filtering time series is to predictably alter the Fourier amplitudes that describe the series. This can be accomplished by modifying a given data sequence with a set of weights called a filter weight function. The filter weight function is related to the variation with frequency of the ratio of the Fourier amplitude of the modified data sequence to that of the given data sequence and is called as filter response function. In the Lanczos filter, the filter response function is expressed as infinite Fourier series so that the weights become the Fourier coefficients. The Fourier coefficient of the smoothed response function is determined by multiplying the original response function by a function in the Lanczos filter called a sigma factor. This sigma factor is the principal feature in the filter as it significantly reduces the amplitude of the Gibbs oscillation (if a response function with a step change in the response is desired, the computed response function would exhibit an oscillation called the Gibbs oscillation). Digital data involve transforming an input data sequence x_i, where i is time, into an output data sequence y_i, using the linear relationship

$$y_i = \sum_{k=-53}^{53} w_k x_{i-k}$$

in which the w_k are the suitably chosen weights. To extract the BWI oscillation, a Lanczos band-pass filter with cutoff periods of 10 and 20 days and 53 weights were applied. The 53 daily weights were observed to provide very sharp cutoffs of response, with negligible Gibbs oscillation. Above mentioned datasets are filtered to BWI oscillations over the SCS using Lanczos filter. These intraseasonally filtered anomalies are used in the present study. To determine the dominant intraseasonal band a wavelet analysis similar to Vaid *et al.* (2007) is carried out. The wavelet analysis is a powerful tool for analyzing multi-scale, nonstationary processes, and can simultaneously determine both the dominant bands of variability and how those bands vary in time (e.g., Mak 1995; Torrence and Compo 1998). Wavelet analysis maintains time and frequency localization in a signal analysis by decomposing or transforming a one-dimensional time series into a diffuse two-dimensional time–frequency image simultaneously. Therefore, it is possible to get information on both the time variable amplitude of any "periodic" signals within the series. We utilize the wavelet analysis program developed by Torrence and Compo (1998) and use the Morlet wavelet as the mother wavelet.

3. *Results*

Analysis of the TRMM TMI data for the period 1998–2012 reveals that the mean SST during the SCS SM period June to September (JJAS) is above 27 °C (Fig. 1a), which is conducive for enhanced convective precipitation (Lau *et al.* 1998) and is of paramount importance. Large biweekly fluctuations in the SST over regions Long. = 115°E–120°E, Lat. = 15°N–20°N (hereafter Region 1) during the study period (Fig. 1b) are observed. It is worth to note that the BWI oscillation over the region 1 is observed to be the dominant band of variability with high statistical significance level (statistical significance at the 90 % confidence level) during the whole study period and has been checked using wavelet analysis. Figure 2b shows a three-dimensional plot, where *x*-axis denotes time (1–122 days correspond to JJAS daily composite during 1998–2012 of original TMI SST), *y*-axis denotes period of the signal and shading gives the information of the power. The black contours in the Fig. 2b are the 10 % significance level, using a red-noise background spectrum. The null hypothesis is defined for the wavelet power spectrum as assuming that the time series has a mean power spectrum; if a peak in the wavelet power spectrum is significantly above this background spectrum, then it can be assumed to be a true feature with a certain percent confidence. For definitions, "significant at the 10 % level" is equivalent to "the 90 % confidence level," and implies a test against a certain background level, while the "90 % confidence interval" refers to the range of confidence about a given value. The 90 % confidence implies that 10 % of the wavelet power should be above this level. More details can be found in Torrence and Compo (1998). Based on wavelet analysis (Fig. 2b), we can interpret that among all other timescales especially the longer intraseasonal time scales, the BWI oscillation is observed to be the dominant band of variability with high statistical significance level (statistically significant at the 90 % confidence level) over the region 1 during the whole study period and therefore signifies the importance of studying 10–20 day oscillations. Also, it can be clearly evident from Fig. 2c that the BWI oscillation is predominant

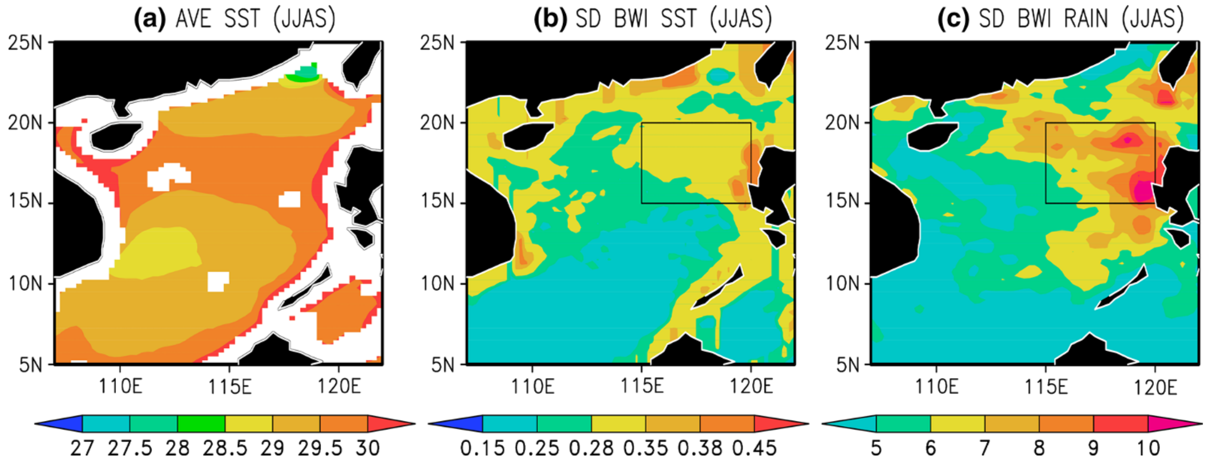

Figure 1

a Averaged SST (°C) over the SCS during June–September (1998–2012). **b** Standard deviation of the BIW oscillations in SST during the same period and **c** standard deviation of the BIW oscillations in rain during the same period

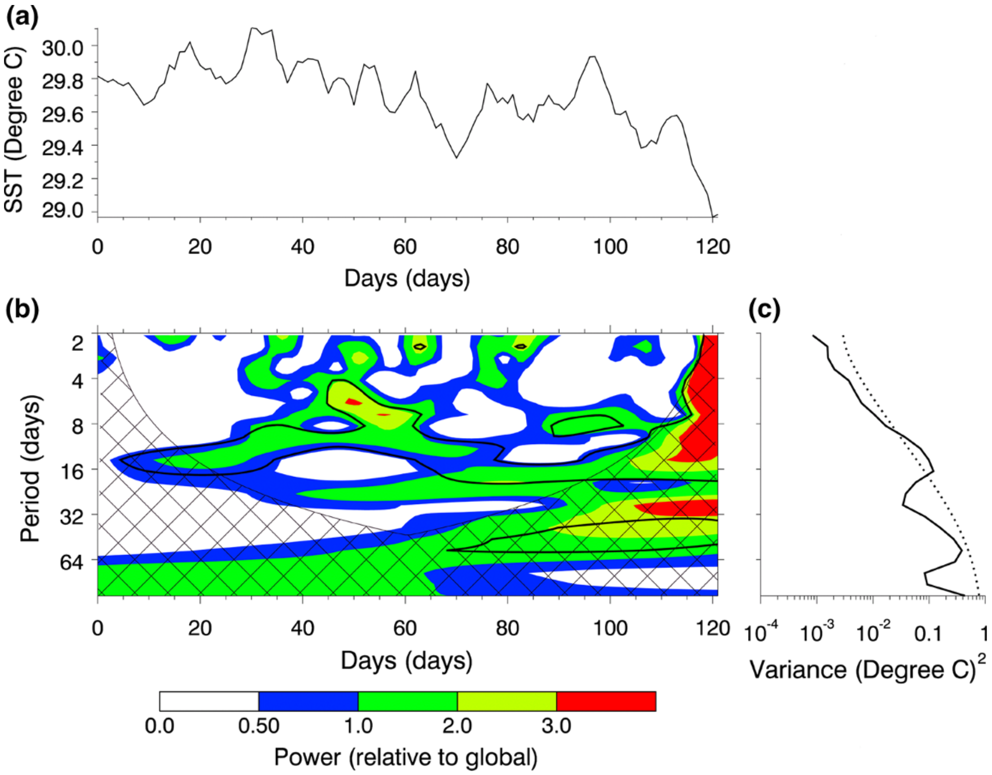

Figure 2

a Daily TMI SST (original) composite of JJAS during 1998–2012 over the Region 1. **b** Normalized wavelet power spectrum using Morlet wavelet. The power has been scaled by the global wavelet spectrum (at *right*). The cross-hatched region is the cone of influence, where zero padding has reduced the variance. *Black* contour is the 10 % significance level (90 % confidence level), using a *red*-noise (autoregressive lag1) background spectrum. **c** The global wavelet power spectrum (*black line*). The *dashed line* is the significance for the global wavelet spectrum, assuming the same significance level and background spectrum as in **b**

among other timescales as its peak can be seen surplussing the dashed line which is the significance for the global wavelet spectrum, assuming the same significance level and background spectrum as in 2(b) and thus it is of paramount interest to study the BWI oscillation over the region 1.

In the present study, we examined the development and sustenance of BWI oscillation over the inset rectangle (Region 1) in the Fig. 1b. Investigation of biweekly SST variability is the first and key step toward understanding air-sea coupling mechanisms on biweekly time scale. Besides, biweekly evolution and degeneration of the SST anomalies, and its association with propagation of the intraseasonal anomalies were also investigated. Further, we analyzed satellite derived rainfall data on a biweekly timescale (Fig. 1c), the significantly large standard deviation of biweekly rainfall over region 1 is observed and it seems to be associated with ocean-to-atmosphere processes as discussed in the later part of the manuscript. The time series of the biweekly SST and biweekly rain averaged over the rectangular box in June–September from 1998 to 2012 years is shown in Fig. 3. It is evident that both the BWI oscillation in SST and rain are coherent. The biweekly SST oscillation clearly leads the biweekly rain throughout the study period. The BWI oscillation in both SST and rain observed to be slightly weaker in 1998, 2006, 2007, 2010 and 2011 years.

To explain the ocean-to-atmosphere interactions, the lead-lag correlations (or correlation function estimates) of the BWI oscillation in SST with respect to the BWI oscillation in rain over the same region are estimated from 8 days before to 8 days after, for the 15 year period (Fig. 4a). A positive correlation is observed when biweekly SST leads the biweekly rain

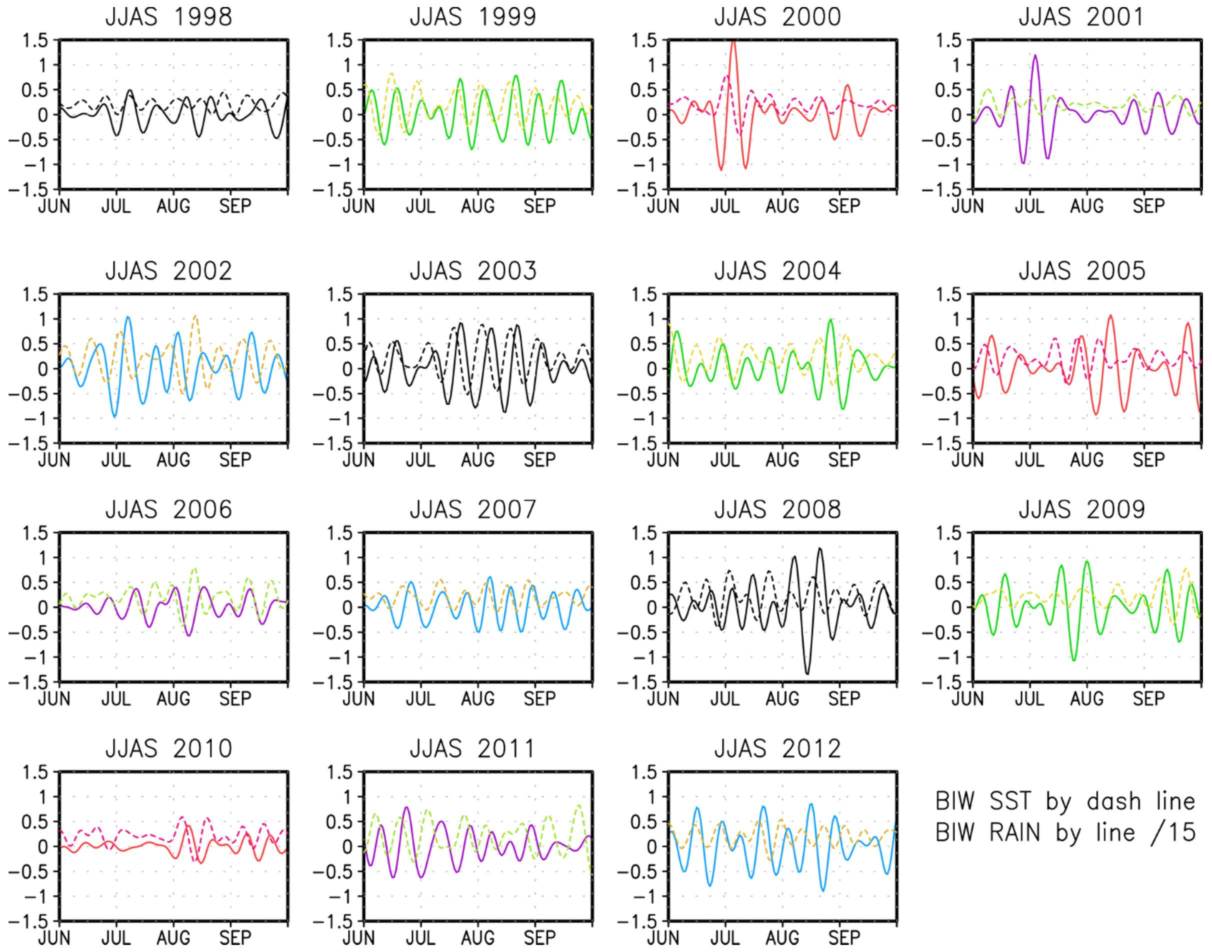

Figure 3
The BIW oscillation time series of SST (*dotted line*) precipitation (*solid line*) averaged over the *inset rectangle* in Fig. 1, in June–September, for the years 1998–2012

which indicates that the biweekly SST is driving the atmosphere and it is denoted as an ocean-to-atmosphere effect. A negative correlation is observed when biweekly SST lags the biweekly rain which implies that the atmosphere is driving the SST and it is denoted as an atmosphere–to-ocean effect. The time lag of the maximum (minimum) correlation denotes how quickly the atmosphere responds to the biweekly SST and vice versa. The correlation is close to zero and insignificant when the biweekly SST and rain are correlated with a 0 time lag (Fig. 4a), and its magnitude increases with the lead/lag. This indicates that the biweekly SST-rain relationship is shifted in time by several days. Maximum positive correlation coefficient ($r = 0.6$, at 99 % significant level) is observed when the SST leads the precipitation by 3 days (Fig. 4a). This suggests that ocean–to-atmospheric processes induced by the intraseasonal SST cause to enhance rain during the SM period. Maximum negative correlation coefficient ($r = -0.69$, at 99 % significant level) is obtained when the SST lags the intraseasonal rains by 3 days, suggesting an ocean cooling as a response to increased cloudiness associated with the rain. To understand the ocean-to-atmosphere interactions involving the SST during the study period, lead-lag correlations between the SST and zonal wind shear (U200-U850), SLP, SSWRF, SSHF, SLHF, SNHF and equivalent potential temperature on biweekly timescale are analyzed. It is evident from lead/lag correlation between biweekly

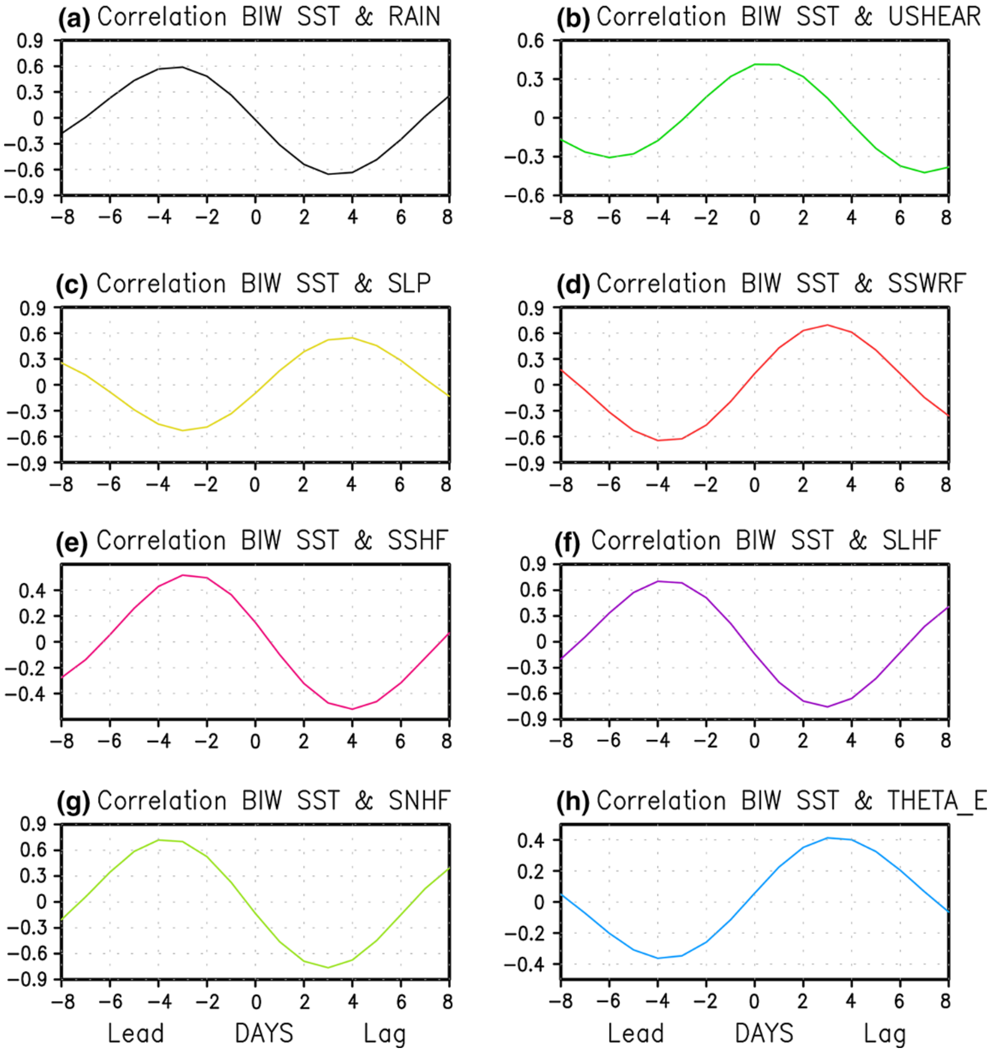

Figure 4

The Lead-lag correlation coefficients between the time series of the BIW oscillation in SST over the rectangular box given in the Fig. 1 and time series over the same *box* for **a** RAIN **b** USHEAR (U200–U850), **c** SLP, **d** SSWRF, **e** SSHF, **f** SLHF, **g** SNHF, **h** THETA_E. The correlation coefficients are statistically significant at 99 % confidence level

SST and zonal wind shear that warm ocean surface induced by wind shear may contribute to a favorable condition of the convective activity over the SCS (Fig. 4). A negative correlation coefficient is observed when biweekly SST leads the biweekly SSWRF and SLP, which indicates that the biweekly SST is driving the atmosphere and it is denoted as an ocean-to-atmosphere effect. Maximum negative correlation coefficient ($r = -0.70$, at 99 % significant level) is observed when the SST leads the biweekly SSWRF and SLP by 3 days (Fig. 4). This suggests that ocean–to-atmospheric processes induced by the intraseasonal SST result in enhancement of SLP and SSWRF during the SM. Maximum negative correlation coefficient ($r = -0.6$, at 99 % significant level) is obtained when the SST leads the intraseasonal SSWRF by 3 days suggesting an ocean cooling as a response to increased cloudiness associated with the rain.

Besides, it is evident from Fig. 4e, f, that biweekly SST changes are closely related to surface heat flux anomalies. A positive correlation coefficient is observed when biweekly SST leads the biweekly

SLHF, SSHF, which indicates that the biweekly SST is driving the atmosphere, and it is denoted as an ocean-to-atmosphere effect. A negative correlation coefficient is observed ($r = -0.61$, at 99 % significance level) when biweekly SST lags the biweekly rain which implies that the atmosphere is driving the SST, and it is denoted as an atmosphere–to-ocean effect. Maximum positive correlation ($r = 0.75$, at 99 % significant level) is observed when the SST leads the biweekly SLHF, SSHF by 3 days (Fig. 4). This suggests that ocean–to-atmospheric processes induced by the intraseasonal SST results in enhancement of SLHF, SSHF during the SCS SM. Maximum negative correlation coefficient ($r = -0.75$, at 99 % significant level) is obtained when the SST lags the intraseasonal SLHF, SSHF by 3 days, suggesting an ocean cooling as a response to increased cloudiness associated with the rain. The results suggest that the SCS involves ocean–atmosphere coupling on biweekly timescales. On biweekly time scale, SST response to the atmosphere is quick and dramatic, the time lag between the SST anomalies and the atmospheric convection response is of the order of 3 days. Moreover, it is observed that changes in the SST cause feedback in the atmosphere which modifies the atmospheric instability. A negative correlation coefficient is observed when biweekly SST leads the biweekly equivalent potential temperature, which indicates that the biweekly change in the SST cause feedback in the atmosphere by modifying the atmospheric instability, and it is denoted as an ocean-to-atmosphere effect. A positive correlation coefficient is observed when biweekly SST lags the biweekly equivalent potential temperature, which implies that the atmospheric instability is driving the SST, and it is denoted as an atmosphere–to-ocean effect. This suggests that the active/break biweekly cycle of the SST over the SCS is related to SLP, surface heat fluxes, and atmospheric instability. The phase relationship suggests that the evolution of biweekly anomalies is a coupled phenomenon.

Modeling studies by Kemball-Cook and Wang (2001) and Fu *et al.* (2008) demonstrated that air-sea coupling on intraseasonal time scales can improve Intraseasonal Oscillation (ISO) phase and propagation, suggesting the importance of air-sea interaction to ISO dynamics. Due to the crucial part played by the SCS intraseasonal anomalies in East Asian SM (Chen and Chen 1995; Lau *et al.* 1998; Mao and Chan 2005), it is imperative that a role of the SCS intraseasonal anomaly in influencing the southward propagating monsoon intraseasonal anomalies, that is in the 10–20 day time scales, during the whole study period is investigated. In the present study, the role of the BWI oscillation in the SST particularly in the SM period is examined. None of the previous studies talked about the role of the BWI oscillation in SST in generating southward propagating biweekly anomalies over the SCS during the SM. Regression analysis is used to understand which, among the atmospheric variables are related to the BWI oscillation in the SST, and to explore the forms of these relationships. The BWI oscillation in different variables like rain, zonal wind shear (U200–U850), SLP, SSWRF, SLHF, SSHF, SNHF, and equivalent potential temperature at 118°E proceed BWI oscillations in SST averaged over the region 1 (Fig. 5). The SSWRF, SLHF, SSHF, SNHF, equivalent potential temperature, SLP and zonal wind shear (U200–U850) at 118°E are clearly revealed southward propagation over the SCS, which can be attributed as a response to the intraseasonal oscillations in the SST within the 10–20 day timescales. Thus, using satellite observations with high temporal resolution we presented the evidence that the BWI oscillations in the SST over the SCS are associated with air–sea interaction and plays very important role in the WNP SM variability. Besides, the present study also showed evidence that biweekly changes in surface heat fluxes, in association with SLP and short wave radiation, induce SST fluctuations in the SCS and that these biweekly SST changes could contribute to the southward propagation of rain during the WNP SM through their impacts on atmospheric instability. In all due fairness, perhaps we can say that biweekly changes in surface heat fluxes, in association with atmospheric wind shear and short wave radiation changes, induce large sub-seasonal SST fluctuations in the SCS and that these SST changes could contribute to the southward propagation of rain during the WNP SM through their impacts on atmospheric instability.

Besides, the BWI SST oscillation in the SCS influences the WNP SM by coherent eastward propagation of biweekly rainfall, wind shear, SLP, surface

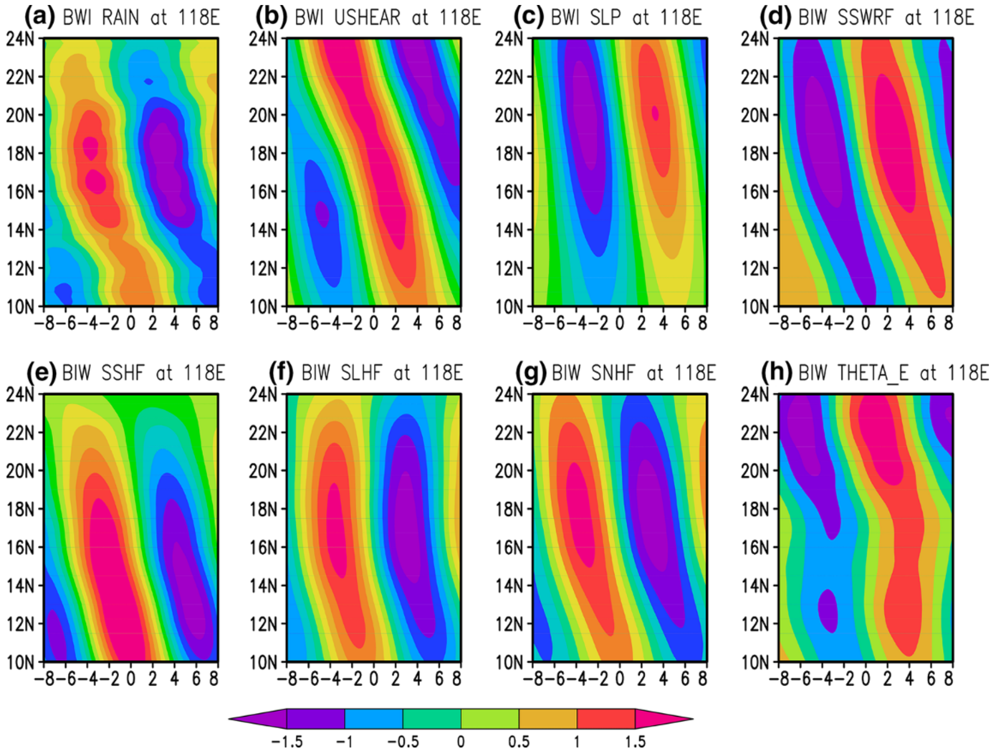

Figure 5
The BWI oscillations **a** RAIN, **b** USHEAR (U200–U850), **c** SLP, **d** SSWRF, **e** SSHF, **f** SLHF, **g** SNHF, **h** THETA_E at 118E, regressed onto the SCS BWI oscillations in SST averaged over the *rectangle box* given in Fig. 1. The regression coefficients are statistically significant at 99 % confidence level

heat flux anomalies is also presented. The East Asian SM is significantly influenced by the convective activity over the WNP (Murakami and Matsumoto 1994; Ueda and Yasunari 1996; Kawamura and Murakami 1998; Lu 2001). It has been pointed out that an atmospheric Rossby wave is generated by anomalous convective activities over the WNP, propagates to the extratropics, and influences the interannual and intraseasonal variations of the East Asian SM. The convective activity over the WNP has considerable influence on the weather and climate in the East Asia (Nitta 1987). Wang and Fan (1999) pointed out that the WNP sea pressure and wind anomalies play a key role in linking ENSO to the East Asian climate, therefore it is important to investigate the role of the SCS SST in influencing the WNP. As pointed out earlier in our manuscript the phase relationship between the SST and rainfall anomalies suggests an important role of ocean–atmosphere interaction in the propagation of biweekly anomalies. This role of biweekly SST anomalies can be explained by the propagation of biweekly surface heat flux anomalies. In Fig. 6 the propagation of SLHF and shortwave radiation anomalies follow clearly those rainfall anomalies. In the western Pacific, the eastward propagation of rainfall is clearly seen due to the SCS SST (Fig. 6). Figure 7 shows the BWI oscillations of rain, SLP, SSWRF, SNHF and THETA_E, regressed onto the SCS BWI oscillations in SST averaged over the rectangle box given in Fig. 1. From the Fig. 7, SCS SST contribution to the southward and eastward propagation of biweekly rainfall anomalies in the western Pacific and over the Philippine Sea can be conspicuously evident. Figures 4, 5, 6 and 7 revealed that large zonal wind shear in the convection region enhance surface heat fluxes and reduce incoming shortwave radiation and SLP. The present study proposes that the SCS SST contribution to the southward and eastward propagation of biweekly rainfall anomalies to the WNP. This

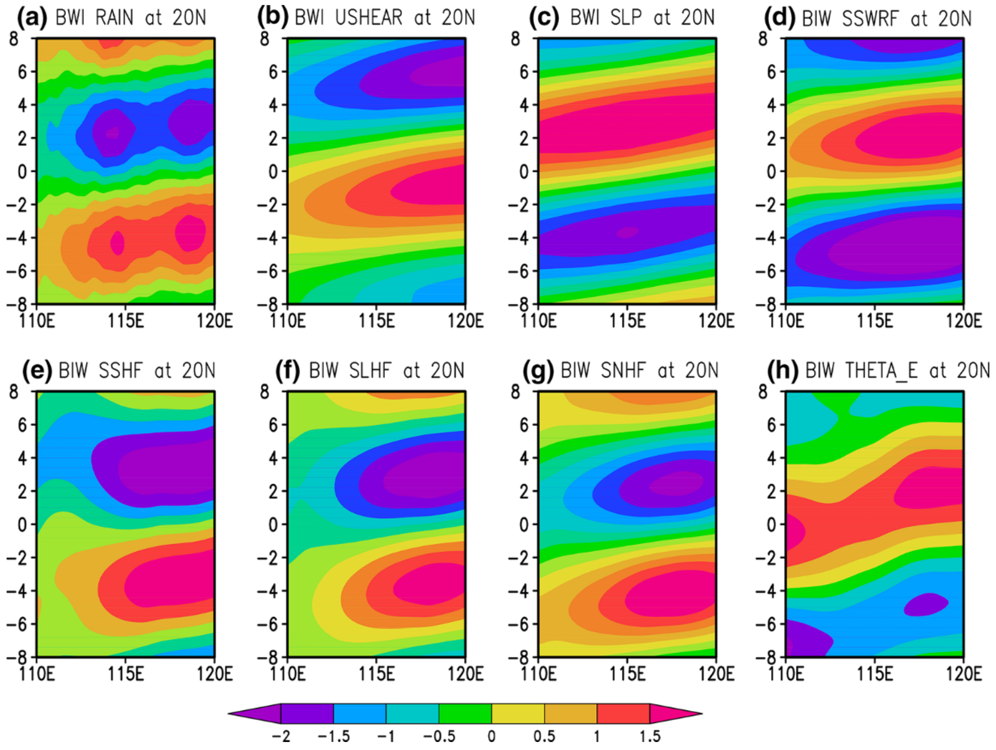

Figure 6
The BWI oscillations **a** RAIN, **b** USHEAR (U200–U850), **c** SLP, **d** SSWRF, **e** SSHF, **f** SLHF, **g** SNHF, **h** THETA_E at 20 N, regressed onto the SCS BWI oscillations in SST averaged over the *rectangle box* given in Fig. 1. The regression coefficients are statistically significant at 99 % confidence level

present study will be helpful for the better understanding of the mechanisms responsible for the intraseasonal variability of the SCS SST, which has been shown to be associated with the WNP monsoons.

4. Concluding Remarks

The new conceptual picture of the BWI oscillation in SST over the SCS obtained here based on data from 1998 to 2012, which provides valuable information on the behavior of the BWI oscillation association with the WNP, which is important for understanding of tropical variability on a time scale between day-to-day weather over the WNP region. Analysis of the TMI data for the period 1998–2012 reveals large biweekly fluctuations in the SST over the SCS during the SCS SM. The study focuses on the biweekly timescale SST and its influence on southward propagating anomalies over the SCS. The propagation of biweekly anomalies is related to the ocean–atmosphere interaction. These biweekly SST changes are closely related to surface heat flux anomalies induced by wind shear. The SST changes feedback in the atmosphere by modifying the atmospheric instability. The results suggest that the SCS involves ocean–atmosphere coupling on biweekly timescales. The positive biweekly SST anomalies lead the rain anomalies over the SCS by 3 days, with a significant correlation coefficient ($r = 0.6$) between the SST-rain anomalies. Based on lead/lag correlation analysis between the biweekly SST and rain, SSWRF, SLHF, SSHF, SNHF, equivalent potential temperature, SLP and zonal wind shear, it is argued that an ocean-to-atmosphere effect over the SCS, where biweekly SST anomalies tend to form a favorable condition for convective activity and sustain enhanced precipitation during the SM. The potential findings here indicate that the biweekly SST

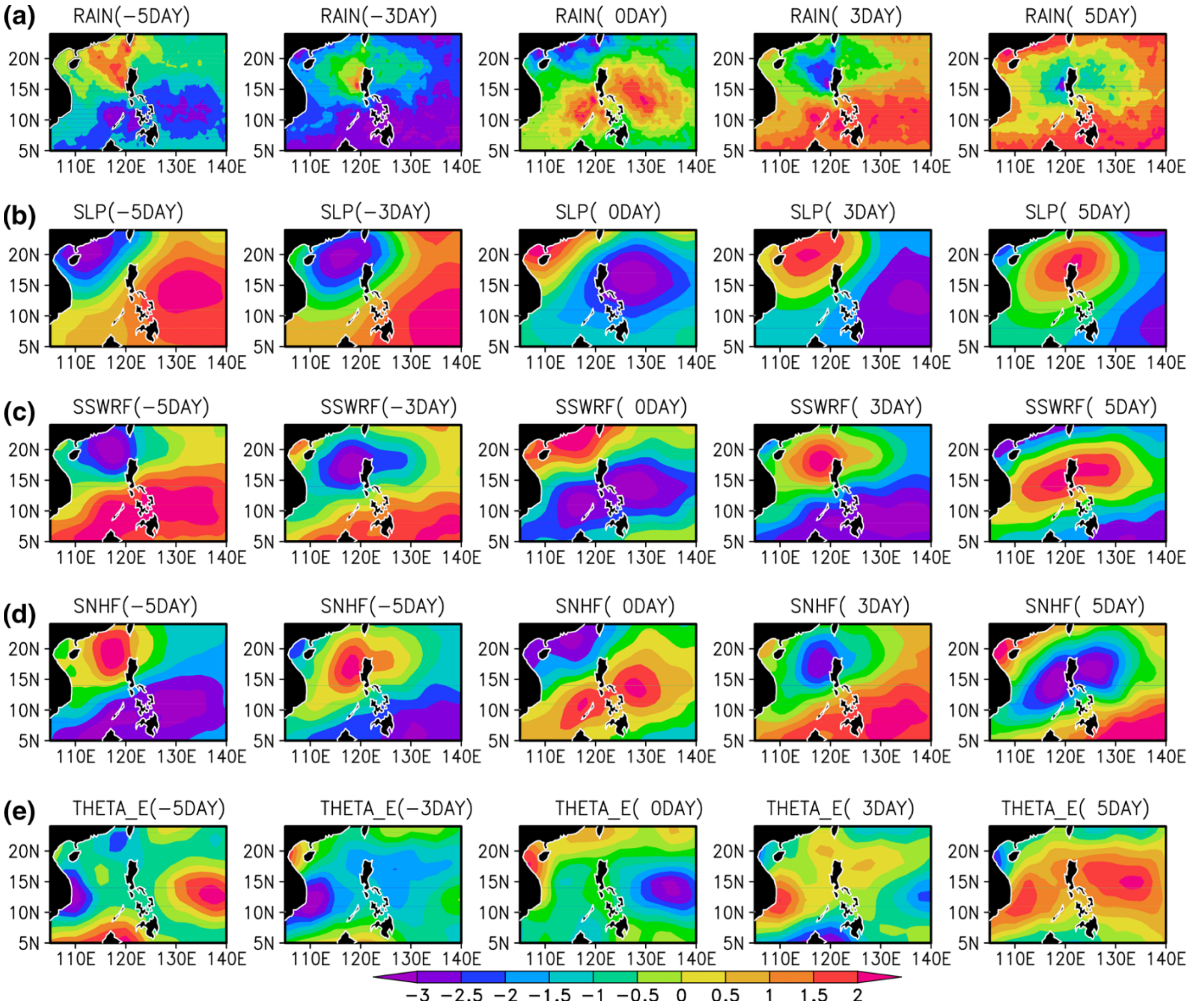

Figure 7

The BWI oscillations **a** RAIN, **b** SLP, **c** SSWRF, **d** SNHF, **e** THETA_E, regressed onto the SCS BWI oscillations in SST averaged over the *rectangle box* given in Fig. 1. The regression coefficients are statistically significant at 99 % confidence level

over the SCS play an important role in the eastward and the southward propagation of the biweekly anomalies to the WNP.

Acknowledgments

The author thanks the editor and anonymous reviewers for their valuable comments and insightful suggestions, which helped us to enhance the manuscript considerably. This research is supported by NUIST through the “Specially-Appointed Professor Program”. B. H. Vaid acknowledges NASA, WHOI OAFlux, NCEP-DOE Reanalysis Version 2 team, Prof. X. San Liang and wavelet by ion research system for kind support. Also, the author thanks to Prof. Gil Compo, Senior Research Scientist, CIRES University of Colorado and Prof. Yijun He, Dean, School of Marine Sciences, NUIST for their valuable suggestions. The figures were prepared using GrADS.

REFERENCES

CHAN, J. C. L., WANG Y. G., and XU, J. (2000), *Dynamics and thermodynamics characteristics associated with the onset of the 1998 South China Sea summer monsoon*, J. Meteorol. Soc., *78*, 367–380

Chan, J. C., Ai., L. W, and Xu, J. (2002), *Mechanisms responsible for the maintenance of the 1998 South China Sea summer monsoon*, J. Meteor. Soc., *80*, 1103–1113

Chatterjee, P., and Goswami, B. N. (2004), *Structure, genesis and scale selection of the tropical quasi-biweekly mode*, Q. J. R. Meteorol. Soc., *130*, 1171–1194

Chen, T. C., and Chen, J. M. (1993), *The 10–20 day mode of the 1979 Indian monsoon: its relation with the time-variation of monsoon rainfall*, Mon. Weather Rev., *121*(9), 2465–2482

Chen, T. C., and Chen, J. M. (1995), *An observational study of the South China Sea monsoon during the 1979 summer: onset and life-cycle*, Mon. Weather Rev., *123*(8), 2295–2318

Duchon, C. E. (1979), *Lanczos fitering in one and two dimensions*, J. Appl. Meteorol. Clim., *18*, 1016–1022

Fu, X., Yang, B., Bao, Q., and Wang, B. (2008), *Sea surface temperature feedback extends the predictability of tropical intraseasonal oscillation*, Mon. Weather Rev., *136*(2), 577–597. doi:10.1175/2007MWR2172.1

Kanamitsu, M., Ebisuzaki, W., Woollen, J., Yang, S. K., Hnilo, J. J., Fiorino, M., and Potter, G. L. (2002), *NCEP-DOE AMIP-II reanalysis (R-2)*, Bull Am Meteorol Soc, *83*, 1631–1643, doi:10.1175/BAMS-83-11-1631(2002)0831631:NAR>2.3.CO;2

Kawamura, R. and Murakami, T. (1998), *Baiu near Japan and its relation to summer monsoons over Southeast Asia and the western North Pacific*, J. Meteor. Soc. Japan, *76*, 619–639

Kemball-Cook, S., and Wang, B. (2001), *Equatorial waves and air-sea interaction in the boreal summer intraseasonal oscillation*, J. Clim., *14*(13), 2923–2942

Krishnamurti, T. N., and Ardanuy, P. (1980), *10- to 20-day westward propagating mode and ''Breaks in the Monsoons''*, Tellus, *32*, 15–26

Krishnamurti, T. N., and Subrahmanyam, D. (1982), *The 30–50 day mode at 850 mb during MONEX*, J. Atmos. Sci., *39*, 2088–2095

Lau, K. M., and Peng, L. (1987), *Origin of low-frequency intraseasonal oscillations in the tropical atmosphere, Part I: basic theory*, J. Atmos. Sci., *44*, 950–972

Lau, K. M., Wu, H. T., and Yang, S. (1998), *Hydrologic processes associated with the first transition of the Asian summer monsoon: a pilot satellite study*, Bull. Am. Meteorol. Soc., *79*(9), 1871–1882

Lu, R. (2001), *Interannual variability of the summertime North Pacific subtropical high and its relation to atmospheric convection over the warm Pool*, J. Meteor. Soc. Japan., *79*, 771–783

Madden, R. A., and Julian, P. R. (1971), *Detection of a 40–50 day oscillation in the zonal wind in the tropical Pacific*, J. Atmos. Sci., *28*, 702–708

Madden, R. A., and Julian, P. R. (1972), *Description of global-scale circulation cells in the tropics with a 40–50 day period*, J. Atmos. Sci., *29*, 1109–1123

Mak, M. (1995), *Orthogonal Wavelet Analysis: Interannual Variability in the Sea Surface Temperature*, Bull. Amer. Meteor. Soc., *76*, 2179–2186

Mao, J. Y. and Chan, J. C. L. (2005), *Intraseasonal variability of the South China Sea summer monsoon*, J. Clim. *18*(13): 2388–2402

Murakami, M., and Frydrych, M. (1974), *On the preferred period of upper wind fluctuations during the summer monsoon*, J. Atmos. Sci., *31*, 1549–1555

Murakami, T., and Matsumoto, J. (1994), *Summer monsoon over the Asian continent and western North Pacific*, J. Meteor. Soc. Japan, *72*, 719–745

Murakami, T., Nakazawa T., and He, J. (1984), *On the 40–50 day oscillations during the 1979 northern hemisphere summer. I: phase propagation*, J. Meteor. Soc., Japan, *62*, 440–468

Nitta, T. (1987), *Convective activities in the tropical Western Pacific and their impact on the Northern Hemisphere summer circulation*, J. Meteor. Soc. Japan, *65*, 373–390

Roxy, M., and Tanimoto, Y. (2011), *Influence of sea surface temperature on the intraseasonal variability of the South China Sea summer monsoon*, Clim. Dyn., *39* (5), 1209–1218, doi: 10.1007/s00382-011-1118-x

Sengupta, D., Goswami, B. N., and Senan, R. (2001), *Coherent intraseasonal oscillations of ocean and atmosphere during the Asian summer monsoon*, Geophys Res Lett, *28*(21), 4127–4130

Tao, S. Y, and Chen, L. X. (1987), A review of recent research on the East Asian summer monsoon in China, In: Chang C-P, Krishnamurti TN (eds) Monsoon meteorology, Oxford University Press, New York, pp 60–92

Torrence, C., and Compo, G. P. (1998), *A practical guide to wavelet analysis*, Bull. Amer. Meteor. Soc., *79*, 61–78

Ueda, H., Yasunari, T. (1996), *Maturing process of the summer monsoon over the western North Pacific - a coupled ocean/atmosphere system*, J. Meteor. Soc. Japan, *74*, 493–508

Vaid, B. H., Gnanaseelan, C., Polito, P. S. and Salvekar, P. S. (2007), *Influence of Pacific on Southern Indian Ocean Rossby Waves*, Pure Appl. Geophys., *164*, 1765–1785

Vaid, B. H., Gnanaseelan, C. and Kumar, J. (2011), *Interseasonal oscillation in Reynold SST over the tropical Indian Ocean and their validation*, Int. J. Rem. Sens, *32*(17), 4835–4856

Vecchi, G. A., and Harrison, D. E. (2002), *Monsoon breaks and subseasonal sea surface temperature variability in the Bay of Bengal*, J, Clim. *15*, 1485–1493. doi:10.1175/1520-0442(2002)015\1485:MBASSS>2.0.CO;2

Wang, B., and Fan, Z. (1999), *Choice of South Asian Summer Monsoon Indices*. Bull. Am. Meteor. Sci., *80*, 629–638

Wang, B. and Lin, H. (2002), *Rainy season of the Asian-Pacific summer monsoon*, J. Clim. *15*, 386–396

Wang, B., and Wu, R. (1997), *Peculiar temporal structure of the South China Sea summer monsoon*, Adv. Atmos. Sci. *14*(2), 177–194

Wentz, F. J., Gentemann, C., Smith, D., and Chelton, D. (2000), *Satellite measurements of Sea surface temperature through clouds*, Science, *288*(5467), 847–850. doi:10.1126/science.288.5467.847

Wu, R., 2010, *Subseasonal variability during the South China Sea summer monsoon onset*, Clim Dyn, *34*(5), 629–642. doi:10.1007/s00382-009-0679-4

Wu, R., and Wang, B. (2000), *Interannual variability of summer monsoon onset over the western North Pacific and the underlying processes*, J. Clim., *13*(14), 2483–2501

Wu, R., and Wang, B. (2001), *Multi-stage onset of the summer monsoon over the western North Pacific*, Clim. Dyn., *17*(4), 277–289

Yu, L., Jin, X., and Weller, R. A. (2008), Multidecade global flux datasets from the objectively analyzed air–sea fluxes (OAFlux), Project: latent and sensible heat fluxes, ocean evaporation, and related surface meteorological variables, vol OA-2008–01. Woods Hole Oceanographic Institution, USA

Zeng, L., and Wang, D. (2009), *Intraseasonal variability of latent-heat flux in the South China Sea*, Theor. Appl. Climatol., *97*(1), 53–64. doi:10.1007/s00704-009-0131-z

Zhou, S., and Miller, A. J. (2005), *The Interaction of the Madden–Julian Oscillation and the Arctic Oscillation*, J. Clim., *18*, 143–159. doi:10.1175/JCLI3251.1

(Received November 17, 2014, revised September 23, 2015, accepted October 17, 2015, Published online October 29, 2015)

Pure Appl. Geophys. 174 (2017), 477–489

DOI 10.1007/s00024-016-1341-9

Pure and Applied Geophysics

North Equatorial Indian Ocean Convection and Indian Summer Monsoon June Progression: a Case Study of 2013 and 2014

RAMESH KUMAR YADAV[1] and BHUPENDRA BAHADUR SINGH[1]

Abstract—The consecutive summer monsoons of 2013 and 2014 over the Indian subcontinent saw very contrasting onsets and progressions during the initial month. While the 2013 monsoon saw the timely onset and one of the fastest progressions during the recent decades, 2014 had a delayed onset and a slower progression phase. The monthly rainfall of June 2013 was +34 %, whereas in 2014 it was −43 % of its long-period average. The progress/onset of monsoon in June is influenced by large-scale circulation and local feedback processes. But, in 2013 (2014), one of the main reasons for the timely onset and fastest progression (delayed onset and slower progression) was the persistent strong (weak) convection over the north equatorial Indian Ocean during May. This resulted in a strong (weak) Hadley circulation with strong (weak) ascent and descent over the north equatorial Indian Ocean and the South Indian Ocean, respectively. The strong (weak) descent over the south Indian Ocean intensified (weakened) the Mascarene High, which in turn strengthened (weakened) the cross-equatorial flow and hence the monsoonal circulation.

Key words: ISM, Mascarene High, Hadley circulation, OLR, Cross-equatorial flow, ENSO.

1. *Introduction*

Rainfall over the Indian subcontinent has a unique annual cycle where more than 80 % of the annual precipitation occurs during a short span of 4 months, which commences in the month of early June and continues till September end, most commonly termed as Indian summer monsoon (ISM) rainfall. ISM, which is a part of the Asian monsoon system, has significant temporal and spatial variations. ISM generally has its onset over the southwest coast around 1 June with a standard deviation of about 8 days, and progresses northward to cover the entire country by 15 July (Pai and Rajeevan 2009).The onset of ISM is the most anxiously awaited weather singularity in the Indian subcontinent as it heralds the rainy season and marks the end of the hot summer. The onset and progression of ISM is represented by the abrupt transition from dry to wet conditions, starting at the southwest coast of India before rapidly blanketing most of the rest of the country (Lau and Yang 1996; Wu and Wang 2001). The onset and progression of ISM have a pronounced interannual variability (Joseph et al. 1994; Wang and LinHo 2002; Gadgil 2003; Li and Zhang 2009) that is partly inherited from large-scale circulation and thermodynamic features. Researchers have tried to explain the onset and progression of ISM by several theories, e.g., land–ocean heat contrast, shifting of the inter-tropical convergence zone due to the effect of varying solar insolation, jet stream theory, etc. Apart from that, there are remote factors (e.g., El Nino, La Nina) that have a profound effect on the ISM (Sikka1980; Angell 1981; Ropelewski and Halpert 1987, 1989; Rasmusson and Carpenter 1983; Shukla 1987; Yadav 2009a, b).

The ISMs of 2013 and 2014 were quite distinct, especially in their onset as well as in initial progression phase during the early monsoon month of June. The year 2013 witnessed the fastest advancement of ISM in the last 70 years (IMD 2013). The monsoon covered the entire country in just 16 days after its onset over the southwest coast on 01 June, i.e., by 16 June, which is almost a month ahead of its climatological date. June 2013 was exceptional due to its strong, timely onset and rapid progression phase. The rainfall over the country during June 2013 was 134 % of its long-term mean (IMD 2013). On the other hand, the 2014 monsoon had a delayed onset on

---

[1] Indian Institute of Tropical Meteorology, Pashan, Pune 411 008, India. E-mail: yadav@tropmet.res.in

06 June, exhibited a sluggish northward progression and covered the whole country by 17 July. During most of June 2014, the rainfall was almost absent over central India. The rainfall over the country during June 2014 was only 56.5 % (source: http://www.imdpune.gov.in/mons_monitor/mm_index.html).

In this study, we have focused on 2013 and 2014 in particular, as none of these 2 years exhibited any strong El Nino or La Nina type of conditions. Though the boreal summer of 2014 initially had the signals of El Nino, it weakened further. In 2014, the cumulative rainfall prior to August was less than the normal. Later in the months of August and September 2014 the ISM recovered, but the initial deficiency during the onset month led to the seasonal rainfall being less than the normal. Hence in particular, the analysis is centered on the early phase of the monsoon. To check the robustness of the feature, we look for other years as well, omitting the strong cases of El Nino or La Nina events. Of course, the conditions which build up over the Indian Subcontinent and around have an established relationship with the seasonal (June–September) rainfall, but the strong cross-equatorial flow of moisture-laden winds is directly influenced by the presence of sustained high pressure over the mid-latitudes in the south Indian Ocean. A buildup of relatively high pressure prior to the month of June, we argue, may lead to the timely onset and supply the initial momentum for faster progression.

2. *Data and Methodology*

The global atmospheric reanalysis dataset ERA-Interim has been used in this study. ERA-Interim is the latest European Centre for Medium-Range Weather Forecasts (ECMWF) global atmospheric reanalysis of the period 1979 to the present. ERA-Interim was originally planned as an 'interim' reanalysis in preparation for the next-generation extended reanalysis to replace ERA-40. It uses a December 2006 version of the ECMWF Integrated Forecast Model (IFS Cy31r2). It originally covered dates from 1 January 1989, but an additional decade, from 1 January 1979, was added later. ERA-Interim is being continued in real time. The spectral resolution is T255 (about 80 km) and there are 60 vertical levels, with the model top at 0.1 hPa (about 64 km). The data assimilation is based on a 12-h four-dimensional variational analysis (4D-Var) with adaptive estimation of biases in satellite radiance data (VarBC). With some exceptions, ERA-Interim uses input observations prepared for ERA-40 until 2002, and data from ECMWF's operational archive thereafter (Dee et al. 2011). Daily and monthly outgoing longwave radiation (OLR) data at 2.5° latitude × 2.5° longitude grid provided by the NOAA/OAR/ESRL PSD, Boulder, USA, from the website http://www.esrl.noaa.gov/psd/ have been used (Liebmann and Smith 1996). Daily and monthly means of different atmospheric fields for the months of May and June have been analyzed to find out the underlying mechanisms for the onset and progression of ISM in the two contrasting consecutive years of 2013 and 2014. The simultaneous correlation coefficient of negative Nino-3 index with sea surface temperature (SST) and 200-hPa velocity potential have been calculated to study the influence of ENSO on SST and Walker circulation. Nino-3 index is obtained by extracting SST data from the box 5°N–5°S and 150°W–90°W. The velocity potential is calculated from the zonal and meridional wind component.

3. *Results*

The years 2013 and 2014 were two consecutive contrasting ISM years with respect to their onset and progression in the month of June. In 2013, the onset was timely (01 June) and the progression was very fast, while in 2014, the onset was delayed (06 June) and the progression was very lethargic. The cumulative rainfall of 2013 June was +34 %, whereas 2014 June recorded −43 % of its long-period average. Therefore, the spatial plots of monthly means for the month of May 2013 and 2014 and their difference in atmospheric parameters are expected to provide further insight into the changes observed in the succeeding months of June. Figure 1 shows the OLR (gray shaded), mean sea level pressure (MSLP; contours) and 850-hPa wind (black arrows) for the month of May 2013 (Fig. 1a), 2014 (Fig. 1b) and the difference of 2013 and 2014

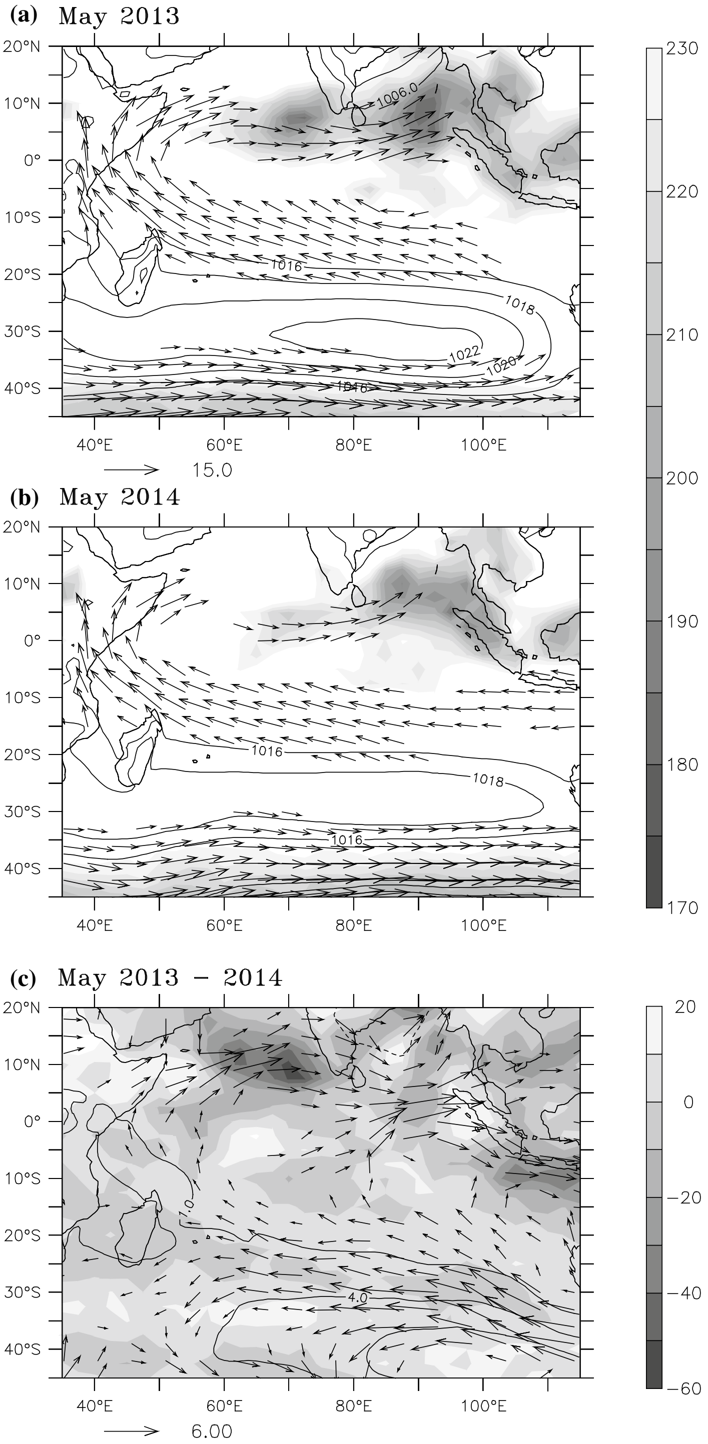

Figure 1
MSLP (*contours*, hPa), 850 hPa winds (*vectors*, ms^{-1}), OLR (*gray shaded*, Wm^{-2}). **a** May 2013 and **b** May 2014. **c** Difference in May 2013 and May 2014 MSLP (*contours*), OLR (*gray shaded*) and 850-hPa wind (*vectors*)

(Fig. 1c). The MSLP over Mascarene High was more intense in 2013 than 2014 (Fig. 1a, b). It caused the buildup of higher north–south (N–S) pressure gradient, resulting in stronger cross-equatorial flow in 2013 as compared to 2014. Since OLR is a good proxy for deep convection: in Fig. 1a, b, low OLR values, less than 220 W/m^2, indicate deep convection and pronounced condensational heating over the tropical and subtropical regions (Liebmann and Smith 1996). As compared to 2013, where the deep convection over the equatorial north Indian Ocean was much wider, during 2014 it was concentrated toward east and deep convection over the north equatorial Indian Ocean was relatively less intense. The difference plot of OLR and 850-hPa wind between 2013 and 2014 (Fig. 1c) shows deep convection over the south Arabian Sea and intense cross-equatorial flow in 2013 as compared to 2014.

Similarly, Fig. 2 shows the SST (color shaded) and 200-hPa velocity potential (contours) for the month of May. The SST was warmer than 28 °C in the tropical Indian and the western Pacific during both years. The velocity potential shows tripole type of structure over the tropical Indo-Pacific Ocean with upper-level divergence (velocity potential minimum) over the warm pool region of Indonesia and the western Pacific and convergence (velocity potential maximum) over the western Indian Ocean and the eastern Pacific. This structure represents the Walker circulation with upper-level divergence and convergence over the warm pool region and the eastern Pacific, respectively. In 2013, the Walker circulation was much stronger than in 2014. The difference between the 2013 and 2014 May month shows cooler SST anomaly all along the equatorial Indo-Pacific Ocean, except the warm pool region. The difference pattern resembles the initial stage of La Nina conditions because 2014 had minor signatures of El Nino during the month which weakened afterward. The difference in SST over the tropical India Ocean was very marginal. This suggests that the tropical Indian Ocean SST was not substantially influential in modulating the deep convection as observed during the mentioned years. The velocity potential shows divergence anomaly all along the tropical Indo-Pacific Ocean except the western Indian Ocean and the eastern Pacific.

To study the upper-level horizontal temperature gradient, the sub-tropical westerly jet stream and tropical easterly jet stream for the month of May during 2013 and 2014, the 200-hPa level temperature (color shaded) and zonal wind (contours) have been plotted in Fig. 3. The horizontal temperature gradient between the northern India and the equatorial Indian Ocean was greater in 2013 than 2014. The sub-tropical westerly jet stream over the north of India and the tropical easterly jet stream over the equatorial Indian Ocean were more intense in 2013 than 2014 (Fig. 3c). This suggests that the deep convection over the north Indian Ocean during May 2013 had intensified the upper-level divergence which is directly correlated with anti-cyclonic circulation. The anti-cyclonic circulation intensified both the sub-tropical westerly jet toward the north of India and the tropical easterly jet stream at the equatorial Indian Ocean. The strong sub-tropical westerly jet stream advected the temperatures to the northern India (Fig. 3a).

Figure 4 shows the Hadley circulation averaged between the longitudes 60°E and 90°E for May 2013 (upper panel), 2014 (middle panel) and the difference between 2013 and 2014 (lower panel). In 2013, the Hadley circulation was more intense than in 2014 (Fig. 4a, b). The difference plot (Fig. 4c) suggests that there was a slightly northward shift in the ascent and descent of the Hadley circulation in 2013 when compared with 2014. In 2013, the ascent and descent were observed around 10°N and 20°S, respectively, whereas in 2014, the ascent and descent were confined to the equator and 25°S, respectively. The strong subsidence over the south Indian Ocean during 2013 was one of the main reasons for the intensification of Mascarene High. The stronger Mascarene High intensified the cross-equatorial monsoonal flow in 2013 and vice versa for 2014 (Krishnamurti and Bhalme 1976). The difference between the wind speed at 850 hPa (Fig. 1) is the confirmation for the same.

It is well known that the onset and progression of ISM are also affected by the northward-propagating intraseasonal variations (ISVs) by transporting moisture and momentum from tropical Indian Ocean to the Indian subcontinent (Zhou and Murtugudde 2014). Therefore, to see the northward propagation of ISVs during 2013 and 2014, we plotted the time–

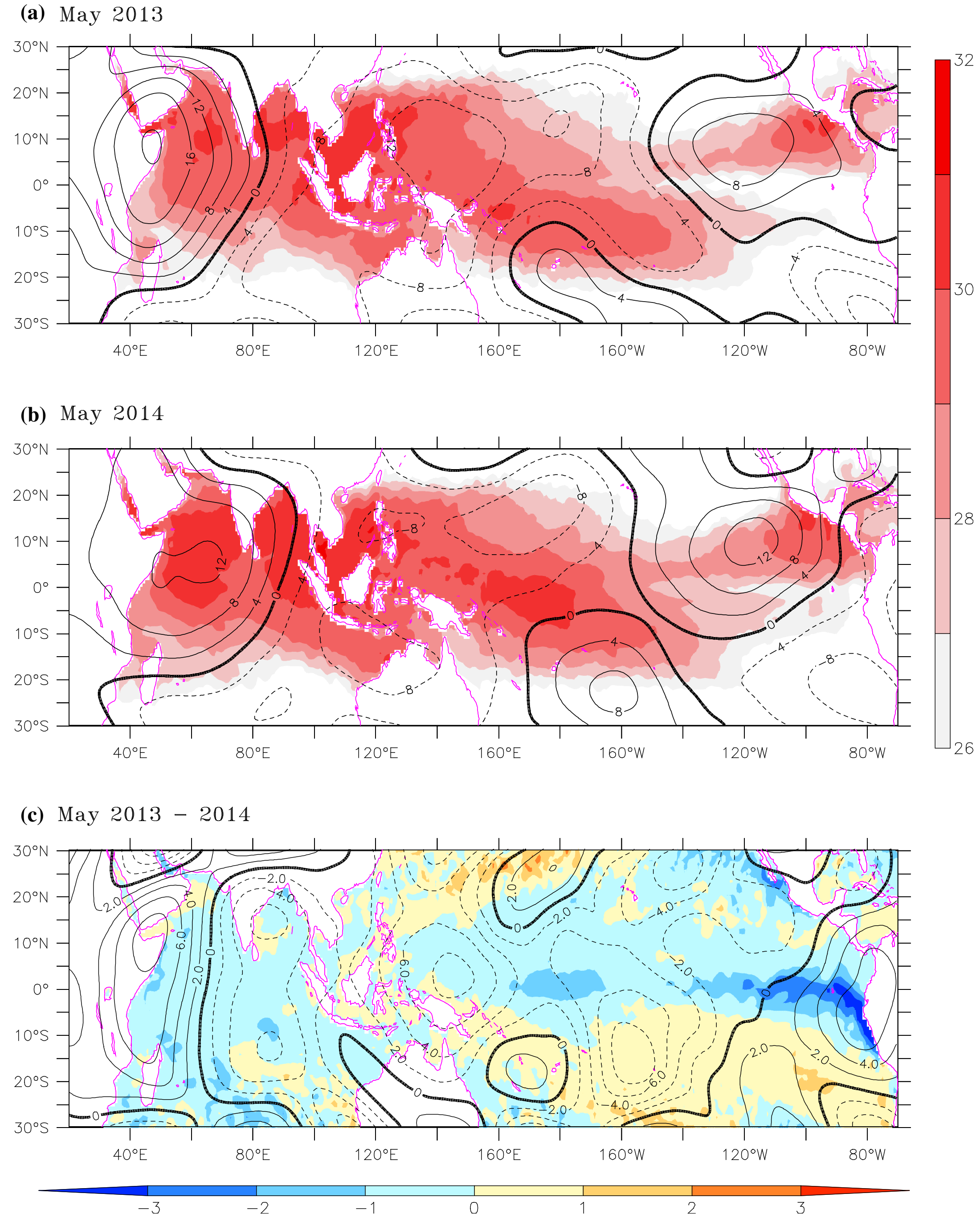

Figure 2

SST (*color shaded*, °C), 200-hPa velocity potential (*contours*, $10^6 m^2 s^{-1}$). **a** May 2013 and **b** May 2014. **c** Difference in May 2013 and May 2014

latitude cross section of OLR averaged over the longitudes 60°E–90°E from 01 May to 15 June for 2013 (Fig. 5a) and 2014 (Fig. 5b). It is seen that the persistent deep convection up to mid-May and last week of May were stagnant over north of the equator, with no northward propagation observed in 2013. In

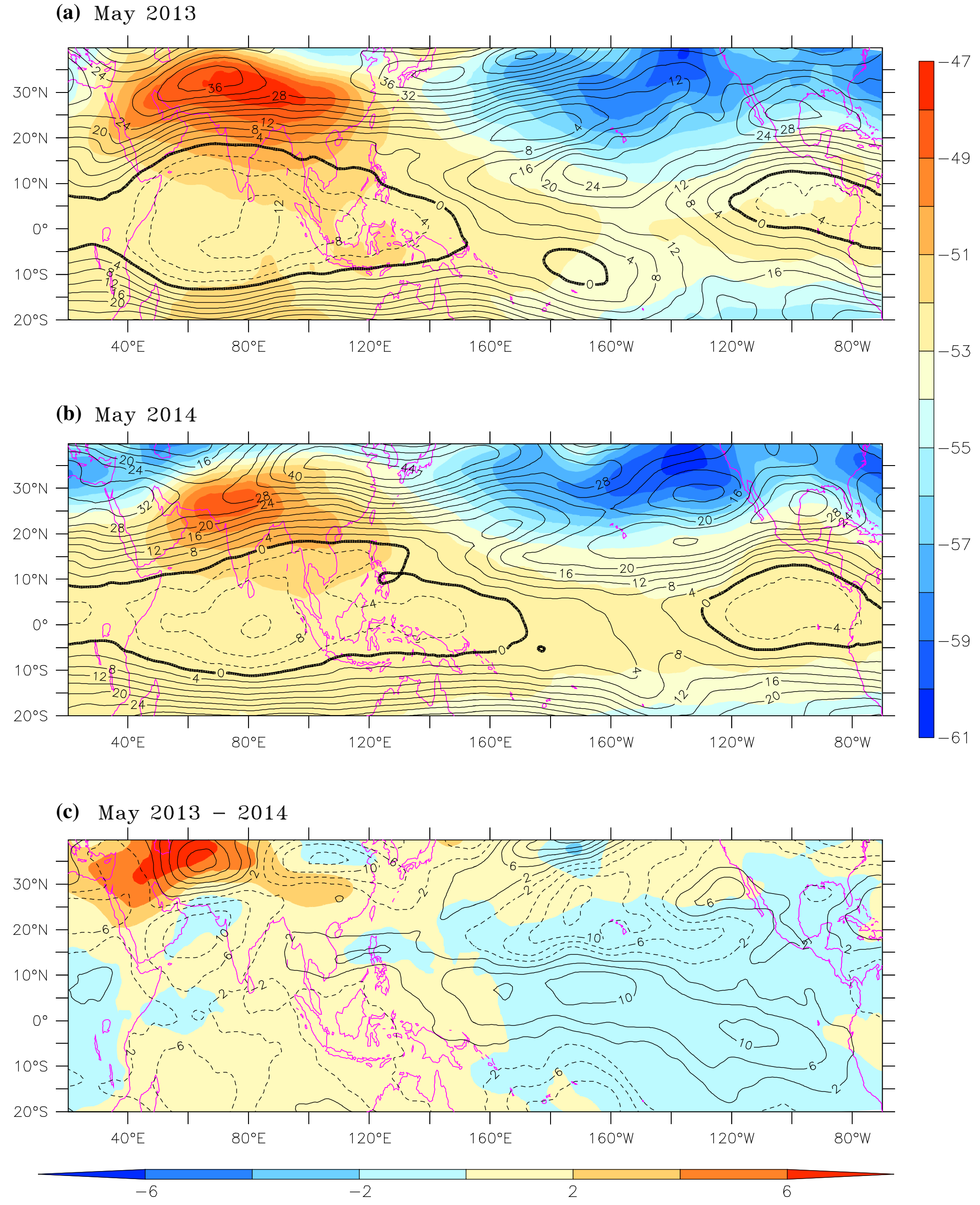

Figure 3
200-hPa temperature (*color shaded*, °C) and zonal wind (*contours*, ms^{-1}). **a** May 2013 and **b** May 2014. **c** Difference in May 2013 and May 2014

the third week of May 2013, tropical deep convection was absent, while in 2014 persistent deep and northward propagation of convection was missing in May. Similarly, we have plotted time–longitude cross section of OLR, averaged over the latitudes 10°S–10°N from 01 May to 15 June to see the eastward

(a) May 2013

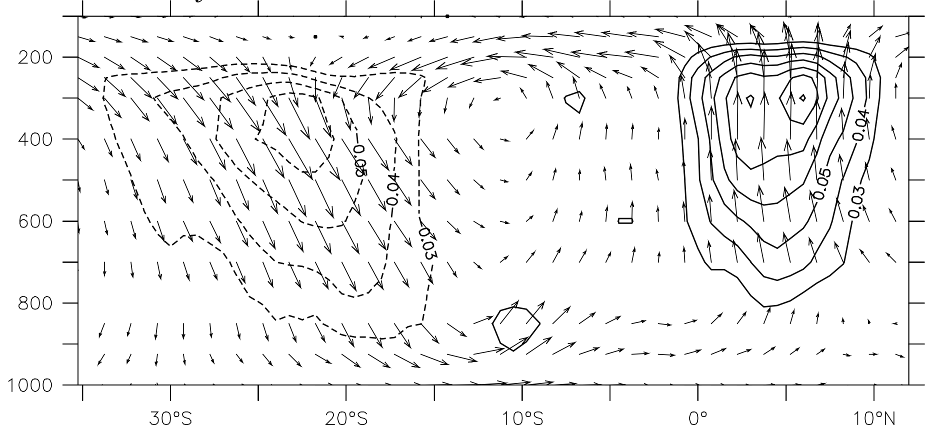

(b) May 2014

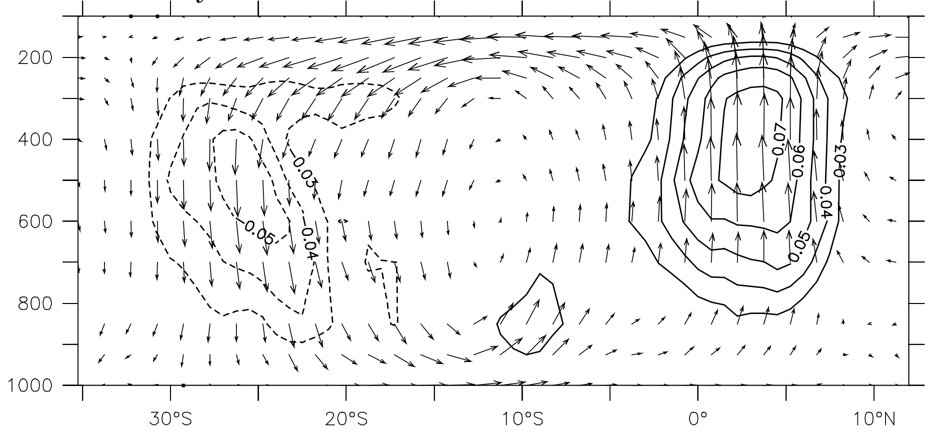

(c) May 2013 – May 2014

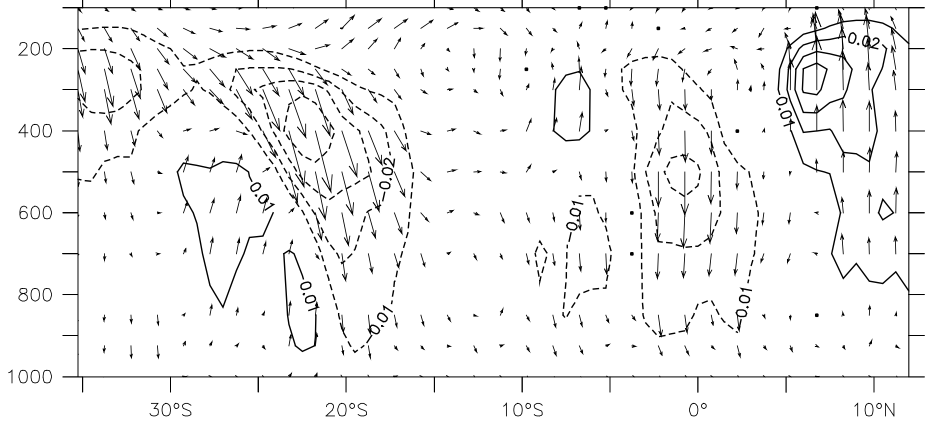

Figure 4

May Hadley circulation, representing the latitude–height section (longitude averaged from 60°E to 90°E) of meridional and pressure vertical velocities for **a** 2013 and **b** 2014 (*vertical velocity* scaled by 100) and **c** 2013 minus 2014 (*vertical velocity* scaled by 500)

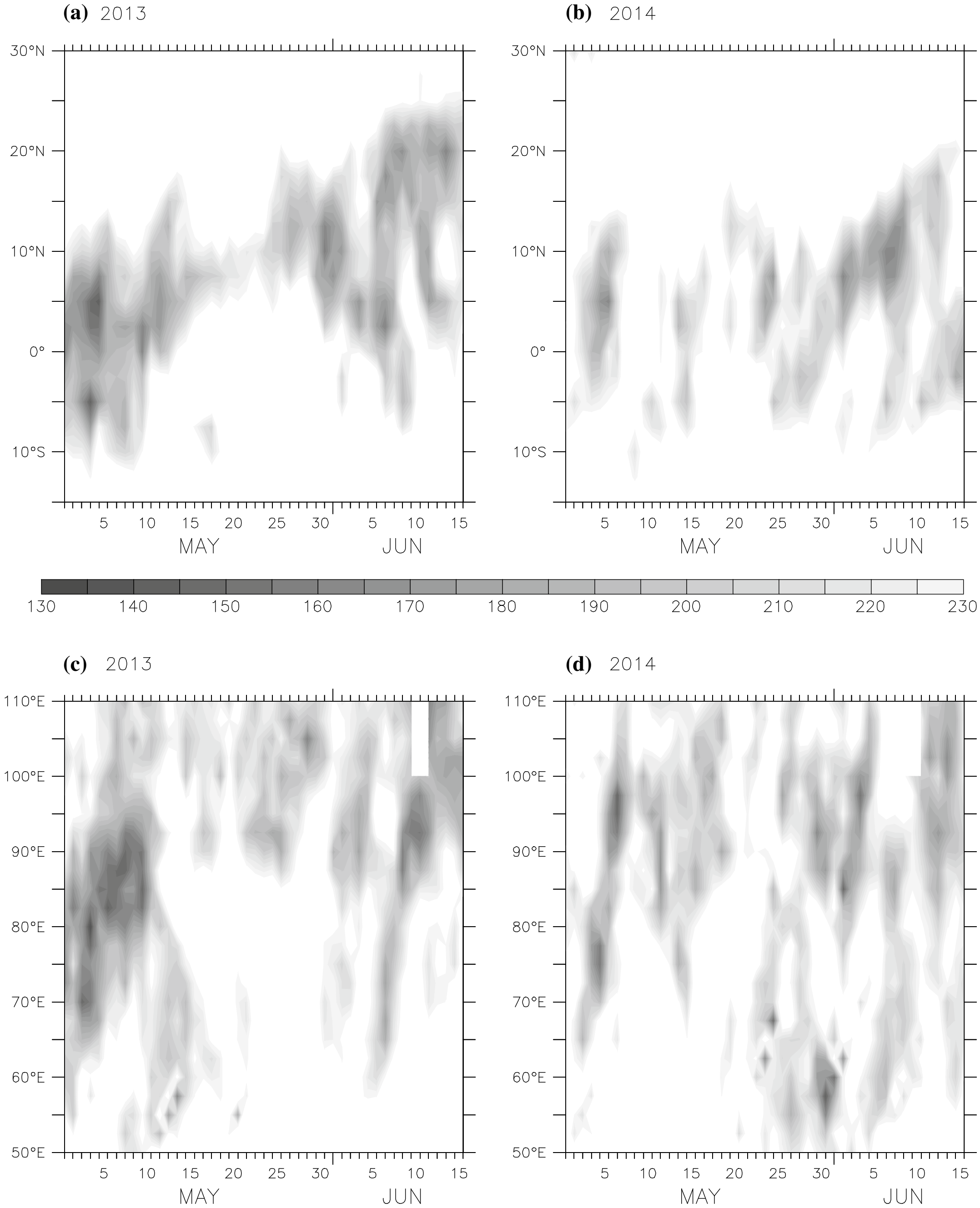

Figure 5
The time–latitude section of OLR (Wm^{-2}) along 15°S to 30°N averaged for the longitude from 60°E to 90°E for **a** 2013 and **b** 2014. The time–longitude section of OLR (Wm^{-2}) along 50°E–110°E averaged for the latitude from 10°S to 10°N for **c** 2013 and **d** 2014. The time length is from 01 May to 15 June

propagation of ISVs in 2013 (Fig. 5c) and 2014 (Fig. 5d). The persistent deep convection observed in the first half of May 2013 shows the eastward propagation, but for the later period of 2013 and the whole of 2014, the eastward propagation was missing. Now, it is clear that the early onset and fast propagation of 2013 ISM was not initiated by the northward propagation of strong ISVs in that year.

From the above results, it is clear that persistent deep convection in the north equatorial Indian Ocean was one of the main reasons which led to the intensification of Mascarene High and hence the ISM circulation. Based on the observed features in Fig. 1, we extracted daily indexes for 2013 and 2014 from the area-averaged OLR in the region 60°E–90°E and 2.5°S–7.5°N and MSLP in the region 60°E–90°E and 20°S–30°S (with special emphasis on the below 220 Wm^{-2} values for OLR and above 1019 hPa for MSLP) termed hereafter as OLRIO and MH, respectively. The daily plots for May OLRIO and MH are shown in Fig. 6a, b, respectively. In 2013, well-organized deep convection was observed in the first half of May which was missing in 2014. Similarly, Mascarene High was intense between 7 and 24 May in 2013, while in 2014 it consistently lacked in intensity throughout the month. This clear distinction in the OLRIO and MH fields in the month of May was one of the important factors which modified the onset and progression of ISM in the successive years of 2013 and 2014.

To see the nature and robustness of the relationship between OLRIO and MH, we calculate the lag correlation of MH with respect to OLRIO from 01 May to 15 June for 2013 and 2014 and have been shown in Fig. 7. In 2013, it shows significantly strong 6–8 days lag correlation at 99.9 % confidence level between MH and OLRIO, which suggests that the deep convection over the north equatorial Indian Ocean had fed and enhanced the MSLP over the Mascarene High through the descent of the Hadley circulation (Fig. 4). In 2014, the lag correlation shows 3 days lead of OLRIO over MH significant at the 95 % confidence level. Since the organized persistent deep convection was missing in 2014, therefore a strong correlation in 2014 is not expected. Hence, the persistent deep convection of May 2013 intensified the Mascarene High which established a good platform with nearly half a month ahead of the commencement of ISM 2013, while the lack of persistent deep convection over the north equatorial Indian Ocean failed to intensify the Mascarene High and remained normal apart from other unfavorable conditions which delayed the onset and progression of ISM 2014.

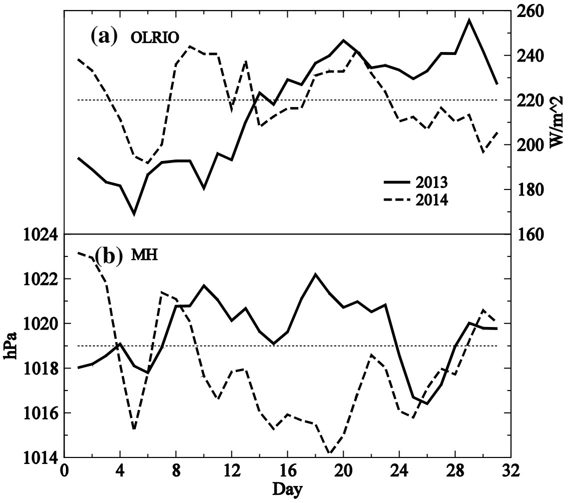

Figure 6
Daily variations of **a** OLRIO (Wm^{-2}) and **b** MH (hPa) for May 2013 and 2014

Further, to find out similar events in the past, we constructed interannual time series for May for OLRIO and MH. The year-to-year variation in the period 1979–2013 shows (Fig. 8a) that the relationship was not persistent throughout the data period. Also the 21-year sliding correlation between the two time series shows (Fig. 8b) positive correlation before central year 1995 and negative correlation after that, suggesting that the relationship has become frequent in the recent years where the deep convection over the north equatorial Indian Ocean intensifies the surface pressure over Mascarene High. In Table 1, we selected the years with OLR values less than 220 Wm^{-2} and MSLP values greater than 1019 hPa in the same year, with their onset date over the southwest peninsular coast and the percentage departure of June rainfall in the respective years. The years with a strong El Nino and La Nina are shown in bold and bold italic, respectively. 2010, 1999 and 1988, which were strong La Nina years, shows early onsets, but the percentage departures in June were not strong. 1997 and 1982 were strong El Nino years; again, the percentage departures in June were not strong. 1997 had a delayed onset, while in 1982 the onset was early. However, during the non-ENSO years such as 1994, 1989 and 1980, the onset and June progressions match with the year 2013.

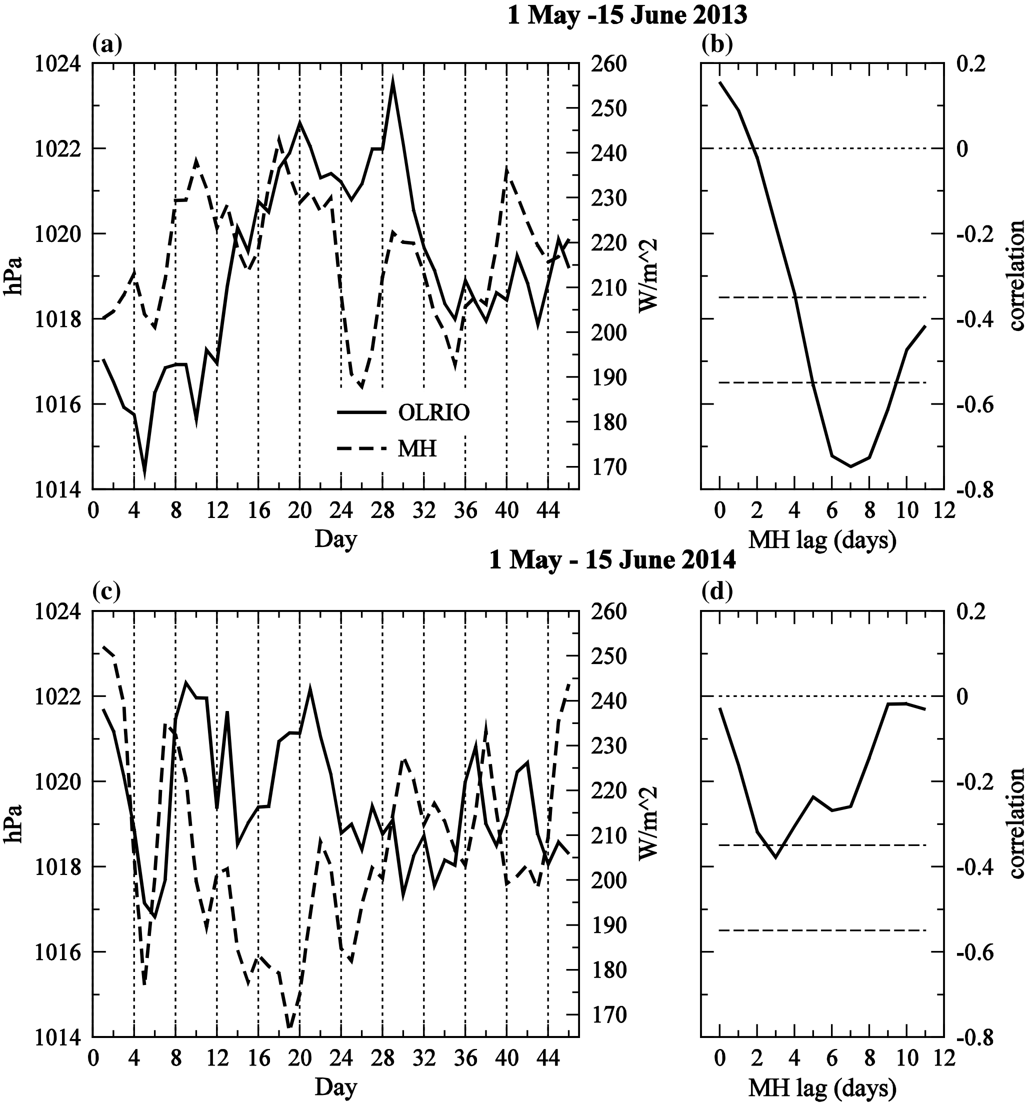

Figure 7
Daily variations of OLRIO (Wm^{-2}) and MH (hPa) from 1 May to 15 June **a** 2013 and **c** 2014. Lag correlations (*black curve*) of MH with respect to OLRIO for the period 1 May to 15 June for **b** 2013 and **d** 2014. The 95 and 99.9 % confidence levels are indicated by the *dashed black line*. The *dotted line* is the zero correlation line

In summary, during the non-ENSO years, the persistent deep convection during the month of May over the north Indian Ocean intensifies the local Hadley cell, which intensifies the Mascarene High. The intensified Mascarene High intensifies the cross-equatorial flow which further pushes the deep convection northward over the Indian subcontinent with abundant moisture supply. This leads to early onset and rapid progression of ISM.

4. Conclusion and Discussion

The Indian summer monsoons (ISMs) of 2013 and 2014 were contrasting in their onset and initial progression phases. In 2013, the onset was timely and the progression of ISM was the fastest in last few decades, whereas in 2014 the onset was delayed and the progression was sluggish. The June monthly rainfall in 2013 was +34 %, whereas in June 2014 it was

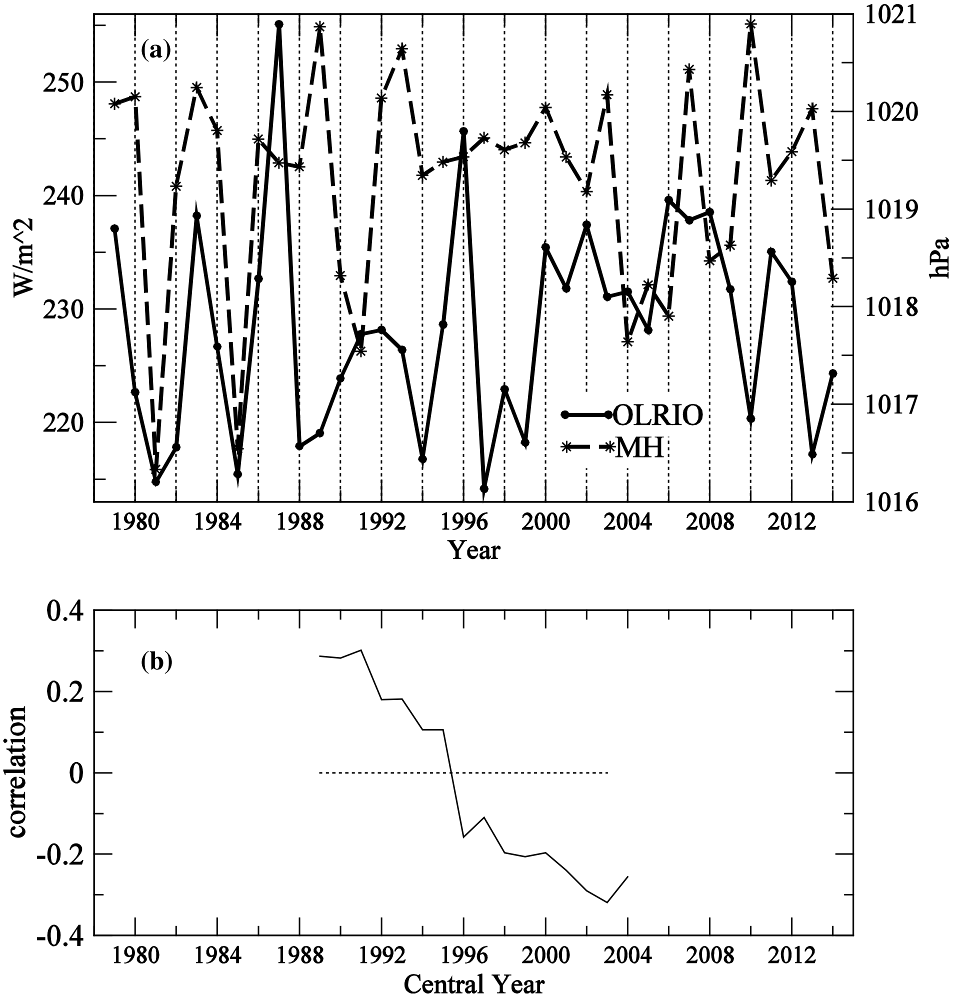

Figure 8
a Yearwise monthly variations of OLRIO and MH from 1979 to 2013. **b** Sliding correlations on a 21 year moving window between OLRIO and MH

−43 % of its long-period average. In this study, we have made an attempt to unravel the factors that generated this discrepancy in the month of June 2013 and 2014. It was found that in 2013, there was persistent deep convection in the first half of May over the north equatorial Indian Ocean, which intensified Mascarene High over the south Indian Ocean through strong Hadley circulation with strong descent over the south Indian Ocean. There was a lead of 6–8 days between deep convection over the north equatorial Indian Ocean to MSLP over the south Indian Ocean, i.e., the Hadley circulation took 6–8 days to feed the Mascarene High over the south Indian Ocean. The intensified Mascarene High intensified the cross-equatorial flow and hence the monsoonal circulation was well established half a month ahead, which caused the timely onset and fastest progression of monsoon in the year 2013. In 2014, the persistent deep convection over the north equatorial Indian Ocean was missing, which led to weaker Hadley circulation that could not feed the Mascarene High. Therefore, the weaker Mascarene High in 2014 as compared to 2013 generated a weaker cross-equatorial flow and hence delayed onset and progression of monsoon 2014 and vice versa. This relationship is more prominent in the recent non-ENSO years.

To see the effect of ENSO on the onset and initial progression of ISM, we have considered Nino-3 index as representative of ENSO. The spatial correlation coefficient of the negative Nino-3 index on SST (color shaded) and 200-hPa velocity potential (contours) are shown in Fig. 9. The negative Nino-3 index represents La Nina conditions. The La Nina years are associated with cool SST anomaly over the equatorial Indian Ocean and warm anomaly over the tropical north-western Pacific. The 200-hPa velocity potential shows significant negative correlation over south-east Asia and positive correlation over the equatorial central and eastern Pacific (Fig. 9). This suggests that the Walker circulation is stronger with rising motion over Cambodia and subsidence over the equatorial eastern Pacific during La Nina years and vice versa during El Nino years. The warming of the tropical north-western Pacific must have shifted and intensified the inter-tropical convergence zone to the Cambodian latitude, which in turn intensifies the Walker circulation during the La Nina years and vice versa during the El Nino years. The upper-level divergence (velocity potential minimum) anomaly over north-east and southern India (Fig. 9) reinforce the convective activity which leads to early onset of ISM during the La Nina years and vice versa for the El Nino years. In 2013, the upper-level divergence was centered over the western Pacific, whose influence on the early onset and fast progression of ISM was not so prominent. Therefore, the persistent deep convection over the north India Ocean in the month of May, like the one observed in 2013, can be a better indicator for the initial buildup of strong cross-

Table 1

Years with simultaneous OLRIO lower than 220 Wm^{-2} and MH greater than 1019 hPa

Year	Onset date	June % departure
2013	01 June	+34.5
2010	***31 May***	***−15.6***
1999	***25 May***	***+5.1***
1997	**09 June**	**+6.4**
1994	29 May	+29.0
1989	03 June	+19.3
1988	***26 May***	***+6.8***
1982	**29 May**	**−16.8**
1980	01 June	+37.7

Bold and bold italic represents the strong El Nino and strong La Nina years, respectively

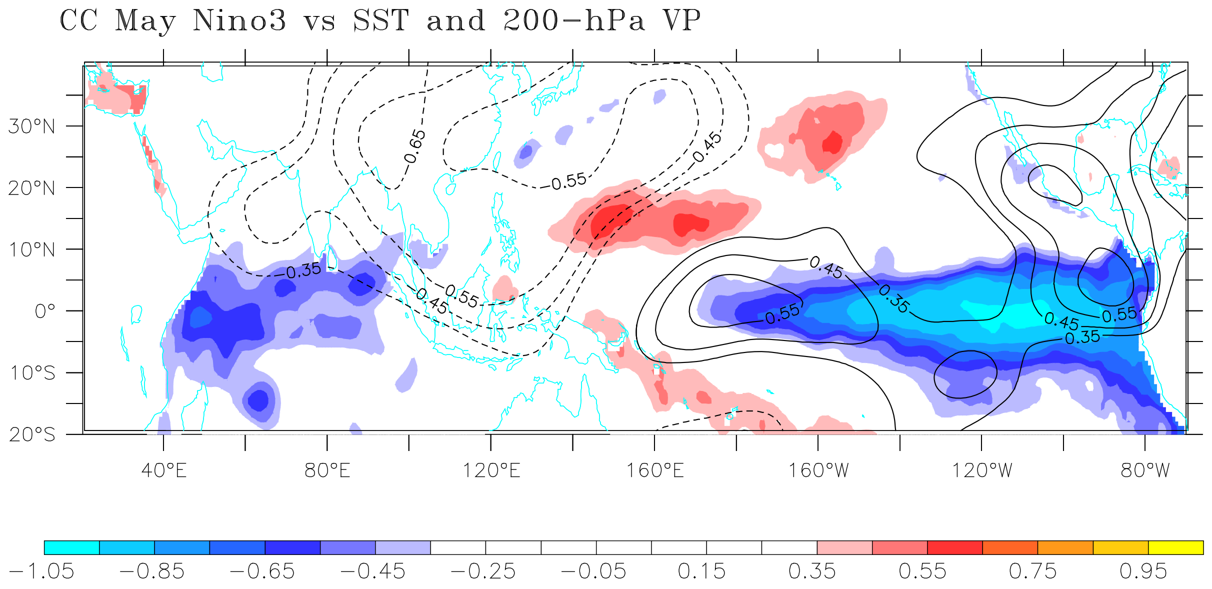

Figure 9

Spatial pattern of simultaneous correlation of May negative Nino-3 index vs SST and 200-hPa velocity potential for the period 1979–2014. SST is shown as *shaded*, and velocity potential as contours. Positive (negative) velocity potential correlations are indicated by *continuous* (*dotted*) *lines*. The velocity potential correlation contours start from 0.35 and the intervals are 0.1

equatorial flow leading to better forecasting of the initial ISM rainfall. This is also an important research topic which will contribute to promote progress in the science of ISM.

Acknowledgments

The authors wish to thank the editor and the two anonymous reviewers for their insightful comments that helped improve the manuscript. The data have been taken from websites and all data sources have been duly acknowledged. Computational and graphical analyses required for the study were completed with the freely available softwares, e.g., Ferret, NCL and xmgrace.

REFERENCES

Angell, J. K. (1981). Comparison of variations in atmospheric quantities with sea surface temperature variations in the equatorial Pacific. *Monthly Weather Review, 109*, 230–243.

Dee, D. P., et al. (2011). The ERA-Interim reanalysis: Configuration and performance of the data assimilation system. *Quarterly Journal Royal Meteorological Society, 137*(656), 553–597.

Gadgil, S. (2003). The Indian monsoon and its variability. *Annual Review of Earth a Planetary nd Sciences, 31*(1), 429–467.

IMD. (2013). Monsoon 2013: A report. IMD Met Monograph No.: ESSO/IMD/SYNOPTIC MET/01-2014/15. India Met Department Eds Pai DS and Bhan SC. http://www.imdpune.gov.in/.

Joseph, P. V., Eischeid, J. K., & Pyle, R. J. (1994). Interannual variability of the onset of the Indian summer monsoon and its association with atmospheric features, El Nino, and sea surface temperature anomalies. *Journal of Climate, 7*, 81–105.

Krishnamurti, T. N., & Bhalme, H. N. (1976). Oscillations of a monsoon system. Part I. Observational aspects. *Journal of the Atmospheric Sciences, 33*(10), 1937–1954.

Lau, K. M., & Yang, S. (1996). Seasonal variation, abrupt transition, and intraseasonal variability associated with the Asian summer monsoon in the GLA GCM. *Journal of Climate, 9*(5), 965–985.

Li, J., & Zhang, L. (2009). Wind onset and withdrawal of Asian summer monsoon and their simulated performance in AMIP models. *Climate Dynamics, 32*, 935–968.

Liebmann, B., & Smith, C. A. (1996). Description of a complete (interpolated) outgoing longwave radiation dataset. *Bulletin of the American Meteorological Society, 77*, 1275–1277.

Pai, D. S., & Rajeevan, M. (2009). Summer monsoon onset over Kerala: New definition and prediction. *Journal of Earth System Science, 118*(2), 123–135.

Rasmusson, E. M., & Carpenter, T. H. (1983). The relationship between eastern equatorial Pacific sea surface temperature and rainfall over India and Sri Lanka. *Monthly Weather Review, 111*, 517–528.

Ropelewski, C. F., & Halpert, M. S. (1987). Global and regional scale precipitation patterns associated with the El Nino/southern oscillation. *Monthly Weather Review, 115*, 1606–1626.

Ropelewski, C. F., & Halpert, M. S. (1989). Precipitation patterns associated with the high index phase of the southern oscillation. *Journal of Climate, 2*, 268–284.

Shukla, J. (1987). Interannual variability of monsoon. In J. S. Fein & P. L. Stephens (Eds.), *Monsoons* (pp. 399–464). New York: Wiley.

Sikka, D. R. (1980). Some aspects of the large-scale fluctuations of summer monsoon rainfall over India in relation to fluctuations in the planetary and regional scale circulation parameters. *Proceedings of the Indian Academy of Sciences (Earth and Planetary Sciences), 89*, 179–195.

Wang, B., & LinHo, (2002). Rainy season of the Asian-Pacific summer monsoon. *Journal of Climate, 15*, 386–398.

Wu, R., & Wang, B. (2001). Multi-stage onset of the summer monsoon over the western North Pacific. *Climate Dynamics, 17*, 277–289.

Yadav, R. K. (2009a). Changes in the large-scale features associated with the Indian summer monsoon in the recent decades. *International Journal of Climatology, 29*, 117–133.

Yadav, R. K. (2009b). Role of equatorial central Pacific and northwest of North Atlantic 2-metre surface temperatures in modulating Indian summer monsoon variability. *Climate Dynamics, 32*, 549–563.

Zhou, L., & Murtugudde, R. (2014). Impact of northward-propagating intraseasonal variability on the onset of Indian summer monsoon. *Journal of Climate, 27*, 126–139.

(Received June 30, 2015, revised May 20, 2016, accepted June 23, 2016, Published online June 28, 2016)

Pure Appl. Geophys. 174 (2017), 491–510

DOI 10.1007/s00024-015-1227-2

Pure and Applied Geophysics

Sensitivity Study of Cloud Cover and Ozone Modeling to Microphysics Parameterization

KINGA WAŁASZEK,[1] MACIEJ KRYZA,[1] MARIUSZ SZYMANOWSKI,[2] MAŁGORZATA WERNER,[1,3] and HANNA OJRZYŃSKA[1]

Abstract—Cloud cover is a significant meteorological parameter influencing the amount of solar radiation reaching the ground surface, and therefore affecting the formation of photochemical pollutants, most of all tropospheric ozone (O_3). Because cloud amount and type in meteorological models are resolved by microphysics schemes, adjusting this parameterization is a major factor determining the accuracy of the results. However, verification of cloud cover simulations based on surface data is difficult and yields significant errors. Current meteorological satellite programs provide many high-resolution cloud products, which can be used to verify numerical models. In this study, the Weather Research and Forecasting model (WRF) has been applied for the area of Poland for an episode of June 17th–July 4th, 2008, when high ground-level ozone concentrations were observed. Four simulations were performed, each with a different microphysics parameterization: Purdue Lin, Eta Ferrier, WRF Single-Moment 6-class, and Morrison Double-Moment scheme. The results were then evaluated based on cloud mask satellite images derived from SEVIRI data. Meteorological variables and O_3 concentrations were also evaluated. The results show that the simulation using Morrison Double-Moment microphysics provides the most and Purdue Lin the least accurate information on cloud cover and surface meteorological variables for the selected high ozone episode. Those two configurations were used for WRF-Chem runs, which showed significantly higher O_3 concentrations and better model-measurements agreement of the latter.

Key words: Cloud mask, meteorological modeling, ozone, WRF, Poland, model evaluation.

1. Introduction

Cloud cover plays important role in many atmospheric processes. Not only does it regulate Earth's water cycle, but also its energy budget, and therefore radiative processes on the surface and atmospheric chemistry, and also interacts with aerosols in the atmosphere. Cloudiness affects ozone and other secondary pollutant formation by limiting incoming radiative fluxes to the surface layer. In meteorological and chemical transport models, e.g. WRF-Chem (GRELL *et al.* 2005; MADRONICH 1987; TIE *et al.* 2003; WILD *et al.* 2000), cloud cover information is passed on to photolysis schemes, thus influencing nitrogen dioxide (NO_2) oxidation rates.

Cloud amount and cloud type are one of the most difficult meteorological parameters to predict. Cloud formation and dynamics depend on a wide variety of factors and processes, which are not accounted for in the model explicitly, simply because the atmospheric system is too complex and the current computational power is insufficient to resolve them. For these reasons, there is a need to apply approximations, which increase the uncertainty of cloud cover prediction (JOHNSON *et al.* 2015; VAN LIER-WALQUI *et al.* 2012). Since cloud microphysics interacts with many other elements of the weather system resolved by the model, those uncertainties are replicated and have an adverse effect on the overall forecast quality. In air quality modeling, it also affects estimation of pollutant concentrations, particularly ozone and other photochemical smog compounds, by regulating the amount of solar energy transferred to the surface.

There are many data types that cloud cover forecast verification can be based on (BRETHERTON *et al.* 1995). The most commonly used and longest data series that can be acquired are cloud fraction reports from ground-based weather stations (e.g. QIAN *et al.* 2012). Surface data are easily accessible in real time and widely used for verification of many other meteorological parameters, such as temperature, pressure or wind speed, but with cloud cover there are

---

[1] Department of Climatology and Atmosphere Protection, University of Wrocław, Wrocław, Poland. E-mail: kinga.walaszek@uni.wroc.pl; kinga.walaszek@uwr.edu.pl
[2] Department of Geoinformatics and Cartography, University of Wrocław, Wrocław, Poland.
[3] National Pollen and Aerobiology Research Unit, University of Worcester, Worcester, UK.

some setbacks. As the density of stations may be sufficient for other meteorological variables, cloudiness measuring network is very irregular and stations are located predominantly on land, so there is disproportion in data density over land and marine areas. There are also manual and automated stations, and the two different methods of gathering cloud fraction information may provide different outcomes (WMO 2008). Additionally, the number of synoptic stations worldwide has been decreasing (PETERSON and VOSE 1997; VOSE *et al*. 1992). Another issue is the frequency of the provided data—surface stations usually report at synoptic times, whereas regional meteorological models provide data at finer temporal resolution (1 h or less). Finally, there is more than one definition of cloud fraction and there are difficulties in transforming it into a variable that would be suitable for model verification.

One data source that solves the problem of irregular and sparse coverage of surface data are meteorological radars; however, they are designed to detect precipitation rather than cloud cover and are not commonly used for that purpose. Finally, there are satellite images, which not only have very large spatial extent, but also high spatial and temporal resolution and data are homogenous across the globe. Satellite data provide images in over a hundred spectral bands which allow the diagnosis of a variety of cloud products, from an unprocessed visible image to cloud mask, cloud top height, liquid water content, or brightness temperatures. Although these data are not always available in real time and go back only a few decades, it may serve a variety of applications related to model verification. There are two main types of satellites providing data for meteorological purposes: geostationary (e.g., the Meteosat series; FENSHOLT *et al*. 2011) and polar-orbiting (e.g. NASA's Terra and Aqua; KING *et al*. 2003). The main advantage of low Earth orbit satellites is their high spatial resolution, which may be even less than 1 km (down to 250 m at sub-satellite point in case of MODIS) and small distortions of the image. However, their orbit characteristics result in the data being available at irregular times, approximately 3–4 times a day. Geostationary satellites, on the other hand, which stay above a fixed point on the equator, have high temporal resolution (15 min for Meteosat Second Generation), but spatial resolution is much lower than the polar-orbiting satellites. Meteosat MSG has 1 and 3 km resolution at sub-satellite point for High Resolution Visible (HRV) and infrared channels, respectively, and it decreases toward the edges of the image. The downside is that their coverage is limited by the satellite's field of view, so polar regions are either invisible or excluded because of large distortions.

Satellite imagery can be processed into a variety of products, and therefore enable various approaches to meteorological model verification (TUINDER *et al.* 2004). One of them is comparison of brightness temperatures (ZINGERLE and NURMI 2008; SÖHNE *et al.* 2008). It is usually not a parameter produced directly by meteorological models, but requires additional post-processing from other model output variables. Much more straightforward approach is to use cloud mask, which can be easily derived from cloud fractions at model levels (CROCKER and MITTERMAIER 2013). Satellite cloud mask is derived from multiple spectral channels, usually based on visible light and supported by infrared wavelengths, through a series of cloud detection tests. These data can then be compared with the modeled cloud mask to evaluate its results.

Meteorological model evaluation can also be based on various methods; one of them, referred to as categorical verification, uses grid-to-grid comparison, and another, object-based verification method, presents the features being verified as objects. In this study, we use both approaches to compare and quantify the differences between the cloud mask derived from the Weather Research and Forecasting (WRF) meteorological model simulation and satellite data. Four different microphysics parameterizations are tested for a selected period, favorable to formation of tropospheric ozone. Finally, for two parameterizations of microphysics, ozone concentrations are calculated with the WRF-Chem model, and the role of microphysics scheme on modeled O_3 is also described with the example of the episode of high ozone concentrations observed in central Europe.

There are two main aims of this study. The first aim is to evaluate the WRF model performance for cloud cover, using satellite data and objective verification approach, and to test the model sensitivity to various microphysics schemes. The second aim is to examine the sensitivity of the WRF-Chem modeled ozone to the selected microphysics schemes. Simulation providing the highest model-measurements agreement will be used in further studies of tropospheric ozone in Poland.

2. *Data and Methods*

2.1. *Study Area and Period*

The analysis is performed for the area of Poland, which is characterized by transitional type of climate, with polar continental and polar maritime air masses being the two main drivers of weather conditions. This makes weather in Poland very changeable and difficult to predict. Episodes with stagnant anticyclone, providing many sunshine hours, high temperatures and low wind speeds, are not uncommon. This type of weather is very favorable for ground-level ozone formation, which is a major issue particularly for large cities and their peripheries. The EU Directive 2008/50/EC goal for 2010 has not been met and threshold values are still being exceeded (Krzyścin *et al.* 2013; Staszewski *et al.* 2012). Because one of the main aims of this study is to quantify the impact of selected microphysics parameterizations on air quality modeling, the test period is a high ozone episode of June 17th–July 4th, 2008. At that time, a vast anticyclone prevailed over Poland (Fig. 1), with low wind speed and high temperatures, which allowed photochemical smog to form in large cities and high concentrations of ground-level ozone were observed in Poland. The threshold value for 1-h average of 180 μg m^{-3} set by aforementioned EU Directive was exceeded at four stations in Poland at least once.

2.2. *The WRF Model*

In this study, a multi-scale meteorological model, the Weather Research and Forecasting (WRF) version 3.5 (Skamarock and Klemp 2008) is used for the area of Poland. Simulations are performed for three one-way nested domains with grid size of 45 km × 45 km for the outermost, 15 km × 15 km for the intermediate, and 5 km × 5 km for the innermost domain, covering the area of interest. The model has 38 vertical layers with model top at 50 hPa. The domain configuration is presented in Fig. 2. Four simulations were run, each with a different microphysics parameterization—Purdue Lin (Lin *et al.* 1983), Eta Ferrier (Rogers *et al.* 2005), WRF Single-Moment 6-class (Hong and Lim 2006), and Morrison 2-Moment (Morrison *et al.* 2009), referred to as SIM1, SIM2, SIM3 and SIM4, respectively. Purdue Lin and Morrison schemes are currently the only two microphysics options that account for aerosol direct effects and are both widely used in WRF-Chem simulations (Forkel *et al.* 2015; Saide *et al.* 2012; Zhang *et al.* 2012). Eta Ferrier and WSM 6-class are also used in many applications, including model evaluation based on satellite data (Grasso *et al.* 2014; Otkin and Greenwald 2008), studies of model sensitivity to microphysics for convective conditions (Hong *et al.* 2009) and heavy precipitation episodes (Segele *et al.* 2013). Other physics options remained the same for all model runs and include the Kain-Fritsch cumulus scheme, Yonsei University PBL scheme, unified Noah land-surface model, and RRTMG (Iacono *et al.* 2008) and RRTM (Mlawer *et al.* 1997) shortwave and longwave radiation, respectively. The model was initialized by the ERA-Interim data, available every 6 h with 0.7° × 0.7° horizontal resolution.

After evaluation of the cloud cover mask for the four WRF model simulations, the best and the worst configurations, in terms of the agreement with the satellite data, were used for the WRF-Chem model runs for the end of the study period—June 31st to July 4th. Details for the WRF and WRF-Chem model configurations are provided in Table 1. Because the differences between the two model runs are of interest here, the simple approach was applied, including restriction of the temporal variations in emissions from nature, while the TNO MACC II emissions (Kuenen *et al.* 2014) are assumed constant during the entire simulation. The chemical boundary conditions of trace gases consist of idealized, northern hemispheric, mid-latitude, clean environmental profiles based upon the results from the NOAA Aeronomy Lab Regional Oxidant Model (Liu *et al.* 1996). With all these simplifications it was

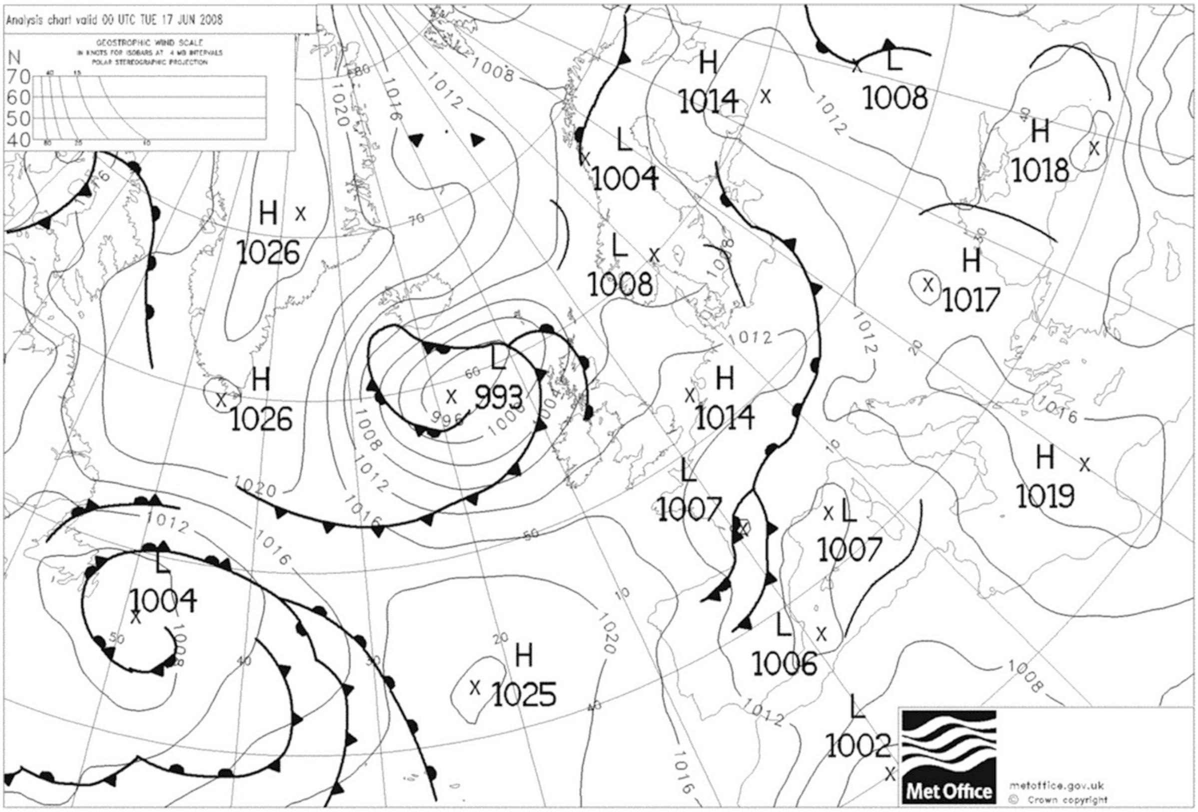

Figure 1
Synoptic situation for the first day of the study period (17.06.2008). Similar conditions prevailed throughout the whole period (17.06-04.07.2008)

computationally efficient to study the impact of microphysics parameterization on ozone concentrations, but it also influenced the chemistry model agreement with the measurements.

2.3. *Measurements for Model Evaluation*

The dataset used for evaluation of the model results is the cloud mask product, derived from the Meteosat Second Generation (MSG) SEVIRI instrument satellite imagery (Derrien and Raoul 2010). This geostationary satellite offers high and constant temporal resolution, consistent with the WRF model output times (1 h), which is why it has been chosen over MODIS even despite its lower spatial resolution.

For generation of this product, a High Resolution Visible (HRV) channel and 11 infrared channels, particularly useful for nighttime hours and necessary for distinction of clouds from e.g. snow cover, were used. Data are available every 15 min, but here the images at full hours were used to match the WRF model output. The final cloud mask product is obtained from Eumetsat, after a series of tests determining whether each grid cell is clear or cloudy. Cloud mask is a pessimistic field, which means that a grid cell can be classified as clear of clouds only if it passes every test. The full methodology of generation of the cloud mask product is described by Derrien and Raoul (2010). HRV channel has a 1 km × 1 km resolution at sub-satellite point, whereas the remaining channels have 3 km × 3 km grid. The final product resolution is reduced to the lower grid resolution. Because of the curvature of the Earth, resolution decreases with distance to sub-satellite point and for Poland it drops to approximately 6–7 km. This is close to the spatial resolution of the

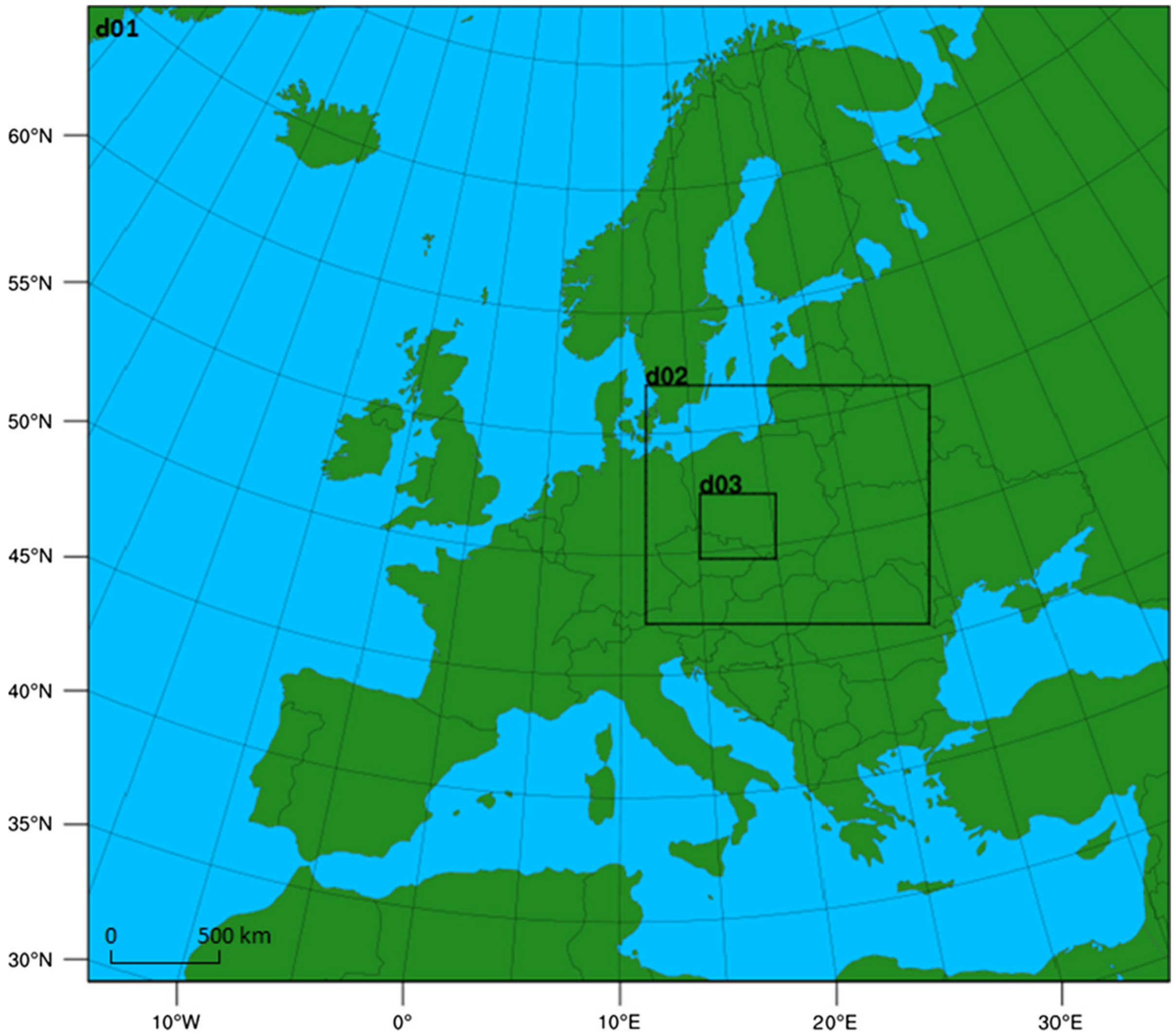

Figure 2
WRF model domain configuration. D01, d02 and d03 domains have spatial resolution of 45 km × 45 km, 15 km × 15 km, and 5 km × 5 km, respectively. Results from domain d03 are analyzed

inner domain (d03) of the WRF model (5 km × 5 km) and the satellite data are resampled to the WRF grid for the spatial comparison.

For evaluation of other meteorological parameters, data from 57 synoptic stations in Poland were used. Ozone concentrations modeled with WRF-Chem were compared with hourly data derived from AirBase, from urban (Wrocław—Korzeniowskiego, WRK), suburban (Wrocław—Bartnicza, WRB), and regional background station (Śnieżka, SNI) in SW Poland.

2.4. *Evaluation of the Model Results Using the Cloud Cover Mask*

There are multiple approaches that can be adopted to verification of cloud cover modeling. Here, two methods are used to evaluate the simulation results. First is categorical verification, which is probably the most widely used method. It is based on grid–to-grid comparison of measured and modeled values. Then, a contingency table is built, based on which various skill scores may be calculated. The main weakness of

Table 1

Physics and chemistry parameterizations used in WRF and WRF-Chem model runs

Parameter	
Cumulus scheme	Kain-Fritsch
Planetary boundary layer	Yonsei University
Land-surface model	NOAH LSM
Shortwave radiation	RRTMG
Longwave radiation	RRTM
Microphysics	Purdue Lin (SIM1) Eta Ferrier (SIM2) WSM6 (SIM3) Morrison 2-Moment (SIM4)
Gas-phase chemistry	RADM2
Aerosol model	MADE/SORGAM
Photolysis scheme	Fast-J
Wet deposition	Simplified parameterization for wet scavenging

this method is underestimation of model skill when analyzed phenomena are shifted in space. To overcome that weakness, an objective verification method can be used. This approach was initially developed for rainfall data and that is how it is commonly used, but it can be adopted to other applications, including cloudiness (Crocker and Mittermaier 2013). In this approach, it is not grid cells, but objects, that are analyzed. An object is a continuous area that fulfills certain criterion, e.g. occurrence of precipitation or cloud cover. In this paper both approaches are used for evaluation of cloud cover simulations and the results are compared. A comparison of example maps, including percentage of area covered by clouds and number of cloud patches for satellite and WRF simulations, is also made.

2.5. *Categorical Verification*

Categorical verification involves a simple and intuitive approach that compares corresponding grid cells of observation and forecast. It can be applied to any phenomenon with values broken into categories; however, the most common use is for binary forecasts, e.g. occurrence of rainfall or cloud cover. In this case, a 2 × 2 contingency table is built, presenting the count of grid cells falling into each of four categories: hits, misses, false alarms, and correct negatives (Table 2). A number of error measures can be calculated based on these data, four of which were selected for this study: Threat Score (TS), Probability of Detection (POD), False Alarm Ratio (FAR), and Frequency Bias Index (FBI; Table 3). Threat Score, also known as the Critical Success Index, measures the fraction of observed and forecast events that were correctly forecast (Gilbert 1884). The range of values is from 0 (no skill) to 1 (perfect score). It is sensitive to climatological frequency of the event and produces lower scores for rare events (Schaefer 1990). However, it allows to compare different model runs for the same domain and period of time, which is one of the aims of this study. Probability of Detection, also known as Hit Rate, measures the fraction of observed events that were correctly forecast. It also ranges from 0 (no skill) to 1 (all observed events were predicted). It is sensitive only to misses and hits and can be improved by overforecasting (Jolliffe and Stephenson 2003). Probability of Detection is usually used with False Alarm Ratio (probability of false detection), which measures the fraction of “yes” forecasts that were false alarms. The range of values is from 0 (no false alarms) to 1 (all “yes” forecasts were incorrect). Opposite to POD, it can be improved by underforecasting (Wilks 2006). Frequency Bias Index determines whether the model is under- or overforecasting the analyzed phenomenon. It ranges from 0 to infinity, with 1 as the perfect score. It should be noted that FBI is not a measure of model accuracy since it does not provide information on the magnitude of forecast errors (Jolliffe and Stephenson 2003). A summary of skill scores used in this study is provided in Table 3. Because in categorical verification only respective grid cells are compared, the so-called double penalty problem is an important issue. For example, when the forecast is even slightly shifted in space, the error may be counted twice—

Table 2

Contingency table used for categorical verification

Forecast	Observed	
	Yes	No
Yes	a (hit)	b (false alarm)
No	c (miss)	d (correct negative)

Skill scores are calculated based on the number of grid cells falling into each category once as a miss, and once as a false alarm. It may falsely reduce the score of model skill, as the event is, in fact, forecasted. In objective verification methods this issue is eliminated, because it is the objects, not individual grid cells, that are analyzed, and the distance of horizontal shift is also being accounted for as a part of the SAL measure.

2.6. *Objective Verification*

The Structure–Amplitude–Location (SAL) method was originally developed as a tool for verification of precipitation field forecasts (Wernli *et al.* 2008). After simplification, the approach can be successfully applied also for other binary variables, such as cloud mask, which has been done previously, for example, by Crocker and Mittermaier (2013) or Zingerle and Nurmi (2008).

First, separate event fields need to be identified within a given domain. These objects are then compared to the respective observed fields, e.g. from Doppler radars or, in this case, satellite images. Afterward, geometric features of the objects, in this case–cloud cover (C_{obs}—cloud cover from satellite image, C_{mod}—from the model), are compared. The first parameter is structure (S), which is defined as the average volume of objects, but because cloud mask field is uniform, it can be treated as a flat object and the structure component describes only its size (denoted as V in Eq. 1). S takes values from -2 to 2, where negative values mean that model underestimates average size of objects and positive values mean overestimation

$$S = \frac{V(C_{\mathrm{mod}}) - V(C_{\mathrm{obs}})}{0.5[V(C_{\mathrm{mod}}) + V(C_{\mathrm{obs}})]}. \tag{1}$$

The second component of the SAL measure is amplitude (A), which calculates the domain-average cloud field. It can be interpreted as the degree to which the model is over- or underestimating the total amount of clouds in the domain. For data with continuous values, the size is understood as the total volume of objects, whereas for binary data it is the total area (D in Eq. 2). A takes values from -2 to 2 as well, with negative values meaning underestimation of total cloud amount within the domain and positive values—overestimation. Please note that structure and amplitude components of SAL are nonlinear, for example $S = -1$ means that model underestimates average cloud size three times, and similar statement is true for amplitude. In general, S and A values depend on observed total cloud amount and cloud size and therefore cannot be directly compared to studies for another region or episode. However, it allows to assess performance of different models for a fixed domain

$$A = \frac{D(C_{\mathrm{mod}}) - D(C_{\mathrm{obs}})}{0.5[D(C_{\mathrm{mod}}) + D(C_{\mathrm{obs}})]} \tag{2}$$

For the location component, two parts of the measure are calculated: one parameter (L_1) determines the distance between the observed and predicted domain-wide center of mass (X in Eq. 3), normalized by the use of the diagonal length of the domain (d in Eqs. 3 and 4). On the other hand, the L_2 parameter measures the observed and predicted average distance between the objects center of mass and the domain

Table 3

Skill scores calculated for cloud cover based on contingency table (above; a hit, b false alarm, c miss, d correct negative)

Name	Definition	Interpretation	Range of values
Threat score or Critical Success Index	$\mathrm{TS} = \frac{a}{a+b+c}$	Fraction of observed and/or forecast events that were correctly predicted	0–1 1: perfect score
Probability of detection or hit rate	$\mathrm{POD} = \frac{a}{a+c}$	Fraction of observed events that were correctly forecast	0–1 1: perfect score
False alarm ratio	$\mathrm{FAR} = \frac{b}{a+b}$	Fraction of forecast events that were false alarms	0–1 0: perfect score
Frequency Bias Index	$\mathrm{FBI} = \frac{a+b}{a+c}$	Ratio of the frequency of forecast events to the frequency of observed events	0–∞ 1: perfect score

Table 4

Error statistics calculated for temperature, relative humidity, wind speed and ozone concentrations

Name	Definition	Range of values
Mean error	$\mathrm{ME} = \frac{\sum(\mathrm{sim}-\mathrm{obs})}{n}$	$-\infty$ to ∞ 0: perfect score
Mean absolute error	$\mathrm{MAE} = \frac{\sum\lvert\mathrm{sim}-\mathrm{obs}\rvert}{n}.$	0 to ∞ 0: perfect score
Index of agreement	$\mathrm{IOA} = \frac{\sum(\mathrm{sim}-\mathrm{obs})^2}{\sum\left(\lvert\mathrm{sim}-\overline{\mathrm{obs}}\rvert+\lvert\mathrm{obs}-\overline{\mathrm{obs}}\rvert\right)}$	0 to 1 1: perfect score

overall center of mass. For binary data, center of mass is simply the geometrical center (denoted as *r;* Eq. 4). The L component is defined as the sum of L_1 and L_2 (Wernli *et al.* 2008)

$$L_1 = \frac{|X(C_{\mathrm{mod}}) - X(C_{\mathrm{obs}})|}{d} \tag{3}$$

$$L_2 = 2\left[\frac{|r(C_{\mathrm{mod}}) - r(C_{\mathrm{obs}})|}{d}\right] \tag{4}$$

The results of object-based verification are then presented on SAL diagrams, which show the values of all components and relationship between them (Fig. 5). Because the values of S and A components have the same range of values, they are represented on the axes, whereas the value of L is represented by the color of the data points. Dotted lines denote mean values of S and A and the sides of the rectangle are the first and third quartiles. These elements facilitate interpretation of the diagram, as the closer the dotted lines are to the center of the diagram and the smaller the rectangle, the more accurate is the forecast.

2.7. *Evaluation of Meteorological Variables and Ozone Concentration*

Besides cloud cover, the impact of the microphysics scheme on three surface meteorological variables was analyzed: air temperature and relative humidity at 2 m, and wind speed at 10 m. Three statistical metrics were calculated for each parameter for all model runs based on observational data from synoptic stations: Mean Error (ME), Mean Absolute Error (MAE), and Index of Agreement (IOA). Mean Error was selected to show how much the model under- or overestimates measured values, whereas Mean Absolute Error shows the absolute value of errors. Index of Agreement is a standardized measure of the overall model-measurement agreement (Willmott 1981). The formulas and value range of the above statistics are presented in Table 4.

After the analysis of meteorological model simulations, the best and the worst simulations were selected for the WRF-Chem model runs. For these simulations, spatial distribution of mean O_3 concentration and the differences between model runs are presented. For three air quality measurement stations representing different environments, temporal variability of measured and modeled 1-h average concentrations were compared.

3. *Results and Discussion*

3.1. *Cloud Cover*

Figures 3 and 4 present example cloud mask images from the satellite product and four WRF simulations for morning (9 AM UTC, 11 AM local time) and afternoon (3 PM UTC, 5 PM local time) hours. In both cases, the locations of modeled cloudy areas correspond to the satellite-derived image, but total cloud amount in the domain is smaller (39 % for SIM4 compared to 59 % on satellite image), particularly in the afternoon. Differences between simulations are much less pronounced than those between the model and satellite product, which suggest that the selection of the microphysics scheme has limited impact on the cloud mask results. The modeled clouds form patches of small cells rather than one vast cloudy area, like the satellite image—every simulation gives at least twice as many cloud cells as satellite. There are two reasons for this. It is related to the fact that cloud mask product

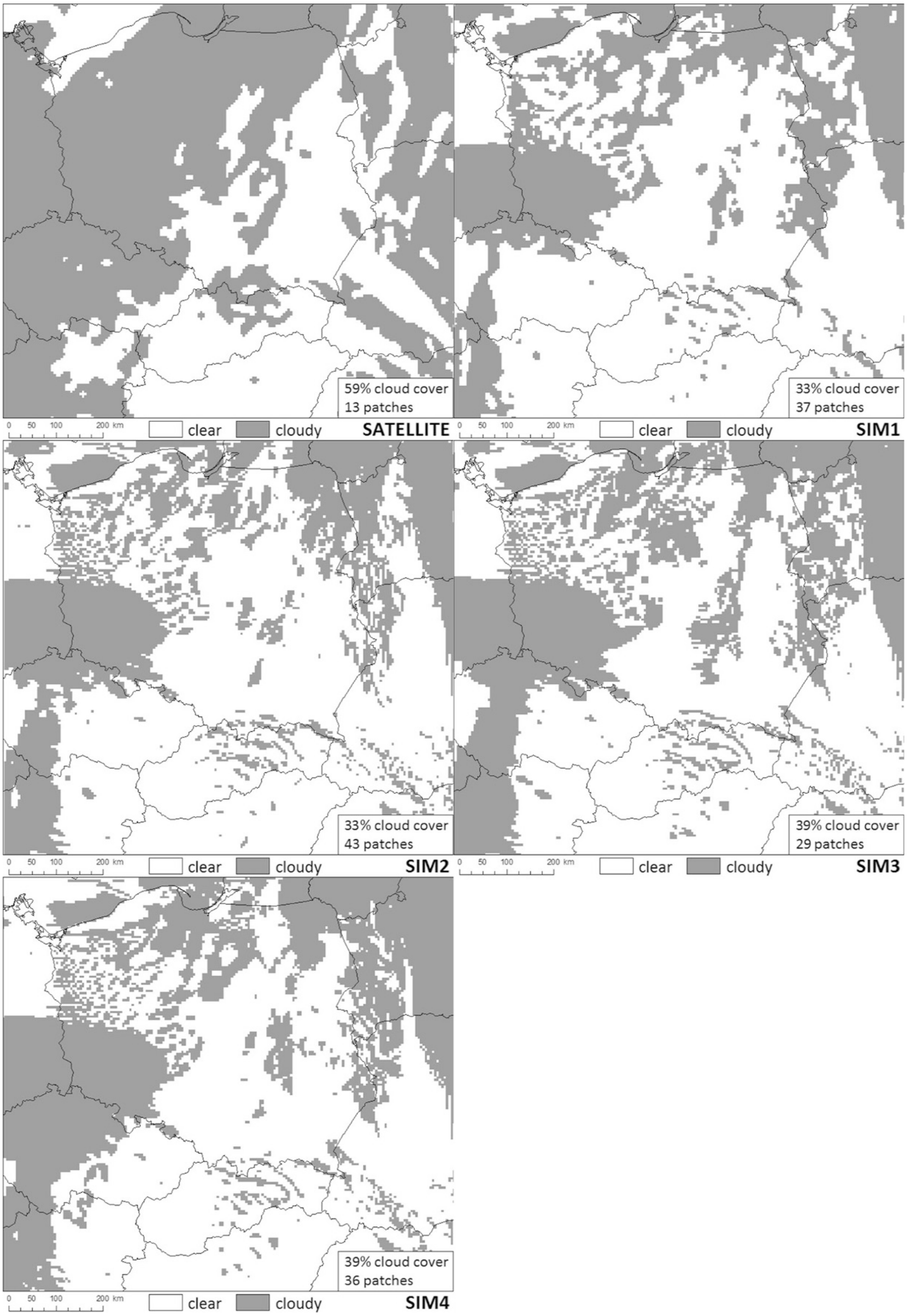

Figure 3
An example of MSG satellite cloud mask product and WRF simulation results for 20 June 2008, 9 AM UTC

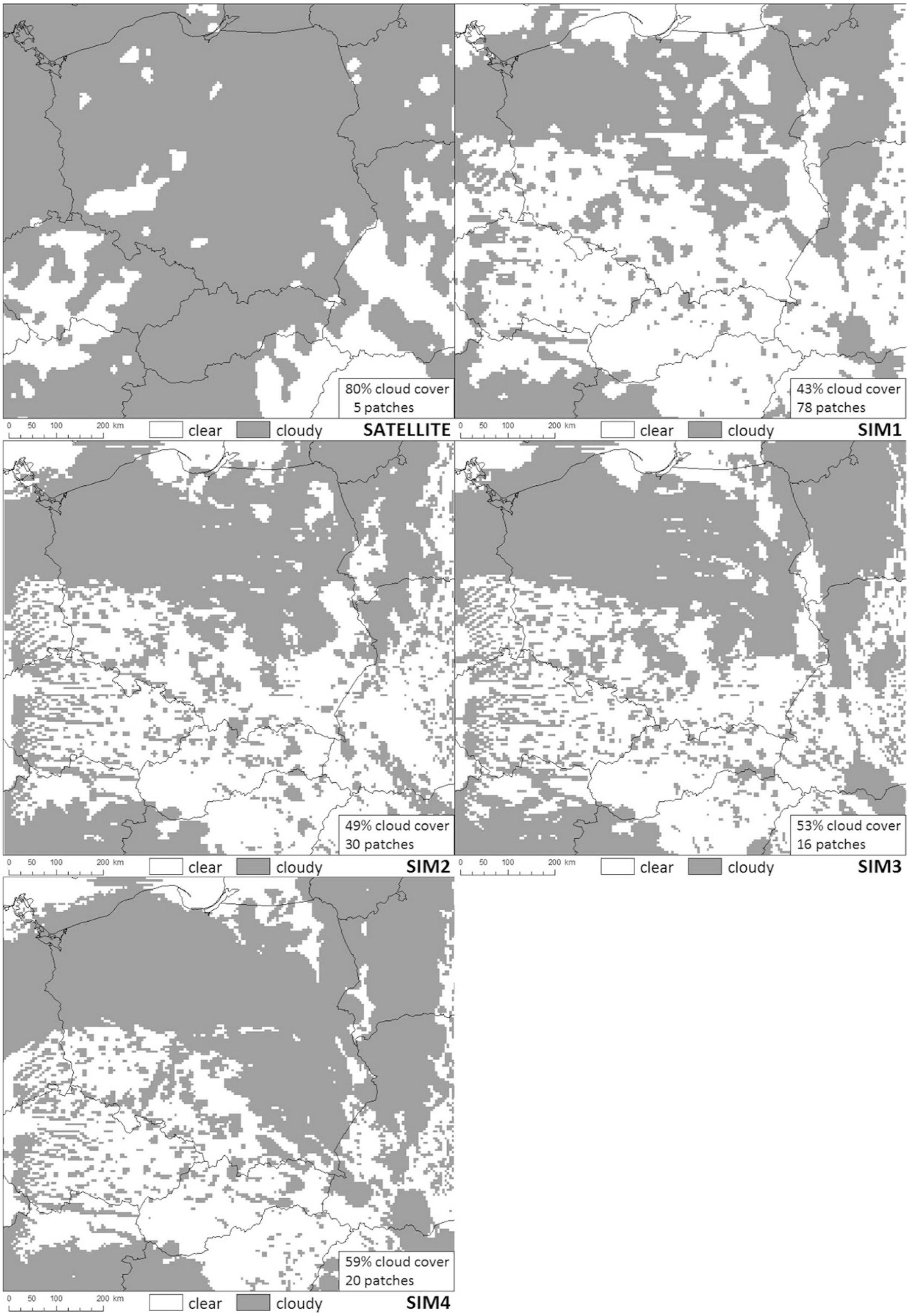

Figure 4
An example of MSG satellite cloud mask product and WRF simulation results for 20 June 2008, 3 PM UTC

generated from Meteosat images has coarser spatial resolution over Poland than the WRF model domains. After resampling to the spatial resolution of the WRF model, the number of cells marked as cloudy might increase. It is also possibly the main reason why for all model simulations a set of orographic clouds in the Carpathians is visible in the morning, which is shown as a single cloud patch in the satellite image. The second reason is that the entire WRF model grid cell has to reach saturation level before it is marked as cloudy. Considering summer convective condition this might be unlikely, therefore the WRF model provides lower number of grid cells with clouds, if compared with satellite data. This is also supported by the larger differences between the WRF and satellite cloud mask for the afternoon hours, if compared to morning (Figs. 3, 4).

Considering the differences between simulations, they are much smaller than differences between any of the simulations and the satellite cloud mask. SIM4 produces the largest cloud amount and SIM1 the smallest. Another noticeable thing is a distinct quantitative difference between SIM4 and other simulations—cloud cells are larger and cover more area, which is supported by the value of FBI (Table 5).

3.2. *The SAL Method*

The results of the simulations evaluated with the SAL method are shown in Fig. 5. It shows that for all simulations both cloud size and total cloud amount, represented by *S* and *A* components, are underestimated by the model, as the majority of data points lie in lower left quadrants of the plots. The main cause is the fact that WRF does not account for subgrid-scale cumulus clouds in the cloud fraction output, which leads to underestimation of modeled cloud cover, as the whole grid cell needs to be saturated to produce cloud. Satellite cloud mask, on the other hand, is a pessimistic field, which means that only the cells which pass all tests can be flagged as cloud-free, which increases the discrepancy between modeled and satellite-derived cloud cover. The best *S* and *A* values are for SIM4, as the rectangle limited by *S* and *A* first and third quartiles is small and located closest to the center of the diagram. It may be explained by the fact that Morrison Double-Moment is the most sophisticated of the selected microphysics options and the only double-moment scheme. SIM3 and SIM2 present similar performance, whereas SIM1 underestimates both cloud amount and size the most. For all simulations, the points with *S* and *A* components close to zero have generally also small *L* values; however, there are some exceptions—particularly in the lower right quadrant. There is a high density of data points with large location component and at the same time structure is significantly underestimated and amplitude is close to the median value. There are very few points with overestimated cloud amount and size, and most of them have small to moderate *L* component value. There are almost no data points with underestimated amount and overestimated cloud size at the same time. This is expected because grid cells on the edges of clouds are less likely to reach saturation, which causes decrease in both cloud size and total cloud cover. A study conducted by Crocker and Mittermaier (2013) for the United Kingdom shows that UK4 and UKV models tend to overestimate cloud cover.

3.3. *Categorical Verification*

Table 5 shows four categorical verification measures. The results present poor model performance,

Table 5

Categorical verification measures calculated for all WRF runs (TS Threat score, POD Probability of Detection, FAR false alarm ratio, FBI Frequency Bias Index)

	TS	POD	FAR	FBI
SIM1	0.39	0.45	0.27	0.71
SIM2	0.40	0.47	0.28	0.74
SIM3	0.42	0.50	0.29	0.82
SIM4	0.42	0.53	0.30	0.94

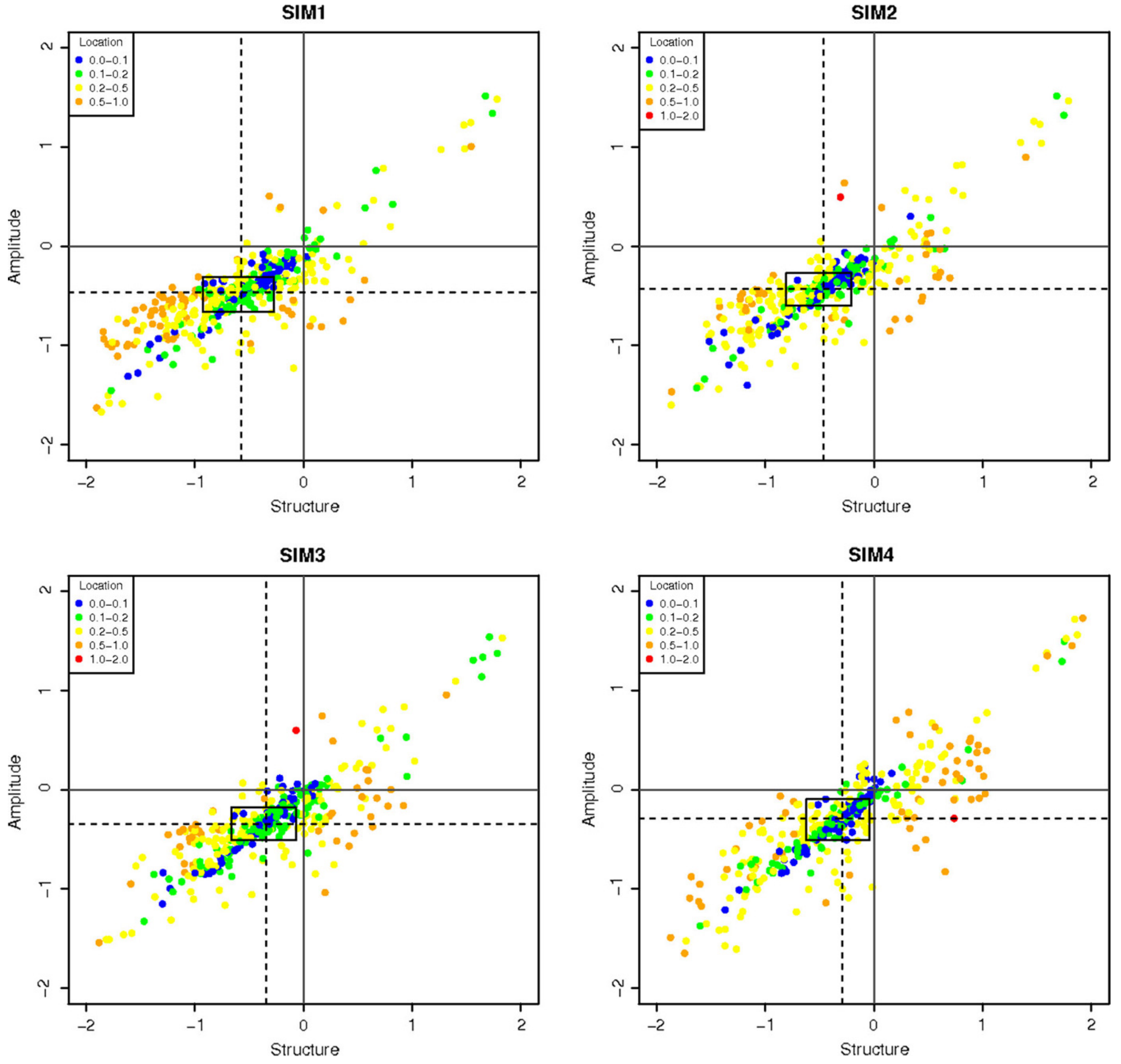

Figure 5
SAL diagrams for all WRF simulations, with Structure (Eq. 1) and Amplitude (Eq. 2) values are given by the position of the point on the diagram and Location (Eqs. 3 and 4) value is given by its color. *Dotted lines* indicate median values and the *rectangles* enclose points within 1st and 3rd quartiles of Structure and Amplitude

with TS not exceeding 0.5. As this measure is sensitive to both misses and false alarms, it is essential to examine which element had the most influence on the results. The values of POD are very low, which indicates large fraction of missed events, therefore it can be concluded that forecasting clear sky when cloud cover is present is a major issue, which is caused by subgrid-scale cloudiness not being resolved by microphysics schemes in WRF. It also shows that nearly half of the observed cloudy grid points are not resolved by the model. SIM4 simulation gives the best result in terms of TS and FBI, which is very close to unity, but False Alarm Ratio is also higher here than for the remaining simulations. It suggests that the reason of high threat score is that this model run forecasts more cloud than other simulations, but otherwise it is not necessarily attributed to model skill.

The values of POD averaged for each hour of day are presented in Fig. 6. All simulations present a similar trend, with the lowest value shortly after sunrise and highest for late afternoon (above 0.6 for SIM4). It indicates that the WRF model is more skilled in resolving afternoon than morning cloudiness. However, one has to be careful in drawing direct conclusions, since most skill scores depend on total observed or modeled cloud amount. SIM4 has the highest values of all simulations for all but 1 h and the differences are the largest for 17:00–19:00 (up to 0.04). The results are much poorer for SIM1 and SIM2, where this parameter falls below 0.4. However, a better POD score is usually associated with larger FAR, because POD may be improved by overforecasting, as the number of hits (to which POD is sensitive) is larger, but the number of false alarms, to which FAR is sensitive, also rises (Fig. 7).

3.4. *Meteorological Variables*

Modeled temperature, relative humidity and wind speed are evaluated based on hourly data from synoptic stations located in Poland. The results are summarized in Table 6. Temperature and humidity are overestimated and wind speed is underestimated by all model runs, which is shown by Mean Error. The differences in Mean Absolute Error between simulations are also small. Model-measurements agreement of wind speed, represented by IOA, shows

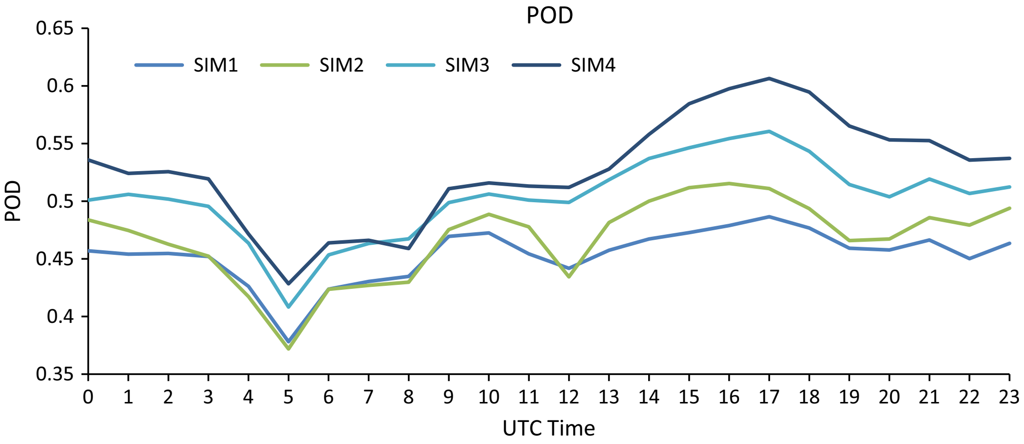

Figure 6
Hourly values of Probability of Detection (POD) averaged for the study period for each of the four simulations

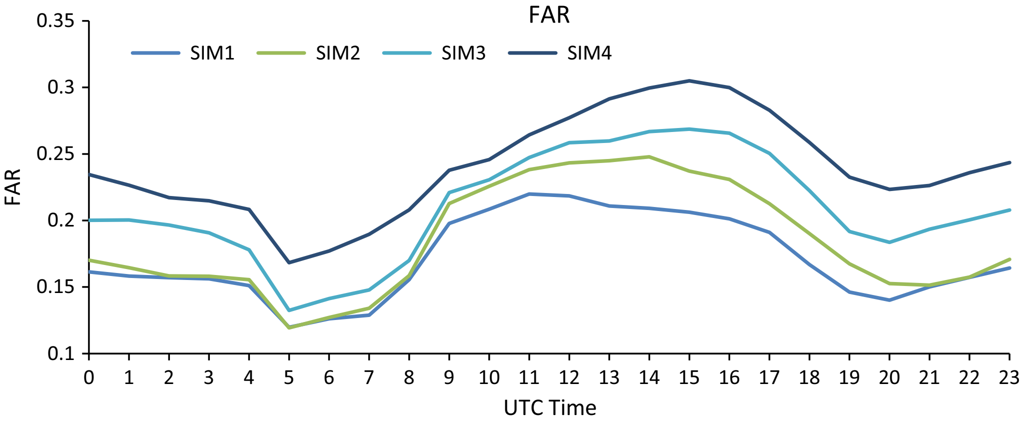

Figure 7
Hourly values of False Alarm Ratio (FAR) averaged for the study period for each of the four simulations

Table 6

Error statistics calculated for WRF simulations of three meteorological variables: temperature (T2), relative humidity (RH2), and wind speed (WSPD)

	T2			RH2			WSPD		
	ME (°C)	MAE (°C)	IOA (–)	ME (%)	MAE (%)	IOA (–)	ME (ms^{-1})	MAE (ms^{-1})	IOA (–)
SIM1	0.135	1.694	0.947	1.998	10.438	0.869	*−0.072*	1.238	0.798
SIM2	*0.098*	*1.672*	*0.949*	1.664	*10.097*	*0.878*	−0.097	1.241	*0.979*
SIM3	0.146	1.692	0.947	2.209	10.491	0.868	−0.083	*1.233*	0.801
SIM4	0.266	1.695	0.947	*0.746*	10.323	0.871	−0.082	1.234	0.800

The numbers in italics denote simulations with lowest values of each statistic

a significant advantage of SIM2 over the other simulations. Generally, there are small differences between the WRF model running with different microphysics schemes, with SIM2 showing slightly better performance. Because the study period is dominated by stagnant anticyclone with low wind speed and no precipitation, the differences between model runs with different microphysics schemes are not pronounced. However, studies conducted for longer and more diverse periods show that Morrison Double-Moment scheme provides the most consistency with observations for meteorological variables and aerosol concentrations (Baró *et al.* 2015).

3.5. *Ozone Concentrations*

Figure 8 presents average 1-h ozone concentrations in the innermost WRF model domain for SIM1 and Fig. 9 for SIM4. Both maps show similar spatial pattern, with O_3 increasing toward the south-west, reaching 90 µg m^{-3} in the Czech Republic. The concentrations modeled with SIM4 are generally higher than SIM1, particularly for areas with higher O_3 levels and over the Baltic Sea in the north, where the differences between SIM4 and SIM1 exceed 7 µg m^{-3} (Fig. 10). The differences between model runs are confirmed by the time series charts in Fig. 11, which show that SIM4 produces higher O_3 levels for all sites. Better performance of the simulation running with Morrison microphysics may be a result of the fact that it is a double-moment scheme that takes into account aerosol direct effects. However, both simulations capture the daily ozone cycle in the urban environment, although the amplitude of changes is much lower than observed. This could be linked to constant temporal emission profile applied, since it does not account for diurnal or weekly changes in anthropogenic emission, mainly from transport (e.g. morning and afternoon peaks in NO_x emission). Another possible source of errors may be inadequate chemistry scheme, underestimating the rate of O_3 formation and destruction processes. Both of these reasons may be verified by changing emission input data or applying a different chemical mechanism. Model errors are on similar level to the study by Forkel *et al.* (2015); however, it should be noted that the study period here is shorter. For rural station O_3 concentration is underestimated for the entire period by both simulations, which may be explained by underestimated background concentrations (default values used with WRF-Chem).

4. *Conclusions*

Although categorical verification of cloud cover forecast provides valuable information about model performance, it may falsely understate model skill in cases when clouds are even slightly dislocated. However, this type of verification can capture the model tendency to underestimate total cloud amount within the domain and enables the identification of possible sources of uncertainties. Objective verification methods may serve as a supplement to categorical approach, as it provides additional information on the structure of model-measurements discrepancies. The objective approach provides both direct information on whether the total cloudiness in the domain is over- or underestimated and to what extent, and also brings more detailed information on

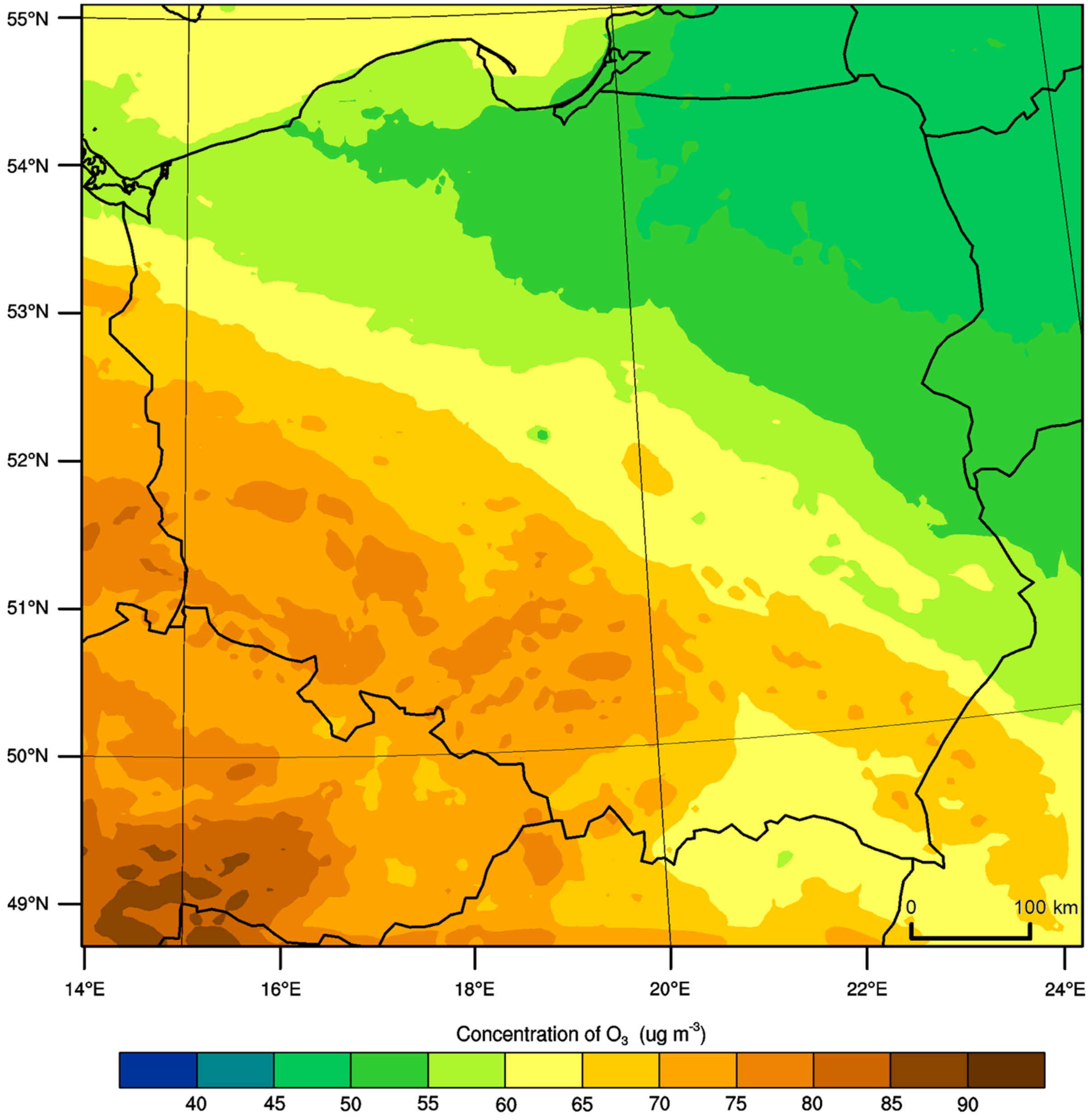

Figure 8
Mean O_3 concentration for the episode of 30 June–4 July 2008 (SIM1, Purdue Lin)

the size and location of modeled cloud patches compared to the observed ones. By analyzing objects (i.e. cloudy areas) instead of individual grid points it also eliminates the double penalty problem, which becomes a large issue with high spatial resolution of meteorological models; therefore, model performance is not underestimated, as in the case of categorical verification method.

Both methods are consistent with the conclusion that all WRF simulations underestimate the amount of cloud cover. This may have further consequences on e.g. overestimation of the summer air temperature by the WRF model which was shown by Kryza *et al.* (2015, this issue) for Central and Eastern Europe. One important factor is that satellite cloud mask is a pessimistic field, meaning that only a grid point that

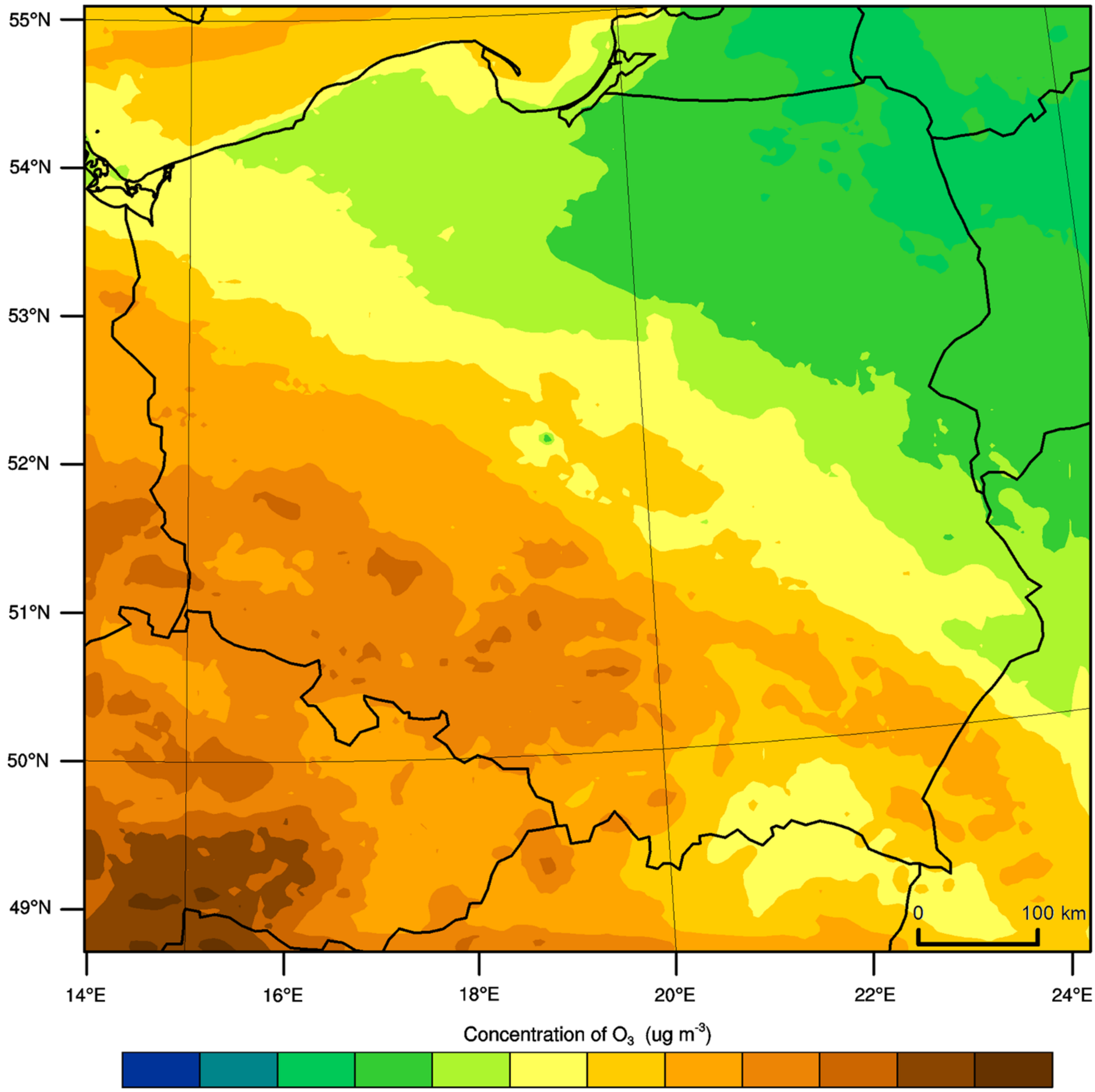

Figure 9
Mean O_3 concentration for the episode of 30 June–4 July 2008 (SIM4, Morrison 2-Moment)

passed all cloud detection tests can be classified as cloud-free. Although these data are consistent with MODIS and point surface observations, it will rather present more than less clouds (Crocker and Mittermaier 2013). Another issue is the resolution of data—satellite cloud mask has similar, but not the same grid size as the model. Coarser resolution results in presenting a set of small cloud cells (e.g. Altocumulus floccus) as one wide patch, whereas the model resolves it differently. It may result in false underestimation of cloud cover and the average size of cloud cells, which may be the case here. Additionally, both methods are agreeable that SIM4 provides the best results of cloud cover and SIM1 presents significantly poorer performance. It refers to all analyzed cloud properties—SIM4 has the least underestimation of

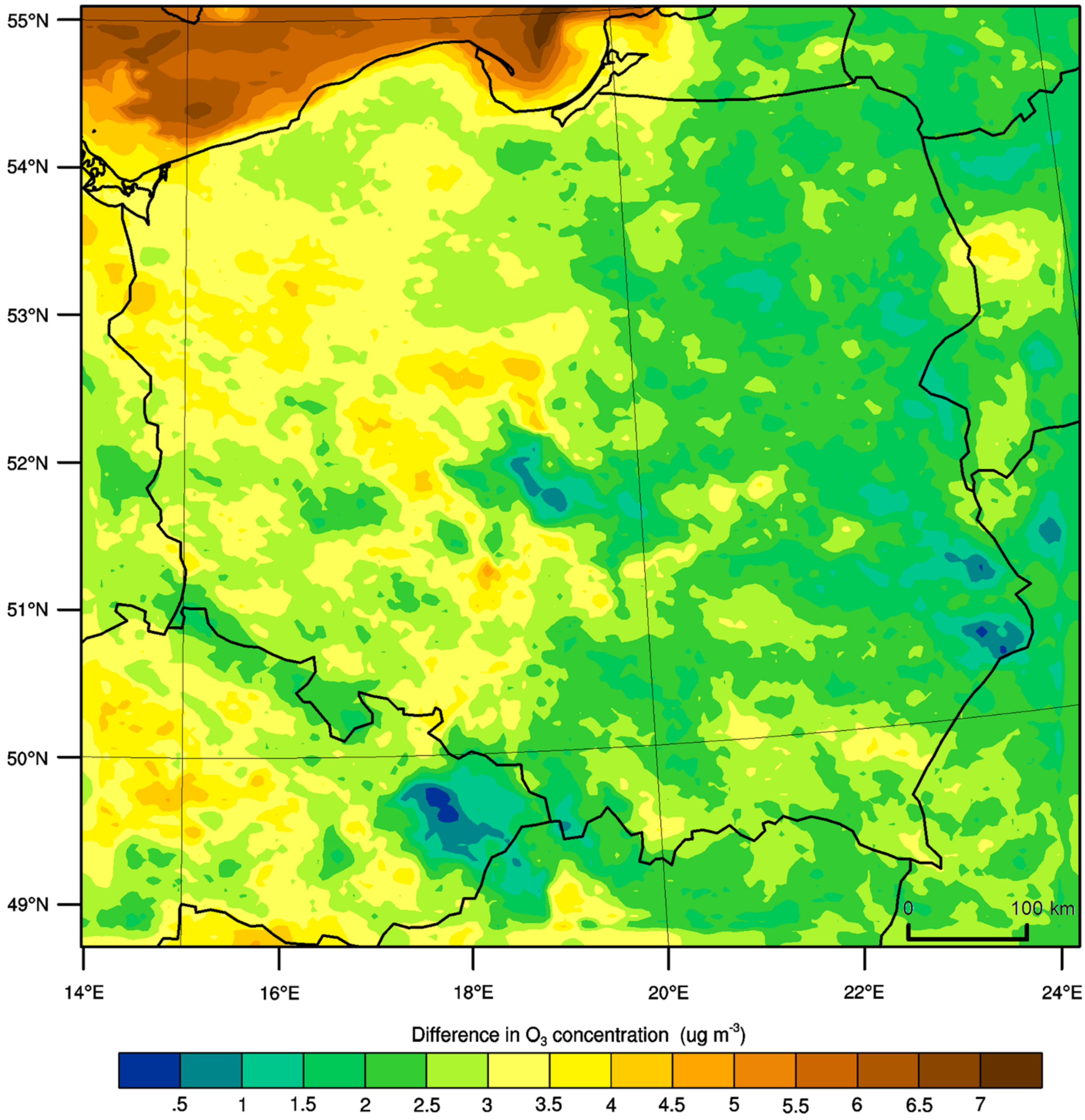

Figure 10
Differences in mean O_3 concentration between SIM4 (Purdue Lin) and SIM1 (Morrison 2-Moment)

cloud size and total cloud amount, as well as its location within the domain. The difference is not as significant for surface meteorological variables, as only one performance measure for wind speed responds to the change in microphysics parameterization. However, the change of microphysics scheme has significant impact on WRF-Chem modeled ozone concentrations, particularly for high ozone conditions. This could be attributed to the fact that cloud cover is used as input for photolysis schemes. It is important for risk assessment of critical ozone levels exceedance and its prediction. Therefore, the Morrison Double-Moment microphysics parameterization will be used in further research regarding the modeling of ozone concentrations during summer episodes in Poland and Central Europe.

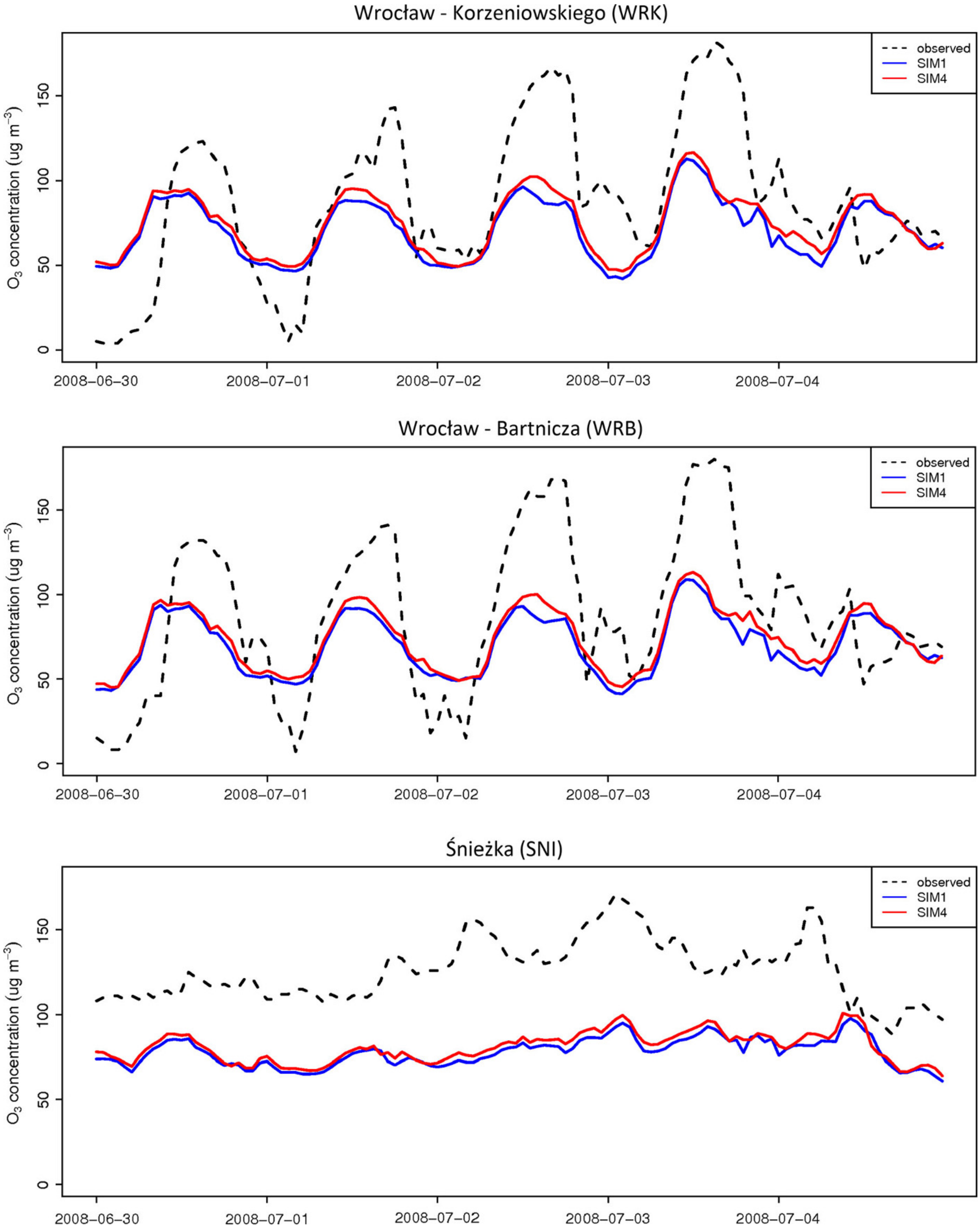
Wrocław - Korzeniowskiego (WRK)

Wrocław - Bartnicza (WRB)

Śnieżka (SNI)

Figure 11
Temporal variability of modeled and measured O_3 concentrations at WRK, WRB, and SNI station

Acknowledgments

The study was supported by the Polish National Science Centre project no. UMO-2013/09/B/ST10/00594. The project was financed with means of the European Union under the Financial Instrument LIFE + and co-financed by the National Fund of Environmental Protection and Water Management. Calculations were carried out in the Wrocław Centre for Networking and Supercomputing (http://www.wcss.wroc.pl), Grant No. 170.

REFERENCES

Baró, R., Jiménez-Guerrero, P., Balzarini, A., Curci, G., Forkel, R., Grell, G., Hirtl, M., Honzak, L., Langerf, M., Pérez, J. L., Pirovano, G., San José, R., Tuccella, P., Werhahn, J., and Žabkar, R. (2015). *Sensitivity analysis of the microphysics scheme in WRF-Chem contributions to AQMEII phase 2*. Atmospheric Environment, *115*, 620–629. doi:10.1016/j.atmosenv.2015.01.047.

Bretherton, C., Klinker, E., Betts, A., and Coakley, J. J. (1995). *Comparison of ceilometer, satellite, and synoptic measurements of boundary-layer cloudiness and the ECMWF diagnostic cloud parameterization scheme during*. Journal of the Atmospheric Sciences, 52(16), 2736–2751. Retrieved from http://ir.library.oregonstate.edu/xmlui/handle/1957/26417.

Crocker, R., and Mittermaier, M. (2013). *Exploratory use of a satellite cloud mask to verify NWP models*. Meteorological Applications, *20*(2), 197–205. doi:10.1002/met.1384.

Derrien, M., Gléau, H. Le, and Raoul, M. (2010). The use of the high resolution visible in SAFNWC/MSG cloud mask. In Proceedings of the 2010 EUMETSAT Meteorological Satellite Conference, 20–24 September 2010, Córdoba, Spain (p. 57 pp.). Retrieved from http://hal.archives-ouvertes.fr/meteo-00604325/.

Fensholt, R., Anyamba, A., Huber, S., Proud, S. R., Tucker, C. J., Small, J., Pak, E., Rasmussen, M. O., Sandholt, I., and Shisanya, C. (2011). *Analysing the advantages of high temporal resolution geostationary MSG SEVIRI data compared to Polar Operational Environmental Satellite data for land surface monitoring in Africa*. International Journal of Applied Earth Observation and Geoinformation *13*(5), 721–729. doi:10.1016/j.jag.2011.05.009.

Forkel, R., Balzarini, A., Baró, R., Bianconi, R., Curci, G., Jiménez-Guerrero, P., Hirtl, M., Honzak, L., Lorenz, C., Im, U., Pérez, J. L., Pirovano, G., San José, R., Tuccella, P., Werhahn, J., and Žabkar, R. (2015). *Analysis of the WRF-Chem contributions to AQMEII phase 2 with respect to aerosol radiative feedbacks on meteorology and pollutant distributions*. Atmospheric Environment, *115*, 630–645. doi:10.1016/j.atmosenv.2014.10.056.

Gilbert, G. K. (1884). *Finley's tornado predictions*. American Meteorological Journal, *1*, 166–172.

Grasso, L., Lindsey, D. T., Sunny Lim, K.-S., Clark, A., Bikos, D., and Dembek, S. R. (2014). *Evaluation of and Suggested Improvements to the WSM6 Microphysics in WRF-ARW Using Synthetic and Observed GOES-13 Imagery*. Monthly Weather Review, *142*(10), 3635–3650. doi:10.1175/MWR-D-14-00005.1.

Grell, G., Peckham, S., and Schmitz, R. (2005). *Fully coupled "online" chemistry within the WRF model*. Atmospheric Environment, *39*, 6957–6975. doi:10.1016/j.atmosenv.2005.04.027.

Hong, S., and Lim, J. (2006). *The WRF single-moment 6-class microphysics scheme (WSM6)*. J. Korean Meteor. Soc, *42*(2), 129–151. Retrieved from http://www.mmm.ucar.edu/wrf/users/docs/WSM6-hong_and_lim_JKMS.pdf.

Hong, S.-Y., Sunny Lim, K.-S., Kim, J.-H., Jade Lim, J.-O., and Dudhia, J. (2009). *Sensitivity Study of Cloud-Resolving Convective Simulations with WRF Using Two Bulk Microphysical Parameterizations: Ice-Phase Microphysics versus Sedimentation Effects*. Journal of Applied Meteorology and Climatology, *48*(1), 61–76. doi:10.1175/2008JAMC1960.1.

Iacono, M. J., Delamere, J. S., Mlawer, E. J., Shephard, M. W., Clough, S. A., and Collins, W. D. (2008). *Radiative forcing by long-lived greenhouse gases: Calculations with the AER radiative transfer models*. Journal of Geophysical Research: Atmospheres, *113*(D13), D13103. doi:10.1029/2008JD009944.

Johnson, J. S., Cui, Z., Lee, L. A., Gosling, J. P., Blyth, A. M., and Carslaw, K. S. (2015). *Evaluating uncertainty in convective cloud microphysics using statistical emulation*. Journal of Advances in Modeling Earth Systems, *7*(1), 162–187. doi:10.1002/2014MS000383.

Jolliffe, I. T., and Stephenson, D. B. (2003). Forecast verification: a practitioner's guide in atmospheric science. John Wiley & Sons, Ltd.

King, M. D., Menzel, W. P., Kaufman, Y. J., Tanré, D., Gao, B. C., Platnick, S., Ackerman, S. A., Remer, L. A., Pincus, R., and Hubanks, P. A. (2003). *Cloud and aerosol properties, precipitable water, and profiles of temperature and water vapor from MODIS*. IEEE Transactions on Geoscience and Remote Sensing, *41*(2 PART 1), 442–456.

Kryza, M., Wałaszek, K., Ojrzyńska, H., Szymanowski, M., Werner, M., and Dore, A. J. *High resolution dynamical downscaling of ERA-Interim using the WRF regional climate model. Part 1: model configuration and statistical evaluation for the 1981-2010 period*. Pure and Applied Geophysics (in revision).

Krzyścin, J. W., Rajewska-Więch, B., and Jarosławski, J. (2013). The long-term variability of atmospheric ozone from the 50-yr observations carried out at Belsk (51.84°N, 20.78°E), Poland. Tellus B; Vol. 65.

Kuenen, J. J. P., Visschedijk, A. J. H., Jozwicka, M., and Denier van der Gon, H. A. C. (2014). *TNO-MACC_II emission inventory; a multi-year (2003–2009) consistent high-resolution European emission inventory for air quality modelling*. Atmos. Chem. Phys., *14*(20), 10963–10976. doi:10.5194/acp-14-10963-2014.

Lin, Y.-L., Farley, R. D., and Orville, H. D. (1983). *Bulk Parameterization of the Snow Field in a Cloud Model*. Journal of Climate and Applied Meteorology, *22*(6), 1065–1092. doi:10.1175/1520-0450(1983)022<1065:BPOTSF>2.0.CO;2.

Liu, S. C., McKeen, S. A., Hsie, E.-Y., Lin, X., Kelly, K. K., Bradshaw, J. D., Sandholm, S. T., Browell, E. V., Gregory, G. L., Sachse, G. W., Bandy, A. R., Thornton, D. C., Blake, D. R., Rowland, F. S., Newell, R., Heikes, B. G., Singh, H., and Talbot, R. W. (1996). *Model study of tropospheric trace species distributions during PEM-West A*. Journal of Geophysical Research, *101*(D1), 2073. doi:10.1029/95JD02277.

Madronich, S. (1987). *Photodissociation in the atmosphere: 1. Actinic flux and the effects of ground reflections and clouds*. Journal of Geophysical Research: Atmospheres, *92*(D8), 9740–9752. doi:10.1029/JD092iD08p09740.

Mlawer, E. J., Taubman, S. J., Brown, P. D., Iacono, M. J., and Clough, S. A. (1997). *Radiative transfer for inhomogeneous atmospheres: RRTM, a validated correlated-k model for the longwave*. Journal of Geophysical Research: Atmospheres, *102*(D14), 16663–16682. doi:10.1029/97JD00237.

Morrison, H., Thompson, G., and Tatarskii, V. (2009). *Impact of Cloud Microphysics on the Development of Trailing Stratiform Precipitation in a Simulated Squall Line: Comparison of One- and Two-Moment Schemes*. Monthly Weather Review, *137*(3), 991–1007. doi:10.1175/2008MWR2556.1.

Otkin, JA., and Greenwald, T. J. (2008). *Comparison of WRF Model-Simulated and MODIS-Derived Cloud Data*. Monthly Weather Review, *136*(6), 1957–1970. doi:10.1175/2007MWR2293.1.

Peterson, T. C., and Vose, R. S. (1997). *An Overview of the Global Historical Climatology Network Temperature Database*. Bulletin of the American Meteorological Society, *78*(12), 2837–2849. doi:10.1175/1520-0477(1997)078<2837:AOOTGH>2.0.CO;2.

Qian, Y., Long, C. N., Wang, H., Comstock, J. M., McFarlane, S. A., and Xie, S. (2012). *Evaluation of cloud fraction and its radiative effect simulated by IPCC AR4 global models against ARM surface observations*. Atmospheric Chemistry and Physics, *12*(4), 1785–1810. doi:10.5194/acp-12-1785-2012.

Rogers, E., Ek, M., Ferrier, B. S., Gayno, G., Lin, Y., Mitchell, K., Pondeca, M., Pyle, M., Wong, V. C. K., and Wu, W. S. (2005). The NCEP North American Mesoscale Modeling System: Final Eta model/analysis changes and preliminary experiments using the WRF-NMM. In 21st Conference on Weather Analysis and Forecasting/17th Conference on Numerical Weather Prediction, Washington, D.C.

Saide, P. E., Spak, S. N., Carmichael, G. R., Mena-Carrasco, M. A., Yang, Q., Howell, S., Leon, D. C., Snider, J. R., Bandy, A. R., Collett, J. L., Benedict, K. B., de Szoeke, S. P., Hawkins, L. N., Allen, G., Crawford, I., Crosier, J., and Springston, S. R. (2012). *Evaluating WRF-Chem aerosol indirect effects in Southeast Pacific marine stratocumulus during VOCALS-REx*. Atmospheric Chemistry and Physics, *12*(6), 3045–3064. doi:10.5194/acp-12-3045-2012.

Schaefer, J. T. (1990). *The Critical Success Index as an Indicator of Warning Skill*. Weather and Forecasting, *5*(4), 570–575. doi:10.1175/1520-0434(1990)005<0570:TCSIAA>2.0.CO;2.

Segele, Z. T., Leslie, L. M., and Lamb, P. J. (2013). Weather Research and Forecasting Model simulations of extended warm-season heavy precipitation episode over the US Southern Great Plains: data assimilation and microphysics sensitivity experiments. Tellus A; Vol 65 (2013).

Skamarock, W., and Klemp, J. (2008). *A time-split nonhydrostatic atmospheric model for weather research and forecasting applications*. Journal of Computational Physics, *227*, 3465–3485. doi:10.1016/j.jcp.2007.01.037.

Söhne, N., Chaboureau, J.-P., and Guichard, F. (2008). *Verification of Cloud Cover Forecast with Satellite Observation over West Africa*. Monthly Weather Review, *136*(11), 4421–4434. doi:10.1175/2008MWR2432.1.

Staszewski, T., Kubiesa, P., and Łukasik, W. (2012). *Response of spruce stands in national parks of southern Poland to air pollution in 1998–2005*. European Journal of Forest Research, *131*(4), 1163–1173. doi:10.1007/s10342-011-0587-0.

Tie, X., Madronich, S., Walters, S., Zhang, R., Rasch, P., and Collins, W. (2003). *Effect of clouds on photolysis and oxidants in the troposphere*. Journal of Geophysical Research: Atmospheres, *108*(D20), 4642. doi:10.1029/2003JD003659.

Tuinder, O. N. E., de Winter-Sorkina, R., and Builtjes, P. J. H. (2004). *Retrieval methods of effective cloud cover from the GOME instrument: an intercomparison*. Atmospheric Chemistry and Physics, *4*(1), 255–273. doi:10.5194/acp-4-255-2004.

Van Lier-Walqui, M., Vukicevic, T., and Posselt, D. J. (2012). *Quantification of Cloud Microphysical Parameterization Uncertainty Using Radar Reflectivity*. Monthly Weather Review, *140*(11), 3442–3466. doi:10.1175/MWR-D-11-00216.1.

Vose, R. S., Schmoyer, R. L., Steurer, P. M., Peterson, T. C., Heim, R., Karl, T. R., and Eischeid, J. K. (1992). The Global Historical Climatology Network: Long-Term Monthly Temperature, Precipitation, Sea Level Pressure, and Station Pressure Data. Environmental Sciences Division Publication no. 3912, doi: 10.3334/CDIAC/cli.ndp041.

Wernli, H., Paulat, M., Hagen, M., and Frei, C. (2008). *SAL—A Novel Quality Measure for the Verification of Quantitative Precipitation Forecasts*. Monthly Weather Review, *136*(11), 4470–4487. doi:10.1175/2008MWR2415.1.

Wild, O., Zhu, X., and Prather, M. (2000). *Fast-J: Accurate Simulation of In- and Below-Cloud Photolysis in Tropospheric Chemical Models*. Journal of Atmospheric Chemistry, *37*(3), 245–282. doi:10.1023/A:1006415919030.

Willmott, C. J. (1981). *On the Validation of Models*. Physical Geography, *2*(2), 184–194.

Wilks, D. S. (2006). Statistical methods in the atmospheric sciences., 704 p., Elsevier Inc., ISBN 9780123850225.

World Meteorological Organization. (2008). Guide to Meteorological Instruments and Methods of Observation. WMO No. 8.

Zhang, Y., Chen, Y., Sarwar, G., and Schere, K. (2012). *Impact of gas-phase mechanisms on Weather Research Forecasting Model with Chemistry (WRF/Chem) predictions: Mechanism implementation and comparative evaluation*. Journal of Geophysical Research, *117*(D1), D01301. doi:10.1029/2011JD015775.

Zingerle, C., and Nurmi, P. (2008). *Monitoring and verifying cloud forecasts originating from operational numerical models*, Meteorological Applications, *15*(3), 325–330. doi:10.1002/met.73.

(Received November 30, 2014, revised November 2, 2015, accepted December 10, 2015, onlinedate January 6, 2016)

Pure Appl. Geophys. 174 (2017), 511–526

DOI 10.1007/s00024-016-1272-5

Pure and Applied Geophysics

High-Resolution Dynamical Downscaling of ERA-Interim Using the WRF Regional Climate Model for the Area of Poland. Part 1: Model Configuration and Statistical Evaluation for the 1981–2010 Period

MACIEJ KRYZA,[1] KINGA WAŁASZEK,[1] HANNA OJRZYŃSKA,[1] MARIUSZ SZYMANOWSKI,[2] MAŁGORZATA WERNER,[1,3] and ANTHONY J. DORE[4]

Abstract—In this work, we present the results of high-resolution dynamical downscaling of air temperature, relative humidity, wind speed and direction, for the area of Poland, with the Weather Research and Forecasting (WRF) model. The model is configured using three nested domains, with spatial resolution of 45 km × 45 km, 15 km × 15 km and 5 km × 5 km. The ERA-Interim database is used for boundary conditions. The results are evaluated by comparison with station measurements for the period 1981–2010. The model is capable of reproducing the main climatological features of the study area. The results are in very close agreement with the measurements, especially for the air temperature. For all four meteorological variables, the model performance captures seasonal and daily cycles. For the air temperature and winter season, the model underestimates the measurements. For summer, the model shows higher values, compared with the measurements. The opposite is the case for relative humidity. There is a strong diurnal pattern in mean error, which changes seasonally. The agreement with the measurements is worse for the seashore and mountain areas, which suggests that the 5 km × 5 km grid might still have an insufficient spatial resolution. There is no statistically significant temporal trend in the model performance. The larger year-to-year changes in the model performance, e.g. for the years 1982 and 2010 for the air temperature should therefore be linked with the natural variability of meteorological conditions.

Key words: Dynamical downscaling, high resolution, WRF model, Poland.

1. *Introduction*

Downscaling is a method used to obtain geographical distribution and time evolution of small-scale features given large-scale coarse-resolution analyses, forecasts or simulations (HONG and KANAMITSU 2014). There are two main downscaling methods: statistical and dynamical (BENESTAD 2008). Dynamical downscaling utilizes a dynamical regional model, forced by coarse-resolution data (GIORGI and BATES 1989). Statistical downscaling is based on the relations between the large-scale parameters and regional-scale observations (KIM *et al.* 1984). Both approaches were compared, e.g. by HUTH *et al.* (2015). There is also a combined approach, named statistical–dynamical downscaling, which has also gained importance in climate research in recent years. Statistical–dynamical downscaling combines the benefit of both the statistical and dynamical approaches, and was presented, e.g. by FUENTES and HEIMANN (2000) and REYERS *et al.* (2015). Here, the work is focused on dynamical downscaling at high spatial resolution. High-resolution models benefit, e.g. from detailed surface forcing information, including topography and land use, and local features, like sea breeze, can be explicitly resolved (HEIKKILA *et al.* 2011; SOARES *et al.* 2012; CZERNECKI 2013). With the grid scale smaller than several kilometres, the explicit treatment of the entrainment process at the top of the planetary boundary layer may be applied and the advantages of this were shown, e.g. by HONG and DUDHIA (2012). There is also certain criticism related with dynamical downscaling and high resolution. This has been addressed, e.g. by

---

[1] Department of Climatology and Atmosphere Protection, Institute of Geography and Regional Development, Wrocław University, ul. Kosiby 8, 51-621 Wrocław, Poland. E-mail: maciej.kryza@uwr.edu.pl
[2] Department of Geoinformatics and Cartography, Institute of Geography and Regional Development, Wrocław University, pl. Uniwersytecki 1, 50-137 Wrocław, Poland.
[3] National Pollen and Aerobiology Research Unit, University of Worcester, Henwick Grove, Worcester WR2 6AJ, UK.
[4] Centre for Ecology and Hydrology, Bush Estate, Penicuik, Midlothian EH26 0QB, UK.

Pielke (2013) and Murphy (1999), and is mainly related to the regional model and its settings. Many parameterization schemes, utilized in regional studies, were developed for coarse resolutions. This may lead to high positive bias in precipitation, which was reported, e.g. by Shrestha *et al.* (2013). The development of the precipitation physics parameterization scheme for a smooth transition to cloud resolving scales is now in progress (Hong and Kanamitsu 2014; Grell and Freitas 2013). Other sources of uncertainty are related with large-scale fields provided by the global climate models, the unphysical treatment of the lateral boundary conditions and inconsistencies in the dynamics and physics between the global and regional climate models.

Central Europe and Poland comprise a geographical region of transitional climate, with large seasonal and year-to-year variability. There are some examples of statistical downscaling applied for this area, presented, e.g. by Marosz *et al.* (2013) and Marosz and Jakusik (2014). Examples of dynamical downscaling at high spatial resolution include simulations for short periods or limited to small areas of selected catchments (Pavlik *et al.* 2011; Czernecki 2013). The results of the European Coordinated Regional Climate Downscaling Experiment (EURO-CORDEX) project show the importance of dynamical downscaling for this area and also address the uncertainties related with this approach (Giorgi and Gutowski 2015). Katragkou *et al.* (2015) show the influence of the various physics scheme on the WRF model performance for Europe. Kotlarski *et al.* (2014) show the role of model grid resolution on the results of dynamical downscaling for the EURO-CORDEX domain. The demand for meteorological information, available for a long-term period, at high spatial and temporal resolution, and developed homogenously for a large area is increasing. This information is a must for other studies, such as ecology and tick diseases (Kiewra *et al.* 2014), air quality (Wałaszek *et al.* 2015; Werner *et al.* 2011; Hernandez-Ceballos *et al.* 2014) or hydrological forecasting (Jeziorska and Niedzielski, this issue).

In this work, we present the application of the WRF model for dynamical downscaling of the ERA-Interim data for the area of Poland, with high spatial resolution of 5 km × 5 km. The model configuration is described and the results are compared with instantaneous surface meteorological measurements of air temperature, relative humidity and wind speed and direction. The model performance is summarized using both the domain-wide statistics and the spatial approach, where individual stations are assessed. In the second part of this work (Ojrzyńska *et al.* 2015, this issue), we address the model performance for daily rainfall and air temperature, and analyse the results in terms of circulation type.

2. *Data and Methods*

2.1. *Study Area*

The study is focused on the territory of Poland in Central Europe, located between 49°00′N and 54°50′N, and 14°07′E and 24°09′E (Fig. 1). The area of Poland is 312 679 km^2, with the altitude varying between 1.8 m below (Northern Poland) and 2499 m above sea level (Southern Poland). The average height of Poland is 173 m a.s.l., and the areas located in zones 100–200 m a.s.l. (49.7 %) and 0–100 m a.s.l. (25.2 %) cover the majority of the country area. The regions with elevation above 1000 m a.s.l. cover about 0.2 %. Poland is characterized by transitional characteristics of climate with strong, varying maritime and continental influences and prevailing western flow. The long-term annual mean air temperature varies from ca. 9 °C in the west, to below 5 °C in the mountains and SE part of Poland. In winter and fall, the west–east gradient in air temperature is pronounced, with a warm belt along the Baltic Sea shore. In summer, the mean air temperature decreases from the south (excluding mountains) to the north. West and south-west wind directions are the most frequent, with the frequency exceeding 20 %. The annual mean wind speed is in the range from 3 to 4 m s^{-1} for the majority of the study area, with the highest values observed close to the Baltic Sea shore and in the mountains (Lorenc 2005). The annual mean relative humidity is the highest in the north of the country (>84 %; Lorenc 2005) and decreases towards the south (except for the mountains).

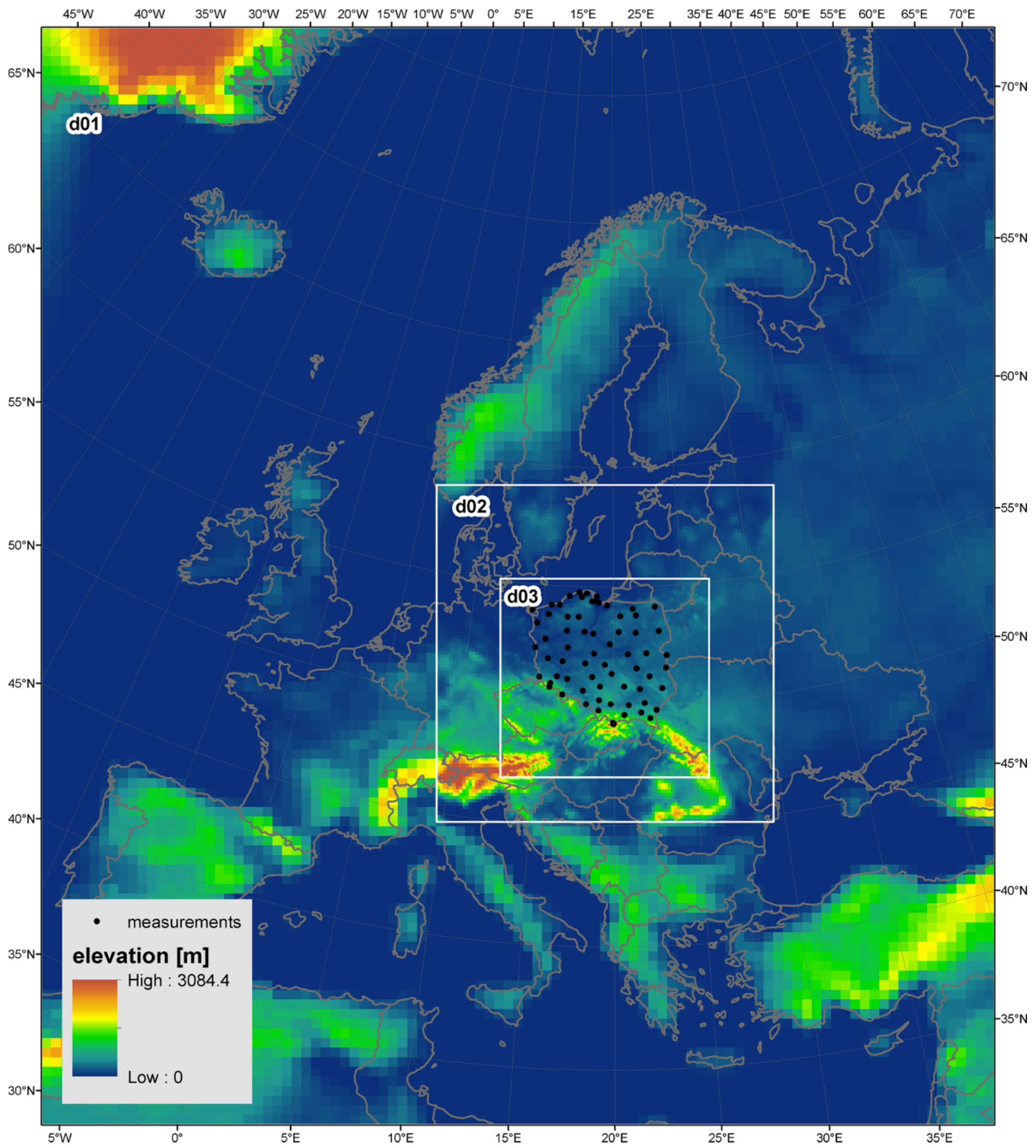

Figure 1
The WRF model domains and meteorological sites used for model evaluation

2.2. *The WRF Model Configuration*

The Advanced Research Weather Research and Forecasting Model (WRF) version 3.4.1 was used in this study (Skamarock *et al.* 2008). The model was run, for each year separately, for the 1981–2010 period. For each year, the simulation was started 14 days in advance, and these 14 days were treated as a spin-up time and removed from the analysis. The large-scale meteorological boundary conditions were taken from the ERA-Interim reanalysis of the European Centre for Medium Range Forecasting (Dee *et al.* 2011). The model configuration was selected after running and evaluation of the model for the chosen test periods (Kryza *et al.* 2013, 2015; Wałaszek *et al.* 2014a). The WRF model configuration applied in this study includes three one-way nested domains, with spatial resolution changing from 45 km × 45 km for the outermost domain (d01, 100 × 115 grid cells; Fig. 1) through 15 km × 15 km (d02, 106 × 106 grid cells), to 5 km × 5 km for the innermost domain (d03, 187 × 195 grid cells). All the domains have 51 vertical layers. The model configuration in terms of physics is summarized in Table 1. All the domains share the same options of physics for radiation, microphysics and boundary layer scheme. For convection, coarse-resolution domains d01 and d02 use the Kain–Fritsch scheme (Kain 2004). For the fine resolution d03, convection is explicitly resolved.

2.3. *Meteorological Measurements*

In this study, we use meteorological measurements provided by the Polish Institute of Meteorology and Hydrology-National Research Institute (IMGW-PIB), available for 66 stations located in Poland (Fig. 1). The focus of this study is on the meteorological variables which are of wide interest for other applications, including ecology and hydrology. The model evaluation is, therefore, presented for air temperature at 2 m (T2), relative humidity at 2 m (RH), wind speed (WSPD) and direction (WDIR) at 10 m. The measurements were available every 3 h. Only the data that passed the quality control at the IMGW-PIB are used for the model evaluation.

2.4. *Evaluation of the Model Results*

The WRF model results are compared with the measurements described above. For this comparison, we used the WRF model domain d03 data from a grid cell, in which the measuring site is located. It should be noticed here that we used the area averages (WRF model grid cell) and point values (measuring sites) in this work. The model error is calculated as the difference between the modelled and observed value, and the model performance was summarized using the following domain-wide error statistics:

- Mean error (ME)—calculated as the arithmetic mean from the model minus observation. This statistic indicates the general tendency for over- (ME >0) or underestimation (ME <0) of the given meteorological value by the model. The expected value is zero. The units are the same as for the analysed meteorological variable. For wind direction, the ME statistic is calculated as the shortest angular distance between the mean modelled and measured wind directions. The mean wind direction was calculated using the R software circular package. The positive/negative values of ME for wind direction mean that the modelled wind direction is shifted clockwise/counterclockwise if compared to the measurements.
- Mean absolute error (MAE)—calculated as an arithmetic mean of the absolute values of the model errors. The expected value is zero, and the units are the same as for the analysed meteorological variable. MAE was calculated for T2, RH and WSPD.
- Index of agreement (IOA)—calculated after Emery *et al.* (2001) as a standardized measure of the degree of model prediction error:

$$\mathrm{IOA} = 1 - \left[\frac{IJ \times \mathrm{RMSE}^2}{\sum_{j=1}^{J} \sum_{i=1}^{I} \left| P_j^i - M_o \right| + \left| O_j^i - M_o \right|} \right],$$

- where RMSE is the square root of the mean-squared difference in prediction–observation pairings with valid data within a given analysis region

Table 1

The WRF model physics options used in this study

	d01	d02	d03
Short-wave radiation	RRTMG (Iacono *et al.* 2008)		
Long-wave radiation	RRTM (Mlawer *et al.* 1997)		
Planetary boundary layer	Yonsei University scheme (Hong *et al.* 2006)		
Cumulus convection	Kain-Fritsch (Kain 2004)		Explicitly resolved
Microphysics	Goddard (Tao *et al.* 1989)		
Land surface model	Noah land surface model		

and for a given time, P_j^i is the individual predicted quantity at site i and time j, O_j^i is the individual observed quantity at site i and time j and M_O is the observed mean. IOA varies between 0 and 1, and the expected value is 1 (perfect model performance). IOA is unitless and was calculated for T2, RH2 and WSPD. The IOA is calculated for a given month using the 3-hourly values from all the stations and all the years considered.

- Pearson's correlation coefficient (R)—calculated using the R circular package suitable for handling circular data. This statistic was calculated for wind direction only. R varies between −1 and +1 and the expected value is +1. R is unitless.

All the above-mentioned statistics were calculated domain-wide for the entire study period of 1981–2010 and separately for each season: winter (December, January and February, DJF), spring (March, April and May, MAM), summer (June, July and August, JJA) and fall (September, October and November, SON). ME and IOA (R in the case of wind direction) were calculated also separately for each station and the season, to spatially assess the model performance. All the statistics were calculated using the model and measurements available every 3 h.

In our study, we evaluate the model performance for the long period of 1981–2010. It is, therefore, of interest to check if the model performance shows some temporal characteristics, e.g. if the model performs better for the more recent years. We analyse this issue using the Taylor diagrams (Taylor 2001). In each plot, prepared separately for each season, we summarize the model performance for each year of the study period. The details on the Taylor diagrams are provided by Taylor (2001). Also, we apply tests for statistical significance of the ME, MAE and IOA trends in the 1981–2010 period, using Mann–Kendall tests (Mann 1945; Kendall 1970).

3. Results

The results are organized as follows. First, the domain-wide error statistics are presented. Second, seasonal and diurnal variability in model performance is addressed and the spatial distribution of the model errors is presented. Finally, the model performance is summarized for each year separately, using the Taylor diagrams.

The model performance is summarized for the entire domain and the period of 1981–2010 in Table 2. The model has a general tendency for overestimation of the observed air temperature. The wind speed is also slightly overestimated. The relative humidity and wind direction have negative ME. For the WDIR, this means that the wind direction is shifted counterclockwise compared with the measurements. MAE is higher compared to ME and reaches 1.7 K for T2, 9 % for RH2 and 1.5 m s^{-1} for WSPD. In terms of Index of Agreement, the model is in very close agreement with the measurements for T2, with IOA above 0.99 (1.0 means a "perfect model performance"). For RH2 and WSPD, the Index of Agreement is lower, but still above 0.8. For WDIR, the Pearson correlation coefficient is close to 0.8 for the entire study period.

The general model performance, summarized with domain-wide statistics for the entire period 1981–2010, changes significantly if the statistics are calculated for months and seasons (Figs. 2 and 3). This is especially noticeable when ME is considered. The air temperature is underestimated for the winter months of January, February and December (Fig. 2). March and November have a mean error close to zero, and for the warm season the model overestimates the observed values of air temperature. For the relative humidity, the annual cycle in model performance is opposite, with an overestimation for cold months and underestimation for spring, summer and fall. For the wind speed, ME is above zero for all the months, except spring. The largest errors, in terms of absolute value of ME, are for late summer and fall. For the wind direction, the ME values are always below zero, and the largest errors, in terms of the absolute value of ME, are for spring and summer. IOA for T2 is very high for all the months, with slightly lower values for summer and fall. There is a strong annual cycle in IOA for relative humidity. The highest values of IOA are for the warm season months, with a drop in IOA for winter. Both the wind speed and direction show a similar annual cycle for the IOA and correlation coefficient, respectively. Cold season months have the highest values of IOA

Table 2

Domain-wide statistics for the entire 1981–2010 period

	T2	RH2	WSPD	WDIR
ME	0.23	−1.45	0.13	−7.60
MAE	1.66	8.93	1.45	–
IOA	0.99	0.86	0.82	–
R	–	–	–	0.78

For ME and MAE, the units are K for T2, % for RH2, m s^{-1} for WSPD and degrees for WDIR. IOA and R are unitless

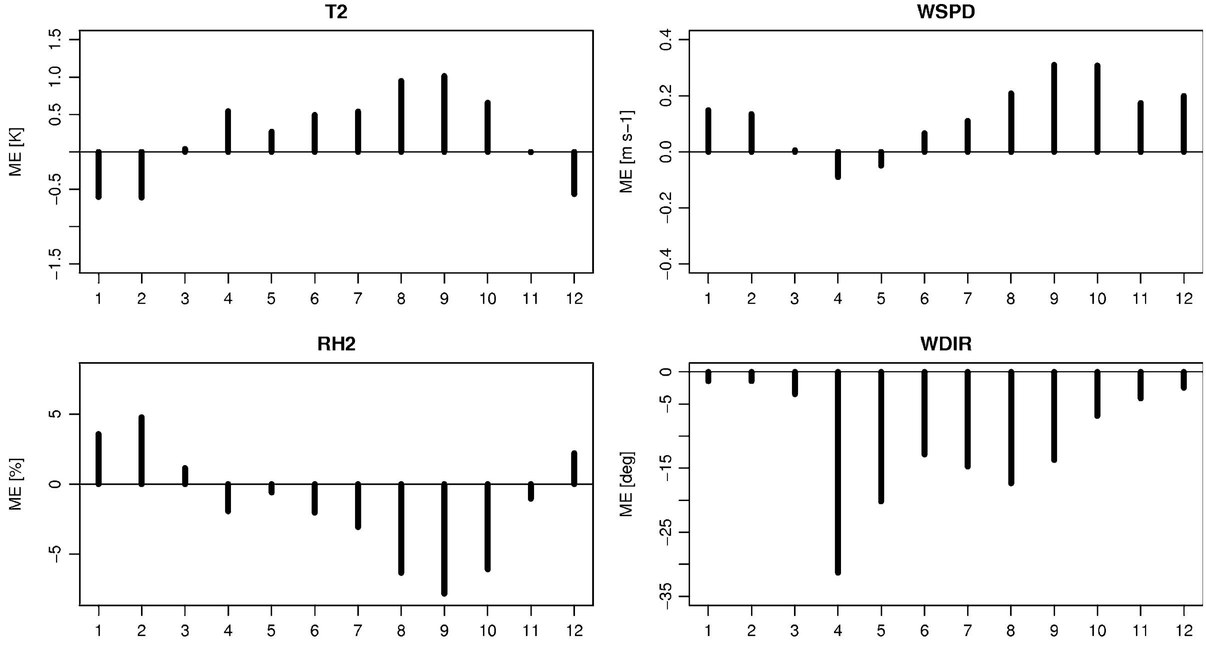

Figure 2
Domain-wide mean error for T2, WSPD, RH2 and WDIR for each month (*x* axis) in the 1981–2010 period

and R. The warm season is characterized by smaller values of these statistics.

For certain months, the model errors are significantly higher compared to the general summary presented in Table 2 and, for some months, the acceptance criteria, defined by Emery *et al.* (2001) for air temperature ME (−0.5 K < ME < 0.5 K), are not met. Noticeably, the annual variability in IOA statistic is very small, especially for T2. Here, the acceptance criteria defined by Emery *et al.* (2001) are met for T2 and WSPD (not defined for RH2 and WDIR).

Apart from the annual cycle in the model performance, the ME, MAE and IOA/R also show a daily pattern, which changes between the seasons (Figs. 4, 5). For the air temperature, ME is negative for all hours in winter and positive for summer and autumn. For winter, the largest ME, in terms of the absolute values, are calculated for night hours. For spring, summer and autumn months, the largest errors are observed for morning hours and, especially for summer and spring, are small in early afternoon. For spring, the air temperature is underestimated for 18 UTC. The relative humidity shows a reversed daily

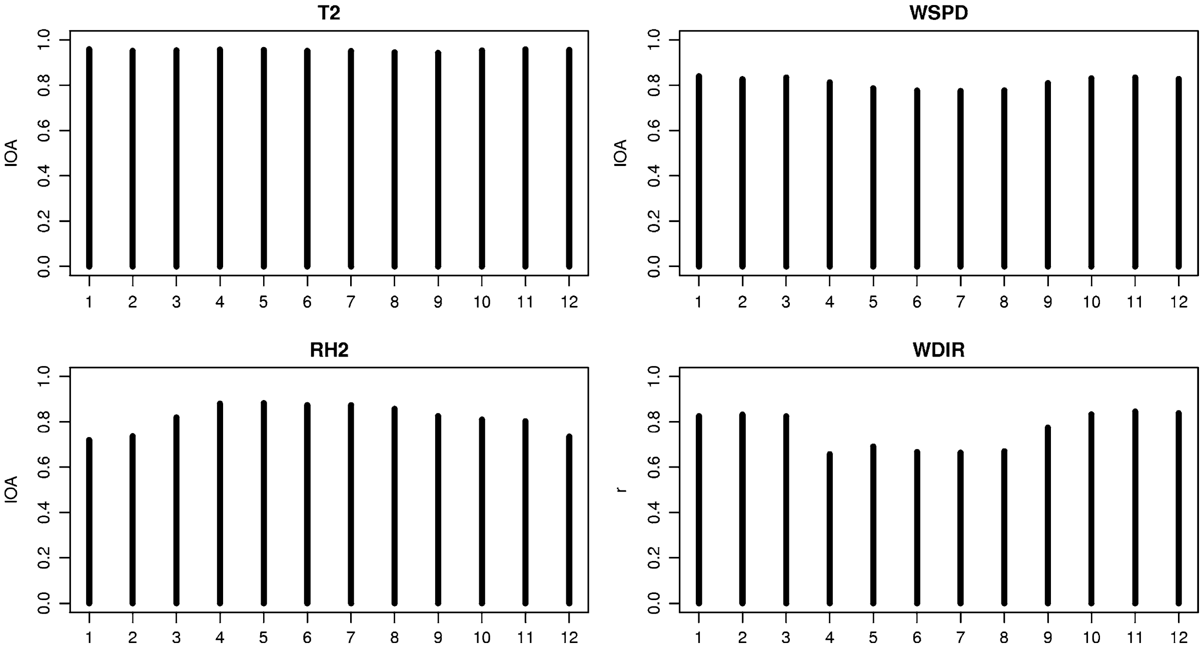

Figure 3
Domain-wide IOA for T2, WSPD, RH2 and R for WDIR for each month (*x* axis) in the 1981–2010 period

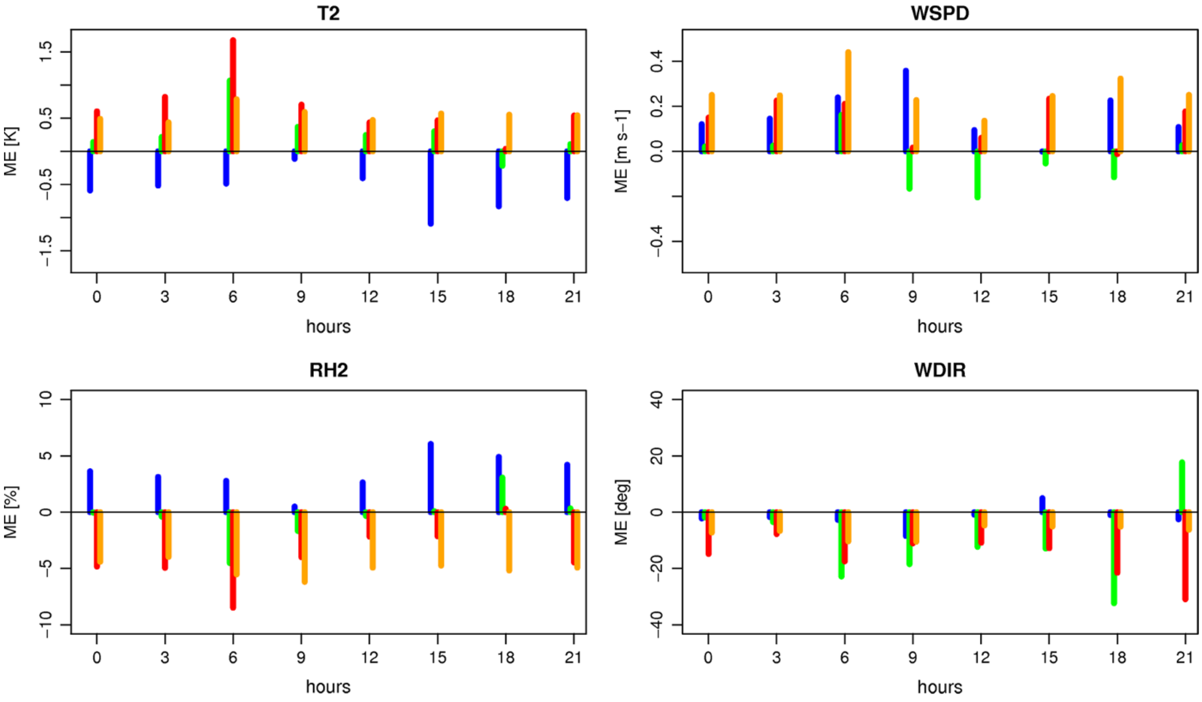

Figure 4
Daily cycle (hours—*x* axis) in ME for T2, WSPD, RH2 and WDIR for DJF (*blue*), MAM (*green*), JJA (*red*) and SON (*orange*)

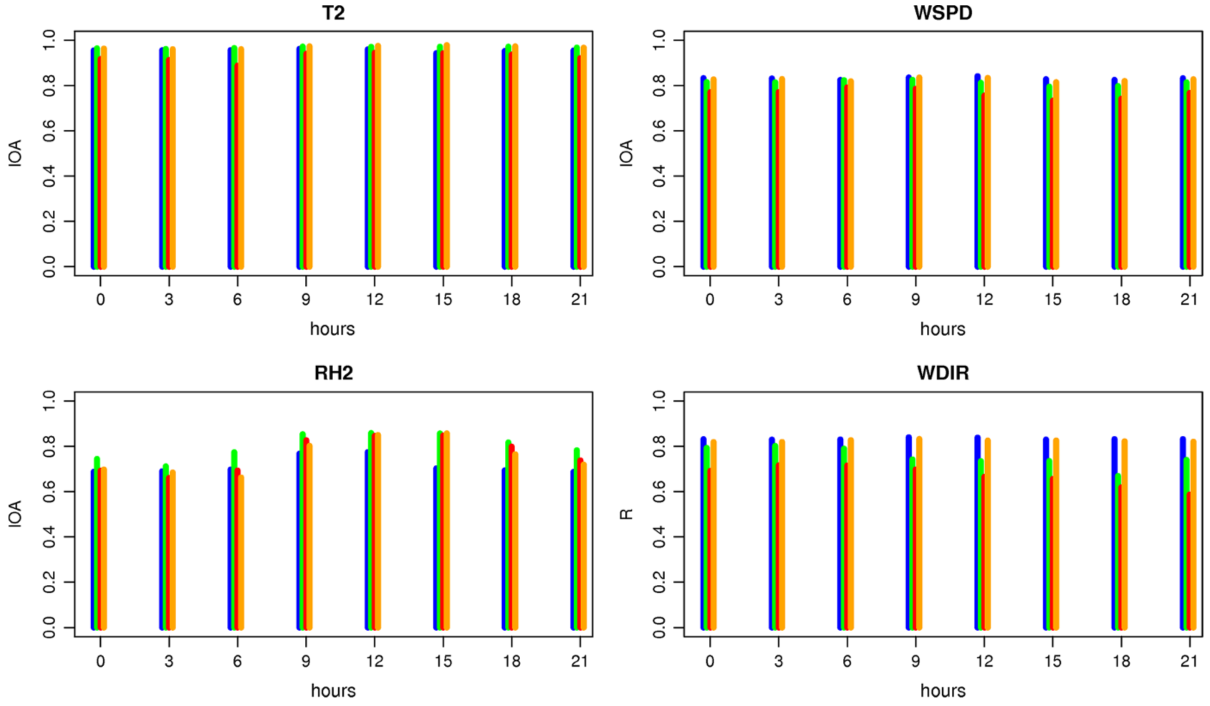

Figure 5
Daily cycle (hours—x axis) in IOA for T2, WSPD, RH2 and R for WDIR for DJF (*blue*), MAM (*green*), JJA (*red*) and SON (*orange*)

cycle. It is overestimated for winter for all hours and underestimated for the remaining seasons. This underestimation shows a pronounced daily pattern for summer, but not for autumn. For autumn, RH2 ME is ca. 5 % for the entire day, with slightly higher ME in terms of the absolute values for morning hours. For spring, ME is underestimated for 6 and 9 UTC and overestimated for 18 UTC. For the remaining hours, ME is close to zero.

The wind speed is overestimated for the entire day during winter, summer and autumn. For winter, ME is the highest for the night and morning hours. A similar pattern is for summer and autumn, but the minimum ME values are shifted towards earlier hours when compared to winter (9 and 12 UTC), and the highest ME are for 6 UTC and afternoon hours. For spring, there is a change of sign for ME during the day. Night and early morning hours are overestimated, with maximum at 6 UTC. For daytime (9–18 UTC), the model underestimates the observed wind speed. For the wind direction, ME is negative for all seasons and hours. The exceptions are for spring 21 UTC and winter 15 UTC. The absolute values of ME for WDIR are very small for winter and are considerably higher for spring and, especially, summer months. For both spring and summer seasons, the largest errors are for 6, 18 and 21 UTC. For 21 UTC, ME is negative for summer and positive for spring.

The daily cycle of IOA for the air temperature is not so pronounced as for ME. Especially for winter, spring and autumn, the IOA is at a very high level throughout the day. For summer, IOA is lower for all hours, if compared to other seasons, and the lowest values are calculated for 3 and 6 UTC. For the relative humidity, the daily cycle is stronger, compared to air temperature, and is similar for all seasons. The maximum values are for 9–15 UTC and there is a decrease in IOA for the night and morning. The IOA values are the highest for spring, when compared with other seasons.

There is practically no daily cycle in IOA for the wind speed. The IOA values differ between the seasons, but remain at ca. the same level for all hours. For wind direction, there is also no daily pattern in

IOA values for winter and autumn. For spring and summer, there is a decrease in IOA for afternoon hours (for summer also for 21 UTC).

The spatial patterns of all simulated meteorological variables analysed are in agreement with the general climatological knowledge for this area (Fig. 6, T2 and WSPD presented as an example). For the winter air temperature, there is a strong decrease in air temperature towards the east, with increasing continentality of climate. The warming effect of the Baltic Sea is noticeable along the coast. The coldest areas are the mountains in the south and lowlands in the north-eastern part of Poland, influenced by a more continental climate. A very similar pattern is observed in the measurements. The model reproduced very well the warm belt along the sea coast and

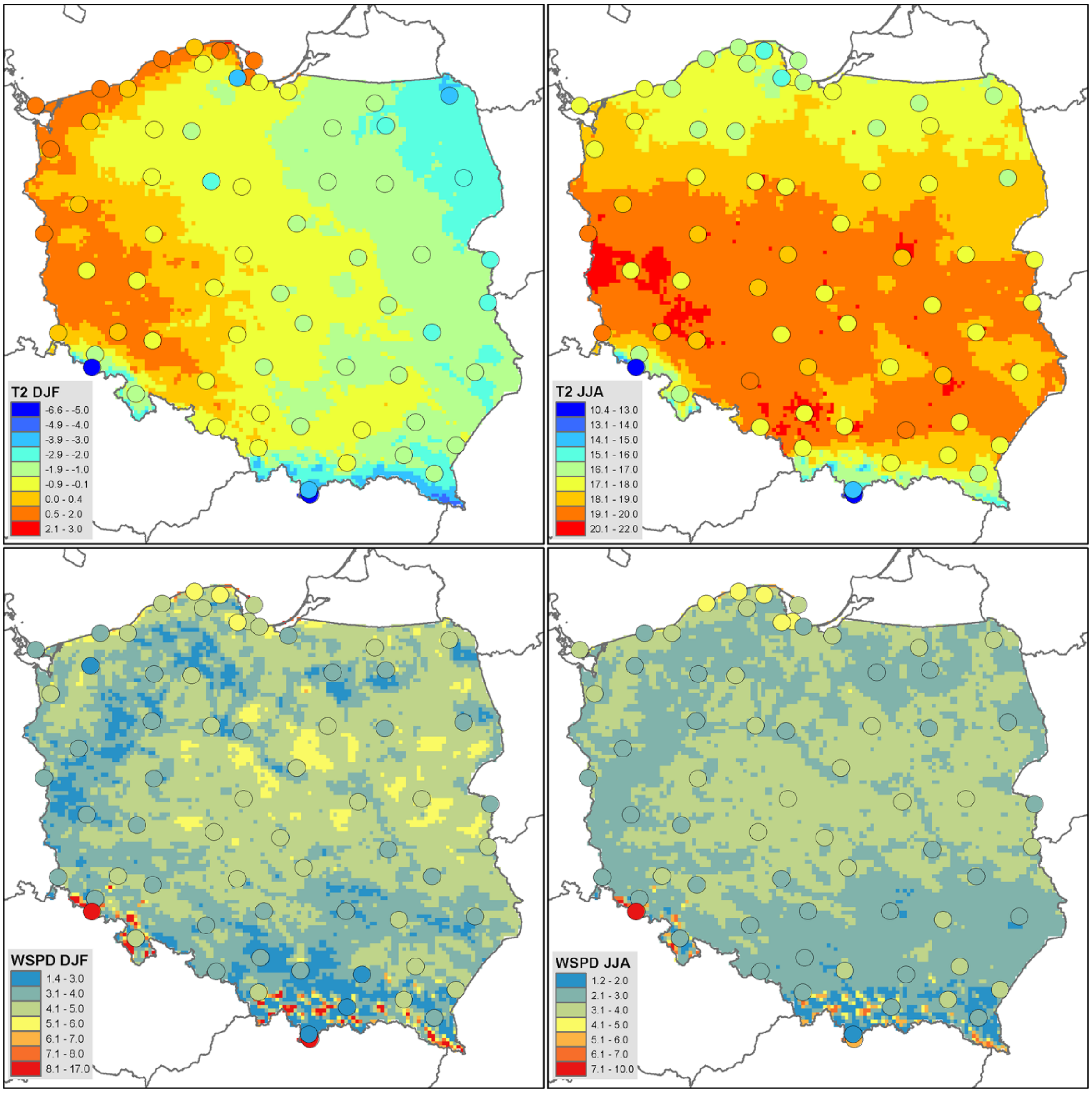

Figure 6
1981–2010 mean T2 (°C) and WSPD (m s^{-1}) for winter (DJF) and summer season calculated with WRF (gridded data) and measurements (points). Please notice inconsistent colour tables for winter and summer

the cold region in NE Poland. However, the warm areas of SW Poland are slightly overestimated compared with the measurements. For summer, the S–N gradient is stronger compared to winter (except for the mountains in the south, where the air temperature is determined by terrain height) and related to the elevation of the sun. The modelled summer air temperature is also higher than that measured for almost all of the stations shown in Fig. 6. This overestimation is stable for the entire area and does not exceed 1 K for the majority of the meteorological stations used in this comparison. The wind speed does not show significant changes in spatial pattern if winter and summer seasons are compared. In general, a higher wind speed is calculated for the winter season, and this is in agreement with the general climatological knowledge for this region. The highest wind speeds are observed and calculated with the WRF model for the narrow belt along the seashore (individual grid cells with wind speed exceeding 6 m s^{-1} for both winter and summer seasons) and for the mountains in the south (above 8 m s^{-1}), both for summer and winter seasons, and this is also confirmed by other studies for this area (e.g. Czernecki 2013). Large area of elevated wind speed in Central Poland is related to large frequency of winds from the west and lack of orographic barrier from this direction.

The spatial distribution of the IOA statistics for winter and summer seasons is presented in Fig. 7 with the example of T2 and WSPD. Both meteorological variables show some similar features. The IOA values are generally lower for the seashore stations and mountains in the south. This is both for winter and, especially, for summer, for which the IOA values are smaller. For the lowland stations of central Poland, the IOA values are very high for T2 for both seasons. For the wind speed, the lowland stations show smaller IOA in summer, compared to winter.

For the wind direction, the Pearson correlation coefficient for each station during the summer and winter seasons is presented in Fig. 8. There is a strong change in the model performance if winter and summer are compared. The correlation coefficient is higher for winter, when wind speed is, on average, stronger and exceeds 0.8 for the majority of the lowland stations. For summer, this statistic shows lower values for all the stations, and the decrease is the strongest for the seashore and the stations located in southern Poland. The station with the lowest R for wind direction, both for DJF and JJA, is Kłodzko, located in the mountain valley in SW Poland. This station is strongly influenced by the local orography (e.g. strong funnelling effects in winter during the frequent advections from the south); therefore, the spatial resolution of the WRF model (5 km × 5 km grid) may not be sufficient to properly resolve all the physical processes in this location.

In this study, the WRF model has been run for the 30-year period of 1981–2010. The question as to whether the model performance changes over time should be considered. This might be related to different reasons, including changes in the quality of the measurements, land use (constant land use was applied for all years) or the quality of the boundary and initial data. To address this question, the model performance has been summarized for each year and season separately and the model performance is summarized using the Taylor diagrams (Fig. 9). There is no statistically significant trend in model performance for all four meteorological parameters considered (only T2 and WSPD are presented for consistency) and all the model performance matrices used. The year-to-year changes in the model performance can be attributed to natural variability of climate. Year-to-year changes are especially large for the winter season and T2, with the two outliers in the plot for years 1982 and 2010. Year 2010 is also away from all the remaining points for winter WSPD (Fig. 9). For summer, all the years are clustered in the plot and characterized by similar values of correlation and standard deviation. For WSPD, some clustering is also present, especially in winter, and lower correlations for the summer season.

4. *Summary and Conclusions*

In our study, we have applied the regional domain Weather Research and Forecasting model to dynamically downscale the coarse-resolution Era-Interim data to a high spatial resolution of 5 km × 5 km grid. The application of the regional meteorological model

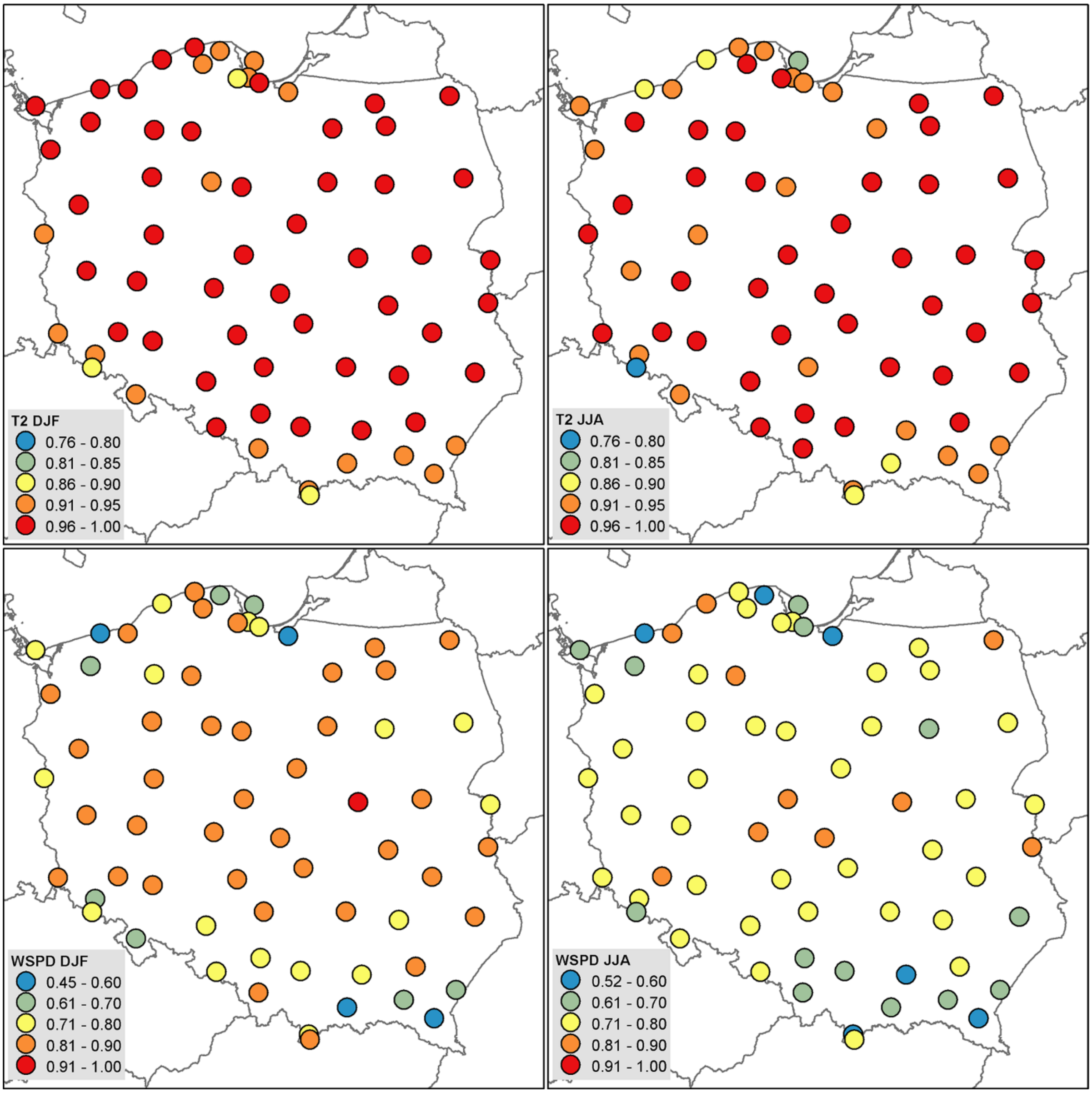

Figure 7
IOA for T2 and WSPD for the 1981–2010 period for the winter (DJF) and summer (JJA) seasons

WRF for the long-term period was undertaken to provide consistent spatial meteorological information for the entire area of Poland to various stakeholders who require this kind of information. Noticeably, this information has already supported ecological studies on tick activity (Kiewra *et al.* 2014) and hydrological forecasting with HydroProg model (Jeziorska and Niedzielski 2015, this issue). To our knowledge, this is the first study that analyses the WRF model performance for this geographical area at high spatial and temporal resolution and for a long-term period of 30 years. Therefore, the main focus of this paper was on the general quantification of the model performance for the meteorological variables, which are of

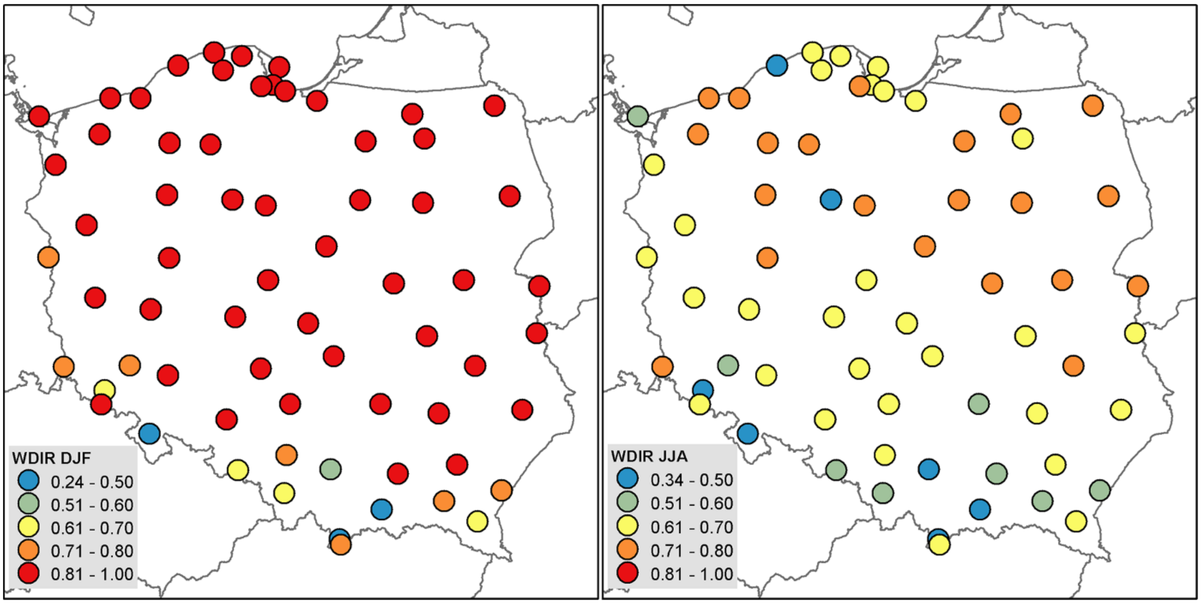

Figure 8
Correlation coefficient for WDIR for the 1981–2010 period for the winter (DJF) and summer (JJA) seasons

wide interest for other researches, e.g. for such problems as air temperature and humidity, wind speed and direction.

The WRF model results are, in general, in good agreement with the measurements. The model performance is better for the cold season and worse for warm months. This is especially clear for the mean error and might be linked with stronger convection in summer and larger variability of meteorological conditions. For summer, the WRF model was also found to be in worse agreement with the measurements for wind direction compared to other variables (T2 and RH2), and this supports the earlier findings by Czernecki (2013). For the wind direction, it is also noticeable that the current spatial resolution of the model domain may not be sufficient to properly resolve the wind conditions in areas of complex terrain. An example is the Kłodzko station, for which the model did not properly reflect strong funnelling effects, caused by specific terrain configuration. The other issues are related with wind measurements, including changes of sensors during this long-term period, e.g. in the 1990s.

There are strong seasonal and diurnal cycles in the model performance, which are especially clear for the mean error statistics. The WRF model underestimates the air temperatures for cold seasons and overestimates them for warm periods. Similar findings were presented for Eastern Europe (EURO-CORDEX subdomain EA) by Kotlarski *et al.* (2014) using the multi-model ensemble approach. The underestimation in winter is observed for the entire day. Also for the warm season, the air temperature is overestimated for the entire day. The cycles are of opposite sign if T2 and RH2 are considered. All these cycles might be of importance for further application of the downscaling results, e.g. in hydrological modelling with the deterministic models. An example is TOPMODEL (Jeziorska and Niedzielski 2015, this issue), for which the temporal variability of evaporation has to be provided. There is a decrease in the model performance for wind speed and direction during hours with low wind speed. Large errors for these hours might also be related with errors in the wind speed measurements, which are of higher uncertainty for calm wind.

The index of agreement statistics is very high for air temperature, regardless of season. The IOA values are above 0.9 for all months and hours, which means that the WRF model results meet the acceptance

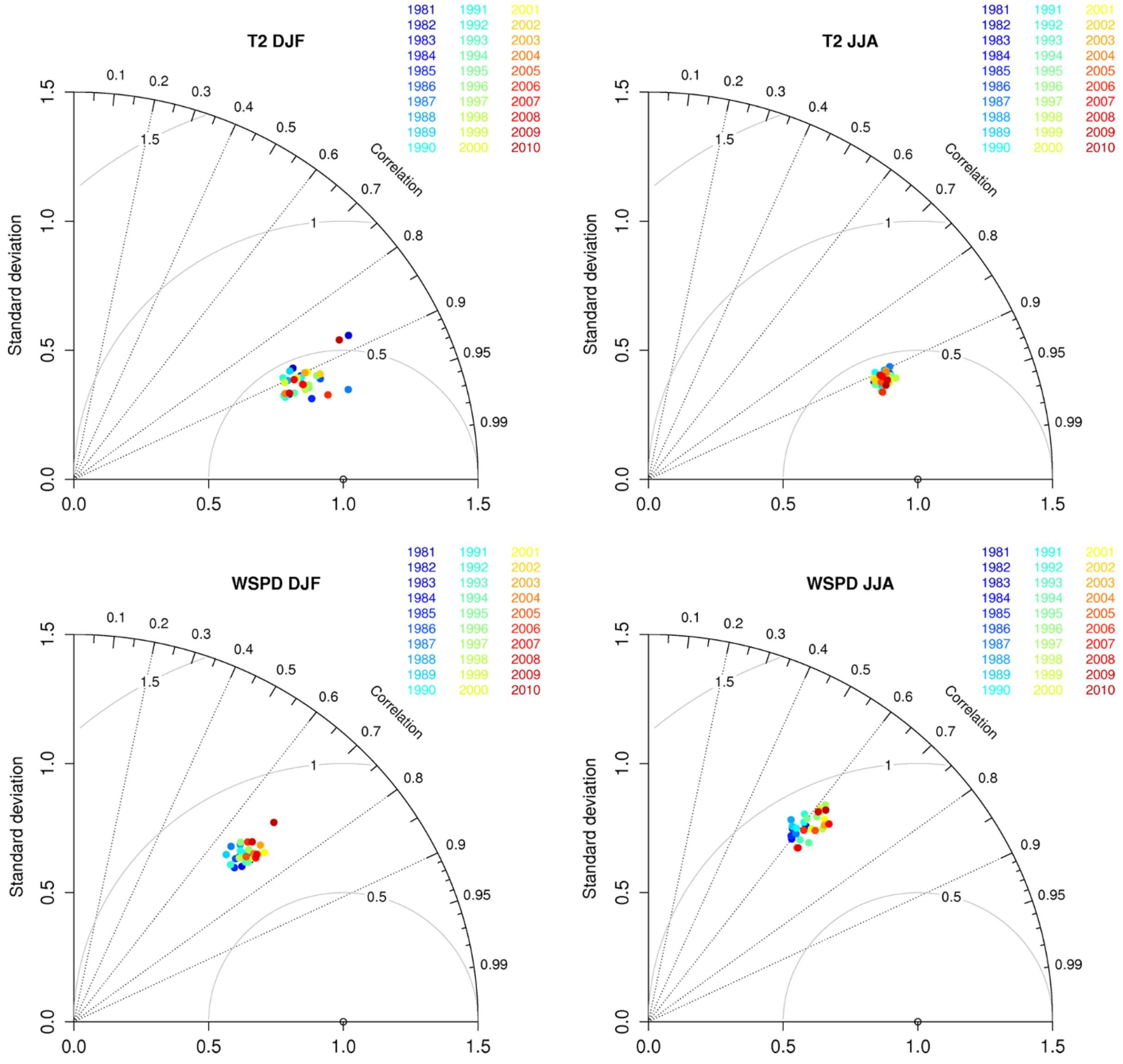

Figure 9
Normalized Taylor diagrams for T2 and WSPD for the winter (*left column*) and summer (*right*)

criteria proposed by Emery *et al.* (2001) for air temperature at IOA >0.7. This means that the results obtained in this study are reliable and applicable for other research. The criteria are also met for wind speed (IOA >0.6). However, the mean error for air temperature usually exceeds the ±0.5 threshold proposed by Emery *et al.* (2001), which suggests the need for application of the bias correction before the results are applied to other studies. For summer, there is a negative bias for air temperature and positive for relative humidity. The magnitude of this bias shows small spatial variability and is below 1 K for air temperature and 5 % for relative humidity.

Spatial and seasonal changes in the index of agreement are small for air temperature and relative humidity. For the wind speed, the changes are more pronounced. For all the meteorological variables considered, the model performance is worse for the seashore and mountain areas. Especially for the mountains, this could be related to insufficient spatial resolution of the WRF model domain. This is especially clear if the specific stations, like Kłodzko, located in a valley, are considered. Here, strong wind funnelling effects are observed, which were not resolved properly by the model because of the smoothing of the terrain topography by the application of the 5 km × 5 km grid. However, the uncertainty related to wind speed and direction measurements, mentioned above, is also of importance here.

Spatial distribution of meteorological variables obtained with the WRF model is in close agreement both with the station measurements and with general climatological knowledge for this area. Some seasonal and spatial features are well resolved by the model, including the warm belt along the sea coast, and the east–west gradient in spatial pattern of air temperature for winter. The 5 km × 5 km model resolution results in a high spatial variability of the meteorological variables, especially for wind speed over mountainous regions. However, this resolution might still not be sufficient for solving local meteorological phenomena, which was demonstrated, e.g. by CZERNECKI (2013).

There is no statistically significant temporal trend in the model performance. The larger year-to-year changes in the model performance, e.g. for year 1982 and 2010 for the air temperature should, therefore, be linked with the natural variability of meteorological conditions.

The results of this study have generated a substantial spatial meteorological data set, which will be made available using the OGC services to a wide community. It is therefore important to know the limitations of this database before this information is used for other research. There is also a need for further evaluation of the WRF model results for the study area. This has already been undertaken by CZERNECKI (2013) for wind speed, WAŁASZEK *et al.* (2014b) solar radiation and cloudiness and KRYZA *et al.* (2015) the planetary boundary layer height. This is especially important as the WRF model becomes widely used for this area for various applications, e.g. aerosol feedback effect studies (WERNER *et al.* 2015a, this issue), emission modelling (WERNER *et al.* 2015b) and wind energy (CZERNECKI 2013).

Acknowledgments

This work was supported by the National Science Centre (NCN), Poland (Grants No. N N404 014 740 and UMO-2011/03/B/ST10/06226). Calculations were carried out in the Wroclaw Centre for Networking and Supercomputing (http://www.wcss.wroc.pl), Grant No. 170. Meteorological measurements for this work were provided by the Institute of Meteorology and Water Management, National Research Institute.

REFERENCES

BENESTAD, R.E., HANSSEN-BAUER, I., CHEN, D., Empirical-Statistical downscaling (World Scientific Publishing, Singapore 2008).

CZERNECKI, B. (2013), *Creating wind field time-series over the Southern Baltic area using a dynamical downscaling approach*, Meteorologische Zeitschrift *22*, 587–593.

DEE, D.P., UPPALA, S.M., SIMMONS, A.J., BERRISFORD, P., POLI, P., KOBAYASHI, S., ANDRAE, U., BALMASEDA, M.A., BALSAMO, G., BAUER, P., BECHTOLD, P., BELJAARS, A.C.M., VAN D BERG, L., BIDLOT, J., BORMANN, N., DELSOL, C., DRAGANI, R., FUENTES, M., GEER, A.J., HAIMBERGER, L., HEALY, S.B., HERSBACH, H., HOLM, E.V., ISAKSEN, L., KALLBERG, P., KOHLER, M., MATRICARDI, M., MCNALLY, A.P., MONGE-SANZ, B.M., MORCRETTE, J.J., PARK, B.K., PEUBEY, C., DE ROSNAY, P., TAVOLATO, C., THEPAUT, J.N. AND VITART, F. (2011), *The Era-Interim reanalysis: configuration and performance of the data assimilation system,* Quarterly Journal of the Royal Meteorological Society *137*, 553–597.

EMERY, C., TAI, E., GREG, Y., 2001. Enhanced Meteorological Modeling and Performance Evaluation for Two Texas Ozone Episodes. Report to the Texas Natural Resource Conservation Commission, College Station, TX, USA, pp 235.

FUENTES U, HEIMANN D (2000): *An improved statistical-dynamical downscaling scheme and its application to the Alpine precipitation climatology*. Theor. Appl. Climatol. *65*: 119–135.

GIORGI, F., and BATES, G.T. (1989), *The climatological skill of a regional model over complex terrain*, Monthly Weather Review *117*, 2325–2347.

Giorgi F., Gutowski W.G., 2015, *Regional dynamical downscaling and the CORDEX initiative*, Annual Review of Environment and Resources, doi: 10.1146/annurev-environ-102014-021217.

Grell, G.A., and Freitas, S.R. (2013), *A scale and aerosol aware stochastic convective parameterization for weather and air quality modelling*, Atmos Chem Phys Discuss *13*, 23845–23893.

Hernandez-Ceballos, M.A., Skjoth, C.A., Garcia-Mozo, H., Bolivar, J.P. and Galan C. (2014), *Improvement in the accuracy of back trajectories using WRF to identify pollen sources in southern Iberian Peninsula*, International journal of biometeorology *58*, 2031–2043.

Heikkila, U., Sandvik, A., Sorteberg, A. (2011), *Dynamical downscaling of ERA-40 in complex terrain using the WRF regional climate model*, Climate Dynamics *37*, 1551–1564.

Hong, S-Y. and Dudhia, J. (2012), *Next generation numerical weather prediction: bridging parameterization, explicit clouds and large eddies*, Bull Amer Meteor Soc 93, http://dx.doi.org/10.1175/2011BAMS3224.1.

Hong, S.Y. and Kanamitsu, M. (2014), *Dynamical Downscaling: Fundamental Issues from a NWP Point of View and Recommendations*, Asia-Pac. J. Atmos. Sci. *50*(1), 83–104.

Hong, S.-Y., Noh, Y., and Dudhia, J. (2006), *A New Vertical Diffusion Package with an Explicit Treatment of Entrainment Processes*, Monthly Weather Review *134*(9), 2318–2341.

Huth, R., Misovsky, J., Stepanek, P., Belda, M., Farda, A., Chladova, Z. and Pisoft, P. (2015), *Comparative validation of statistical and dynamical downscaling models on a dense grid in central Europe: temperature*, Theoretical and Applied Climatology doi: 10.1007/s00704-014-1190-3.

Iacono, M. J., Delamere, J. S., Mlawer, E. J., Shephard, M. W., Clough, S. A., and Collins, W. D. (2008), *Radiative forcing by long-lived greenhouse gases: Calculations with the AER radiative transfer models*, Journal of Geophysical Research: Atmospheres *113*(D13), D13103. doi:10.1029/2008JD009944.

Jeziorska, J. and Niedzielski, T. (2015), Applicability of TOPMODEL in the mountainous catchments in the upper Nysa Kłodzka River basin (SW Poland), Pure and Applied Geophysics (in revision, this issue).

Katragkou E., Garcia-Diez M., Vautard R., Sobolowski S., Zanis P., Alexandri G., Cardoso R.M., Colette A., Fernandex J., Gobiet A., Goergen K., Karacostas T., Knist S., Mayer S., Soares P.M.M., Pytharoulis I., Tegoulias I., Tsikerdekis A., Jacob D., 2015, *Regional climate hindcast simulations with EURO-CORDEX: evaluation of a WRF multi-physics ensemble*, Geosci. Model Dev. doi:10.5194/gmd-8-603-2015.

Kain, J. S. (2004), *The Kain–Fritsch Convective Parameterization: An Update*, Journal of Applied Meteorology *43*(1), 170–181.

Kendall, M.G., (1970), *Rank Correlation Methods.* 4th Ed. (Griffin 1976).

Kiewra, D., Kryza, M. and Szymanowski, M. (2014), *Influence of selected meteorological variables on the questing activity of Ixodes ricinus ticks in Lower Silesia, SW Poland*, Journal of Vector Ecology *39*, 138–145.

Kim, J.-W., Chang, J.-T., Baker, N.L., Wilks, D.S. and Gates, W.L. (1984), *The statistical problem of climate inversion: determination of the relationship between local and large-scale climate*, Monthly Weather Review *112*, 2069–2077.

Kryza, M., Werner, M., Waiaszek, K. and Dore, A.J. (2013), *Application and evaluation of the WRF model for high-resolution forecasting of rainfall—a case study of SW Poland*, Meteorologische Zeitschrift *22*, 595–601.

Kryza, M., Guzikowski, J., Werner, M., Szymanowski, M., Waiaszek, K. and Dore A.J. (2015), Performance of the WRF model and sensitivity to microphysics, planetary boundary layer and radiation schemes: a case study from Poland, Atmospheric Research (in revision).

Kotlarski S., Keuler K., Christensen O.B., Colette A., Deque M., Gobiet A., Goergen K., Jacob D., Luthi D., van Meigaard E., Nikulin G., Schar C., Teichmann C., Vautard R., Warrach-Sagi K., Wulfmeyer V., 2014, *Regional climate modelling on European scales: a joint standard evaluation of the EURO-CORDEX RCM ensamble*, Geosci. Model Dev. doi:10.5194/gmd-7-1297-2014.

Lorenc, H., Atlas Klimatu Polski, (IMGW 2005) (in Polish).

Mann, H.B. (1945), *Nonparametric tests against trend*, Econometrica *13*, 245–259.

Marosz, M. and Jakusik, E. (2014), *Downscaling of PDFs of daily air temperature on northern Poland: assessment of predictors*, Meteorologische Zeitschrift *23*, 167–174.

Marosz, M., Wójcik, R., Pilarski, M. and Miętus, M. (2013), *Extreme daily precipitation totals in Poland during summer: the role of regional atmospheric circulation*, Clim Res *56*, 245–259.

Mlawer, E. J., Taubman, S. J., Brown, P. D., Iacono, M. J., and Clough, S.A. (1997), *Radiative transfer for inhomogeneous atmospheres: RRTM, a validated correlated-k model for the longwave*, Journal of Geophysical Research: Atmospheres *102*(D14), 16663–16682.

Murphy, J. (1999), *An evaluation of statistical and dynamical techniques for downscaling local climate*, J. Climate *12*, 2256–2284.

Ojrzyńska, H., Kryza, M., Waiaszek, K., Szymanowski, M., Werner, M. and Dore A.J. (2015), High resolution dynamical downscaling of ERA-Interim using the WRF regional climate model for the area of Poland. Part 2: model performance with respect to automatically derived circulation types, Pure and Applied Geophysics. doi:10.1007/s00024-016-1273-4.

Pavlik, D., Soehl, D., Pluntke, T., Mykhnovych, A. and Bernhofer, C. (2011), *Dynamical downscaling of global climate projections for Eastern Europe with a horizontal resolution of 7 km*, Environ Earth Scie *65*, 1475–1482.

Pielke, R.A. Sr (2013), *Comments on "The North American Regional Climate Change Assessment Program: Overview of Phase I results"*, Bull Amer Meteor Soc 1075–1077.

Reyers M, Pinto JG, Moemken J (2015): Statistical-dynamical downscaling for wind energy potentials: evaluation and applications to decadal hindcasts and climate change projections. Int. J. Climatol. *35*: 229–244.

Skamarock, W.C., Klemp, J.B., Dudhia, J., Gill, D.O., Barker, D.M., Duda, M., Huang, X.-Y., Wang, W. and Powers J.G., A description of the advanced research WRF version 3, (Technical report TN-475 + STR, NCAR 2008).

Shrestha, D.L, Robertson, D.E., Wang, Q.J., Pagano, T.C. and Hapuarachchi H.A.P. (2013), *Evaluation of numerical weather prediction model precipitation forecasts for short-term streamflow forecasting purpose*, Hydrol Earth Syst Sci *17*, 1913–1931.

Soares, P.M.M., Cardoso, R.M., Miranda, P.M.A., de Medeiros, J., Belo-Pereira, M., Espirito-Santo, F. (2012), *WRF high resolution dynamical downscaling of ERA-Interim for Portugal*, Climate Dynamics *39*, 2497–2522.

Tao, W.-K., Simpson, J., and McCumber, M. (1989), *An Ice-Water Saturation Adjustment*, Monthly Weather Review *117*(1), 231–235.

TAYLOR, K.E. (2001), *Summarizing multiple aspects of model performance in a single diagram*, Journal of Geophysical Research *106*, 7183–7192.

WAŁASZEK, K., KRYZA, M. and WERNER, M. (2014), *Evaluation of the WRF meteorological model results during a high ozone episode in SW Poland—the role of model initial conditions*, International Journal of Environment and Pollution *54*, 193–202.

WAŁASZEK, K., KRYZA, M. and WERNER M. (2014), A Sensitivity Analysis of the WRF Model to Shortwave Radiation Schemes for Air Quality Purposes and Evaluation with Observational Data, Air Pollution Modeling and its Application XXIII, pp. 539–543.

WAŁASZEK, K., KRYZA, M., SZYMANOWSKI, M., WERNER, M. and OJRZYŃSKA H. (2015), Sensitivity study of cloud cover and ozone modeling to microphysics parameterization, Pure and Applied Geophysics (this issue).

WERNER, M., KRYZA, M., DORE, A.J., BŁAŚ, M., HALLSWORTH, S., VIENO, M., TANG, Y.S. and SMITH R.I. (2011), *Modelling of marine base cation emissions, concentrations and deposition in the UK*, Atmospheric Chemistry and Physics *11*, 1023–1037.

WERNER, M., KRYZA, M., SKJØTH A.C., WAŁASZEK, K., DORE A.J. and OJRZYŃSKA, H. (2015a), Aerosol-radiation feedback and PM10 air concentrations over Poland, Pure and Applied Geophysics (this issue).

WERNER, M., SKJØTH A.C., KRYZA, M. AND DORE, A.J. (2015b), Understanding emissions of ammonia from buildings and application of fertilizers: an example from Poland, Biogeosciences Discuss.

(Received January 20, 2015, revised February 16, 2016, accepted March 11, 2016, Published online March 30, 2016)

Pure Appl. Geophys. 174 (2017), 527–550

DOI 10.1007/s00024-016-1273-4

Pure and Applied Geophysics

High-Resolution Dynamical Downscaling of ERA-Interim Using the WRF Regional Climate Model for the Area of Poland. Part 2: Model Performance with Respect to Automatically Derived Circulation Types

Hanna Ojrzyńska,[1] Maciej Kryza,[1] Kinga Wałaszek,[1] Mariusz Szymanowski,[2] Małgorzata Werner,[1,3] and Anthony J. Dore[4]

Abstract—This paper presents the application of the high-resolution WRF model data for the automatic classification of the atmospheric circulation types and the evaluation of the model results for daily rainfall and air temperatures. The WRF model evaluation is performed by comparison with measurements and gridded data (E-OBS). The study is focused on the area of Poland and covers the 1981–2010 period, for which the WRF model has been run using three nested domains with spatial resolution of 45 km × 45 km, 15 km × 15 km and 5 km × 5 km. For the model evaluation, we have used the data from the innermost domain, and data from the second domain were used for circulation typology. According to the circulation type analysis, the anticyclonic types (AAD and AAW) are the most frequent. The WRF model is able to reproduce the daily air temperatures and the error statistics are better, compared with the interpolation-based gridded dataset. The high-resolution WRF model shows a higher spatial variability of both air temperature and rainfall, compared with the E-OBS dataset. For the rainfall, the WRF model, in general, overestimates the measured values. The model performance shows a seasonal pattern and is also dependent on the atmospheric circulation type, especially for daily rainfall.

Key words: Atmospheric circulation, rainfall, air temperature, WRF, dynamical downscaling, ERA-Interim, circulation types.

1. Introduction

Spatial meteorological information is a key element in various environmental studies, including air pollution, hydrology (Jeziorska and Niedzielski 2015, this issue) and wind energy production (Badger *et al.* 2014; Mendez *et al.* 2014). This information can be provided in various ways, including GIS-based interpolation (Szymanowski *et al.* 2013) and statistical or dynamical downscaling (Giorgi and Bates 1989; Lo *et al.* 2008; Czernecki 2013). There is also a combined approach, named statistical–dynamical downscaling, which has also gained importance in climate research in recent years. Statistical–dynamical downscaling combines the benefit of both techniques and was presented, e.g. by Fuentes and Heimann (2000) and Reyers *et al.* (2015). The performance of these approaches is also evaluated in different ways, by comparing the results with available measurements and with other reference spatial data, including gridded information.

Atmospheric circulation plays a major role in daily, seasonal and spatial distribution of weather-related parameters, including air temperature and rainfall. Poland (Central Europe) is notable for transitional characteristics of climate, from maritime in the west to more continental in the east, and this region is the focus of the current study. There are many studies that link the local meteorological features, usually based on station measurements, with large-scale circulation patterns, classified into different groups using various approaches. For example, Osuchowska-Klein (1992) and Niedźwiedź (1981) analysed the relation between the air temperature and

---

[1] Department of Climatology and Atmosphere Protection, Institute of Geography and Regional Development, Wrocław University, ul. Kosiby 8, 51-621 Wrocław, Poland. E-mail: maciej.kryza@uwr.edu.pl

[2] Department of Geoinformatics and Cartography, Institute of Geography and Regional Development, Wrocław University, pl. Uniwersytecki 1, 50-137 Wrocław, Poland.

[3] National Pollen and Aerobiology Research Unit, University of Worcester, Henwick Grove, Worcester WR2 6AJ, UK.

[4] Centre for Ecology and Hydrology, Bush Estate, Penicuik, Midlothian EH26 0QB, UK.

atmospheric circulation using a classification based on sea level pressure, while other authors proved that the spatial variability of air temperature and precipitation is highly correlated with the geopotential height at upper isobaric levels (Wibig 1991, 2001; Kożuchowski *et al.* 1992). Ustrnul (2000) and Ustrnul *et al.* (2010) have shown that a circulation type with anticyclonic ridge forms the most favourable conditions for the high air temperatures in summer. For winter, anticyclonic types with easterly flows are favourable for extremely low air temperatures. Synoptic conditions favourable to frosty, freezing and severe freezing days for Poland were analysed by Bielec-Bąkowska and Łupikasza (2009) and Ustrnul *et al.* (2014). Bednorz (2012) and Bednorz and Wibig (2008) showed that the atmospheric circulation has a large impact on intense thaws and snow conditions. Łupikasza (2010) analysed the relationship between atmospheric circulation and high daily precipitation in Poland, using various methods of classifications of circulation types. Niedźwiedź (1981), Twardosz and Niedźwiedź (2001) and Twardosz *et al.* (2011) analysed the role of synoptic circulation patterns on daily rainfall in south-west Poland for a long period and found that the advection of air masses from the west and cyclonic troughs are the most favourable to precipitation events. Finally, the circulation patterns were used during the construction of the GIS-based maps of meteorological elements spatial variability (Ustrnul 2006; Ojrzyńska 2015).

A detailed weather and climate analysis based on various data sets should be supported by the analysis of atmospheric circulation. There are different approaches to the classification of circulation types, and several of these methods were applied for the study area addressed in this paper (e.g. Litynski 1969; Niedźwiedź 1981; Osuchowska-Klein 1978; Gerstengarbe *et al.* 1993; Ustrnul 1997; Wibig 2001; Huth *et al.* 2008; Piotrowski 2009; Woyciechowska and Ustrnul 2011; Bednorz 2012). The results of the 733 COST action *Harmonisation and applications of weather type classification for European Regions* (cost733.met.no/FinalEvent.html) emphasize that high spatial variability of atmospheric circulation patterns preclude a general and universal method for circulation type classification and justifies the development and application of regional methodology. A long time series of meteorological data provides the opportunity to apply complex classification schemes with large numbers of distinct types. This kind of classifications could be troublesome in statistical analysis and practical applications, but also more circulation types allow a more detailed weather description in case studies. In this study, we develop an approach similar to the Objective Weather Type Classification (Die objective Wetterlagenklassifikation) of the German Weather Service (Bissolli and Dittmann 2001), which, apart from e.g. cyclonality and direction of the air masses advection, utilizes information on the humidity of the air. A modification of the original classification scheme described by Bissolli and Dittmann (2001) was previously successfully applied for the Sudetes Mountains (SW Poland) and their foreland (Ojrzyńska 2015), using coarse resolution gridded meteorological data. Here, the objective classification scheme is fed with the WRF-derived meteorological information, available at high spatial resolution. This is a novelty, as previous studies used coarse resolution meteorological information for classification of circulation types, coming from global reanalysis databases like NCEP or ERA (Ustrnul 1997; Bissolli and Dittmann 2001; Piotrowski 2009; Woyciechowska and Ustrnul 2011; Ojrzyńska 2015).

In the first part of this twin paper (Kryza *et al.* 2016), we have evaluated the results of the ERA-Interim dynamical downscaling with the Weather Research and Forecasting (WRF) model for the period 1981–2010 using 3-hourly measurements of air temperature, humidity and wind speed and direction. Here, the focus is on evaluation of daily rainfall and air temperature for the same period, with the context of synoptic situation. Earlier reports by Jiménez *et al.* (2013) suggest that the model performance might rely on the synoptic situation, and their analysis was focused on wind condition for complex terrain.

In this work, we first describe and apply a method for automatic classification of the circulation types (ACCT) in Poland and then apply the method to the extended period of 1981–2010 with WRF model data. Secondly, we compare the WRF model for daily rainfall and air temperature with respect to the circulation types derived by application of the ACCT method. The analysis of the regional dynamical downscaling with the WRF model is complemented by comparison with spatial data obtained through a geostatistical (spatial interpolation) method. This spatial comparison is also performed with respect to the circulation type, to assess if the model performance changes with the atmospheric circulation pattern.

2. *Data and Methods*

2.1. *The WRF Model*

The details of the WRF model (Skamarock *et al.* 2008) configuration are provided in the first part of this twin paper (Kryza *et al.* 2016). Here, we only provide some important remarks on the model configuration. The model has been run for a 30-year long period of 1981–2010, using ERA-Interim data as initial and boundary conditions. The model was applied for three one-way nested domains: d01 (45 km × 45 km grid for Europe), d02 (15 km × 15 km grid for Central Europe) and d03 (5 km × 5 km grid for Poland). In this study, we compare the measurements with the results from the innermost domain (d03) covering Poland with a 5 km × 5 km grid resolution, and the d02 results are used for classification of the circulation types. The model results are available for every 3 h, and the daily mean air temperature is calculated by averaging all time frames available for a given day. The WRF model rainfall is available for every 3 h as accumulated precipitation and was recalculated into daily sums. The same time spans (6 UTC–6 UTC) were used both for the model data and the measurements.

2.2. *Calculation of Circulation Types*

The methodology of classification refers to the assumptions of “Die objective Wetterlagenklassifikation” (Bissolli and Dittmann 2001), modified according to Ojrzyńska (2015). One circulation type for each day is determined, using the daily meteorological data available for the domain d02. Four criteria of the classification are calculated individually for every grid cell of the model domain. Each of the criteria results in two to five different types. The domain-wide type of the particular criterion is calculated as the mode grid cell type within the model domain. The final circulation types (40) are composed of types of classification criteria in the following order: direction of advection (characters in positions 1–2 in type name), cyclonality at 825 hPa (position 3), cyclonality at 500 hPa (position 4), and humidity type (position 5; Fig. 1). The algorithm was applied here using the WRF d02 meteorological data, with 15 km × 15 km spatial resolution, and the calendar of atmospheric circulation types for the area of Poland for the years 1981–2010 was prepared. The classification scheme applied here utilizes the following meteorological information:

2.2.1 *Direction of Advection*

The direction of advection is calculated directly from the u and v wind components, provided by the WRF model for 700 hPa isobaric level. If the wind speed exceeds 2 m s^{-1}, the wind direction for the analysed grid cell is assigned, using four main directions: NE, NW, SE, SW. Otherwise, if the wind speed is below the threshold value, the XX class is assigned to the grid cell. The dominant wind direction for the entire domain is the one that occurs for more than 50 % of the grid cells in this domain. If there is no prevailing wind direction for the area, the final type of criterion “direction of advection” is classified as XX.

2.2.2 *Cyclonality for 825 (Lower) and 500 (Upper) Isobaric Level*

Cyclonality is calculated as an approximated value of $\nabla^2\phi$, where ∇ is the nabla operator and ϕ is a value of the geopotential. Cyclonality is calculated separately for the 500 and 825 hPa isobaric levels. A positive value of $\nabla^2\phi$ is classified for the cyclonic type (C), and negative for the anticyclonic (A) type. The calculation of grid cell cyclonality is a two-step procedure, based on the 3 × 3 grid neighbourhood. In the first step, every grid cell from a given neighbourhood is multiplied by value 1, while the analysed grid cell (centre of a given 3 × 3

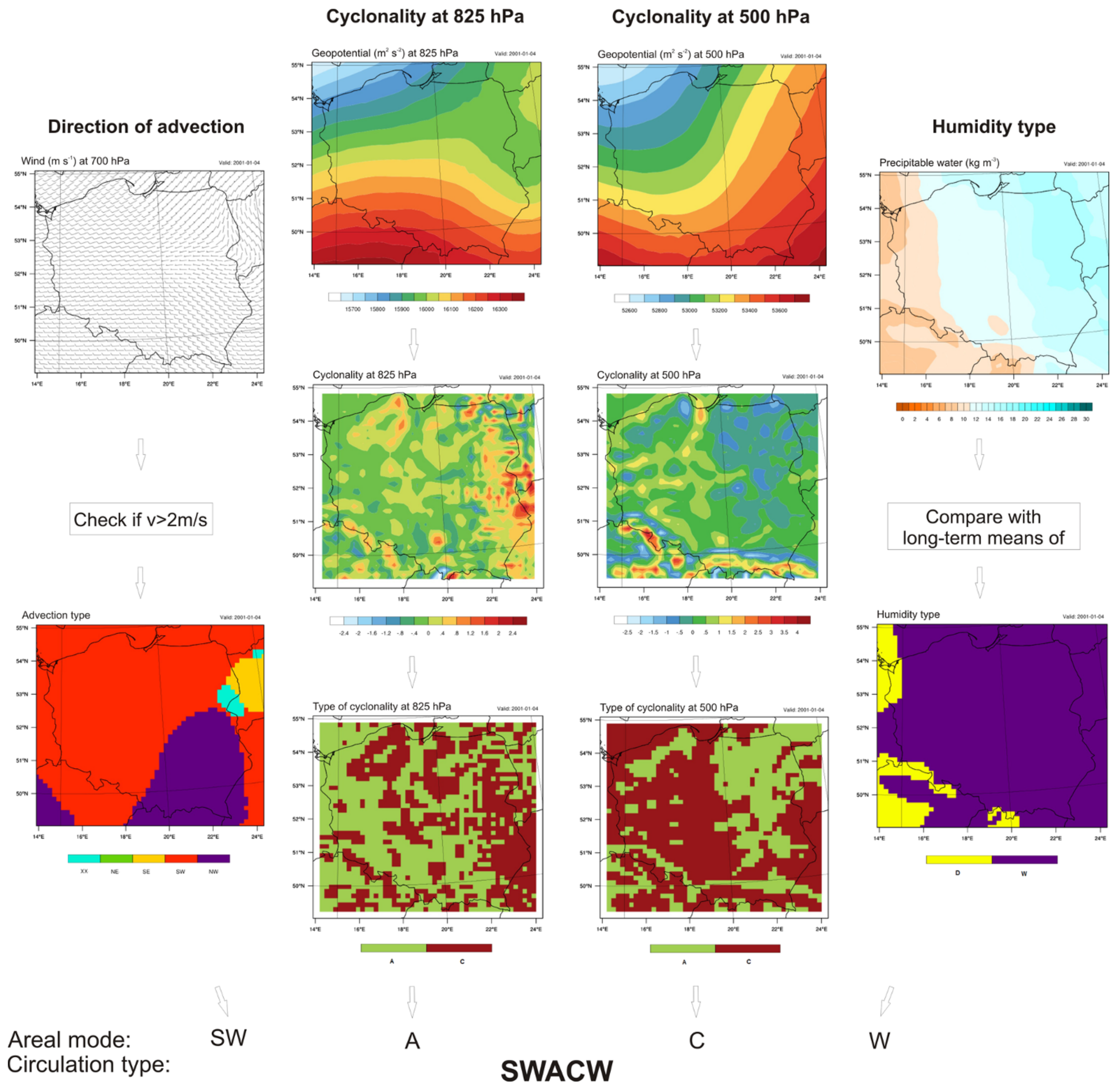

Figure 1
Circulation type classification scheme—real case for 01.04. 2001. The SWACW acronym, used here as an example, stands for: *SW* advection direction from south-west, *A* anticyclonic type at 825 hPa, *C* cyclonic type for 500 hPa, *W* wet type according to humidity-type class

neighbourhood) is multiplied by −8. In the second step, the mean value from all nine grid cells is calculated. The result is attributed to the analysed grid as an approximate value of $\nabla^2\phi$. The calculation of $\nabla^2\phi$ is preceded by the generalization of the geopotential, which is averaged using a low-pass filter with size 3 × 3 grid cells.

2.2.3 *Humidity Type*

The humidity type for each grid cells is calculated as a result of subtracting the daily mean value of tropospheric precipitable water (PW) and the suitable areal long-term monthly mean of PW. A positive value of the difference is classified for wet (W) type and negative for dry type (D). The long-term mean PW is calculated using the WRF model data for the d02 domain.

An automatic tool for the circulation type classification took a form of script, prepared using the NCAR Command Language (NCL Software, Version 6.1.2, 2013). The script reads sequential netCDF files, which contain the outputs from the WRF model. The above-mentioned meteorological information, needed to determine the circulation type, is calculated for each grid cell and classified according to the classification criteria. The atmospheric circulation type is determined by the combination of the four classification criteria described above (direction of advection, lower and upper cyclonality and humidity type). This method allows for easy grouping of the detailed classification and reduction of particular classification criteria. This characteristic was utilized for the results of this study. The algorithm is flexible in terms of, e.g. the incorporation of additional meteorological parameters and can be applied for other areas and the WRF model configuration (e.g. in terms of spatial extent and grid resolution).

2.3. Meteorological Data for the WRF Model Evaluation

In this work, first we compare the 5 km × 5 km WRF model results with the meteorological measurements of daily rainfall and daily mean air temperature, gathered at 66 synoptic stations in Poland for the 1981–2010 period. For comparison, we used the WRF model domain d03 data from a grid cell, in which the measuring site is located. It should be noted here that we used the area averages (WRF model grid cell) and point values (measuring sites) in this work. The spatial distribution of the measurement sites is presented in the first part of this twin paper (please see Fig. 1 at Kryza *et al.* 2016). Secondly, we compare the WRF model results with the gridded meteorological information available for Europe and described by Haylock *et al.* (2008).

The European land-only daily high-resolution gridded data (E-OBS; Haylock *et al.* 2008) for daily rainfall and daily mean air temperature are available for all Europe with 0.25° × 0.25° spatial resolution. This dataset was developed by three-step spatial interpolation. First, the monthly mean values are interpolated with thin-plate splines. Second, the anomalies with regard to the monthly mean are interpolated using the kriging algorithm. The final map is calculated by applying the interpolated anomaly to the interpolated monthly mean (Haylock *et al.* 2008). In this work we used E-OBS data version 10.0.

2.4. The WRF Model Evaluation

The WRF model results are compared with the measurements of the rainfall and daily mean air temperatures. The WRF modelled rainfall and air temperature were extracted for the nearest grids where the synoptic stations are located and compared with the station measurements. A grid-to-point comparison is performed. In the same way, the E-OBS database is compared with the measurements. This is done to assess the differences between these two approaches that provide the spatial climatological information: dynamical regional climate model and geostatistical method, and to address the uncertainty related to each dataset. The model error is calculated as the difference between the modelled (by WRF or from E-OBS) and the observed value and the results are summarized using three error statistics:

- *Mean error* (*ME*) calculated as an arithmetic mean from the model error for the air temperature in °C. A positive value of ME suggests a tendency for overestimation, while a negative value suggests underestimation of the air temperature by the model. For the rainfall, ME is given in percent, with the values >100 % showing overestimation of rainfall and <100 % showing underestimation.
- *Mean absolute error* (*MAE*) calculated as the mean value of the absolute model error. The units are °C for the air temperature and mm/day for rainfall.
- *Index of agreement* (*IOA*) calculated using the formula proposed by Emery *et al.* (2001), as a standardized measure of the degree of model prediction error. Details for IOA are provided in part 1 of this paper. The values vary between 0 (no agreement) and 1 (perfect match). IOA is unitless.

The error statistics are calculated using the data from all available stations and for the entire study period, each month and for each determined groups of circulation types. Histograms and the quantile–quantile plots are provided both for the WRF and E-OBS comparison with the measurements. The WRF and E-OBS are also compared spatially for long-term periods. Additionally, the IOA statistic was calculated for each grid separately for selected groups of atmospheric circulation types to give an insight into spatial differences between the WRF and the E-OBS datasets.

Similar to the approach used for the WRF model evaluation, the rainfall and air temperature values from E-OBS datasets were extracted for the grid in which the meteorological stations were located. It must be emphasised that the E-OBS database is based on the same measurements that are used here to evaluate the results of the WRF model and, therefore, should show very similar values as the measurements. However, because of the relatively coarse grid of 0.25°, there might be some issues related with spatial averaging and reduction of the extremes, which is one of the key points of this work. This includes, among others, averaging of the extreme values, both for air temperature and rainfall (Wibig *et al.* 2014). Additionally, for rainfall, the coarse resolution of the E-OBS database makes it less prone to incorrect spatial allocation of rainfall. The quantification of the differences between the E-OBS data and the measurements is important, because the E-OBS is used later in this work for the WRF model spatial evaluation.

The spatial distribution of the long-term mean values of rainfall and air temperatures was calculated with the WRF and E-OBS data and compared, using the original spatial resolutions of both datasets. This was done to show the value added by the higher spatial resolution of the WRF model. Secondly, we aggregated the WRF model data to the coarser E-OBS grid, and for each common grid cell we calculated the index of agreement and mean error statistics. This was possible, because for the entire period and each grid cell, time series of the WRF and E-OBS meteorological information was available. The IOA and ME were calculated for selected types of atmospheric circulation and presented as maps.

3. *Results*

The results are organized as follows. First, the general comparison of the WRF and E-OBS data with measurements is presented, including spatial comparison of the WRF and E-OBS data. Both datasets are also compared spatially, using the source spatial resolutions of WRF and E-OBS. Secondly, the information on the circulation types and frequency is provided. Finally, the WRF model and E-OBS performance are summarized with respect to the circulation types, and spatial distribution of the rainfall and air temperature, calculated with these two sources, is compared, using the common E-OBS spatial resolution.

3.1. *WRF and E-OBS Comparison with Meteorological Measurements*

Comparison of the WRF and E-OBS performance for the entire 1981–2010 period is summarized in Fig. 2 for the air temperature and rainfall. For the air temperature, both WRF and E-OBS databases have a small positive bias if the entire period and all months are considered. However, if the seasonal performance is analysed, ME changes significantly for WRF, with negative values in winter months and the highest positive values for autumn. The seasonal changes in E-OBS ME are smaller. There is also a seasonal pattern in MAE, both for WRF and E-OBS. For WRF, MAE is the highest for winter and autumn, while for E-OBS there is also a secondary maximum in summer. Noticeably, the MAE is significantly smaller for WRF, compared with E-OBS, for all months. The WRF model performance is also better in terms of IOA, which is higher when compared with E-OBS for all months of the study period. The differences in IOA are especially large for the summer months. The better agreement of the WRF model in terms of MAE and IOA, compared with E-OBS, shows the strength of the dynamical downscaling approach for providing long-term meteorological information, even before applying the bias correction techniques.

For the rainfall, the E-OBS is in closer agreement with the measurements in terms of all three statistics considered. The WRF model significantly overestimates the observed rainfall, while the

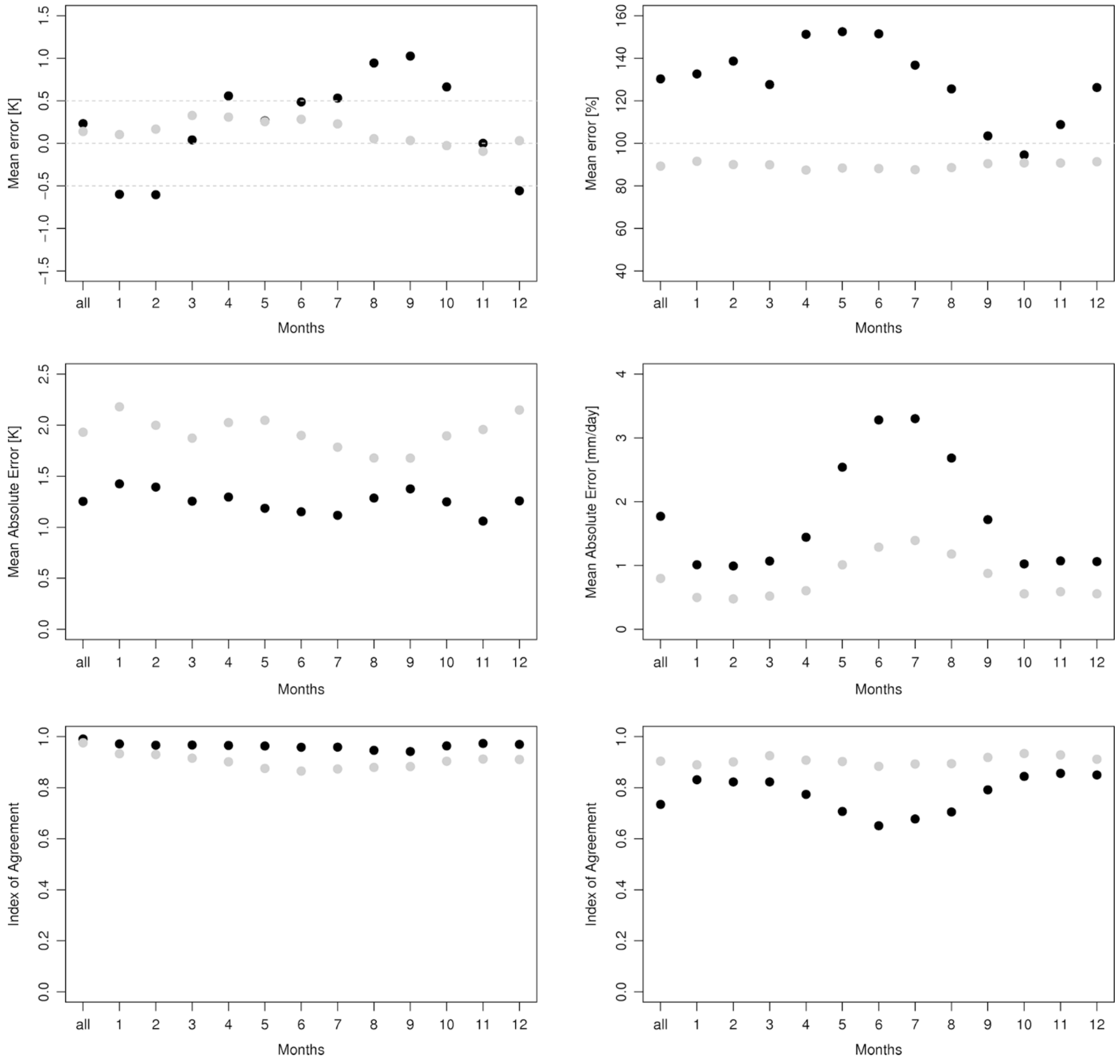

Figure 2
Summary of the WRF (*black points*) and E-OBS (*grey points*) error statistics for daily air temperature (*left column*) and rainfall (*right*) for the 1981–2010 period (all) and each month

E-OBS gridded values are slightly underestimated. There is also a clear seasonal pattern in the WRF model performance for rainfall. The largest differences between the WRF modelled and the observed daily precipitation are for summer months, when the convective rainfall dominates the total precipitation. For this season, local, intensive rainfall episodes may contribute to the majority of the monthly precipitation sum, and these events are likely to be missed or shifted both in time and space by WRF because of its local character.

The histograms of the daily 2 m air temperatures for the period 1981–2010, calculated with observations, WRF and E-OBS data, are presented in Fig. 3 for each season separately: winter (December–February, DJF), spring (March–May, MAM), summer (June–August, JJA) and fall (September–November, SON). The E-OBS data reproduce the air

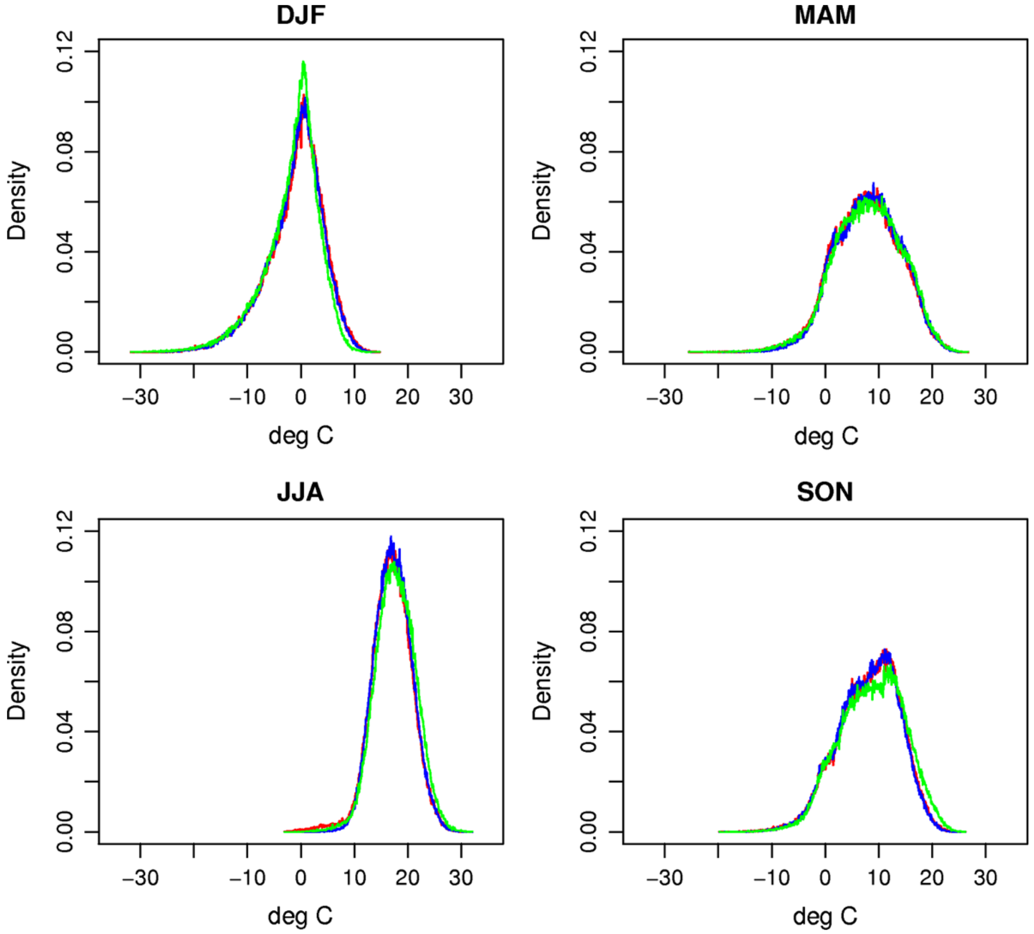

Figure 3
Histograms of daily mean air temperatures observed (*red*) from E-OBS (*blue*) and WRF (*green*)

temperatures very well. The WRF modelled air temperature is shifted towards cold values for December–February, which is in agreement with the ME plot shown in Fig. 2. For spring (March–May), all three sources are in close agreement, with slightly lower frequencies of air temperatures close to 8–9 °C for the WRF model. For summer (June–August) and fall (September–November), the WRF air temperature is shifted towards warm values. For all seasons, the WRF model reproduces the minimum observed air temperatures better than E-OBS. This might be linked with the higher spatial resolution of the WRF model. The highest air temperatures are overestimated except for winter (Fig. 3).

Similar features are shown if the modelled quantiles are plotted against the observed quantiles (Fig. 4). For WRF, higher quantiles are overestimated for all seasons except winter. Low quantiles are well reproduced by WRF for all seasons.

The frequency and intensity of the precipitation events are addressed with the observed, WRF and E-OBS rainfall distribution, presented in histograms (Fig. 5). The WRF model fails to reproduce the lower end of the spectrum, with lower frequencies for all the seasons, except for autumn. The E-OBS reproduces the lower values and no rainfall days well for all the seasons. The WRF model shows a considerably lower number of cases with no rain. For rainfall in the range from 0.2 to 0.5 mm, the WRF model is closer to the measurements compared to E-OBS. The WRF model overestimates the daily rainfall, especially the high values, for all the seasons, except for

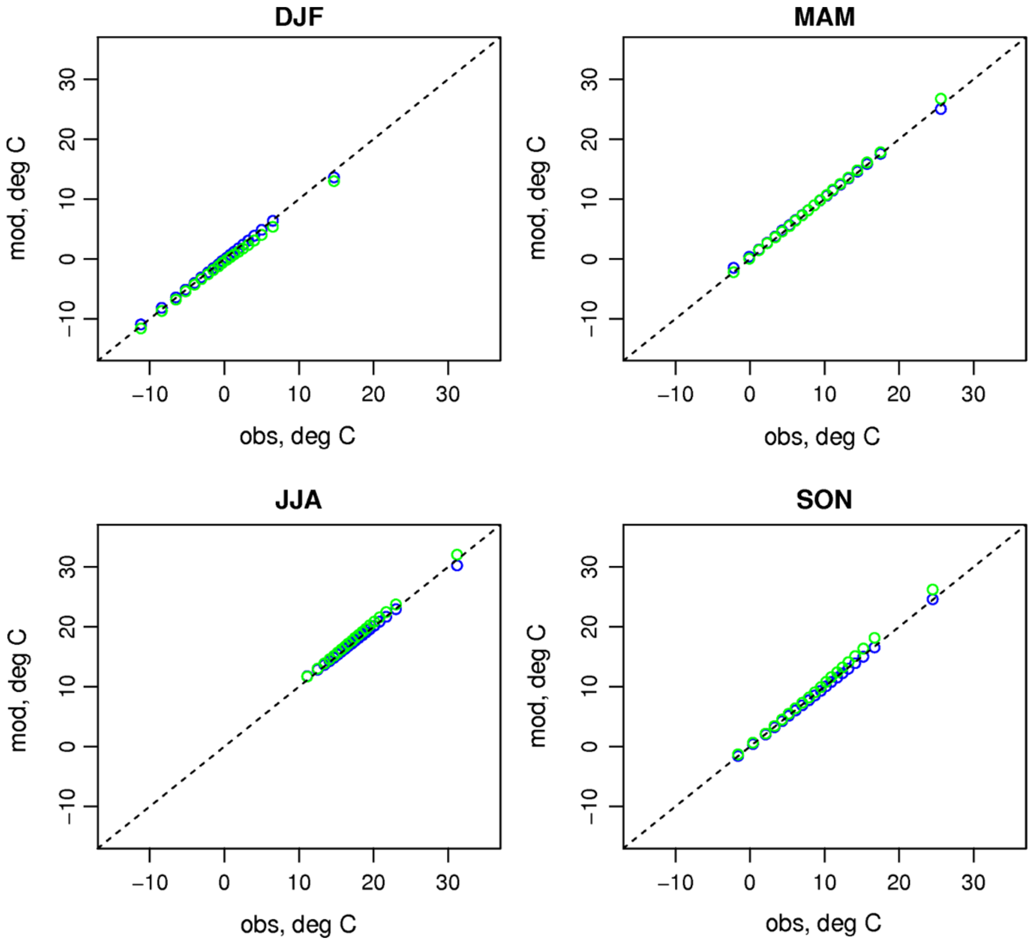

Figure 4
Quantiles (from 0.05 to 1 in steps of 0.05) for daily air temperature at 2 m for E-OBS (*blue*) and WRF (*green*). Mod is for modelled (WRF and E-OBS, *y* axis) and obs is for observed values (*x* axis)

autumn (Fig. 6). The E-OBS, on the contrary, underestimates the values, which is the largest for summer and autumn.

The spatial patterns of the mean monthly air temperature and rainfall sums, calculated with the WRF and E-OBS gridded data, are presented in Figs. 7 and 8. There is a large spatial variability in the WRF-based maps, both for the air temperature and rainfall. This is related to the significantly higher spatial resolution of the WRF data. For the air temperature, both WRF and E-OBS show similar spatial patterns. The grid-to-grid correlation coefficient is 0.94 for January and 0.87 for July. The WRF model shows higher values of the air temperatures, if summarized for the entire model domain, with the mean grid-to-grid difference at 0.26 and 1.28 for January and July, respectively. Some features, e.g. warm areas of the cities, are missing entirely in the E-OBS map.

For the rainfall, grid-to-grid correlations are smaller, and are close to 0.5, both for January and July. The WRF maps also show higher rainfall values, compared to E-OBS, with mean differences of 14 and 41 mm for January and July, respectively. Both WRF and E-OBS show the highest rainfall for the mountainous areas in the south. However, the second area of increased rainfall, located in northern Poland, is shifted westward in the E-OBS maps, when compared with WRF. This is both for January and July.

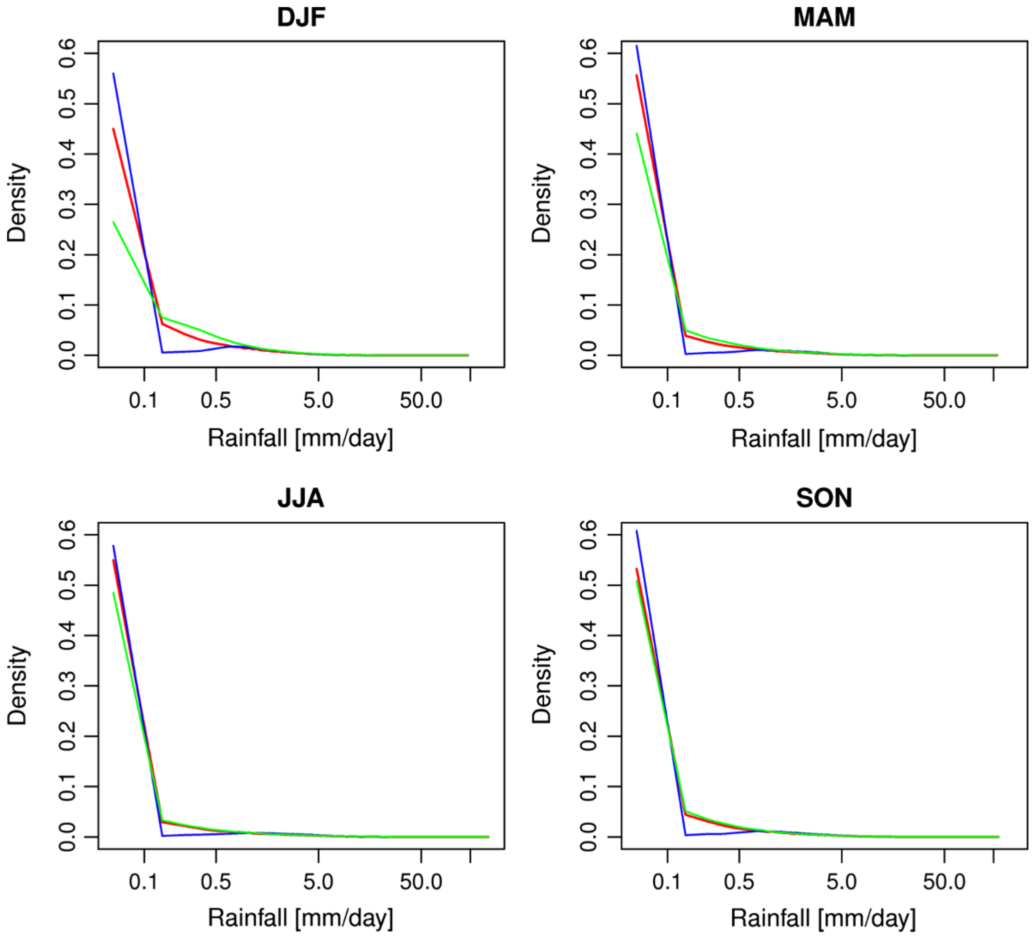

Figure 5
Histograms of daily rainfall: observed (*red*), from E-OBS (*blue*) and WRF (*green*)

3.2. Circulation Types Analysis

The circulation types classification applied in this study resulted in 40 distinct circulation types. There are seven most frequent types, with frequency exceeding 4 % in the years 1981–2010, mainly anticyclonic: SWAAW, SWAAD, NWAAW, NWAAD, NEAAD and NWACD, NWCCD and SWCAW (Fig. 9). The next four most frequent types (2–4 %) are characterised with advection from the SW sector: SWACD, SWACW, SWCCD and SWCCW. The least frequent circulation types are those of the XX sector and some types with the advection from sectors NE (NEACW, NECAD, NECAW) and SE (SEACD, SEACW, SECAD). To assure the meaningful statistical analysis of the WRF model performance for rainfall and air temperature regarding the circulation types, the least frequent types were aggregated for further analysis. Finally, nine groups of various circulation types were distinguished (Table 1). Three groups contain only dry circulation types: AAD, ACD and CdD. The five groups of wet types are: AAW, WACW, EACW, WCdW and ECdW. All types from the XX sector are classified to group XX. This group, together with EACW, has the lowest frequency (~1 %) in the 1981–2010 period, but both are specified because of their specific air temperature and rainfall distribution. The frequency for most of the remaining groups exceeds 10 % (Fig. 10).

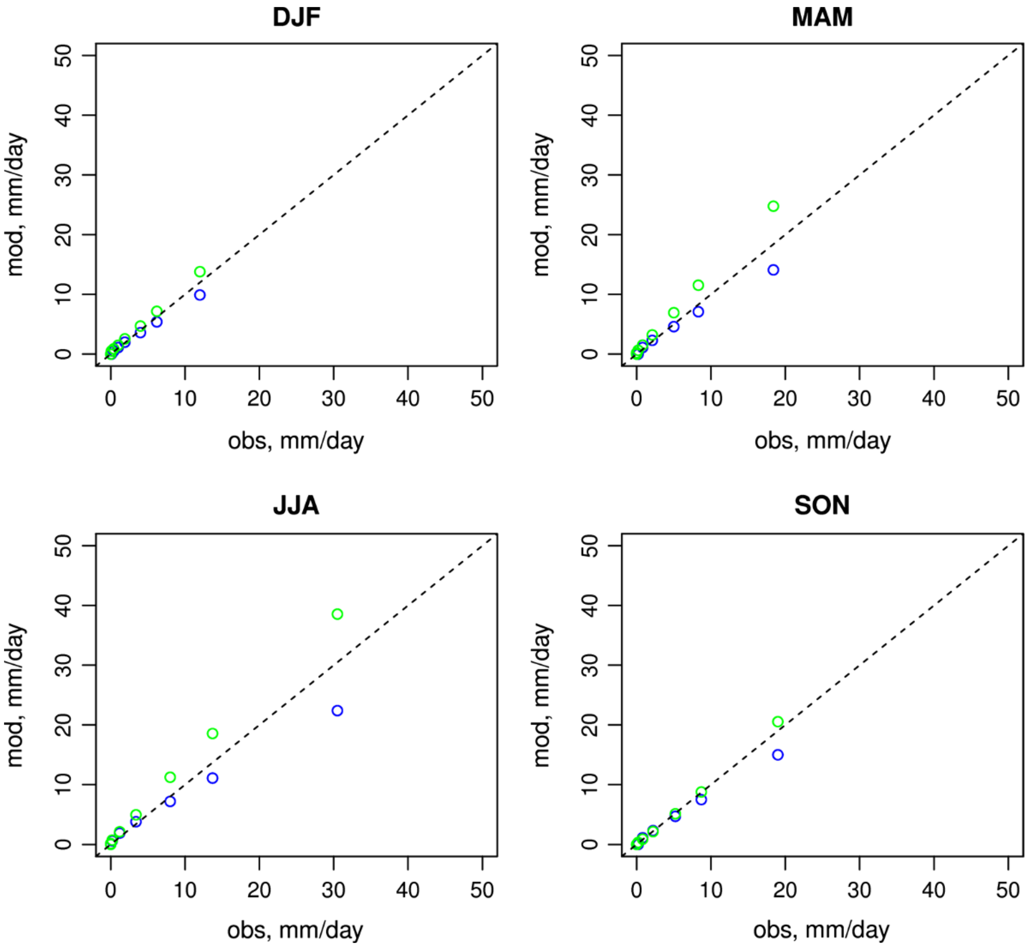

Figure 6
Quantiles (0.025, 0.1, 0.25, 0.5, 0.6, 0.7, 0.8, 0.9, 0.95 and 0.99) for daily rainfall at 2 m for E-OBS (*blue*) and WRF (*green*). Mod is for modelled (WRF and E-OBS, *y* axis) and obs is for observed values (*x* axis)

The WRF and E-OBS agreement with the measurements for the air temperature and rainfall, with respect to the circulation types, is summarised in Fig. 11. For the air temperature, the WRF data have small positive ME for all groups, and the ME is below 0.5 °C for most of the circulation types analysed, except for ECdW. For the E-OBS data, small ME is found for WACW, XX, ECdW and EACW types, for which the frequency of the occurrence is relatively low. For more frequent groups of types, e.g. groups ACD and AAD, the E-OBS data overestimate the air temperatures above 0.5 °C, and the ME is significantly higher, compared with WRF. For the wet groups of AAW and WCdW, the E-OBS is underestimated and has the largest MAE, while the WRF model shows small overestimation. The IOA for both datasets are very high for all the circulation types, both for E-OBS and WRF. The WRF model results have slightly higher values of IOA, especially for the wet circulation types with advection from the western sector (e.g. WCdW).

The WRF model overestimates the measured rainfall for all circulation types. This is especially the case for eastern or unidentified direction of advection (e.g. ECdW, EACW and XX; Fig. 11). Especially for group XX, ME shows almost two times higher rainfall in the period 1981–2010 than the measured value. On the contrary, the E-OBS database shows significant underestimation for the XX group. The MAE and IOA also show worse performance of

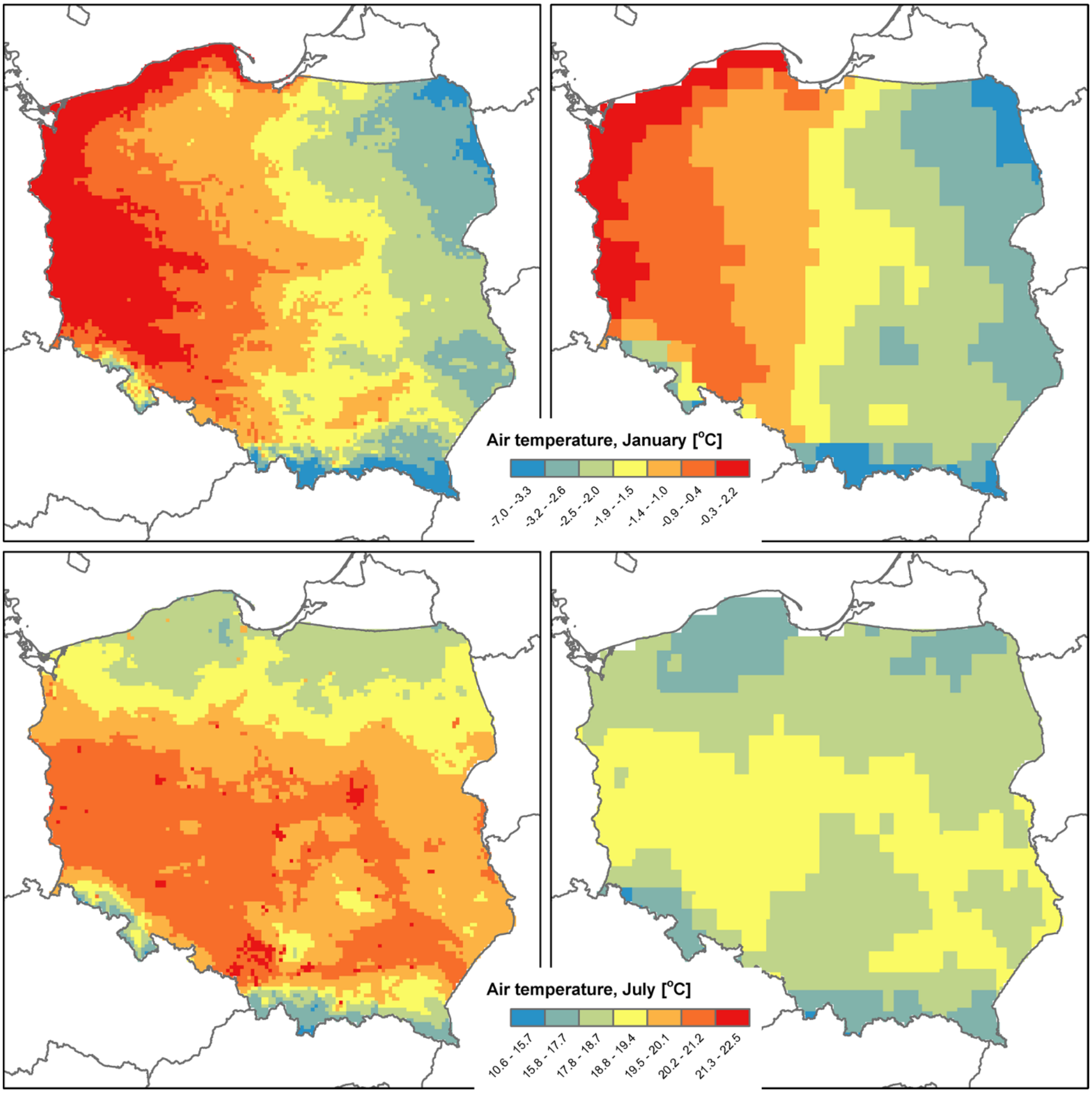

Figure 7
Spatial pattern of mean (1981–2010) air temperature for January (*top row*) and July (*bottom*) for WRF (*left column*) and E-OBS (*right*)

the WRF model for rainfall, compared to the E-OBS database, and MAE is especially large if the eastern wet types are considered (e.g. ECdW). For dry circulation types, MAE for the WRF model is below 1.5 mm/day, and for the majority of circulation types, the E-OBS MAE does not exceed 1.0 mm/day, except for the wet types of eastern advection. There were similar findings for the IOA statistics, which was higher for all the circulation types for E-OBS, compared to WRF. Both E-OBS and WRF show the lowest IOA for XX.

The statistical summary of the daily air temperature and rainfall is presented for the measurements, WRF and E-OBS data in Figs. 12 and 13. The variability of the air temperature and rainfall within each of the circulation type group is relatively small

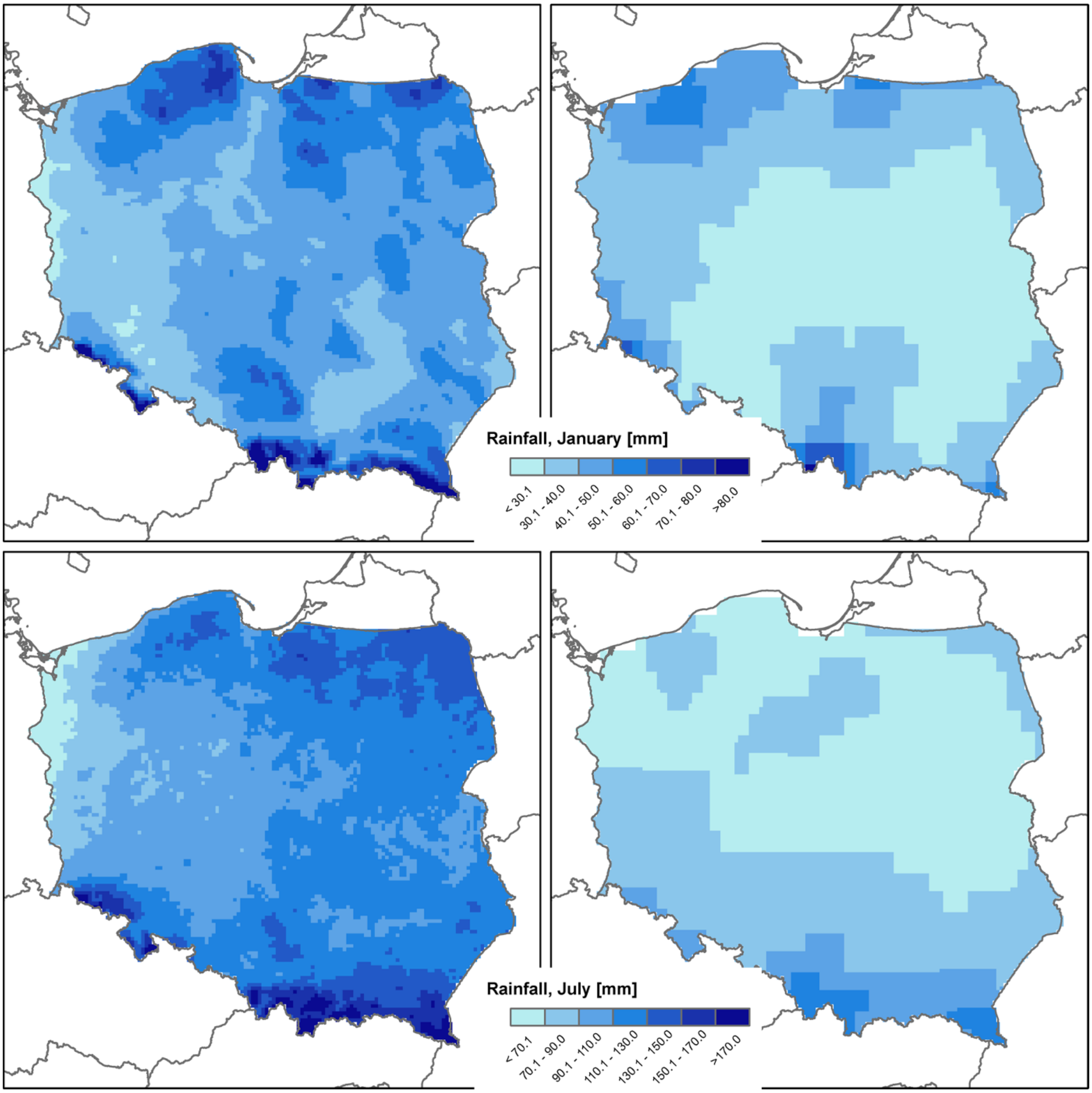

Figure 8
Spatial pattern of mean (1981–2010) monthly rainfall for January (*top row*) and July (*bottom*) for WRF (*left column*) and E-OBS (*right*)

and the groups are different in terms of, e.g. the median value. This suggests that the classification method properly distinguishes the circulation types, according to, e.g. Kalkstein *et al.* (1987) and Ustrnul *et al.* (2010). The largest differences in the median value between the circulation types and air temperature are observed in spring and reach 8 °C in CdD and EACW. The interquartile range is also the largest for spring, for which it reaches 8 °C. The smallest differences in the median value between the groups of circulation types (about 1 °C) concern dry type groups in the winter seasons (AAD, ACD, CdD) and wet, lower cyclonic groups in autumn (WCdW, ECdW). For all the seasons, the largest spread of air temperatures is the lower anticyclonic group of circulation types: AAD, AAW and ACD, which are

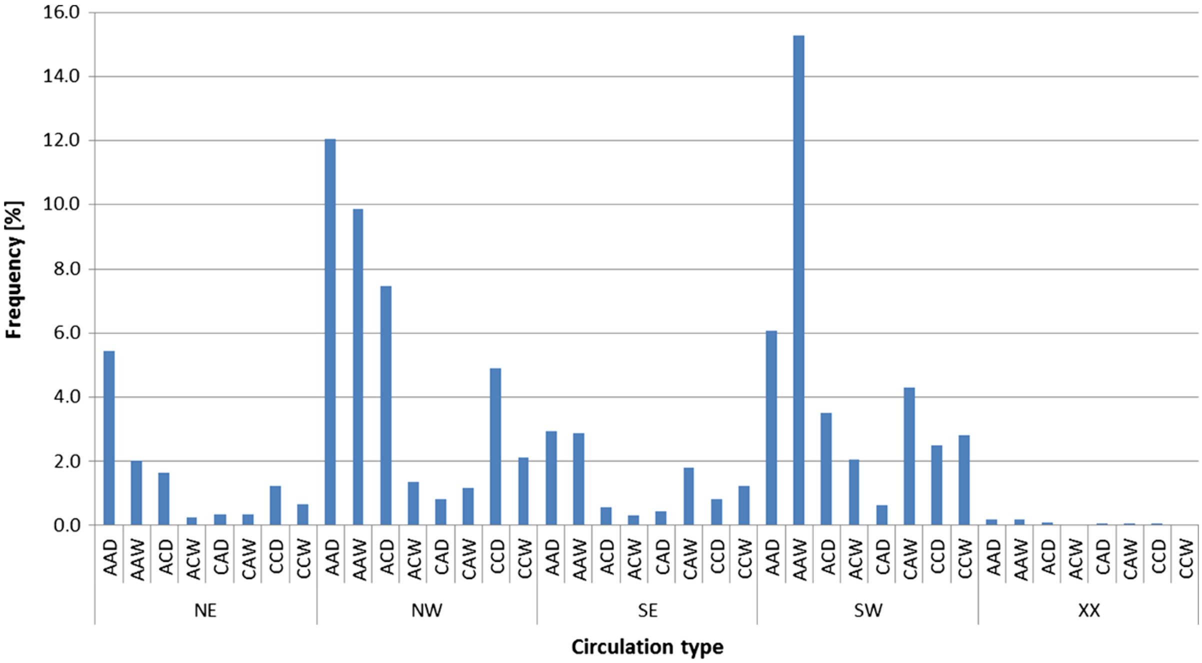

Figure 9
Frequency of circulation types for Poland in the years 1981–2010

Table 1

Circulation types and groups of circulation types determined using ACCT for the 1981–2010 period

Group of circulation types		Circulation types belong to the group
Acronym	Long name	
AAD	Lower anticyclonic, upper anticyclonic dry	SWAAD, NWAAD, NEAAD, SEAAD
ACD	Lower anticyclonic, upper cyclonic dry	SWACD, NWACD, NEACD, SEACD
CdD	Lower cyclonic dry	SWCCD, NWCCD, NECCD, SECCD, SWCAD, NWCAD, NECAD, SECAD
AAW	Lower anticyclonic, upper anticyclonic wet	SWAAW, NWAAW, NEAAW, SEAAW
WACW	Western, lower anticyclonic, upper cyclonic wet	SWACW, NWACW
EACW	Eastern, lower anticyclonic, upper cyclonic wet	NEACW, SEACW
WCdW	Western, lower cyclonic wet	SWCCW, NWCCW, SWCAW, NWCAW
ECdW	Eastern, lower cyclonic wet	NECCW, SECCW, NECAW, SECAW
XX	Unidentified direction of advection/without advection	XXAAD, XXAAW, XXACD, XXACW, XXCAD, XXCAW, XXCCD, XXCCW

also the most frequent. For spring to autumn, an increased dispersion is found in the types with advection from the eastern sector (EACW, ECdW). The higher dispersion of the air temperatures for summer types with eastern advection could be related with the large variability of cloudiness and humidity in convective unstable air masses. The high extremes of temperature in XX and anticyclonic groups may be linked with long-lasting occurrence of this types and intense insolation and irradiation.

For precipitation, the differences between groups of circulation types are the highest for summer and winter (differences exceed 2 mm/day for the median value). The dispersion of precipitation values, according to the interquartile range, is the highest for the wet-type group, especially for AAW, WACW and

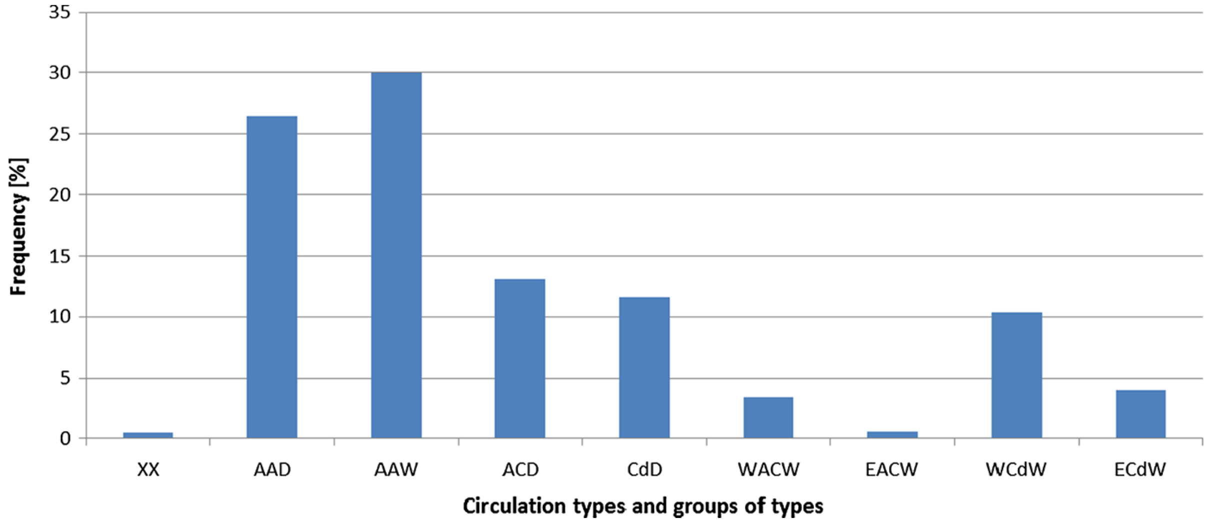

Figure 10
Frequency of groups of circulation types for Poland in the years 1981–2010

WCdW. Days with advection from the east (ECdW, EACW) have a large interquartile range, except for the winter months. The outliers here reach 100 mm/day. There is a strong seasonal variability in the interquartile range for all groups of atmospheric circulation types. The values vary from 1.4 to 3.6 mm/day for winter months, to 3.2–7.2 mm/day for autumn. In summer, the interquartile range for most of the circulation-type groups is in the range from 5.2 to 7.0 mm/day and reaches the maximum (14 mm/day) for group ECdW, which contains the types with unstable convective air masses.

The box plots presented in Figs. 12 and 13 also show the differences in the WRF and E-OBS data and the observations. This is especially true for the outliers, which were covered in the general model performance statistics presented above. For the air temperature and the winter months, there is a close agreement between the E-OBS and the measurements for the group types with high frequency (AAD, AAW, ACD, CdD) in terms of quartiles and the high outliers (Fig. 12). For groups ACD and CdC, the WRF model also shows a very good agreement with the measurements, but for the lower and upper anticyclonic group types (AAD, AAW) and most of the less frequent groups of circulation types, the median temperature together with the first and third quartile is lower, compared with the measurements. The WRF model, in general, better reproduces the lower outliers when compared with E-OBS, and for the majority of the groups in winter, the lower outliers are underestimated by WRF and overestimated by E-OBS. For the less frequent type of group, excluding XX, the WRF model shows closer agreement with the measured air temperatures than the E-OBS..

For spring and summer, both E-OBS and the WRF models reproduce the air temperatures well, especially for the wet type (Fig. 12). For summer, the WRF model overestimates the median value for the majority of the circulation types. The differences between the temperature quartiles from WRF and observed datasets are small and usually do not exceed 1 °C. For groups AAW and WCdW, the WRF model shows higher maximum values of air temperatures, compared with the measurements, for both spring and summer. In summer, WRF shows closer agreement with the measurements for the low outliers, but, similar to E-OBS, the model overestimates air temperature. In spring, the WRF model reproduces well the higher air temperatures.

For autumn, the WRF model reproduces well the median value both for frequent and rare circulation types. The high values are usually overestimated, especially for the most common circulation types of AAD, AAW and ACD, for which the E-OBS shows a

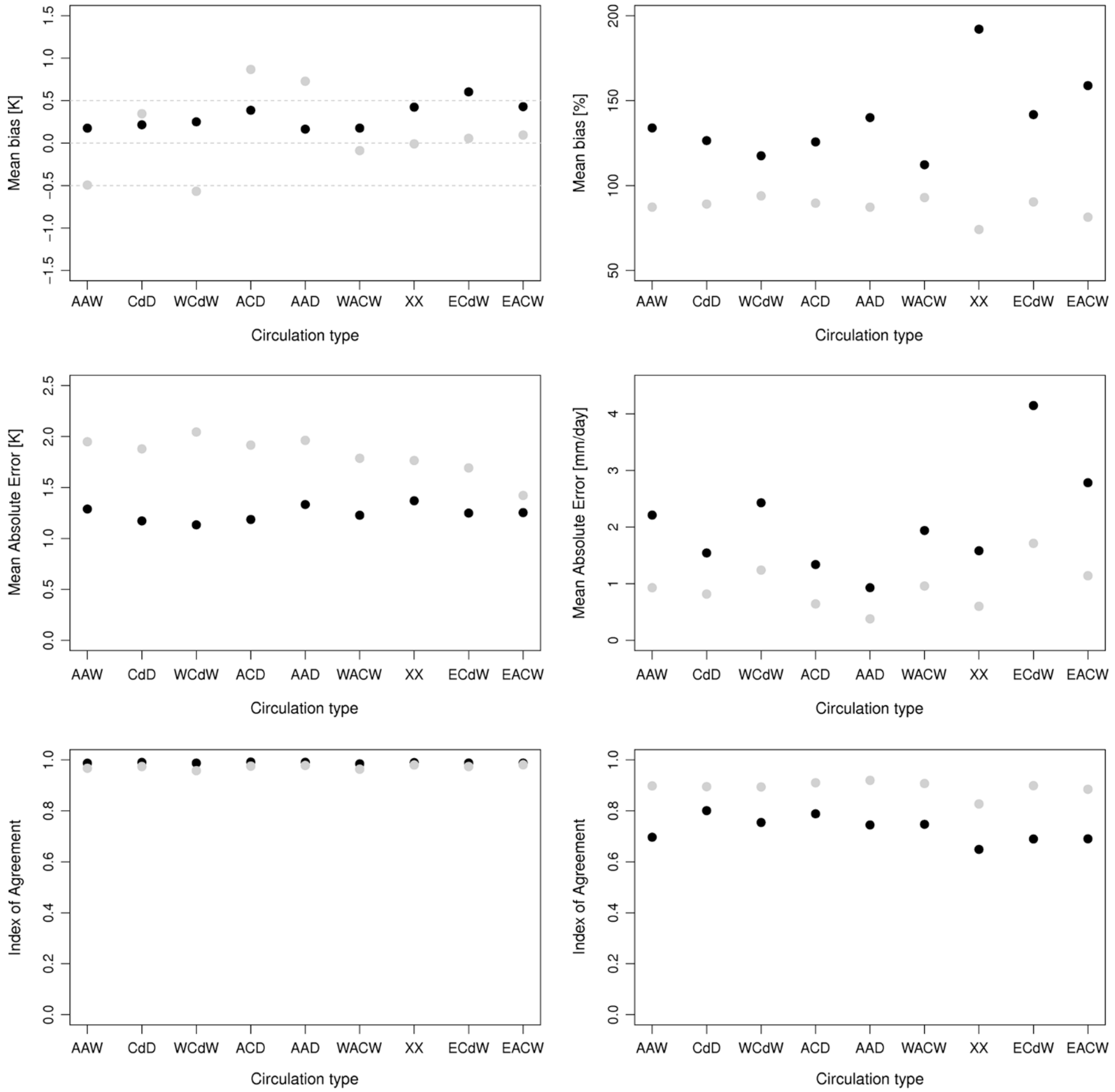

Figure 11
Statistical performance of WRF (*black points*) and E-OBS (*grey points*) for daily air temperature (*left column*) and rainfall above 0.1 mm/day (*right column*) according to the group of circulation types

closer agreement with the measurements than WRF. However, for the less frequent groups, like WCdW or EACW, the upper outliers are better represented by the WRF model.

For rainfall, the box plots show that for the WRF model there is a significantly higher number of days with rainfall, compared to the measurements (Fig. 13). On the contrary, the E-OBS data give a

▶

Figure 12
Comparison of the observed (*red*) and WRF (*green*) and E-OBS (*blue*) modelled air temperature for the 1981–2010 period for circulation types. *Box plot* width is proportional to the group of circulation-type frequency. The *box plot* hinges show the first and third quartiles, the *whiskers* are 1.5 times the hinges spread or to the data extreme (if 1.5* the hinge spread is smaller than the extreme value) and *circles* are the outliers, which are above/below the 1.5 times the *box* length

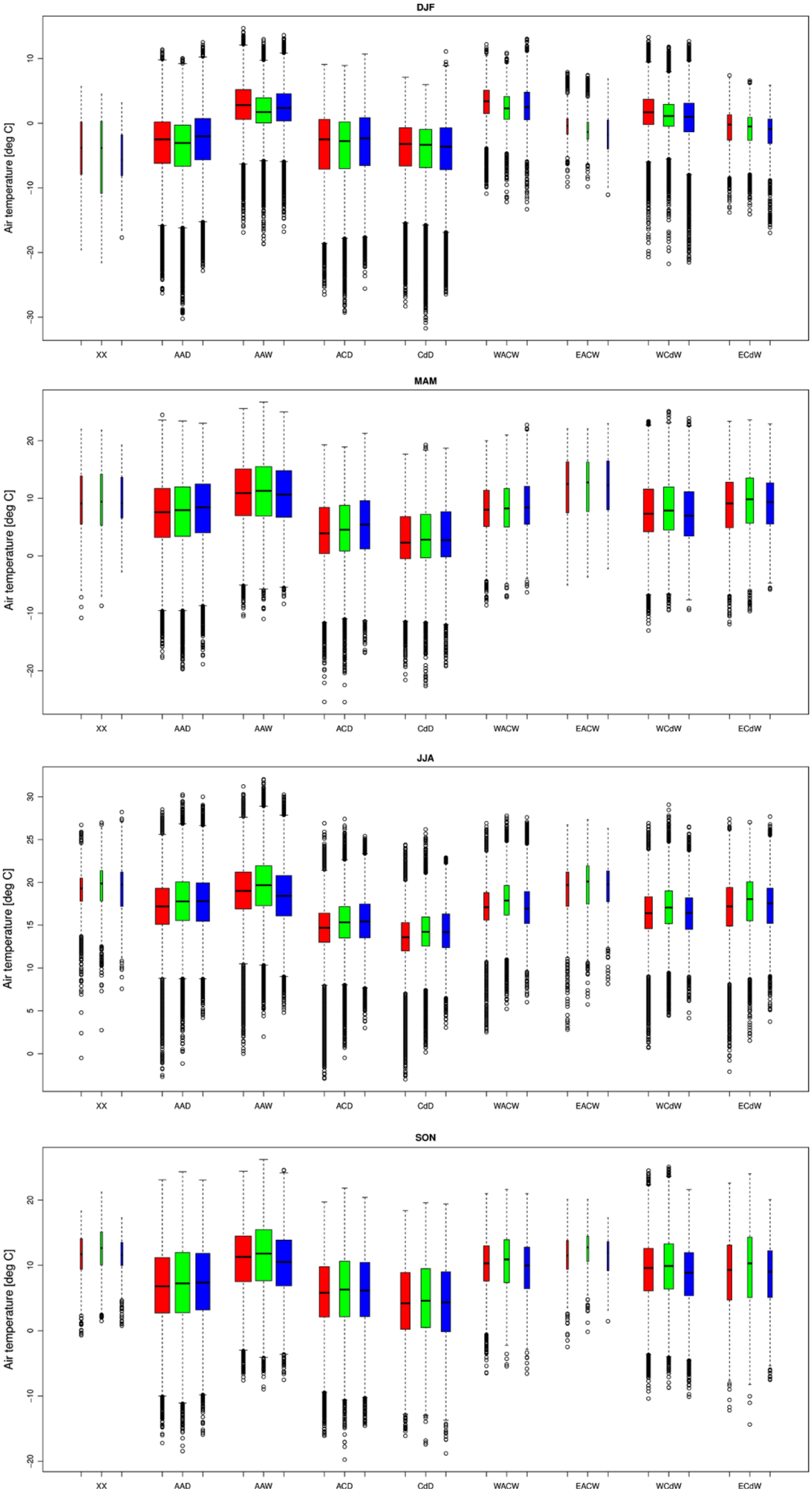
DJF
Air temperature [deg C]
10
0
-10
-20
-30
XX
AAD
AAW
ACD
CdD
WACW
EACW
WCdW
ECdW
MAM
Air temperature [deg C]
20
10
0
-10
-20
XX
AAD
AAW
ACD
CdD
WACW
EACW
WCdW
ECdW
JJA
Air temperature [deg C]
30
25
20
15
10
5
0
XX
AAD
AAW
ACD
CdD
WACW
EACW
WCdW
ECdW
SON
Air temperature [deg C]
20
10
0
-10
-20
XX
AAD
AAW
ACD
CdD
WACW
EACW
WCdW
ECdW

smaller number of days with rainfall compared to the measurements. Regardless of the season, the median values of precipitation for WRF data are in a better agreement with the measurements than E-OBS for the majority of the circulation types, especially in groups AAW, WCdW and ACD. For summer, the WRF model gives higher daily rainfall for all the circulation types. The same is observed for winter and spring in the lower cyclonic types of the group. For autumn, the WRF median is higher, compared to the measurements only for AAW and ECdW.

For the majority of the circulation types and regardless of the season, the first quartile for the WRF model is about 0.1 mm higher, compared with the observations, while this difference for E-OBS exceeds 1.0 mm, especially for the spring and summer months (Fig. 13). For higher daily rainfall values, represented by the third quartile, the E-OBS is in better agreement with the measurements for all circulation types, except for the autumn and winter months. For all the circulation types, the third quartiles of precipitation in the WRF model are 0.5–2.0 mm higher than in the observed datasets in spring and summer. In the winter and autumn months, they are about 1.0 mm lower, but only for lower anticyclonic groups of circulation types, with any differences in other groups. The WRF model also shows higher than measured highest daily rainfall values for all the circulation types, but these extreme values are in closer agreement with the observation than for E-OBS.

For a spatial evaluation of the WRF model results for the daily mean air temperature and rainfall, with respect to the circulation type, we used the E-OBS data. The most important result is that the differences between the WRF and E-OBS are not spatially constant and change with the circulation type. The example is presented in Fig. 14 for the air temperature, with the most common lower/upper anticyclonic wet circulation type (AAW) and eastern, lower anticyclonic, upper cyclonic wet type (EACW). For the AAW circulation type, the highest IOA is for northern and eastern Poland. For EACW, the highest values are for northern and western areas of the country. For EACW, there is a large area of decreased IOA in SE Poland, which is not visible for AAW. The absolute minimum values are different for AAW and EACW, but cover approximately the same area of southern Poland. Similarly, there are large changes in spatial distribution of ME for these circulation types. The lowest ME covers the northern and eastern areas of Poland for AAW, while for EACW it is N and NW. The largest values are for central and southern Poland in AAW, while for EACW there is a large area of high ME in SE Poland. The same changes in the WRF and E-OBS spatial agreement are found for rainfall (Fig. 15). There are also large changes, e.g. in IOA which is significantly lower for AAW compared to EACW.

Figure 13 ▶
Comparison of the observed (*red*) and WRF (*green*) and E-OBS (*blue*) modelled daily rainfall (above 0.1 mm/day) for the 1981–2010 period for circulation types. *Box plot* width is proportional to the number of days with rainfall for a given circulation type. Please notice the log *Y* axis. The *box plot* hinges show the first and third quartiles, the whiskers are 1.5 times the hinges spread or to the data extreme (if 1.5* the hinge spread is smaller than the extreme value) and *circles* are the outliers, which are above/below 1.5 times the *box* length

4. Summary and Conclusions

In our study, we have presented the results of high-resolution dynamical downscaling of daily rainfall and air temperature with the regional climate model WRF. The results were evaluated by comparison with measurements and gridded data. Additionally, we presented the method for automatic classification of atmospheric circulation types, which utilize the high-resolution WRF model output. The method for the automatic classification of the circulation types (ACCT) for Poland, based on the WRF data (wind direction, cyclonality and humidity of air masses), was applied for the entire period of 1981–2010. The WRF model performance was evaluated for daily precipitation and air temperature, individually for each month and also with respect to the group of circulation types. The analysis of the regional dynamical downscaling with the WRF model was complemented by comparison with spatial data obtained with the geostatistical method (E-OBS).

The main findings of this work are:

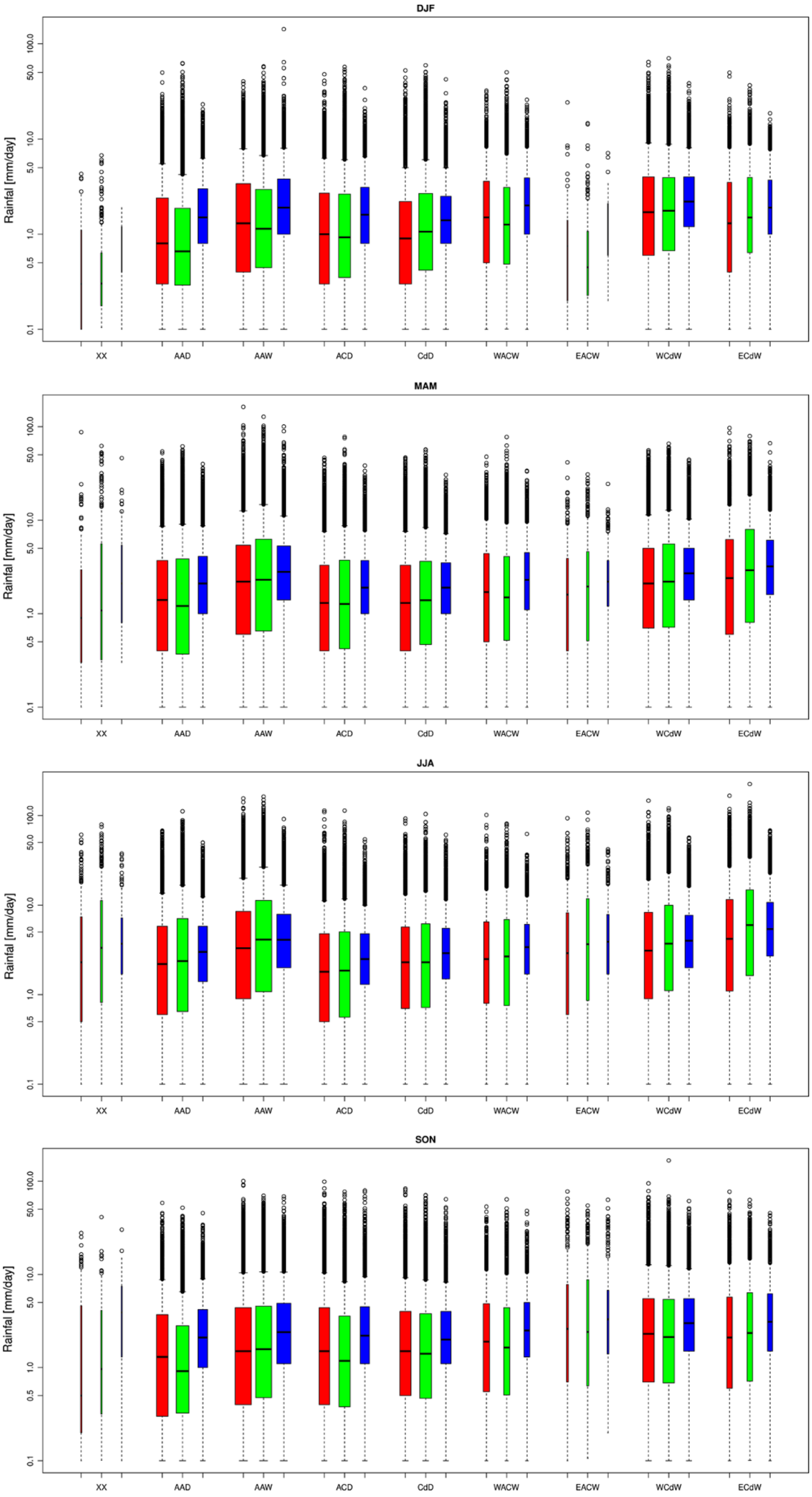
DJF
MAM
JJA
SON
Rainfal [mm/day]
0.1
0.5
1.0
5.0
10.0
50.0
100.0
XX
AAD
AAW
ACD
CdD
WACW
EACW
WCdW
ECdW

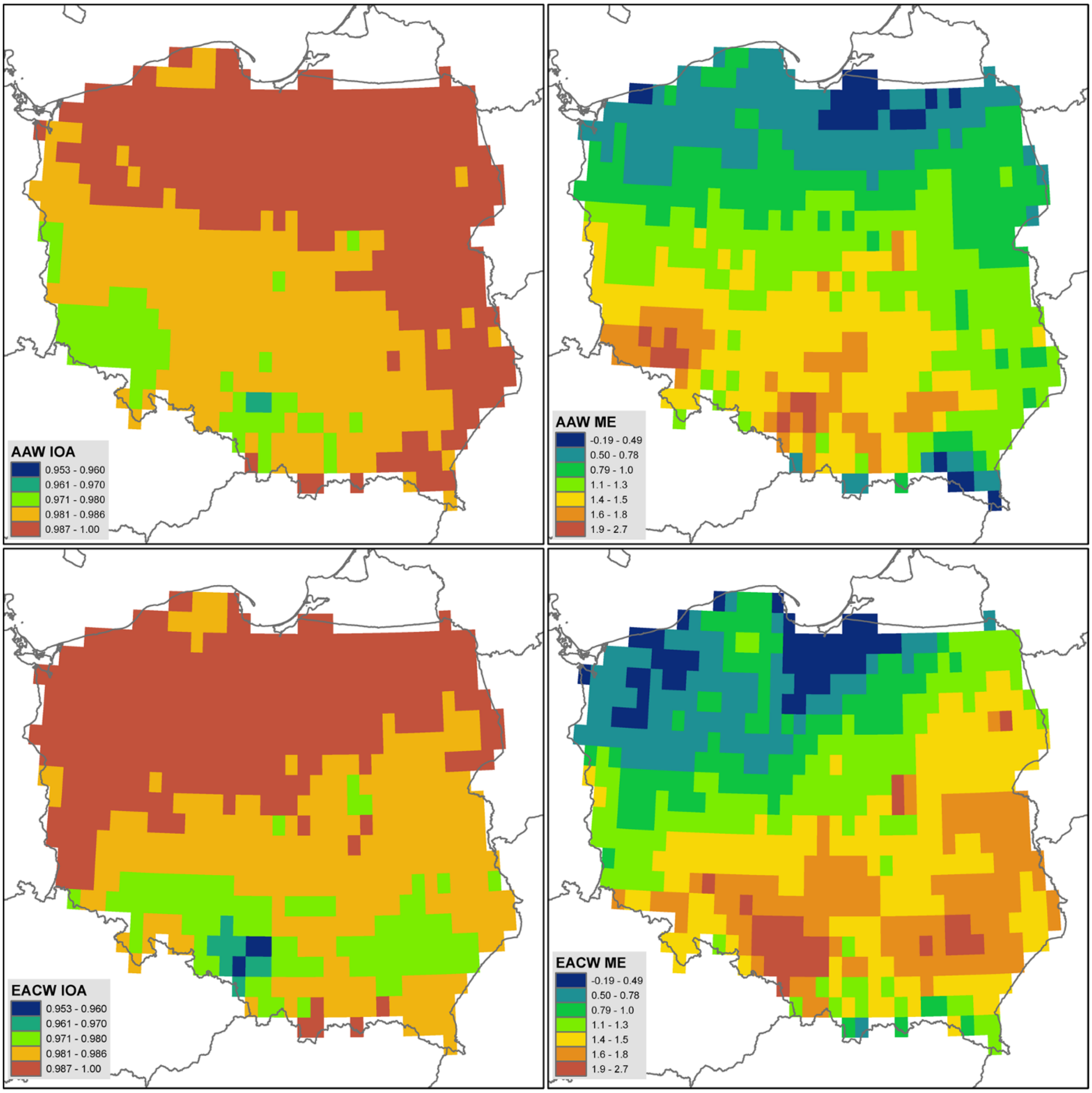

Figure 14
ME and IOA between the WRF and E-OBS air temperature data for AAW and EACW circulation types in the 1981–2010 period

- A tool for automatic derivation of circulation schemes was developed and used with high-resolution gridded meteorological data. The tool is flexible in terms of spatial domain resolution, location and meteorological input. The advantage of ACCT classification is that it provides the opportunity of type grouping depending on the research aim, while in long time series, a large number of circulation types permit detailed case studies. The classification scheme can also be extended by incorporating other classification criteria.
- The variability of the air temperature and precipitation between particular types and groups of circulation types confirmed the usefulness of the classification methodology. The worst results were connected with the anticyclonic group type and with the types with unstable convective air masses.

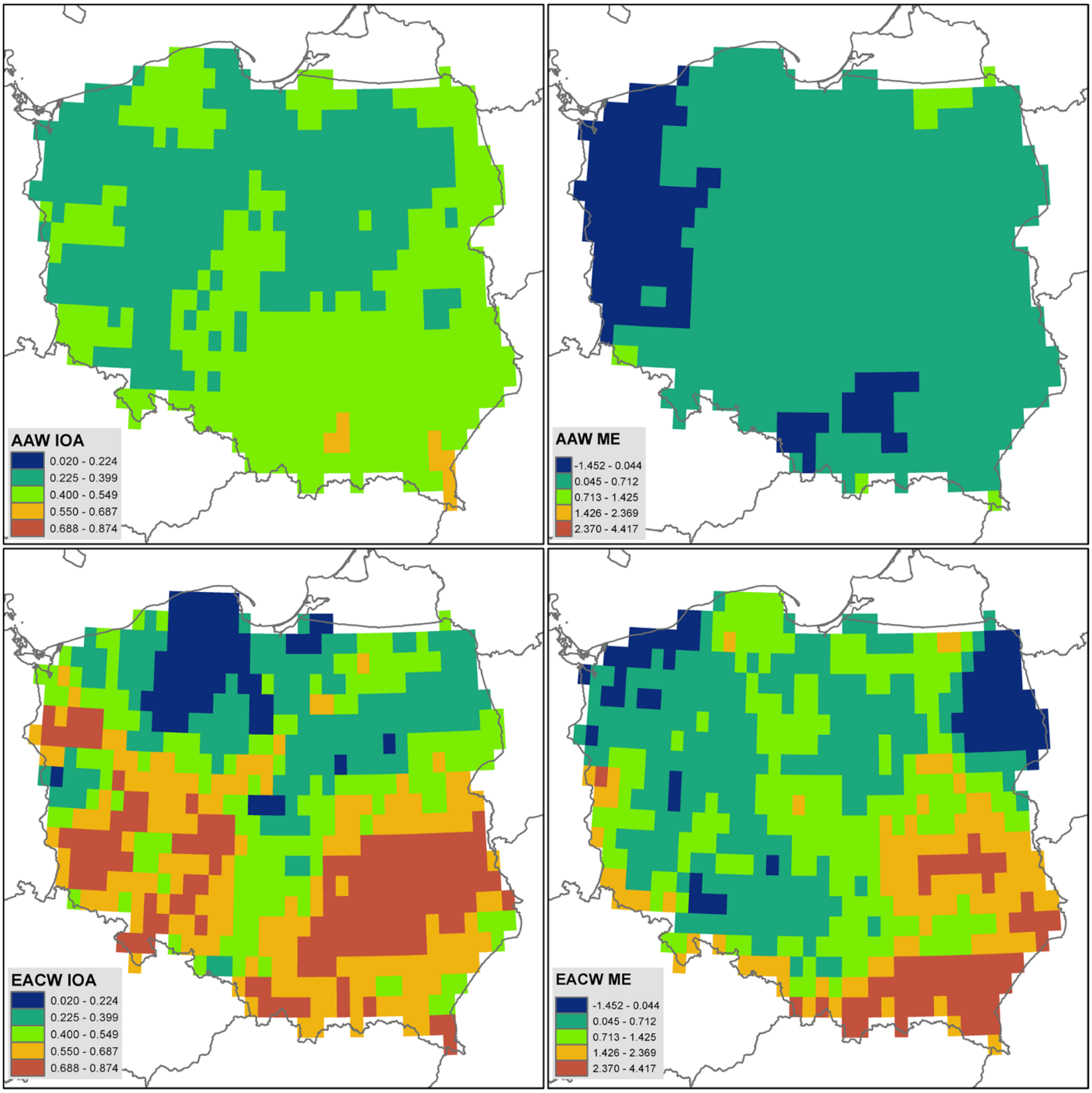

Figure 15
ME and IOA between the WRF and E-OBS rainfall data for AAW and EACW circulation types in the 1981–2010 period

The authors are aware that worse results, in terms of larger variability of meteorological parameters, could be caused by the difficulty in choosing the mode value of classification types for the large area of Poland, with its considerable spatial variability. The classification scheme will therefore be modified to allow for spatial variability of circulation type for a given day within the area that is analysed.

- In general, the WRF model shows a good agreement with the observed daily air temperature, especially for its lowest values. The higher air temperatures are, except for the winter months, overestimated. The error statistics of ME, MAE and IOA for WRF also show a better model–measurements agreement compared to E-OBS. The E-OBS overestimates the lower air temperatures in most seasons, which might be linked with the coarser spatial resolution compared to WRF. The spatial patterns of the air temperature and rainfall are similar for both WRF and E-OBS, when the long-term mean values are compared. The WRF model shows a larger spatial variability because of the higher spatial resolution.

- The close WRF–measurements agreement, quantified by ME, MAE and IOA for the air temperatures, is independent of group of circulation types. However, there is a seasonal variability in temperature agreement in particular circulation types considered. In contrast to small overestimation for all circulation types for spring and autumn, the winter months are underestimated, especially for frequent lower and upper anticyclonic groups of types (AAW, AAD). For all the seasons, except the summer, the WRF model shows lower, compared with the measurements, minima of the air temperature. In winter, the WRF model better reproduces the air temperatures for the coldest groups of circulation types (ACD, CdD). For warmer groups of circulation types in winter and autumn, E-OBS is in better agreement with the measurements. In spring and summer months, the mean air temperatures are in closer agreement with the measurements for the WRF model.
- The error statistics for the rainfall shows a worse performance of the WRF model, compared with E-OBS. This is especially the case for the summer months. The WRF model overestimates the measured rainfall, especially the higher daily values. The WRF model also gives more days with rainfall, compared to the measurements. However, the E-OBS underestimates the precipitation values mainly in the summer and autumn months.
- The differences between WRF and E-OBS for precipitation are similar in all groups of circulation types. For the spring and summer months, the WRF model overestimates the daily precipitation sums. This overestimation is especially large for the XX and eastern groups of circulation types. The maximum sums of precipitation for WRF are higher than the observed values, but are in better agreement with the measurements when compared to E-OBS. In winter and autumn, the modelled precipitation sums are close to the measurements (e.g. in WCdW) or underestimated for the lower anticyclonic-type groups.
- The spatial distribution of the differences between the WRF and E-OBS data changes significantly according to the atmospheric circulation type. This is of significant practical importance, as the large-scale atmospheric circulation pattern determines the uncertainty related to the meteorological information provided by the WRF model.

In this work we have shown that the WRF model performance depends strongly on the type of atmospheric circulation. This is especially the case for rainfall. This suggests that the model evaluation should also consider some indices related with circulation types, as presented in this study. Also, it means that the circulation type can be used to assess the uncertainty related with the numerical weather forecasting. High-resolution WRF model data can be used to determine the circulation types using the ACCT, with respect to, e.g. humidity of air mass.

The overall poor WRF model performance for rainfall shows the need for improvement. The uncertainty in the WRF model prediction for rainfall is high and changes both seasonally and with circulation type. The model performance could be improved, e.g. by data assimilation (e.g. GNSS data, as suggested by SCHWITALLA *et al.* 2011).

Acknowledgments

This work was supported by the National Science Centre (NCN), Poland (Grants Nos. NN404 014 740 and UMO-2011/03/B/ST10/06226). Calculations have been carried out in the Wroclaw Centre for Networking and Supercomputing (http://www.wcss.wroc.pl), Grant No. 170. Meteorological measurements for this work were provided by the Institute of Meteorology and Water Management, National Research Institute.

References

Badger, J., Frank, H., Hahmann, A.N., Giebel, G. (2014), *Wind-climate estimation based on mesoscale and microscale modelling: statistical-dynamical downscaling for wind energy applications*, Journal of Applied Meteorology and Climatology *53*, 1901–1919.

Bednorz, E. (2012), *Atmospheric conditions of intense thaws in the Polish lowlands*, Meteorologische Zeitschrift, Vol. *21*, No. 1, 89–98, doi:10.1127/0941-2948/2012/0228.

Bednorz, E., Wibig, J. (2008), *Snow depth in eastern Europe in relation to circulation patterns*, Annals of Glaciology *48*, 135–149, doi:10.3189/172756408784700815.

Bielec-Bąkowska, Z., Łupikasza, E. (2009), *Frosty, freezing and severe freezing days and their synoptic implications in Małopolska, Southern Poland, 1951–2000*, Bulletin of Geography—physical geography series, No. *1*, 39–62.

Bissolli, P., Dittmann, E. (2001), *The objective type classification of the German Weather Service and its possibilities of application to environmental and meteorological investigations*, Meteorologische Zeitschrift, Vol. *10*, No. 4, 253–260.

Czernecki, B. (2013), *Creating wind field time-series over the Southern Baltic area using a dynamical downscaling approach*, Meteorologische Zeitschrift Vol. *22*, 587–593.

Emery, C., Tai, E., Greg, Y. (2001) Enhanced Meteorological Modeling and Performance Evaluation for Two Texas Ozone Episodes. Report to the Texas Natural Resource Conservation Commission, College Station, TX, USA, pp 235

Fuentes U, Heimann D (2000): *An improved statistical-dynamical downscaling scheme and its application to the Alpine precipitation climatology*. Theor. Appl. Climatol. *65*: 119–135.

Gerstengarbe, F.W., Werner, P.C., Busold, W., Rüge, U., Wegener, K.O., Katalog der Grosswetterlagen Europas nach Paul Hess und Helmut Brezowsky 1881–1992 (Deustcher Wetterdienst, Offenbach am Main 1993).

Giorgi, F., Bates, T. (1989) *The climatological skill of a regional model over complex terrain*, Monthly Weather Review *117*, 2325–2347.

Haylock, M.R., Hofsta, N., Klein Tank, A.M.G., Klok, E.J., Jones, P.D., New, M. (2008), *A European daily high-resolution gridded data set of surface temperature and precipitation for 1950–2006*, Journal of Geophysical Research *113*, doi:10.1029/2008JD010201.

Huth, R., Beck, C., Philipp, A, Demuzere, M., Ustrnul, Z., Cahynova, M., Kysely, J., Tveito, O.E. (2008), *Classifications of Atmospheric Circulation Patterns Recent Advances and Applications*, Trends and Directions in Climate Research *1146*, 105–152.

Jeziorska, J., Niedzielski, T. (2015), *Applicability of TOPMODEL in the mountainous catchments in the upper Nysa Kłodzka River basin (SW Poland)*, Pure and Applied Geophysics (this issue).

Jiménez, P.A., Dudhia, J., González-Rouco, J.F., Montávez, J.P., García-Bustamante, E., Navarro, J., Vilà-Guerau de Arellano, J., Muñoz-Roldán, A. (2013), *An evaluation of WRF's ability to reproduce the surface wind over complex terrain based on typical circulation patterns*, Journal of Geophysical Research: Atmospheres *118*, 7651–7669.

Kalkstein, L.S., Tan, G., Skindlov, J.A. (1987), *An evaluation of three clustering procedures for use in synoptic climatological classification*, Jour. Appl. Meteor., *26*, 17–730.

Kryza, M., Wałaszek, K., Ojrzyńska, H., Szymanowski, M., Werner, M., Dore, A.J. (2016), High-Resolution Dynamical Downscaling of ERA-Interim Using the WRF Regional Climate Model for the Area of Poland. Part 1: Model Configuration and Statistical Evaluation for the 1981–2010 Period, Pure and Applied Geophysics, doi:10.1007/s00024-016-1272-5

Kożuchowski, K., Wibig, J., Maheras, P. (1992), *Connections between air-temperature and precipitation and the geopotential height of the 500-hpa-level in a meridional cross-section in Europe*, International Journal of Climatology *12*, 343–352.

Lityński, J. (1969), Liczbowa klasyfikacja typów cyrkulacji i typów pogody dla Polski, Prace PIHM, *97*, 3–14.

Lo, J.C.F., Yang, Z.L., Pielke, R.A. (2008), *Assessment of three dynamical climate downscaling methods using the Weather Research and Forecasting (WRF) model*, Journal of Geophysical Research-Atmospheres *113*.

Łupikasza, E. (2010), *Relationships between occurrence of high precipitation and atmospheric circulation in Poland using different classifications of circulation types*, Physics and Chemistry of the Earth, *35*(9), 448–455, doi:10.1016/j.pce.2009.11.012.

Mendez, M., Garcia-Diez, M., Fita, L., Fernandez, J., Mendez, F.J., Gutierrez, J.M. (2014), *High-resolution sea wind hindcasts over the Mediterranean area*, Climate Dynamics *42*, 1857–1872.

Niedźwiedź, T., Sytuacje synoptyczne i ich wpływ na zróżnicowanie przestrzenne wybranych elementów klimatu w dorzeczu górnej Wisły (Rozpr. Hab. UJ 58, Kraków 1981).

Ojrzyńska, H., Circulation conditionings of air temperature spatial differentiation in morphologically diverse area with the use of an example of the Western Sudeten (pl. Cyrkulacyjne uwarunkowania przestrzennego rozkładu temperatury powietrza w terenie zróżnicowanym morfologicznie na przykładzie Sudetów), (Rozprawy Naukowe Instytutu Geografii i Rozwoju Regionalnego, 36, Wrocław 2015).

Osuchowska- Klein, B., Katalog typów cyrkulacji atmosferycznej (WKiŁ, Warszawa 1978).

Osuchowska-Klein, B., Związek miedzy temperatura a cyrkulacją atmosferyczną (Mat. Bad. IMGW, ser. Meteorologia 17, Warszawa 1992).

Piotrowski, P., Obiektywna metoda klasyfikacji cyrkulacji atmosferycznej dla Polski, (Acta Universitatis Lodziensis, Folia Geographica Physica, 10, Wyd. UŁ, Łódź 2009).

Reyers M, Pinto JG, Moemken J (2015): *Statistical-dynamical downscaling for wind energy potentials: evaluation and applications to decadal hindcasts and climate change projections*. Int. J. Climatol. *35*: 229–244.

Schwitalla, T., Bauer, H.-S., Wulfmeyer, V., Aoshima, F. (2011), *High-resolution simulation over central Europe: assimilation experiments during COPS IOP 9c*, Quarterly Journal of the Royal Meteorological Society *137*: 156–175. doi:10.1002/qj.721.

Skamarock, W.C., Klemp, J.B., Dudhia, J., Gill, D.O., Barker, D.M., Duda, M., Huang, X.-Y., Wang, W., Powers, J.G. (2008), A description of the advanced research WRF version 3, Technical report TN-475 + STR, NCAR.

Szymanowski, M., Kryza, M., Spallek, W. (2013), *Regression-based air temperature spatial prediction models: an example from Poland*, Meteorologische Zeitschrift *22*, 557–585.

The NCAR Command Language (Version 6.1.2) [Software]. (2013). Boulder, Colorado: UCAR/NCAR/CISL/VETS. doi:10.5065/D6WD3XH5.

Twardosz, R., Niedźwiedź, T. (2001), *Influence of synoptic situations on the precipitation in Krakow (Poland)*, International Journal of Climatology, Vol. *21*, 4, 467–481, doi:10.1002/joc.620.

Twardosz, R., Niedźwiedź, T., Łupikasza, E. (2011), *The influence of atmospheric circulation on the type of precipitation (Kraków, southern Poland)*, Theoretical and Applied Climatology, *104*, 233–250, doi:10.1007/s00704-010-0340-5.

Ustrnul, Z., Zmienność cyrkulacji atmosfery na półkuli północnej w XX wieku (Mat. Bad. IMGW, ser. Meteorologia, 27, Warszawa 1997).

Ustrnul, Z. (2000), *Synoptic—climatic structure of the extreme air thermal phenomena in Poland*, Geographia Polonica *73*(2), 99–109.

Ustrnul, Z. (2006), *Spatial differentiation of air temperature in Poland using circulation types and GIS*, Int. J. Climatol., Vol. *26*, 1529–1546.

Ustrnul, Z., Czekierda, D., Wypych, A. (2010), *Extreme values of air temperature in Poland according to different atmospheric circulation classifications*, Physics and Chemistry of the Earth, *35*, 429–436.

Ustrnul, Z., Wypych, A., Winkler, J.A., Czekierda, D. (2014), *Late spring freezes in Poland in relation to atmospheric circulation*, Quaestiones Geographicae *33*(3), 165–172.

Wibig, J., Związki wybranych elementów klimatu Polski z cyrkulacjąna powierzchni izobarycznej 500 hPa nad Europą i północnym Atlantykiem (Phd dissertation, Katedra Meteorologii i Klimatologii UŁ, Łódź 1991).

Wibig, J., Wpływ cyrkulacji atmosferycznej na rozkład przestrzenny anomalii temperatury i opadów w Europie (Rozprawy habilitacyjne UŁ, Wyd. UŁ, Łódź 2001).

Wibig, J., Jaczewski, A., Brzoska, B., Konca-Kędzierska, K., Pianko-Kluczyńska, K. (2014), *How does the areal averaging influence the extremes? The context of gridded observation data sets*, Meteorologische Zeitschrift, Vol. *23*, No. 2, 181–187, doi:10.1127/0941-2948/2014/0470.

Woyciechowska, J., Ustrnul, Z. (2011), *Fuzzy logic circulation types based on the Osuchowska-Klein classification system created for Poland*, Theoretical and Applied Climatology *104*, 543–549, doi:10.1007/s00704-010-0366-8.

(Received January 22, 2015, revised February 17, 2016, accepted March 11, 2016, Published online March 30, 2016)

Pure Appl. Geophys. 174 (2017), 551–568

DOI 10.1007/s00024-016-1267-2

Pure and Applied Geophysics

Aerosol-Radiation Feedback and PM_{10} Air Concentrations Over Poland

MAŁGORZATA WERNER,[1,2] MACIEJ KRYZA,[1] CARSTEN AMBELAS SKJØTH,[2] KINGA WAŁASZEK,[1] ANTHONY J. DORE,[3]
HANNA OJRZYŃSKA,[1] and JAN KAPŁON[4]

Abstract—We have implemented the WRF-Chem model version 3.5 over Poland to quantify the direct and indirect feedback effects of aerosols on simulated meteorology and aerosol concentrations. Observations were compared with results from three simulations at high spatial resolutions of 5 × 5 km: (1) BASE—without any aerosol feedback effects; (2) DIR—with direct aerosol-radiative effects (3) INDIR—with direct and indirect aerosol-radiative effects. We study the overall effect during January 2011 as well as selected episodes of the highest differences in PM_{10} concentrations between the three simulations. For the DIR simulation, the decrease in monthly mean incoming solar radiation (SWDOWN) appears for the entire study area. It changes geographically, from about −8.0 to −2.0 W m^{-2}, respectively for the southern and northern parts of the country. The highest changes do not correspond to the highest PM_{10} concentration. Due to the solar radiation changes, the surface mean monthly temperature (T2) decreases for 96 % of the area of Poland, but not more than 1.0 °C. Monthly mean PBLH changes by more than ±5 m for 53 % of the domain. Locally the differences in PBLH between the DIR and BASE are higher than ± 20 m. Due to the direct effect, for 84 % of the domain, the mean monthly PM_{10} concentrations increase by up to 1.9 μg m^{-3}. For the INDIR simulation the spatial distribution of changes in incoming solar radiation as well as air temperature is similar to the DIR simulation. The decrease of SWDOWN is noticed for the entire domain and for 23 % of the domain is higher than −5.0 W m^{-2}. The absolute differences of PBLH are slightly higher for INDIR than DIR but similarly distributed spatially. For daily episodes, the differences between the simulations are higher, both for meteorology and PM_{10} concentrations, and the pattern of changes is usually more complex. The results indicate the potential importance of the aerosol feedback effects on modelled meteorology and PM_{10} concentrations.

Key words: WRF-Chem, feedback, aerosol, PM10, Poland.

1. Introduction

Aerosol particles have an important role in the climate system acting on the global radiation budget in two ways—directly by scattering and absorbing the incoming radiation or indirectly by altering the cloud properties (e.g. CHARLSON *et al.* 1992; ANDREAE *et al.* 2005; ROSENFELD *et al.* 2008). Furthermore, a climate-biosphere feedback mechanism on diffuse radiation can alter net ecosystem exchange significantly (MERCADO *et al.* 2009) and it has been suggested that this process will also be very important on the emission of particle precursors such as isoprene from nature (WILTON *et al.* 2011). Additionally, studies of human health indicated that there are significant correlations between particulate matter levels and increased respiratory and cardiovascular diseases, and mortality (POPE *et al.* 2002; PEREZ *et al.* 2008). Many chemical transport models (CTMs) have been developed to better understand the physical and chemical processes of gas-phase species and particulate matter. The models generally underestimate $PM_{2.5}$ and PM_{10} mass concentrations by 4.0–14.0 μg m^{-3} (10–50 %) and 6.5–18.0 μg m^{-3} (20–50 %), respectively (TUCCELLA *et al.* 2012). It is, therefore, important to explore the processes that relate to PM concentrations to explain this underestimation.

Most CTMs are implemented as offline models, where the meteorological input data are provided by

---

Electronic supplementary material The online version of this article (doi:10.1007/s00024-016-1267-2) contains supplementary material, which is available to authorized users.

[1] Department of Climatology and Atmosphere Protection, University of Wrocław, ul. Kosiby 8, 51-521 Wrocław, Poland. E-mail: malgorzata.werner@uwr.edu.pl; maciej.kryza@uwr.edu.pl; kinga.walaszek@uwr.edu.pl; hanna.ojrzynska@uwr.edu.pl

[2] National Pollen and Aerobiology Research Unit, Institute of Science and the Environment, University of Worcester, Henwick Grove, Worcester WR2 6AJ, UK. E-mail: c.skjoth@worc.ac.uk

[3] Centre for Ecology and Hydrology, Bush Estate, Penicuik, Midlothian EH26 OQB, UK. E-mail: todo@ceh.ac.uk

[4] Department of Satellite Geodesy, Wroclaw University of Environmental and Life Sciences, ul. Grunwaldzka 53, 50-357 Wrocław, Poland. E-mail: jan.kaplon@igig.up.wroc.pl

an independent model. In that solution it is impossible to simulate the complexity of the aerosol-cloud-radiation feedback process. Additionally, the decoupling between the meteorological and chemical model leads to a loss of information because of the physical and chemical processes occurring on a time scale smaller than the output time step of the meteorological data (ZHANG 2008). It is well accepted that weather has a profound impact on air quality as well as that atmospheric composition can influence both weather and climate. Coupling of atmospheric dynamics, pollutant transport, chemical reactions and atmospheric composition will remain one of the most challenging tasks over the next decades as they are strongly integrated processes (JACOBSON 2002; ZHANG 2008; BAKLANOV *et al.* 2014).

Accurately simulating these feedbacks requires the use of online-coupled meteorology-chemistry models, e.g. GATOR-MMTD (JACOBSON *et al.* 1996), WRF-Chem (GRELL *et al.* 2005), GEM-AQ (KAMINSKI *et al.* 2007), GEM-MACH (MORAN *et al.* 2010), among which the weather research and forecasting with chemistry (WRF-Chem) model represents a state-of-the-science online model. ZHANG (2008) applied WRF-Chem over eastern Texas and showed that the presence of aerosols leads to a decrease in surface temperature by up to 0.18 °C. By coupling a cloud microphysics module with WRF, LYNN *et al.* (2007) illustrated the suppression of precipitation by continental aerosol in the Sierra Nevada Mountains. ZHANG *et al.* (2010) applied WRF-Chem over North America at a 36 km × 36 km resolution to examine the influence of direct and indirect feedback effects on meteorology and photolysis rate. Despite the relatively coarse resolution, the results of ZHANG *et al.* (2010) indicated the potential importance of the aerosol feedbacks on a regional scale, even at a time scale of a month. Similar studies on feedback effects have been undertaken for Europe by FORKEL *et al.* (2012), where the WRF-Chem model was implemented at a resolution of 22.5 × 22.5 km. This work has shown that over the European continent, many of the spatial changes in meteorological parameters and pollutants due to aerosol effects are not only a general feature but also a result of the prevailing meteorological situation. It was suggested that a more pronounced feedback mechanism from aerosols can be expected with increased horizontal resolution (e.g. 5 vs. 50 km) or by focusing on episodes compared to long term means.

In this study we explored the direct and indirect feedback effects of aerosols on both meteorology and PM concentrations. We focused on the difference between specific episodes and long-term means and

Table 1

Model components and configuration

Category	D01	D02	D03
Simulation period	01–30 of January 2011		
Domains	Europe	Central Europe	Poland
Horizontal resolutions	45 km	15 km	5 km
Vertical resolution	35 layers		
Shortwave and longwave radiation	RRTMG		
Land-surface model	Noah LSM		
Boundary layer scheme	YSU		
Cumulus parameterization	GRELL and DENVENYI (2002)	GRELL and DENVENYI (2002)	Explicitly resolved
Microphysics	LIN *et al.* (1983)		
Prognostic cloud droplet number	Prognostic equation used only for the INDIR simulation		
Analysis nudging (FDDA)	Yes	Yes	No
Gas-phase mechanism	RADM2		
Aerosol model	MADE/SORGAM		
Photolysis scheme	Fast-J		
Wet deposition	Simplified parameterisation for wet scavenging		
Sea salt parameterisation	Yes (MADE/SORGAM sea salt emission)		

Please refer to the WRF and the WRF-Chem user's guides for a complete description of the options

Table 2

Mean spatial error statistics (58 stations, January 2011) for meteorological surface variables (T2, RH2, W10) for the BASE, DIR and INDIR simulations

	T2			RH2			PSFC			W10		
	BASE	DIR	INDIR	BASE	DIR	INDIR	BASE	DIR	INDIR	BASE	DIR	INDIR
MB	−2.081	−2.224	−2.226	3.858	4.013	4.032	1.539	1.555	1.564	0.593	0.587	0.589
MGE	2.540	2.637	2.636	6.925	6.937	6.918	4.067	4.070	4.074	1.504	1.503	1.507
NMB	−16.356	−18.095	−18.186	0.044	0.046	0.046	0.002	0.002	0.002	0.264	0.262	0.262
NMGE	17.576	18.879	18.953	0.078	0.078	0.078	0.004	0.004	0.004	0.485	0.485	0.486
RMSE	3.168	3.275	3.275	9.671	9.694	9.678	4.151	4.153	4.158	1.896	1.896	1.898
IOA	0.853	0.848	0.848	0.612	0.609	0.610	0.907	0.907	0.907	0.787	0.787	0.787

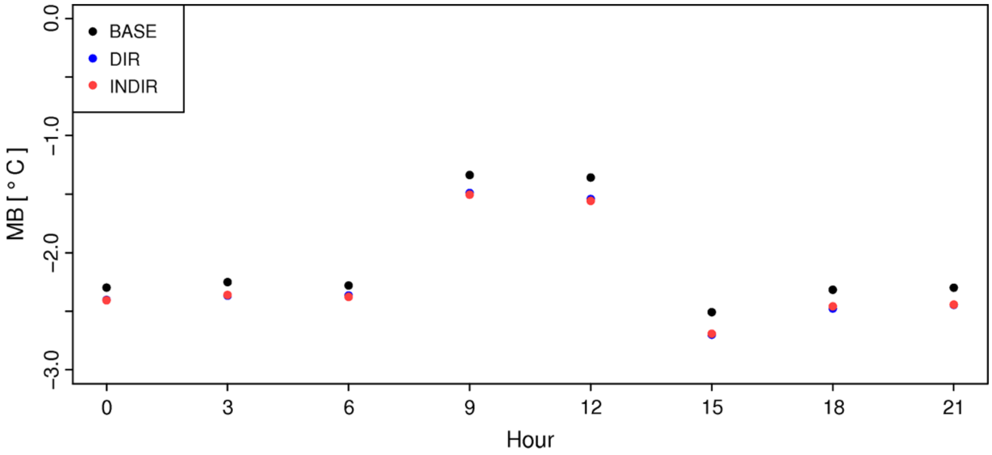

Figure 1
Diurnal cycle in mean bias for T2 for Poland for January 2012

Table 3

Error statistics for SWDOWN for Warszawa, Sopot and Strzyżów

	Warszawa			Sopot			Strzyżów		INDIR
	BASE	DIR	INDIR	BASE	DIR	INDIR	BASE	DIR	
MB	67.470	58.178	57.522	31.435	27.587	27.379	55.318	42.491	43.842
MGE	73.233	64.354	64.408	44.987	41.191	42.099	71.316	61.163	61.003
NMB	1.703	1.468	1.452	0.495	0.434	0.431	0.652	0.500	0.516
NMGE	1.848	1.624	1.626	0.708	0.648	0.663	0.840	0.720	0.719
RMSE	108.739	95.871	96.049	62.713	57.626	59.870	101.156	85.810	85.662
IOA	0.510	0.551	0.548	0.854	0.870	0.860	0.780	0.821	0.824

implemented for this purpose the WRF-Chem model version 3.5 at high spatial resolution (5 km × 5 km) over Poland. With this we studied an extended period that contains several episodes of high measured PM10 concentrations: January 2011. The aim of this study was twofold: first we wanted to compare the model results of meteorological variables and PM_{10} concentrations with available measurements. Second, we quantified the feedback effects on modelled aerosol concentrations and meteorological parameters.

2. *Methodology*

2.1. *WRF-Chem Setup*

The Weather Research and Forecasting (WRF) model is a mesoscale non-hydrostatic meteorological model that includes a large number of options. These options include parameterisations of the Planetary Boundary Layer, the land surface description, cloud microphysics, radiation and convection processes. WRF-Chem is a version of WRF coupled online with a chemistry model where meteorological and chemical components of the model are predicted simultaneously. A complete description of the model is given by Grell *et al.* (2005) and Fast *et al.* (2006). The main options for physical and chemical schemes used here are listed in Table 1. These include the Noah Land Surface Model (Chen and Dudhia 2001), YSU boundary layer physics (Hong *et al.* 2006), RRTMG long- and short-wave radiation scheme (Iacono *et al.* 2008), Grell 3D parameterisation with radiative feedback and shallow convection (Grell 2002), the Lin microphysics scheme (Lin *et al.* 1983). The convection was explicitly resolved for the innermost domain (d03), which is of the main focus of this paper, and no analysis nudging (FDDA) was included for this domain. For the BASE and DIR simulation we used the Lin *et al.* (1983) scheme with the prognostic cloud droplet number turned off. In the INDIR simulation the cloud droplet number of grid scale clouds was calculated by a prognostic equation.

The gas phase chemistry model used in this study was the regional acid deposition model, version 2 (RADM2, Stockwell *et al.* 1990). The aerosol module included the Modal Aerosol Dynamics Model for Europe (MADE, Ackermann *et al.* 1998) for the inorganic fraction and the Secondary Organic Aerosol Model (SORGAM, Schell *et al.* 2001) for the carbonaceous secondary fraction.

The model was run for January 2011 with three one-way nested domains. This study focuses on domain 3, which covers Poland at 5 km × 5 km spatial resolution and hourly temporal resolution. The simulations were driven by the NCEP final analysis, available every 6 h, with 1° × 1° spatial resolution and TNO MACC II emissions, with 1/8° × 1/16° spatial resolution (Kuenen *et al.* 2014). Temporal variations in emissions are restricted to emissions from nature, while the TNO MACC II emissions are assumed constant during the entire simulation. The chemical boundary conditions of trace gases consist of idealised, northern hemispheric, mid-latitude, clean environmental profiles based upon the results from the NOAA Aeronomy Lab Regional Oxidant Model (Liu *et al.* 1996). The simulation uses a spin up, with the model simulation started on 30 December 2010. To study the influence of the feedback effects, we run three simulations: (1) BASE—baseline simulation, without any aerosol feedback effects; (2) DIR—direct aerosol-radiative effects only (also includes semi-direct effects); (3) INDIR—direct aerosol-radiative effects and indirect effects (also includes semi-direct and second indirect effects).

2.2. *Evaluation of the WRF-Chem Model Results*

The WRF modelled air temperature at 2 m (T2), relative humidity at 2 m (RH2), surface pressure (PSFC) and wind speed at 10 m (W10) were compared with 3-hourly measurements from 58 sites provided by the Institute of Meteorology and Water Management in Poland. The model evaluation was done for all three simulations—BASE, DIR and INDIR. The following statistics were calculated for all available stations as mean values for January 2011: mean bias (MB), mean gross error (MGE), normalised mean bias (NMB), normalised mean gross error, root mean square error (RMSE) and index of agreement (IOA).

Modelled downward short wave flux at ground surface (SWDOWN) was compared with measurements from three stations under the Poland-AOD network (Warszawa, Sopot, Strzyżów) and provided by the Institute of Geophysics, University of Warsaw. For Warszawa and Strzyżów the data were available for the entire analysed period and for Sopot for the first 18 days of January. The time series of modelled and observed values were provided for all stations and individual statistics for daylight hours for each station were calculated. Additionally we used all stations from the World Radiation Data Centre available for Poland for January 2011. This included three stations (Kołobrzeg, Belsk and Zakopane) available at daily temporal resolution. For these stations we plotted time series with measured and aggregated to daily modelled values SWDOWN.

Measured hourly PM_{10} concentrations were provided by the Chief Inspectorate of Environmental Protection in Poland. 55 stations with data availability above 75 % were used to validate the modelled results. First, the average statistics, for the entire domain (FAC2, MB, RMSE, IOA) for all three simulations were calculated and presented in a table and a mean scatter plot was plotted. Then, for three sites located in the large Polish cities (Warszawa, Poznań, Łódź, marked in Fig. 8), time series of modelled and observed data were plotted and individual scatter plots presented. To check the importance of station location on model performance we used additional information on station types and plotted three Taylor diagrams (for the INDIR simulation):

1. according to type of station (background, industrial and traffic)
2. according to station type of area (rural, suburban and rural)
3. using only background stations and plotted according to station area type.

Finally the spatial distribution of MB between the INDIR simulation and observations is presented.

3. Results

3.1. Meteorology

The summary of domain-wide error statistics for all sites and the entire period of January 2011 is presented in Table 2. For all the simulations (BASE, DIR, INDIR) the lowest NMB and NMGE is for PSFC and the highest for T2. A high Index of Agreement occurs for all meteorological parameters, with only RH2 below 0.70. Inclusion of feedback effects slightly changes the statistics for T2, RH2, PSFC and W10. The highest decrease in model performance between BASE and INDIR simulation is for the air temperature. The mean bias of T2 was plotted at 3-hourly temporal resolution (Fig. 1). MB changes during the day but for all the simulations the lowest bias (below 1.5 °C) is at 9 and 12 am, whereas for the rest hours is above 2.0 °C. These diurnal changes are consistent with results reported by Kryza *et al.* (2015) for a long-term WRF simulation for Poland for years 1981–2010.

There is a reasonably good Index of Agreement (above 0.75) between modelled and observed solar radiation (SWDOWN) for Sopot and Strzyżów but observed values are overestimated by the model (Table 3; Fig. 2). The best performance has been obtained for the station located at the sea coast (Sopot) and the worse for Warszawa. Inclusion of the direct feedback improves all error statistics for the three sites; however, inclusion of indirect feedback increases MGE and RMSE for two of them, if compared to DIR. Time series plotted for daily values available from the World Radiation Data Centre for Belsk, Kołobrzeg and Zakopane (Fig. 1 in supplementary materials) present a similar trend as for hourly measurements from POLAND-AOD. The measurements are overestimated by the model, with the best agreement between model and observations for the sea cost station (Kołobrzeg) and worst for Zakopane (at the base of the mountains).

Temporal changes in SWDOWN, T2, PBLH and differences for the BASE, DIR and INDIR simulations are described for two locations—Łódź and Łeba (Fig. 3, figures for WSPD and RH2 are available in supplementary materials, Fig. 2). The first station is in the area with the highest positive differences of PM_{10} concentrations between INDIR and BASE, and the second is located in the area of the negative differences. Generally, the peak values of SWDOWN are highest for BASE and appear at the same time for all simulations. An exception is, e.g., the 12th and 17th January in Łódź, where the highest solar radiation is for INDIR and DIR, respectively. The highest differences in T2 appear for the same episodes as for SWDOWN. For selected periods the temperature in Łódź, for the INDIR simulation is up to 2.5 °C lower than that for BASE. High variability between DIR and INDIR simulations appears on 02nd–04th of January at Łódź station and 10–14th, 10–24th of January at Łeba. For several episodes

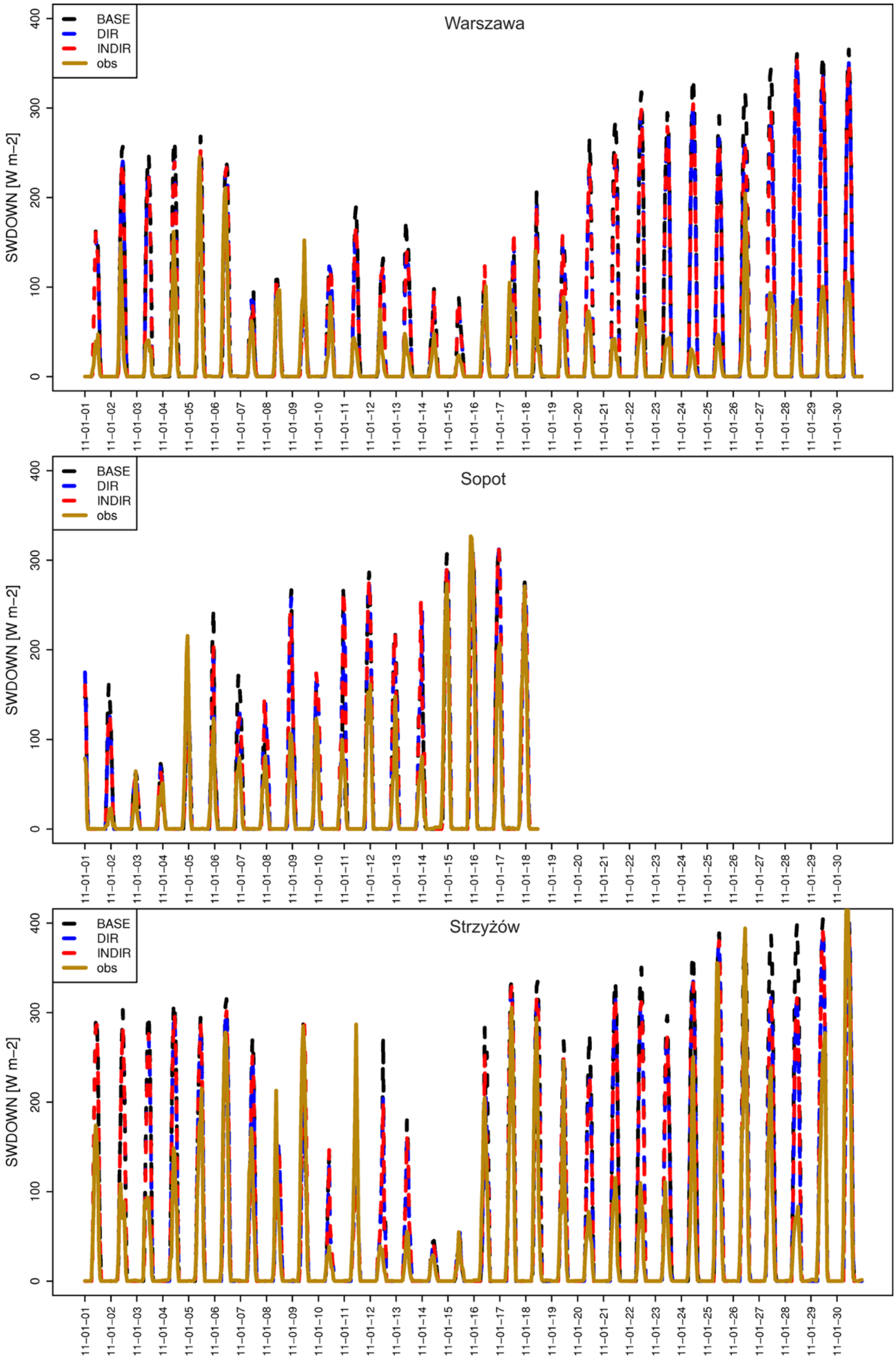

Figure 2
Modelled vs. observed hourly variation of SWDOWN

PBLH differs between DIR and INDIR simulation by more than 200 m. For Łódź, the lowest differences between the simulations are for the 4–9th and 11–15th of January, which also coincide with small differences in the air temperature. This is also a period with relatively lower values of solar radiation at the surface in comparison to the last 10 days of the month.

Mean monthly solar radiation for the BASE simulation for January 2011 in Poland domain was 53.3 W m^{-2}. Inclusion of direct effects in the model decreases the monthly mean solar radiation by 3.5 W m^{-2}. It changes geographically from about -8.0 to -2.0 W m^{-2}, respectively, for the southern and northern parts of the country. The lowest decrease is for the Baltic Sea. Solar radiation decrease is observed for the entire domain and it is more than -5.0 W m^{-2} for about 15 % of the area (Table 4). The highest changes do not correspond to the highest surface PM_{10} concentrations (Figs. 4, 9). Daily mean solar radiation changes from about -20.0 up to 10.0 W m^{-2}, both for 19th and 29th of January (Fig. 5). For the 19th the increase in SWDOWN was noticed for about 24 % of the domain. Inclusion of both direct and indirect feedback causes a decrease in monthly mean solar radiation equal to 3.8 W m^{-2}. The spatial distribution of changes are similar to changes for DIR, both for monthly and daily values (Figs. 4, 5). The decrease is apparent for the entire domain and for 23 % of the domain it is higher than 5.0 W m^{-2}. Due to the solar radiation changes, the surface mean monthly temperature (T2) decreases

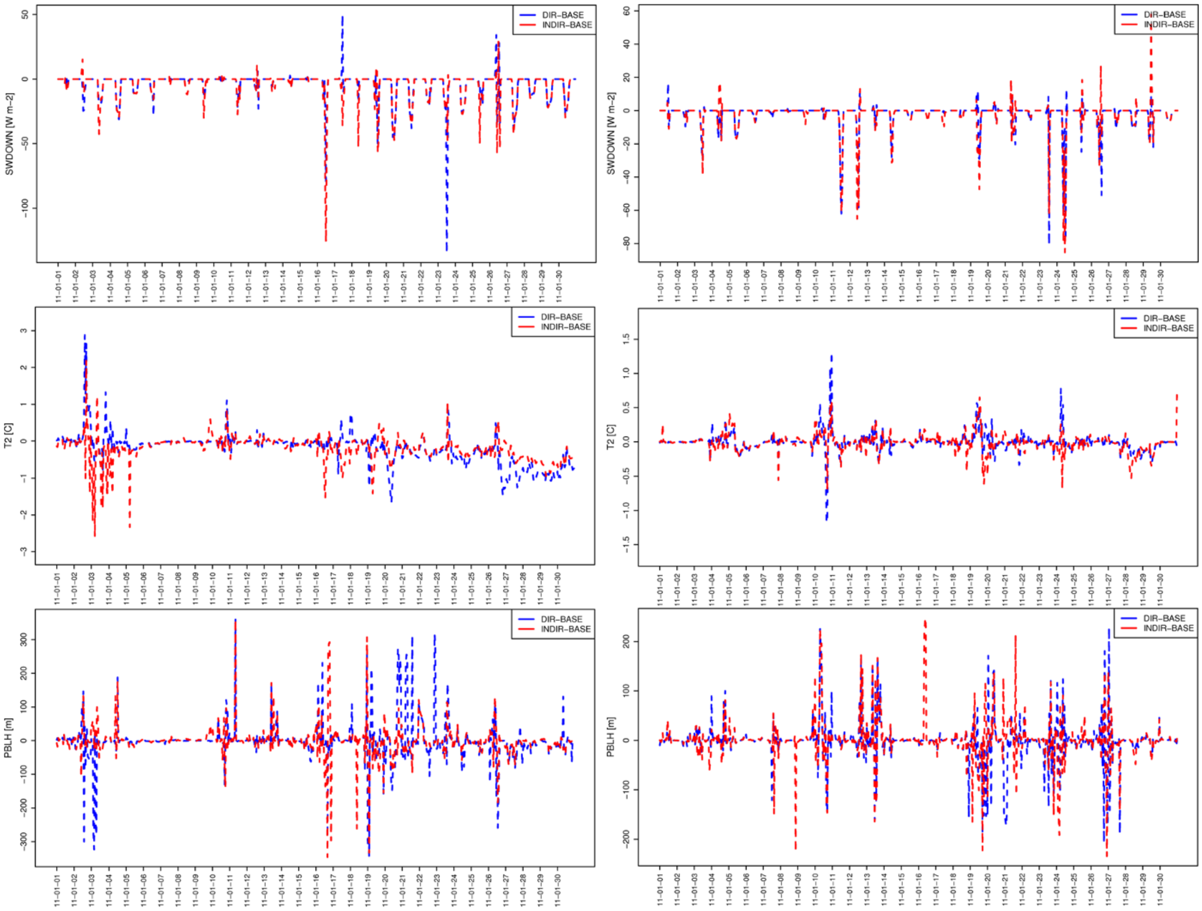

Figure 3
Hourly time series of differences in SWDOWN, T2 and PBLH between the DIR and BASE and INDIR and BASE simulations for two selected locations (*left*: Łódź, *right*: Łeba)

over 96 % of the domain, but the decrease is less than 1.0 °C (Table 4). Locally, in the north part of the country an increase was observed, of up to 0.5 °C. Daily variability is higher than monthly and for the 19th January varies between −1.5 and 2.0 °C, but for the majority of the area (about 75 %) it is negative. There are no significant differences between the results for the INDIR and DIR simulations (Table 4).

Mean PBLH for the BASE simulation in January 2011 was 243.3 m and varied from 62 to 502 m. The highest was over sea and the lowest in the south-eastern Poland. PBLH changes by more than ±5 m for 42 % of the domain when the direct feedback effect was included. The highest differences, both in the case of the DIR and INDIR simulations, were modelled for northern and southern Poland. For the northern part of the domain, DIR gives higher PBL than the BASE simulation up to 14 m, whereas for the southern part PBLH is lower for DIR by up to 23 m. For the episodes of the 19th and 29th January the differences exceed 20 m, respectively, for about 33 and 10 % of the domain; however, for some regions the difference is above 50 m and locally even exceeds 100 m.

Figure 4 ▶
Monthly mean spatial differences in SWDOWN, T2 and PBLH between DIR and BASE (*left column*) and INDIR and BASE (*right column*)

3.2. PM_{10} Concentrations

The model results for all three simulations have been compared with the surface PM_{10} measurements. There are no large differences in mean model performance among the simulations (Table 5; Fig. 6). For all of the three runs the FAC2 statistic is 0.89, MB equal from −9.54 to −9.70 µg m^{-3} and

Table 4

Percentage area with differences between simulations in the following ranges given in the table

SWDOWN [W m^{-2}] (monthly mean = 53.3)

Range	≤−10	(−10, −5>	(−5, −1>	(−1, 0>	(0, 1>	(1, 5>	(5, 10>	>10
Mon DIR	0.00	14.97	82.52	2.47	0.02	0.01	0.00	0.00
Mon INDIR	0.01	22.83	76.88	0.26	0.03	0.00	0.00	0.00
19 Jan DIR	3.87	16.28	46.21	14.98	8.59	8.43	1.40	0.25
19 Jan INDIR	5.26	16.91	40.43	12.88	9.13	12.12	2.80	0.49
29 Jan DIR	2.04	30.73	66.44	0.52	0.11	0.08	0.01	0.07
29 Jan INDIR	1.97	30.74	66.46	0.54	0.12	0.09	0.01	0.06

T2 [C] (monthly mean = −3.3)

Range	≤−1.5	(−1.5, −1.0>	(−1.0, −0.5>	(−0.5, 0>	(0, 0.5>	(0.5, 1.0>	(1.0, 1.5>	>1.5
Mon DIR	0.00	0.00	0.06	95.70	4.24	0.00	0.00	0.00
Mon INDIR	0.00	0.00	0.57	94.71	4.71	0.00	0.00	0.00
19 Jan DIR	0.13	0.24	1.27	73.53	24.18	0.53	0.09	0.03
19 Jan INDIR	0.17	0.38	1.92	64.32	32.15	0.90	0.13	0.04
29 Jan DIR	0.81	10.30	40.89	46.21	1.77	0.01	0.01	0.00
29 Jan INDIR	1.75	10.49	39.77	36.30	1.68	0.02	0.00	0.00

PBLH [m] (monthly mean = 243.3)

Range	<−20.0	(−20, 10>	(−10, −5>	(−5, 0>	(0, 5>	(5, 10>	(10, 20>	>20
Mon DIR	0.04	7.11	33.62	45.99	12.63	0.59	0.02	0.00
Mon INDIR	0.07	7.07	31.08	44.33	16.34	1.08	0.05	0.00
19 Jan DIR	18.00	15.68	12.17	18.05	11.24	6.93	8.15	9.77
19 Jan INDIR	21.05	14.98	10.09	14.56	10.81	7.06	9.16	12.29
29 Jan DIR	8.97	23.89	32.72	27.26	4.78	1.56	0.62	0.20
29 Jan INDIR	9.63	23.95	31.01	28.41	4.40	1.57	0.74	0.29

Mon DIR—mean monthly differences between DIR and BASE, Mon INDIR mean monthly differences between INDIR and BASE, and the same for daily differences for the 19th and 29th of January

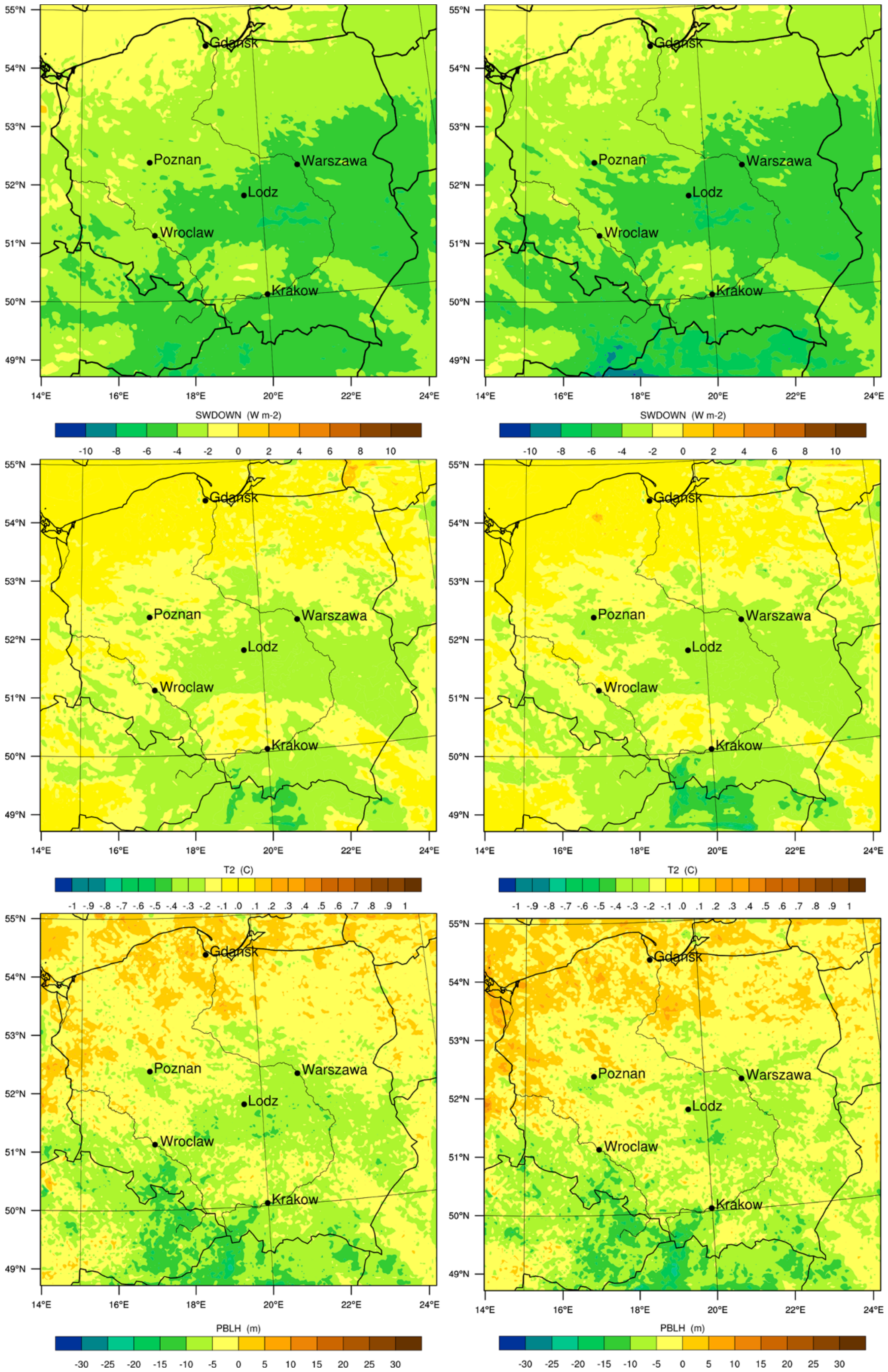
55°N
54°N
53°N
52°N
51°N
50°N
49°N
14°E
16°E
18°E
20°E
22°E
24°E
Gdansk
Poznan
Warszawa
Lodz
Wroclaw
Krakow
SWDOWN (W m-2)
-10 -8 -6 -4 -2 0 2 4 6 8 10
T2 (C)
-1 -.9 -.8 -.7 -.6 -.5 -.4 -.3 -.2 -.1 .0 .1 .2 .3 .4 .5 .6 .7 .8 .9 1
PBLH (m)
-30 -25 -20 -15 -10 -5 0 5 10 15 20 25 30

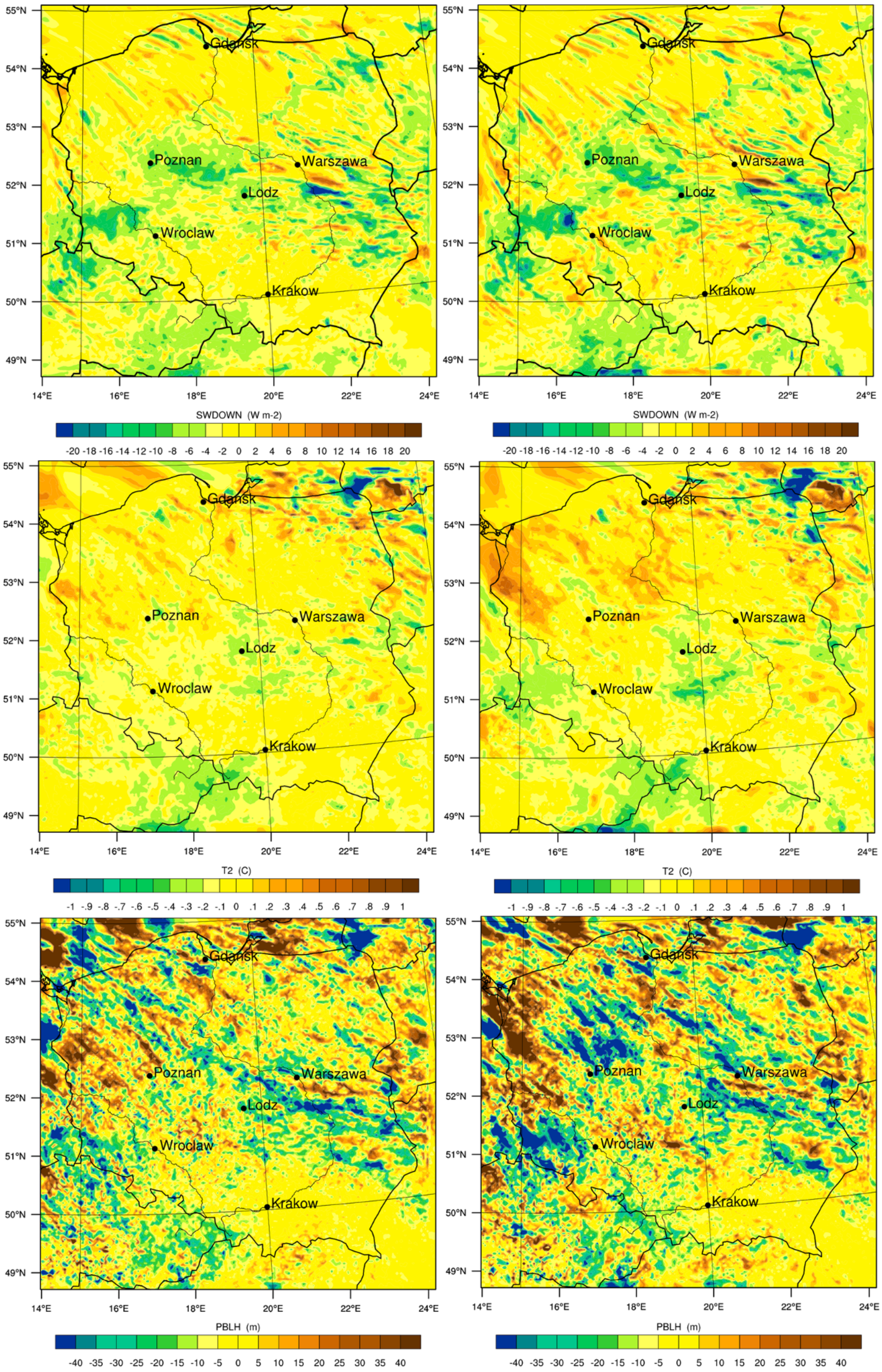
55°N
54°N
53°N
52°N
51°N
50°N
49°N
14°E
16°E
18°E
20°E
22°E
24°E
Gdansk
Poznan
Warszawa
Lodz
Wroclaw
Krakow
SWDOWN (W m-2)
-20 -18 -16 -14 -12 -10 -8 -6 -4 -2 0 2 4 6 8 10 12 14 16 18 20
T2 (C)
-1 -.9 -.8 -.7 -.6 -.5 -.4 -.3 -.2 -.1 0 .1 .2 .3 .4 .5 .6 .7 .8 .9 1
PBLH (m)
-40 -35 -30 -25 -20 -15 -10 -5 0 5 10 15 20 25 30 35 40

◄ Figure 5
Daily mean spatial differences in SWDOWN, T2 and PBLH between DIR and BASE (*left column*) and INDIR and BASE (*right column*) for the 19nd of January 2011

R between 0.67 and 0.69. However, the largest error statistics are for the simulation with no feedback effects (BASE), and inclusion of the direct and indirect effects leads to improvements in the model performance.

For three selected sites, located in the large Polish cities (Warszawa, Poznań, Łódź), time series of modelled (BASE, DIR, INDIR) and observed concentrations and scatter plots for INDIR are presented in Fig. 7. The model generally captures the variability induced by some pollution episodes (e.g. 4–7, 28–30 of January), but in some cases underestimates their magnitude. The main reason for this is the flat annual emission profile applied for anthropogenic sources. In Poland, anthropogenic emission changes seasonally for both primary PM_{10} and their gaseous precursors, especially for SNAP sector 2 emission (residential combustion) which is largely responsible for emission of PM_{10}. For INDIR the spatial distribution of MB is presented in Fig. 8. There is a tendency towards overestimation of observed values at the stations located at the sea coast, whereas for the stations located in the central and southern Poland the model has a tendency to underestimate of PM_{10} concentration.

Mean temporal changes of PM_{10} concentrations for the total domain are presented in Fig. 9. Significantly higher concentrations for DIR and INDIR in comparison to BASE are for 27th–29th of January. This episode is also quite well reproduced in Fig. 7 which presents PM_{10} concentrations for Warszawa, Poznań and Łódź.

Table 5

Domain-wide error statistics (55 stations, January 2011) for PM_{10} concentrations for the BASE, DIR and INDIR simulations (N total number of measurements)

	BASE	DIR	INDIR
N	720	720	720
FAC2	0.89	0.89	0.89
R	0.67	0.68	0.69
MB	−9.70	−9.56	−9.54
RMSE	17.84	17.58	17.55

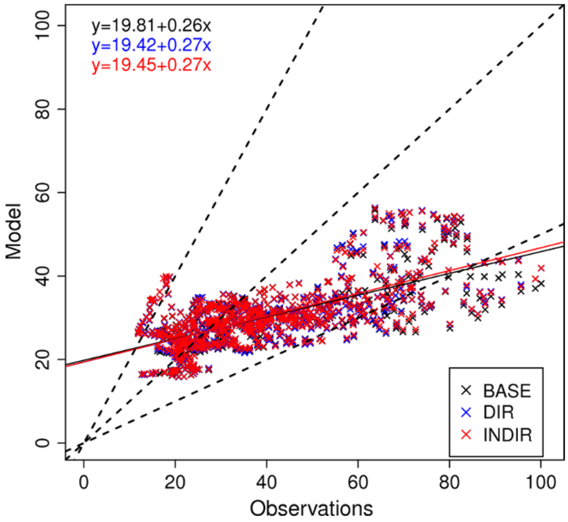

Figure 6
Scatter plot between modelled and observed PM_{10} concentrations for 55 stations for January 2011 (unit: µg m^{-3}). Different colours applied for BASE, DIR and INDIR. *P* values of fitted slopes are below 0.05

Taylor diagrams plotted according to station location (Fig. 10) show small differences with respect to the type of station. The results for background, industrial and traffic stations show very small differences. Nevertheless, the WRF-Chem results showed slightly worse results for urban stations when compared to suburban and rural. The correlation coefficients and centred RMSE for the background stations are slightly better for rural stations in comparison to suburban and urban stations.

The mean monthly modelled PM_{10} concentration for the domain of Poland (BASE simulation) in January 2011 is 26.0 µg m^{-3}. The highest concentrations concern the central part of the country and locally exceed 45.0 µg $m^{-3.}$

The monthly mean differences between DIR and BASE simulations range between −0.4 and 1.9 µg m^{-3} (Fig. 11). For 84 % of the area PM_{10} concentration is higher when indirect effects are present. The differences between INDIR and BASE simulations range between −0.5 and 2.0 µg m^{-3} with the spatial distribution similar to DIR.

When the direct feedback effect is included, daily differences in PM10 concentrations for the episodes of the 19th and 29th of January are between −5.0 and 13.0 µg m^{-3}. The PM_{10} concentrations are higher than for the BASE simulation for about 55 and 32 %

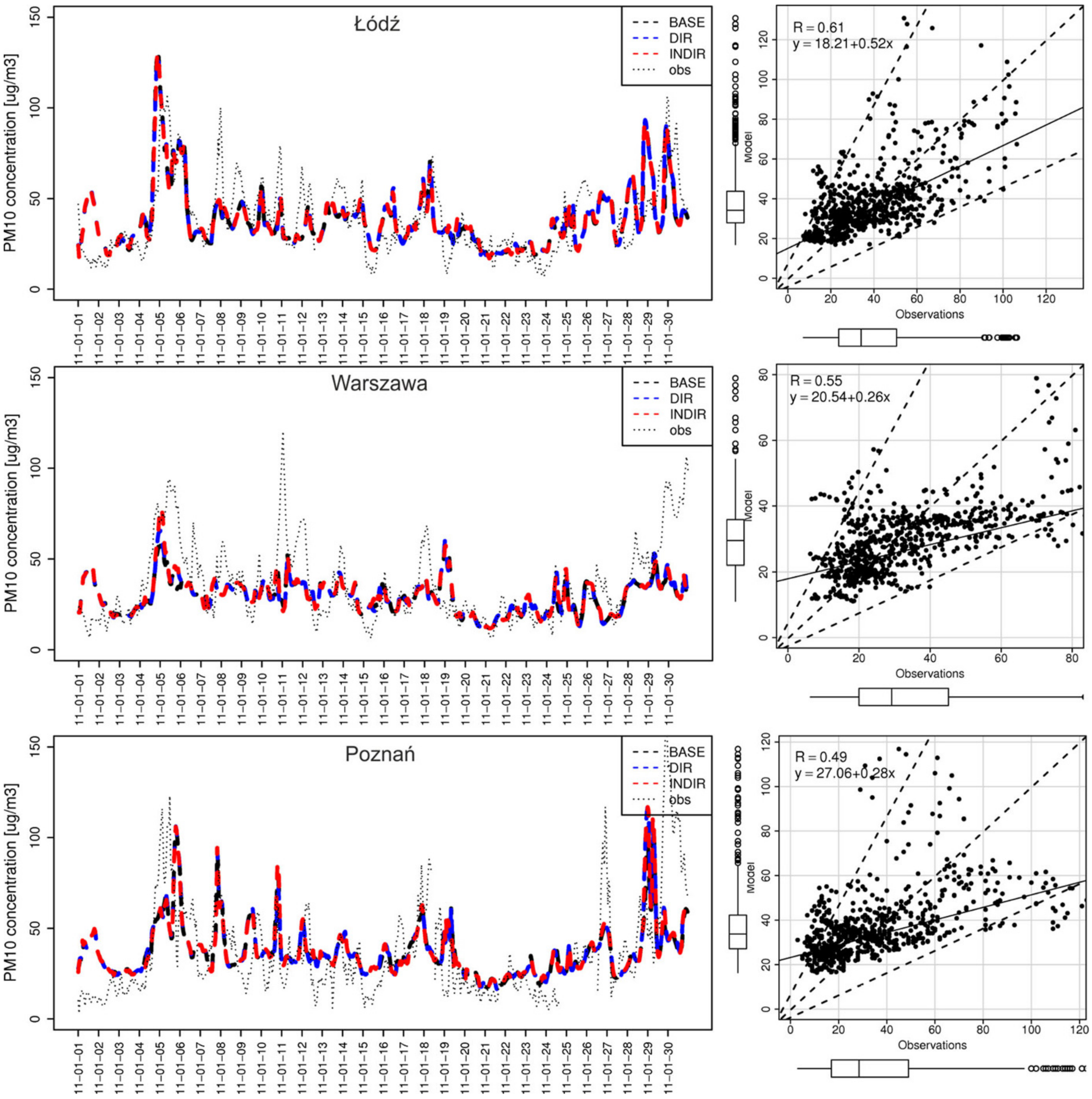

Figure 7
Time series of modelled (BASE, DIR, INDIR) and observed PM_{10} concentrations for selected stations for January 2011. *Scatter plots* of PM_{10} concentrations for the stations for INDIR simulation. *P* values of fitted slopes are below 0.05

of the domain, respectively, for the 19th and 29th of January. The highest differences are for central Poland for both 19th and 29th. In the case of the INDIR simulation the PM_{10} concentrations change in the range of −7.0 to 8.0 in comparison to DIR. The hourly variability between the DIR or INDIR and BASE simulation is higher than the daily variability. For the 19th of January at 12.00, the direct effect changes the PM_{10} concentration in the range of −13.0 and 20.0 μg m^{-3} and inclusion of the indirect effect changes the concentration from −33.0 to 28.0 μg m^{-3}, in comparison to the BASE simulation.

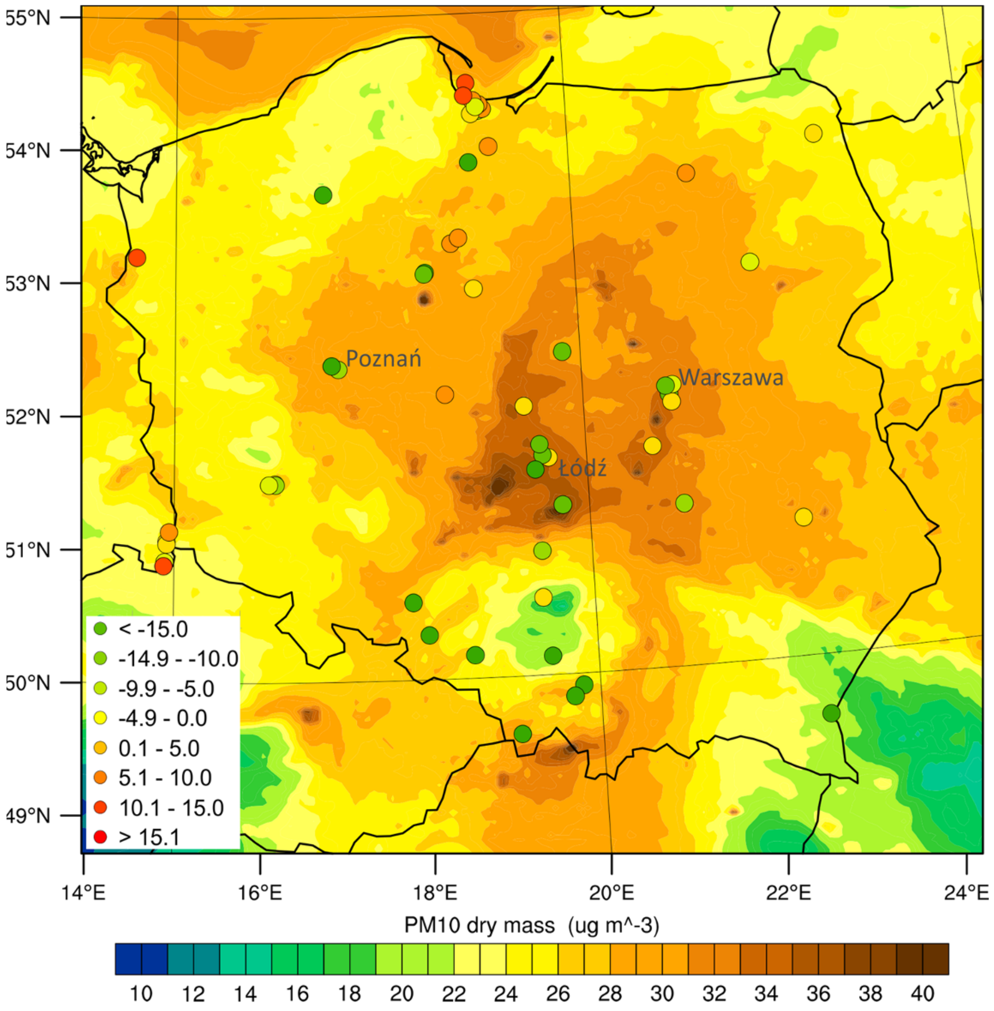

Figure 8
Monthly average PM_{10} concentrations (INDIR) and MB statistics marked by dots (MB = INDIR-observation)

4. Discussion and Conclusion

The online meteorology-chemistry model WRF-Chem has been implemented to investigate the direct and indirect feedback effects of aerosols on both meteorology and PM_{10} concentrations with the focus on the difference between specific episodes and monthly means. The simulations with high spatial resolution of 5 km × 5 km were run for Poland, for January 2011. The modelled meteorological parameters and PM_{10} concentrations have been evaluated against observations.

Aerosols affect radiation and temperature in several ways due to different radiative effects of different aerosol components (Jacobson *et al.* 1996). They can reduce incoming solar radiation via backscattering, therefore increasing the surface albedo and decreasing surface temperature. In our study a decrease in monthly mean incoming solar radiation appears for the entire area, whereas a decrease in surface air temperature is observed for about 96 % of the domain. The direct effect of aerosols on solar radiation is clearly noticeable for days with relatively high solar radiation. For these days the difference between DIR and BASE often reaches 50 W m^{-2} (e.g. between 20th and 30th January at Łódź, Fig. 3).

A higher cooling effect corresponds to the higher decrease in solar radiation. Absorption of solar radiation by black carbon and other absorbing aerosol

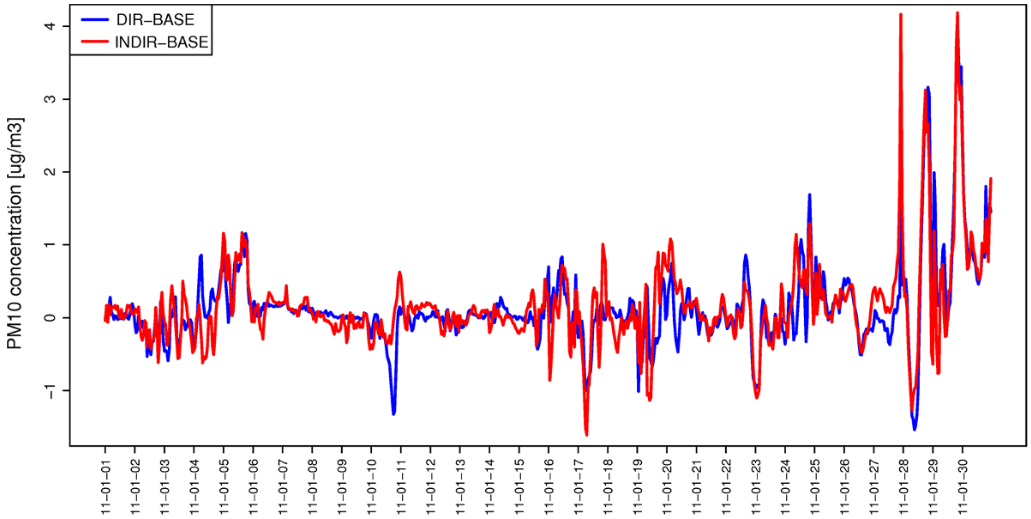

Figure 9
Time series of average differences in modelled PM_{10} concentrations between the DIR and BASE and INDIR and BASE simulations

compounds can result in regional heating of the atmosphere. Aerosols can also absorb and emit infrared radiation, also offsetting the cooling effect of backscattering during daytime. An increase in monthly mean temperature is noticed over about 4.5 % of the domain. For daily episodes on 19th and 29th January a local increase in solar radiation appears of up to 10.0 W m^{-2}. A similar effect of atmospheric heating by up to 26.0 W m^{-2} was noticed by Zhang *et al.* (2010) over the ocean and western US

Changes in air temperature in the atmosphere cause changes in monthly mean PBLH. Monthly mean PBLH changes in the range of ±5 m for 58 % of the study area. Locally the differences between DIR and BASE were higher than ±20 m. An increase appears in the northern and a decrease in the southern part of the domain. PBLH reduces because of enhanced stability as a result of the warming caused by black carbon in the PBL and the cooling at surface resulting from reduced solar radiation. Lack of this effect in the northern part of the study domain may be related to the relatively warm sea surface and local increase in air temperature. In the case of daily values the differences in PBLH for some regions reach ± 100 m. These changes may have a great impact on air pollution behaviour in the air. Reduced PBLH indicates a more stable planetary boundary layer and can thus further increase air pollution over areas where air pollution is already severe (Zhang *et al.* 2010).

Inclusion of direct feedback increases specific humidity for the western and north-western part of the domain (Fig. 3, supplementary materials). Inclusion of indirect feedback intensifies this effect for some parts of these regions. There is a strong impact of the indirect effect on specific cloud water content (QCLOUD) over the Baltic Sea and north-western and southern regions of the domain. Specific cloud water content increases notably for INDIR in comparison to the BASE and also DIR simulations and these changes are opposed to changes in Q2 (Fig. 3, supplementary material). For the region with the highest difference in QCLOUD between INDIR and BASE and relatively small difference between them, the vertical profile of QCLOUD was plotted (LOC1: 49.0°N, 20.0°E, LOC2: 52.0°N, 20.0°E, Fig. 4 in supplementary material). For the first location the vertical profile shows higher QCLOUD values for the INDIR simulation in comparison to BASE and DIR between the 1st and 5th model layers, but above these layers the results for the three simulations are the same. The highest difference between INDIR and BASE is for the 1st and 4th model layer. For the second location the QCLOUD profile is more diverse and differences appear both between the DIR and BASE and INDIR and BASE simulation. Generally, the

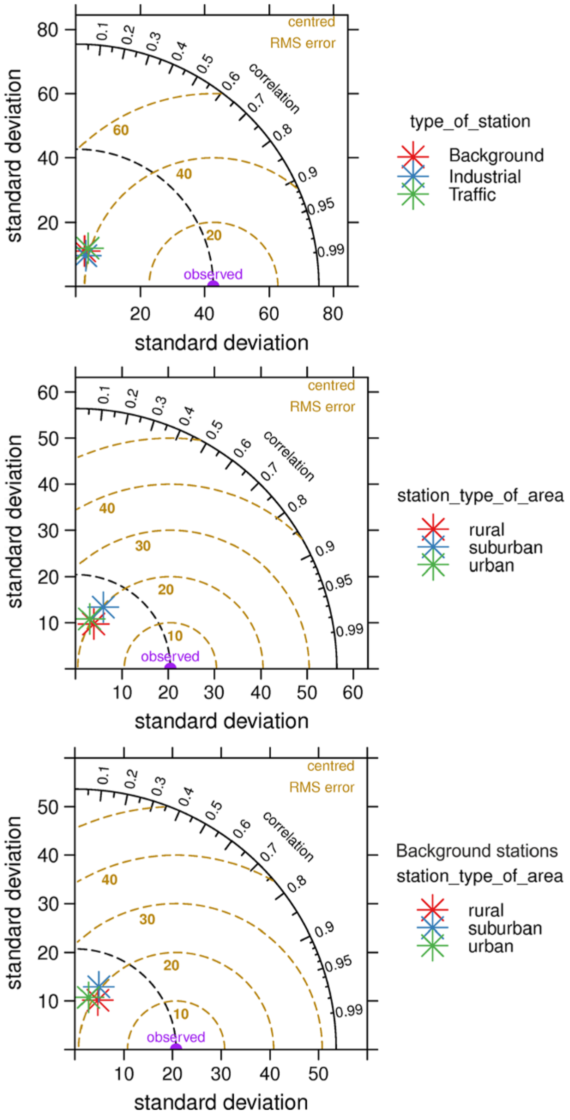

Figure 10
Taylor diagrams for PM10 concentrations for the INDIR simulation: according to type of station (background, industrial and traffic, the *upper figure*), according to station type of area (rural, suburban and rural, the *middle figure*) and using only background stations and plotted according to station area type (the *lower figure*)

highest values are for INDIR but for some areas (model layer 5) QCLOUD is the highest for BASE.

For the episodes of the 19th and 29th January, for some areas the decrease in QCLOUD is higher than 0.02 g kg^{-1} (Table 1 and Fig. 5, supplementary material). In the case of the INDIR simulation the spatial distribution of mean monthly changes is similar to DIR and ranges mainly between 0.001 and 0.300 g kg^{-1}. Considerable changes in monthly sum of rainfall for DIR simulation were found in contrast to the comparatively small changes in solar radiation for these regions. The pattern of the precipitation is not related to SWDOWN or QCLOUD.

Due to the direct effect, for 85 % of the domain, the mean monthly PM_{10} concentrations increase by up to 1.9 µg m^{-3}. A decrease of up to -0.4 µg m^{-3} was noticed over Baltic sea as well as in the western and partially also southern parts of Poland. For the INDIR simulation, generally a decrease is observed by $-0.1 \div -1.0$ µg m^{-3} in comparison to DIR but locally in central Poland an increase appears. Partially, it could be explained by liquid phase aerosols formation, as suggested in Forkel *et al.* (2012). In the case of daily values, differences in PM_{10} concentration between DIR and BASE reach 14.0 µg m^{-3} and are positive for about 80 % of the domain. Comparison of hourly PM_{10} concentrations between INDIR and BASE for the 19th and 29th of January at 12.00 gives differences of $-33.0 \div 28.0$ µg m^{-3} and $-12 \div 24$ µg m^{-3}, respectively.

The meteorological WRF model results for T2, RH2, PSFC and W10 perform well when compared with observations, with a high IOA for all parameters. Inclusion of feedback effects slightly decreases the error statistics for air temperature and relative humidity. Modelled solar radiation (SWDOWN) is in good correlation with observations, but observed values are overestimated by the model. Inclusion of feedback effects improves MB and MGE statistics. There are no large differences in mean model performance for PM_{10} concentration among the simulations. However, the worst results are obtained for the BASE simulation. The model has a tendency towards overestimation of observed PM_{10} concentrations at the sea coast station. This may be related to overestimation of sea salt aerosol emission as modelled wind speed is higher than observed values from meteorological stations in this region.

The results illustrate the potential importance of the aerosol feedback effects on modelled meteorology and PM_{10} concentrations. This influence is noticeable for mean monthly values but is evidently higher for daily and hourly episodes. This agrees well with previous studies with the COSMO-ART model on Saharan dust (Stanelle *et al.* 2010) and experiments from the EUCAARI campaign

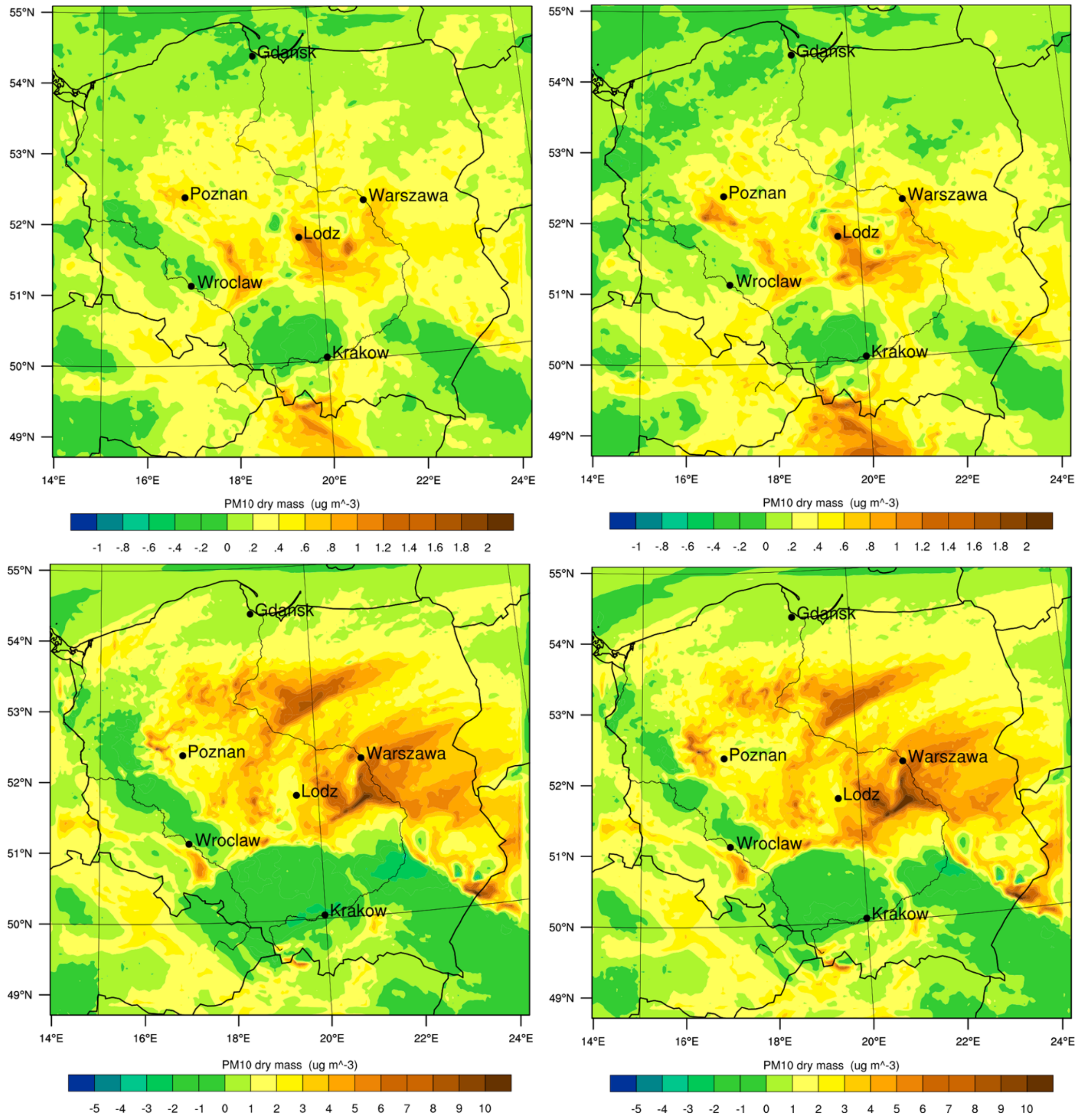

Figure 11
Mean monthly (*upper line*) and mean daily for the 29th of January spatial differences in PM_{10} concentrations between DIR and BASE (*left*) and INDIR and BASE (*right*) (different scales for monthly and daily maps)

(Athanasopoulou *et al.* 2013). We made our simulations for a winter month which due to low temperatures and limited sun-shine has limited emissions from nature. A summer simulation should, therefore, provide a much higher impact from feedback effects. This suggests that for studies in high temporal resolution the online models are necessary to describe the processes and feedback effects correctly to obtain the most reliable results. For long-term studies the offline models in most cases meet the requirements as the overall feedback effect is reduced over longer periods. This study has been based on the winter period, which is characterised in Poland by high anthropogenic emissions of particulate matter and severe meteorological conditions. However, it was noticed that the highest feedback effects are not strictly related with the highest particulate matter concentrations. We suggest to carry out a similar study for this region for the summer period, which is characterised by higher solar radiation, high BVOC emissions from nature and more dynamic PBL, or during episodes with substantial transport of particles due to Saharan dust.

Acknowledgments

The authors acknowledge the Aerosol Research Network Poland-AOD and the Institute of Geophysics, University of Warsaw for the provision of radiation data, the Institute of Meteorology and Water management for the provision of measurements of: air temperature, relative humidity, surface pressure and wind speed and the Chief Inspectorate of Environmental Protection in Poland for PM$_{10}$ measurements. This study has received support from the Polish National Science Centre through project no. UMO-2013/09/B/ST10/00594.

References

Ackermann, I.J., Hass, H., Memmesheimer, M., Ebel, A., Binkowski, F.S., Shankar, U., (1998). *Modal aerosol dynamics model for Europe*. Atmos. Environ. *32*, 2981–2999.

Andreae, M.O., Jones, C.D., Cox, P.M., (2005. *Strong present-day aerosol cooling implies a hot future*. Nature *435*, 1187–90.

Athanasopoulou, E., Vogel, H., Vogel, B., Tsimpidi, A. P., Pandis, S. N., Knote, C., Fountoukis, C., (2013). *Modeling the meteorological and chemical effects of secondary organic aerosols during an EUCAARI campaign*, Atmos. Chem. Phys., *13*(2), 625–645, doi:10.5194/acp-13-625-2013.

Baklanov, A., Schlünzen, K.., Suppan, P., Baldasano, J., Brunner, D., Aksoyoglu, S., Carmichael, G., Douros, J., Flemming, J., Forkel, R., Galmarini, S., Gauss, M., Grell, G., Hirtl, M., Joffre, S., Jorba, O., Kaas, E., Kaasik, M., Kallos, G., Kong, X., Korsholm, U., Kurganskiy, a., Kushta, J., Lohmann, U., Mahura, a., Manders-Groot, a., Maurizi, a., Moussiopoulos, N., Rao, S.T., Savage, N., Seigneur, C., Sokhi, R.S., Solazzo, E., Solomos, S., Sørensen, B., Tsegas, G., Vignati, E., Vogel, B., Zhang, Y., (2014. *Online coupled regional meteorology chemistry models in Europe: current status and prospects*. Atmos. Chem. Phys. *14*, 317–398.

Charlson, R.J., Schwartz, S.E., Hales, J.M., Cess, R.D., Coakley, J.A., Hansen, J.E., Hofmann, D.J., (1992). *Climate forcing by anthropogenic aerosols*. Science *255*, 423–30.

Chen, F., Dudhia, J., (2001). *Coupling an Advanced Land Surface–Hydrology Model with the Penn State–NCAR MM5 Modeling System. Part I: Model Implementation and Sensitivity.* Mon. Weather Rev. *129*, 569–585.

Fast, J.D., Gustafson, W.I., Easter, R.C., Zaveri, R.A., Barnard, J.C., Chapman, E.G., Grell, G.A., Peckham, S.E., (2006). *Evolution of ozone, particulates, and aerosol direct radiative forcing in the vicinity of Houston using a fully coupled meteorology-chemistry-aerosol model.* J. Geophys. Res. *111*, D21305.

Forkel, R., Werhahn, J., Hansen, A.B., McKeen, S., Peckham, S., Grell, G., Suppan, P., (2012). *Effect of aerosol-radiation feedback on regional air quality – A case study with WRF/Chem.* Atmos. Environ. *53*, 202–211.

Grell, G. A., Peckham, S.E., Schmitz, R., McKeen, S. a., Frost, G., Skamarock, W.C., Eder, B., (2005). *Fully coupled "online" chemistry within the WRF model.* Atmos. Environ. *39*, 6957–6975. doi:10.1016/j.atmosenv.2005.04.027.

Grell, G.A., (2002). *A generalized approach to parameterizing convection combining ensemble and data assimilation techniques*. Geophys. Res. Lett. *29*, 1693.

Hong, S.Y., Noh, Y., Dudhia, J., (2006). *A New Vertical Diffusion Package with an Explicit Treatment of Entrainment Processes.* Mon. Weather Rev. *134*, 2318–2341.

Iacono, M.J., Delamere, J.S., Mlawer, E.J., Shephard, M.W., Clough, S.A., Collins, W.D., (2008). *Radiative forcing by long-lived greenhouse gases: Calculations with the AER radiative transfer models*. J. Geophys. Res. *113*, D13103.

Jacobson, M.Z., Lu, R., Turco, R.P., Toon, O., (1996). *Development and application of a new air pollution model system e Part I: Gas-phase simulations*. Atmos. Env *30*, 1939–1963.

Jacobson, M., Z., (2002). Atmospheric Pollution History, Science, and Regulation, Cambridge University Press.

Kaminski, J., Neary, L., Lupu, A., McConnell, J., Struzewska, J., Zdunek, M., Lobocki, L., (2007). High Resolution Air Quality Simulations with MC2-AQ and GEM-AQ, in: Borrego, C., Norman, A.-L. (Eds.), Air Pollution Modeling and Its Application XVII SE - 86. Springer US, pp. 714–720.

Kuenen, J.J.P., Visschedijk, a. J.H., Jozwicka, M., Denier van der Gon, H. A. C., (2014). *TNO-MACC_II emission inventory: a multi-year (2003–2009) consistent high-resolution European emission inventory for air quality modelling*. Atmos. Chem. Phys. Discuss. *14*, 5837–5869.

Kryza, M., Wałaszek, K., Ojrzyńska, H., Szymanowski, M., Werner, M. and Dore, A. J., (2015). High resolution dynamical downscaling of ERA-Interim using the WRF regional climate model (Part 1) – model configuration and statistical evaluation for the 1981-2010 period, Pure Appl. Geophys., in review.

Lin, Y.L., Farley, R.D., Orville, H.D., (1983). *Bulk Parameterization of the Snow Field in a Cloud Model.* J. Clim. Appl. Meteorol. *22*, 1065–1092.

Liu, S.C., McKeen, S.A., Hsie, E.-Y., Lin, X., Kelly, K.K., Bradshaw, J.D., Sandholm, S.T., Browell, E. V., Gregory, G.L., Sachse, G.W., Bandy, A.R., Thornton, D.C., Blake, D.R., Rowland, F.S., Newell, R., Heikes, B.G., Singh, H., Talbot, R.W., (1996). *Model study of tropospheric trace species distributions during PEM-West* A. J. Geophys. Res. *101*, 2073.

Lynn, B., Khain, A., Rosenfeld, D., Woodley, W.L., (2007). *Effects of aerosols on precipitation from orographic clouds.* J. Geophys. Res. *112*, D10225.

Mercado, L.M., Bellouin, N., Sitch, S., Boucher, O., Huntingford, C., Wild, M., Cox, P.M., (2009). *Impact of changes in diffuse radiation on the global land carbon sink.* Nature *458*, 1014–7.

Moran, M.D., Ménard, S., Talbot, D., Huang, P., Makar, P.A., W., G., Landry, H., Gravel, S., Gong, S., Crevier, L.-P., K.A., Sassi, M., (2010). Air Pollution Modeling and Its Application XX, in: Steyn, D.G., Rao, S. (Eds.), Air Pollution Modelling and Its Application XX. Springer Science & Business Media, pp. 289–292.

Perez, L., Tobias, A., Querol, X., Künzli, N., Pey, J., Alastuey, A., Viana, M., Valero, N., González-Cabré, M., Sunyer, J., (2008). *Coarse particles from Saharan dust and daily mortality.* Epidemiology *19*, 800–7.

Pope, C.A., Burnett, R.T., Thun, M.J., Calle, E.E., Krewski, D., Ito, K., Thurston, G.D., (2002). *Lung cancer, cardiopulmonary mortality, and long-term exposure to fine particulate air pollution.* JAMA *287*, 1132–41.

Rosenfeld, D., Lohmann, U., Raga, G.B., O'Dowd, C.D., Kulmala, M., Fuzzi, S., Reissell, A., Andreae, M.O., (2008). *Flood or drought: how do aerosols affect precipitation?* Science *321*, 1309–13.

Schell, B., Ackermann, I.J., Hass, H., Binkowski, F.S., Ebel, A., (2001). *Modeling the formation of secondary organic aerosol within a comprehensive air quality model system.* J. Geophys. Res. Atmos. *106*, 28275–28293.

Stanelle, T., Vogel, B., Vogel, H., Bäumer, D., Kottmeier, C., (2010). Feedback between dust particles and atmospheric processes over West Africa during dust episodes in March 2006 and June 2007, Atmos. Chem. Phys., 10(22), 10771–10788, doi:10.5194/acp-10-10771-2010.

Stockwell, W.R., Middleton, P., Chang, J.S., Tang, X., (1990). The second generation regional acid deposition model chemical mechanism for regional air quality modeling. J. Geophys. Res. 95, 16343.

Tuccella, P., Curci, G., Visconti, G., Bessagnet, B., Menut, L., Park, R.J., (2012). *Modeling of gas and aerosol with WRF/Chem over Europe: Evaluation and sensitivity study*. J. Geophys. Res. *117*, D03303.

Wilton, D.J., Hewitt, C.N., Beerling, D.J., (2011). *Simulated effects of changes in direct and diffuse radiation on canopy scale isoprene emissions from vegetation following volcanic eruptions*. Atmos. Chem. Phys. *11*, 11723–11731.

Zhang, Y., 2008. *Online coupled meteorology and chemistry models: history, current status, and outlook*. Atmos. Chem. Phys. Discuss. *8*, 1833–1912.

Zhang, Y., Wen, X.Y., Jang, C.J., (2010). *Simulating chemistry–aerosol–cloud–radiation–climate feedbacks over the continental U.S. using the online-coupled Weather Research Forecasting Model with chemistry (WRF/Chem).* Atmos. Environ. *44*, 3568–3582.

(Received November 26, 2014, accepted March 3, 2016, Published online March 16, 2016)

Pure Appl. Geophys. 174 (2017), 569–594

DOI 10.1007/s00024-016-1297-9

Pure and Applied Geophysics

The Relevance of Surface Roughness Data Qualities in Diagnostic Modeling of Wind Velocity in Complex Terrain: A Case Study from the Śnieżnik Massif (SW Poland)

Kacper Jancewicz[1] and Mariusz Szymanowski[1]

Abstract—Numerical modeling of wind velocity above complex terrain has become a subject of numerous contemporary studies. Regardless of the methodical approach (dynamic or diagnostic), it can be observed that information about surface roughness is indispensable to achieve realistic results. In this context, the current state of GIS and remote sensing development allows access to a number of datasets providing information about various properties of land coverage in a broad spectrum of spatial resolution. Hence, the quality of roughness information may vary depending on the properties of primary land coverage data. As a consequence, the results of the wind velocity modeling are affected by the accuracy and spatial resolution of roughness data. This paper describes further attempts to model wind velocity using the following sources of roughness information: LiDAR data (Digital Surface Model and Digital Terrain Model), database of topographical objects (BDOT10k) and both raster and vector versions of Corine Land Cover 2006 (CLC). The modeling was conducted in WindStation 4.0.2 software which is based on the computational fluid dynamics (CFD) diagnostic solver Canyon. Presented experiment concerns three episodes of relatively strong and constant synoptic forcing: 26 November 2011, 25 May 2012 and 26 May 2012. The modeling was performed in the spatial resolution of 50 and 100 m. Input anemological data were collected during field measurements while the atmosphere boundary layer parameters were derived from the meteorological stations closest to the study area. The model's performance was verified using leave-one-out cross-validation and calculation of error indices such as bias error, root mean square error and index of wind speed. Thus, it was possible to compare results of using roughness datasets of different type and resolution. The study demonstrates that the use of LiDAR-based roughness data may result in an improvement of the model's performance in 100 and 50 m resolution, comparing to CLC and BDOT10k. Furthermore, a slight improvement of these results can be accomplished if the LiDAR-based roughness calculation process includes the variable of prevailing wind direction. Qualities of both CLC and BDOT10k raw datasets (imposed land coverage classes, necessity of the roughness classes assignment) induce relatively high values of the modeled velocity error indices. Hence, these and other similar datasets need to be carefully analyzed (e.g. compared with aerial or satellite imagery) before they are used in the process of roughness length parameterization.

Key words: Roughness length, LiDAR, diagnostic wind velocity modeling, computational fluid dynamics, sudetes.

1. Introduction

Proper surface roughness estimation is considered as one of the most important aspects of microscale and mesoscale meteorological modeling (Hansen 1993; Emeis and Knoche 2007). Regardless of the methodical approach (dynamic or diagnostic) it can be assumed that roughness input data significantly affects results of the near-ground wind velocity modeling; only proper roughness parameterization may result in a realistic spatial distribution of modeled wind velocity. Hence, preparation of the input roughness dataset involves consideration of two issues: a method of roughness estimation and properties of the source of information.

The aerodynamic surface roughness z_0 value is the height above a surface at which the logarithmic profile of wind speed versus altitude extrapolates to zero wind speed (Jacobson 2005). Under neutral conditions, the idealized near-surface wind velocity profile can be expressed as:

$$u(z) = \frac{u_*}{\kappa} \ln\left(\frac{z}{z_0}\right) \tag{1}$$

where u_* denotes friction velocity, κ von Karman's constant ($\kappa = 0.4$), z height above reference plane and z_0 aerodynamic surface roughness length (Emeis and Knoche 2007). The z_0 value can be treated as a fixed property of the surface; it is usually derived from measured wind profiles. The empirical estimation of roughness length has been considered by many authors since 1950s for both natural and

---

[1] Institute of Geography and Regional Development, University of Wrocław, pl. Uniwersytecki 1, 50-137 Wrocław, Poland. E-mail: kacper.jancewicz@uni.wroc.pl

anthropogenic surfaces. Hence, some analyses consist of exhaustive lists of z_0 values assigned to specific forms of land coverage (e.g. HANSEN 1993; CHO *et al.* 2012). A detailed review of roughness data from boundary-layer experiments was provided by WIERINGA (1993), who stated that the classification created by DAVENPORT (1960) describes roughness of landscape types in the most reliable way. After several updates (WIERINGA *et al.* 2001), it has become probably the best field-validated roughness classification to date (HAMMOND *et al.* 2012) (Appendix 1).

On the other hand, numerous authors have focused on the relation between z_0 value and parameters of surface obstacles. This approach resulted in a broad range of roughness definitions. For instance, roughness length can be described simply as a function of surface objects height (e.g. PLATE 1982; GARRATT 1994; LOPES 2013):

$$z_0 = fh_c \tag{2}$$

where h_c denotes height of the roughness element. The f value of 0.15 is recommended for most natural surfaces (PLATE 1982). In fact, it depends on the layout and shape of roughness elements. Hence, the f range is variously specified, depending on the author, e.g. 0.03–0.25 (LOPES 2013) or 0.07–0.14 (GARRATT 1994). Subsequently, the exploration of properties of roughness elements (and their relation to z_0) resulted in the inclusion of much more sophisticated morphometric analyses in the process of surface roughness estimation. These methods are usually applied in order to determine aerodynamic parameters of dense urban areas, where empirical anemometric estimation of z_0 may not give sufficient results or is impossible to perform (GRIMMOND and OKE 1999; SUDER and SZYMANOWSKI 2014).

Direct application of the logarithmic law (Eq. 1) encounters difficulties in the areas which are densely built-up or covered by high vegetation. Thus, an additional parameter, a zero-plane displacement height (d), was added to roughness description (THOM 1971; JACKSON 1981), resulting in:

$$u(z) = \frac{u_*}{\kappa} \ln\left(\frac{z-d}{z_0}\right) \tag{3}$$

where d value can be regarded as a datum height above which normal turbulent exchange takes place (HANSEN 1993). It is comparable to the depth of an air layer trapped in vegetation (or in urban structure) and depends on the density of the obstacles—the d becomes negligible when they are sparsely distributed (WIERINGA 1993). However, some authors raise the controversial aspect of the zero-plane displacement, stating that much information concerned with d can be included in z_0 by increasing its value (DONG *et al.* 2001).

Aforementioned roughness parameters refer only to homogenous surfaces. In practice, the single grid cell of the numerical flow model usually represents heterogeneous land use, which should be parameterized by the effective roughness length $z_{0\mathrm{eff}}$ (EMEIS and KNOCHE 2007). According to TAYLOR (1987), the $z_{0\mathrm{eff}}$ can be approximated by an ensemble average of local z_0 values inside the grid cell. A different approach was proposed by YAMAZAWA and KONDO (1989) who considered that $z_{0\mathrm{eff}}$ should be calculated for the windward fetch areas which was a wedge with 45° angle and a radius $R = 100\ h_\mathrm{a}$ (where h_a denotes height of the anemometer placement). Similarly, HAMMOND *et al.* (2012) calculated $z_{0\mathrm{eff}}$ as an arithmetic average of z_0 values within fans of various radius lengths (from 100 to 500 m).

An utterly different concept of surface drag parameterization concerns sub-grid scale orographic effects (WOOD *et al.* 2001, JIMENEZ and DUDHIA 2012). In reality, orography is not uniform—there are concave and convex terrain forms which are too small to be represented explicitly within a single grid of assumed resolution. Hence, additional parameterization (of momentum equation) should be made in order to include terrain characteristics inside every grid. This problem applies mainly to mesoscale meteorological models—a fine example is provided by JIMENEZ and DUDHIA (2012), who demonstrate improvements of WRF model's performance (resolution—2 km) by use of the standard deviation of the subgrid-scale orography as well as the Laplacian of the topographic field.

In reference to the aforementioned methodical background, it is possible to focus on potential sources of information about roughness. The current state of remote-sensing techniques and GIS systems development allows one to access a number of datasets from which roughness length z_0 can be derived. They can be, in general, classified into four categories—three of which are remote-sensing-based (Table 1).

The first two groups of datasets provide information about distribution of land-coverage types inside the selected area. Thus, the values of surface roughness length (z_0) can be assigned to the consecutive land-coverage classes. Therefore, the quality of roughness information depends on the initial data resolution, the number of included land-use types and the accuracy of assignment of roughness length values. The last issue is considerably dependent upon the choice of appropriate roughness values from those proposed by various authors (e.g. Corine Land Cover roughness length values—Silva *et al.* 2007). Regardless of the processing issues, an unquestionable advantage of these datasets is their accessibility.

The third group of datasets—the multi-spectral satellite images—allows to parameterize roughness as a derivative of vegetation indices, calculated from the bands of particular spectrum. For instance, the use of the normalised difference vegetation index (NDVI) (Ramli *et al.* 2009) and the leaf area index (LAI) (Schaudt and Dickinson 2000) to calculate z_0 should be mentioned in this context.

The last group contains high-resolution digital surface models (DSMs) and digital terrain models (DTMs). They are usually derived from data gathered by the airborne light detection and ranging (LiDAR) devices. Subtracting DTM from DSM results in a dataset containing a height of surface objects (h_c from the Eq. 2) (Hammond *et al.* 2012). In consequence it is possible to estimate z_0 values within very high (2 m or less) resolution and then recalculate it into $z_{0\mathrm{eff}}$ which represents a surface appropriate to model grid size. Another advantage of LiDAR-based data is the fact that obtained z_0 has a continuous form. Thus, it should give much better approximation of real surface properties than pre-classified land-cover data.

In consequence, the present authors intend to consider how the properties and the quality of roughness data affect the results of the wind velocity modeling. The starting point is a recent research on using the CLC data in a case study of near ground wind field diagnostic modeling (solver: Canyon, Lopes 2003) in mountainous terrain. Jancewicz (2014) demonstrated that including CLC-derived input roughness information generally adjusts model's performance, comparing to the results achieved with spatially-uniform roughness (root mean squared error of velocity = 1.0 m/s instead of 1.6 m/s). However, he also concluded that raw CLC data may generate incorrect spatial distribution of roughness values due to the terrain complexity. Therefore, one could cautiously suppose that the use of a more detailed (or higher-quality) source of roughness information may further improve the performance of the model. An opportunity of using airborne LiDAR-derived data and a detailed topographical database is, in that case, especially promising.

This study concerns continued attempts of wind-field modeling in a part of the Śnieżnik Massif, which

Table 1

Main sources of data used in the roughness length estimation

Data type	Examples of studies concerning roughness determination or wind velocity modelling
Land-use components of vector topographic databases	*Top10DK*: Hasager *et al.* (2003)
Remote-sensing-based land coverage qualitative datasets	*Corine Land Cover*
	Hasager *et al.* (2003), Silva *et al.* (2007), Truhetz (2010), Jancewicz (2014) and De Meij and Vinuesa (2014)
	Global land cover characterization
	Morales *et al.* (2012)
Multi-spectral satellite images	*Landsat TM*: Jasinski and Crago (1999) and Ramli *et al.* (2009)
	SPOT-5 Tian *et al.* (2011)
	NOAA-AVHRR: Schaudt and Dickinson (2000)
Remote-sensing-based high-resolution digital surface models (DSMs) and digital terrain models (DTMs)	*Airborne LiDAR-based DSM and DTM* Colin and Faivre (2010), Tian *et al.* (2011) and Hammond *et al.* (2012)

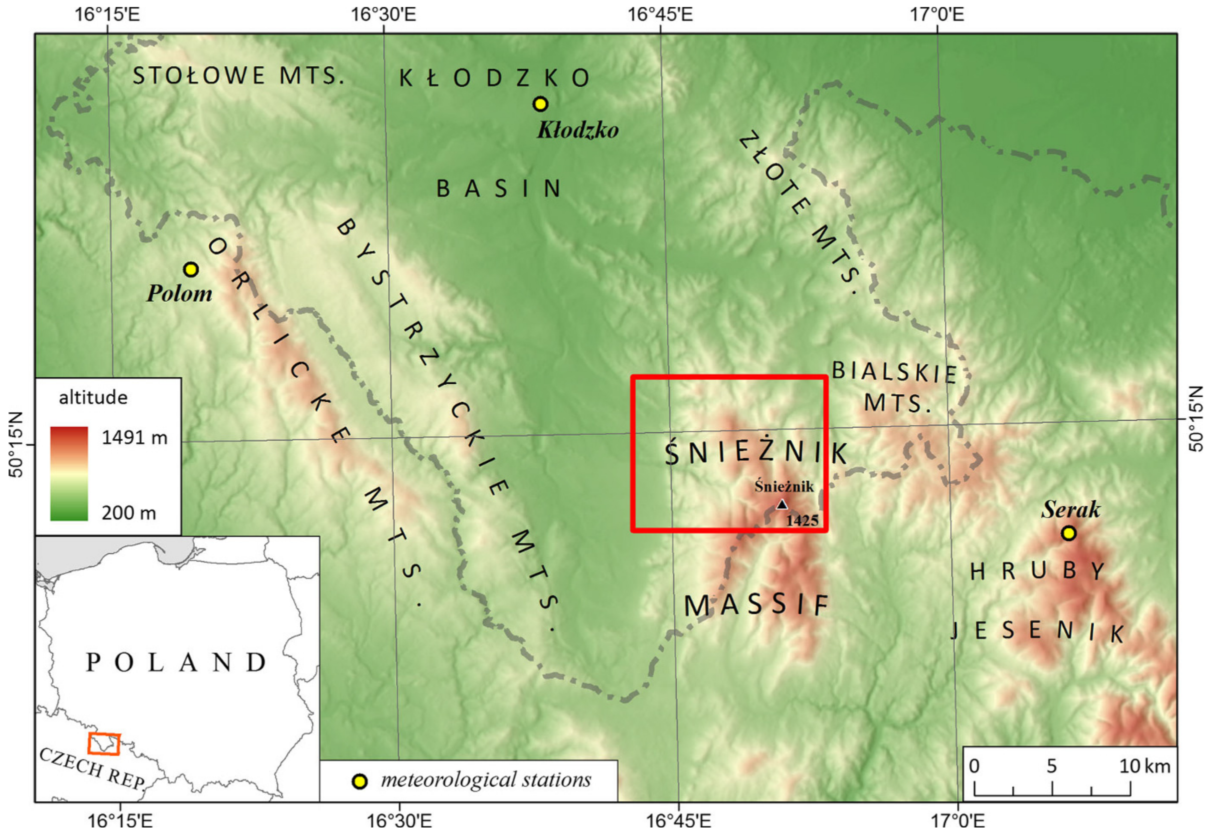

Figure 1
Position of the study area (marked by the *red rectangle*)

were undertaken in order to settle an issue of the potential impact of roughness data properties (resolution, data type) on the results of near-ground wind velocity diagnostic modeling.

2. *Study Area*

The Śnieżnik Massif, divided by the border of Poland and the Czech Republic (known there as Králický Sněžník) (Fig. 1), is the second highest mountain terrain in the Eastern Sudetes. The highest peak of the massif is Śnieżnik (1425 m a.s.l.). The massif itself represents a prominent orographic barrier, as it is surrounded by valleys and basins. Therefore, its morphology, containing deep valleys and long ridges (altitude range 1100–1300 m a.s.l.), causes local deformations of air flow. Prevailing wind directions are W, SW, S. If they are combined with strong synoptic forcing, then air-flows follow valley axes in the windward part of the massif. If conditions are favourable, foehn winds occur and the adaptation of flow direction may be also observed in leeward valleys (Piasecki 1996; Piasecki and Sawiński 2009).

Since 2011, the Śnieżnik Massif has been an area of studies focused on diagnostic modeling of near-ground air-flow using GIS techniques and remote-sensing data (Jancewicz 2014). The research polygon covers an area of 120 sq km in the north-western part of the massif (Fig. 1); within this area the altitude varies from 421 to 1425 m a.s.l. A detailed map of this area is presented on Fig. 2.

3. *Methods*

The modeling process was carried out using WindStation 4.0.2 software. It is based on the CFD

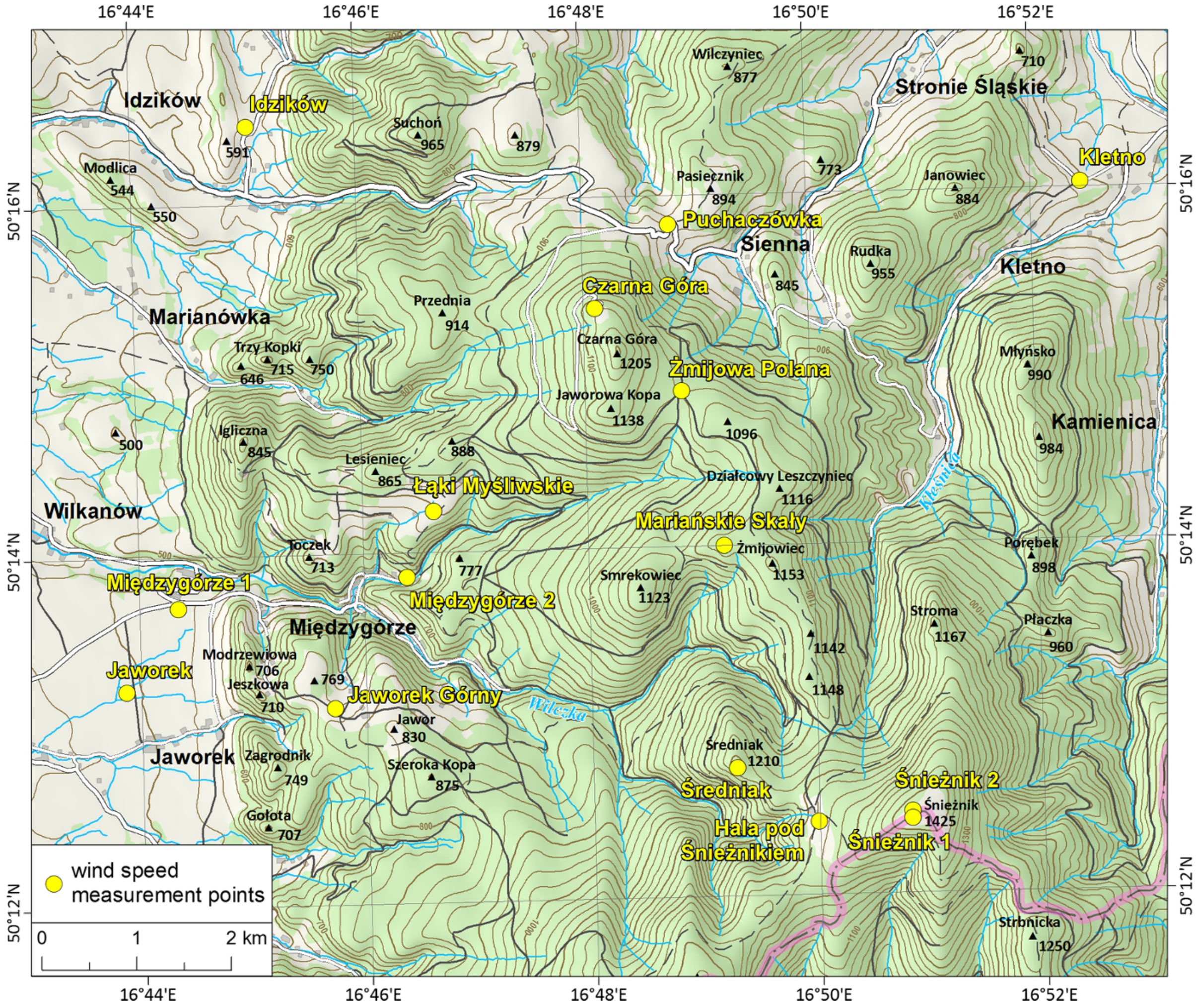

Figure 2
Distribution of wind measurement points inside the study area (after Jancewicz 2014)

solver Canyon, which solves for mass conservation, momentum conservation (Navier–Stokes equations), energy conservation and turbulence quantities (k–ε model) (Lopes 2003, 2013). The first version of WindStation was presented in 2003—its performance was validated using data obtained from the Askervein Hill site and two test areas in Portugal (Lopes 2003). Later versions were used in several studies. Colin and Faivre (2010) applied Canyon in the process of aerodynamic roughness length estimation in Heihe basin (China), using high-resolution LiDAR elevation data. Abbes and Belhadj (2012) used it to estimate resources of wind energy in the El-Kef region (Tunisia). Eventually, Canyon solver was used by Jancewicz (2014) in an experiment concerning the modeling of near-ground wind velocity and direction at the test-site in the Śnieżnik Massif (SW Poland).

The input anemological data were obtained during short periods (6 h a day—from 9:00 to 15:00 CET/CEST)—velocity measurements were taken at a height of 2 m above ground at 5 min intervals, using Kaindl Windmaster 2 anemometers. Wind direction was estimated to the nearest of the 16 points of the compass as a result of observation of banners mounted on poles—in accordance with official guidelines (WMO 2008). Spatial distribution and the

Table 2

Measurement points used in the wind velocity modeling case study (after Jancewicz 2014)

ID	Measurement point	λ	φ	Altitude (m)	Measurements					
					26-11-2011		25-05-2012		26-05-2012	
					Mean V (m/s)	Mean direction	Mean V (m/s)	Mean direction	Mean V (m/s)	Mean direction
1	Czarna Góra	16°48′06.3″E	50°15′21.9″N	1122	–	–	–	–	2.6	45
2	Hala p. Śnieżnikiem	16°49′59.6″E	50°12′24.9″N	1229	3.6	270	3.5	0	–	–
3	Idzików	16°45′03.2″E	50°16′26.9″N	567	–	–	–	–	4.1	0
6	Jaworek	16°43′52.3″E	50°13′14.3″N	494	–	–	4.3	7.5	–	–
4	Jaworek Górny	16°45′42.7″E	50°13′07.5″N	759	–	–	–	–	3.6	7.5
5	Kletno	16°52′26.8″E	50°16′01.7″N	611	–	–	4.7	348.8	–	–
7	Łąki Myśliwskie	16°46′37.6″E	50°14′14.0″N	795	1.3	247.5	–	–	2.8	45
8	Mariańskie Skały	16°49′12.4″E	50°14′00.1″N	1133	3.9	225	–	–	4.8	22.5
9	Międzygórze 1	16°44′20.8″E	50°13′42.6″N	520	2.8	202.5	2.2	0	–	–
10	Międzygórze 2	16°46′23.1″E	50°13′51.8″N	636	–	–	–	–	1.7	191.3
11	Puchaczówka	16°48′46.4″E	50°15′50.3″N	868	–	–	3.3	45	–	–
12	Śnieżnik 1	16°50′49.5″E	50°12′25.5″N	1424	3.5	213.8	–	–	–	–
13	Śnieżnik 2	16°50′49.6″E	50°12′28.1″N	1423	–	–	9.0	22.5	–	–
14	Średniak	16°49′16.7″E	50°12′43.9″N	1199	5.5	247.5	4.2	22.5	–	–
15	Żmijowa Polana	16°48′51.4″E	50°14′53.1″N	1047	2.8	202.5	–	–	3.2	22.5

list of measurement points are presented respectively in Fig. 2 and Table 2. This distribution pattern of anemometers was premeditated—the velocity was recorded within a broad range of altitude, relative exposure to mean wind direction, yet in the locations of minimized screening by topographic objects or vegetation (except Czarna Góra and Międzygórze 2 sites—Jancewicz 2014).

Similarly to the previous study, the experiment presented here concerns three episodes of relatively strong and constant synoptic forcing: 26 November 2011, 25 May 2012 and 26 May 2012 (Fig. 3). Differences between the velocity ratio at Kłodzko and Mt Šerak synoptic stations (Fig. 1) (Jancewicz 2014) can be partly explained by prevailing wind direction (November—WNW, both May days—NE/NNE), also diurnal local convection should be considered during May episode. A slow decrement of wind velocity on Mt Šerak (May 26, Fig. 3c) may also be a consequence of gradual weakening of horizontal pressure gradient. However, field measurements did not indicate such changes of velocity ratio between points placed at high and low altitudes during measurement periods. In consequence, these 3 days were recognized as the most suitable for further modeling regarding vices and virtues of the diagnostic solver.

Further anemological data preparation involved calculation of hourly mean velocity values and prevailing directions in order to create an input dataset for the model. Wind conditions from the upper parts of the atmospheric boundary layer were obtained from upper air soundings performed in stations nearest to the study area: Prague-Libus, Prostějov and Wrocław. Those stations are relatively far from the study area, nevertheless the mean values of upper wind velocity and direction had to be introduced as the only available approximation. The results of the soundings were provided by the Department of Atmospheric Science at the University of Wyoming (http://www.weather.uwyo.edu/upperair/sounding.html, access date: June 10, 2012).

The second component of the input data was a LiDAR-based high resolution (1 m) Digital Terrain Model (DTM)—a product of IT System of the

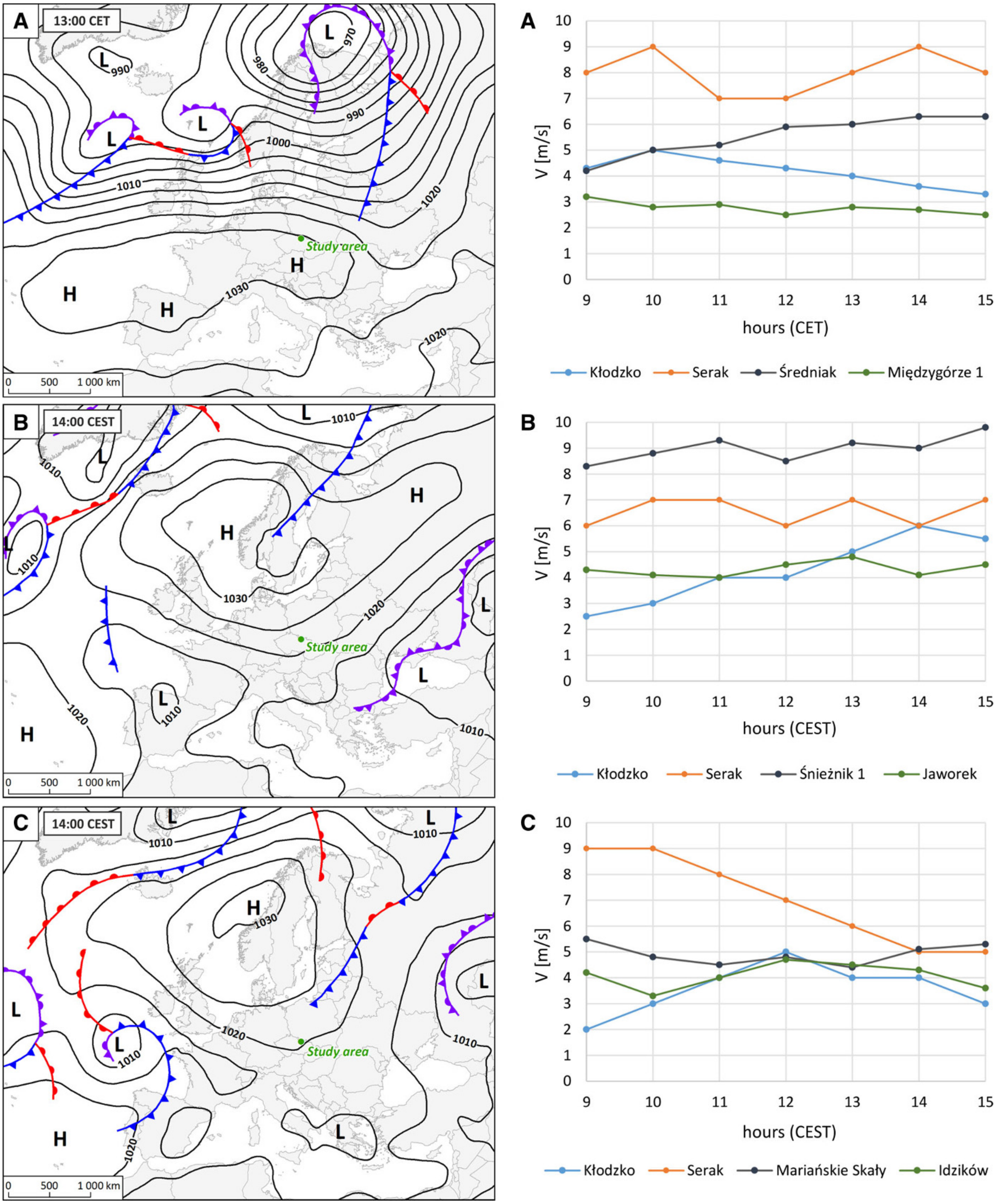

Figure 3
Atmospheric pressure field over Europe (*left*) and wind velocity observed within study area and in Serak and Kłodzko synoptic stations (*right*) during measurement time-periods : **a** 26 November 2011; **b** 25 May 2012; **c** 26 May 2012 (after Jancewicz 2014)

Table 3

Roughness classes assigned to CLC and BDOT10k datasets

Land-use class names	z_0 (m)	h_c (m)	% of total area		
			CLC (raster)	CLC (vector)	BDOT 10k
Inland water	0.0	0.0	0.0	0.0	0.1
Bare rock; dump sites; mineral extraction sites	0.01	0.07	0.0	0.0	0.2
Natural grasslands; non-irrigated arable land; pastures	0.03	0.2	17.4	17.2	24.3
Roads and associated land	0.04	0.3	0.0	0.0	0.2
Complex cultivation patterns; land principally occupied by agriculture with significant areas of natural vegetation	0.1	0.7	9.9	10.0	0.0
Sparsely vegetated areas	0.2	1.3	0.0	0.0	0.2
Agro-forestry areas; construction sites; fruit trees and berry plantations; green urban areas	0.3	2.0	0.0	0.0	1.3
Transitional woodland-shrub	0.4	2.7	7.2	7.2	1.1
Discontinuous urban fabric	0.6	4.0	1.4	1.4	1.0
Broad leaved forest; coniferous forest; mixed forest	1.4	9.3	64.0	64.2	71.5
Continuous urban fabric	1.5	10.0	0.0	0.0	0.1

Country's protection against extreme hazards (ISOK) Project (http://www.isok.gov.pl/en/products-of-isok-project, access date: May 30th, 2015). The model was resampled using cubic convolution method to 100 and 50 m in order to fit the settings of calculation domain.

The third input data component contained roughness information derived from four different datasets:

1. Corine Land Cover 2006 raster dataset ($\mathrm{CLC_R}$) (version 15) (2011)—100 m resolution, provided by the European Environmental Agency (EEA);
2. Corine Land Cover 2006 vector dataset ($\mathrm{CLC_V}$) (version 17) (2013)—provided by EEA;
3. Database of topographical objects (BDOT10k)—vector database, corresponding to topographic map scale 1:10,000—provided by the Polish Head Office of Geodesy and Cartography.
4. LiDAR-based DSM and DTM, spatial resolution: 1 m, provided by the Polish Head Office of Geodesy and Cartography.

Due to different properties, each dataset had to be individually pre-processed in order to fit the domain's resolution and to provide input roughness information required by WindStation—the height of surface objects (h_c). Thus, the $\mathrm{CLC_R}$ data were resampled to 50 m with use of the majority technique, while $\mathrm{CLC_V}$ and BDOT10k were converted to raster format in the appropriate resolutions using maximum combined area approach (in consequence, the raster values reflected a dominant type of land coverage inside every cell). The next step was assignment of roughness length, which was based on the Finnish Wind Atlas (http://www.tuuliatlas.fi/modeling/mallinnus_3.html, access date: March 20th, 2014) and SILVA *et al.* (2007). In the case of BDOT10k, original land use classes had to be matched with CLC classification. Finally, the assigned z_0 values allowed calculating the h_c values according to the transformed Eq. 2 (PLATE 1982; LOPES 2013):

$$h_c = \frac{z_0}{0.15} \tag{4}$$

The results of the roughness classes' assignment are presented in Table 3.

A different approach was required in case of LiDAR data. Firstly, the h_c was calculated, with reference to HAMMOND *et al.* (2012):

$$h_c = 0.6(\mathrm{DSM} - \mathrm{DTM}) \tag{5}$$

where 0.6 is the value of porosity factor P (HEISLER and DEWALLE 1988) and approximates the porosity of forest canopy. Secondly, the initial h_c raster was recalculated to obtain mean values of h_c for every 50 and 100 m grid.

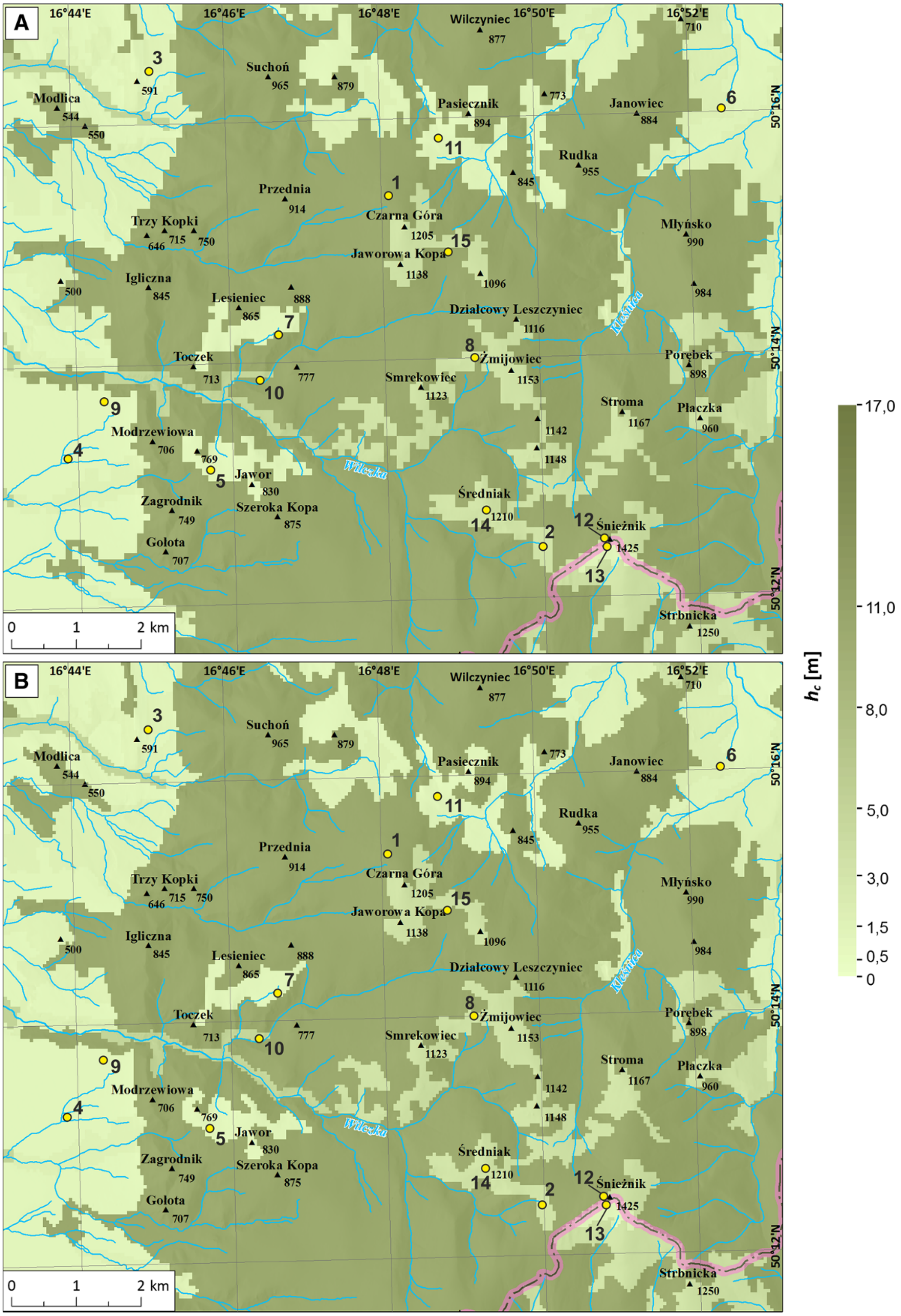

Figure 4

Distribution of the height of surface objects (h_c) inside the study area, according to the: **a** CLC raster version, **b** CLC vector version. *Yellow dots* indicate measurement/validation points

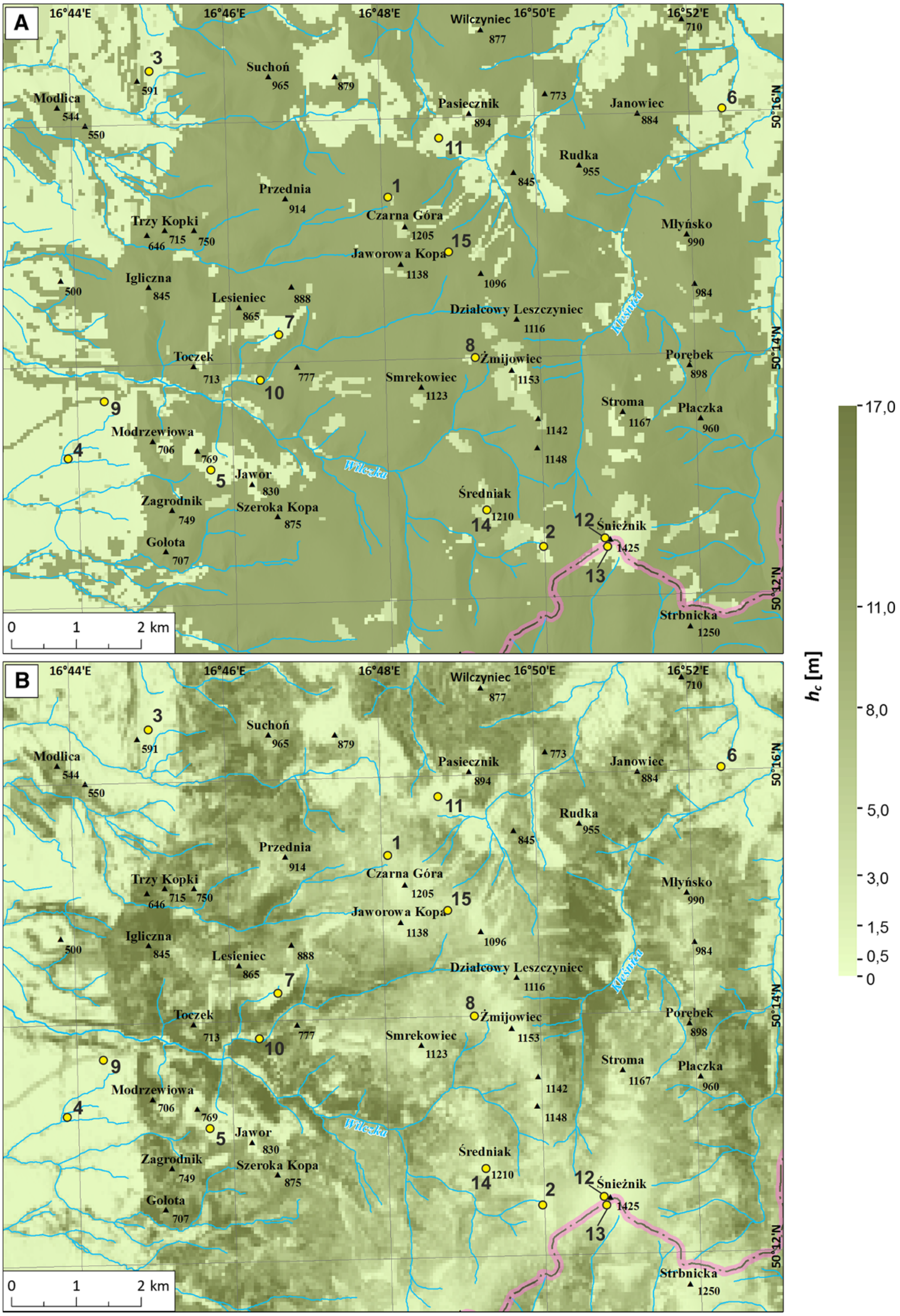

Figure 5

Distribution of the height of surface objects (h_c) inside the study area, according to the: **a** BDOT10k vector database, **b** LiDAR-based DEM and DSM. *Yellow dots* indicate measurement/validation points

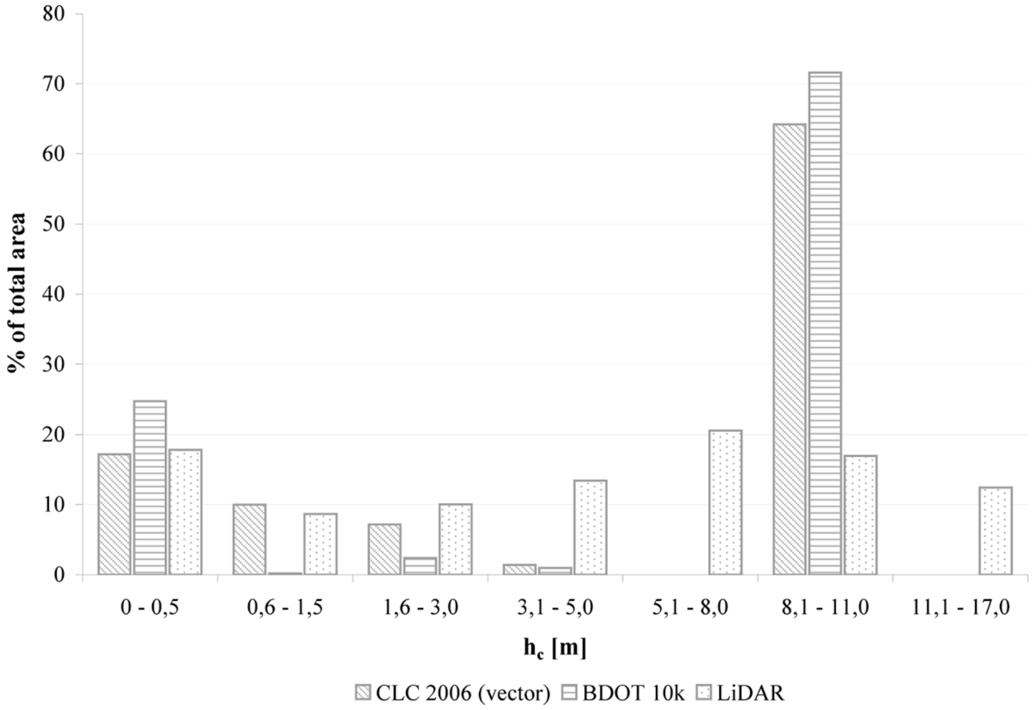

Figure 6
Percentage share of roughness parameter h_c classes inside the study area, depending on the initial source of roughness information

The results of the foregoing procedure are presented on roughness maps (Figs. 4, 5), which clearly demonstrate how the spatial distribution of roughness can differ according to the source's properties. Unsurprisingly, the LiDAR data provided the most detailed and realistic spatial distribution of h_c (Fig. 5), reflecting gradual decrease of forest vegetation height towards higher altitudes. This phenomenon is shown by neither $\mathrm{CLC_R}$, $\mathrm{CLC_V}$ nor BDOT10k, which rely on an average roughness value for "forest" class. However, both CLC datasets include class of "transitional woodland-shrub", which gives lower roughness values on the ridges (Table 3; Fig. 4), while BDOT10k presents forest as completely uniform. On the other hand, this dataset provides (comparing to both CLCs) a much more detailed spatial distribution of roughness elements in the areas dominated by agricultural or post-agricultural land-use forms (Fig. 5). Overall, the different ways of representing roughness of forested areas by particular datasets cause significant differences among the range of high roughness values (Fig. 6).

The aforesaid roughness data were calculated according to the TAYLOR's (1987) concept of effective roughness length, which is insensitive to the variable of wind direction. However, the authors also recalculated h_c values of LiDAR data basing on the upwind fetch approach (YAMAZAWA and KONDO 1989; HAMMOND *et al.* 2012). This resulted in "windward effective h_c" (h_{ceff}) which is a mean value for fans of 45° angle, 200 m radius from the initial cell and the azimuth value matched to the wind direction which was prevailing during the modeled episode.

Eventually, modeling was conducted, using consecutively four prepared roughness datasets. The computational grid had 292 × 252 × 20 nodes, with the first node placed at 4 m. Similarly to the previous studies (LOPES 2003; JANCEWICZ 2014), a neutral atmospheric stability was assumed. This decision was supported by analyses of aerological soundings conducted at stations in Wrocław, Prague and Prostějov. Again, it should be emphasized that those are the *nearest* stations, yet they are still very far from the study area (ca. 100 km). Hence, the results of soundings cannot be uncritically considered as a source of detailed information on vertical changes of atmospheric stability within the calculation domain. Furthermore, the model setup requires choosing between stable, neutral or unstable conditions for an entire altitude range of the domain. In these circumstances, an assumption of neutral conditions seems to be a justified simplification. Nonetheless, while interpreting the results of modeling, one should consider possible occurrence of shallow layers characterized by low values of temperature gradient (or even thermal inversion), especially on 26 November 2011, though it is not explicitly indicated by wind velocity field measurements nor background data from stations at Kłodzko and Mt Šerak. Consequently, the results and the following conclusions apply only to the aforesaid assumptions.

Raw output data were converted to a point vector layer and, subsequently, to a raster format using the spline interpolation method. Additionally, the mean velocity was calculated for selected hours and different roughness data setups; this calculation based on the raster representations of wind velocity at 2 m above ground, which were a result of the model's consecutive runs. Finally, it was possible to present examples of spatial variability of modeled velocity and to compare the effects of using different roughness datasets.

The model's performance was evaluated through the execution of a modified leave-one-out cross-validation. The measured wind velocity data served as a base to create two subsets ("training" data and validation data). Per every observational hour, 20 different training datasets were randomly chosen with the stipulation that all of them had to contain at least two measurement points. In consequence, 120 runs of the model were performed per every day and roughness setup (Jancewicz 2014). As a result, the following indices were calculated: velocity Bias (B_v), root mean square error of velocity (RMSE$_v$), index of wind speed (I_v); the equations are presented in Table 4.

4. Results and Discussion

The procedure applied created possibility to compare spatial differences between near-ground wind-velocity fields, which were calculated on the basis of different roughness input data. Examples of velocity maps are presented on Figs. 7, 8 and 9, while maps presenting the spatial distribution of mean velocity differences are displayed on Figs. 10 and 11. It becomes clear that the spatial variability of velocity strongly reflects the distribution of h_c parameter (see roughness maps in Figs. 4, 5). Therefore, it is not surprising that the use of CLC$_R$ and CLC$_V$ roughness data yielded very similar wind-fields (Fig. 7)—some slight differences may be noticed only if the boundaries of land-use classes differ in location due to the properties (raster/vector) of the initial datasets. Fine examples of these differences can be observed on the northern slopes of Jawor peak (SW part of the study area) or on the slopes of Średniak and Żmijowiec (Fig. 10a).

The use of BDOT10k roughness resulted in a wind-field characterized by relatively low velocities above ridges and peaks at altitude of 1000–1300 m a.s.l. (e.g. Żmijowiec, Czarna Góra and southern slopes of Śnieżnik) (Fig. 10b). This is because

Table 4

Error measures used in evaluation of overall wind velocity modeling results

Variable	Error measure	Equation	Remarks
Wind velocity	Bias error (Emery *et al.* 2001)	$B_v = \frac{1}{N}\sum_{i=1}^{N}(v_m - v_o)$	v_m—Modelled wind velocity v_o—Observed wind velocity
	Root mean square error (Emery *et al.* 2001)	$\mathrm{RMSE}_v = \sqrt{\frac{1}{N}\sum_{i=1}^{N}(v_m - v_o)^2}$	v_m—Modelled wind velocity v_o—Observed wind velocity
	Index of wind speed Lopes (2003)	$I_v = \frac{1}{N}\sum_{i=1}^{N} 100e^{\left[-0.692\left(\frac{v_1}{v_2}-1\right)\right]}$	v_1, v_2—Observed and simulated velocities or vice versa, with $v_1 > v_2$

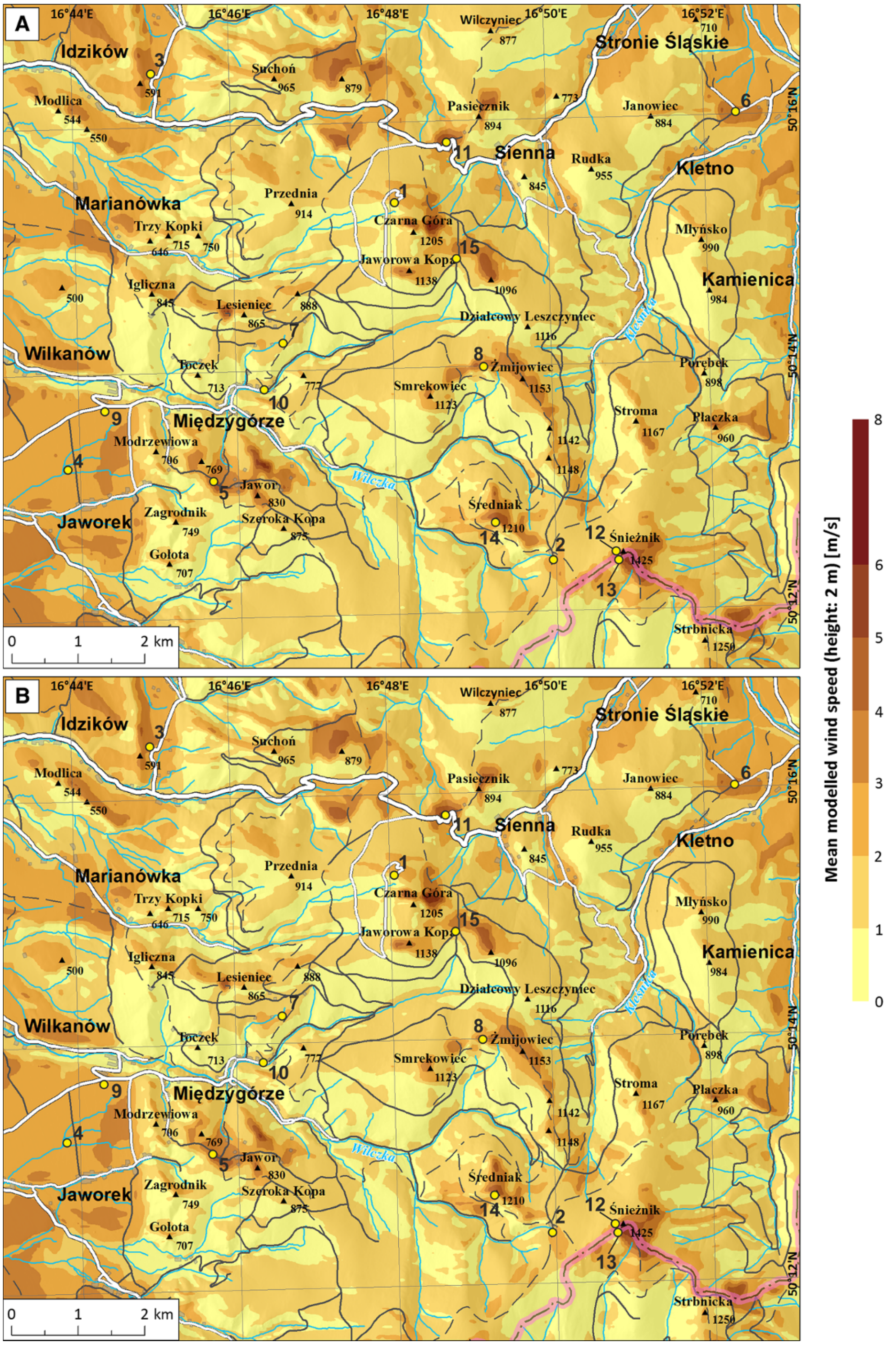

Figure 7
Spatial distribution of mean modeled wind velocity at height of 2 m above ground (26 May 2012; 13:00); roughness length information derived from: **a** CLC raster version, **b** CLC vector version. The velocity values were calculated from the results of 20 simulations based on various combinations of the input measurement points (containing at least two points). *Yellow dots* indicate measurement/validation points, *numbers* indicate point ID—see Tables 2 and 5

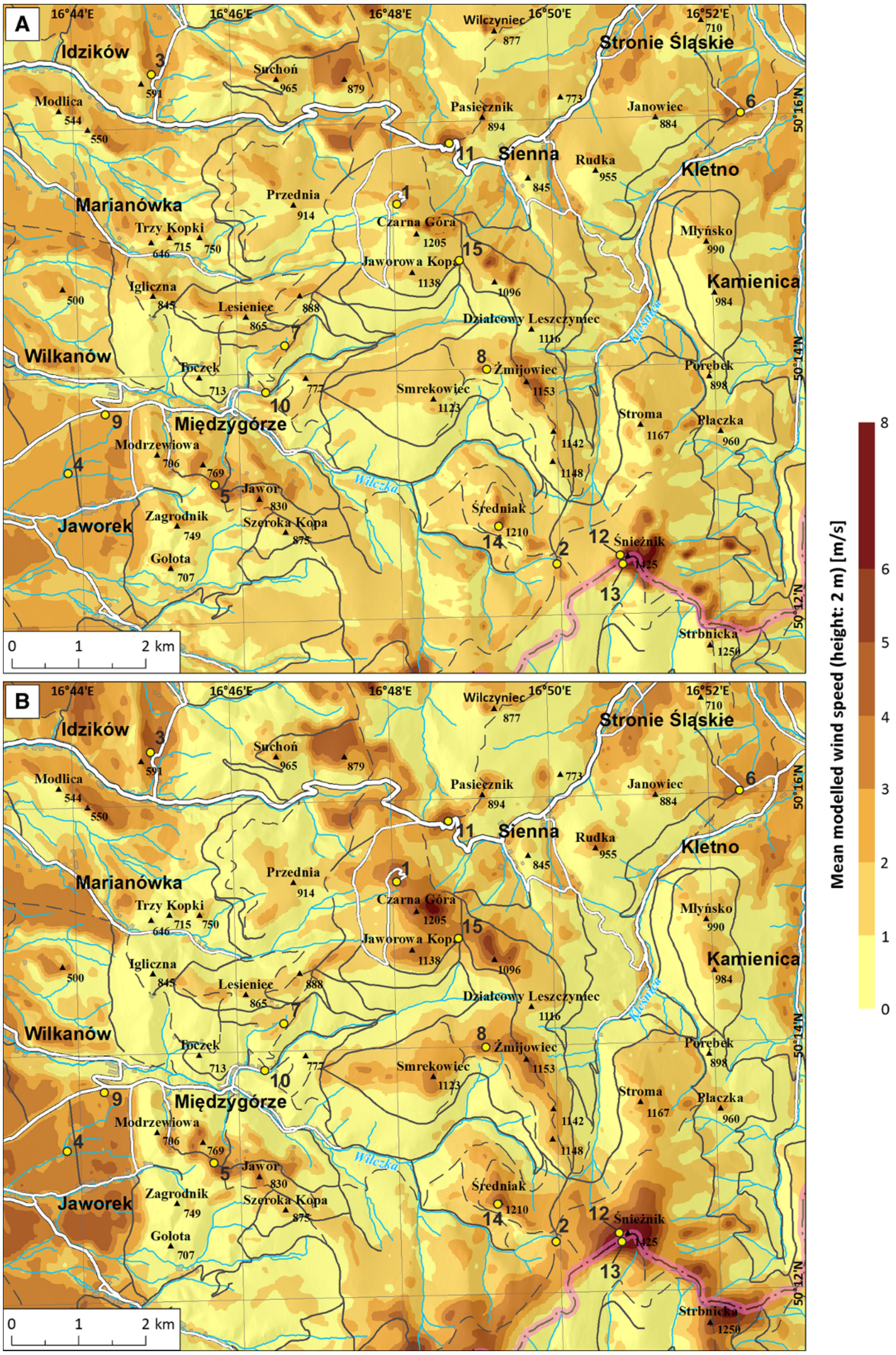

Figure 8
Spatial distribution of mean modeled wind velocity at height of 2 m above ground (26 May 2012; 13:00); roughness length information derived from: **a** BDOT10k vector database, **b** LiDAR-based DEM and DSM. The velocity values were calculated from the results of 20 simulations based on various combinations of the input measurement points (containing at least two points). *Yellow dots* indicate measurement/validation points, *numbers* indicate point ID—see Tables 2 and 5

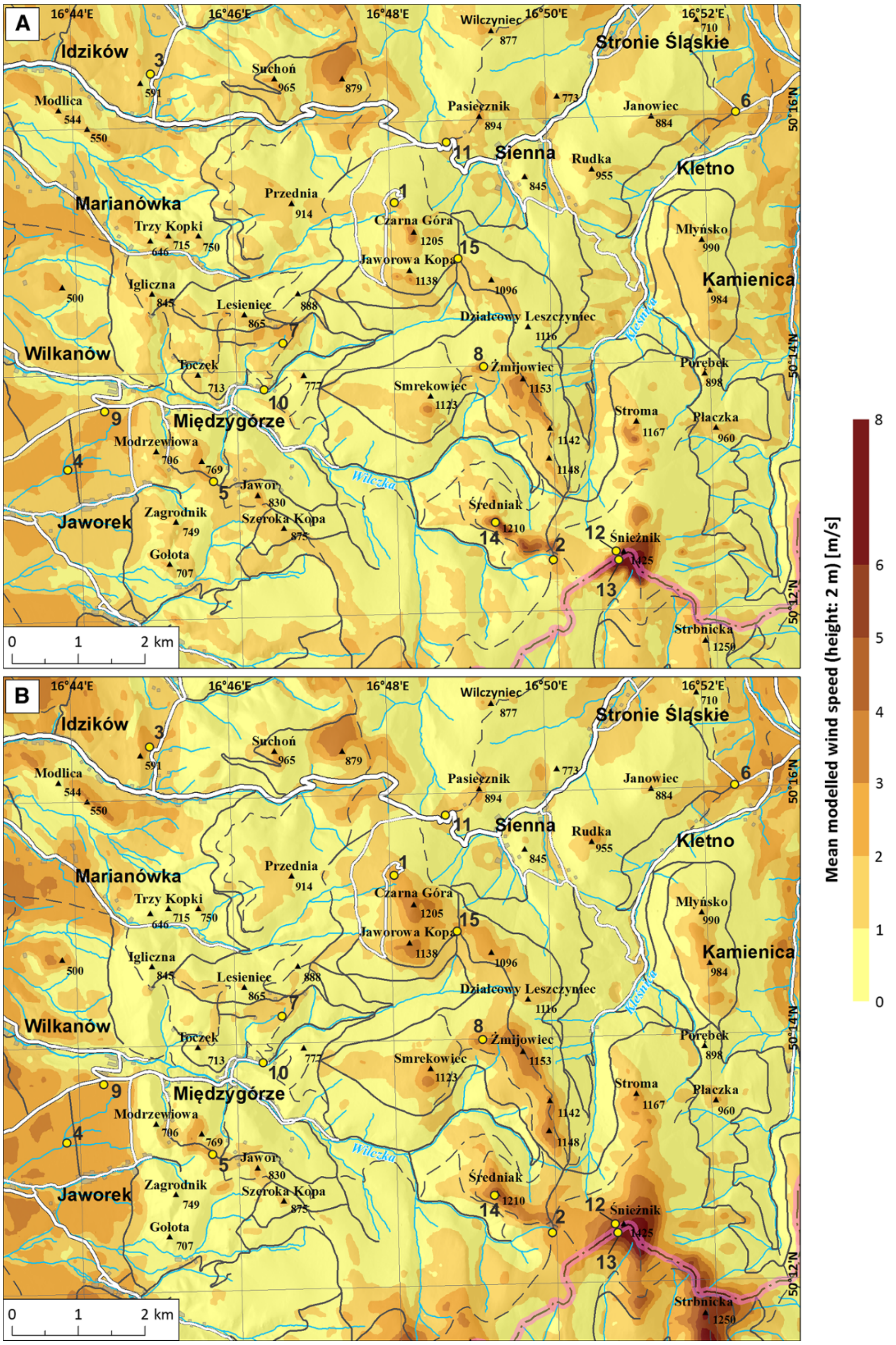

Figure 9
Spatial distribution of mean modeled wind velocity at height of 2 m above ground (26 November 2011; 13:00); roughness length information derived from: **a** BDOT10k vector database, **b** LiDAR-based DEM and DSM. The velocity values were calculated from the results of 20 simulations based on various combinations of the input measurement points (containing at least two points). *Yellow dots* indicate measurement/validation points, *numbers* indicate point ID—see Tables 2 and 5

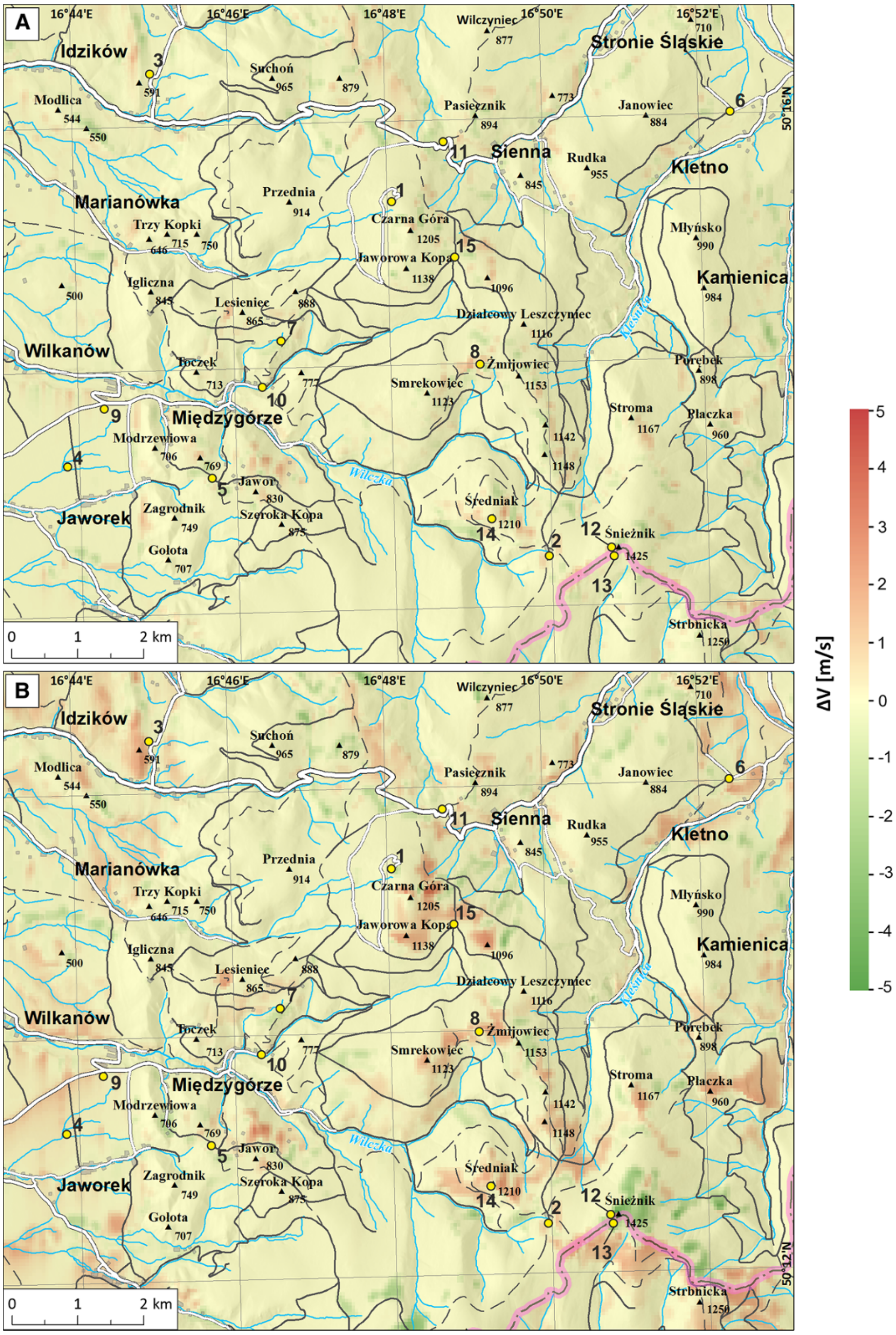

Figure 10

Spatial distribution of mean modeled wind velocity differences (ΔV) at height of 2 m above ground (26 May 2012; 13:00). The comparison concerns the following input roughness datasets: **a** CLC raster and CLC vector ($\Delta V = V_{\mathrm{CLCr}} - V_{\mathrm{CLCv}}$); **b** CLC raster and BDOT10k vector database ($\Delta V = V_{\mathrm{CLCr}} - V_{\mathrm{BDOT10k}}$). *Yellow dots* indicate measurement/validation points, *numbers* indicate point ID—see Tables 2 and 5

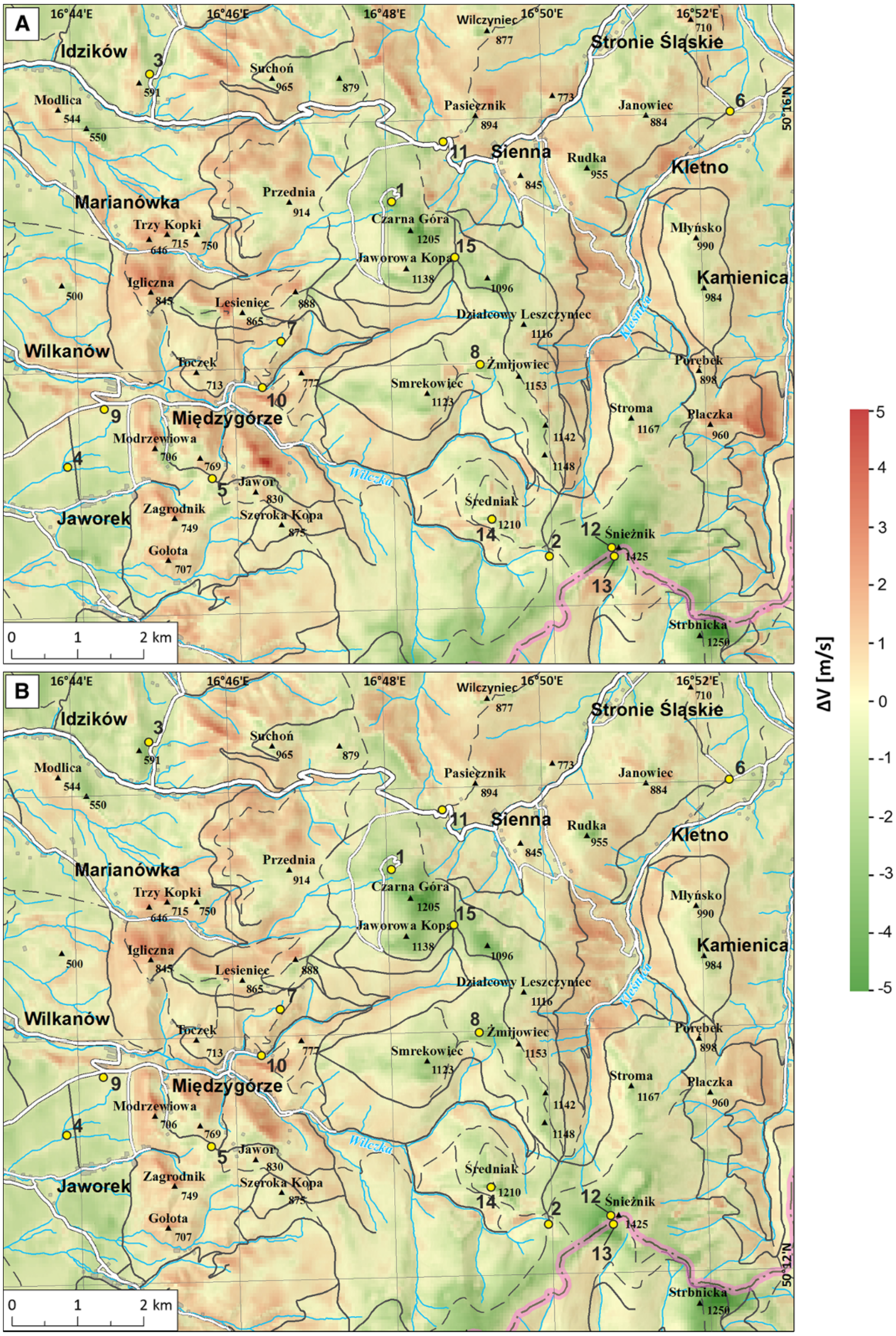

Figure 11

Spatial distribution of mean modeled wind velocity differences (ΔV) at height of 2 m above ground (26 May 2012; 13:00). The comparison concerns the following input roughness datasets: **a** CLC raster and LiDAR-based DEM and DSM ($\Delta V = V_{\mathrm{CLCr}} - V_{\mathrm{LiDAR}}$); **b** BDOT10k vector database and LiDAR-based DEM and DSM ($\Delta V = V_{\mathrm{BDOT10k}} - V_{\mathrm{LiDAR}}$). *Yellow dots* indicate measurement/validation points, *numbers* indicate point ID—see Tables 2 and 5 original BDOT10k land-use classes neglect "transitional woodland-shrub" CLC category, thus sparse coniferous forests (typical land coverage for these altitudes in the Śnieżnik Massif and the whole Sudetes range) are not represented properly. On the other hand, BDOT10k data were accurate enough to reflect the effects of linear obstacles such as trees and bushes along the roads (e.g. a road leading westwards from Międzygórze—Fig. 10b; see also Fig. 2) and small vegetation canopies in foothill areas (e.g. NW part of the area, near Idzików) (Fig. 10b). Moreover, the distribution of velocity above the Śnieżnik dome is completely different, comparing to CLC-based results. This is caused by more realistic roughness approximation due to avoidance of relief-induced errors, as mentioned by Jancewicz (2014).

The wind-field modeled with use of LiDAR data distinguishes itself by much higher velocity values at high altitudes and relatively low velocities in densely forested valleys (Figs. 8, 9, 11). This is an effect of roughness data continuity which reflect details of spatial variability of vegetation height inside the canopies (Fig. 6).

The analysis of model performance indices enables a more detailed insight into model's performance with an application of the aforementioned roughness data. It is conspicuous that CLC_R, CLC_V and BDOT10k datasets result in overall underestimation of the wind velocity (Fig. 12) (Table 5), though 100 m resolution induces greater underestimation than 50 m, especially in case of CLC_V and BDOT10k. This is mostly caused by improper land cover classification nearby measurement/validation points (e.g. Śnieżnik 2; Mariańskie Skały, Żmijowa Polana). To the contrary, the LiDAR data result in overall overestimation of the velocity ($B_v = 0.11$ m/s within 100 m and 0.26 m/s within 50 m resolution).

In respect of $RMSE_v$, Canyon model performed best while using the LiDAR-based roughness ($RMSE_v = 0.87$ and 0.80 m/s for 100 and 50 m resolution). BDOT10k and CLC_V induced relatively similar results (respectively: 1.41 and 1.42 m/s for 100 m grid; 1.09 and 1.15 m/s for 50 m grid), while the highest error value characterized the CLC_R output (1.47 for 100 m and 1.33 for 50 m grid) (Table 5; Fig. 12). These changes of mean error values might be caused by emergence of some roughness details, which were "sub-grid" in lower resolution—land-use data are especially fragile to this type of effects due to the their qualitative character. However, this cannot be univocally stated within the presented experimental setup and should be a subject of further investigation. The detailed review of B_v and $RMSE_v$ for particular validation points (Table 5) reveals that the biggest differences between the results obtained with different roughness datasets appear at Śnieżnik 2 and Mariańskie Skały locations. In the first case CLC data lead to considerable underestimation of velocity (up to -5.6 m/s in 50 m grid), BDOT10k results fitted better (-1.2 m/s), while LiDAR-based results tend to slightly overestimate it (0.4 m/s). The case of Mariańskie Skały was similar—only LiDAR dataset provided roughness information which could make Canyon solve properly for this station. In this case, the pre-classified land-use data do not give a proper approximation of the pattern of roughness elements nearby the measurement point. The big improvement of model's performance due to the growing number of roughness details could be also observed at Żmijowa Polana, Jaworek, and Idzików. On the other hand, at Czarna Góra site, the use of LiDAR data caused a noticeable overestimation of velocity. This single case implies conjecture of roughness underestimation—it can be caused by the value of porosity factor which might be unfitting for the predominant shapes of trees' crowns at this altitude. Finally, the most disturbing case is Śnieżnik 1 point, which is characterized by high velocity overestimation regardless of the input roughness data. This may be caused by a local change of atmospheric stability (shallow stable layer), which might have led to decrement of wind velocity—if so, this problem cannot be solved using mean parameterization for atmospheric stability inside the whole calculation domain. Unfortunately, there is no undeniable proof that the aforementioned meteorological conditions actually appeared, thus this explanation should only be treated as a possibility.

According to the aforesaid observations, the LiDAR data appeared to induce the best Canyon performance. An additional application of the direction-dependent roughness parameter (h_{ceff}), applied only for 50 m grid, resulted in further minor decrement of the error values (Table 6). For instance, the

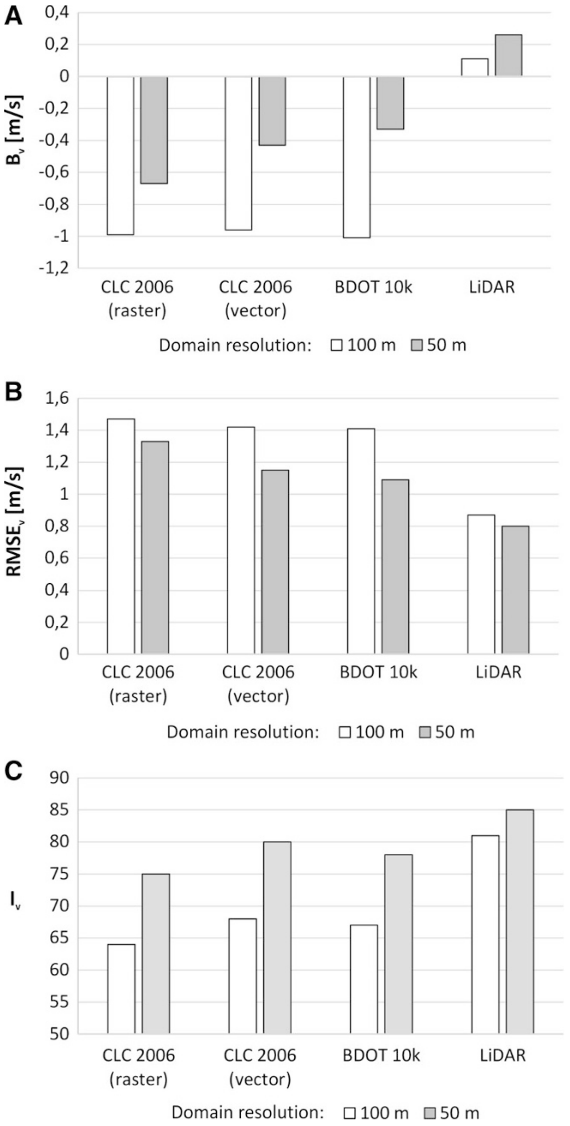

Figure 12
Impact of the particular roughness datasets on the overall values of wind velocity modeling performance indices: **a** mean B_v, **b** mean RMSE_v, **c** mean I_v

mean RMSE_V decreased by 0.04 m/s comparing to the "standard" h_c. This error measure also did not change more than ±0.2 m/s in any measurement point. Figure 13 provides the best illustration of the subtlety of changes in the modeled velocity field. Nonetheless, h_{ceff}-based results are characterized by the mean B_v value of 0.17 m/s, which indicates that the overall tendency to overestimate wind velocity is slightly lower.

Comparing to the previous study at the Śnieżnik Massif test site, the overall performance of the model was improved. The mean RMSE_V value was reduced from 1.0 m/s (Jancewicz 2014) to little less than 0.8 m/s, while the mean I_v value increased from 82 to 85 (Table 7). However, in this study a different elevation model was used than in the previous study.

Probably, there is a possibility to achieve further improvements of model's performance, as the LiDAR data offer such a high level of details that could be used in the process of roughness parameterization. However, a certain part of generated errors may be a consequence of solver's limitations.

5. *Summary*

This study demonstrates that the near-ground diagnostic wind velocity modeling in mountainous terrain (with an assumption of atmospheric neutral stability and relatively constant wind conditions) needs to be supported by apt roughness information. The use of LiDAR-based input roughness dataset improves performance of the diagnostic model, comparing to the qualitative datasets. It is distinctly expressed by calculated error indices. Moreover, the change of grid resolution from 100 m up to 50 m adjusts further model's performance. A slight improvement can be accomplished while modeling with use of re-calculated "windward" roughness values. One can observe that, while using various input qualitative data, the differences between calculated wind-velocity fields are caused by interference of following key factors: data properties (format and spatial resolution) and land-use classification.

These observations lead to a major conclusion that roughness information pre-processing should be inevitably considered in relation to the qualities of the available datasets.

On one hand there are pre-classified land coverage sets which provide categorical information, hence the estimated roughness is discrete. In consequence, roughness information may contain errors due to.

(a) Insufficient number of land cover classes.
(b) Inappropriate roughness values assignment.

Table 5

Roughness values and mean error measures of wind velocity calculated for particular validation points, considering the results of using different input roughness datasets in the wind velocity modeling within 100 and 50 m grid resolution

			ID	1	2	3	4	5	6	7	8
			Roughness dataset	Czarna Góra	Hala pod Śnieżnikiem	Idzików	Jaworek	Jaworek Górny	Kletno	Łąki Myśliwskie	Mariańskie Skały
Domain resolution —100 m	*Roughness*	h_c (m)	CLC (raster)	*9.3*	*2.7*	*0.7*	*0.2*	*0.2*	*0.7*	*9.3*	*2.7*
			CLC (vector)	*9.3*	*2.7*	*0.7*	*0.2*	*0.2*	*0.7*	*0.2*	*2.7*
			BDOT 10k	*9.3*	*9.3*	*0.2*	*0.2*	*0.2*	*0.2*	*0.2*	*9.3*
			LiDAR	*1.9*	*0.4*	*0.0*	*0.1*	*0.3*	*0.4*	*1.1*	*1.2*
	Error measure	B_{v} (m/s)	CLC (raster)	−1.2	−1.3	−1.1	−0.7	**0.1**	**−0.1**	−1.5	−2.2
			CLC (vector)	−1.2	−1.5	−1.2	**−0.6**	0.2	**−0.1**	−0.8	−2.1
			BDOT 10k	**−1.0**	−1.0	−1.0	−0.9	0.2	−0.4	**−0.3**	−3.3
			LiDAR	1.3	**−0.4**	**−0.2**	−0.7	0.4	−0.4	**−0.3**	**−1.0**
		RMSE$_{\mathrm{v}}$ (m/s)	CLC (raster)	1.2	1.3	1.2	**0.8**	**0.5**	**0.2**	1.6	2.2
			CLC (vector)	1.2	1.5	1.2	**0.8**	**0.5**	**0.2**	1.1	2.2
			BDOT 10k	**1.0**	1.0	1.0	1.0	**0.5**	0.4	**0.8**	3.3
			LiDAR	1.3	**0.5**	**0.3**	**0.8**	0.6	0.4	**0.8**	**1.0**
		I$_{\mathrm{v}}$	CLC (raster)	57	67	78	88	**91**	**97**	38	54
			CLC (vector)	57	61	77	**89**	**91**	94	66	55
			BDOT 10k	64	76	81	83	**91**	95	**73**	16
			LiDAR	**71**	**91**	**95**	88	90	94	**73**	**83**
Domain resolution – 50 m	Roughness	h_c (m)	CLC (raster)	*9.3*	*2.7*	*0.7*	*0.2*	*0.2*	*0.7*	*9.3*	*2.7*
			CLC (vector)	*9.3*	*2.7*	*0.7*	*0.2*	*0.2*	*0.7*	*0.2*	*2.7*
			BDOT 10k	*9.3*	*0.2*	*0.2*	*0.2*	*0.2*	*0.2*	*0.2*	*9.3*
			LiDAR	*3.0*	*0.2*	*0.0*	*0.0*	*0.3*	*0.2*	*0.3*	*0.4*
	Error measure	B_{v} (m/s)	CLC (raster)	**−0.3**	−0.9	−1.3	−1.1	0.4	−0.3	−1.0	−1.6
			CLC (vector)	**−0.3**	−0.8	−1.4	−1.1	0.4	−0.3	**−0.1**	−1.2
			BDOT 10k	**0.3**	−0.3	−1.3	−1.4	0.3	−0.2	**0.1**	−2.9
			LiDAR	1.3	**−0.1**	**−0.6**	**−0.6**	**0.1**	**0.1**	−0.4	**−0.3**
		RMSE$_{\mathrm{v}}$ (m/s)	CLC (raster)	**0.3**	0.9	1.3	1.2	0.5	**0.3**	1.2	1.6
			CLC (vector)	**0.3**	0.8	1.4	1.2	0.5	**0.3**	**0.7**	1.3
			BDOT 10k	**0.3**	0.4	1.3	1.4	0.5	**0.3**	**0.7**	2.9
			LiDAR	1.3	**0.3**	**0.7**	**0.8**	**0.4**	**0.3**	0.8	**0.4**
		I_{v}	CLC (raster)	91	80	72	79	92	96	65	68
			CLC (vector)	91	80	70	79	92	96	**79**	78
			BDOT 10k	**92**	93	74	73	**93**	**97**	**79**	31
			LiDAR	71	**96**	**89**	**89**	92	96	71	**94**

Table 5

continued

			ID Roughness dataset	9 Międzygórze 1	10 Międzygórze 2	11 Puchaczówka	12 Śnieżnik 1	13 Śnieżnik 2	14 Średniak	15 Żmijowa Polana	Mean value
Domain resolution —100 m	*Roughness*	h_c (m)	CLC (raster)	*0.2*	*9.3*	*0.2*	*0.3*	*9.3*	*2.7*	*9.3*	–
			CLC (vector)	*0.2*	*2.7*	*0.2*	*0.3*	*2.7*	*2.7*	*9.3*	–
			BDOT 10k	*0.2*	*0.2*	*0.2*	*0.3*	*0.2*	*2.7*	*9.3*	–
			LiDAR	*0.2*	*5.5*	*0.1*	*0.0*	*0.0*	*0.5*	*2.6*	–
	Error measure	B_v (m/s)	CLC (raster)	0.9	−1.1	**−0.1**	1.7	−4.1	−2.0	−2.2	−0.99
			CLC (vector)	0.9	−1.0	**−0.1**	**1.4**	−4.6	−2.0	−1.7	−0.96
			BDOT 10k	0.5	**−0.9**	−0.2	**1.4**	−3.4	−2.6	−2.3	−1.01
			LiDAR	**0.4**	−1.1	**−0.1**	3.6	**0.3**	**0.0**	**−0.2**	**0.11**
		$RMSE_v$ (m/s)	CLC (raster)	0.9	1.2	**0.6**	1.8	4.1	2.2	2.2	1.47
			CLC (vector)	0.9	1.1	**0.6**	**1.5**	4.6	2.2	1.7	1.42
			BDOT 10k	0.6	**0.9**	0.7	**1.5**	3.4	2.7	2.3	1.41
			LiDAR	**0.4**	1.2	**0.6**	3.7	**0.3**	**0.9**	**0.3**	**0.87**
		I_v	CLC (raster)	77	24	**86**	70	56	66	16	64
			CLC (vector)	77	39	**86**	**74**	49	65	41	68
			BDOT 10k	85	**49**	85	**74**	66	51	11	67
			LiDAR	**89**	24	**86**	46	**97**	**88**	**92**	**81**
Domain resolution – 50 m	Roughness	h_c (m)	CLC (raster)	*0.2*	*9.3*	*0.2*	*0.3*	*9.3*	*2.7*	*9.3*	–
			CLC (vector)	*0.2*	*4.0*	*0.2*	*0.3*	*2.7*	*2.7*	*9.3*	–
			BDOT 10k	*0.2*	*4.0*	*0.2*	*0.3*	*0.1*	*2.7*	*9.3*	–
			LiDAR	*0.1*	*1.0*	*0.1*	*0.0*	*0.0*	*0.2*	*2.8*	–
	Error measure	B_v (m/s)	CLC (raster)	**0.1**	−0.6	**0.2**	3.0	−5.6	0.4	−1.5	−0.67
			CLC (vector)	**0.1**	**−0.3**	0.3	**2.9**	−4.1	0.5	−1.1	−0.43
			BDOT 10k	−0.2	**−0.3**	0.3	3.3	−1.2	**0.2**	−1.6	−0.33
			LiDAR	0.2	−0.6	**0.2**	3.4	**0.4**	0.9	**0.1**	**0.26**
		$RMSE_v$ (m/s)	CLC (raster)	**0.2**	0.6	**0.6**	**3.0**	5.6	1.2	1.5	1.33
			CLC (vector)	**0.2**	0.4	**0.6**	**3.0**	4.1	1.3	1.1	1.15
			BDOT 10k	0.4	**0.3**	0.7	3.3	1.2	**1.1**	1.6	1.09
			LiDAR	**0.2**	0.6	0.7	3.4	**0.4**	1.4	**0.4**	**0.80**
		I_v	CLC (raster)	94	72	87	53	32	86	50	75
			CLC (vector)	**96**	86	**88**	**54**	57	86	68	80
			BDOT 10k	89	**89**	**88**	50	90	**87**	45	78
			LiDAR	**96**	72	86	49	**97**	84	**92**	**85**

Bold font indicates the lowest error values

Italic values indicate roughness values

Table 6

Mean error measures calculated for particular validation points, considering results of modeling with use of standard LiDAR−based roughness and its "windward" modification

Station name	Czarna Góra	Hala pod Śnieżnikiem	Idzików	Jaworek	Jaworek Górny	Kletno	Łąki Myśliwskie	Mariańskie Skały
B_v								
LiDAR	1.3	**−0.1**	**−0.6**	−0.6	0.1	0.1	−0.4	**−0.3**
LiDAR (windward)	**1.2**	−0.2	−0.7	−0.6	**0.0**	**0.0**	**−0.3**	−0.4
RMSE_v								
LiDAR	1.3	0.3	**0.7**	0.8	0.4	0.3	0.8	**0.4**
LiDAR (windward)	**1.2**	0.3	0.8	0.8	**0.3**	**0.2**	0.8	0.5
I_v								
LiDAR	71	96	**89**	89	92	96	71	**94**
LiDAR (windward)	**73**	96	87	89	**94**	**97**	**73**	93

Station name	Międzygórze 1	Międzygórze 2	Puchaczówka	Śnieżnik 1	Śnieżnik 2	Średniak	Żmijowa Polana	Mean value
B_v								
LiDAR	0.2	−0.6	0.2	3.4	0.4	0.9	0.1	**0.26**
LiDAR (windward)	**−0.1**	−0.6	**−0.1**	3.4	**0.0**	**0.7**	0.1	**0.17**
RMSE_v								
LiDAR	0.2	0.6	**0.7**	**3.4**	0.4	1.4	0.4	**0.80**
LiDAR (windward)	0.2	0.6	0.7	3.5	**0.0**	**1.2**	**0.3**	**0.76**
I_v								
LiDAR	**96**	72	86	49	97	84	92	**84.9**
LiDAR (windward)	94	72	86	49	**100**	**86**	**93**	**85.4**

Bold font indicates the lowest error values

(c) Method of data collecting.

Accordingly, qualitative data have to be thoroughly analyzed (and corrected if necessary) before being used as a source of an input roughness information. Then, these datasets can provide a valuable improvement of model's performance, to be used consistently with previous experience with empirical roughness length estimation and classification.

On the other hand, high-resolution LiDAR-based continuous elevation data offer plenty of possibilities during the pre-processing stage. It is possible to prepare a roughness dataset which is suitable for any grid resolution. Furthermore, the continuous quantitative datasets seem to be exceptionally interesting within the scope of the optimization of "effective roughness length" calculation process. Accordingly, there are numerous issues which should be examined in an experimental way:

(a) Calculation of roughness inside the windward fan.
(b) Spatially variable canopy porosity.
(c) Application of solutions used in the modeling of wind fields in urban areas.
(d) Sub-grid effects induced by micro relief.

Thus, it seems that it is still possible to refine the roughness estimation process which may lead to further improvements of diagnostic wind-velocity modeling.

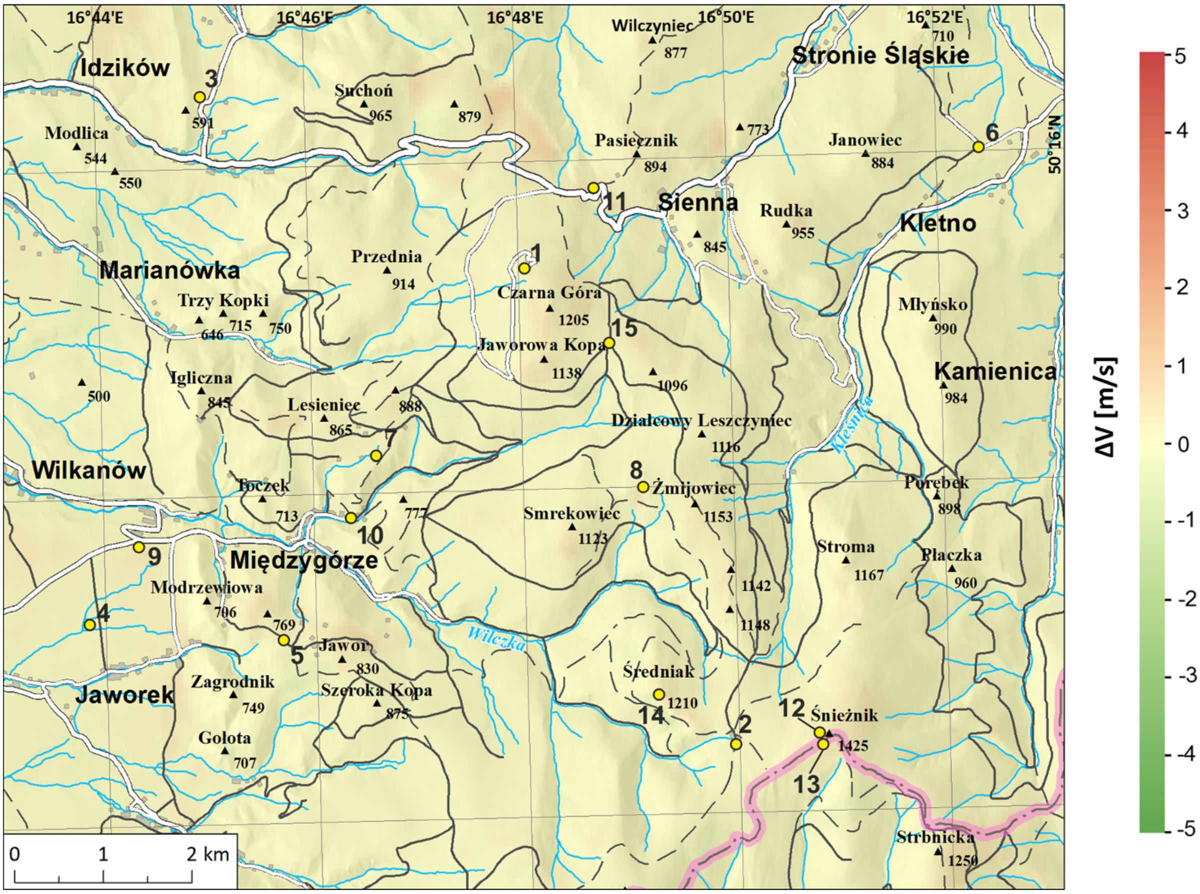

Figure 13
Spatial distribution of mean modeled wind velocity differences (ΔV) at height of 2 m above ground (26 May 2012; 13:00). The comparison concerns two methods of LiDAR-based roughness parameterization: mean height inside grid cell (h_c) and mean height inside windward-placed fan of 200 m radius ($h_{c\ \mathrm{eff}}$) – ($\Delta V = V_{hc} - V_{hc\mathrm{eff}}$). *Yellow dots* indicate measurement/validation points, *numbers* indicate point ID—see Tables 2 and 5

Table 7

Comparison of Canyon CFD solver performance indices calculated for various test sites

Test site	Poiares Region (Lopes 2003)	Trevim Region (Lopes 2003)	Śnieżnik Massif (constant roughness) (Jancewicz 2014)	Śnieżnik Massif [CLC 2006 (2011) roughness] (Jancewicz 2014)	Śnieżnik Massif (LiDAR-based roughness)
Mean I_v	56	41	71	80	**85**

Acknowledgments

The authors are grateful to: Romuald Jancewicz, Marzena Józefczyk, Aleksandra Karbowniczak, Maurycy Urbanowicz and Remigiusz Żukowski for their support during field measurements of wind velocity, Tymoteusz Sawiński for technical support and Piotr Migoń for proofreading. Kaindl Windmaster 2 anemometers were used by kind permission of the Department of Climatology and Atmosphere Protection, University of Wrocław. WindStation 4.0.2 software was developed and provided by António Manuel Gameiro Lopes (Department of Mechanical Engineering, University of Coimbra). LiDAR and BDOT10k data were provided by the Head Office of Geodesy and Cartography under the license no. DIO.DFT.DSI.7211.1619.2015_PL_N. Corine Land Cover 2006 raster and vector datasets were provided by European Environmental Agency. Meteorological data used in presented study were provided by Department of Atmospheric Science at the University of Wyoming, National Oceanic and Atmospheric Administration, The Austrian Central Institute for Meteorology and Geodynamics (ZAMG), German Weather Service and The Institute for Meteorology at the Free University of Berlin. Finally, the author greatly appreciate reviewers for their valuable comments and constructive suggestions to improve the manuscript.

Appendix

See Table 8.

Table 8

Davenport classification of terrain roughness (Wieringa *et al.* 2001)

z_0 (m)	Landscape description
0.0002 "Sea"	Open sea or lake (irrespective of wave size), tidal flat, snow-covered flat plain, featureless desert, tarmac and concrete, with a free fetch of several kilometres
0.005 "Smooth"	Featureless land surface without any noticeable obstacles and with negligible vegetation; e.g. beaches, pack ice without large ridges, marsh and snow-covered or fallow open country
0.03 "Open"	Level country with low vegetation (e.g. grass) and isolated obstacles with separations of at least 50 obstacle heights; e.g. grazing land without wind breaks, heather, moor and tundra, runway area of airports. Ice with ridges across-wind
0.10 "Roughly open"	Cultivated or natural area with low crops or plant covers, or moderately open country with occasional obstacles (e.g. low hedges, isolated low buildings or trees) at relative horizontal distances of at least 20 obstacle heights
0.25 "Rough"	Cultivated or natural area with high crops or crops of varying height, and scattered obstacles at relative distances of 12–15 obstacle heights for porous objects (e.g. shelterbelts) or 8–12 obstacle heights for low solid objects (e.g. buildings)
0.5 "Very rough"	Intensively cultivated landscape with many rather large obstacle groups (large farms, clumps of forest) separated by open spaces of about eight obstacle heights. Low densely-planted major vegetation like bush land, orchards, young forest. Also, area moderately covered by low buildings with interspaces of 3–7 building heights and no high trees
1.0 "Skimming"	Landscape regularly covered with similar-size large obstacles, with open spaces of the same order of magnitude as obstacle heights; e.g. mature regular forests, densely built-up area without much building height variation
≥2.0 "Chaotic"	City centres with mixture of low-rise and high-rise buildings, or large forests of irregular height with many clearings

REFERENCES

ABBES, M., BELHADJ, J. (2012), *Wind resource estimation and wind park design in El-Kef region, Tunisia*, Energy *40*, 348–357.

CHO, J., MIYAZAKI, S., YEH, P.J.-F., KIM, W., KANAE, S., OKI T. (2012), *Testing the hypothesis on the relationship between aerodynamic roughness length and albedo using vegetation structure parameters*, International Journal of Biometeorology *56*, 411–418.

COLIN, J., FAIVRE, R. (2010), *Aerodynamic roughness length estimation from very high-resolution imaging LIDAR observations over the Heihe basin in China*, Hydrology and Earth System Sciences *14*, 2661–2669.

Corine Land Cover 2006 raster dataset (version 15) (2011); http://www.eea.europa.eu/data-and-maps/data/corine-land-cover-2006-raster-1. Accessed date 13 Mar 2012.

Corine Land Cover 2006 vector dataset (version 17) (2013); http://www.eea.europa.eu/data-and-maps/data/clc-2006-vector-data-version-3. Access date 20 Mar 2014.

Database of Topographical Objects (BDOT10k)—vector database; http://www.codgik.gov.pl/index.php/zasob/baza-danych-obiektow-topograficznych.html. Accessed date 30 May 2015.

DAVENPORT, A.G. (1960), *Rationale for determining design wind velocities*, Journal of Structural Division *86*, 39–68.

DE MEIJ, A., VINUESA, J.F. (2014), *Impact of SRTM and Corine Land Cover data on meteorological parameters using WRF*, Atmospheric Research *143*, 351–370.

DONG, Z., GAO, S., FRYREAR, D.W. (2001), *Drag coefficients, roughness length and zero-plane displacement height as disturbed by artificial standing vegetation*, Journal of Arid Environments *49*, 485–505.

EMEIS, S., KNOCHE, H.R., Applications in meteorology. In Geomorphometry: concepts, software, applications. (eds. Hengl T., Reuter H. I.) (Elsevier 2007) pp. 603–623.

EMERY, C., TAI, E., YARWOOD, G., Enhanced meteorological modeling and performance evaluation for two Texas ozone episodes. (ENVIRON International Corporation, 2001).

GARRATT, J.R., The atmospheric boundary layer (Cambridge, New York, 1994).

GRIMMOND, C.S.B., OKE, T.R. (1999), *Aerodynamic properties of urban areas derived from analysis of surface form.* Journal of Applied Meteorology *38*, 1262–1292.

HAMMOND, D.S., CHAPMAN, L., THORNES, J.E. (2012), *Roughness length estimation along road transects using airborne LIDAR data,* Meteorological Applications *19*, 420–426.

HANSEN, F.V., Surface roughness lengths (Army Research Laboratory, 1993).

HASAGER, C.B., NIELSEN, N.N., JENSEN, N.O., BOEGH, E., CHRISTENSEN, J.H., DELLWIK, E., SOEGAARD, H. (2003), *Effective roughness calculated from satellite-derived land cover maps and hedge-information used in a weather forecasting model*, Boundary-Layer Meteorology *109*, 227–254.

HEISLER, G.M., DE WALLE, D.R. (1988), *Effects of windbreak structure on airflow*, Agriculture, Ecosystems & Environment *22/23*, 41–69.

JACKSON, P.S. (1981), *On the Displacement Height in the Logarithmic Velocity Profile*, Journal of Fluid Mechanics *111*, 15–25.

JACOBSON, M.Z., Fundamentals of atmospheric modeling (University Press, Cambridge 2005).

JANCEWICZ, K. (2014), *Remote sensing data in wind velocity field modeling: a case study from the Sudetes (SW Poland),* Pure and Applied Geophysics *171*, 941–964.

JASINSKI, M.F., CRAGO, R.D. (1999), *Estimation of vegetation aerodynamic roughness of natural regions using frontal area density determined from satellite imagery*, Agricultural and Forest Meteorology *94*, 65–77.

JIMENEZ, P.A., DUDHIA, J. (2012), *Improving the representation of resolved and unresolved topographic effects on surface wind in the WRF model*, Journal of Applied Meteorology and Climatology, *51*(2), 300–316.

LOPES, A.M.G. (2003), *WindStation—a software for the simulation of atmospheric flows over complex topography*, Environmental Modeling & Software *18*, 81–96.

LOPES, A.M.G. (2013), WindStation 3.1.0: User's Manual.

MORALES, L., LANG, F., MATTAR, C. (2012), *Mesoscale wind speed simulation using CALMET model and reanalysis information: An application to wind potential,* Renewable Energy *48*, 57–71.

PIASECKI, J., Wybrane cechy klimatu Masywu Śnieżnika, In Masyw Śnieżnika. Zmiany w środowisku przyrodniczym (eds. JAHN A., KOZIOWSKI S., PULINA M.) (PAE, Warszawa 1996) pp. 189–206.

PIASECKI, J., SAWIŃSKI, T., The Niedźwiedzia Cave in the climatic environment of the Kleśnica Valley (Śnieżnik Massif), In Karst of the Częstochowa Upland and of the Eastern Sudetes: palaeoenviroments and protection (eds. STEFANIAK K., TYC A., SOCHA P.) (University of Silesia, Sosnowiec – Wrocław 2009) pp. 423–454.

PLATE, E.J., Engineering meteorology (Elsevier, New York, 1982).

RAMLI, N.I., IDRIS ALI, M., SAAD, M.S.H., MAJID, T.A (2009), Estimation of the roughness length (z_o) in malaysia using satellite image, Conference Proceedings of The Seventh Asia-Pacific Conference on Wind Engineering, http://www.iawe.org/Proceedings/7APCWE/T2D_1.pdf.

SCHAUDT, K.J., DICKINSON, R.E. (2000), *An approach to deriving roughness length and zero-plane displacement height from satellite data, prototyped with BOREAS data*, Agricultural and Forest Meteorology *104*, 143–155.

SILVA, J., RIBEIRO, C., GUEDES, C. (2007), Roughness length classification of Corine Land Cover Classes, Conference Proceedings of European Wind Energy Conference 2007, http://www.ewea.org/ewec2007/allfiles2/545_Ewec2007fullpaper.pdf.

SUDER, A., SZYMANOWSKI, M. (2014), *Determination of ventilation channels in urban area: a case study of Wrocław (Poland)*, Pure and Applied Geophysics *171*, 965–975.

TAYLOR, P.A. (1987), *Comments and further analysis of effective roughness lengths for use in numerical three-dimensional models*, Boundary-Layer Meteorology *39*, 403–418.

THOM, A.S. (1971), *Momentum absorption by vegetation*, Quarterly Journal of Royal Meteorological Society *97*, 414–428.

TIAN, X., LI, Z.Y, VAN DER TOL, C., SU, Z., LI, X., HE, Q.S., BAO, Y.F., CHEN, E.X., LI, L.H. (2011), *Estimating zero-plane displacement height and aerodynamic roughness length using synthesis of LiDAR and SPOT-5 data,* Remote Sensing of Environment *115*, 2330–2341.

TRUHETZ, H., High resolution wind field modeling over complex topography: analysis and future scenarios. (Wegener Center for Climate and Global Change, Scientific Report No. 32-2010, Graz 2010).

WIERINGA, J. (1993), *Representative roughness parameters for homogenous terrain*, Boundary-Layer Meteorology *63*, 323–363.

WIERINGA, J., DAVENPORT, A.G., GRIMMOND, C.S.B., OKE, T.R. (2001) New revision of Davenport roughness classification. Proceedings of the 3rd European & African Conference on Wind Engineering.

WOOD, N., BROWN, A.R., HEWER, F.E., (2001), *Parametrizing the effects of orography on the boundary layer: An alternative to effective roughness lengths*, Q. J. R. Meteorol. Soc., *127*(573), 759–777.

World Meteorological Organization, Guide to meteorological instruments and methods of observation, Tech. Rep. 8 (Seventh Edition). (Secretariat of World Meteorological Organization, Geneva 2008).

YAMAZAWA, H., KONDO J. (1989), *Empirical-statistical method to estimate the surface wind speed over complex terrain*, Journal of Applied Meteorology and Climatology *28*, 996–1001.

(Received November 30, 2014, revised February 17, 2016, accepted April 12, 2016, Published online April 29, 2016)

Pure Appl. Geophys. 174 (2017), 595–621

DOI 10.1007/s00024-015-1199-2

Pure and Applied Geophysics

The Role of Auxiliary Variables in Deterministic and Deterministic-Stochastic Spatial Models of Air Temperature in Poland

MARIUSZ SZYMANOWSKI[1] and MACIEJ KRYZA[2]

Abstract—Our study examines the role of auxiliary variables in the process of spatial modelling and mapping of climatological elements, with air temperature in Poland used as an example. The multivariable algorithms are the most frequently applied for spatialization of air temperature, and their results in many studies are proved to be better in comparison to those obtained by various one-dimensional techniques. In most of the previous studies, two main strategies were used to perform multidimensional spatial interpolation of air temperature. First, it was accepted that all variables significantly correlated with air temperature should be incorporated into the model. Second, it was assumed that the more spatial variation of air temperature was deterministically explained, the better was the quality of spatial interpolation. The main goal of the paper was to examine both above-mentioned assumptions. The analysis was performed using data from 250 meteorological stations and for 69 air temperature cases aggregated on different levels: from daily means to 10-year annual mean. Two cases were considered for detailed analysis. The set of potential auxiliary variables covered 11 environmental predictors of air temperature. Another purpose of the study was to compare the results of interpolation given by various multivariable methods using the same set of explanatory variables. Two regression models: multiple linear (MLR) and geographically weighted (GWR) method, as well as their extensions to the regression-kriging form, MLRK and GWRK, respectively, were examined. Stepwise regression was used to select variables for the individual models and the cross-validation method was used to validate the results with a special attention paid to statistically significant improvement of the model using the mean absolute error (MAE) criterion. The main results of this study led to rejection of both assumptions considered. Usually, including more than two or three of the most significantly correlated auxiliary variables does not improve the quality of the spatial model. The effects of introduction of certain variables into the model were not climatologically justified and were seen on maps as unexpected and undesired artefacts. The results confirm, in accordance with previous studies, that in the case of air temperature distribution, the spatial process is non-stationary; thus, the local GWR model performs better than the global MLR if they are specified using the same set of auxiliary variables. If only GWR residuals are autocorrelated, the geographically weighted regression-kriging (GWRK) model seems to be optimal for air temperature spatial interpolation.

Key words: Air temperature, spatial interpolation, auxiliary variables, geographically weighted regression-kriging.

1. Introduction

Providing accurate, high-resolution spatial information is one of the most challenging tasks of contemporary environmental sciences. However, this particularly concerns climatological and meteorological data as they are used not only for climatological analysis itself, but they are frequently applied as the significant input for modelling and studies in many other scientific disciplines or applications, for example, in bioclimatology, dispersion of atmospheric pollutants, or for planning and supporting location decisions. There are two general approaches to the development of continuous spatial climatological information: physically based and data based. The first is performed by means of the climatological models in either global [General Climate Models (GCMs)] or regional/mesoscale models [Regional Climate Models (RCMs)]. To the RCMs class belong such models as, e.g. Weather Research and Forecasting (WRF; SKAMAROCK *et al.* 2008) or Regional Atmospheric Modeling System (RAMS; PIELKE *et al.* 1992). The GCMs are typically run at coarse spatial resolution (max. ~50 km) and do not account for local scale features and phenomena caused, e.g. by topography, local land use/land cover or clouds. To overcome these problems, various

---

[1] Department of Geoinformatics and Cartography, Institute of Geography and Regional Development, University of Wrocław, pl. Uniwersytecki 1, 50-137 Wrocław, Poland. E-mail: mariusz.szymanowski@uwr.edu.pl

[2] Department of Climatology and Atmosphere Protection, Institute of Geography and Regional Development, University of Wrocław, ul. Kosiby 8, 51-621 Wrocław, Poland.

dynamical or statistical downscaling techniques can be applied to process GCMs' outputs (Wilby and Wigley 1997). For example, the WRF model can be used to dynamically downscale GCM simulations even up to a few kilometres spatial grid (Kryza *et al.* 2012; Bowden *et al.* 2012). But still, even if RCMs are continuously developing and their accuracy and spatial resolution are increasing, spatial interpolation allowing for transformation from discretely distributed point data into continuous high-resolution spatial information is the most frequently used for mapping climatological/meteorological elements. However, the final choice between physically based or data-based spatialization procedures is strongly dependent on many factors, including, e.g. the specific user's needs and skills, and the access to required datasets, specialized software or computational resources.

There are dozens of methods available to perform the spatial interpolation of various elements of the natural environment. For example, Li and Heap (2008) reviewed 62 methods and their variations applied and described in 51 publication. These methods can be considered as universal which means that they can be used for various environmental features. The choice of the optimal algorithm in a given case is a difficult task as it depends on characteristics of the spatial process, properties of the modelled variable, the expectations of the modeller, e.g. assumed accuracy and resolution, the number and spatial distribution of input data and many others. In the selection of interpolation procedure, the classifications of the algorithms, presented, e.g. by Hengl (2007), Li and Heap (2008) or in COST Action 719 Final Report (2008), or the decision trees (Hengl 2007; Szymanowski *et al.* 2013) allowing for selection and grouping methods accordingly to their theoretical basis and properties, might become useful. Most of the "universal" spatialization methods have been used for the interpolation of climatological elements, like air temperature and atmospheric precipitation. There are also some methods that have been intentionally developed or modified for the use in climatology, e.g. lapse rate method (LR; Lennon and Turner 1995; Willmott and Matsuura 1995), thin-plate splines (TPS; Hutchinson 1995), AURELHY (Benichou and Le Breton 1987), PRISM (Daly *et al.* 1994, 2008) and MISH (Szentimrey and Bihari 2004). There are also significant advances in hierarchical Bayesian and non-stationary process modelling techniques (Huerta *et al.* 2004; Al-Awadhi and Al-Awadhi 2006; Cressie and Johannesson 2008; Yue and Speckman 2010; Wilson and Silander 2014).

In the case of the air temperature spatialization, where the physical processes and environmental covariables determining spatial distribution are quite well known, the multivariable techniques based on deterministic or geostatistical (or both) assumptions are the most frequently used. The reviews of papers and applications show that the most proper and frequently applied for air temperature spatial interpolation are residual kriging (regression-kriging, RK), regression methods—mostly multiple linear (MLR), and TPS (COST Action 719 Final Report 2008; Szymanowski *et al.* 2012). Less frequently, other techniques, such as LR, PRISM, co-kriging (CK), kriging with external drift (KED) or combination MLR + IDW [inverse distance weighting (IDW)], are also applied. All of them are multivariable approaches, performed with the use of one or more environmental auxiliary variables.

In multivariate climatological interpolation, the role of an explanatory variable is to replicate the impact of environmental factor on the magnitude and the distribution of the interpolated climate element. A review of previous works, taking into account the multidimensional techniques in air temperature spatialization, indicates that there are variables that can be considered as universal and almost always included in the analysis (e.g. elevation for air temperature), and those that are used depending on the climate (geographical) characteristic of a study area and the scale of impacts (usually macro- to local scale) taken into account. Altitude is the major factor determining the spatial pattern of air temperature at global/regional scales and when the longer averaging periods are considered. Its level of influence on temperature is usually many times greater than that of other environmental factors (Szymanowski *et al.* 2012). In practice, one can be assured that if the multivariate technique is used for air temperature interpolation, the altitude is included in the set of explanatory variables. However, there can be some exceptions, as, for example, in the case of the urban heat island interpolation for a city located in a flat terrain (Szymanowski and Kryza 2012).

The same, general group of auxiliary variables is represented by coordinates, even if they are used less frequently than altitude. Latitude and longitude (or their counterparts in local coordinate systems) are used to reflect an overall spatial trend. This trend can be, for instance, a consequence of systematic changes in insolation, the impact of the oceans, lands, or mountain ranges and, in some cases, circulation-driven regularities with the advection of air masses (e.g. Nalder and Wein 1998; Ninyerola *et al.* 2000; Ustrnul and Czekierda 2005; Perry and Hollis 2005a, b; Szymanowski *et al.* 2012, 2013). As the coordinates are used to characterize general tendencies over a study area, they are usually less applicable for small areas with strong locally determined air temperature fields (Szymanowski and Kryza 2009, 2012). In some papers, in addition to coordinates, the index of continentality has also been used (Attorre *et al.* 2007; Hogewind and Bissolli 2011; Krahenmann *et al.* 2011).

Another, very frequently used variable is a distance from the sea (White 1979; Bjornsson *et al.* 2007; Boi *et al.* 2011; Joly *et al.* 2011) or distance from other major bodies of water (Holdaway 1996; Hiebl *et al.* 2009; Tietavainen *et al.* 2010). Distance from water bodies, like most of the variables capturing the impact of land use/land cover, is typical of regional or local scale. Their impact, decreasing with distance, is clearly marked up to 10 km and negligible in practice for distances exceeding 100 km from the sea (Daly 2006). The influence of other land cover classes can also be observed locally (Jarvis and Stuart 2001a, b; Percec Tadic 2010). Here, the specific role is played by the impact of urban areas, especially due to well-known phenomena of air temperature rise in cities—the urban heat island (Choi *et al.* 2003; Hiebl *et al.* 2009; Szymanowski *et al.* 2013).

Terrain relief usually also has a local influence on the air temperature field. Various terrain derivatives can be used to reflect the relief-controlled effects. One of the most frequently applied is slope inclination (Lennon and Turner 1995; Szymanowski *et al.* 2013); however, its role in physical processes determining air temperature is ambiguous. This variable probably should not stand alone but rather in conjunction with terrain aspect (Agnew and Palutikof 2000; Attorre *et al.* 2007; Hiebl *et al.* 2009; Apaydin *et al.* 2011). The role of the relief, particularly associated with the disposal of cooler air from the slopes and a tendency to the accumulation of cold air in concave terrain forms, is expressed in such variables as concavity/convexity, relative height and terrain curvature (Ninyerola *et al.* 2007; Esteban *et al.* 2009; Hiebl *et al.* 2009; Szymanowski *et al.* 2013).

Relatively rarely used explanatory variable of air temperature is solar irradiation (Vicente-Serrano *et al.* 2003; Attorre *et al.* 2007; Benavides *et al.* 2007; Esteban *et al.* 2009; Joly *et al.* 2011), even if this variable is complex, representing general geographic, atmospheric and astronomic energetic conditions, as well as local influence of terrain height and relief (slope, aspect, and hillshades).

The above-mentioned variables can be used in various shapes, for example, taking into account the feature in certain directions only (Vicente-Serrano *et al.* 2003; Perry and Hollis 2005a, b). Explanatory variables can also be further modified by application of various moving window filters (focal functions) to simulate the effect of the so-called source area (defined by the window size) on the air temperature distribution (Agnew and Palutikof 2000; Jarvis and Stuart 2001a, b; Szymanowski *et al.* 2013). Auxiliary variables can also be created as combinations of environmental factors using map algebra or grouping in principal components to reduce the dimension of the model (White 1979; Lennon and Turner 1995; Bjornsson *et al.* 2007; Percec Tadic 2010).

In previous studies focused on multivariate interpolation of air temperature, two main strategies of appointing the set of explanatory variables were used to specify the regression model. These were the stepwise regression selection (Kurtzman and Kadmon 1999; Brown and Comrie 2002; Apaydin *et al.* 2011; Boi *et al.* 2011) or mandatory appointment of auxiliary variables accordingly only to known physical processes but without in-depth analysis of statistical interrelations (Chuanyan *et al.* 2005; Hogewind and Bissolli 2011). However, in all these attempts, it was assumed that the more spatial variation of air temperature is deterministically explained, the better is the quality of spatial interpolation. The correctness of this assumption, although intuitively justified, has not been thoroughly verified. Thus, one of the purposes of this paper is to review the above thesis—does the incorporation of additional explanatory variables lead to the statistically significant improvement of the model performance, compared with simpler models?

In the above-mentioned research, significantly correlated variables were usually also introduced to the model by the fact that their spatial patterns were "reproduced" on the maps of air temperature. However, there are some reports claiming that the introduction of certain auxiliary variables to the spatial models, even if they are significantly correlated with air temperature, may lead to the unexpected artefacts seen on the maps, if the expert judgment is applied (Szymanowski *et al.* 2012).

This work addresses the role of the explanatory variable selection for spatial interpolation of climatological elements with air temperature used as an example. We evaluate the role of auxiliary variables in the spatial air temperature models, and present how the environmental co-variables affect the quality of spatial interpolation and how they affect the final maps. This is the novelty of this paper both for climatologists and for the researchers that perform spatial interpolation of climate data with multivariate geostatistical methods and use these data for their own studies at various fields. We demonstrate the importance of proper, conscious application of spatial statistical approaches, and we quantitatively show that over-reliance on physical deterministic relationships may lead to less reliable results than finding a balance between deterministic and stochastic model components. Spatialization in this study is performed with two spatial models frequently used for air temperature interpolation: deterministically applied regression and deterministic-stochastic combined model—the residual kriging. Regression techniques are represented here by two models: global—MLR, and local—geographically weighted regression (GWR), which are also extended to a deterministic-stochastic form. These are relatively frequently used multiple linear regression-kriging (MLRK) and recently developed geographically weighted regression-kriging (GWRK), respectively. All four methods are included in the decision scheme for selection an optimal interpolation method and have been used for spatial modelling of air temperature in Poland (Szymanowski *et al.* 2012, 2013). Two main aspects of the models' quality are considered. First, how introducing the additional co-variables affects the goodness-of-fit and the model errors in the points of measurements. Second, how the auxiliary variables visually modify the air temperature maps.

2. *Study Area*

The study area is the territory of Poland, located in Central Europe, between 49°00′N and 54°50′N, and 14°07′E and 24°09′E. The overall area of Poland is 312 679 km^2 (with 791 km^2 of marine internal waters included). The altitude in the country varies from 1.8 m below (N Poland) to 2499 m above sea level (S Poland). The average height of Poland (173 m a.s.l) is about 100 m less than that for Europe. The areas located in zones: 100–200 m a.s.l. (49.7 %) and 0–100 m a.s.l. (25.2 %) cover the majority of the country area, and the areas located over 1000 m a.s.l. cover only about 0.2 % (Fig. 1). Poland is characterized by transitional climate with strong, varying maritime and continental influences and prevailing western flow.

The annual mean temperature in Poland changes from below 0 °C in the upmost parts of the highest mountains (Tatra Mts.) to >8.5 °C in W and SW Poland (Słubice, Legnica, Wrocław; Fig. 1). However, in the lowland areas, mean values <7 °C are observed only in the NE part of the country. Differences of mean air temperature in the coldest and warmest years in relation to the long-term annual average do not exceed 3 °C (Woś 2010), except for the mountains. The spatial distribution of long-term annual mean temperature, with general increasing tendency to the south-west, indicates a general impact of latitude and oceanic influences, strongly affected by altitude. The highest values are observed in lowlands and in the valleys of large rivers, and the lowest annual means are noticed on the mountain tops (Kożuchowski 2011).

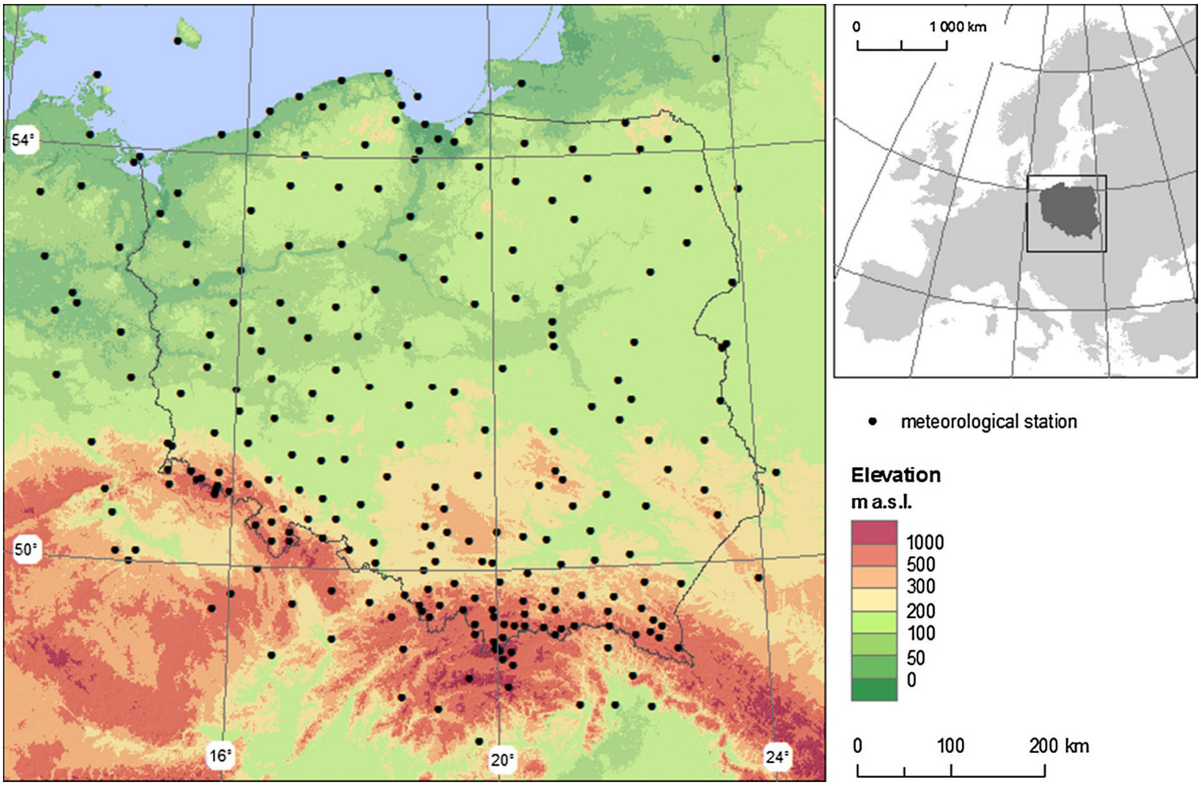

Figure 1
Study area and location of meteorological stations

There are large annual changes in the spatial distribution of air temperature due to large scale climatological factors. The W–E-oriented isotherms are shaped by the insolation energy and compounded by the impact of the Baltic Sea in the north and latitudinally stacked mountain ranges in the south. The effect of altitude, regardless of the season, is constant (decrease in temperature with height), while the role of the Baltic Sea changes seasonally from warming in autumn and winter, to cooling in spring and summer. Zonal arrangement of isotherms is most clearly visible in summer. Azonal factors, such as circulation-driven impact of the Atlantic Ocean, are apparently showed up in winter, forming a N–S course of isotherms.

Regardless of the season, the coldest areas are the uppermost parts of the mountains and the lowland parts in NE Poland. In winter, except for the coldest mountain areas, the temperature decreases from west to east, where it reaches an average below −3 °C. In the west of the country, especially in the coastal zone, where warming effects of the Baltic Sea are clearly marked, the average winter air temperature is above 0 °C. The temperature field in spring is transitional between winter and summer conditions—isotherms are NW–SE oriented, with the highest temperatures (>8 °C) in the SW part of the country. In summer, most of the area of Poland is characterized by seasonal average temperatures exceeding 18 °C, with the exception of lakeland areas in the north of the country and uplands and mountains in the south. In autumn, the warming influence of the Baltic Sea is already seen; however, a general decrease in temperature into the north-east is also clearly visible. The average seasonal air temperature in NE Poland is below 7 °C.

On average, the coldest and warmest months in Poland are January and July, respectively, and the characteristics of the spatial distribution of temperature in these months are analogous to those seen in winter and summer. Changing effects of various climate factors result in significantly different spatial distribution and values of the air temperature from the long-term averages (Ustrnul 2006).

The highest temperature, 39.5 °C, was observed in Słubice (W Poland) on 30 Jul 1956, and the lowest one, −36.9 °C, in Jelenia Góra (SW Poland) on 10 Feb 1956 (Ustrnul and Czekierda 2009). The highest maximum temperatures can be observed in Poland in various circulation types, but mainly in anticyclonic situations. In the case of the lowest minimum temperatures, the coldest, below −35 °C, are observed in areas in the east of the country (Białystok, Rzeszów). The only exception is station Jelenia Góra, located in a valley where a tendency to accumulate cold air masses is typical. As in the case of the maximum temperature, minimum temperatures are also observed mainly in anticyclonic circulation types, especially in winter, during the continental cold air advections from Eastern Europe and Asia, and also under a cloudless weather conditions in nighttime (strong radiation loss).

Maps of the mean daily temperature usually show a significant variability of the air temperature field and rather slight similarity of thermal field pattern, in comparison with climatologic, highly aggregated maps for the corresponding months or seasons. This reflects the greater role of dynamic, circulation factors influencing the daily temperature field in comparison to the impact factors of more static geo-environmental features such as altitude or distance from the sea (Ustrnul and Czekierda 2009).

3. Data

3.1. Air Temperature Data

Air temperature measurements for this study were gathered mostly in the meteorological network operated by the Institute of Meteorology and Water Management (IMGW) in Poland. Data were available from 197 stations and were next complemented by data from 53 meteorological stations located in the closest neighbourhood of Poland (up to about 100 km from the country boundaries; Fig. 1). The inclusion of these additional stations was done to avoid extrapolation for grids located outside the convex hull of Polish stations. Second, this additional set has increased the number of stations located in the higher elevated area, which allows for a more precise modelling of relation between temperature and altitude—one of the most significant environmental correlations of air temperature. And third, the enlarged set of stations, allowed improving the relevance of statistical inference accordingly to the increased number of observations in statistical models and, as a result, enhanced the quality of air temperature estimation.

Meteorological stations used in the study are rather evenly distributed over the study area. The spatial distribution is dispersed, according to the nearest neighbour analysis (Mitchell 2005), although there are clear regional differences in network density. 83 % of the study area is located no further than 30 km from the nearest station, and less than 0.3 % of the area is located further than 50 km, mainly in the central and north-eastern parts of the country. On average, for the whole country, station density is about 6.3 stations/10,000 km^2, with the highest density, reaching 16 stations/10,000 km^2 in the western part of the Polish Carpathians (Fig. 1). The representativeness of the stations in relation to one of the most dominant climate factors, which is the altitude, is of particular importance for the quality of modelling the air temperature using multivariate spatialization techniques. In the case of the Polish meteorological network, low-elevated areas are characterized by relatively large number of stations, mainly due to numerous stations located close to the seashore. Areas located up to 50 m a.s.l., covering 6.4 % of the country are represented by ca 9 % of the stations. Only 33 % of the stations are located in the zone of 100–200 m a.s.l., which covers 49.7 % of the area of Poland, so this zone is slightly underrepresented. Above 200 m a.s.l., there is some over-representation of the number of stations in relation to altitude. The areas elevated above 500 m a.s.l. ($\sim$3.5 % of the country area) are covered by 13.2 % of stations. However, a problem is that stations are not evenly distributed over the highest altitude zones. For example, there are no Polish stations between 900 m (Bukowina Tatrzańska) and 1520 m a.s.l. (Hala Gąsienicowa). The extension of a dataset by foreign stations allowed for getting additional 4 stations located in the zone above 900 m a.s.l.: Lysa Hora, Štrbské Pleso, Chopok and Lomnický Štít (Fig. 1). The last two are situated higher than the highest Polish station at Kasprowy Wierch (1991 m a.s.l.).

Data from the Polish stations were provided by the Institute of Meteorology and Water Management. Daily temperatures for Polish and foreign stations were calculated using the same formula: (T06 + T18 + TMAX + TMIN)/4. The measurements for the foreign stations were taken from the Global Summary of the Day, and the Deutscher Wetterdienst (http://www.dwd.de) databases. Sixty-nine cases on five levels of data aggregation from the decade 1996–2005 were prepared for spatial interpolation:

- Level 1: 1996–2005 annual mean air temperature (one case),
- Level 2: annual means of the warmest (2000) and coldest (1996) years of the decade 1996–2005 (two cases),
- Level 3: 1996–2005 monthly mean air temperatures (12 cases),
- Level 4: monthly means of the warmest and coldest months of the 1996–2005 decade (24 cases),
- Level 5: daily means, selected to represent varying synoptic conditions, seasons and ranges of variability (30 cases).

The study encompasses all cases of annual and monthly air temperature means from the period 1996–2005 (levels 1 and 3). The selection of cases of individual years and months (levels 2 and 4) was performed based on the highest and lowest areal air temperature mean, calculated with the measurements from the Polish meteorological stations. This made it possible to select the coolest and the warmest year (month) in the analysed decade. Daily cases (level 5) were selected considering thermal and circulation criteria. Cases of high and low spatial variability of air temperature, occurring at different temperature ranges and in different seasons, were included. In addition, selected cases covered a variety of situations in terms of synoptic circulation types, air masses advections and the occurrence of atmospheric fronts. This allowed for spatial modelling of cases characterized by diversified overall level of environmental correlations, as well as by different proportions of deterministic impacts of particular environmental features.

All the cases are summarized in this work. Two cases of air temperature were selected for a detailed analysis. These were the level 1—1996–2005 annual mean (TY) air temperature and one case from the level 5—daily mean of 8 Jan 2003 (TD). The first was characterized by a very high degree of the variance explained by regression model, and the latter was characterized by the lowest determination coefficient of all cases.

3.2. Environmental Variables

Taking into account the causes of climate determining air temperature distribution in Poland (Sect. 2) and former attempts to multidimensional spatial interpolation of air temperature (Sect. 1), a set of potential environmental predictors for the study was prepared, including (Fig. 2):

- Variables describing general spatial tendency (e.g. continentality of climate): coordinates (*X*, *Y*) and the sea distance index (SDI),
- Digital elevation model (DEM) and its derivatives: slope inclination (SLP), concavity/convexity index (CCI), foehn index (FI) and potential total insolation (IT),
- Land use/land cover derivatives: percentage share of natural (NS) and artificial (AS) surfaces in the vicinity of a given location and the normalized difference vegetation index (NDVI).

All variables were prepared as raster layers of 250 m resolution, projected to the Polish local coordinate system PUWG1992. *X* and *Y* coordinates of each cell's centre were assigned to the corresponding raster cells. Coordinate *X* was assumed to represent changes in longitude, reflecting the macro-scale impact of lands and oceans in central Europe, while coordinate *Y*—corresponding to the latitude and general solar energy distribution. Both variables, together or separately, may also express the impact of air masses advections and atmospheric circulation (Fig. 2a, b).

The influence of the Baltic Sea on air temperature is described by SDI. Former studies (Szymanowski

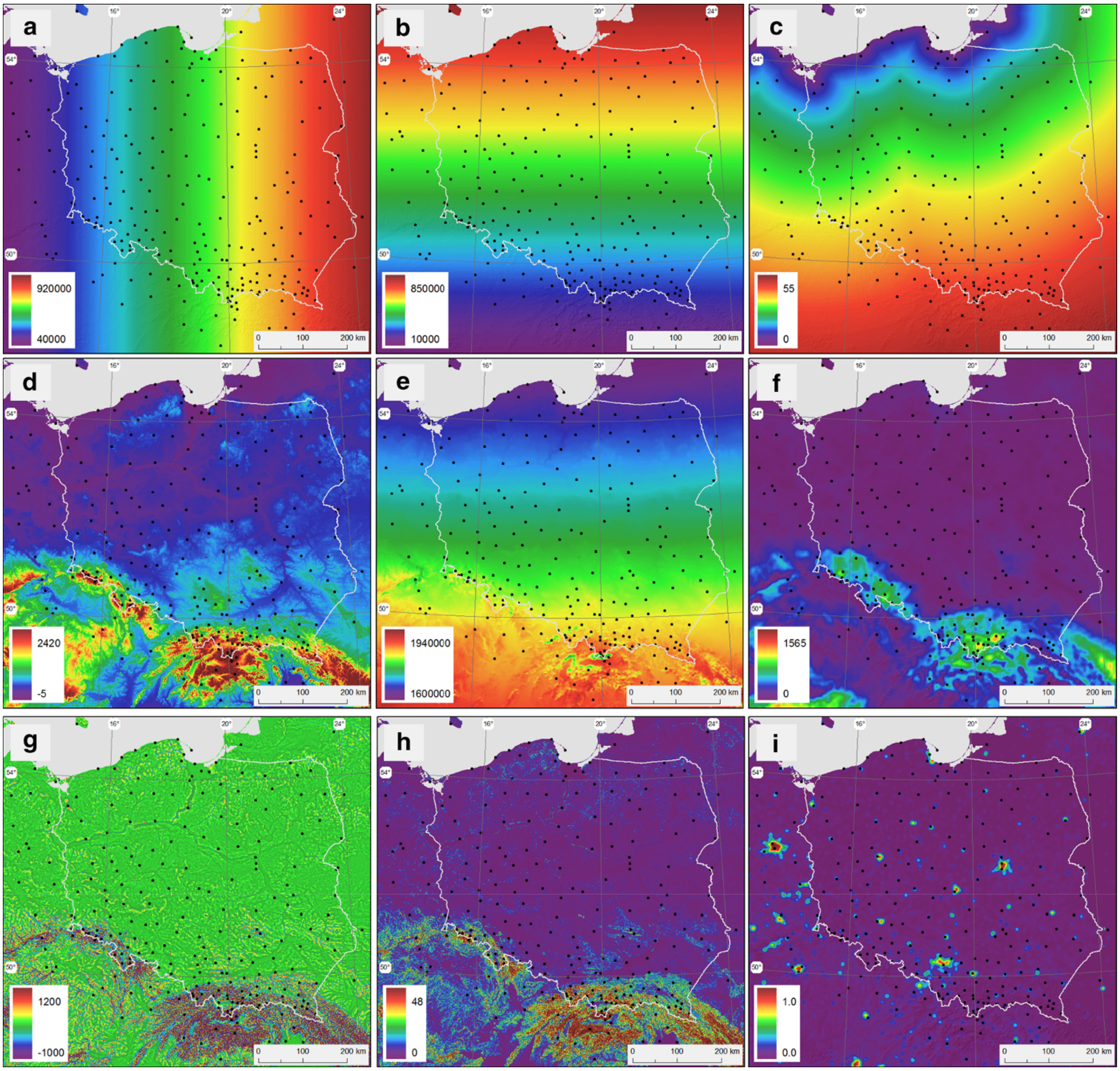

Figure 2
Sample layers of potential predictors of air temperature in Poland used in this study: **a** *X*, **b** *Y*, **c** SDI, **d** DEM, **e** IT, **f** FI, **g** CCI, **h** SLP, **i** AS (explanation of acronyms in the text)

et al. 2012, 2013) showed that this impact decreases non-linearly with distance; therefore, the index was constructed as the square root of the shortest Euclidean distance (expressed in number of 250 m raster cells) from the coastline (Fig. 2c).

Altitude (DEM) was taken from the SRTM-3 digital elevation model (http://www2.jpl.nasa.gov/srtm), which was projected to PUWG1992 and resampled to 250 m resolution (Fig. 2d). DEM was then used to calculate derivatives: IT, FI, CCI and SLP.

Potential insolation for a given period/day, IT, expressed spatial distribution of potential incoming solar energy (Fig. 2e). Insolation was calculated on the real, inclined surface by the r.sun model, implemented in GIS-GRASS software (GRASS Development Team 2011).

The thermal effect of the foehn wind is well-known in the forelands of various mountain ranges, which can also be found in Poland. So far, however, attempts to simulate the effect of foehn wind were limited to the variables based only on distance from the mountain barrier (Carrega 1995). Because it is not only the distance alone, but, first of all, the combination of distance and height difference that determines the temperature rise on the leeward side of the mountain, a new foehn index (FI) was introduced and tested in the interpolation of selected thermal parameters for the south-western Poland (Szymanowski *et al.* 2007). The index combines the distance to the mountain barrier with the maximum difference in elevation between the given raster cell and the highest raster in the foehn-favourable direction of advection (Fig. 2f).

The CCI, describing the cold air accumulation in concave landforms, was defined as the difference between the altitude in a given location and DEM averaged in a moving window (circular shape; radii: 1250, 2500 or 5000 m). CCI values close to zero mean that the area is flat, positive values indicate a convex landform, and negative—concave landform.

Local, land use/land cover impact on temperature was described by AS, NS and NDVI variables. The first two were calculated for the surrounding of each grid cell using the same radii of moving window filter as in the case of CCI. The percentage share was calculated using the CORINE Land Cover 2000 (2004) and, for the areas of Ukraine, Belarus and Russia, USGS Land Cover (2011) databases (Fig. 2i). Additionally, the vegetation index NDVI (Tucker 1979) was used to characterize local land cover features. The relationship between NDVI and air temperature is known and proven, both at the country (Kożuchowski and Żmudzka 2001) and local scales (Szymanowski and Kryza 2012). NDVI values were prepared based on MODIS and AVHRR data processed by Clark Labs, Clark University, USA (http://www.clarklabs.org/products/global-gis-image-processing-data.cfm). NDVI was used as a potential predictor of air temperature only for the cases of levels 4 and 5 of data aggregation (Fig. 2j).

4. Methods

Extensive set of statistical methods were used in this study, with the most important

- regression methods: MLR and GWR, as well as their extensions to the regression-kriging form: MLRK and GWRK were used to spatialize the air temperature,
- stepwise regression (SWR) was applied to select sets of significant auxiliary variables, to specify and calibrate regression models and to evaluate a goodness-of-fit of these models in each step of SWR forward selection,
- cross-validation (CV) results were applied to evaluate the quality of interpolation and to compare spatial models, based mostly on CV mean absolute error (MAE) as a main diagnostic measure used together with MAE error bars as the method to assess the statistical significance of differences between models.

4.1. Spatial Interpolation Methods

The basic assumption of this study is that the air temperature can be treated as a regionalized variable (Matheron 1963), which suggests that spatial variation can be modelled as the sum of deterministic and stochastic components. Such a model was termed the ‘universal model of spatial variation’ (Matheron 1969) and its mathematical representation is the regression-kriging (residual kriging; RK) model, which is the implementation of the best linear unbiased predictor (BLUP) for spatial data (Hengl 2007). Until recently, residual kriging for spatial interpolation of the air temperature was used in the conventional way: the deterministic part was modelled using MLR, and then regression residuals were spatialized using the kriging technique (e.g. Holdaway 1996; Courault and Monestiez 1999; Brown and Comrie 2002; Szymanowski and Kryza 2009). However, recent studies on spatial variation of the air temperature (Szymanowski and Kryza 2012; Szymanowski *et al.* 2012, 2013) draw attention to two issues:

1. The spatial process determining the air temperature can be expected to be non-stationary. This was shown both for the local and regional scales, with the examples of the urban heat island in Wrocław (Szymanowski and Kryza 2011) and air temperature in Poland (Szymanowski *et al.* 2012, 2013). The non-stationary spatial process has different spatial correlation in different regions. In such a case, the local, dedicated for non-stationary conditions GWR model, is better fitted to the observations than global MLR (Fotheringham *et al.* 2002). Consequently, it is a prerequisite to use GWR instead of MLR to perform modelling of the deterministic part of air temperature spatial variation. Such solution was suggested and applied in the selection scheme of the optimal interpolation method by Szymanowski *et al.* (2012, 2013). The goodness-of-fit of the regression models and, indirectly, non-stationarity of the spatial process, can be assessed by various measures as, e.g. determination coefficient (R^2) or standard error of estimation (STE), which were used in the study.
2. The full applicability of the RK scheme may be limited in some cases. The reason is the lack of spatial autocorrelation of regression residuals. In the absence of autocorrelation, the variogram takes the form of a pure nugget effect, and hence, prediction at each point in the study area is equal to the average of the regression residuals, which, by the assumption, is in the MLR model equal to zero. In the GWR model, an unbiased estimate of the local coefficients is not possible because the bias results from inferring the outcome of a non-stationary process at given location from data collected at other locations. This means that the average regression residual is likely to be different but sufficiently close to zero (Fotheringham *et al.* 2002). Thus, when GWR residuals are not autocorrelated (pure nugget variogram), we are allowed to assume that the modification of the GWR prediction contributed by kriging of the GWR residuals is negligible in the RK model. Therefore, when a stochastic component can be omitted, the entire variation in the spatial model is explained deterministically only by either MLR or GWR. The decision on the existence of positive spatial autocorrelation was taken in the study based on the Moran's I statistics (Moran 1950), assuming its statistical significance at $p < 0.05$. In GWRK, similarly to the general RK scheme, the deterministic component is modelled using GWR and after that regression residuals are modelled with the kriging technique.

The spatialization models for predicting variable $\hat{z}$ in location s_0 can be mathematically expressed as MLR:

$$\hat{z}(s_0) = \sum_{k=0}^{p} \hat{\beta}_k q_k(s_0)$$

GWR:

$$\hat{z}(s_0) = \sum_{k=0}^{p} \hat{\beta}_k(s_0) q_k(s_0)$$

MLRK:

$$\hat{z}(s_0) = \sum_{k=0}^{p} \hat{\beta}_k q_k(s_0) + \sum_{i=1}^{n} \lambda_i e(s_i)$$

GWRK:

$$\hat{z}(s_0) = \sum_{k=0}^{p} \hat{\beta}_k(s_0) q_k(s_0) + \sum_{i=1}^{n} \lambda_i e(s_i),$$

where $\hat{\beta}_k$ are estimated deterministic model coefficients ($\hat{\beta}_0$—estimated intercept), q_k are explanatory variables, λ_i are kriging weights determined by the spatial dependence structure of the residual and $e(s_i)$ is the residual at location s_i.

All four types of models (or only two types if the regression residuals' autocorrelation was not statistically significant) were used to evaluate the impact of auxiliary variables on the quality of air temperature spatial interpolation.

4.2. *Stepwise Selection of Auxiliary Variables*

The basic question in the initial phase of the analysis was which variables from the entire set of potential predictors should be included in the model for a given case. Generally, it is probably the most subjective part of modelling and it is likely that each modeller may consider various determinant factors of the spatial process, prepare different sets of potential predictors, establish different criteria to include variables to the model, etc. Nevertheless, if the set of potential predictors is prepared, the selection of statistically significant auxiliary variables could be done in an objective way using, for example, a stepwise regression approach (Draper and Smith 1998). SWR is an automatic procedure for statistical model selection in cases where there are a large number of potential explanatory variables. The goal is to choose a small subset from the larger set so that the resulting regression model is simple, in the sense that it only includes the significant predictors. Here, the SWR forward selection based on partial F tests (with F to include >1.0, slightly less than F critical for 250 observations at $p = 0.05$) was applied in the initial phase of variable selection and model calibration. The partial F test performs fitting of two models: full and reduced, and assesses whether the improvement in model fit is too large to be ascribed to chance alone (Jamshidian *et al.* 2007). The model is accepted for final analysis based on two conditions: F test result (model is significant at $p < 0.05$) and statistical significance of all the predictors included, which is described by the t test (all the model parameters are significant at $p < 0.05$). The SWR technique starts with no variables in the model, tests the addition of each variable based on assumed criterion, adds the variable that improves the model the most, and then repeats this process until adding any of the omitted variables does not improve the model.

Stepwise regression forward selection is subject to various imperfections (e.g. Wilkinson and Dallal 1981; Hurvich and Tsai 1990); however, for this study it was found a good mechanism for tracking the quality of the interpolation model when entering step by step the significant explanatory variables. Despite the fact that properties of the selection scheme are known, the form of the regression model is still dependent on the set of potential predictors that can be prepared in different ways by different researchers. In such situations, the initial selection of explanatory variables can have a decisive influence on the final result of interpolation. Checking whether this claim is true is one of the primary objectives of this study. The best way to assess this would be a comparison of the results of interpolation performed, based on the models selected by the stepwise procedure from all possible subsets of the initial (full) set of predictors. However, taking into account 11 variables in the initial set of predictors (Sect. 3.2) would require analysing thousands of possible combinations for each of the 69 cases of air temperature, which was beyond the computational capabilities of this project. Instead, the evaluation of models in each step of the SWR (with additional criteria described below), based on the full initial set of predictors, was performed. For each air temperature case, the aim was to specify and calibrate the regression model including all the statistically significant variables indicated by stepwise selection. These kinds of models are referred to as the MP models in this paper, as they include the maximum (for each case) possible number of significant predictors (n). This purpose has been achieved by specification of the series of models that include a limited number of not more than $n - 1$, significant predictors (LP models). The comparison between MP and LP models in each step allows assessing the effect of introducing additional explanatory variables on the air temperature spatialization process.

Some additional criteria were also incorporated to complete each model specification. Multicollinearity was checked using the value inflation factor ($\mathrm{VIF} < 10$), statistical significance was assumed when $p < 0.05$ and the maximum number of variables in the model should not exceed seven with the number of observations $n = 250$ (Szymanowski *et al.* 2012, 2013). The same variables at each step were then used in MLR and GWR models. Given the irregular spatial distribution of meteorological stations, the GWR model was calibrated using adaptive kernels with bi-square weighting scheme. The size of the adaptive kernel, called a bandwidth, was defined as the number of data points used to calibrate the local linear regression function. Due to a known property of GWR, termed a ‘bias-variance trade-off’ (Fotheringham *et al.* 2002), the bandwidth size was chosen to be the smallest possible, but with respect to two limitations. First, the bandwidth size should be large enough to include at least 25 measuring sites to assure sufficient number of data for proper specification of the local regression model (using up to seven explanatory variables). Second, the sign of the regression coefficient should be in agreement with the assumed physical process to allow for the possibility of deterministic explanation of spatial process in each part of the study area (Szymanowski and Kryza 2012; Szymanowski *et al.* 2012). Once the Moran's I statistic confirmed significant spatial autocorrelation, the variogram of regression residuals was modelled automatically with the use of a spherical function (best fit) with a nugget effect included.

4.3. Validation of Model Errors

The model errors were evaluated using the leave-one-out cross-validation approach (CV). The mean absolute error (MAE) was applied as the basic diagnostic statistics of the model quality. MAE is considered as one of the most natural summary measures for the model performance (Willmott and Matsuura 1995) and it can also be used to determine statistical difference between models' performance (Szymanowski *et al.* this issue). This can be done by compering severability of MAE error bars. The model with the smallest MAE can be considered as performing best only if its MAE error bar does not overly the MAE error bar of any other model for the same case. The error bar was determined as MAE ± $\hat{\sigma}_{\mathrm{MAE}}$, where $\hat{\sigma}_{\mathrm{MAE}}$ was the error of MAE calculation. For the n-element set with standard deviation σ_{CV}, it can be calculated as (Kalarus *et al.* 2010):

$$\hat{\sigma}_{\mathrm{MAE}} = \frac{\sigma_{\mathrm{CV}}}{\sqrt{nc}}, \quad c = \frac{\pi}{\pi - 2}.$$

Cross-validation approach results allow for the assessment of the model quality with respect to the data measured in meteorological stations. The model performance in other locations was based on visual inspection of the maps, paying special attention to the artefacts and the incredible values of the modelled air temperature (Szymanowski *et al.* 2012). The maps of air temperature for the case analysis were prepared in two ways. The overall changes in air temperature for a given case, depending on the set of variables in the model and the type of interpolation model, were presented as classified (every 0.5°) colour ramp. These maps were complemented by spatial distribution of CV errors in data points shown using point symbols. To introduce the local effect and very detailed changes in the air temperature field caused by some explanatory variables, maps were drawn with the use of stretched colour scale.

5. Results and Discussion

5.1. Deterministic Component of Spatial Model

The frequency of occurrence of individual auxiliary variables in MP models for all 69 air temperature cases in Poland shows that each of the considered potential predictors (Sect. 3.2) is included in at least a few models (Fig. 3). Some of variables are introduced to almost all models, e.g. DEM (in 66 of 69 models) and X coordinate (65). Some are included very frequently: SDI (52), coordinate Y (40), SLP (34) and land use/land cover surfaces AS and NS (43 times in total). Variables AS and NS should be treated as complementary because they are strongly collinear and, accordingly to the assumptions (Sect. 4), only one of them is included in a model specified for a given case. Less often such variables as NDVI (24 out of 54 models—analysed only at levels 4 and 5), IT (21) and FI (17) are included in MP models. CCI is the least frequent (only six times) variable introduced into the regression models. This may be the consequence of the features of input air temperature dataset because meteorological stations are located in open, flat terrain, usually free from the local impact of relief.

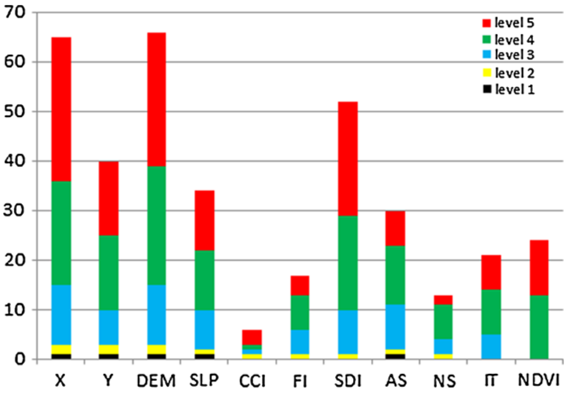

Figure 3
Number of MP models including individual explanatory variables for each level of data aggregation

Digital elevation model is most frequently introduced as the first variable to the regression model which means that, due to assumptions of SWR forward selection, it is most significantly correlated with air temperature, taking into account the *F* statistics. DEM is selected as the first in all the models at levels 1–3, and in 21 out of 24 models at level 4. However, it is included only in 12 out of 30 cases at level 5. This shows that the lower the levels of data aggregation, the less significant is the impact of terrain height and more significant are, e.g. synoptic factors. However, it is strongly case dependent and this statement cannot be generalized with the set of 30 cases presented here. In some level 5 cases, the air temperature can be strongly correlated with elevation, whereas in other cases the correlation may be relatively weak or even statistically insignificant. In situations where the DEM is not the first variable introduced to the MP model, it is usually substituted by coordinate *X*, which is selected as first in 3 of 24 models at level 4 and in 11 of 30 models at level 5. Only in 6 models, different variables are introduced as the most significant (all only at level 5): SDI—4 times, NDVI—2 times and IT—once. Both coordinates (*X*—18 times, *Y*—17 times) and DEM (12 times) are introduced most frequently as a second significant explanatory variable. The role (expressed in terms of statistical significance) of locally determined factors expressed by such variables as AS/NS, SLP or CCI is relatively low. Even if some of them are frequently introduced into the regression models, they are never added as the first and very rarely as the second most important variable (AS/NS—1 time, SLP—2 times, CCI—none).

Each MP model includes from 3 to 7 statistically significant explanatory variables. Most frequently, the models are specified based on six auxiliary variables (21 cases), and less frequently based on 4, 5 or 7 variables (15, 15 and 13 cases, respectively). The least frequent are models including only three additional variables (five cases). There is also no clear dependence of the number of predictors included in the model on the aggregation level, but 3- or 4-variable models are more typical of lower level of data aggregation (levels 4 and 5).

According to the assumptions, all MP models are statistically significant (in terms of the *F* test, detailed description in Sect. 4.2), even if they differ significantly in terms of goodness-of-fit. In individual cases, these models explain over 90 % (max. 96 %) of the air temperature variance at aggregation levels 1–3 but, in some cases, it falls to 70 % on level 4, and can be as low as 31 % for daily means cases (level 5). Generally, it can be stated that the higher the level of data aggregation, the higher the determination coefficients. The level of air temperature variance explained by the MP model is shown in Fig. 3—the value corresponding to the last step of the SWR procedure. The lower the level of data aggregation, the larger the observed variability of R^2. This suggests that for short-time averaged air temperature (e.g. daily means), some models can fit the data as well as for the long-term means, but there are also cases for which the overall fitting of the regression model is relatively poor ($R^2 < 0.6$; Fig. 4).

The next questions are, however, what the level of determination is when only the most significant variable is introduced to the model and how does the goodness-of-fit of the model change when adding subsequent variables. One-variable LP models are characterized by very different values of determination coefficients depending also on the level of data aggregation (Fig. 4). The R^2 of such models at level 1 is 0.82; at levels 2–4, they change in the range of 0.78–0.81 (level 2), 0.61–0.86 (level 3) and 0.31–0.92 (level 4). At level 5, there is one case for which the one-variable model explains only about 3 % of the air temperature variance. This is the case of 8 Jan 2003

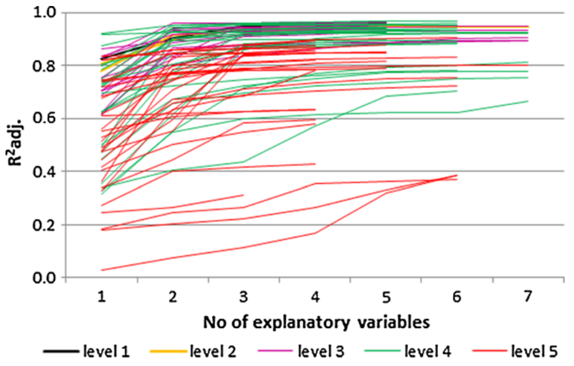

Figure 4
Determination coefficients depending on the level of the air temperature aggregation and the number of explanatory variables in the SWR model

that will be analysed in detail below. However, it is very surprising that the model with such a low determination coefficient meets the criterion of statistical significance (in terms of the F test, detailed description in Sect. 4.2). Nevertheless, the lower the level of data aggregation, the more one-variable models explain smaller amount of variance, even if well-explaining one-variable models can be found at each level of aggregation as well. At levels 1–3, all one-variable models explain >60 % of air temperature variance, while at levels 4 and 5, it is only 16 out of 24 and 10 out of 30, respectively (Fig. 4). At level 4, lower values of the determination coefficients are observed for the winter months, which may indicate a declining role of environmental factors with respect to synoptic conditions that are not directly included in the regression model. This is also the case at level 5, where atmospheric circulation with passing fronts and air masses advections deteriorate the statistical relation of air temperature with static environmental factors represented by the set of potential predictors prepared for this study.

The most significant changes in the determination coefficient are observed mostly when adding second and third variables to the model. The second variable in the model increases the explained variance by more than 10 %, mostly at lower aggregated levels (3–5). This happens in 8 out of 12 models at level 3, 17 out of 24 models at level 4 and 16 out of 30 models at level 5. The third variable added to the model rarely increases the variance explained by more than 10 %. This is the case in 4 out of 24 models at level 4 and 6 out of 30 at level 5 (Fig. 4).

In some cases, the introduction of subsequent variables to the model does not make significant changes in the coefficient of determination in comparison to the one-variable model. In such cases, the curves of the determination coefficient are flattened and the LP and MP models do not differ significantly. This can be observed not only in cases when the first auxiliary variable explains 80 % or more of air temperature variance, but also in cases in which the determination coefficient of one-variable model is quite low (Fig. 4).

As it was indicated in earlier studies (Szymanowski *et al.* 2012, 2013), in each of the analysed cases for Poland, the local GWR model, with the same explanatory variables, provides a better fit to the data compared to the MLR. While comparing the MP models, GWR is characterized by the same or greater determination coefficients (up to 15 % of variance explained) and lower standard errors of estimation, residual sums of squares and Akaike Information Criterion in comparison to MLR (Szymanowski *et al.* 2013). This means that the process can be considered as non-stationary, and the change of the global to local model with the same explanatory variable leads to an increase in the explained variance.

5.2. Deterministic-Stochastic Interpolation—a Case Study

Due to significant computational load, GWR models as well as all RK models are not analysed in this study for all 69 cases in each step of SWR, as it would again require calibrating and validating more than a thousand additional models. Here, two cases representing different levels of air temperature aggregation: level 1—decadal annual mean (TY) and level 5—daily mean on 8 Jan 2003 (TD) are analysed in details, comparing all four types of spatialization algorithms for all LP and MP models. These two cases are characterized also by one of the highest (TY) and lowest (TD) determination coefficients independently on the subset of explanatory variables included in the regression model.

The air temperature in the TY case is strongly determined by static environmental explanatory variables (Table 1). The most significant variable is elevation and it explains 83 % of the variance while using the MLR model and even 96 % using the GWR approach. Other statistically significant variables are coordinates, artificial surfaces and slope, and they increase the determination coefficient to 0.95 for MLR and 0.97 for GWR. A significant change of R^2 and decrease of standard error (STE) are especially pronounced for the first three LP-MLR models. In the LP-GWR approach, introducing additional variables does not produce any significant change in neither R^2 nor STE (Table 1).

Additional analysis of regression residuals' spatial autocorrelation shows that residuals are not autocorrelated for all 3-, 4- and 5-variable MLR and GWR

Table 1

Selected statistics of regression models and autocorrelation of regression residuals for 1996–2005 annual mean air temperature in Poland (TY)

Regression model					Spatial autocorrelation of residuals	
No of variables	Explanatory variables (in the order of stepwise selection)	Model	Determination coefficient (R^2)	Standard error of estimation (STE)	Moran's I statistics $E(I) = -0.004$	p value
1	DEM	MLR	0.83	0.67	0.597	0.000
		GWR	0.96	0.33	0.222	0.000
2	DEM, Y	MLR	0.90	0.50	0.494	0.000
		GWR	0.96	0.33	0.135	0.000
3	DEM, Y, X	MLR	0.95	0.36	0.045[a]	0.079
		GWR	0.96	0.32	−0.025[a]	0.456
4	DEM, Y, X, AS	MLR	0.95	0.34	0.008[a]	0.666
		GWR	0.96	0.31	−0.048[a]	0.116
5	DEM, Y, X, AS, SLP	MLR	0.96	0.33	0.028[a]	0.245
		GWR	0.97	0.28	−0.029[a]	0.361

[a] No spatial autocorrelation (random distribution of residuals)

models. This means that regression and regression-kriging models are considered as identical in these cases (Table 1). Changes in CV MAE are analogous to changes in the goodness-of-fit for both regression models. The MAE decreases significantly for the first three LP models, and the decrease is larger for the MLR and smaller for the GWR (Fig. 5). The extension of the spatial model to the RK form produces a significant decrease in MAE for both MLRK and GWRK models, starting already from the one-variable model. It can be summarized that for 1- and 2-variable models, GWR performs significantly better than the MLR, both RK models perform significantly better than the corresponding regression models, and that MLRK and GWRK perform similarly. Adding the third (X) and next (AS, SLP) variables does not improve the MAE significantly, as the error bars overlap for MLR and GWR models and their extensions by residual kriging (Fig. 5).

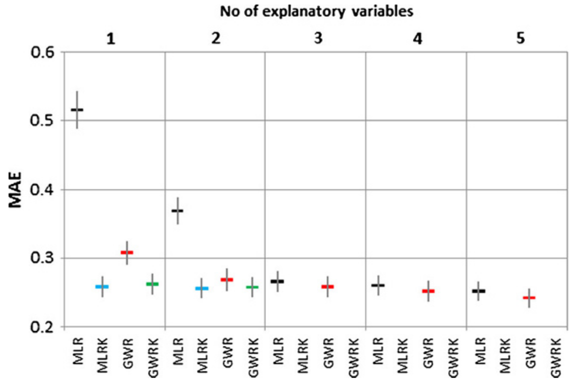

Figure 5
Cross-validation mean absolute errors (MAE) together with *error bars* depending on model type and number of explanatory variables included in the model for the 1996–2005 annual mean air temperature in Poland (TY)

Tendencies discussed above are also seen in the maps of air temperature and CV errors distribution (Figs. 6, 7, 8, 9, 10). The most significant changes are observed for maps prepared using 1-, 2- and 3-variable MLR models. The least accurate, in terms of CV errors, is the map prepared using only elevation as predictor in a global regression approach (Fig. 6a). Distinct spatial pattern in CV error is observed showing the tendencies to overestimate the air temperature over NE Poland and to underestimate the air temperature over SW Poland. Similar features are noticed on the corresponding GWR map (Fig. 6b), but the CV errors are smaller. Visually, both MLR and GWR regression-kriging maps are very similar, starting already from the one-variable models. Introduction of additional explanatory variables does not change the modelled air temperature field, but involve local adjustments (Figs. 6, 7, 8, 9,

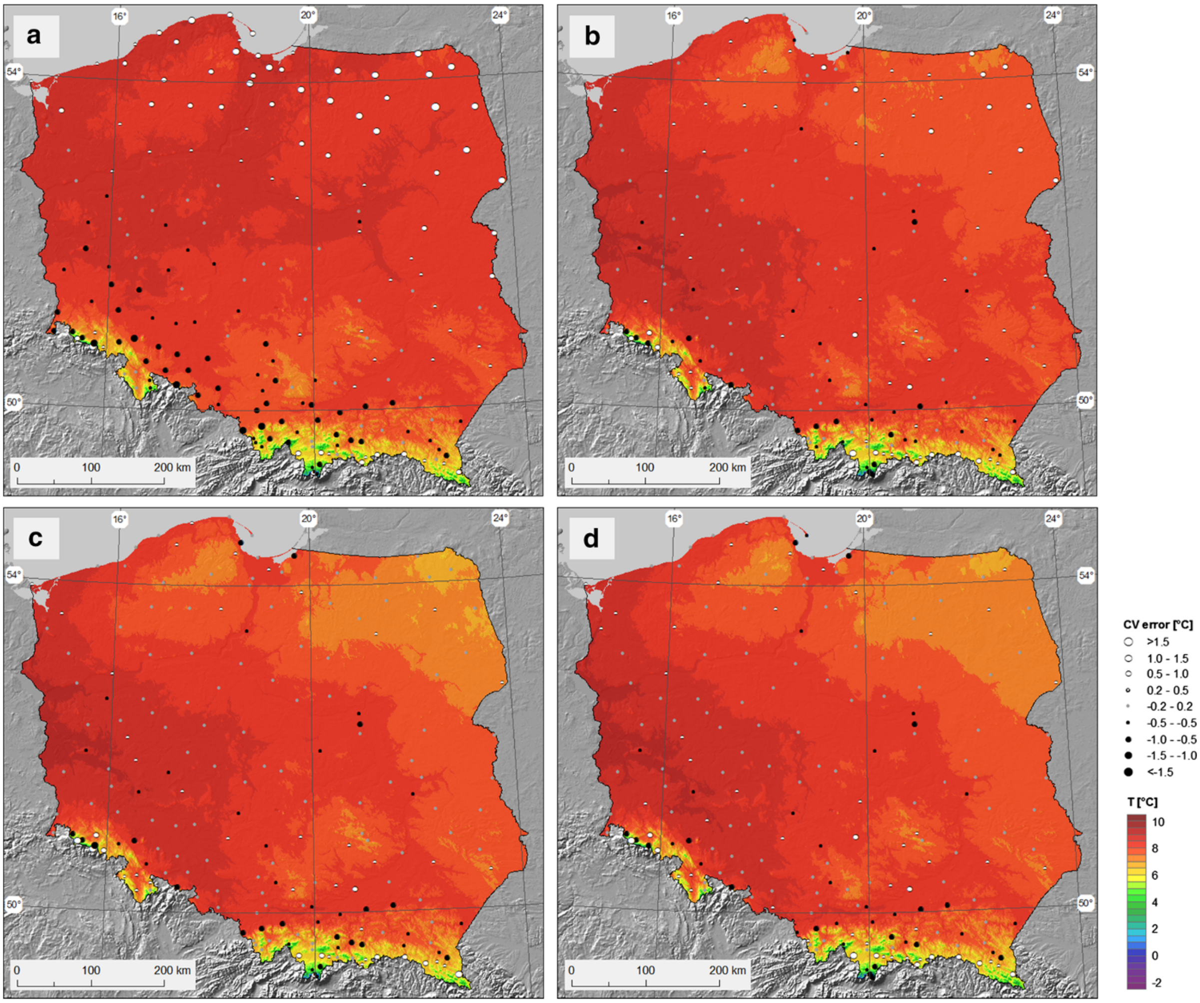

Figure 6
1996–2005 annual mean air temperature in Poland (TY) mapped using **a** MLR, **b** GWR, **c** MLRK and **d** GWRK algorithms with the use of DEM as the only explanatory variable in the regression model

10). This issue will be discussed in details later in this section.

The TD case differs significantly from TY. First of all, globally the air temperature is only determined to a small extent by static environmental factors, described by explanatory variables. The MP-MLR model, with six predictors included, explains only 38 % of the observed variance (Table 2). The spatial process is significantly non-stationary; therefore, the MP-GWR model is much better fitted to observation than MLR, with 67 % of the variance explained. The LP-GWR with four predictors included explains 71 % of the variance and its STE is significantly lower than STE of the corresponding MP model (Table 2).

Regression residuals are autocorrelated for all the global and local models for the TD case, and all the models can be extended to the deterministic-stochastic form. Low determination causes the stochastic component to play a dominating role in the regression-kriging algorithm, and significantly affects the modelled air temperature field (Fig. 11).

It is surprising that the first variable introduced to the model by stepwise procedure is NDVI, of which the correlation with air temperature in this winter case is rather ambiguous. This time most of the

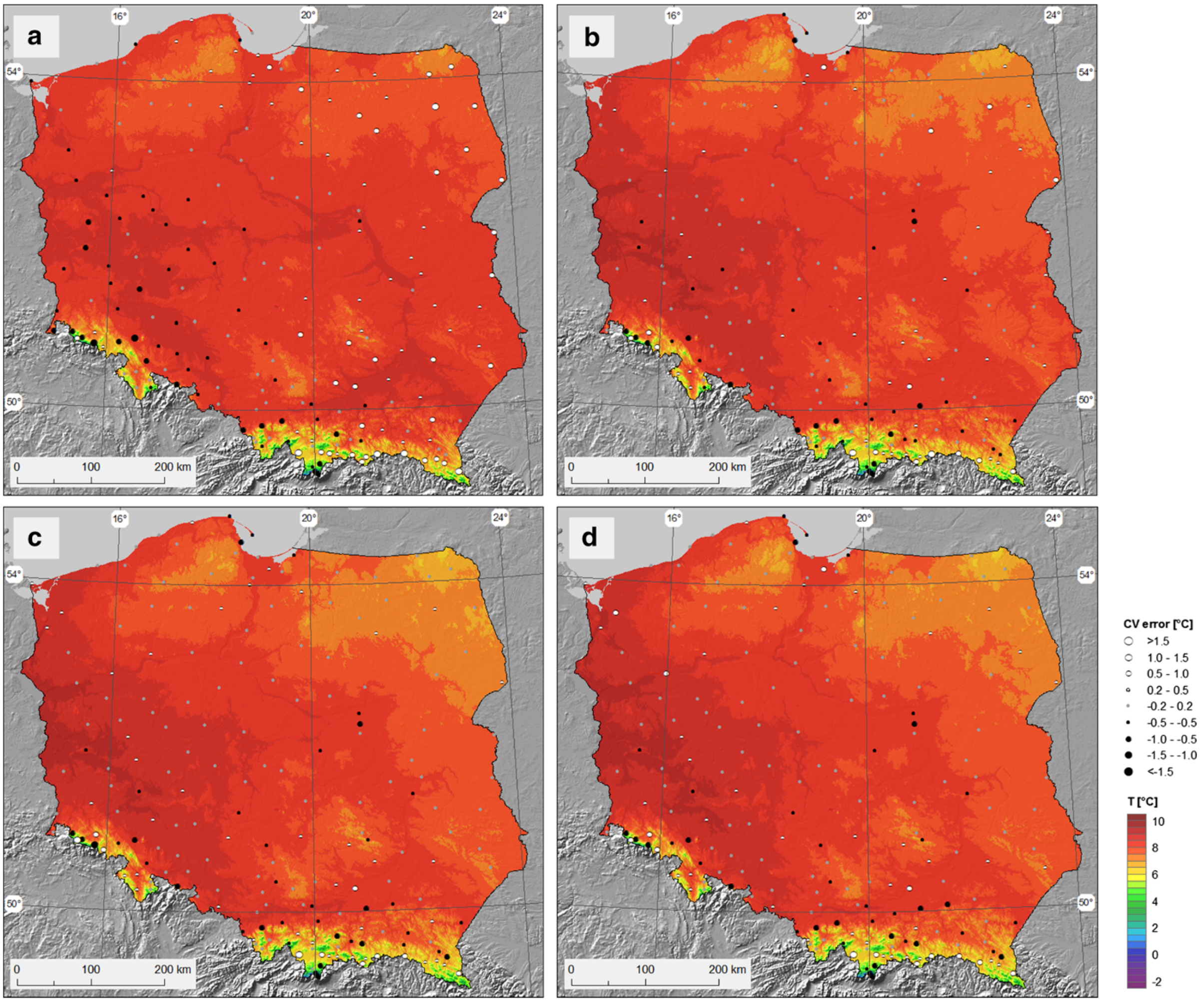

Figure 7

1996–2005 annual mean air temperature in Poland (TY) mapped using **a** MLR, **b** GWR, **c** MLRK and **d** GWRK algorithms with the use of DEM and *Y* as the explanatory variables in the regression model

territory of Poland was covered by snow that resulted in very small differences in NDVI values between vegetated and non-vegetated areas. There is probably no clear physical explanation of air temperature—NDVI dependence in this case. The relation was detected "by chance", and even though it is statistically significant, NDVI explains only 2 % of air temperature variance in the MLR model (Table 2). The air temperature field determined by NDVI is very "rough" (Fig. 12). The changes in the CV MAE show that the introduction of second (*X*) and third (DEM) variables does not improve the quality of spatial interpolation (Fig. 11). What is more, in this case the temperature is also very slightly determined by elevation. The last three variables (IT, SDI, *Y*) improve the interpolation done by the MLR model and, to a smaller extent, by GWR (Fig. 11). More interesting are the changes in quality of both RK models while introducing subsequent auxiliary variables. For the predictors' subsets, GWRK performs better than MLRK, but not significantly better. Both MP-RK models perform best; however, they do not differ significantly (according to MAE error bars) from the results achieved by the corresponding one-variable LP models (Fig. 11). As the geostatistical component brings large information on modelled air

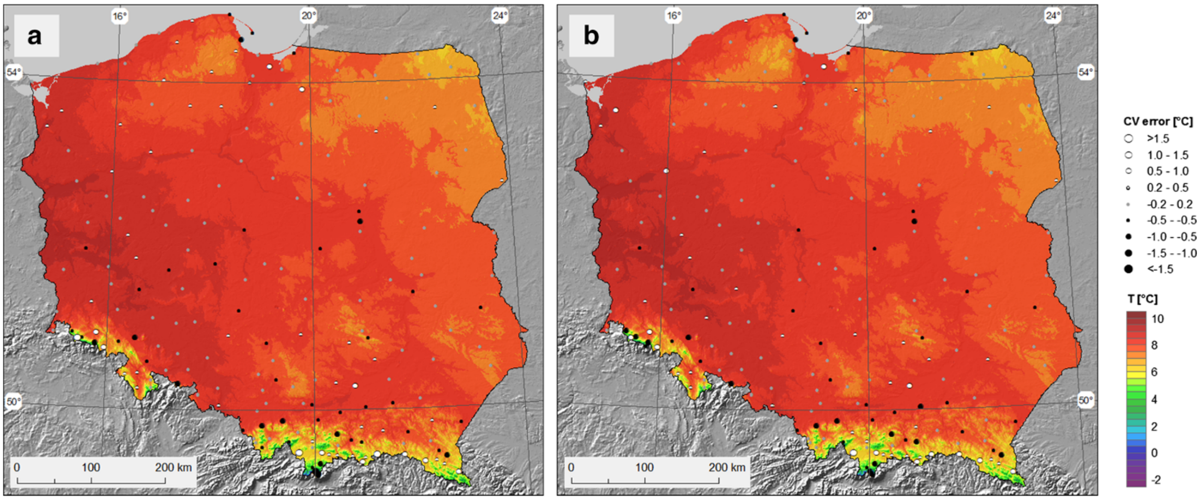

Figure 8
1996–2005 annual mean air temperature in Poland (TY) mapped using **a** MLR and **b** GWR algorithms with the use of DEM, *Y* and *X* as the explanatory variables in the regression model

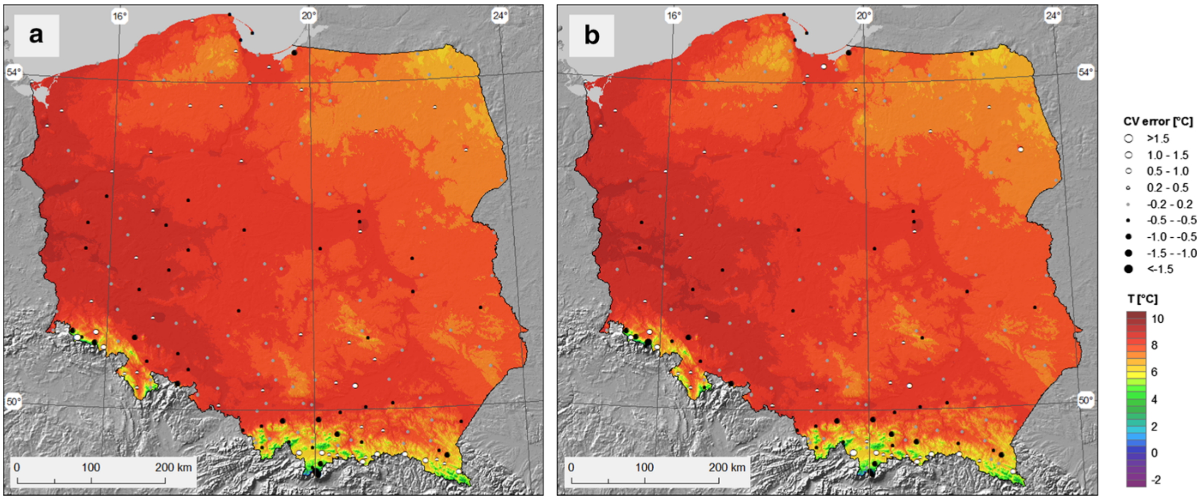

Figure 9
1996–2005 annual mean air temperature in Poland (TY) mapped using **a** MLR and **b** GWR algorithms with the use of DEM, *Y*, *X* and AS as the explanatory variables in the regression model

temperature in the TD case, the maps prepared by both regression models differ significantly from those done using RK algorithms (Figs. 12, 13). Some interesting features of air temperature distribution are different to the to "expected" characteristics of averaged field (as for examples in the TY case). Due to the cold eastern air mass advection, a belt of low temperatures in central Poland is noticeable. Apart from that, a zone of relatively high temperature, caused by the impact of the Baltic Sea, is observed along the coast. Quite interesting and unexpected is also the area of high temperature in the part of mountains in SE Poland (the Bieszczady Mts.), which might be explained by the air mass subsidence in anticyclonic pressure system (Fig. 13). Except for the warming influence of the sea, the remaining features

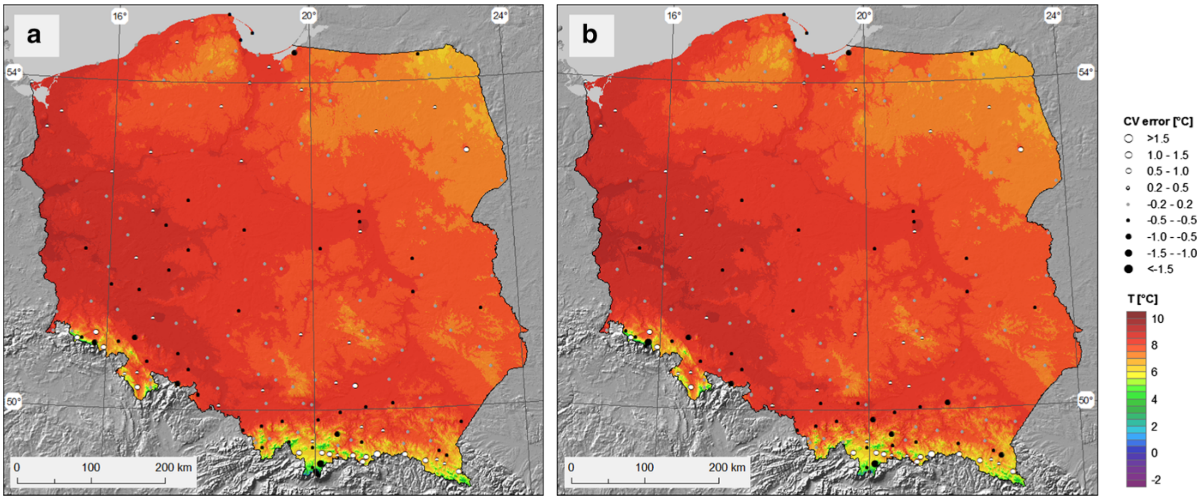

Figure 10
1996–2005 annual mean air temperature in Poland (TY) mapped using **a** MLR and **b** GWR algorithms with the use of DEM, Y, X, AS and SLP as the explanatory variables in the regression model

Table 2

Selected statistics of regression models and autocorrelation of regression residuals for the air temperature on 8 Jan 2003 in Poland (TD)

Regression model					Spatial autocorrelation of residuals	
No of variables	Variables (in the order of stepwise selection)	Model	Determination coefficient (R^2)	Standard error of estimation (STE)	Moran's I statistics $E(I) = -0.004$	p value
1	NDVI	MLR	0.02	3.07	0.606	0.000
		GWR	0.42	2.35	0.592	0.000
2	NDVI, X	MLR	0.07	2.99	0.570	0.000
		GWR	0.40	2.41	0.553	0.000
3	NDVI, X, DEM	MLR	0.11	2.93	0.595	0.000
		GWR	0.51	2.17	0.571	0.000
4	NDVI, X, DEM, IT	MLR	0.16	2.84	0.563	0.000
		GWR	0.71	1.68	0.504	0.000
5	NDVI, X, DEM, IT, SDI	MLR	0.32	2.56	0.451	0.000
		GWR	0.58	2.02	0.434	0.000
6	NDVI, X, DEM, IT, SDI, Y	MLR	0.38	2.44	0.495	0.000
		GWR	0.67	1.80	0.474	0.000

of dynamic/synoptic origin are not explained deterministically and are modelled by the geostatistical component of the RK model.

5.3. *The Signal of Explanatory Variables in Air Temperature Maps—a Case Study*

Concerning the large added value introduced by interpolation of regression residuals in RK algorithms, one could conclude that the large variance explained by the deterministic component is not crucial for the quality of interpolation. If the 3 or 4 most significant explanatory variables are included in the regression model, the remaining variance is well explained by the stochastic component of the RK model. It was shown that introducing additional auxiliary variables does not necessarily lead to the improvement of the CV MAE. However, in some

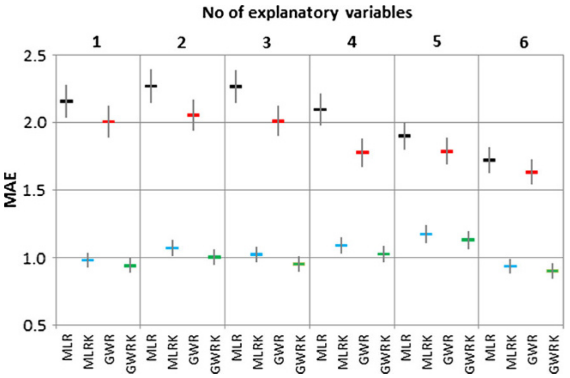

Figure 11
Cross-validation mean absolute errors (MAE) together with *error bars* depending on the model type and number of explanatory variables included in the model for air temperature on 8 Jan 2003 in Poland (TD)

cases, additional explanatory variables may significantly change the spatial distribution of the CV errors because of the reduction of regional/local tendencies leading to over or under-estimation. This is of large importance for the final distribution of air temperature, but it is missed if only the CV MAE is analysed. More importantly, the additional variables may lead to formation of effects in the modelled field that are "imprinted" by these variables, like the effects of urban heat island or warm slopes. Such effects, even if statistically justified, may also lead to undesired artefacts in the maps. This problem will be discussed based on TY case again, but this time the attention is put on not only to the statistical evaluation of the model, which significance has been confirmed above, but also on the global (Poland) and local (surrounding of the city of Cracow) changes in the modelled air temperature field induced by introduction of additional, to DEM, *Y* and *X*, explanatory variables.

According to the changes in MAE, the 3-variable TY regression model (including DEM, *Y* and *X*) that explains 95 % (MLR) or 96 % (GWR) of variance is not significantly different from the 4- and 5-variable models (Fig. 5). In both cases, the regression residuals are not autocorrelated and the stochastic components of the RK models can be omitted (Sect. 4.1). Therefore, the question is whether it makes sense to introduce additional variables and if so, what changes in modelled air temperature field will be observed? This will be considered starting from the 3-variable model, where temperature is determined by elevation and both coordinates (Fig. 14a). In the next two steps, AS and SLP will be added. It will show how these variables influence the spatial pattern of the modelled air temperature, with no statistically significant effects on statistical model performance.

The incorporation of AS, as the fourth explanatory variable, increases the modelled air temperature over the urban areas (Fig. 14b). This warming effect might be considered as realistic, both when it comes to the location and magnitude of change, which was confirmed with measurements of the urban heat island for Wrocław (SZYMANOWSKI and KRYZA 2012). The incorporation of the SLP variable leads to lower MAE but the change is not statistically significant (Fig. 5). However, SLP results in noticeable local changes in the modelled air temperature field. Steep slopes are now relatively warmer, regardless to the slope aspect, comparing to surrounding flat areas (Fig. 14c). This does not look realistic, even if there are no measurements to verify this effect quantitatively. It is very likely that the temperature over most of steep slopes, especially in the highest parts of the highest mountain ranges (the Tatra Mts.), will be significantly overestimated. This effect is caused in fact by the extrapolation process that "exports" the relation between temperature and inclination to the slopes inclined more than the range of SLP observed for available meteorological stations. Meteorological stations are located mostly on flat terrains—248 of 250 stations in this study are characterized by slope inclination less than 10°, and the most inclined station has inclination of about 15°. The regression model is linear, so the relation estimated for the 0–15° range is then extrapolated for the slopes inclined by >15° with the same assumption of linearity, which is barely realistic. The only solution would be to fit non-linear function; however, the lack of stations located on steep slopes prevents to confirm any considered theoretical model. The conclusion is that in this case (given set of meteorological stations for Poland), the SLP should be probably removed from the set of potential predictors, because its introduction to linear regression models may lead to unrealistic results, seen as artefacts in the air temperature maps. The SLP should be excluded even if it is so frequently

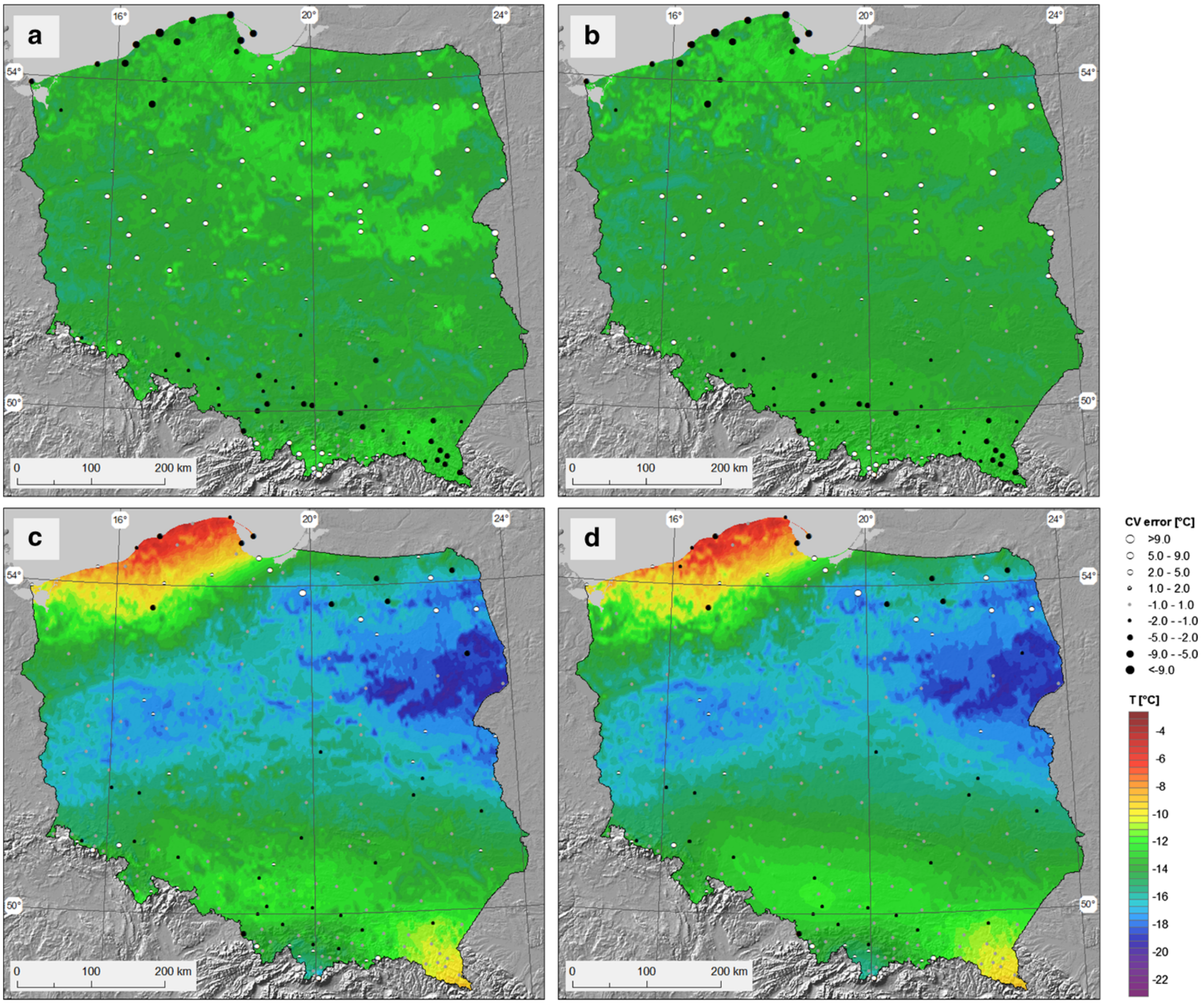

Figure 12
Air temperature on 8 Jan 2003 in Poland (TD) mapped using **a** MLR, **b** GWR, **c** MLRK and **d** GWRK algorithms with the use of NDVI as the only explanatory variable in the regression model

introduced to the regression models by stepwise selection (Fig. 3).

6. *Summary and Conclusions*

Taking into account the results of analysis carried out on 69 cases of air temperature in Poland, aggregated on five different levels (from long-term annual mean to daily means), the following main conclusions can be formulated:

1. The environmental factors, most significantly determining spatial distribution of air temperature in Poland, are elevation, geographical location and the distance from the sea, expressed in this study by variables: DEM, *X*, *Y* and SDI, respectively. The leading role is played by DEM and *X* (corresponding to longitude), which were introduced to almost all MP regression models. Using the stepwise method, these factors were usually introduced as the first (mainly DEM) or second most significant explanatory variable. DEM and *X* were most frequently followed in the model structure by SDI and *Y* (corresponding to latitude). The role of regional [e.g. foehn impact (FI)] and local—land use and relief factors (e.g. AS/NS,

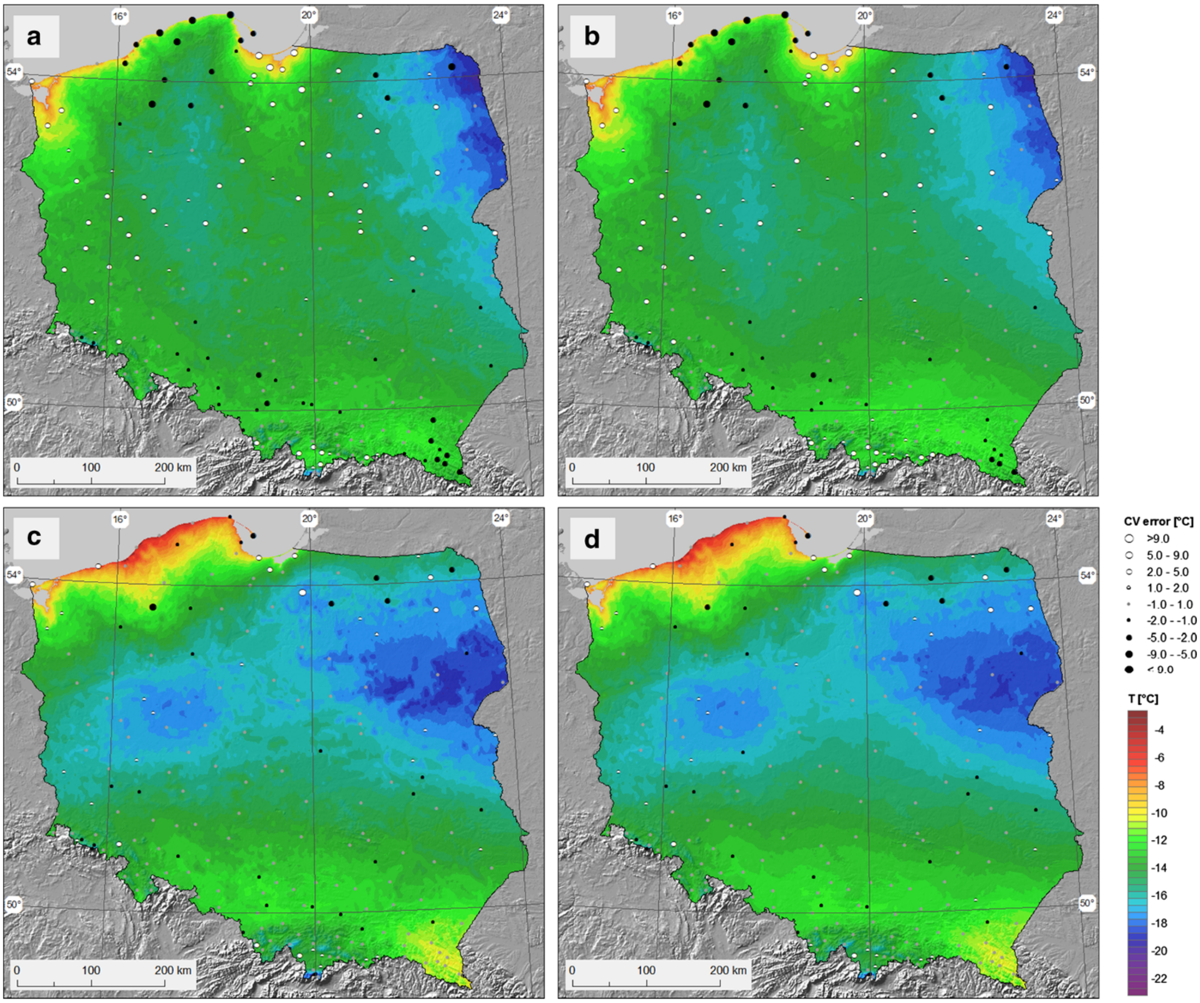

Figure 13
Air temperature on 8 Jan 2003 in Poland (TD) mapped using **a** MLR, **b** GWR, **c** MLRK and **d** GWRK algorithms with the use of NDVI, *X*, DEM, IT, SDI and *Y* as the explanatory variables in the regression model

NDVI, SLP, CCI) should be considered as complementary, and, as was shown for SLP, these variables should be very carefully introduced to the regression models. Even if some of them were very often introduced into the regression models (e.g. AS/NS), they have never been added as the first and very rarely as the second variable.

2. The fully specified MP models included from 3 to 7 explanatory variables. In individual cases, these models explained over 90 % (maximum 96 %) of the air temperature variance, but only at data aggregation levels 1–3. In some cases, the explained variance was as low as 70 % at level 4, and dropped to 31 % at aggregation level 5. Generally, it can be stated that the higher the level of data aggregation, the higher determination coefficients are observed.

Figure 14 ▶
1996–2005 annual mean air temperature in Poland (TY) mapped using GWRK algorithm with the use of **a** DEM, *Y* and *X*, **b** DEM, *Y*, *X* and AS and **c** DEM, *Y*, *X*, AS and SLP as the explanatory variables in the regression model

3. The first variable introduced to the model, accordingly to stepwise selection's assumptions, usually explained the majority of the air

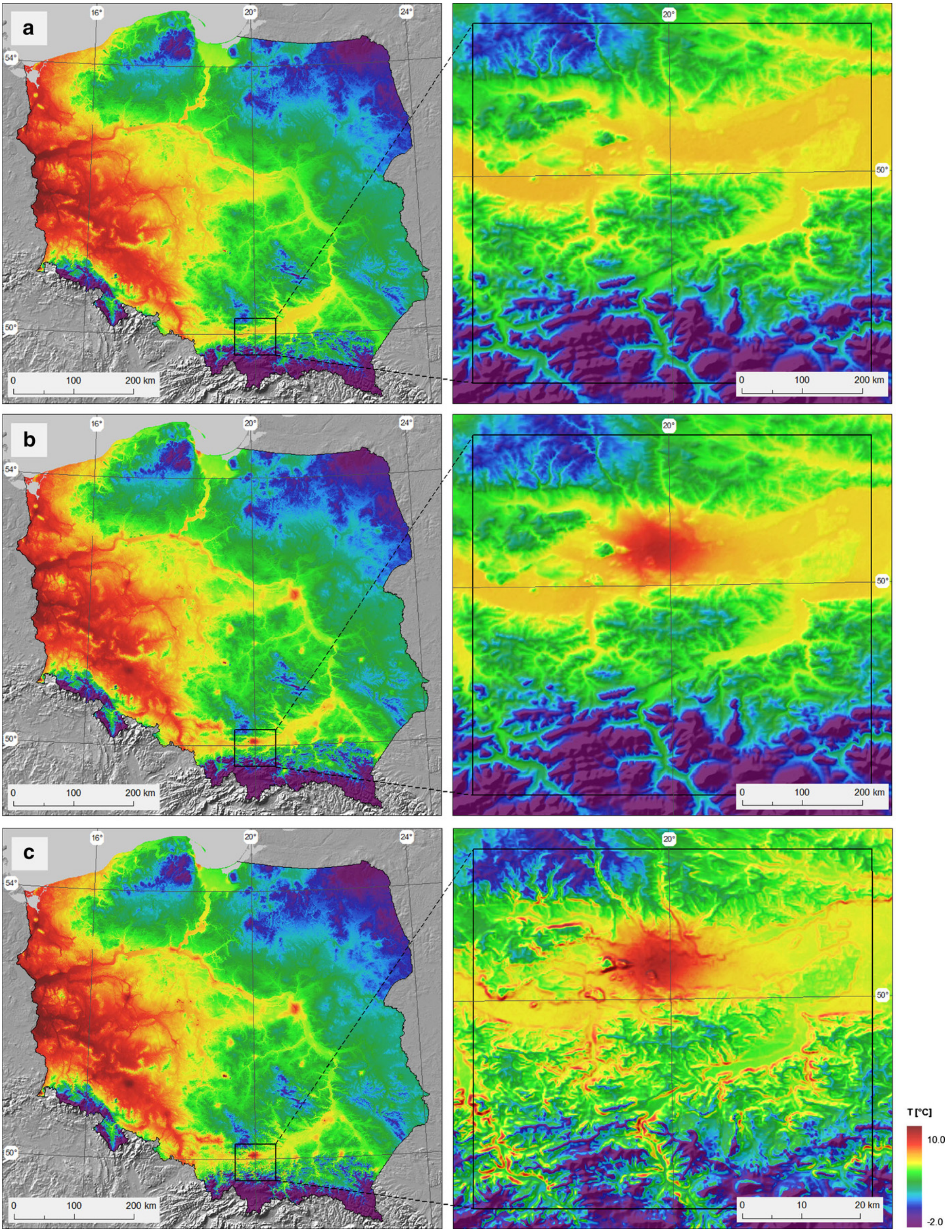
a
b
c
16°
20°
24°
54°
50°
0
100
200 km
10
20 km
T [°C]
10.0
-2.0

temperature variance, but it is not a general rule. For the lower levels of data aggregation, there are more one-variable models that explain only a small part of variance, even if well-explaining one-variable models can be found at each level of aggregation as well. The reason might be a declining significance of static environmental factors and increasing role of atmospheric dynamics and weather conditions on spatial pattern of air temperature, which are not directly represented in the regression models.

4. The most significant changes in determination coefficients are observed mostly when adding the second and third variables to the regression model. However, there are also cases in which the first, most significant variable explains the majority of air temperature variance and the incorporation of additional variables does not lead to further improvement of the deterministic model.
5. For all the MP models and for all analysed cases, local GWR models are better fitted to the observations than global MLR models. This means that the spatial process determining the air temperature distribution over Poland can be considered as non-stationary.

A detailed study of two selected cases from levels 1 and 5 additionally revealed that

6. Introducing significantly correlated explanatory variables improves the goodness-of-fit of the regression model (MLR or GWR), but it does not necessarily mean a significant improvement of the quality of spatial interpolation expressed by CV errors. Thus, the thesis from many previous interpolation attempts, claiming that the more spatial variation is explained by the deterministic part of the model, the better is the quality of spatial interpolation, cannot be indisputably accepted.
7. Regression-kriging models (MLRK, GWRK) as spatial interpolators usually perform better than their corresponding regression models (MLR, GWR), but the improvement strongly depends on the particular case.
8. If the GWR or MLR residuals are autocorrelated, the model should be expanded to residual kriging. GWRK usually gives better results of spatial interpolation than MLRK; however, the difference in performance quality is very rarely statistically significant.
9. The signal of each explanatory variable, even if it explains relatively small part of the air temperature variance, might introduce large and noticeable effects in the final map prepared by using either regression alone or regression-kriging interpolation algorithm. However, despite a statistically significant correlation, the effect of the introduction of certain variables into the model may not be climatologically justified. This is due to the extrapolation of air temperature—variable relation in the case of not representative distribution of measuring points with respect to the environmental feature (variable) determining the air temperature distribution. In the analysed TY case, it was seen, while introducing SLP as a 5th variable in the model, that it led to significant changes in air temperature over steep slopes.

Although the analysis was performed on only a limited number of cases for Poland, some general conclusions can also be drawn. The Matheron's universal model of spatial variation and its mathematical representation—the regression-kriging, are very effective models for spatial interpolation and mapping the air temperature. The air temperature spatial variation can be assumed non-stationary, so it is justified to model deterministic part using local GWR model instead of global MLR. If regression residuals are spatially autocorrelated, it is recommended to extend the spatialization model to the regression-kriging form: GWRK. It should be emphasized that some of the processes that are deterministic in nature, for example, caused by atmospheric circulation, cannot be modelled in the deterministic part of the model. This is because it is hardly possible to prepare proper layers of variables expressing such dynamic features. Thus, this part of spatial variation is explained by the stochastic part of the model.

Although the leading explaining role is played by such environmental variables as elevation, location and the distance from the sea, and usually most of air temperature variance is explained by the first 1–3 auxiliary variables, the set of potential predictors for deterministic part specification should be as wide as possible. This is because each statistically significant predictor is reflected in the final map regardless whether regression or regression-kriging method is used for spatialization. It is up to the modeller to decide which statistically justified effects are desired and climatologically realistic, and should be expressed on the air temperature map, depending for example on the map purpose. The expert judgment is, therefore, necessary to compliment the cross-validation statistics of the models performance.

Acknowledgments

The authors thank Ryszard Kryza for his help in improving the manuscript.

REFERENCES

AGNEW, M.D., and PALUTIKOF, J.P. (2000), *GIS-based construction of baseline climatologies for the Mediterranean using terrain variables*, Clim. Res. *14*, 115–127.

AL-AWADHI F.A., and AL-AWADHI S.A. (2006), *Spatial-temporal model for ambient air pollutants in the state of Kuwait*, Environmetrics *17*, 739–752.

APAYDIN, H., ANLI, A.S., and OZTURK, F. (2011), *Evaluation of topographical and geographical effects on some climatic parameters in the Central Anatolia Region of Turkey*, Int. J. Climatol. *31*, 1264–1279.

ATTORRE, F., ALFO, M., DE SANCTIS, M., FRANCESCONIA, F., and BRUNOA, F. (2007) *Comparison of interpolation methods for mapping climatic and bioclimatic variables at regional scale*, Int. J. Climatol. *27*, 1825–1843.

BENAVIDES, R., MONTES, F., RUBIO, A, and OSORO K. (2007), *Geostatistical modelling of air temperature in a mountainous region of Northern Spain*, Agr. Forest Meteorol. *146*, 173–188.

BENICHOU, P., and LE BRETON, O. (1987), *Prise en compte de la topographie pour la cartographie des champs pluviométriques statistiques*, La Météorologie *7*, 23–34.

BJORNSSON, H., JONSSON, T., GYLFADOTTIR, S.S., and OLASON, E.O. (2007), *Mapping the annual cycle of temperature in Iceland*, Meteorol. Z. *16*(1), 45–56.

BOI, P., FIORI, M., and CANU, S. (2011), *High spatial resolution interpolation of monthly temperatures of Sardinia*, Meteorol. Appl. *18*, 475–482.

BOWDEN, J.H., OTTE, T.L., NOLTE, C.G., and OTTE, M.J. (2012), *Examining interior grid nudging techniques using two-way nesting in the WRF model for regional climate modeling*, J. Climate. *25*, 2805–2823.

BROWN, D.P., and COMRIE , A.C. (2002), *Spatial modeling of winter temperature and precipitation in Arizona and New Mexico, USA*, Clim. Res. *22*, 115–128.

CARREGA, P. (1995), *A method for the reconstruction of mountain air temperatures with automatic cartographic applications*, Theor. Appl. Climatol. *52*(1), 69–84.

CHOI, J., CHUNG, U., and YUN, J.I. (2003), *Urban-effect correction to improve accuracy of spatially interpolated temperature estimates in Korea*, J. Appl. Meteorol. *42*, 1711–1719.

CHUANYAN, Z., ZHONGREN, N., and GUODONG, C. (2005), *Methods for modelling of temporal and spatial distribution of air temperature at landscape scale in the southern Qilian mountains, China*, Ecol. Model. *189*, 209–220.

COST ACTION 719 FINAL REPORT: The use of Geographic Information Systems in climatology and meteorology (ed. Tveito O.E., Wegehenkel M., van der Wel F., and Dobesch H.) (Office for Official Publications of the European Communities, Luxembourg 2008).

COURAULT, D., and MONESTIEZ, P. (1999), *Spatial interpolation of air temperature according to atmospheric circulation patterns in southeast France*, Int. J. Climatol. *19*, 365–378.

CRESSIE N., and JOHANNESSON G. (2008), *Fixed rank kriging for very large spatial data sets*, J. Roy Stat. Soc. B. *70*, 209–226.

DALY, C. (2006), *Guidelines for assessing the suitability of spatial climate data sets*, Int. J. Climatol. *26*, 707–721.

DALY, C., HALBLEIB, M., SMITH, J.I., GIBSON, W.P., DOGGETT, M.K., TAYLOR, G.H., CURTIS, J., and PASTERIS, P.P. (2008), *Physiographically sensitive mapping of climatological temperature and precipitation across the conterminous United States*. Int. J. Climatol. *28*, 2031–2064.

DALY, C., NEILSON, R.P., and PHILLIPS, D.L. (1994), *A statistical-topographic model for mapping climatological precipitation over mountainous terrain*. J. Appl. Meteorol. *33*, 140–158.

DRAPER, N., and SMITH, H., Applied Regression Analysis, 3rd Edition (John Wiley & Sons Inc., New York 1998).

ESTEBAN, P., NINYEROLA, M., and PROHOM, M. (2009), *Spatial modelling of air temperature and precipitation for Andorra (Pyrenees) from daily circulation patterns*, Theor. App. Climatol. *96*, 43–56.

FOTHERINGHAM, A.S., BRUNSDON, C., and CHARLTON, M., Geographically weighted regression: the analysis of spatially varying relationships (Wiley, Chichester 2002).

GRASS DEVELOPMENT TEAM (2011), Geographic Resources Analysis Support System (GRASS) Software, Version 6.4.0. Open Source Geospatial Foundation. http://grass.osgeo.org.

HENGL, T., A practical guide to geostatistical mapping of environmental variables (Office for Official Publications of the European Communities, Luxembourg 2007).

HIEBL, J., AUER, I., BÖHML, R., SCHÖNER, W., MAUGERI, M., LENTINI, G., SPINONI, J., BRUNETTI, M., NANNI, T., PERCEC TADIC, M., BIHARI, Z., DOLINAR, M., and MÜLLER-WESTERMEIER, G. (2009), *A high-resolution 1961–1990 monthly temperature climatology for the greater Alpine region*, Meteorol. Z. *18*(5), 507–530.

HOLDAWAY, M.R. (1996), *Spatial modeling and interpolation of monthly temperature using kriging*, Clim. Res. *6*, 215–225.

Hogewind, F., and Bissolli, P. (2011), *Operational maps of monthly mean temperature for WMO Region VI (Europe and Middle East)*, Idojaras *115*(1–2), 31–49.

Huerta G., Sanso B., and Stroud J.R. (2004), *A spatiotemporal model for Mexico City ozone levels*, J. Roy Stat. Soc. C-App. *53*, 231–248.

Hurvich, C.M., and Tsai, C.L. (1990), *The impact of model selection on inference in linear regression*, Am. Stat. *44*, 214–217.

Hutchinson, M.F. (1995), *Interpolating mean rainfall using thin plate smoothing splines*, Int. J. Geogr. Inf. Syst. *9*(4), 385–403.

Jamshidian, M., Jennrich, R.I., and Liu, W. (2007), *A study of partial F tests for multiple linear regression models*, Comput. Stat. Data Anal. *51*, 6269–6284.

Jarvis, C.H., and Stuart, N. (2001a), *A comparison among strategies for interpolating maximum and minimum daily air temperature. Part I: the selection of "guiding" topographic and land cover variables*, J. Appl. Meteorol. *40*, 1060–1074.

Jarvis C.H., and Stuart, N. (2001b) *A comparison among strategies for interpolating maximum and minimum daily air temperature. Part II: the interaction between number of guiding variables and the type of interpolation method*, J. Appl. Meteorol. *40*, 1075–1084.

Joly, D., Brossard, T., Cardot, H., Cavailhes, J., Hilal, M., and Wavresky, P. (2011), *Temperature interpolation based on local information: the example of France*, Int. J. Climatol. *31*, 2141–2153.

Kalarus, M., Schuh, H., Kosek, W., Akyilmaz, O., Bizouard, C., Gambis, D., Gross, R., Jovanović, B., Kumakshev, S., Kutterer, H., Mendes Cerveira, P.J., Pasynok, S., and Zotov, L. (2010), *Achievements of the Earth orientation parameters prediction comparison campaign*, J. Geodesy *84*, 587–596.

Kożuchowski, K., Klimat Polski. Nowe spojrzenie (Wydawnictwo Naukowe PWN, Warszawa 2011).

Kożuchowski, K., and Żmudzka, E. (2001), *Assessment of relations between the normalised difference vegetation index (NDVI), frequency of forest fires, air temperature, sunshine, precipitation in Poland*, Geographia Polonica *74*(2), 29–40.

Krahenmann, S., Bissolli, P., Rapp, J., and Ahrens, B. (2011) *Spatial gridding of daily maximum and minimum temperatures in Europe*, Meteorol. Atmos. Phys. *114*, 151–161.

Kryza, M., Werner, M., Dore, A.J., Vieno, M., Błaś, M., Drzeniecka-Osiadacz, A., and Netzel, P. (2012), *Modelling meteorological conditions for the episode (December 2009) of measured high PM10 air concentrations in SW Poland—application of the WRF model*, Int. J. Environ. Pollut. *50*, 41–52.

Kurtzman, D., and Kadmon, R. (1999), *Mapping of temperature variables in Israel: a comparison of different interpolation methods*, Clim. Res. *13*, 33–43.

Lennon, J.J., and Turner J.R.G. (1995), *Predicting the spatial distribution of climate: temperature in Great Britain*, J. Anim. Ecol. *64*, 370–392.

Li, J., and Heap, A.D., A review of spatial interpolation methods for environmental scientists (Geoscience Australia, Canberra 2008).

Matheron, G. (1963), *Principles of geostatistics*, Econ. Geol. *58*, 1246–1266.

Matheron, G., Le Krigeage universel (Cahiers du Centre de Morphologie Mathematique, Ecole des Mines de Paris, Fontainebleau 1969).

Mitchell, A., The ESRI guide to GIS analysis. Spatial measurements and statistics, vol 2 (ESRI Press, Redlands, California 2005).

Moran, P.A.P. (1950), *Notes on Continuous Stochastic Phenomena*, Biometrika *37*(1), 17–23.

Nalder, I.A., and Wein, R.W. (1998), *Spatial interpolation of climatic normals: test of a new method in the Canadian boreal forest*, Agr. Forest Meteorol. *92*, 211–225.

Ninyerola, M., Pons, X., and Roure, J.M. (2000), *A methodological approach of climatological modelling of air temperature and precipitation through GIS techniques*, Int. J. Climatol. *20*, 1823–1841.

Ninyerola, M., Pons, X., and Roure, J.M. (2007), *Objective air temperature mapping for the Iberian Peninsula using spatial interpolation and GIS*, Int. J. Climatol. *27*, 1231–1242.

Perčec Tadić M. (2010), *Gridded Croatian climatology for 1961–1990*, Theor. Appl. Climatol. *102*, 87–103.

Perry, M., and Hollis, D. (2005a), *The development of a new set of long-term climate averages for the UK*, Int. J. Climatol. *25*, 1023–1039.

Perry, M., and Hollis D. (2005b), *The generation of monthly gridded datasets for a range of climatic variables over the UK,* Int. J. Climatol. *25*, 1041–1054.

Pielke, R.A., Cotton, W.R., Walko, R.L., Tremback, C.J., Lyons, W.A., Grasso, L.D., Nicholls, M.E., Moran, M.D., Wesley, D.A., Lee, T.J., and Copeland, J.H. (1992), *A comprehensive meteorological modeling system—RAMS*, Meteorol. Atmos. Phys. *49*, 69–91.

Skamarock, W.C., Klemp, J.B., Dudhia, J., Gill, D.O., Baker, D.M., Duda, M.G., Huang, X., Wei, W., and Powers, J.G. (2008), A Description of the Advanced Research WRF Version 3, NCAR Technical Note NCAR/TN-475 + STR, National Center for Atmospheric Research, Boulder, Colorado, USA. doi:10.5065/D68S4MVH.

Szentimrey, T., and Bihari, Z., Mathematical background of spatial interpolation, meteorological interpolation based on surface homogenized data bases (MISH), In COST Action 719: The use of Geographic Information Systems in climatology and meteorology (ed. Szalai, S., Bihari, Z., Szentimrey, T., and Lakatos M.) (Proceedings from the Conference on Spatial Interpolation in Climatology and Meteorology, Budapest, 25–29 October 2004) pp. 17–27.

Szymanowski, M., and Kryza, M. (2009), *GIS-based techniques for urban heat island spatialization*, Clim. Res. *38*, 171–187.

Szymanowski, M., Kryza, M. (2011), *Application of geographically weighted regression for modelling the spatial structure of urban heat island in the city of Wroclaw (SW Poland)*, Procedia Environmental Sciences *3*, 87–92, doi:10.1016/j.proenv.2011.02.016.

Szymanowski, M., and Kryza M. (2012), *Local regression models for spatial interpolation of urban heat island—an example from Wrocław, SW Poland*. Theor. App. Climatol. *108*, 53–71.

Szymanowski, M., Kryza, M., and Smaza, M. (2007), A GIS approach to spatialize selected climatological parameters for wine-growing in Lower Silesia, Poland, In Střelcová, K., Škvarenina, J. & Blaženec, M. (ed.) Bioclimatology and natural hazards, International Conference, Pol'ana nad Detvou, Slovakia, 17–20 September 2007, CD-ROM, ISBN 978-80-228-17-60-8.

Szymanowski, M., Kryza, M., and Spallek, W., Air temperature atlas for Poland: the methodical approach (Uniwersytet Wrocławski, Wrocław 2012) (in Polish, English summary).

Szymanowski, M., Kryza, M., and Spallek, W. (2013), *Regression-based air temperature spatial prediction models: an example from Poland*, Meteorol. Z. *22*, 577–585.

Tietavainen, H., Tuomenvirta, H., and Venalainen, A. (2010), *Annual and seasonal mean temperatures in Finland during the last 160 years based on gridded temperature data*, Int. J. Climatol. *30*, 2247–2256.

Tucker, C.J. (1979), *Red and Photographic Infrared Linear Combinations for Monitoring Vegetation*, Remote Sens. Environ. *8*(2), 127–150.

Ustrnul, Z. (2006), *Spatial differentiation of air temperature in Poland using circulation types and GIS*, Int. J. Climatol. *26*(11), 1529–1546.

Ustrnul, Z., and Czekierda, D. (2005), *Application of GIS for the development of climatological air temperature maps: an example from Poland*, Meteorol. Appl. *12*, 43–50.

Ustrnul, Z., and Czekierda, D., Atlas of extreme meteorological phenomena and synoptic situations in Poland (IMGW Warszawa 2009).

Vicente-Serrano , S.M., Saz-Sánchez, M.A. and Cuadrat, J.M. (2003), *Comparative analysis of interpolation methods in the middle Ebro Valley (Spain): application to annual precipitation and temperature*, Clim. Res. *24*, 161–180.

White, E.J. (1979), *The prediction and selection climatological data for ecological purposes in Great Britain*, J. Appl. Ecol. *16*, 141–160.

Wilby, R.L., and Wigley, T.M.L. (1997), *Downscaling general circulation model output: a review of methods and limitations*, Prog. Phys. Geog. *21*, 530–548.

Wilkinson, L., and Dallal, G.E. (1981), *Tests of significance in forward selection regression with an F-to-enter stopping rule*, Technometrics *23*, 377–380.

Willmott, C.J., and Matsuura, K. (1995), *Smart interpolation of annually averaged air temperature in the United States*, J. Appl. Meteorol. *34*, 2577–2586.

Wilson, A.M., and Silander J.A. (2014), *Estimating uncertainty in daily weather interpolations: a Bayesian framework for developing climate surfaces*, Int. J. Climatol. *34*, 2573–2584.

Woś, A., Klimat Polski w drugiej połowie XX wieku (Wydawnictwo Naukowe UAM, Poznań 2010).

Yue U., and Speckman P.L. (2010), *Nonstationary Spatial Gaussian Markov Random Fields*, J. Comput. Graph. Stat. *19*, 96–116.

(Received November 24, 2014, revised September 25, 2015, accepted October 17, 2015, Published online November 3, 2015)

Pure Appl. Geophys. 174 (2017), 623–642

DOI 10.1007/s00024-016-1413-x

Pure and Applied Geophysics

Spatial Interpolation of Ewert's Index of Continentality in Poland

Mariusz Szymanowski,[1] Piotr Bednarczyk,[2] Maciej Kryza,[3] and Marek Nowosad[4]

Abstract—The article presents methodological considerations on the spatial interpolation of Ewert's index of continentality for Poland. The primary objective was to perform spatial interpolation and generate maps of the index combined with selection of an optimal interpolation method and validation of the use of the decision tree proposed by Szymanowski et al. (Meteorol Z 22:577–585, 2013). The analysis involved four selected years and a multi-year average of the period 1981–2010 and was based on data from 111 meteorological stations. Three regression models: multiple linear regression (MLR), geographically weighted regression (GWR), and mixed geographically weighted regression were used in the analysis as well as extensions of two of them to the residual kriging form. The regression models were compared demonstrating a better fit of the local model and, hence, the non-stationarity of the spatial process. However, the decisive role in the selection of the interpolator was assigned to the possibility of extension of the regression model to residual kriging. A key element here is the autocorrelation of the regression residuals, which proved to be significant for MLR and irrelevant for GWR. This resulted in exclusion of geographically weighted regression kriging from further analysis. The multiple linear regression kriging was found as the optimal interpolator. This was confirmed by cross validation combined with an analysis of improvement of the model in accordance with the criterion of the mean absolute error (MAE). The results obtained facilitate modification of the scheme of selection of an optimal interpolator and development of guidelines for automation of interpolation of Ewert's index of continentality for Poland.

Key words: Ewert's index of continentality, spatial interpolation, regression kriging, geographically weighted regression, Poland.

1. Introduction

The concept of continentality in climatology refers to all characteristics of climate influenced by continents and is regarded as a notion opposed to climate oceanity. The continental impact is most frequently considered in the context of its effect on air temperature (thermal continentality) and precipitation (pluvial or hygric continentality). The continental climate is characterised by higher diurnal and annual amplitude of air temperature, hot summers, and cold winters. As the distance from the ocean increases, the cloudiness and precipitation rates decline and the annual distribution of precipitation changes and exhibits a distinct summer maximum. The oceanic climate is characterised by high air humidity and high rates of precipitation distributed evenly throughout the year, with low annual air temperature amplitudes, cool summers, and mild winters.

In a macroscale, it can be assumed that climate features of any place on the globe comprise a signal coming from the continents and a supposedly opposite signal from the oceans. To quantify these interactions, a number of indices, primarily describing the "strength" of land impacts, have been developed. Given the disproportion between the land and ocean cover (ca. 30 %—lands and 70 %—oceans), they can be regarded as a specific modification of the prevailing oceanic climate on the planet. As a rule, indicators of continentality express the relation between continental and oceanic features of climate and, hence, underline the relative nature of continentality. The continentality has been assigned particular importance in characterisation of areas with the so-called transitional climate combining continental and oceanic impacts, which exhibit high year-to-year variability depending on macro-circulation features. For Poland, such analyses have been

---

[1] Department of Geoinformatics and Cartography, Institute of Geography and Regional Development, University of Wrocław, pl. Uniwersytecki 1, 50-137 Wrocław, Poland. E-mail: mariusz.szymanowski@uwr.edu.pl

[2] Laboratory of Geoinformatics, Maria Curie-Skłodowska University in Lublin, al. Kraśnicka 2cd, 20-718 Lublin, Poland.

[3] Department of Climatology and Atmosphere Protection, Institute of Geography and Regional Development, University of Wrocław, ul. Kosiby 8, 51-621 Wrocław, Poland.

[4] Department of Meteorology and Climatology, Maria Curie-Skłodowska University in Lublin, al. Kraśnicka 2cd, 20-718 Lublin, Poland.

performed by Kożuchowski and Marciniak (1986, 1992), Kożuchowski and Wibig (1988), and Kożuchowski (2003). Recently, continentality indices have been applied in environmental analyses, particularly as a variable supporting the analysis of variability and spatial distribution of, e.g., air temperature (Hogewind and Bissolli 2011), evapotranspiration (Marti and Gasque 2010) and bioclimatic changes (Torregrosa et al. 2013). The analytical usefulness of continentality indices has also been corroborated in the investigations of glacier mass balance (Holmlund and Schneider 1997), plant species range and the treeline (Caccianiga et al. 2008), and plant pollen in northern Europe (Salonen et al. 2012).

Given the recent climate changes, it is expected that continentality indices bring important signs of these changes, particularly when research-based thereon will address the dynamic year-to-year changes, multi-year trends, and predictions supplemented with detailed analysis of extreme values and circulation relationships. On the one hand, maps of continentality indices can provide data concerning a number of environmental elements, thereby being an important variable in multi-dimensional spatial modelling of these elements, as mentioned above. Methodology for accurate spatialization of continentality indices based on discrete point observations is a prerequisite for generation of such maps. This paper is focused on spatial interpolation of the thermal continentality index for Poland. It has a methodological character allowing indication of a preferable spatialization algorithm in accordance with the environmental characteristics of the study area and the nature of the input data set.

The annual temperature amplitude, i.e., the difference between the mean temperature of the warmest and coldest month, is the simplest absolute measure of thermal continentality. The drawback of this indicator lies in its dependence on seasonal changes in the quantity of incoming solar energy, which results in an increase in the annual amplitude with latitude. The effect is compensated for in the thermal continentality indices by dividing the temperature amplitude by the sine of latitude with concurrent introduction of empirical parameters facilitating rescaling of the index into the assumed interval in accordance with theoretical assumptions (Conrad 1946).

Various continentality indices used in climatology are based on the average annual temperature amplitude scaled with the sine of latitude. However, Driscoll and Yee Fong (1992) suggest that there is no conclusive evidence for the validity of the use of this divisor with respect to amplitude changes determined by the incoming solar energy. This group comprises indicators specified by Gorczyński (1920), Johansson (1926), Raunio (1948), Conrad (Conrad and Pollak 1950), Hela (1953), Ivanov (1953), Khromov (1957), Ewert (1963), and Hogewind and Bissolli (2011). Formulas extending this type of thermal continentality indices with other environmental parameters include indicators developed by Spitaler (1922), Ringleb and Johansson (after Szreffel 1961), and Ivanov (1959). Berg (1944), Bailey (1968), and Oliver (1970) proposed formulas based on other assumptions than annual temperature amplitude. These ideas have been put forward by Driscoll and Yee Fong (1992) and Mikolášková (2009).

Classic approach to present continentality indices uses hand-drawn isolines (Swoboda 1922; Kożuchowski and Marciniak 1992), with generalisation typical of this technique, especially in small scales. In recent studies, index maps are generated in the GIS environment, taking advantage of raster maps and showing more details (Mikolášková 2009; Torregrosa et al. 2013). The spatialization approaches applied are relatively simple, one-dimensional, and disregard selection of an optimal interpolation method and accuracy of the results.

Currently, environmental research, including climatology, employs various interpolation techniques (Hengl 2007; Li and Heap 2008; Szymanowski et al. 2012), which often leads to difficulties in choosing a method that is appropriate in a given case. This problem has been addressed, e.g., in the COST 719 research project “The Use of GIS in Climatology and Meteorology” (Dobesch et al. 2007; COST Action 719 Final Report 2008), but the investigations did not yield a conclusive solution. The spectrum of methods employed for spatial interpolation of climate elements is very wide and comprises deterministic and geostatistical techniques and their combinations. The best results are usually obtained with multivariate methods considering the role of environmental factors, in particular the elevation and coordinates (Szymanowski et al. 2012). This group includes, among others, the multiple linear regression (MLR) and residual kriging (MLRK, regression kriging) methods. Analyses of the spatial properties of climate elements, particularly non-stationarity, indicate that the local geographically weighted regression (GWR) model with residual kriging (geographically weighted regression kriging, GWRK) is more suitable for modelling the spatial variability of these elements (Szymanowski and Kryza 2011, 2012). Methodological research aiming at interpolation of the temperature field for Poland resulted in construction of a decision tree for selection of an optimal multivariate interpolation method considering the potential non-stationarity of the spatial process (Szymanowski et al. 2012, 2013).

The main objective of this study is to perform spatial interpolation and generate maps of Ewert's index of continentality (1972) for selected cases in Poland representing long-term annual mean values and years with extreme values or characteristics of the spatial distribution of this indicator. This methodological paper emphasises the choice of an optimal interpolation method and indication of guidelines for automated or semi-automated interpolation of the indicator for a large data set (multi-year series) to identify the trend in climate change. Second aim is to validate the usefulness of the scheme of selection of the optimal interpolation method developed by Szymanowski et al. (2012, 2013) for interpolation of the continentality indices.

2. Study Area

Poland (312,679 km^2) is situated in the central part of Europe. The terrain elevation in the country ranges from −1.8 m in the north to 2499 m above sea level in the highest, mountainous area in the south of the country. The north-western border of Poland is delimited by the Baltic Sea, and in the south, the border extends along the main ridge of the Sudetes and Carpathians (Fig. 1).

Poland is located in the temperate transitional climate zone with clear continental and oceanic impacts. Westerly winds and polar air masses are predominant. The spatial distribution of the lowest values of the mean annual air temperature is determined by elevation, with the top parts of the mountains (−0.7 °C), and continentality, with the north-eastern part of the country being the second coolest region (<7 °C). The mean annual temperature increases from the north-east to the south-west, where it exceeds 8.5 °C (Woś 2010). July, with temperatures ranging from 17.3 to 18.8 °C (except for the mountains), is the warmest month, and January, with temperatures in the range between −3.4 and −1.3 °C, is the coldest (Kożuchowski 2011). In January, longitudinal distribution of isotherms dominates, with temperatures decreasing eastwards. In July, the course of isotherms exhibits latitudinal distribution with temperatures decreasing from the central regions northwards, towards the Baltic Sea, and southwards along the increasing elevation in the mountains. The mean annual temperature amplitude varies between ca. 15 °C in high mountain areas and 22 °C in the eastern part of the country. The longitudinal course of isoamplitudes typical for the east of the country is deformed in the west. The longitudinal distribution is only observed there in the central part, whereas in the north and south, the arrangement has a latitudinal direction similar to the course of the coast and mountain ranges (Woś 2010). A similar distribution is characteristic for the multi-year continentality indices. The areal average value of Ewert's index of continentality is 44.3 % (Kożuchowski 2011). In decades dominated by oceanic influences, it ranges from below 38 % at the Baltic Sea to over 48 % in the east of the country. In decades dominated by continental influences, the values of Ewert's index range from below 44 % and over 56 %, respectively (Kożuchowski and Marciniak 1992).

3. Data and Methods

3.1. Ewert's Index of Continentality

One of the thermal continentality indices presented in the Introduction section, i.e., Ewert's index

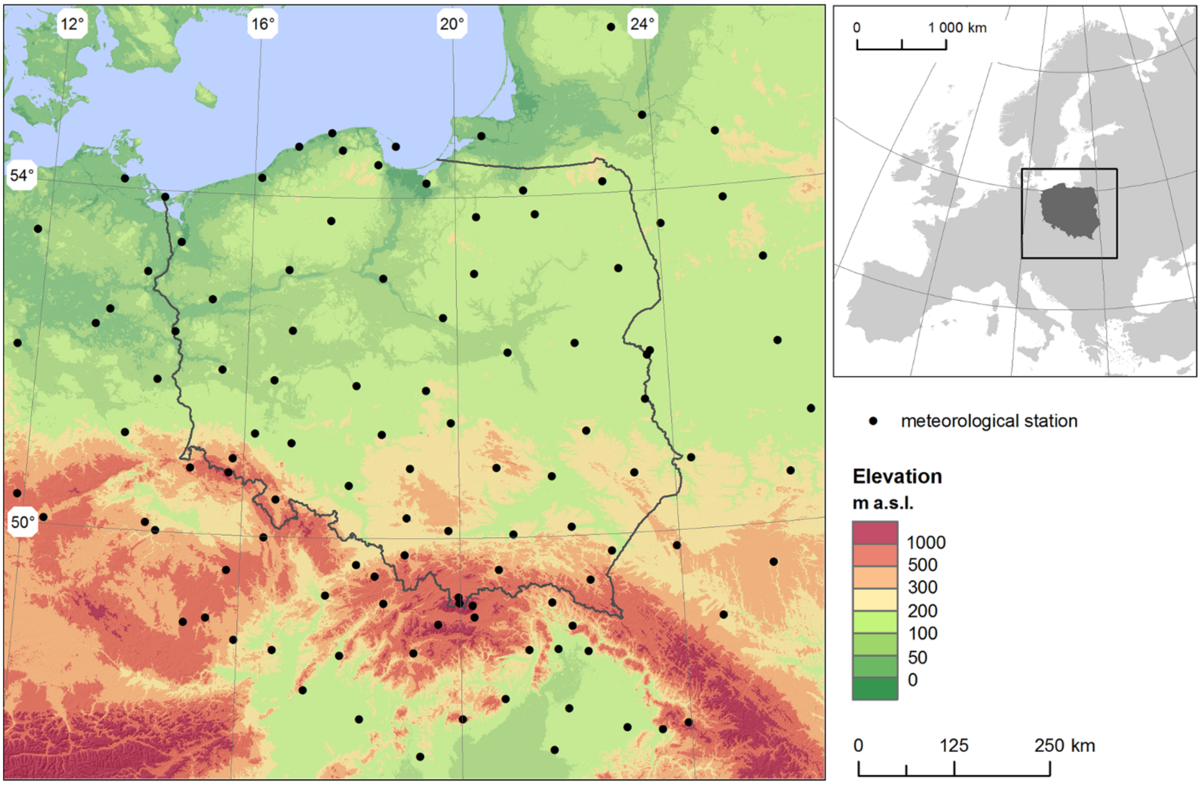

Figure 1
Study area and location of meteorological stations used in the study

(1972), was selected for the analysis. Compared with other indicators involving compensation of the influence of latitude, Ewert's index includes additional parameterization considering the impact of land cover on the value of the annual air temperature amplitude in the individual latitude zones. These relationships were estimated particularly carefully for Central Europe, where the best results are achieved (Ewert 1972). Additional important assumptions for the development of the index include the possibility of applying it to all latitudes and any—annual or multi-year—period. Ewert's index of continentality K [%] is expressed by the formula:

$$K = \frac{A - (3.81 \sin \varphi + 0.1)}{38.39 \sin \varphi + 7.47} \times 100, \qquad (1)$$

where A is the annual temperature amplitude and φ is latitude. The index is not limited to the range of 0–100 %, but it has the values from -1.5 % for Turk Island to 141.5 % for Yakutsk. Areas with negative index values are characterised by "hyperoceanity" and those with the values >100 % by "hypercontentality" (Ewert 1972). Minimal "hyperoceanity" has been identified at several Pacific stations and "hypercontentality" in a large part of eastern Siberia (Ewert 1972).

To achieve one of the objectives of this study, i.e., development of a method and general guidelines for spatial interpolation of Ewert's index of continentality for Poland, the analyses were based on five data sets representing mean and extreme values of the index from 1981 to 2010 (Table 1):

- the mean value of the index ($K_{1981\text{–}2010}$);
- the years 1989 and 2006 with the lowest and highest areal means for Poland, respectively (K_{1989}, K_{2006}); and
- the years 1990 and 2002 with the smallest and largest index ranges, respectively (K_{1990}, K_{2002}).

The study was based on measurement data provided by 111 synoptic meteorological stations,

Table 1

Summary of statistics of Ewert's index of continentality (K) in Poland for the four selected years and the 1981–2010 average

Statistics	K_{1989}	K_{1990}	K_{2002}	K_{2006}	$K_{1981–2010}$
Mean	36.19	38.52	58.71	67.52	50.26
Minimum	22.79	31.26	35.36	49.25	39.54
Maximum	40.88	42.78	70.10	75.92	55.52
Range	18.09	11.51	34.74	26.67	15.97
Standard deviation	3.43	2.72	7.01	6.03	4.18

including 53 Polish stations and 58 stations located outside Polish borders (Fig. 1). The localization of each station was carefully verified by comparing station metadata with ortophotomaps and digital elevation model. The values of the annual amplitude of air temperature were calculated based on information contained in global summary of the day (GSOD) database and provided by German weather service—Deutscher Wetterdienst (Klimadaten für Deutschland—online—frei; http://www.dwd.de).

3.2. Environmental Variables

The findings of the COST 719 project (COST Action 719 Final Report 2008) and the previous experience related to interpolation of meteorological elements for Poland (Ustrnul and Czekierda 2005, 2009; Szymanowski et al. 2012) indicate a significant value of multivariate interpolation algorithms constituted for large range of climatological applications. The methods consider the deterministic relationships between the modelled element and environmental variables—predictors. The spatial distribution of the predictors is represented in the interpolation procedure by raster layers with a fixed spatial resolution. Variables prepared previously for interpolation of temperature (Szymanowski et al. 2012, 2013), which could have a significant impact on the distribution of the continentality index, were used in the study. Three groups of variables were included in the set of potential predictors:

- variables of the overall spatial trend comprising layers of raster cell coordinates (X, Y) and the sea distance index (SDI);
- terrain elevation represented by the digital elevation model (DEM) and derivative layers: the concavity/convexity index (CCI), the foehn index (FI), and insolation (IT); and
- land cover and its derivatives: the percentage of natural surfaces (NS) and artificial surfaces (AS) in the neighbourhood of the data point.

Variables X and Y denote coordinate values in the local coordinate system PUWG-92. The influence of the Baltic Sea is illustrated by the SDI index. To consider the decreasing impact of the Baltic Sea along with distance, the index was constructed as a square root of the smallest Euclidean distance (expressed by the number of cells) of a raster cell from the coastline. SRTM-3 elevation data (http://www2.jpl.nasa.gov/srtm) were used as a digital elevation model (DEM). To achieve the goal of this study, the data were transformed into the PUWG-92 system and resampled into 250-m resolution. This resolution is a compromise between the computational costs and details of information introduced to the models and expressed on the maps. High resolution is of special importance when the interpolated variable is potentially strongly dependant on local factors (including changes in altitude). The choice of spatial resolution applied is supported by earlier studies of Szymanowski et al. (2012, 2013) and Szymanowski and Kryza (2015). Based on the 250-m DEM, the concavity/convexity index (CCI) expressing the cool air accumulation effects of concave terrain forms and the foehn index (FI) illustrating the thermal impact of the foehn wind were calculated (Szymanowski et al. 2007). Insolation (IT), expressed by sums of energy of potential total radiation incoming to the terrain surface, is a variable illustrating the role of energy factors. The calculations were performed with the use of the r.sun program implemented in the GIS—GRASS software (GRASS Development Team 2011). The r.sun program is a functionally best-developed module for calculation of radiation in GIS, which can be successfully applied to large areas (Šuri and Hofierka 2004) and works with high-resolution terrain models (Kryza et al. 2010). Variables describing the percentage of the surface area arbitrarily called "artificial" (AS) and "natural" (NS) in the surroundings with a radius of 2500 m around each point were prepared on the basis of CLC2000—CORINE Land Cover 2000 database (2004) for European Union countries and the USGS Land Cover database (2011) for Ukraine, Belarus, and Russia. The values of all environmental variables were extracted from raster layers at the coordinates of localization of each meteorological station and were used to specify regression models as described below.

3.3. *Statistical and Spatial Analysis Methods*

In this study, a scheme of selection of an optimal interpolation method developed with an example of air temperature is employed (Szymanowski et al. 2012, 2013). The scheme is based on Hengl's decision tree (2007), and was extended with methods dedicated to non-stationary spatial processes. It is generally assumed that the analysed continentality index is characterised by a statistically significant correlation with at least one environmental variable; therefore, the deterministic component can be modelled with the regression method. In the absence of the correlation, spatial interpolation would have to be performed using one of the one-dimensional methods, e.g., ordinary kriging (OK) or inverse distance weighting (IDW), depending on the degree of spatial autocorrelation of the analysed variable (Hengl 2007). In the scheme discussed, the modelled indicator is regarded as a regionalised variable (Matheron 1971), i.e., a random variable comprising structural, local, and random components. This cumulative model was termed a universal model of spatial variability by Matheron. The structural—deterministic ($\hat{m}(s_0)$) and local—stochastic (deterministic model residuals—$\hat{e}(s_0)$) components of variability can be modelled separately and the estimated value of variable z in position s_0—$\hat{z}(s_0)$ is a sum of these components (Eq. 2):

$$\hat{z}(s_0) = \hat{m}(s_0) + \hat{e}(s_0). \tag{2}$$

If the deterministic component is modelled with the regression method, and kriging is used for modelling regression residuals, such a model is called residual kriging (Hengl 2007). The decision scheme is based on Matheron's model and offers a possibility of application of one of the four interpolation methods at a general assumption of existence of a correlation between the modelled variable and environmental variables. The choice of an optimal method follows decisions that are taken in two steps. Initially, based on the goodness-of-fit of the model to the observations, the stationarity of the spatial process is assessed. The choice is made between the global, multiple linear regression (MLR) model dedicated to stationary processes, and the local, geographically weighted regression (GWR) model employed for non-stationary processes.

The global multiple linear regression MLR model can be expressed as the following equation:

$$\hat{m}\ (s_0) = \sum_{k=0}^{p} \hat{\beta}_k q_k(s_0), \tag{3}$$

where $\hat{\beta}_k$ are estimated regression coefficients ($\hat{\beta}_0$—estimated intercept and $q_k(s_0)$—explanatory variables). The explanatory variables were selected for the model with the stepwise regression method. The prerequisite for inclusion of a variable was its statistically significant ($p < 0.05$) correlation with the continentality index and the absence of collinearity with other explanatory variables determined by the variance inflation factor, VIF (VIF <10).

The strongest reservations concerning the MLR model in the context of spatial interpolation are that the possible local variations and non-constant spatial relation between the predictor and the estimated variable are ignored both during model calibration and in the prediction stage. These factors are considered in the geographically weighted regression model (Fotheringham et al. 2002). The validity of the application of this model for air temperature in Poland has been demonstrated by Szymanowski et al. (2012). When the GWR model is employed, the deterministic component of the spatial variability model will be expressed as the following equation:

$$\hat{m}(s_0) = \sum_{k=0}^{p} \hat{\beta}_k(s_0) q_k(s_0), \tag{4}$$

where $\hat{\beta}_k(s_0)$ are estimated regression coefficients in location s_0 and $q_k(s_0)$—explanatory variables. Estimation of regression parameters is performed locally using the weighted least-squares method. The schemes of weighing in GWR moving windows are developed in such a way that the weight would decrease with the distance between the estimation point and the data point. In this study, we used the bi-square function in adaptive kernels, whose value was selected on the basis of minimisation of the Akaike information criterion (AIC; Fotheringham et al. 2002). Exactly, the same auxiliary variables as in the MLR were used in the GWR model.

In practice, the decision concerning the choice of the regression model for approximation of the deterministic component of the universal model can be taken only on the basis of the degree of the goodness-of-fit of the model to the observation data. It was based on such measures of the fit as the adjusted coefficient of determination ($R^2_{\mathrm{adj.}}$), standard error of estimation (STE), corrected Akaike information criterion (AICc), and analysis of variance (ANOVA) for regression model residuals. ANOVA was used to check whether the improvement of the model fit, expressed as a decrease in the sum of squared residuals of the model, was statistically significant (Szymanowski and Kryza 2012).

The justification for the use of the GWR model instead of MLR was tested using two tests of the spatial variability of local geographically weighted regression coefficients, i.e., Monte Carlo implemented in the GWR3.0 software (Fotheringham et al. 2002) and the geographical variability (GV) test from the GWR4.0 software (Nakaya 2016). In the case of stationarity of any of the explanatory variables, it would be justified to apply a mixed GWR (MGWR) model instead of a fully local approach (Nakaya et al. 2005). The mixed models allow to mix in one model the explanatory variables which are spatially non-stationary (like for ordinary GWR) and the stationary predictors (like used in MLR). Calibration of the semiparametric GWR model was performed for comparison using the GWR4.0 software.

The other decision in the presented scheme of selection of an optimal interpolation method concerns the possibility of extending the model with a stochastic component, i.e., interpolation of regression model residuals with ordinary kriging. This procedure is employed when there is a significant spatial autocorrelation of regression residuals, which is a basis for modelling a variogram that is different from the pure nugget effect. If the pure nugget effect was the only variogram possible to fit to the experimental variogram of regression residuals, the deterministic model would be corrected at each studied point by an average of the residuals, which equals zero, in accordance with the assumptions of MLR as a best linear unbiased predictor (BLUP) model. In the GWR model, which does not meet the criterion of unbiasedness, the average of the residuals varies, although it is sufficiently close to zero (Fotheringham et al. 2002) to assume that the modification of prediction by residual kriging is negligible in the absence of autocorrelation (Fotheringham et al. 2002). Therefore, the absence of autocorrelation of the residuals excludes the extension of the MLR or GWR models into MLRK or GWRK, respectively (Szymanowski et al. 2012).

Spatial autocorrelation is a mathematical expression of spatial relationships described by Tobler's first law of geography (Tobler 1970), i.e., decreasing similarity of features of geographical objects along the increasing distance between them. It describes the degree of correlation of the variable value in one location with the value of the same variable in a different location, which implies that the values of the analysed variable determine and, concurrently, are determined by realisation of the variable in different locations. These relationships result in spatial clustering of similar values, which is referred to as positive autocorrelation. The value of the autocorrelation and its statistical significance was determined by calculating Moran's I statistics (Moran 1950).

The deterministic component residuals were modelled with ordinary kriging (Eq. 5):

$$\hat{e}(s_0) = \sum_{i=1}^{n} \lambda_i e(s_i), \tag{5}$$

where λ_i are kriging weights determined from the spatial dependence of the deterministic component residuals and $e(s_i)$—residual in position s_i. Hence, the full model of residual kriging based on the global regression MLRK model (Eqs. 2, 3, 5) can be expressed as the following equation:

$$\hat{z}(s_0) = \hat{m}(s_0) + \hat{e}(s_0) = \sum_{k=0}^{p} \hat{\beta}_k q_k(s_0) + \sum_{i=1}^{n} \lambda_i e(s_i), \tag{6}$$

whereas residual kriging based on the geographically weighted regression (GWR) model (Eqs. 2, 4, 5) can be expressed as the following equation:

$$\begin{aligned}\hat{z}(s_0) &= \hat{m}(s_0) + \hat{e}(s_0)\\ &= \sum_{k=0}^{p} \hat{\beta}_k(s_0) q_k(s_0) + \sum_{i=1}^{n} \lambda_i e(s_i).\end{aligned} \tag{7}$$

Modelling of variograms of the regression residuals was carried out using automated fitting procedure in ArcGIS Geostatistical Analyst. This approach is based on the Levenberg–Marquardt method (Press et al. 1988) of non-linear least-squares approximation. The choice between candidate variogram models (spherical, circular, and exponential) was done basing on the fit quality, using the criterion of the lowest root-mean-squared error (RMSE). To avoid inconsistencies on the edges of local neighbours' search area and subsequent artificial tearing of continuity of interpolated variable, global settings were used to specify kriging models, i.e., all data points were considered in determination of the weights at any interpolation point.

Due to the limited 111-element input data set, the quantification of the modelling results was performed using the leave-one-out cross-validation (CV) technique. It yielded a 111-element set of CV errors, which were used in the validation of the model in two ways. The values of the summary diagnostic measures were calculated and analysis of the spatial distribution of the CV errors was carried out, particularly in terms of systematic local and regional trends.

Three synthetic measures, i.e., mean error (ME), mean absolute error (MAE), and RMSE, were used in the analysis of the CV errors. The relationship between the sizes of the aforementioned errors can be defined as ME $\leq$ MAE $\leq$ RMSE, with the two latter measures having only non-negative values with the predicted zero value. The use of the square of the CV errors in the RMSE index makes the measure substantially biased even by an inconsiderable number of large errors, although the other errors may be small and acceptable. According to some researchers, MAE is regarded as the most natural diagnostic measure (Willmott and Matsuura 1995).

Since the differences in the MAE of CV errors may be negligible in the compared methods, the decision as to whether any of the methods yielded significant improvement, i.e., has a significantly lower MAE, was made by comparison of MAE $\pm\ \hat{\sigma}_{\mathrm{MAE}}$ intervals, where $\hat{\sigma}_{\mathrm{MAE}}$ was a MAE calculation error. Assuming that the mean μ of CV errors is $\mu_{\mathrm{CV}} \cong 0$, and $\hat{\sigma}_{\mathrm{MAE}}$ for an n element set with standard deviation σ_{CV} can be calculated with the formula (Kalarus et al. 2010; Eq. 8):

$$\hat{\sigma}_{\mathrm{MAE}} = \frac{\sigma_{\mathrm{CV}}}{\sqrt{\mathrm{nc}}}, \quad c = \frac{\pi}{\pi - 2}. \tag{8}$$

Therefore, if the MAE $\pm\ \hat{\sigma}_{\mathrm{MAE}}$ intervals for the two methods are disjoint, the method with a smaller MAE can be considered better. If, however, the analysed intervals have a certain common range, this statement is not justified.

The quantitative analysis of the model was also accompanied by visual evaluation, which by definition serves identification of features of the model that cannot be shown by methods based on the actual values of the interpolated variable. In particular, it facilitates detection of such little realistic effects as spatial discontinuity, unusually large or small values of the modelled variable, strong directional or regional trends, and various artefacts illustrating the characteristics of the interpolation algorithm rather than those of the interpolated variable. Although it is based on the expert knowledge of the modelled element, such validation is subjective and only complementary to quantitative evaluation.

A number of various computer programs were used in the study, both commercial packages and free software. The spatial analyses primarily concerning the structure of the layers of the explanatory variables and spatial interpolation as well as the final maps were generated in the ArcGIS and GIS GRASS software. The analysis of stepwise regression and the global model was carried out in the STATISTICA program, and the complementary analyses of geographically weighted regression (ANOVA, non-stationarity tests, calibration o semiparametric GWR model) were performed using the GWR3.0 (Fotheringham et al. 2002) and GWR4.0 (Nakaya 2016) packages. For cross validation, the R scripts were developed, using gstat and spgwr packages.

4. Results and Discussion

4.1. Ewert's Index Spatial Predictors

The specification of the multiple linear regression (MLR) model using the stepwise method showed that only four environmental variables in the five analysed cases significantly determined the value of Ewert's index: coordinates (*X* and *Y*), elevation (DEM), and the distance from the sea (SDI; Table 2). These variables indicate the global nature of the determinants of the continentality index distribution. It should be stressed that variables combining global and local factors, such as insolation (IT), regional factors, such as the foehn index (FI), or local factors reflecting the effect of the terrain relief (CCI) or land cover (AS, NS), were not introduced into the model in any of the analysed cases. These variables were, therefore, not correlated significantly with the continentality index based on air temperature amplitude, although they often proved to be significantly correlated with air temperature alone (Szymanowski et al. 2012, 2013). This may have been caused by the fact that the input data for the analysis presented in this paper were only obtained from synoptic stations that, in accordance with the WMO guidelines, had been located in a way to minimise local impacts; no data from climatological stations were available in the study.

Table 2

Explanatory variables and standardized regression coefficients in multiple linear regression (MLR) models of Ewert's index of continentality (K) for the four selected years and the 1981–2010 average (descriptions of variables in the text)

Model parameter (in the order of significance)	Standardized coefficients	*P* value
K_{1989}		
SDI	0.753	0.000
DEM	−0.612	0.000
X	0.121	0.050
K_{1990}		
Y	−0.956	0.000
DEM	−0.359	0.000
K_{2002}		
X	0.725	0.000
DEM	−0.569	0.000
SDI	0.101	0.014
K_{2006}		
DEM	−0.525	0.000
X	0.323	0.000
$K_{1981–2010}$		
SDI	0.754	0.000
DEM	−0.576	0.000
X	0.363	0.000

DEM elevation, *SDI* sea distance index, *X* easting coordinate, *Y* northing coordinate

Each time, a maximum of three variables was introduced into one model, and only elevation was included in all the five models. This is related to the expected decline in the temperature amplitude together with elevation. Variable *X* describing the rate of change in the east–west orientation was introduced four times, except for the index calculated for 1990 (Table 2). Similarly, one of the variables characterising the zonal distribution of Ewert's index, *Y*, or SDI was introduced in four cases. Importantly, in none of the models, do these variables appear simultaneously. In the geographical conditions of Poland with the Baltic Sea in the north of the country, and given arrangement of meteorological stations, variable *Y* (northing) and the sea distance index SDI are correlated, and hence, only one of them was introduced into the regression model even if both were significantly correlated with the continentality index (SDI—3 times, *Y*—1 time; Table 2). There was no significant correlation with one of the zonal variables *Y* or SDI only in 2006.

Table 3

Selected statistics of multiple linear regression (MLR), geographically weighted regression (GWR), and mixed geographically weighted regression (MGWR) models of Ewert's index of continentality (K) for the four selected years and the 1981–2010 average

Regression model	Auxiliary variables (in the order of significance)	Bandwidth size	Adjusted R^2	Corrected Akaike information criterion (AICc)	Standard error of estimation (STE)
K_{1989}					
MLR	SDI, DEM, X	–	0.66	586.36	3.33
GWR		65	0.77	550.19	2.74
MGWR		65	0.77	549.32	2.74
K_{1990}					
MLR	Y, DEM	–	0.76	510.86	2.38
GWR		48	0.84	472.13	1.92
K_{2002}					
MLR	X, DEM, SDI	–	0.87	566.53	3.05
GWR		65	0.91	538.4	2.59
MGWR		65	0.91	537.07	2.59
K_{2006}					
MLR	DEM, X	–	0.37	684.13	5.20
GWR		32	0.75	596.74	3.27
$K_{1981\text{–}2010}$					
MLR	SDI, DEM, X	–	0.90	427.45	1.63
GWR		65	0.91	538.4	2.59

DEM elevation, *SDI* sea distance index, *X* easting coordinate, *Y* northing coordinate

The values of standardized regression coefficients indicate a varying impact of the environmental variables on the individual cases, which concurrently imply significant differences in the distribution of the continentality index. The sign of the coefficients identifies the direction of the relationships: in general, Ewert's index of continentality decreases together with the terrain elevation and northwards and increases along the distance from the sea and eastwards (Table 2).

4.2. Regression Models

Global regression model (MLR) explains over 66 % of the Ewert's index variability in four analysed cases (Table 3). The coefficient of determination was as low as 0.37 only for 2006. The model for the 1981–2010 average was the best fitted one ($R^2_{\text{adj.}} = 0.90$) with a 1.63 % standard error of estimation. In the poorest fitted model for 2006, STE was found to be 5.20 %.

Local geographically weighted regression models (GWR) for all the cases were characterised by a better fit to the observations. The highest increase in the coefficient of determination was found for 2006: from 0.37 for MLR to 0.75 for GWR. In the other cases, there was an increase in the explanation of the variance of Ewert's index from +2 % for the multi-year average to +11 % for 1989. Increase in explained variance was accompanied by a simultaneous decrease in the STE value and a significant (>3) reduction in the Akaike information criterion (AICc, Table 3). The ANOVA analysis indicated a statistically significant decrease in the residual sum of squares of the GWR models, compared with MLR (Table 4).

The Monte Carlo and geographical variability (GV) tests for spatial non-stationarity indicated possible spatial stationarity of the DEM variable GWR coefficients in two cases: for 1989 (GV test only) and 2002 (both tests, but the result of the GV test was not significant at 0.05; Table 5).

The mixed MGWR models for the two cases considered were characterised by a slightly lower residual sum of squares than the GWR models (Table 4). However, the coefficients of determination and estimation errors were similar to the GWR model, and AICc did not indicate a significant improvement in the fit to the observations (Table 3).

Table 4

ANOVA of multiple linear regression (MLR), geographically weighted regression (GWR), and mixed geographically weighted regression (MGWR) models of Ewert's index of continentality (K) for the four selected years and the 1981–2010 average

Source	K_{1989} Sum of squares	K_{1990}	K_{2002}	K_{2006}	$K_{1981–2010}$
MLR residuals	1186.5	612.8	992.3	2918.9	283.5
GWR residuals	733.3	353.1	659.6	945.9	195.0
GWR improvement	453.2	259.7	332.7	1972.9	88.5
MGWR residuals	748.4	–	670.2	–	–
MGWR improvement	438.1	–	322.1	–	–

The analysis presented in this section shows a better fit of the local GWR regression model than that of the global MLR model. This suggests the non-stationarity of the spatial process in each analysed case of the spatial distribution of Ewert's index of continentality. No significant difference between the GWR and mixed MGWR models was found either. Thus, accordingly to Occam's razor principle, where simpler models are preferable to more complex ones, because they are better testable and falsifiable, simpler GWR model was used for further analysis.

4.3. Residual Kriging Models

Extension of the regression models to the form of residual kriging was preceded by an analysis of the spatial autocorrelation of the regression residuals. Moran's I statistics showed a statistically significant positive autocorrelation, i.e., clustering of similar values of residuals, for all the MLR models (Table 6). For the GWR residuals, a tendency towards clustering of similar values was observed in four cases, but the autocorrelation was not significant at the 0.05 level. In the case of year 2002, a random distribution of the GWR residuals, i.e., the absence of autocorrelation, was observed (Table 6).

Here, as in the previous studies (Szymanowski et al. 2012, 2013), an exclusion criterion was used, i.e., the absence of a significant (<0.05) positive autocorrelation prevented correct fitting of the theoretical variogram different from the pure nugget effect. Thus, according to none significant autocorrelation of all GWR residuals (Table 6), variogram modelling was performed only for MLR residuals (Table 7). In all the cases, the spherical model was the best fitted (lowest or at least the same RMSE) while comparing to exponential and circular ones (Table 7).

4.4. Cross-Validation Results

The diagnostic measures of CV errors of the continentality index for Polish synoptic stations are presented in Table 8. Summary statistics were calculated for the two regression models (MLR and GWR) and one residual kriging model (MLRK). The choice of the model that would be optimal considering cross-validation results was made based on ME, MAE, and RMSE measures and extreme errors (Table 8). MAE was regarded as the main measure in this case, since it facilitated assessment of the statistically significant difference between the error sizes and, consequently, identification of significant improvement provided by the model with lower MAE values. This is particularly important, as the differences in the diagnostic measures, including MAE, are often inconsiderable, particularly when similar categories of models, e.g., regression or residual kriging, are compared (Table 8).

The better fit of the GWR models, comparing with MLR, was also confirmed by cross validation. In general, the GWR model was characterised by better CV summary statistics in each analysed case. This did not imply that the model was better in terms of all the five measures employed. Sometimes, the ME or one of the extreme errors was closer to zero in MLR than in GWR. However, the MAE and RMSE for GWR were always lower than for MLR. Importantly, GWR was characterised by a significantly lower MAE only in 2006 (Table 8).

Table 5

Local parameter variability tests for geographically weighted regression (GWR) models of Ewert's index of continentality (K) for the four selected years and the 1981–2010 average

GWR model parameter	Monte Carlo test (GWR3.0 software) *p* value	Geographical variability test (GWR4 software) difference of criterion
K_{1989}		
Intercept	0.000	−6.234
DEM	0.020	**0.874**
SDI	0.000	−29.289
X	0.000	−10.570
K_{1990}		
Intercept	0.000	−15.714
DEM	0.000	−0.843
Y	0.000	−24.766
K_{2002}		
Intercept	0.000	−6.920
DEM	**0.140***	**1.363***
SDI	0.000	−28.086
X	0.000	−16.900
K_{2006}		
Intercept	0.000	−0.305
DEM	0.000	−5.312
X	0.000	−22.551
$K_{1981-2010}$		
Intercept	0.000	−12.387
DEM	0.000	−0.286
SDI	0.000	−14.413
X	0.000	−11.086

* Not significant at 0.05; bold numbers suggest no spatial variability

Table 6

Spatial autocorrelation of multiple linear regression (MLR) and geographically weighted regression (GWR) residuals of Ewert's index of continentality (K) for the four selected years and the 1981–2010 average

Model	Moran's I statistics $E(I) = -0.009$	*p* value
K_{1989}		
MLR	0.380	0.000
GWR	0.083	0.145*
K_{1990}		
MLR	0.357	0.000
GWR	0.049	0.357*
K_{2002}		
MLR	0.244	0.000
GWR	−0.019	0.870*
K_{2006}		
MLR	0.585	0.000
GWR	0.098	0.095*
$K_{1981-2010}$		
MLR	0.313	0.000
GWR	0.078	0.165*

* Not significant at 0.05

The absence of autocorrelation of GWR residuals limits the model of spatial variation only to explanation of the deterministic component. Thus, even if the fit of the GWR model is significantly better than that of MLR (as in the case of 2006; Table 3), GWRK is not effective when regression residuals are randomly distributed. Paradoxically, this may imply that a better fitted deterministic model does not necessarily guarantee better spatial interpolation. Consequently, the scheme of the optimal interpolator selection applied so far (Szymanowski et al. 2012, 2013) requires revision, so that it will consider the above-mentioned possibility of the absence of autocorrelation of GWR residuals accompanied by a significant positive autocorrelation of MLR residuals (Fig. 2). Therefore, a question arises whether a reverse situation, i.e., the absence of autocorrelation of MLR residuals accompanied by a significant positive autocorrelation of GWR residuals, should be considered in such scheme. Such situation is highly unlikely, since it would have to result from a better fit of the MLR than the GWR model. In fact, MLR can be regarded as a special case of GWR with the constant weight along the distance and all observation data points used for model calibration. This implies that the GWR model may work better or be comparable to MLR, but the reverse situation should be rather excluded. Thus, such option is not included in the proposed selection tree (Fig. 2).

In all the analysed cases, the MLRK models have smaller errors than both the regression models. Moreover, due to MAE criterion, MLRK was significantly different from MLR and GWR, so it can be assumed the optimal spatial interpolation algorithm. To confirm the choice, an additional visual assessment of maps of the continentality index was carried out.

4.5. Maps of Ewert's Index of Continentality

To present the characteristics and differences between the maps generated with the three spatial models analysed, two cases were selected, i.e., the

Table 7

Variogram fitting evaluation and parameters of spherical variograms of multiple linear regression (MLR) residuals of Ewert's index of continentality (K) for the four selected years and the 1981–2010 average

Variogram model fitting—RMSE			Spherical model parameters		
Spherical	Circular	Exponential	Partial sill	Range	Nugget
K_{1989}					
2.61	2.62	2.66	5.3279	382,579	5.9659
K_{1990}					
2.34	2.34	2.34	2.3679	870,121	4.0273
K_{2002}					
2.69	2.70	2.72	3.0954	709,466	6.7452
K_{2006}					
2.83	2.83	2.96	23.618	380,159	5.1770
$K_{1981–2010}$					
1.43	1.44	1.44	0.29,026	500,120	2.3367

years 2002 and 2006. Due to the large range and considerable variability of the index (Table 1), these were the most demanding cases in terms of spatial interpolation of the analysed data set. This was also reflected in the largest cross-validation errors (Table 8).

The largest differences between the fit of the MLR and GWR models were found for 2006 (Table 3). This was clearly reflected on maps generated with these two methods (Fig. 3a, b). The DEM and X variables included in the MLR model are responsible for the overall decrease in the index with elevation and an increase eastwards. The process, however, is highly non-stationary (Table 5) and the model significantly overestimates the values obtained on the Baltic Sea coast and underestimates the values from the rest of the country (Fig. 3a). The considerably better fitted GWR model substantially increases the value of the index in the central part of the country and slightly decreases it on the coast, contributing to the reduction of the CV errors size. The general tendency towards overestimation is still visible in the northern part of Poland (Fig. 3b). The map generated using the GWR method clearly emphasises the role of terrain relief, particularly in the northern part of the country. This is related to the small kernel bandwidth (32 points), i.e., the smallest of all the analysed cases (Table 3), which can locally emphasise the effect of the explanatory variable. The correction introduced by the geostatistical component is significant in the MLRK model (Fig. 3c) which can be regarded as optimal in this case.

In the case of 2002, although the improvement of the fit introduced by the GWR model compared with MLR is statistically significant (Table 4), the maps of Ewert's index do not show significant differences, the spatial distribution and size of the CV errors are similar (Fig. 4a, b), and the MAE criterion does not indicate a significant difference between the methods. All three models for 2002 exhibit a poor local fit to the observations in the central-northern part of the country (Fig. 4). Despite this limitation, MLRK, which is statistically significantly better than MLR and GWR in terms of the MAE criterion, can be regarded as an optimal model for 2002 (Table 8).

In the other analysed cases, MLRK were also regarded as optimal models. This supported the conclusions drawn from the analysis of the cross-validation errors also confirming the necessity of introduction of a modified scheme of selection of an optimal predictor (Fig. 2).

The differences in the size, range, and variation of Ewert's index indicated in the observations (Table 1) were also reflected on the maps (Fig. 5). The spatial distribution of the 1981–2010 multi-year average is characterised by a distinct upward trend from NW to SE with a clearly decreased value of the index in the top parts of the highest mountains. This is particularly visible in the western part of the Sudetes, SW Poland (Fig. 5a).

Table 8

Summary statistics of cross-validation (CV) errors for multiple linear regression (MLR), geographically weighted regression (GWR), and multiple linear regression—kriging (MLRK) models of Ewert's index of continentality (K) for the four selected years and the 1981–2010 average

Statistics	MLR	GWR	MLRK
K_{1989}			
ME	1.080	1.068	0.408
MAE	2.180 (1.991 ÷ 2.369)	2.065 (1.893 ÷ 2.237)	1.109 (1.000 ÷ 1.218)
RMSE	2.526	2.385	1.400
MIN	−4.054	−3.254	−2.520
MAX	5.504	5.117	3.690
K_{1990}			
ME	1.010	0.862	0.434
MAE	1.797 (1.652 ÷ 1.942)	1.739 (1.599 ÷ 1.879)	1.399 (1.275 ÷ 1.523)
RMSE	2.111	2.018	1.660
MIN	−3.452	−2.977	−2.631
MAX	4.341	4.135	3.649
K_{2002}			
ME	−0.479	−0.518	−0.111
MAE	2.158 (1.938 ÷ 2.378)	2.071 (1.866 ÷ 2.276)	1.819 (1.621 ÷ 2.017)
RMSE	2.982	2.848	2.690
MIN	−5.582	−6.134	−7.992
MAX	9.654	8.956	8.496
K_{2006}			
ME	−2.989	−2.171	−0.442
MAE	5.078 (4.727 ÷ 5.429)	4.317 (3.998 ÷ 4.636)	1.645 (1.500 ÷ 1.790)
RMSE	5.748	5.044	2.107
MIN	−9.414	−7.551	−5.536
MAX	10.631	11.024	6.357
$K_{1981-2010}$			
ME	0.341	0.323	0.243
MAE	1.331 (1.223 ÷ 1.439)	1.285 (1.182 ÷ 1.388)	1.118 (1.025 ÷ 1.211)
RMSE	1.608	1.565	1.398
MIN	−3.233	−2.975	−2.557
MAX	3.353	3.598	3.664

ME mean error, *MAE* mean absolute error, *RMSE* root-mean-square error, *MIN* minimum, *MAX* maximum; in brackets—*MAE* error range (description in the text)

Although discussion of the reasons for this situation lies beyond the scope of this paper, it should be noted that the differences in the distribution between the individual years in relation to the averaged field are significant. In 1990, there was a pronounced zonal trend in the distribution of the continentality index; in 2002, the distribution was longitudinal, and in 2006, high values of the continentality index covered large areas of the central Poland (Fig. 5). Such strong variability of the index distribution may indicate its analytical usefulness as a complementary indicator of macro- and mesoscale atmospheric processes.

5. *Summary and Conclusions*

The primary aim of the paper was to perform spatial interpolation and to generate maps of Ewert's index of continentality in Poland for the selected years and an average from the period 1981–2010. The main emphasis was placed on the methodological side of spatial interpolation to develop guidelines for automation of the interpolation process.

Additional objective was to test, on the example of Ewert's index, the validity of the scheme of selection of an optimal interpolation method developed by Szymanowski et al. (2012, 2013) for

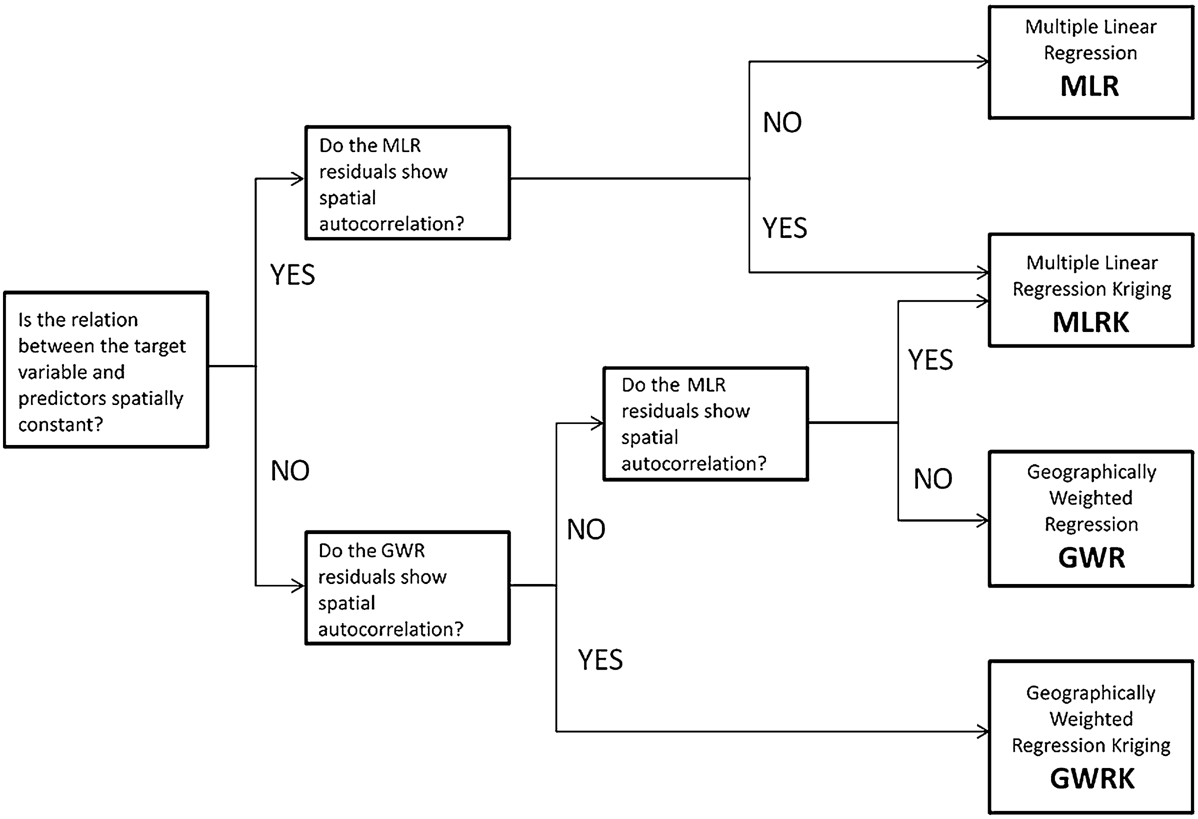

Figure 2
Decision tree for selecting a suitable spatial prediction model under the assumption of existing environmental correlations (after Szymanowski et al. 2012, 2013, extended)

spatialization of air temperature. An optimal method was yielding the smallest errors and simultaneously allowing generation of an acceptable map on the basis of expert knowledge about the spatial characteristics of the interpolated variable.

The continentality index for the period 1981–2010 was calculated based on the daily data from 111 meteorological stations. Four years (1989, 1990, 2002, and 2006) characterised by extreme values of the areal average and index range were selected for the analysis. The set of analysed cases was complemented with the mean value of Ewert's index for the multi-year period 1981–2010.

The set of potential predictors of the continentality index comprised nine environmental variables previously used for spatial interpolation of air temperature in Poland (Szymanowski et al. 2012, 2013). However, the stepwise regression analysis demonstrated that only four variables in the analysed cases exhibited a significant correlation with Ewert's index, i.e., coordinates X and Y, elevation, and the distance from the sea. Regional or local variables were not significantly correlated with the index, which implies that the features of the continentality index field are mainly determined by macroscale and regional factors (distance from the Baltic Sea) with modification depending on terrain elevation. Noteworthy, the analysis was performed on the basis of the index calculated for the synoptic stations; the location of which, by definition, minimises the local impacts on climate elements. Data from lower-rank, climatological stations, where the impact may be more significant, were not included.

The correlation analysis performed to eliminate collinearity in the regression model additionally showed that variables Y (northing) and SDI were

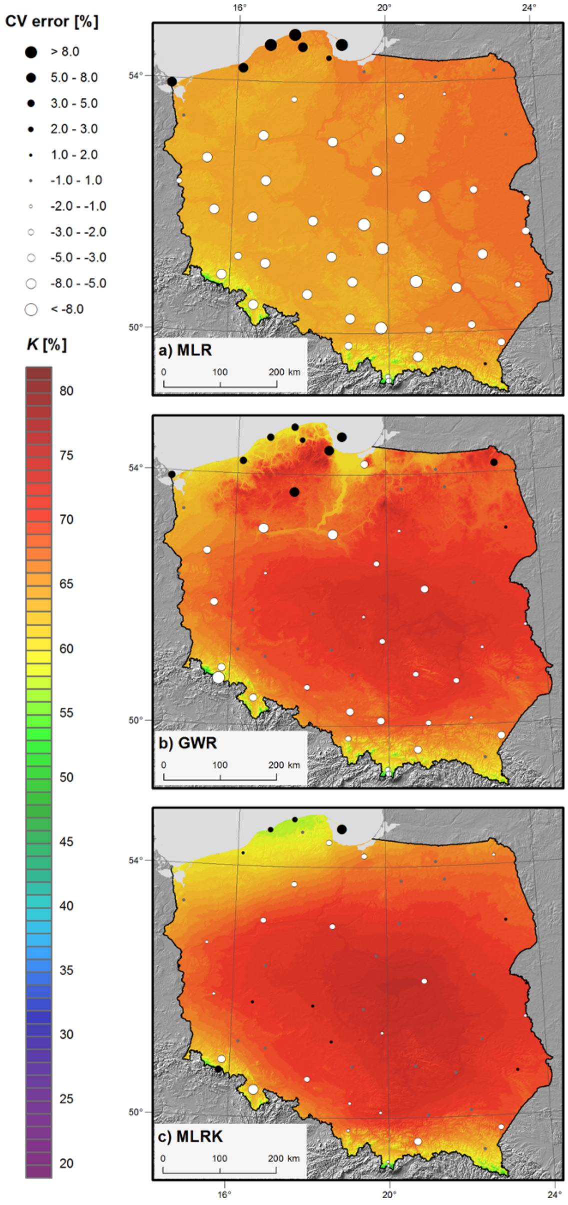

Figure 3
Ewert's index of continentality (K) in Poland in 2006 spatialized using selected interpolation methods

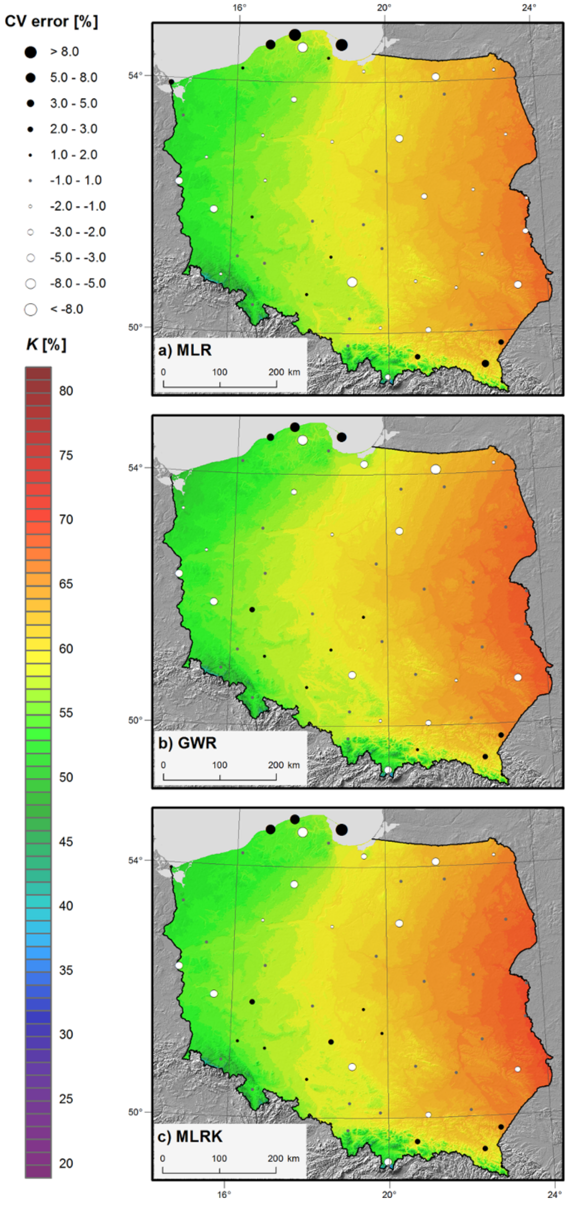

Figure 4
Ewert's index of continentality (K) in Poland in 2002 spatialized using selected interpolation methods

correlated in the geographical conditions of Poland and considering given set of meteorological station. Therefore, only one of them was included in the multiple linear regression MLR model (SDI—3 times, *Y*—1 time). The elevation variable was included in the models of each of the five cases, although this does not mean that its role was dominant. In fact, the role of the explanatory variables in the regression models varied between the cases, which indicates significant changes in the determinants and, hence, variable features of the Ewert's index distribution. The general regularities of the distribution allow a conclusion that the continentality index for Poland decreases with elevation and northwards and increases along the distance from the sea and eastwards, which is also supported by

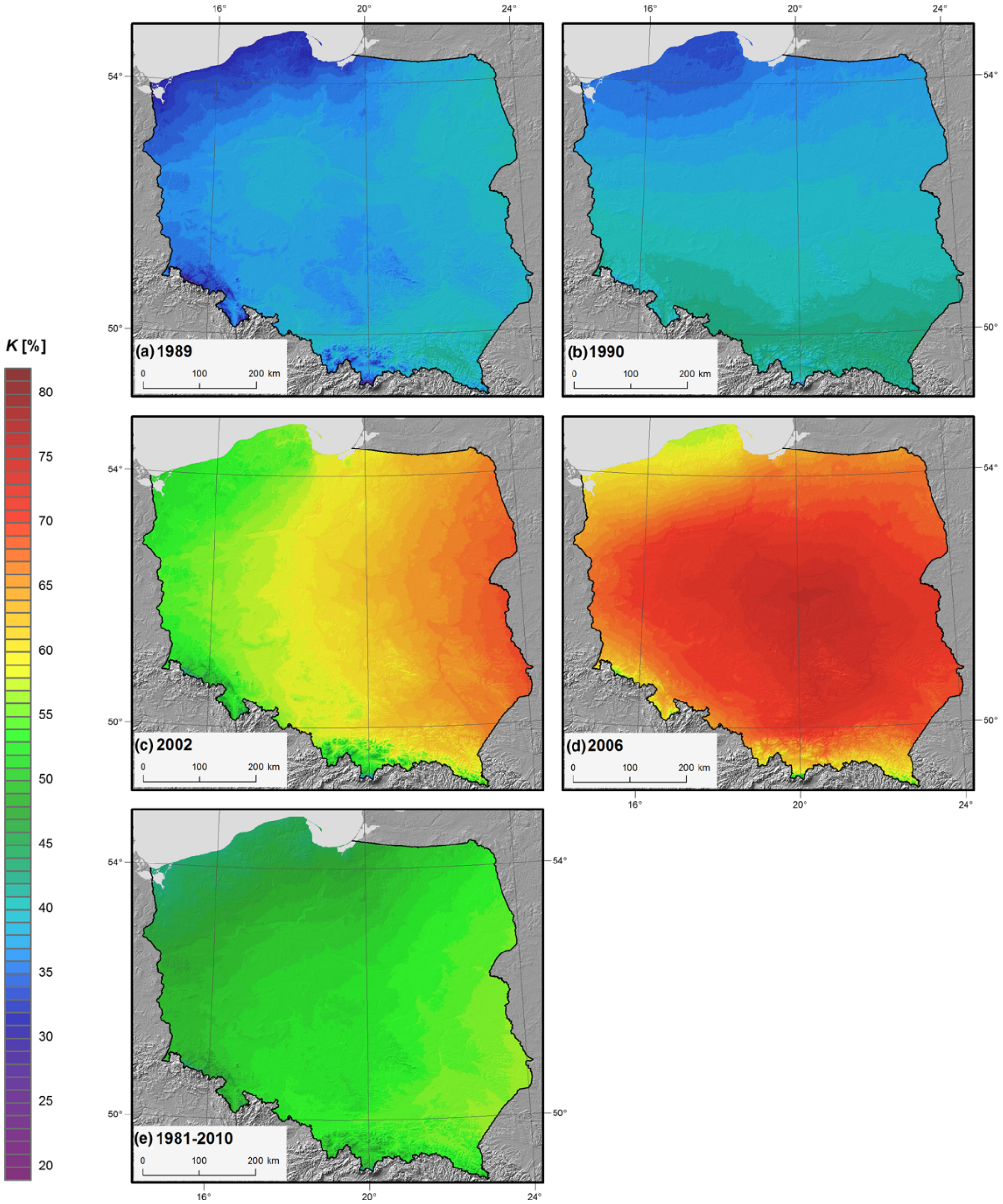

Figure 5
Maps of Ewert's index of continentality in Poland for the four selected years and the 1981–2010 average

the previous studies (Kożuchowski and Marciniak 1992).

The environmental correlation for each of the analysed cases was statistically significant, although for 2006, the MLR model explained solely 37 % of the Ewert's index variation. In each case, the local GWR model was better fitted to the observations and it significantly improved the MLR regression results. The tests of the spatial variability of the GWR regression coefficients indicated their stationarity. However, compared with the GWR, the use of mixed local–global regression models (MGWR) did not significantly improve the fit.

The residuals of the MLR models were characterised by a positive spatial autocorrelation, which clearly justified extension of the model to the form of residual kriging, MLRK. In contrast, no statistically significant autocorrelation was found in any case of GWR, so the GWRK model was excluded from further considerations.

The cross validation was carried out for three models of each case of Ewert's index. The local GWR model was characterised by smaller errors. In terms of the MAE criterion, MLR was found to be statistically significantly worse than GWR only for 2006. CV carried out for residual kriging models clearly indicated that the MLRK models produced smaller errors than both regression models. However, the specification of GWRK was not justified and gave grounds for modification of the scheme of optimal interpolator selection in the presence of the environmental correlation. The modified scheme of Szymanowski et al. (2013) now allows a situation where the absence of an autocorrelation of GWR residuals is accompanied by an autocorrelation of MLR residuals, which indicates that MLRK is an optimal method, even if GWR is better fitted to observations than MLR.

The visual assessment of the maps confirmed the results of the cross validation and the MAE criterion. The MLRK model is recommended to spatialize the Ewert's index for Poland.

Based on the results obtained, it can be postulated that the following elements should be considered in the procedure of automation of the interpolation of the continentality index for Poland:

- Regression models should be specified using four potential predictors: coordinates (X, Y), elevation (DEM), and distance from the sea (SDI).
- The decision concerning selection of the interpolator should in each case be based on the proposed scheme (Fig. 2), including comparison of the fit of the regression models to observations by, e.g., comparing the coefficient of determination and autocorrelation regression residuals using Moran's I statistics.
- For autocorrelated residuals, the automatic fitting of the variogram can be done using the spherical model.

In the previous papers (Szymanowski and Kryza 2012; Szymanowski et al. 2012, 2013), it was assumed that the choice of an optimal interpolation method was determined by the stationarity or non-stationarity of the spatial process, which could be inferred from the better fit of one of the regression models, i.e., global or local. The results obtained in this study demonstrated greater importance of the geostatistical component in the universal model of spatial variation (Hengl 2007). Residual kriging is highly efficient if regression residues exhibit a strong positive autocorrelation contributing to the well fit of the theoretical variogram to the experimental one. This does not imply, however, a possibility of exclusion of the deterministic component if the environmental correlation is significant. Although this would lead to maintenance of the good fit of the model to observation in measurement points, the spatial distribution of the index would simultaneously "diverge" from environmental features beyond these points.

REFERENCES

Bailey, H. (1968). Hourly temperatures and annual range. *Yearb. Assoc. Pac. Coast Geogr., 32*, 25–40.

Berg, H. (1944). Zum Begriff der Kontinentalitat. *Meteorologische Zeitschrift, 61*, 283–284.

Caccianiga, M., Andreis, C., Armiraglio, S., Leonelli, G., Pelfini, M., & Sala, D. (2008). Climate continentality and treeline species distribution in the Alps. *Plant Biosyst., 142*, 66–78.

Conrad, V. (1946). Usual formulas of continentality and their limits of validity, Eos T. *American Geophysical Union, 27*, 663–664.

Conrad, V., & Pollak, L. W. (1950). *Methods in climatology* (2nd ed.). Cambridge: Harvard University Press.

CORINE Land Cover 2000 in Poland. (2004). Final Report, Warsaw. http://www.igik.edu.pl/images/stories/sip/clc_final_report_pl.pdf. Accessed Aug 2012.

COST Action 719 Final Report. (2008). In O. E. Tveito, M. Wegehenkel, F. van der Wel, & H. Dobesch (Eds.), *The use of geographic information systems in climatology and meteorology*. Luxembourg: Office for Official Publications of the European Communities.

USGS Land Cover (2011). http://landcover.usgs.gov/usgslandcover.php. Accessed Mar 2011.

Dobesch, H., Dumolard, P., & Dyras, I. (Eds.). (2007). *Spatial interpolation for climate data: The use of GIS in climatology and meteorology*. London: ISTE Ltd.

Driscoll, D. M., & Yee Fong, J. M. (1992). Continentality: A basic parameter re-examined. *International Journal of Climatology, 12*, 185–192.

Ewert, A. (1963). Kontynentalizm termiczny klimatu. *Przegl. Geofiz. XVI, 3*, 143–150.

Ewert, A. (1972). O obliczaniu kontynentalizmu termicznego klimatu. *Przegl. Geogr. XLIV, 2*, 273–286.

Fotheringham, A. S., Brunsdon, C., & Charlton, M. (2002). *Geographically weighted regression: The analysis of spatially varying relationships*. Chichester: Wiley.

Gorczyński, W. (1920). Sur le Calcul du Degré du Continentalisme et son Application dans la Climatologie. *Geografiska Annaler, 2*, 324–331.

Johansson, O. V. (1926). Über die Asymmetrie der Meteorologische Schwankungen, *Societas Scientiarum Fennica Communications in Mathematical Physics*, 3 I, Helsingfors, 124.

Matheron, G. (1971). The theory of regionalised variables and its applications (Les Cahiers du Centre de Morphologie Mathematique de Fontainebleau, 5. Ecole Nationale Superieure' des Mines de Paris).

GRASS Development Team. (2011). Geographic resources analysis support system (GRASS) Software, Version 6.4.0. Open Source Geospatial Foundation. http://grass.osgeo.org.

Hela, I. (1953). Regional distribution of the continentality in the climate of the oceans. *Geophysica, 4*, 41–47.

Hengl, T. (2007). *A practical guide to geostatistical mapping of environmental variables*. Luxembourg: Office for Official Publications of the European Communities.

Hogewind, F., & Bissolli, P. (2011). Operational maps of monthly mean temperature for WMO Region VI (Europe and Middle East). *Idojaras, 115*, 31–49.

Holmlund, P., & Schneider, T. (1997). The effect of continentality on glacier response and mass balance. *Annals of Glaciology, 24*, 272–276.

Ivanov, N. (1953). Ob opredelenyi welichyny kontinentalnosti klimata, Izv. Vses. Geogr. Obshch, *85*.

Ivanov, N. (1959). Belts of continentality on the globe. *Izv Vses Geogr Obshch, 91*, 410–423.

Kalarus, M., Schuh, H., Kosek, W., Akyilmaz, O., Bizouard, C., Gambis, D., et al. (2010). Achievements of the Earth orientation parameters prediction comparison campaign. *Journal of Geodesy, 84*, 587–596.

Khromov, S. P. (1957). K voprosu o kontinentalnosti klimata, Izv. Vses. Geogr. Obshch. *89.*

Kożuchowski, K. (2003). Cyrkulacyjne czynniki klimatu Polski. *Czasopismo Geograficzne, LXXIV, 1–2*, 93–105.

Kożuchowski, K. (2011). *Klimat Polski. Nowe Spojrzenie*. Warszawa: Wydawnictwo Naukowe PWN.

Kożuchowski, K., & Marciniak, K. (1986). Fluktuacje kontynentalizmu klimatu Polski na tle warunków cyrkulacyjnych i solarnych (1881–1980). *Przegląd Geofizyczny, 31*(39), 139–152.

Kożuchowski, K., & Marciniak, K. (1992). Kontynentalizm termiczny klimatu na obszarze Polski, Wiad. IMGW XV(XXXVI), *4*, 89–93.

Kożuchowski, K., & Wibig, J. (1988). Kontynentalizm pluwialny w Polsce: Zróżnicowanie geograficzne i zmiany wieloletnie. *Acta Geographica Lodziensia, 55*, 102.

Kryza, M., Szymanowski, M., Migała, K., & Pietras, M. (2010). Spatial information on total solar radiation: Application and evaluation of the r.sun model for the Wedel Jarlsberg Land, Svalbard, Pol. *Polar Research, 31*(1), 17–32.

Li, J., & Heap, A. D. (2008). *A review of spatial interpolation methods for environmental scientists*. Canberra: Geoscience Australia.

Marti, P., & Gasque, M. (2010). Ancillary data supply strategies for improvement of temperature-based ET_o ANN models. *Agricultural Water Management, 97*, 939–955.

Mikolášková, K. (2009). A regression evaluation of thermal continentality, Geografie—Sbornik České Geografické Společnosti, *114*(4), 350–362.

Moran, P. A. P. (1950). Notes on continuous stochastic phenomena. *Biometrika, 37*(1), 17–23.

Nakaya, T. (2016). GWR4 User Manual. GWR 4 Windows Application for Geographically Weighted Regression Modelling, GWR4 Development Team. https://raw.githubusercontent.com/gwrtools/gwr4/master/GWR4manual_409.pdf.

Nakaya, T., Fotheringham, A. S., Brunsdon, C., & Charlton, M. (2005). Geographically weighted Poisson regression for disease associative mapping. *Statistics in Medicine, 24*, 2695–2717.

Oliver, J. (1970). An air mass evaluation of the concept of continentality. *The Professional Geographer, 22*, 83–87.

Press, W. H., Teukolsky, S. A., Vetterling, W. T., & Flannery, B. P. (1988). *Numerical recipes in C, the art of scientific computing*. New York: Cambridge University Press.

Raunio, N. (1948). The effect of local factors on meteorological observations at Tórshavn. *Geophysica, 3*, 173–179.

Salonen, J. S., Seppä, H., Luoto, M., Bjune, A. E., & Birks, H. J. B. (2012). A North European pollen—climate calibration set: Analysing the climatic responses of a biological proxy using novel regression tree methods. *Quaternary Science Reviews, 45*, 95–110.

Spitaler, R. (1922). Klimatische Kontinentalität und Ozeanität. *Petermann's Geographische Mitteilungen, 68*, 113.

Šuri, M., & Hofierka, J. (2004). A new GIS-based solar radiation model and its application to photovoltaic assessments. *Transactions in GIS, 8*, 175–190.

Swoboda, G. (1922). Linien gleicher Kontinentalität und Ozeanität 1. Weltkarte 2. Europa, Justus Perthes/Petermanns Mitteilungen, Gotha.

Szreffel, C. (1961). Przegląd ważniejszych sposobów charakterystyki stopnia kontynentalizmu. *Przegląd Geograficzny VI, 3*, 191–199.

Szymanowski, M., & Kryza, M. (2011). Application of geographically weighted regression for modelling the spatial structure of urban heat island in the city of Wroclaw (SW Poland). *Procedia Environmental Sciences, 3*, 87–92.

Szymanowski, M., & Kryza, M. (2012). Local regression models for spatial interpolation of urban heat island—an example from Wrocław, SW Poland. *Theoretical and Applied Climatology, 108*, 53–71.

Szymanowski, M., & Kryza, M. (2015). The role of auxiliary variables in deterministic and deterministic-stochastic spatial models of air temperature in Poland. *Pure and Applied Geophysics,*. doi:10.1007/s00024-015-1199-2.

Szymanowski, M., Kryza, M., Smaza, M. (2007). A GIS approach to spatialize selected climatological parameters for wine-growing in Lower Silesia, Poland. In: Střelcová, K., Škvarenina, J., Blaženec, M (Ed.) Bioclimatology and natural hazards, International Conference, Pol'ana nad Detvou, Slovakia, 17–20 September 2007, CD-ROM, ISBN 978-80-228-17-60-8.

Szymanowski, M., Kryza, M., & Spallek, W. (2012). *Air temperature atlas for Poland: The methodical approach*. Wrocław: Uniwersytet Wrocławski. **(in Polish, English summary)**.

Szymanowski, M., Kryza, M., & Spallek, W. (2013). Regression-based air temperature spatial prediction models: An example from Poland. *Meteorologische Zeitschrift, 22*, 577–585.

Tobler, W. (1970). A computer movie simulating urban growth in the Detroit region. *Econ. Geogr., 46*, 234–240.

Torregrosa, A., Taylor, M. D., Flint, L. E., & Flint, A. L. (2013). Present, future, and novel bioclimates of the San Francisco, California Region. *PLoS ONE, 8*(3), e58450. doi:10.1371/journal.pone.0058450.

Ustrnul, Z., & Czekierda, D. (2005). Application of GIS for the development of climatological air temperature maps: An example from Poland. *Meteorological Application, 12*, 43–50.

Ustrnul, Z., & Czekierda, D. (2009). *Atlas of extreme meteorological phenomena and synoptic situations in Poland*. Warszawa: IMGW.

Willmott, C. J., & Matsuura, K. (1995). Smart interpolation of annually averaged air temperature in the United States. *Journal of Applied Meteorology, 34*, 2577–2586.

Woś, A. (2010). *Klimat Polski w Drugiej Połowie XX Wieku*. Poznań: Wydawnictwo Naukowe UAM.

(Received September 22, 2014, revised September 22, 2016, accepted October 5, 2016, Published online October 19, 2016)

Pure Appl. Geophys. 174 (2017), 643–659

DOI 10.1007/s00024-016-1250-y

Pure and Applied Geophysics

Geospatial Predictive Modelling for Climate Mapping of Selected Severe Weather Phenomena Over Poland: A Methodological Approach

EWELINA WALAWENDER,[1,2] JAKUB P. WALAWENDER,[2,1] and ZBIGNIEW USTRNUL[2,1]

Abstract—The main purpose of the study is to introduce methods for mapping the spatial distribution of the occurrence of selected atmospheric phenomena (thunderstorms, fog, glaze and rime) over Poland from 1966 to 2010 (45 years). Limited in situ observations as well the discontinuous and location-dependent nature of these phenomena make traditional interpolation inappropriate. Spatially continuous maps were created with the use of geospatial predictive modelling techniques. For each given phenomenon, an algorithm identifying its favourable meteorological and environmental conditions was created on the basis of observations recorded at 61 weather stations in Poland. Annual frequency maps presenting the probability of a day with a thunderstorm, fog, glaze or rime were created with the use of a modelled, gridded dataset by implementing predefined algorithms. Relevant explanatory variables were derived from NCEP/NCAR reanalysis and downscaled with the use of a Regional Climate Model. The resulting maps of favourable meteorological conditions were found to be valuable and representative on the country scale but at different correlation (r) strength against in situ data (from $r = 0.84$ for thunderstorms to $r = 0.15$ for fog). A weak correlation between gridded estimates of fog occurrence and observations data indicated the very local nature of this phenomenon. For this reason, additional environmental predictors of fog occurrence were also examined. Topographic parameters derived from the SRTM elevation model and reclassified CORINE Land Cover data were used as the external, explanatory variables for the multiple linear regression kriging used to obtain the final map. The regression model explained 89 % of annual frequency of fog variability in the study area. Regression residuals were interpolated via simple kriging.

Key words: Geospatial modelling, severe weather phenomena, regression kriging, climate mapping, Poland.

1. *Introduction*

Severe weather is an extreme meteorological event or phenomenon, which represents a real threat to human life and property (World Meteorological Organization 2004). Weather hazards may occur suddenly and not leave much time for reaction. Furthermore, these occurrences are spatially varied and should be identified by an area. Hence, knowledge about the spatial distribution and strength of dangerous atmospheric phenomena is crucial for reliable local risk assessment as well as effectiveness in preventing and mitigating weather disasters. Some of the most common dangerous weather phenomena that occur over Poland are fog, thunderstorms (lightning and hail) and icing (rime and glaze).

Understanding the spatial variability and intensity of severe weather phenomena makes it possible to determine regional sensitivity to extreme atmospheric hazards at different risk levels. Spatial prediction methods for several weather elements are relatively well recognized and widely described (e.g. HARTKAMP *et al.* 1999; CHAPMAN and THORNES 2003; DOBESCH *et al.* 2007; LI and HEAP 2008; TVEITO *et al.* 2008; SLUITER 2009). The most frequently studied were: air temperature (e.g. NINYEROLA *et al.* 2000, 2007b; BROWN and COMRIE 2002; VICENTE-SERRANO *et al.* 2003; USTRNUL and CZEKIERDA 2005, BENAVIDES *et al.* 2007; SZYMANOWSKI and KRYZA 2013), solar radiation (e.g. HEUVELINK and GRIFFITH 2010; KRYZA *et al.* 2010; RUIZ-ARIAS *et al.* 2011; WANG *et al.* 2014), precipitation (e.g. NINYEROLA *et al.* 2000, 2007a; MARTÍNEZ-COB 1996; BROWN and COMRIE 2002; VICENTE-SERRANO *et al.* 2003; WAGNER *et al.* 2012; DI PIAZZA *et al.* 2011), evapotranspiration (e.g. MARTÍNEZ-COB 1996; VICENTE-SERRANO *et al.* 2007;

---

[1] Institute of Geography and Spatial Management, Jagiellonian University, 7 Gronostajowa St., Krakow, Poland. E-mail: ewelina.walawender@doctoral.uj.edu.pl

[2] Institute of Meteorology and Water Management—National Research Institute, 14 Borowego St., Krakow, Poland.

Shirin Manesh *et al.* 2013) and snow cover (e.g. López-Moreno and Nogués-Bravo 2005, 2006; López Moreno and Vicente-Serrano 2007; Blanchet and Lehning 2010). Thus far, not much attention has been paid so far to techniques for mapping some visually observed atmospheric phenomena (e.g. fog, dew, hoarfrost, icing, rime, glaze, thunderstorms), which are usually small-scale, often spatially discontinuous, inherently complicated and difficult to predict and/or measure. The volume of source data is also usually too small for interpolation because phenomena are visually observed only at synoptic and research weather stations where a human observer records observations. For spatially continuous mapping of atmospheric phenomena characteristics, estimation based on selected physical relationships is recommended (World Meteorological Organization 2011). This often requires application of predictive modelling and mapping techniques also known as geospatial data mining (Yuan *et al.* 2005; Shekhar *et al.* 2005) instead of traditional spatial interpolation methods (Berry 2005; Diem and Comrie 2002). In this case, geospatial predictive modelling and mapping techniques were used for estimating the spatial distribution of selected atmospheric phenomena over the area of Poland on the basis of rasterised environmental variables (Franklin 1995).

The main purpose of the study is to present an improved climate mapping method for evaluating the spatial distribution of selected small-scale atmospheric phenomena based on limited input data. Geospatial predictive models of thunderstorms, fog, glaze, and rime were developed to obtain spatially continuous maps. Cartographic versions of similar maps have already been published in the Meteorological hazard atlas of Poland (Ustrnul *et al.* 2014) where the spatial and temporal variability of each given phenomenon is discussed. In this study, the methodological approach is presented.

2. Study Area and Data

2.1. Weather Observation Data (in Situ Data)

The study area is Poland, a central European country (313,000 km^2) characterized by a transitional climate with both oceanic and continental influences. Elevation varies from almost 2500 m above sea level in the Tatra Mountains in the south to 2 m below sea level in the north. Changing oceanic and continental influences together with complex physiography make weather phenomena in Poland difficult to predict.

Even though advanced measurement methods of weather parameters do exist, there is still an evident shortage of objective and quantitative observational data on atmospheric phenomena. Taking into account weather phenomena such as fog, thunderstorms, glaze, and rime, visual observations performed at weather stations serve as the only available data source for Poland.

However, there are several limitations of in situ observations, which have to be considered:

- Subjectivity of the observations, which depend on the knowledge and experience of the observer,
- The way observations are coded in the SYNOP dispatch; current weather code makes it impossible to obtain information on the intensity of each given phenomenon (no quantifiers available),
- The local nature of atmospheric phenomena strongly depends on the variability of key local environmental conditions, such as topography and land cover.

All such limitations seriously complicate the use of interpolations method for the purpose of creating spatially continuous maps of hazardous atmospheric phenomena. Nevertheless, visual observation data were presented directly in form of graduated symbol maps (Fig. 1) to gain general view on variability of a given phenomenon over the Poland territory and gather an input data to modelling results validation.

Daily observational data for a period of 45 years (1966–2010) were used. Careful verification and homogenisation of the time series was done in accordance with WMO recommendations (World Meteorological Organization 2011) in order to complete the missing values. Finally, daily data on observed thunderstorms, fog, glaze, and rime obtained from 61 weather stations spread across Poland were included in the analysis (Fig. 2a).

For favourable meteorological conditions algorithms construction (see Sect. 3.1) and RegCM modelling validation, data from every 3 h observations were also used. Additionally, aerological data

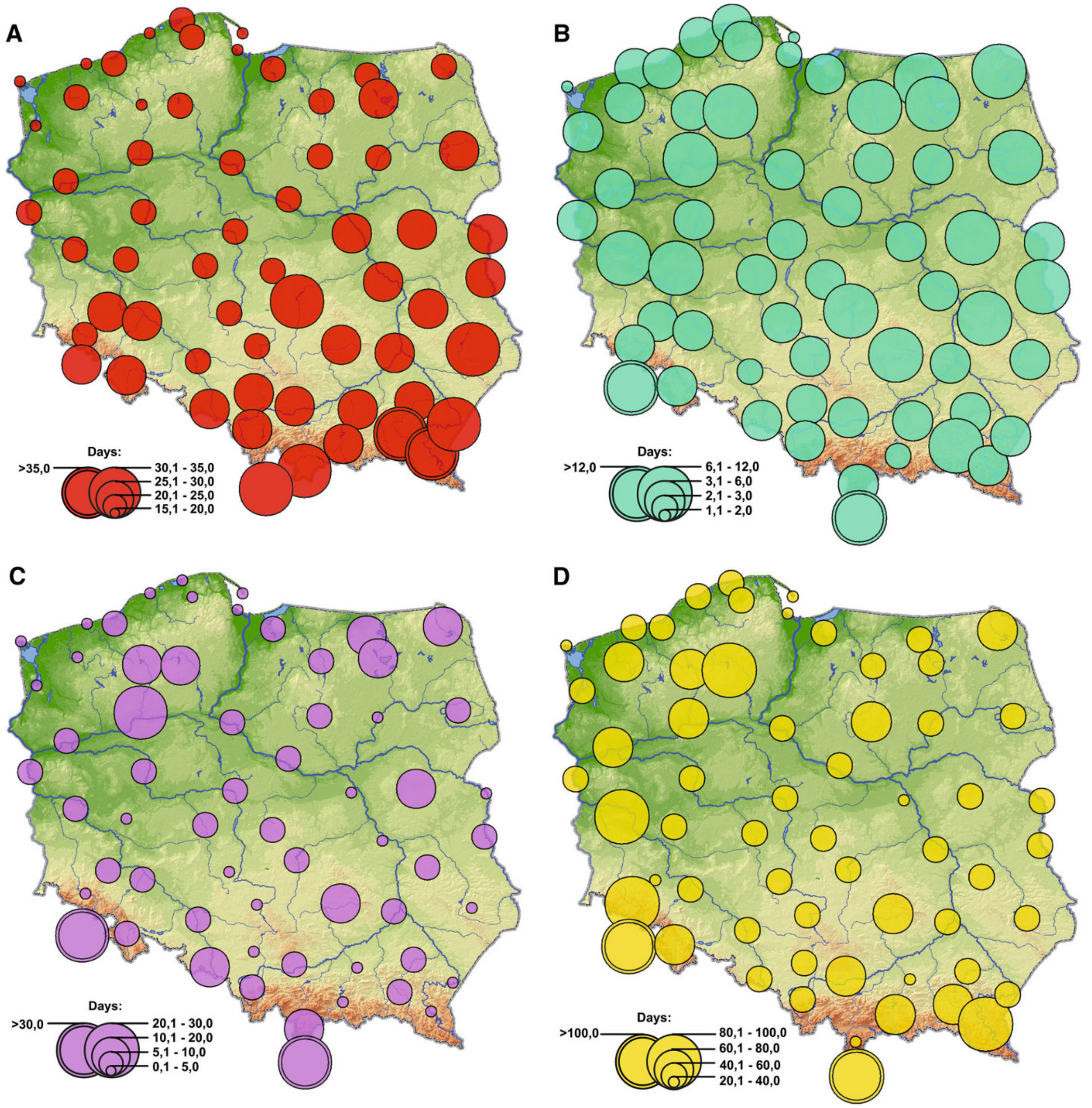

Figure 1
Average annual number of days with thunderstorms (**a**), glaze (**b**), rime (**c**), and fog (**d**) observed at weather stations

(soundings from 00 UTC and 12 UTC) from three Polish upper-air stations (Łeba, Wrocław, and Legionowo) were derived and used in glaze and thunderstorms algorithm construction and modelling results validation.

All observation data were derived from meteorological stations which work within the national network and were provided by the Institute of Meteorology and Water Management—National Research Institute.

2.2. *Reanalysis and Regional Climate Model Data*

Due to the lack of objective quantitative data derived from an adequate number of observations,

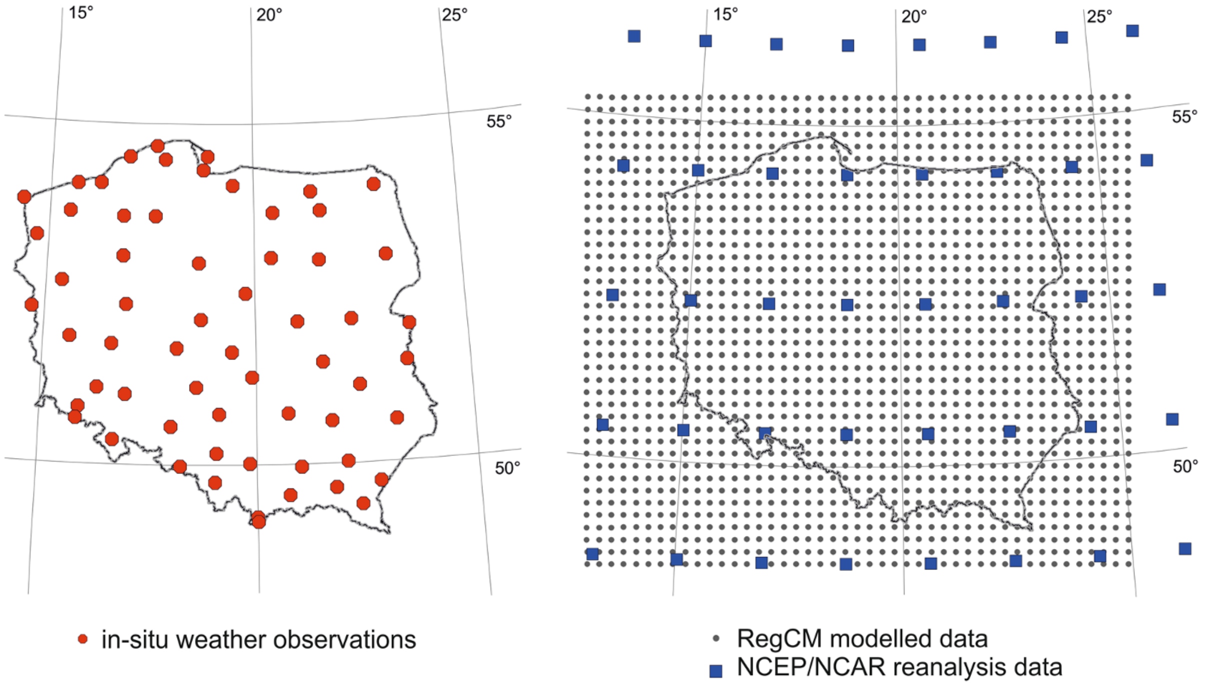

Figure 2
Location of the weather stations used in the study (**a**) in comparison to NCEP/NCAR reanalysis and RegCM model gridded data (**b**)

additional environmental data were tested for statistical dependence (predictor testing). To obtain regularly-gridded coverage, a 45-year study period (1966–2010) was used with NCEP/NCAR reanalysis data (Kalnay *et al.* 1996; Kistler *et al.* 2001) with 6-h temporal resolution ([1] NCEP 2015). A 2.5 × 2.5 decimal degree gridded dataset contained information at the surface level (2 m above the ground) and 17 different pressure levels in the atmosphere. It was used as an input for dynamical downscaling (Wilby and Wigley 1997) carried out with the use of the RegCM model, version 4.1.1. (Elguindi *et al.* 2011). Thanks to its improved parameters associated with atmospheric physics and land cover patterns, the RegCM regional climate model is suitable for modelling weather conditions on a regional scale (Giorgi and Anyah 2012). As a result, homogenous gridded datasets for the surface layer (2 m) and 23 upper atmospheric levels were obtained with a spatial resolution of 20 km and a temporal resolution of 3 h (Fig. 2b).

2.3. Environmental Variables

Some atmospheric phenomena vary considerably even over a relatively small area. Because of this, valuable data on local meteorological conditions as well as information on several key environmental variables need to be included for proper climate mapping. In this study, fog was the variable most dependent on local environmental characteristics. According to COST Action 722 (Short range forecasting methods of fog, visibility and low clouds, Jacobs *et al.* 2007), topography and land use (connected also with soil moisture and vegetation) were concerned as the most important predictors. Several auxiliary parameters were extracted from an SRTM Digital Elevation Model v.4.1 (Jarvis *et al.* 2008) with spatial resolution at 90 m and from the CORINE Land Cover 2000 vector database (Bossard *et al.* 2000; [2] EEA Data and Maps 2015) with the smallest mapping unit at 25 hectares. Final maps were generated with a spatial resolution of 250 m,

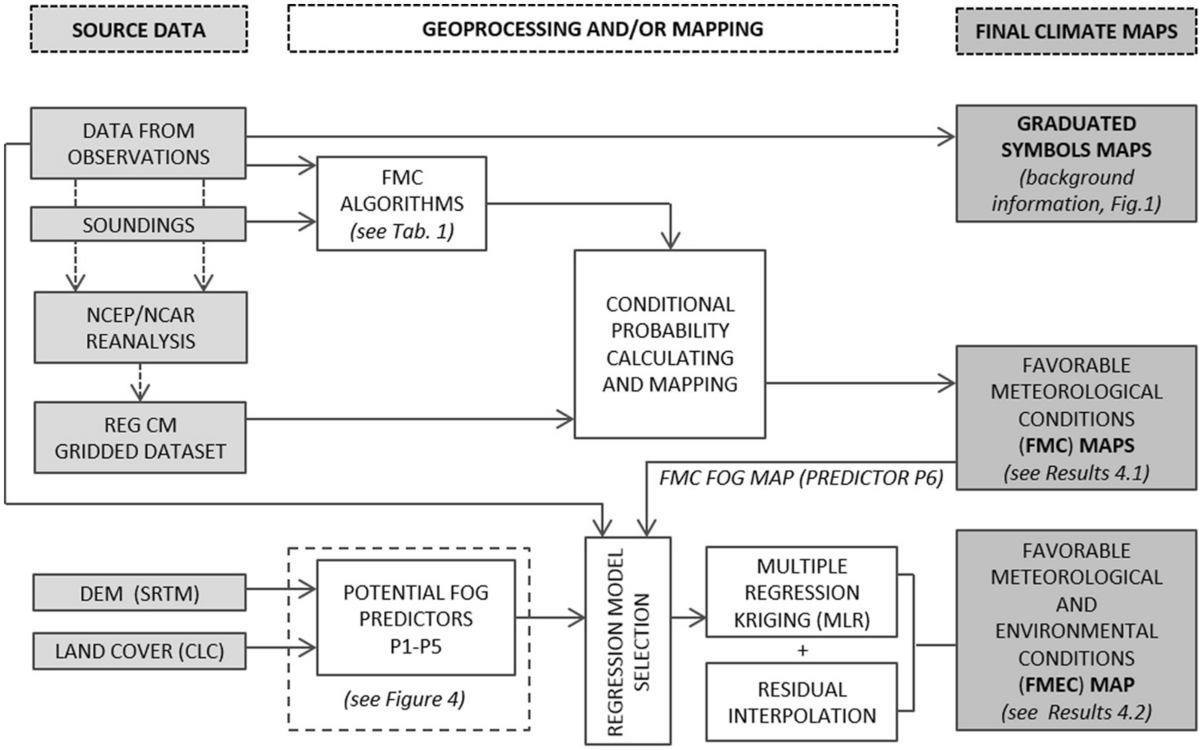

Figure 3
General workflow scheme

which seems to be adequate for climate mapping on the scale of Poland.

3. Methodology

Section 3 outlines the methods used for the map generation process, including a proposed approach to discontinuous phenomena mapping.

The whole workflow (Fig. 3) consisted of three steps which were finalised by three different types of climate maps:

1. Direct presentation of in situ observation (graduated symbols maps) (Sect. 2.1).
2. Conditional probability mapping based on favourable meteorological conditions algorithms (FMC maps) (Sects. 3.1 and 4.1).
3. Extending FMC map with environmental predictors employed in multiple linear regression kriging (FMEC map) (Sects. 3.2 and 4.2).

3.1. *Predictive modelling based on favourable meteorological conditions (fmc) algorithms and gridded data*

In order to obtain spatially continuous climate maps of the probability of occurrence of fog, thunderstorms, glaze, and rime an approach based on conditional probability algorithms and predictive modelling was employed. These methods are widely used in weather forecasting (Lorenc 1986; Keller and Kuchera 2004), but since they are based on the detailed analysis of real data, they can also be successfully applied in climate research (Thorne *et al*. 2012). The first step consisted of an extended analysis of long-term data from daily and 3 h weather observations. Favourable meteorological conditions for each phenomenon were determined through an analysis of all measured and observed weather parameters during the occurrence of each studied phenomenon. In the case of thunderstorms and glaze, upper-air soundings were additionally analysed for characteristic patterns. Finally, empirical formulas and thresholds were defined for all the selected phenomena. The entire process of algorithm definition was undertaken as a part of a task called “Maps of Meteorological Hazards” which was done within the framework of the EU co-financed project “IT system of the country’s protection against extreme hazards” (Polish acronym: ISOK) (Wypych *et al.* 2014; Ustrnul *et al.* 2015). The detailed procedure for the construction and validation of each algorithm is beyond the scope of this paper (an example for thunderstorms can be found in Walawender *et al.* 2015), which focuses mainly on mapping methods. Simplified versions of favourable weather conditions algorithm for each given phenomenon are shown in Table 1.

Subsequently, algorithms were implemented with the use of RegCM modelled data (1966–2010) (see Sect. 2.2). Finally, the mean annual frequency of favourable conditions was calculated for each of the four studied phenomena. Gridded values were interpolated via an exact method (radial basis function—completely regularized spline) to keep the grid point values in the output geostatistical surface.

Validation of obtained RegCM modelling results was performed through implementation of FMC algorithms into available in situ data. Every 3 h data from weather stations without any missing values were used in the process. Finally, 1966–2010 data from 42 weather station were used for rime and fog FMC modelling validation. Validation of thunderstorms and glaze FMC map (RegCM results) was performed only for three weather-stations (Leba, Legionowo, Wroclaw—as FMC algorithms demanded data from upper-air soundings) using the data from 2003–2010 period because of the very poor upper weather data availability (described in Walawender *et al.* 2015).

3.2. Environmental Predictors and Regression Kriging: Fog Map Example

As the occurrence of fog is usually highly dependent on local environmental conditions, more predictors (apart from certain weather parameters) are needed to explain its spatial variability. The distribution of fog is first of all determined by relief

Table 1

Components of favourable weather conditions algorithms (simplified version)

	Favorable meteorological conditions
Fog	Visibility as a function of relative humidity $VIS = 800 \times (101 - RH)/RH^{1.75} \rightarrow VIS < 1.3$ $P < 0.1$
Thunderstorms	Convective available potential energy (CAPE) together with convective precipitation MUCAPE >200 (calculated from 23 isobaric (sigma) levels) Type of precipitation
Glaze	Precipitation, air temperature at 700, 850 and 925 hPa isobaric levels (°C) and near the surface (2 m and 5 cm above the ground) T 700 hPa < −2 T 850 hPa: > −4 T 925 hPa: > −6 T 2 m > −6 °C and T 2 m < +2 T 5 cm < 0 $P > 0.1$
Rime	Probability of rime as a function of relative humidity and air temperature 2 m a.g.l. Lack of precipitation (different functions depending on T value) T 2 m < 0.1 $P < 0.1$ RH > 0.715 × T 2 m + 94

VIS visibility (km), *RH* relative humidity (%), *P* precipitation (mm), *MUCAPE* Most Unstable CAPE (J/kg), T_{5cm} air temperature 5 cm above the ground (°C), T_{2m} air temperature 2 m above the ground (°C) and its interactions with the air. There exists a strong and complex relationship between fog occurrence and local topography (elevation and landform) and land cover patterns (e.g. amount of water bodies or green areas). These parameters are crucial for spatial prediction of fog (Jacobs *et al.* 2007). Predictive mapping makes it possible to integrate both meteorological and geographic data (Vicente-Serrano *et al.* 2010) to estimate the spatial distribution of a given variable.

In this study multiple linear regression (MLR, also known as environmental correlation) with additional residual interpolation (so called Multiple Linear Regression Kriging—MLRK, Hengl *et al.* 2004; Hengl 2007, 2009) was tested for mapping fog occurrences over the territory of Poland.

Exploratory analysis was carried out first to select an appropriate set of key environmental variables. The locations of all available weather stations were verified with the use of high resolution aerial photographs and orthophotomaps. All improperly assigned XY coordinates were adjusted by geocoding postal addresses. Finally, a location accuracy of 90 m (consistent with nominal SRTM pixel size) was achieved and made it possible to check relationships between predictors and input data with greater precision and reliability. Selected environmental predictors were converted into raster format. The diagram in Fig. 4 illustrates the process.

Topographic predictors were obtained from SRTM data. Elevation (meters above sea level) (P1) was extracted directly from SRTM data and further used as an input raster to calculate the Topographic Position Index (TPI) (Gallant and Wilson 2000). A dedicated ArcGIS extension developed by Jenness (2006) was used to calculate TPI on the basis of elevation data. TPI (P2) is an objective semi-automated landform classifier based on neighbourhood analyses. It shows the difference between the elevation in each pixel and the average elevation in its neighbourhood defined by a circle of arbitrary radius which depends on the level of detail assumed in the analysis. In this study, for the resampled 250 m DEM raster dataset, the radius of 200 cells was defined in order to extract large terrain features that differentiate key regional climate conditions. To obtain the final raster predictor (P2), TPI was recalculated into absolute values as both uplands ($TPI \gg 0$) and valleys ($TPI \ll 0$) favour the occurrence of fog.

Corine Land Cover (CLC), which was originally created as a vector dataset was transformed to a raster with 250 m resolution. Urban areas, green (vegetated) areas, as well as wetlands and water bodies were extracted from reclassified CLC data (Table 2).

Regarding conditions of fog occurrence, buffer and focal analyses were applied to obtain the percentage of urban/green/water areas within a 2.5 km buffer zone around each available weather station and similarly around each CLC raster cell. The analysis was repeated three times in order to compute three raster datasets (three predictors): percentage share of urban areas (P3), percentage share of green areas (P4), and percentage share of wetlands and water bodies (P5). The entire set of predictors (including P6—fog favourable meteorological conditions described in Sect. 2.2) are shown in Table 3.

The selected predictors were examined with stepwise regression analysis to check the spatial relationships between the occurrence of key phenomena and corresponding predictors. The following statistical criteria were taken into account to identify the best fitted Multiple Linear Regression (MLR) model based on the ordinary least squares (OLS) method: adjusted R-squared ($AdjR^2$), corrected Akaike Information Criterion (AICc), Koenker Statistic p value (K(BP)) and the Maximum Variance Inflation Factor (MaxVIF). Jarque–Bera (JB) test was performed on model residuals to indicate whether they are normally distributed. Global Moran's I statistic p values (SA) were calculated to decide whether the regression residuals are spatially autocorrelated and further interpolation is required.

The probability of fog favourable meteorological and environmental conditions (FMEC) was calculated using map algebra on predictor raster datasets, applying selected MLR model—*MLR output raster dataset*. Regression residuals were then interpolated via simple kriging (recommended by Hengl *et al.*

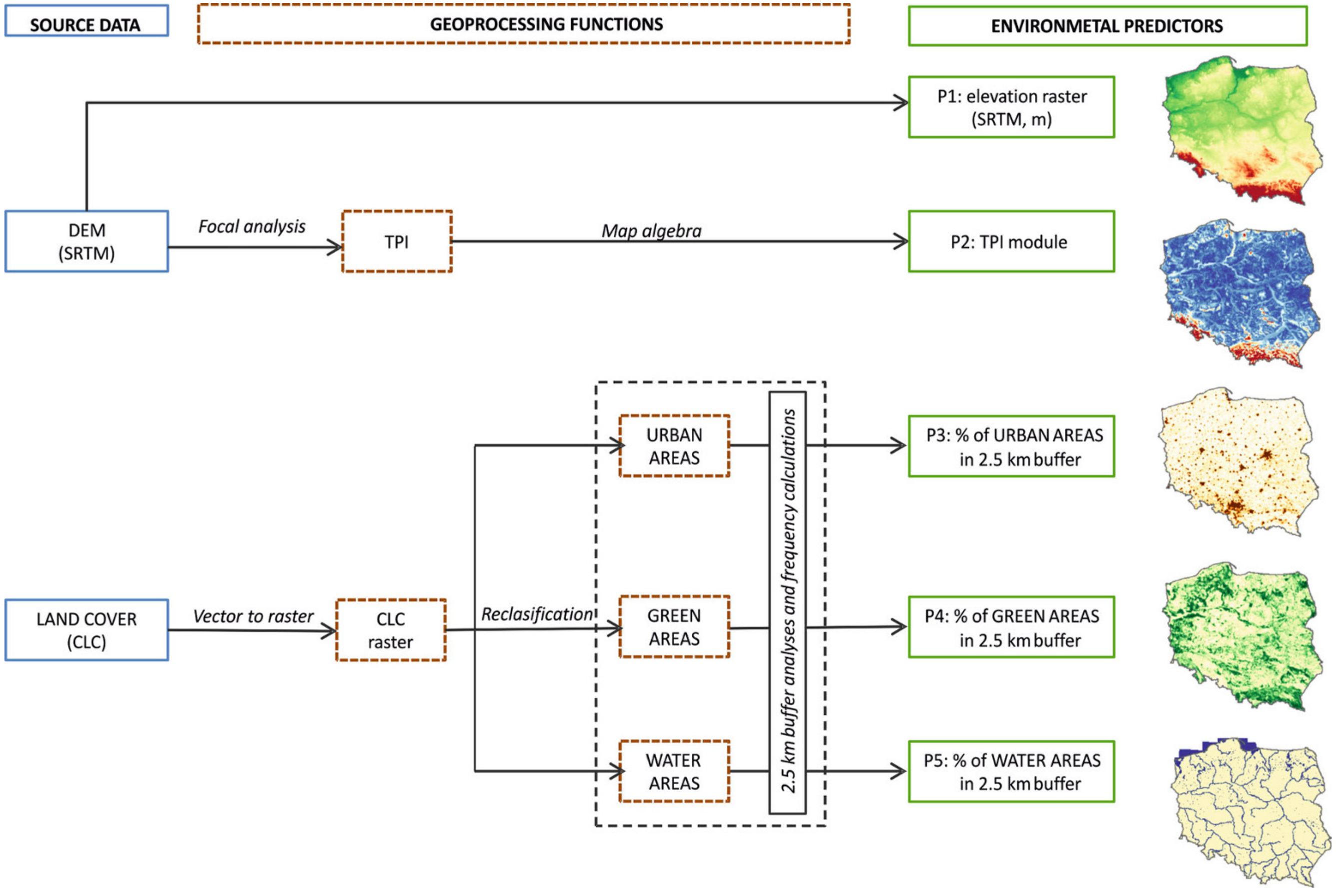

Figure 4
Fog environmental predictors (*P1–P5*) and geoprocessing functions used (see Sects. 2.3 and 3.2 for explanations)

Table 2

Reclassified and aggregated CLC Classes

New aggregated class	Original CLC class
Urban areas	1.1 Urban fabric
	1.2 Industrial, commercial and transport units
	1.3 Mine, dump and construction sites
Green areas	1.4 Artificial, non-agricultural vegetated areas
	2.2 Permanent crops
	2.3 Pastures
	2.4 Heterogeneous agricultural areas
	3.1 Forests
	3.2 Scrub and/or herbaceous vegetation
Wetlands and water bodies	4.1 Inland wetlands
	5.1 Inland waters

Table 3

Fog environmental predictors chosen for testing

Code	Predictor
P1	Elevation (DEM)
P2	Landform (TPI)
P3	Percentage of urban areas in 2.5 km radius circle buffer (CLC)
P4	Percentage of green areas in 2.5 km radius circle buffer (CLC)
P5	Percentage of wetlands and water in 2.5 km radius circle buffer (CLC)
P6	Favourable meteorological conditions (FMC)

2004; Hengl 2007, 2009)—*SK output raster dataset*. The final result (*MLRK output raster dataset*) was achieved by adding both the MLR raster dataset and the interpolated residuals raster dataset:

$$MLRK\ \ raster\ = MLR\ \ raster\ +\ SK\ \ raster$$

An appropriate FMEC map was then created. The prediction results of both the MLR and the MLRK procedures were cross-validated via a classic leave-one-out approach (Geisser 1975; Isaaks and Srivastava 1989). Error statistics including: mean error (ME), mean absolute error (MAE) and root mean square error (RMSE) were calculated to evaluate the obtained results (summarized in Table 4 after Li and Heap 2008). Their use in spatial interpolation and interpretation is widely known and well described (e.g. Willmott and Matsuura 2006; Szymanowski *et al*. 2012).

Table 4

Error metrics used in FMEC model validation

Symbol	Error metrics	Mathematical Expression
ME	Mean error	$\frac{1}{N}\sum_i (M_i - O_i)$
MAE	Mean absolute error	$\frac{1}{N}\sum_i \lvert M_i - O_i \rvert$
RMSE	Root mean square error	$\sqrt{\frac{1}{N}\sum_i (M_i - O_i)^2}$

N total number of pairs, M_i modelled fog frequency (days with fog favourable conditions), O_i observed fog day frequency

4. Results

4.1. Favourable meteorological conditions (fmc) maps

Predictive modelling based on FMC algorithms applied to RegCM gridded data was used to identify favourable conditions for selected weather phenomena (see Sect. 3.1 for details). FMC maps (Fig. 5) show spatially continuous probability of a day with favourable conditions for the occurrence of certain weather phenomena during the whole year. In other words, FMC maps show regional variability of weather conditions favouring the occurrence of phenomena such as thunderstorms, glaze, rime, and fog.

Validation of RegCM modelling itself was done through the calculation of FMC algorithms using available in situ data (Table 5). For thundersotrms, glaze and rime RegCM FMC calculation resulted as very similar to in situ FMC calculation with mean bias smaller than 1.5 %. In case of the fog FMC map RegCM results were strongly underestimated.

FMC maps do not correspond exactly with observational data, as they present the probability of the occurrence of favourable conditions, which is not the same as the observed frequency of weather phenomena. Local variability of atmospheric phenomena makes FMC maps quite difficult to subject to any form of objective verification and validation of modelling results against actual observations. One weather station is often not representative of a particular climate region at mesoscale level (3–100 km). Standardized WMO instructions indicate typical location characteristics but it is not easy to confirm them, especially due to weather station exposure (World Meteorological Organization 2008). Of the created maps, only the thunderstorms frequency map can be interpreted as highly representative on a regional scale, which can be clearly seen from the results of correlation analysis between FMC maps and weather station data (Table 6). Thunderstorms FMC probability was found to be very strongly correlated (Pearson's coefficient $r > 0.8$, at significance level $p < 0.001$) with the frequency of thunderstorm observations calculated via in situ data. Despite the occurrence of thunderstorms over a rather limited geographic area at a particular time of day, they usually are associated with convective processes arising within unstable air masses or frontal systems.

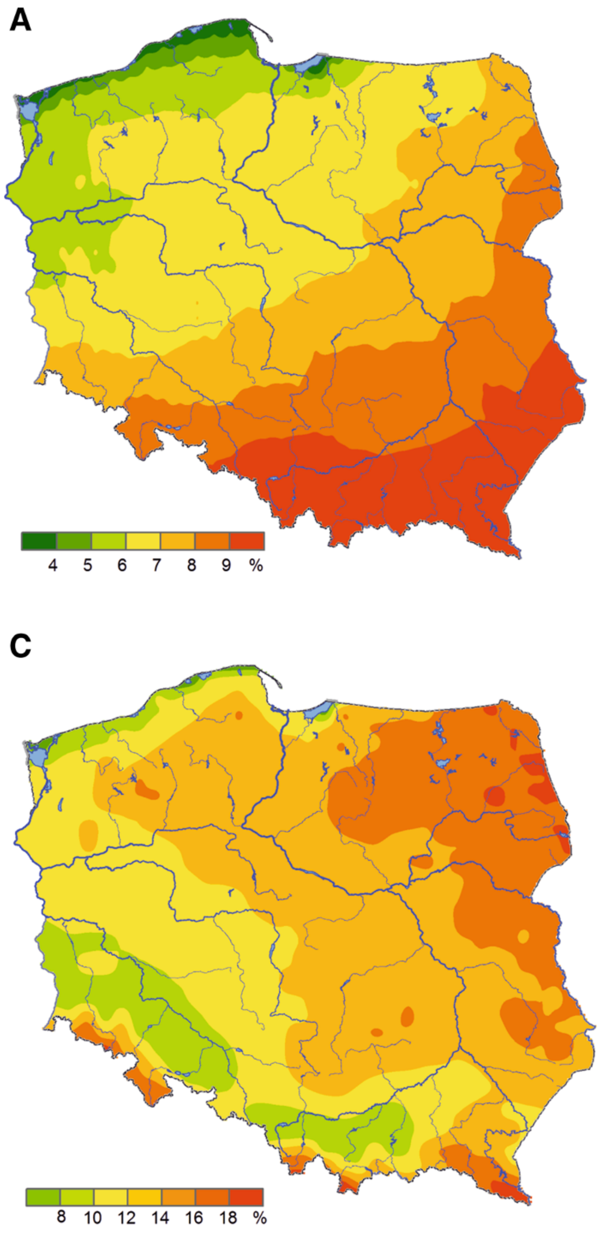

Figure 5
Average annual probability (%) of a day with thunderstorms (**a**), glaze (**b**), rime (**c**) and fog (**d**) favourable conditions occurrence. FMC maps

Table 5

Validation of RegCM FMC results against FMC calculated from available in situ data

Modelled phenomenon	Number of stations/grid points	Validation period	RegCM FMC Mean	Observations FMC Mean	RegCM Mean Bias	RegCM Bias Std
Thunderstorms	3	2003–2010	5.0	5.1	−0.1	1.4
Glaze	3	2003–2010	1.3	1.5	−0.2	0.2
Rime	42	1966–2010	20.8	19.4	1.4	5.7
Fog	42	1966–010	6.2	19.8	−13.7	8.2

Explanations: FMC MEAN, mean annual probability (%) of a day with a given phenomenon favourable conditions occurrence averaged for all stations/grid points used in the validation process (RegCm FMC MEAN—calculated from RegCM data, Observations FMC MEAN—calculated from in situ data); RegCM MEAN BIAS, average difference between RegCM FMC result and observation FMC result; RegCM BIAS STD, standard deviation of calculated biases among all stations/grid points

Table 6

Correlation analysis between FMC results and phenomena observations (n = 61)

Modelled phenomenon	Pearson's coefficient (r)	Coefficient of determination (R^2)	Correlation significance (p)
Thunderstorms	0.84	0.71	<0.001
Glaze	0.60	0.36	<0.001
Rime	0.39	0.15	0.002
Fog	0.15	0.02	0.253

In such situations the overall annual frequency of observations may be related to the whole region. In addition, the probability of glaze FMC is relatively strongly ($r > 0.6$, $p < 0.001$) correlated with observations. The occurrence of glaze is induced by freezing precipitation: hence it can be considered regionally dependent as well. Nevertheless, detailed regional variability remains beyond the spatial resolution of modelled maps.

Statistical relationship between probabilities of rime and fog FMC and observations are low ($r = 0.39$ for rime) and weak ($r = 0.15$ for fog), correspondingly. Rime is in fact, a form of frozen fog caused mostly by the same environmental factors that affect the occurrence of fog. However, the meteorological conditions favouring the deposition of rime are slightly easier to recognize (Ahti and Makkonen 1982) and are also easier to predict. Rime occurrence is also limited to the cold season (in Poland from October to April), whereas fog may appear year-round in Poland and is strongly affected by local environmental conditions. This means some of the very local fog occurrences might not be identified due to the relatively coarse spatial resolution of RegCM data. The fog FMC map was found to be in agreement with the satellite-based map of fog and low stratus frequency created by Cermak *et al.* (2009) at comparable spatial resolution to that of the RegCM data but FMC frequency values were underestimated.

Table 7

Summary of variables significance

Variable	Significant (%)	Negative (%)	Positive (%)
P1	71.9	0.0	100.0
P2	100.0	0.0	100.0
P3	75.0	100.0	0.0
P4	65.6	0.0	100.0
P5	6.3	62.5	37.5
P6	75.0	0.0	100.0

4.2. Favourable Meteorological and Environmental Conditions (FMEC) MAP: Fog Example

Statistical significance of additional fog predictors was examined through the stepwise regression analysis. The results were summarized in Table 7. Five out of six explanatory variables turned out to be statistically significant for most of the iterations and showed a consistent and stable relationship with the dependent variable. Predictors P1 (elevation), P2 (landform), P4 (% of green areas), and P6 (favourable meteorological conditions) were positively correlated with the dependent variable in 100 % of iterations and P3 (% of urban areas) was negatively correlated, which came into agreement with the initial assumptions made for this study. The predictor P5 (% of

Table 8

Stepwise regression analysis results

Step	AdjR2	AICc	JB	K (BP)	MaxVIF	SA	Cov1	Cov2	Cov3	Cov4	Cov5
1	0.84	369.99	0.30	0.16	1.00	0.10	+P2***				
1	0.76	394.51	0.00	0.00	1.00	0.00	+P1***				
2	0.87	359.87	0.46	0.26	1.00	0.07	+P2***	+P6***			
2	0.85	366.44	0.23	0.39	1.02	0.13	+P4**	+P2***			
3	0.89	351.43	0.00	0.01	5.10	0.01	+P2***	+P6***	+P1		
3	0.88	357.37	0.57	0.69	1.03	0.11	+P4**	+P2***	+P6***		
3	0.87	360.44	0.46	0.54	1.15	0.04	−P3	+P2***	+P6***		
3	0.88	357.37	0.57	0.69	1.03	0.11	+P4**	+P2***	+P6***		
3	0.86	363.21	0.57	0.45	1.07	0.12	+P4**	−P3**	+P2***		
4	0.89	351.44	0.00	0.03	5.44	0.02	+P4*	+P2***	+P6***	+P1	
4	0.89	351.77	0.00	0.06	5.12	0.01	−P3	+P2***	+P6***	+P1	
4	0.88	357.38	0.45	0.97	1.16	0.07	+P4**	−P3	+P2***	+P6***	
5	0.89	351.40	0.00	0.11	5.45	0.01	+P4	−P3	+P2***	+P6***	+P1***

Explanations: AdjR^2, AICc, JB, K(BP), MaxVIF and SA—abbreviations explained in part 3.2

Cov1, Cov2, Cov3, Cov4, Cov5—regression model covariates

* 0.10, ** 0.05, *** 0.01—model variable significance

water/wetlands) resulted as insignificant and was excluded from the analysis—it seems that the water and wetlands identified within the buffer zones around weather stations seemed not to be sufficiently representative for the purpose of analysis.

The final MLR model was determined taking into account both the stepwise regression results (Table 8) and knowledge-based experience. The most complex model with five covariates (P1, P2, P3, P4 and P6) was selected. The model explained 89 % of variation in annual foggy day frequency (adj $R^2 = 0.89$). The corrected Akaike information criterion (AICc) was found to be the smallest for the selected model, which also show that it is relatively well-fitted. Maximum (from all VIF values checked for every environmental variable) VIF factor was also acceptable (<7.5); in effect, there is no redundancy (multicollinearity) among the model's explanatory variables. The Koenker Statistic p-value test resulted in a not statistically significant value [K(BP) > 0.05], hence, the relationships modelled are consistent. Although covariates P3 and P4 in the selected regression model were not statistically significant at $p < 0.1$, it was decided to use them anyway because of their proven influence on fog occurrence (e.g. Sachweh and Koepke 1997; Jacobs *et al.* 2007), and overall high significance in the stepwise regression analysis (Table 8).

While geographically weighted regression (GWR) (Brunsdon *et al.* 1996; Fotheringham *et al.* 1998, 2002) may seem to be more suitable for capturing local variability, it could not be used with reliable results in this study. First of all, the performed Koenker Test did not indicate a spatial nonstationarity which should characterised the GWR input data (Brunsdon *et al.* 1996; Gao and Li 2011). Moreover, number of observation points is regarded as insufficient for sensible GWR calibration. It is suggested that at least 150 data points should be employed in the analysis to build reliable local regressions models and capture local (not regional or global) trends (Fotheringham 2010). There are also a few weather stations in the East Poland which are spatially isolated by large areas over which no data are recorded. It could produce excessive bias in local estimation.

JB test indicated that regression residuals are not normally distributed and the model may need additional geostatistical modelling performed on its residals. Global Moran's I test was performed (Table 9), as SA statistics (SA $= 0.01$) had shown spatial autocorrelation among regression residuals. Given a z-score of 2.02, there is a less than 5 % likelihood ($p = 0.043$) that the clustered pattern could be the result of random events and spatial autocorrelation is statistically significant.

Due to the positive result of the spatial autocorrelation test performed on regression residuals, Simple Kriging with normal score transformation

Table 9

Global Moran's I test summary

Moran's I statistic parameter	Value
Moran's index	0.194
Expected index	−0.017
Variance	0.011
z-score	2.018
p value	0.043

was employed for their interpolation. Figure 6 shows the output fog FMEC probability map generated through a combination of a deterministic regression part and residual interpolation (MLRK method).

Cross-validation resulted in satisfying values of error statistics which were improved for the MLRK model (Table 10) compared to results achieved with the deterministic part (MLR) alone. Both the validation results and visual evaluation make it possible to regard the final FMEC map as valuable and representative on the scale of Poland. It reflects both the general trends presented in the Climatic atlas of Poland (Lorenc 2005) and detailed information on environmental variability. Moreover, the FMEC map was found to be in substantial accordance with some high resolution (1 km) remote sensing derivative products presenting the fog frequency (Musial *et al*. 2014).

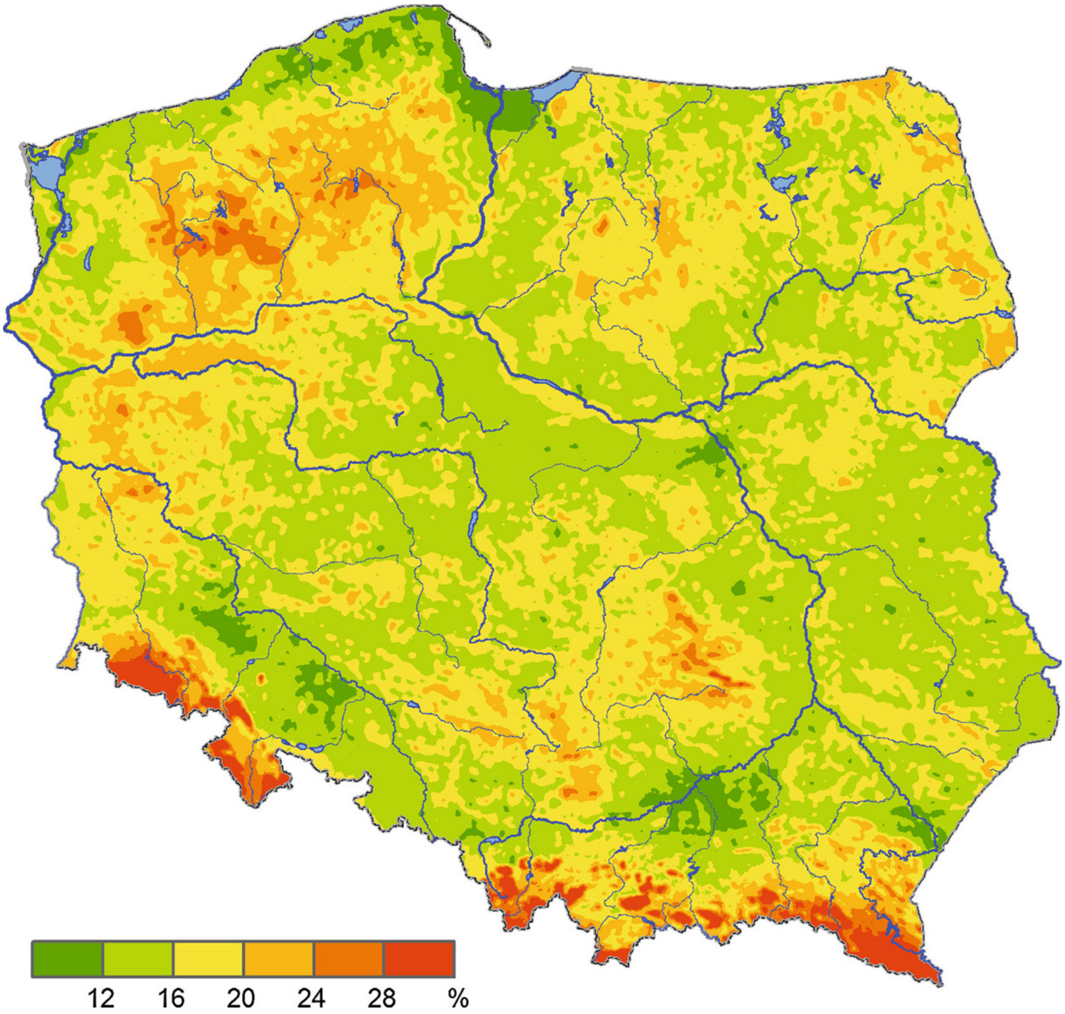

Figure 6
Average annual probability (%) of day with fog occurrence. FMEC map

Table 10

Cross-validation results

	ME	MAE	RMSE
MLR	0.000	2.839	3.954
MLRK	0.100	1.168	1.604

5. Conclusions

This study describes climate mapping techniques used for spatially discontinuous atmospheric phenomena. Thunderstorms, glaze, rime and fog were selected to test some of the existing methods and develop a predictive modelling approach for mapping location-dependent phenomena. Climatological maps based on a 45-year analysis (1966–2010) were created for Poland in order to identify distinct regions with a higher frequency and intensity of selected weather hazards. In case of hugely location dependent phenomena, observational data obtained from only 61 weather stations are definitely not sufficient for spatial interpolation over the entire territory of Poland. The number of data points is extremely important for spatial interpolation—the more data available, the better—but the complex nature of atmospheric phenomena makes interpolation even more difficult unless additional, environmental factors are also taken into account.

This study introduces quite an innovative method of using predictive modelling for climatological analysis of atmospheric phenomena over Poland. The presented approach remains valid for every relatively large area where orography and land cover are not homogeneous. The method proposed in this study uses a Regional Climate Model to yield regularly distributed gridded data and to assimilate them into algorithms describing favourable meteorological conditions for each given weather phenomenon. The algorithms have been previously validated on both observational and modelled weather data (Wypych *et al.* 2014; Ustrnul *et al.* 2015). The resulting FMC maps exhibit an adequate quality of prediction. Both quantitative validation and visual knowledge-based interpretation have confirmed a good estimation of the spatial distribution of selected phenomena over the entire territory of Poland. The maps show general patterns and relationships (Lorenc 2005) and allow to avoid wrong estimation which can occur during traditional interpolation of strongly local data from observations. As FMC maps were designed as regional, they are determined by the resolution of the input data (RegCM grid—20 km). For this reason, it is not possible to identify local differences in the maps, which should rather be considered as moderately generalized—but still valuable for regional analysis. The thunderstorm frequency FMC map is considered to be the most accurate map with very strong correlation with observational data ($r = 0.84$). The annual glaze and rime frequency FMC maps are also representative for the country area—considering the complexity of factors affecting these phenomena. Only the fog frequency FCM map proved to be strongly underestimated for southern Poland, as it does favour less heterogeneous areas in terms of orography and land cover.

Consequently, an additional fog frequency FMEC map was created with the use of multiple linear regression kriging (MLRK). Environmental correlation was based on several relevant predictors derived from elevation model and land-cover data—together with a previously obtained FMC map. The final map was found to be more accurate for analyzing the spatial patterns on a regional scale.

Although the generated maps cover just the area of Poland, the methodological background presented in this paper may be considered broadly applicable. An appropriate approach to geospatial predictive modelling should be preceded by detailed analysis of physical processes behind the analysed atmospheric phenomena. An extended exploration of key environmental factors affecting the modelled variable should be performed in order to recognise predictors, which may help to explain properly its spatial variability. The proper selection of predictors must avoid underestimation of the model, but also redundancy among proposed variables.

The modelling approach is characterised by some uncertainties, which one should be aware of in the analytical process. Some of these uncertainties can be at least partially eliminated. First, algorithms designed for favourable meteorological conditions may be improved by employing additional parameters or changing coefficients. Second, modelled data

(RegCM in this study) are often biased because of certain model assumptions, so an improvement can be made in the model's physical and topographical parameters' configuration and downscaling techniques.

In this study, linear regression was used as a deterministic element of a spatial interpolation procedure which may cause some simplification in the final outcome. Although the results were found to be satisfactory, additional methods including nonlinear models (Vicente-Serrano *et al.* 2010) or artificial neural networks should be tested in the future to verify the possibility of further improvements. Among new and very powerful, spatially continuous environmental datasets which may be used as predictors for this type of analysis, satellite data seem to be invaluable and are increasingly being used for climatological analysis of fog (e.g. Bendix 2002; Cermak *et al.* 2009; Musial *et al.* 2014; Avotniece *et al.* 2015). The importance of climate maps based on remotely sensed data is even greater because of potential use for validation of modelling results in case of limited data from weather observations. Lightning detection and weather radar imagery complemented by conventional meteorological measurements offer opportunities for the validation of predictions of thunderstorms as well as freezing rain.

In addition to the limitations already mentioned, geospatial predictive modelling based on physical relationships between meteorological and environmental parameters favouring the occurrence of a particular atmospheric phenomenon possesses great potential for climate mapping and weather forecasting. Algorithms used to create maps in this study will be also incorporated into an operational numerical weather model.

Acknowledgments

This work was performed as a part of the ISOK project (IT system for country protection against extreme hazards; POIG.07.01.00-00-025/09) which was co-financed by the European Fund of Regional Development under the Operational Programme Innovative Economy and the Polish Government. Authors would like to thank Łukasz Harasimowicz, Rafał Kielar, Tomasz Knopik, Szymon Pysz and Witold Wiążewski from the Institute of Meteorology and Water Management–National Research Institute whose previous work on fog, glaze, rime and thunderstorm detection algorithms in the project has contributed to this article. The authors would like to also thank the anonymous reviewers for their helpful comments and remarks.

REFERENCES

Ahti, K., and Makkonen, L. (1982), *Observations on rime formation in relation to routinely measured meteorological parameters*, Geophysica *19*, 75–85.

Avotniece, Z., Klavins, M., and Lizuma, L. (2015), *A Fog climatology in Latvia*, Theor. Appl. Climatol *122*(1), 97–109.

Benavides, R., Montes, F., Rubio, A., and Osoro, K. (2007), *Geostatistical modelling of air temperature in a mountainous region of Northern Spain*, Agr. Forest Meteorol. *146*, 173–188.

Bendix, J. (2002), *A satellite-based climatology of fog and low-level stratus in Germany and adjacent areas*, Atmos. Res. *64*, 3–18.

Berry, J.K., *Predictive Modeling*, In Analyzing Geo-Spatial Resource Data—A hands-on case study in spatial analysis and data mining (ed. Berry J.K.) (W.M. Keck Scholar in Geosciences, University of Denver, Denver, Colorado 2005) chapter 13, pp 13.1–13.12.

Blanchet, J., and Lehning, M. (2010), *Mapping snow depth return levels: smooth spatial modeling versus station interpolation*, Hydrol. Earth Syst. Sci. *14*, 2527–2544.

Bossard, M., Feranec, J., and Otahel, J. (2000), *CORINE land cover technical guide—Addendum* 2000, http://www.eea.europa.eu, accessed in Jan. 2015.

Brown, D.P., and Comrie, A.C. (2002), *Spatial modeling of winter temperature and precipitation in Arizona and New Mexico, USA*, Clim. Res. *22*, 115–128.

Brunsdon, C., Fotheringham, A. S., and Charlton, M. E. (1996), *Geographically Weighted Regression: A Method for Exploring Spatial Nonstationarity*, Geographical Analysis *28*, 281–298. doi:10.1111/j.1538-4632.1996.tb00936.x.

Cermak, J., Eastman, R.M., Bendix, J., and Warren, S.G. (2009), *European climatology of fog and low stratus based on geostationary satellite observations*, Q. J. R. Meteorol. Soc. *135*, 2125–2130.

Chapman, L., and Thornes, J.E. (2003), *The use of geographical information systems in climatology and meteorology* Prog. Phys. Geogr. *27*(3), 313–330.

Diem, J.E., and Comrie, A.C (2002), *Predictive mapping of air pollution involving sparse spatial observations*, Eniron. Pollution *119*, 99–117.

Di Piazza, A, Lo Conti, F., Noto, L.V., Viola, F., and La Loggia, G. (2011), *Comparative analysis of different techniques for spatial interpolation of rainfall data to create a serially complete monthly time series of precipitation for Sicily, Italy*, Int. J. Appl. Earth Obs. Geoinf. *13*, 396–408.

Dobesch, H., Dumolard, P., and Dyras, I. (eds.), *Spatial Interpolation for Climate Data : the Use of GIS in Climatology and Meteorology* (ISTE, London 2007).

Elguindi, N., Bi, X., Giorgi, F., Nagarajan, B., Pal, J., Solmon, F., Rauscher, S., Zakey, A., and Giuliani, G. (2011), *Climatic Model RegCM User Manual-Version 4.1*. Trieste, Italy.

Fotheringham, A.S., Brunsdon, C., and Charlton, M.E. (1998), *Geographically weighted regression: a natural evolution of the expansion method for spatial data analysis*, Environment and Planning A, *30*(11), 1905–1927.

Fotheringham, A. S., Brunsdon, C., and Charlton, M. (2002), *Geographically weighted regression: the analysis of spatially varying relationships*, Wiley, ss. 282.

Fotheringham, A. S. (2010), *Geographically weighted regression*. In: Warf, B. (Ed.), Encyclopedia of geography, SAGE Publications, Thousand Oaks, 1225-1232.

Franklin, J. (1995), *Predictive vegetation mapping: geographic modelling of biospatial patterns in relation to environmental gradients*, Prog. Phys. Geogr. *19*(4), 474–499, doi:10.1177/030913339501900403.

Gallant, J.C., and Wilson, J.P. (2000), *Primary topographic attributes*. In: Wilson, J.P., Gallant, J.C. (Eds.), Terrain Analysis: Principles and Applications, Wiley, New York, 51–85.

Gao, J., and Li, S. (2011), *Detecting spatially non-stationary and scale-dependent relationships between urban landscape fragmentation and related factors using Geographically Weighted Regression*, Applied Geography *31* (1), 292–302.

Geisser, S. (1975), *The predictive sample reuse method with applications*, J. Amer. Statist. Assoc. *70*, 320–328.

Giorgi, F., and Anyah, R.O. (2012), *The road towards RegCM4*, Clim Res *52*, 3–6.

Hartkamp, A.D., De Beurs, K., Stein, A., and White, J.W., *Interpolation techniques for climate variables, NRG-GIS Series 99-01* (CIMMYT, Mexico D.F., 1999).

Hengl, T. (2007), *A practical guide to geostatistical mapping of environmental variables*. EUR 22904 EN. Office for Official Publications of the European Communities, Luxembourg.

Hengl, T. (2009), *A practical guide to geostatistical mapping*, 2nd ed. Amsterdam: University of Amsterdam.

Hengl, T., Heuvelink, G.B.M., and Stein, A. (2004), *A generic framework for spatial prediction of soil variables based on regression-kriging*, Geoderma *120* (1–2), 75–93.

Heuvelink, G.B.M., and Griffith, D.A. (2010), *Space–Time Geostatistics for Geography: A Case Study of Radiation Monitoring Across Parts of Germany*, Geogr. Anal. *42*, 161–179.

Isaaks, E.H., and Srivastava, R.M. (1989), *An introduction to applied geostatistics*, Oxford Univ. Press, New York.

Jacobs, W., Nietosvaara, V., Bott, A., Bendix, J., Cermak, J., Silas, M., and Gultepe, I. (2007), *Short range forecasting methods of fog visibility and low clouds*, Earth System Science and Environmental Management Final Rep. on COST-722 Action.

Jarvis, A., Reuter, H.I., Nelson, A., and Guevara, E. (2008), *Hole-filled SRTM for the globe Version 4*, available on-line from the CGIAR-CSI SRTM: http://srtm.csi.cgiar.org, accessed in Jan. 2015.

Jenness, J. (2006), *Topographic Position Index (tpi_jen.avx) extension for ArcView 3.x, v. 1.3a., Jenness Enterprises*, available on-line: http://www.jennessent.com/arcview/tpi.htm, accessed in Jan. 2015.

Kalnay, E., Kanamitsu, M., Kistler, R., Collins, W., Deaven, D., Gandin, L., Iredell, M., Saha, S., White, G., Woollen, J., Zhu, Y., Chelliah, M., Ebisuzaki, W., Higgins, W., Janowiak, J., Mo, K.C., Ropelewski, C., Wang, J., Leetmaa, A., Reynolds, R., Jenne, R., and Joseph, D. (1996), *The NCEP/NCAR 40-year reanalysis project*, Bull Amer Meteor Soc *77*, 437–470.

Keller, D. L., and Kuchera, E.L. (2004), *Model-output post-processor algorithm development with interactive visualization software*, Natl. Wea. Dig. *28*, 47–53.

Kistler, R., Kalnay, E., Collins, W., Saha, G., White, G., Woollen, J., Chelliah, M., Ebisuzaki, W., Kanamitsu, M., Kousky, V., van den Dool, H., Jenne, R., and Fiorino, M. (2001), *The NCEP–NCAR 50-year reanalysis: Monthly means CD-ROM and documentation*, Bull Amer Meteor Soc *82*, 247–267.

Kryza, M., Szymanowski, M., Migaia, K., and Pietras, M. (2010), *Spatial information on total solar radiation: Application and evaluation of the r.sun model for the Wedel Jarlsberg Land, Svalbard,* Polish Polar Research *31*, 17–32.

Li, J., and Heap, A.D., *A review of spatial interpolation methods for environmental scientists*, Geoscience Australia Records 23, (Australian Government, Canberra 2008).

López-Moreno, J.I., and Nogués-Bravo, D. (2005), *A generalized additive model for modelling the spatial distribution of snowpack in the Spanish Pyrenees*, Hydrol. Process *19*, 3167–3176.

López-Moreno, J.I., and Nogués Bravo, D. (2006), *Interpolating snow depth data: a comparison of methods*, Hydrol. Process. *20*(10), 2217–232.

López Moreno, J.I., and Vicente-Serrano, S.M. (2007), *Mapping snowpack distribution over large areas using GIS and interpolation techniques*, Clim. Res. *33*, 257–270.

Lorenc, A. C. (1986), *Analysis methods for numerical weather prediction*. Q.J.R. Meteorol. Soc. *112*, 1177–1194.

Lorenc, H. (ed.), *Climatic atlas of Poland*, (Institute of Meteorology and Water Management, Warsaw, 2005) *(in Polish)*.

Martínez-Cob, A. (1996), *Multivariate geostatistical analysis of evapotranspiration and precipitation in mountainous terrain*, J. Hydrol. *174*, 19–35.

Musial, J.P., Hüsler, F., Sütterlin, M., Neuhaus, C., and Wunderle, S. (2014) *Daytime Low Stratiform Cloud Detection on AVHRR Imagery*, Remote Sens. *6*, 5124–5150.

Ninyerola, M., Pons, X., and Roure, J.M. (2000), *A methodological approach of climatological modelling of air temperature and precipitation through GIS techniques* International Journal of Climatology *20*: 1823–1841.

Ninyerola, M., Pons, X., and Roure, J.M. (2007), *Monthly precipitation mapping of the Iberian Peninsula using spatial interpolation tools implemented in a Geographic Information System*. Theoretical and Applied Climatology *89*: 195–209.

Ninyerola, M., Pons, X., and Roure, J.M. (2007), *Objective air temperature mapping for the Iberian Peninsula using spatial interpolation and GIS*. International Journal of Climatology *27*: 1231–1242.

RUIZ-ARIAS, J.A., POZO-VÁZQUEZ, D., SANTOS-ALAMILLOS, F.J., LARA-FANEGO, and TOVAR-PESCADOR, V. (2011), *A topographic geostatistical approach for mapping monthly mean values of daily global solar radiation: A case study in southern Spain*, Agr. Forest Meteorol. *151*(12), 1812–1822.

SACHWEH, M., and KOEPKE, P. (1997), *Fog dynamics in an urbanized area*, Theoretical and Applied Climatology *58*(1), 87–93.

SHEKHAR, S., ZHANG, P., and HUANG, Y. (2005), *Spatial Data Mining* [in:] Maimon, O. and Rokach, L. (eds.) The data mining and knowledge discovery handbook, Springer 2005, chapter 39, 833–852.

SHIRIN MANESH, S.S., AHANI, H., and REZAEIAN-ZADEH, M. (2013) *ANN-based mapping of monthly reference crop evapotranspiration by using altitude, latitude and longitude data in Fars province, Iran*, Environ. Dev. Sustain, doi: 10.1007/s10668-013-9465-x.

SLUITER, R., *Interpolation methods for climate data*. Literature review, KNMI Intern Raport (R&D Information and Observation Technology, De Bilt 2009).

SZYMANOWSKI, M., KRYZA, M., and SPALLEK, W. (2012), *Air temperature atlas for Poland: the methodical approach*. Rozprawy Naukowe Instytutu Geografii i Rozwoju Regionalnego Uniwersytetu Wrocławskiego 26, Uniwersytet Wrocławski, Wrocław (in Polish, English summary).

SZYMANOWSKI, M., KRYZA, M., and SPALLEK W. (2013), *Regression-based air temperature spatial prediction models: an example from Poland*, Meteoroloische Zeitschrift *22*(5), 577–585.

THORNE, J., BOYNTON, R., FLINT, L., FLINT, A., and LE, T.N. (2012), *Development and Application of Downscaled Hydroclimatic Predictor Variables for Use in Climate Vulnerability and Assessment Studies*, California Energy Commission, Publication number: CEC-500-2011-010.

TVEITO, O.E., WEGEHENKEL, M., VAN DER WEL, F., and DOBESCH, H., *The Use of Geographic Information Systems in Climatology and Meteorology—Final Report COST Action 719* (Official Publications of the European Communities, Luxembourg 2008).

USTRNUL, Z., and CZEKIERDA, D. (2005), *Application of GIS for the development of climatological air temperature maps: an example from Poland*, Meteorol. Appl. *12*, 43–50.

USTRNUL, Z., WYPYCH, A., HENEK, E., CZEKIERDA, D., WALAWENDER, J., KUBACKA, D., PYRC, R., and CZERNECKI, B., *Meteorological hazard atlas of Poland* (Institute of Meteorology and Water Management and ATTYKA, Krakow, 2014).

USTRNUL, Z., WYPYCH, A., HENEK, E., MACIEJEWSKI, M., and BOCHENEK, B. (2015), *Climatologically based warning system against meteorological hazards and weather extremes—the example for Poland*, Natural Hazards, doi:10.1007/s11069-015-1673-2.

VICENTE-SERRANO, S.M., LANJERI, S., and LÓPEZ-MORENO, J.I. (2007), *Comparison of different procedures to map reference evapotranspiration using geographical information systems and regression-based techniques*, Int. J. Climatol. *27*, 1103–1118.

VICENTE-SERRANO, S.M., LÓPEZ-MORENO, J.I., VEGA-RODRIGUEZ, M.I., BEGUERÍA, S., and CUADRAT, J.M. (2010), *Comparison of regression techniques for mapping fog frequency: application to the Aragon region (northeast Spain)*, Int. J. Climatol. *30*, 935–945.

VICENTE-SERRANO, S.M., SAZ, M.A., and CUADRAT, J.M. (2003), *Comparative analysis of interpolation methods in the middle Ebro valley (Spain): application to annual precipitation and temperature*, Clim. Res. *24*, 161–180.

WAGNER, P.D., FIENER, P., WILKEN, F., KUMAR, S., and SCHNEIDER, K. (2012), *Comparison and evaluation of spatial interpolation schemes for daily rainfall in data scarce regions*, J. Hydrol. 464–465, 388–400.

WALAWENDER, E., KIELAR, R., and USTRNUL, Z. (2015), *Use of RegCM gridded dataset for thunderstorm favorable conditions analysis over Poland—climatological approach*, Theoretical and Applied Climatology, doi:10.1007/s00704-015-1620-x.

WANG, C., YUE, T., and FAN, Z. (2014), *Solar Radiation Climatology Calculation in China*, Journal of Resources and Ecology *5*(2), 132–138.

WILBY, R.L., and WIGLEY, T.M.L. (1997), *Downscaling general circulation model output: a review of methods and limitations*. Progr in Phys Geogr, *21*, 530–548.

WILLMOTT, C.J., and MATSUURA, K. (2006), *On the use of dimensioned measures of error to evaluate the performance of spatial interpolators*, International Journal of GIS *20*, 89–102.

World Meteorological Organization (2004), *Establish Guidelines for implementation of a demonstration project of severe weather forecasting (proposal)*, Workshop On Severe and Extreme Events Forecasting (Toulouse, 26–29 October 2004). Available online at: http://www.wmo.int/pages/prog/www/DPS/Meetings/Wshop-SEEF_Toulouse2004/Doc3-1(1).doc (Accessed on: March 2015).

World Meteorological Organization (2008), *Guide to Meteorological Instruments and Methods of Observation*, 7th ed., WMO-No. 8.

World Meteorological Organization (2011), *Guide to climatological practices*, WMO no.100, third edition, Available online at: http://www.wmo.int/pages/prog/wcp/ccl/guide/documents/WMO_100_en.pdf (Accessed on: March 2015).

WYPYCH, A., USTRNUL, Z., and HENEK, E. (2014), *Meteorological Hazards—Visualization System for National Protection Against Extreme Hazards for Poland*, Meteorol. Hydrol. and Water Manag. *2*(1), 37–42.

YUAN, M.B., BUTTERNFIELD M., GAHEGAN M., and MILLER H., *Geospatial data mining and knowledge discovery*, In Research Challenges in Geographic Information Science (eds. McMaster R. and Usery) (John Wiley & Sons, CRC Press, Boca Raton, FL. 2005), chapter 14, pp. 365–388.

ONLINE DATA SOURCES

NCEP *Reanalysis data provided by the NOAA/OAR/ESRL PSD, Boulder, Colorado, USA*, http://www.esrl.noaa.gov/psd/data/reanalysis/reanalysis.shtml, accessed in March 2015.

EEA Data and Maps, *CORINE Land Cover*, http://www.eea.europa.eu/data-and-maps, accessed in March 2015.

(Received March 27, 2015, revised January 6, 2016, accepted January 29, 2016, Published online February 25, 2016)

Pure Appl. Geophys. 174 (2017), 661–678

DOI 10.1007/s00024-016-1296-x

Pure and Applied Geophysics

Geocomputation and Spatial Modelling for Geographical Drought Risk Assessment: A Case Study of the Hustopeče Area, Czech Republic

Aleš Ruda,[1] Jaromír Kolejka,[2] and Kateřina Batelková[3]

Abstract—The phenomenon of drought is serious in many landscapes with continental patterns of climate. In fact, drought risk is usually assessed in terms of prevailing issue (meteorological, hydrological, agronomical, etc.) and not in terms of complex landscape features. A procedure for detailed geographical drought risk modelling has been developed using recent meteorological data of dry period and prior precipitations, as well as a digital elevation model and geographic data layers of natural landscape features and land cover. The current version of the procedure starts with meteorological data (temperature and precipitation) processing followed by the use of soil and geological data and land cover, the national CORINE LC 2006 CZ database, for assessing the impact of the local natural features on drought risk. The methodology is based on GIS tools, geodata of the geological structure of the area (water holding capacity of the substrate, the horizontal and vertical water conductivity), soil cover (in agricultural and forested areas, soil types and kinds), landscape cover (land use), relief (digital elevation model and its derivatives), temperature and precipitation data from neighbouring representative meteorological and climate stations. The procedure uses regression equation for temperature and precipitation risk modelling, fuzzy standardization for estimation of different water retention within land cover categories and expert estimation for risk categories within rocks and soils. The final calculation is based on spatial decision-making techniques, especially the weighted sum method with a natural breaks reclassification algorithm. Combining geodata of soils, the geological environment and the active surface with their computed humidity conditions, it is possible to identify areas with a graded risk of geographic drought. The final results do not represent partial values, but identify five risk classes in the study area illustrating a possible level of geographical drought risk.

Key words: Geographical drought, aridity, spatial decision making, geocomputation, risk levels, environmental modelling.

1. Introduction

Geographic drought is a perceived drought, based on a geographic model of susceptibility to drought that includes interacting factors in a given area. Climate and meteorological factors of drought are assumed to control subsequent events with a lack of moisture in the area (Wilhite *et al*. 2000a, b). The deficit of groundwater or surface water can be amplified or attenuated by other factors of the geographical environment—both natural and anthropogenic. The aim of this article is to develop an area evaluation methodology based on geodata, which are publicly available for the Czech Republic. This approach will be such that the method can be applied anywhere in the Czech Republic or neighbouring countries to improve national or European regional policy (Hájek *et al*. 2014) dealing with the drought issue. The procedure is assumed to start to operate after the maximum daily temperature exceeds 30 °C and the period of tropical days begins regardless of the length of the consequent real "hot and dry" period. The method will address the response to drought of precisely selected areas.

In addition to established ideas of long-term (climatic) and seasonal (meteorological) drought, it is necessary to distinguish drought which is also the product of variously combined effects of all components of the landscape (Dracup *et al*. 1980). This means that the actual deficiency of water in the area may be locally and specifically increased or decreased by such effects. The Czech Republic is located in the temperate climatic zone in a transitional position on the border between the oceanic and continental climates (Munzar 2004). Its position in the centre of Europe leads to differences of available

---

[1] Department of Regional Development, Public Sector Administration and Law, Faculty of Management and Economics, Tomas Bata University in Zlin, Mostní 5139, 760 01 Zlín, Czech Republic. E-mail: ruda@fame.utb.cz

[2] Department of Geography, Faculty of Education, Masaryk University, Poříčí 7, 603 00 Brno, Czech Republic.

[3] Institute of Geonics, Drobného 28, 602 00 Brno, Czech Republic.

water, which should correspond to the potential climax vegetation. However, local effects can lead to drought conditions (Crutchfield 1983).

2. *Drought Phenomena Within Drought Indices*

Many parts of the world experience growing intensity, duration and frequency of water deficit in the landscape (Hayes 2003). In this context, the most frequently used terms are drought and aridity. This increasing trend in water deficit has resulted in a decrease in biomass production during the year (Potts 2003). Because of serious social, economic and environmental consequences of drought, monitoring has become an integral part of science and research. The drought is counted as one of the most damaging natural hazards (Bryant 1991). Arid areas are complex adaptive systems, which in fact are one of the least environmentally resilient ecosystems (see North American Drought 1996). This point is illustrated in reference to soil erosion, salinization and desertification. Fraisse *et al.* (2006) defines drought as a temporary condition in which the amount of water is due to lack of precipitation. In general, drought indicates a lack of water (Rožnovský 1998) or might be defined as a moisture deficit, compared to normal conditions that is generally caused by precipitation deficit, although other climatic factors cannot be excluded (Dracup *et al*. 1980; Oladipo 1985; Wilhite and Glantz 1985). It is also an integral part of climatic conditions (in Europe, especially in the continental moderate zone in south-eastern Europe and Mediterranean region; see Hawkes 2004) and has always affected human society with agriculture undoubtedly most clearly and most severely affected as a consequence of insufficient precipitation and soil moisture reserve (Sima *et al.* 2015). Brázdil and Kirchner (2007) state for dry periods that droughts represent a relatively short-term negative deviation from the normal water balance. In practice, this means that the water output in the landscape outweighs the water intake. It is not a random or rare phenomenon, but a normal, recurring situation of climate. Such transient climate anomalies are seen in all rainfall regimes of different climatic zones (Crutchfield 1983). This distinguishes it from aridity, which we consider as a permanent characteristic of climate (Munzar 2004). The effects of drought are cumulative in nature, because the intensity of the drought increases with time. The losses caused by drought can be considerable and we encounter its impacts years after a return to a normal precipitation regime.

Crutchfield (1983) further considers that drought is a deficiency that occurs when soil moisture is insufficient to meet the requirements of potential evapotranspiration. In contrast to the above-mentioned difference between drought and aridity, he divides drought into three categories: permanent drought associated with arid climates, seasonal drought, which represents annually recurring distinct periods of dry weather, and drought caused by considerable variability in precipitation. For these reasons, a universally valid definition of drought cannot be given (Blinka 2002). Many authors have distinguished the types of drought according to its dominant manifestations: meteorological drought, agricultural drought, hydrological drought and socioeconomic drought. It is clear that between these four types, there is a certain time sequence and the various manifestations can occur simultaneously (Brázdil and Kirchner 2007). The occurrence of agricultural, hydrological and socioeconomic drought may also be conditioned by meteorological drought. Agronomical (agricultural) drought, when the amount of soil moisture does not meet the needs of the plants, occurs after meteorological drought, but always before hydrological drought. It is primarily related to a water deficit in soil; agriculture constitutes moreover the first sector of the economy which is affected by this natural hazard (Brázdil and Kirchner 2007). Factors such as above-average temperatures, lower relative humidity, reduced cloudiness and longer duration of sunshine result in greater evapotranspiration. Drought is an issue not only for the livelihood of the population, but also for the protection of biodiversity (Potts 2003). However, not all the causes of reduced biodiversity are connected with drought.

Identification of factors causing drought is the subject of much research (Mo 2011; Vitas and Erlickytė 2007; Hayes 2003). Drought-related reduction of the efficiency of photosynthetically active radiation has also a great impact on crops which is very important for farmers and landscape planners (Earl and Davis 2003) and animal production (Palát *et al*. 2012). The effect of drought on plants has been investigated predominantly as a response to water deficit. Drought has an effect on the physiological and anatomical characteristics of stems, roots and leaves of plants (Makbul *et al*. 2011). Trnka *et al*. (2009) identify two main processes associated with drought–desertification and aridization. Desertification means land degradation in arid, semiarid and sub-humid areas resulting from a climate change and direct human activities (Reynolds and Stafford Smith 2002). The most affected zone is the Sahel, which is found south of the Sahara desert as a comprehensive and continuous belt. Desertification is an extreme form of aridization describing the effects of a process of long-term desiccation.

Drought can be defined both from spatial and temporal as well as from intensity points of view. Spatially, the areal extent of drought is monitored ranging from several hundred square kilometres to areas of hundreds of thousands of square kilometres or in extreme cases up to millions of square kilometres. In terms of time, drought is usually defined as duration, based on the beginning and end of a dry period. Other factors for assessing drought are used including air temperature, wind speed and humidity, which can significantly increase the intensity of drought (McKee *et al*. 1993; Heathcote 1999).

Indices of drought based on monthly mean values are not always wholly meaningful. They do not consider water supply decreases in time as a function of runoff and evapotranspiration, and do not reflect the impact of drought, which will take effect with a certain delay (Blinka 2002). Probably, the most commonly used indices are the Palmer Drought Severity Index (PDSI)—whose calculation takes into account the value of precipitation, evapotranspiration, runoff and soil and depth infiltration (Palmer 1965) and the standardized precipitation index (SPI) (McKee *et al*. 1993; Dragota *et al*. 2012). The original PDSI has undergone a series of modifications (Rhee 2007). The agronomical drought index and the index of moisture crops have been developed to measure short-term moisture conditions with regard to crop yields (Palmer 1968). The standardized runoff index (SRI, Shukla and Wood 2008) and the surface water supply index (Dezman *et al*. 1982) are hydrological drought indexes using data of flowing water in rivers for calculation, which represent hydrometeorological processes in a particular basin. Recently, due to the development of remote sensing techniques, a satellite-based index of drought has been developed. The vegetation condition index (VCI) is used to detect drought and also measures the intensity, duration and impact of drought on the landscape in different regions. Furthermore, daily climate data are being used to build a hydrological simulation model—precipitation runoff modelling system (PRMS) (Tsakiris and Vangelis 2005). PRMS also simulates water balance and energy balance of the water and is also used to determine the water quality, to estimate the impact of climate change and so on. For some indices, a large number of parameters for their calculation are only estimated, which noticeably reduces their quality. Therefore, there is also an argument that using only precipitation for meteorological drought determination is better than working with complex indexes for this reason (Wilhite *et al*. 2000a, b; Tsakiris and Vangelis 2005).

Wilhite *et al*. (2000a, b) also mention another approach used for the drought monitor system, which is intended to avoid the shortcomings associated with the current methods of drought assessment. They developed a composite index using seven key parameters (Palmer Drought Index, crop moisture index, CPC soil moisture model (percentiles), USGS daily streamflow (percentiles), percent of normal precipitation, USDA/NASS topsoil moisture (percent short and very short) and a remotely sensed satellite vegetation health index). The daily loss of water in their calculations is represented by effective rainfall for which determination it is sufficient to have only daily totals of precipitation of a station. At least ten consecutive days with no measurable precipitation, or a very small amount, or where a total precipitation reached a maximum of 5 mm within 1–5 days are considered periods without precipitation.

3. *Study Area: Hustopeče Area*

The Hustopeče research area (425 km^2) is a typical example of the Carpathian region of South

Moravia (Fig. 1). It includes both lowlands and highlands. The drainage axis of the valley and floodplain of the Thaya River is from NW to SE. It is followed by the river network of the Svratka River and the Trkmanka River north of the Thaya River plains. These streams drain the southern foothills of the Ždánický les Mountains, which is a part of the Central Moravian Carpathians region. The highest elevation in this area reaches Přední kout peak (410 m a.s.l.) and lies approximately in the middle of the test area. The geology of this part of the Ždánický les Mountains consists of flysch layers alternating with thin layers of sandstone, claystone and marl. The highest parts are underlain by massive layers of sandstone. The lower parts are covered by loess. Foot slopes are mostly covered with loamy slope foot deposits that in dry valleys pass into deluvial sandy–loamy deposits, and in valleys drained by rivers into fluvial floodplains. The area east of the river Trkmanka belongs to the rolling plains of the Dolnomoravský úval Graben, which is covered with Neogene deposits, mainly clayey marine sediments and locally covered with loess. Neogene sediments form the bedrock of the Thaya River plain. The southwest corner of the area extends to the South Moravian Carpathians, represented by Pavlovské vrchy Mountains, and is also covered with flysch sediments. The lowest parts of the study area, in the oak vegetation zone, have a very warm climate with average annual temperatures around 10 °C, and the highest positions reach the oak and beech vegetation zone with average annual temperatures around 8 °C. Higher cool shady slopes belong to the beech vegetation zone with temperature around 7 °C. The area is fairly dry, and rainfall varies from 400 mm per year in the lowlands to about 600 mm per year in the highest positions. Gleysols and fluvisols cover floodplains, while loess and weathered flysch are covered with Chernozem of different subtypes, switching at higher levels to Luvisols. Areas of Rendzic Leptosols are found on limestones and Haplic Arenosols on aeolian sands.

Figure 1
Study area localization (*red polygon*) in the South Moravian Region

4. *Methodology Background*

The concept of geographical drought is based on the assumption that the development of water deficit in each locality is jointly conditioned by factors representing all natural components of the geographical environment [atmosphere, hydrosphere, relief, geological environment, soil and vegetation (land) cover] and that generating the final level of risk can bring decision makers more evident results then strict value representation (Heathcote 1999; Blinka 2002). These components determine the water regime through their indicators (Wilhite and Glantz 1985):

- Atmosphere—incidence of periods with extremely high temperatures above 30 °C (tropical days) causing high evaporation.
- Hydrosphere—significant amount of available water moisture (precipitation, snowmelt) in the upper layer of the soil and weathered rock.
- Relief—elevation, slope and exposure conditions and the height above the local source of surface water and groundwater in alluvium, which define the moisture regime.
- Geological environment—different rocks affect the infiltration speed of surface water away from plant roots and capillary rise affects the movement of groundwater to the surface.
- Soil—soil type and texture define the moisture regime in the soil; the soil then has different water regimes forming the amount of moisture in the soil.
- Vegetation (land) cover—is affected by influences on the basis of retention susceptibility to evaporation from the surface, infiltration intensity and the speed of surface runoff.

Mentioned indicators have different relative weights in their impact on the water regime (Loucks and Gladwell 1999). To ensure the compliance of indicators for evaluating geographical drought, it showed up not to work only with measured values, but especially with their categories graded according to their impact on the formation and continuance of geographical drought.

The objective is to determine the site and, therefore on the basis of this, the landscape sensitivity to drought. The minimum size of the site is essentially determined by the resolution of the research data, in this case at the approximate lower chorological level (generally up to n. 10^3 km^2). Susceptibility to the drought means that any component of the natural environment is susceptible to water deficit. The more the elements of the landscape show this tendency, the higher is the risk of drought. A semiarid state of landscape unit is when at least one component shows lack of moisture, while an arid state is when all components show a moisture deficit (in biota, soil, geological environment, surface and underground water bodies, atmosphere). All the natural landscape components and a wide range of human activities in the region are involved, albeit to varying degrees in the determination of the water deficit.

The assessment of the drought risk in this way will reflect local natural conditions and land use, which potentially will be beneficial for long-term operational solutions for its mitigation. With respect to the known level of risk and to the contribution of the main factors to this risk, it will be possible to formulate, select and locate the necessary measures automatically using a procedure based on GIS, possibly tightening it up to the "step-by-step" automation and develop a DSS (decision support system). This will be able to design these measures for any area possessing similar geodata abundance and tentatively for long and short events of the rainfall deficit. Using available geodata, it is possible, based on terrain, to model the available precipitation amounts contributing to site moisture with respect to the prevailing wind directions as well as temperature and evapotranspiration conditions and the susceptibility to the formation of atmospheric inversions. By combining the calculated values of redistributed rainfall amounts, the intensity of evaporation, water runoff and infiltration values with regard to the nature of the geological environment, soils and the active surface (land cover), we can identify areas where on the one hand, despite the occurrence of climatic or meteorological drought, there is no geographic drought, and on the other hand locate dry areas although no rain deficit is indicated.

Direct values are calculated using various equations (mainly regression) to cover the study area, but there is no way to verify computed values in the field. When qualitative data are being used (geology, soils, land cover), only risk categories of these factors can be applied in further data processing (Ruda 2010). That is why the variables and their numerical or qualitative values were reclassified according to expert estimation into risk categories. The final value is calculated as a weighted sum of partial risk categories. Following reclassification into five risk values with respect to all variables applied in the data processing provides decision makers quite realistic outputs. The five classes represent risk categories: very low, low, average, high and very high (risk of drought). Finer classes cannot be justified. Anyway, a classification of the importance of everyone (weight of factor) of them is possible.

4.1. Air Temperature

Four key stations (Kobylí, Nemochovice, Staré město and Luhačovice) were taken as representative of the area and were used for temperature data. Their maximum daily air temperatures were analysed and from the time series (Fig. 2) a period from 18 July to 9 August 2013, with prevailing daytime temperatures (above 30 °C) and minimal rainfall, was identified as arid. This period served as a basis from which an arithmetic mean was calculated for each station and subsequently used for the calculation of temperature changes related to elevation. Meteorological data (not climate data) provide an operational drought risk assessment in each area. The results of such type of modelling support the immediate decision making and are suitable for identifying areas at risk of drought. The procedure described below represents an example from a real territory using real temperature and precipitation conditions (and other local natural conditions) for the total “hot and dry” period. In fact, in practical applications the modelling starts after the first day of high temperatures.

For this purpose, an environmental model (Fig. 3) reflecting the change in air temperature with altitude, slope and aspect was created. The means of the maximum daily temperatures were calculated with regard to their altitude by regression analysis. A calculated regression equation, $-0.0122x + y = 34.376$, was used for further processing. Using map algebra, a raster image of vertical temperature gradient in relation to digital model elevation (T1 grid) was created. The equation for T1 grid enables regression estimation of temperatures related to elevation, but does not reflect the local (zonal) temperature trend. For this, temperature normality (a proportion between the actually measured temperature and the temperature detected by calculating a regression equation) can be used as input data. Interpolating the values of individual temperature normality, followed by multiplying with the T1 raster results, in the zonal correction for the applied regression relationship. Using the experimental equation T2 (Vašků 1971) to refine the calculated temperature (T1 grid), the resulting potential temperature is given by the sum of the calculated values for the equation of T1 and T2 grid (Fig. 4). For this purpose, a raster layer combining reclassified values of the mentioned elevation characteristics was created and used to derive information of the coefficient of relative insolation (Table 1).

Because spatial decision-making process works with standardized values, the values of the air temperature model were reclassified using the algorithm of natural breaks into five classes. Class value 1 represents the coldest areas and therefore the areas of least risk for drought occurrence. Class value 5 represents the areas with the highest risk of drought.

4.2. Precipitation

The distribution of precipitation is similarly influenced by the characteristics of the relief. In addition to the current precipitation regime, the current rainfall totals reflect variable elevation, slope and aspect (Basist *et al.* 1994). Particularly strong rainfall comes to the Czech Republic from the northwest. It has been shown that the raindrops fall on average at a 5° angle to the vertical (Kolejka and Kretek 1997, 2001). On this basis, the distribution of precipitation was derived taking into account the slope and aspect (Table 2).

Recalculation of total rainfall from the previous period of precipitation is based on several simplifying assumptions. The recalculation is based on data available from precipitation stations mentioned above and located in the area of interest or in its neighbour. Although we cannot prove particular precipitation values, in the lowland areas at a particular altitude (summer precipitation may have a patchy pattern

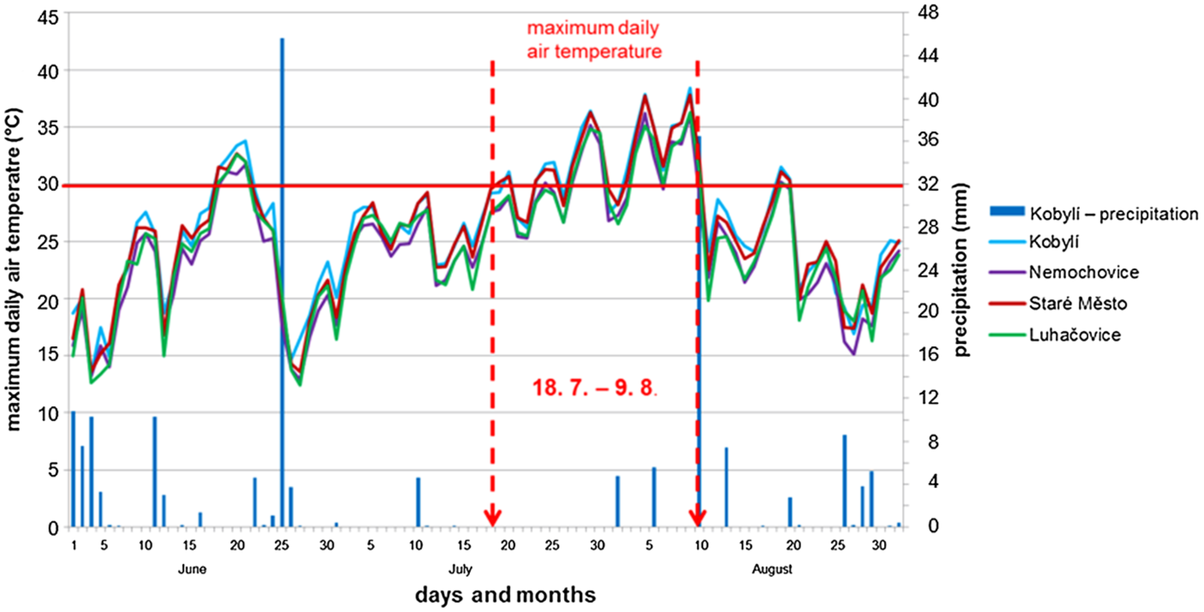

Figure 2
Identification of an arid period based on actual data from 2013

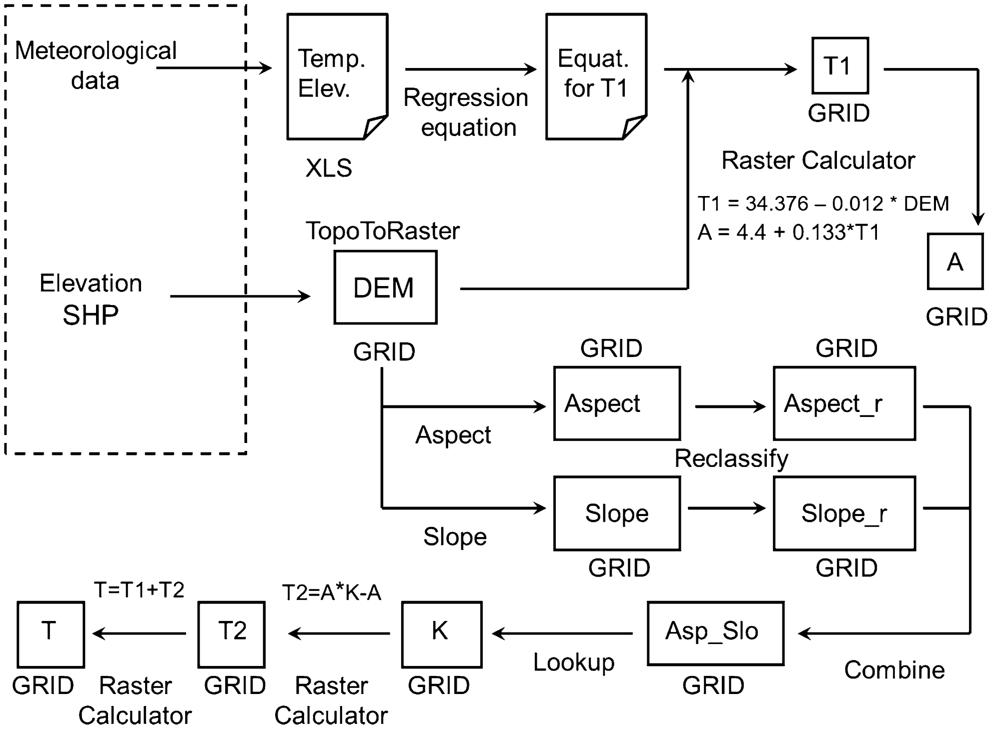

Figure 3
Flowchart of air temperature model

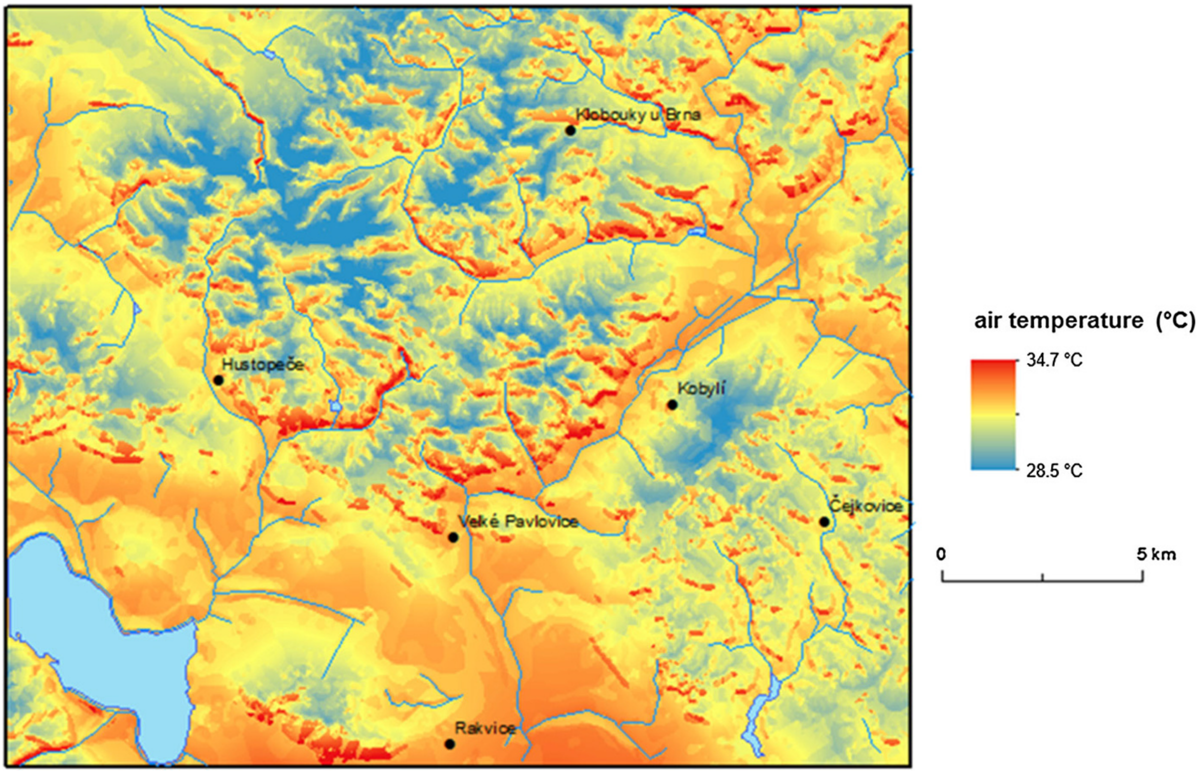

Figure 4
Air temperature results visualization of the Hustopeče area

Table 1

Derivation of coefficient of relative insolation for aspect and slope. Source: Vašku (1971)

K	Slope							
Aspect	(1) 0°–5°	(2) 5°–10°	(3) 10°–15°	(4) 15°–20°	(5) 20°–25°	(6) 25°–30°	(7) 30°–40°	(8) 40°–50°
(1) S	1.05 (04)	1.33 (03)	1.17 (06)	1.22 (08)	1.26 (31)	1.31 (34)	1.34 (35)	1.37 (40)
(2) SE, SW	1.04 (05)	1.10 (02)	1.16 (01)	1.20 (07)	1.24 (30)	1.26 (33)	1.28 (32)	1.30 (39)
(3) E, W	1.02 (09)	1.06 (20}	1.09 (21)	1.11 (14)	1.12 (27)	1.12 (26)	1.10 (29)	1.07 (38)
(4) SW, NW	1.00 (10)	1.02 (11)	1.01 (15)	1.00 (17)	0.99 (22)	0.97 (24)	0.92 (28)	0.84 (36)
(5) N	0.99 (13)	1.00 (12)	0 98 (16)	0 96 (18)	0.93 (19)	0.87 (23)	0.81 (25)	0.75 (37)

reflecting convective precipitation) we used simplifying assumptions that the theoretically homogeneous precipitation field is interrupted by the relief with respect to altitude, slope and aspect during the expected northwest direction of rain-bearing winds. Linear regression was used to determine the dependence of total rainfall on altitude. Recalculation using slope and aspect characteristics required further simplification, namely that rainfall-bearing wind changes the direction of rain drops from the vertical axis by up to 5°. Using descriptive geometry calculations, precipitation falling on a horizontal surface (100 % at an angle of 85°) was recalculated to combinations of eight aspect categories and four slope categories (0°–3°—plain; 3.1°–8°—flat slope; 8.1°–15°—low slope; above 15°—steep slope). Precipitation values were the total rainfall recorded before the expected drought period as mentioned during air temperature model calculation data from the Kobylí station. Precipitation values were

Table 2

Percent correction for supposed distribution of rainfall. Source: Kolejka and Kretek (1997, 2001)

	0°–3°	3.1°–8°	8.1°–15°	More than 15°
N	100	100.5	100.5	99
NE	100	100	100	100
E	100	99.5	98	94.5
SE	100	99	97.5	91.3
S	100	99.5	98	94.5
SW	100	100	100	100
W	100	100.5	100.5	99
NW	100	101	100	97.5

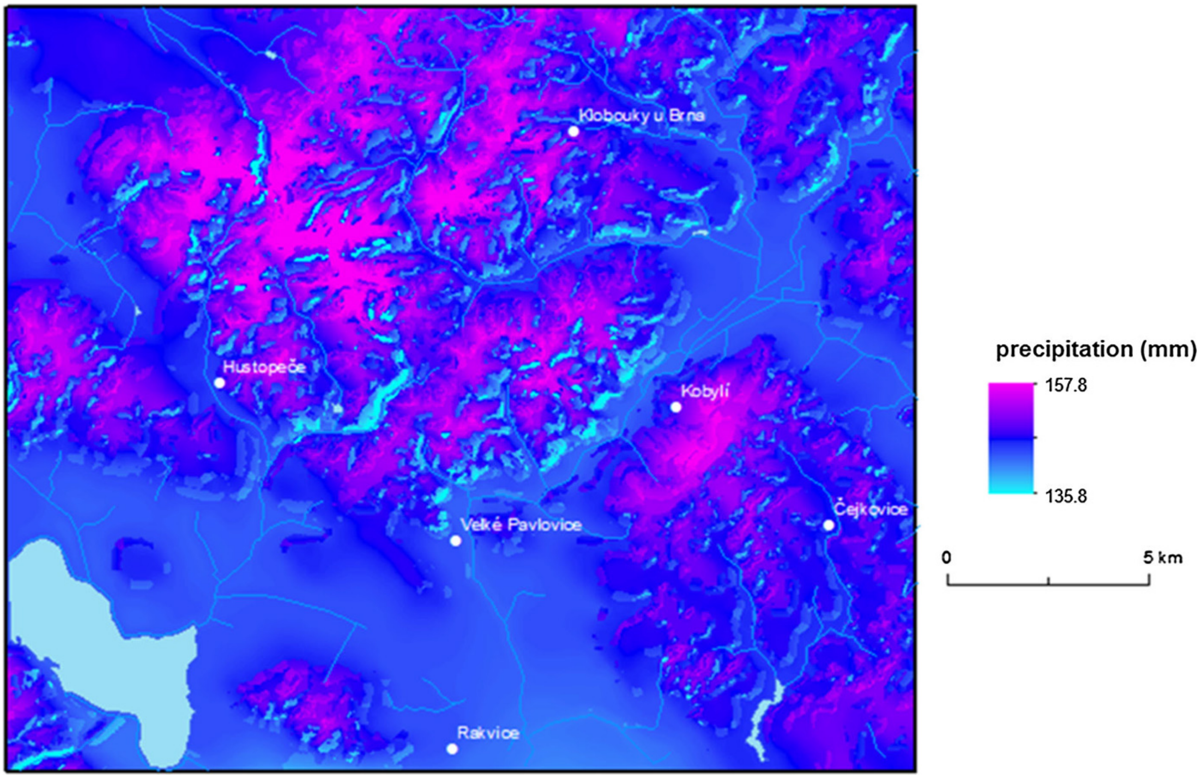

Figure 5
Precipitation results visualization of the Hustopeče area before the drought period

calculated based on rainfall and elevation of stations located inside or near the area of interest (Hustopeče, Kobylí, Klobouky, Ždánice, Prušánky, Těšany a Dolní Věstonice). The resulting image of computed precipitation is shown in Fig. 5. The data were reclassified by natural breaks algorithm grouping close values where the lowest point value is given to areas with the highest precipitation.

4.3. *Geology and Soils*

Soils data were derived from recent soil map (Tomášek 1994) and geologic data from geology maps (Stráník 1978, 1982; Matejka and Stráník 1960a, b; Palusková 1967). These represent local factors that can change the water situation-determined precipitation and air temperature. Soils and rocks (Fig. 6) with high water permeability (sandy

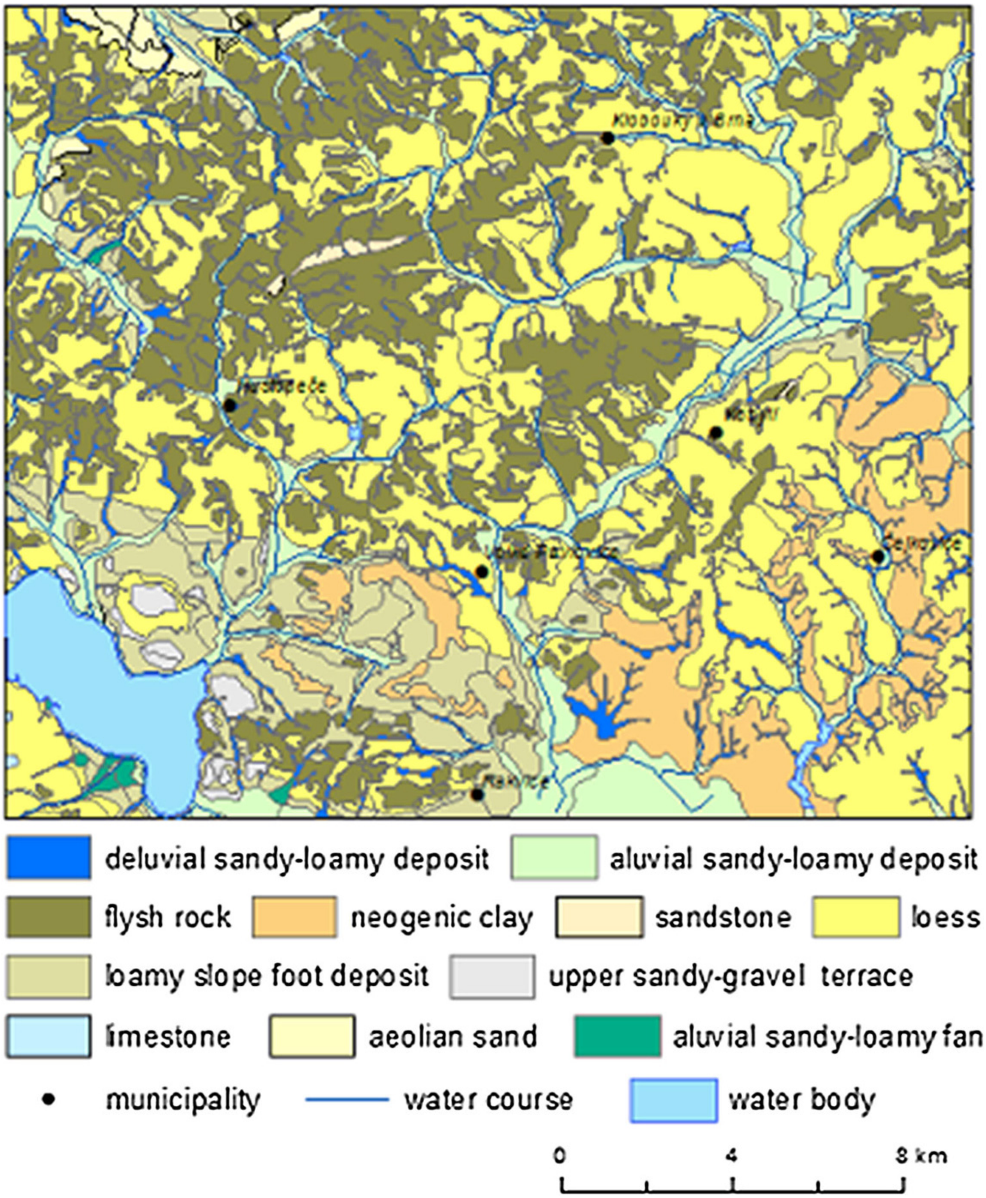

Figure 6
Geological composition of the Hustopeče area

soil: regosols, aeolian sands, gravel terraces, sandstones and fractured limestones) take water away from the reach of crop roots. Therefore, they are associated with water deficit of the surface, soil and upper parts of the geological environment shortly after rainfall. Soils with high content of clay and the clay-like particles (many soils on Neogene clays, flysch formations and loess) have high retention, but low infiltration and low permeability and promote surface water runoff.

Soils (Fig. 7) with strong vapour water regime and increased salinity strengthen the loss of water (i.e., Chernozems and partly Gleysols). Such regime can be found at the foot slope deposits where water lost by evaporation can be replaced with subsurface drainage from the upper part of the slope or capillary

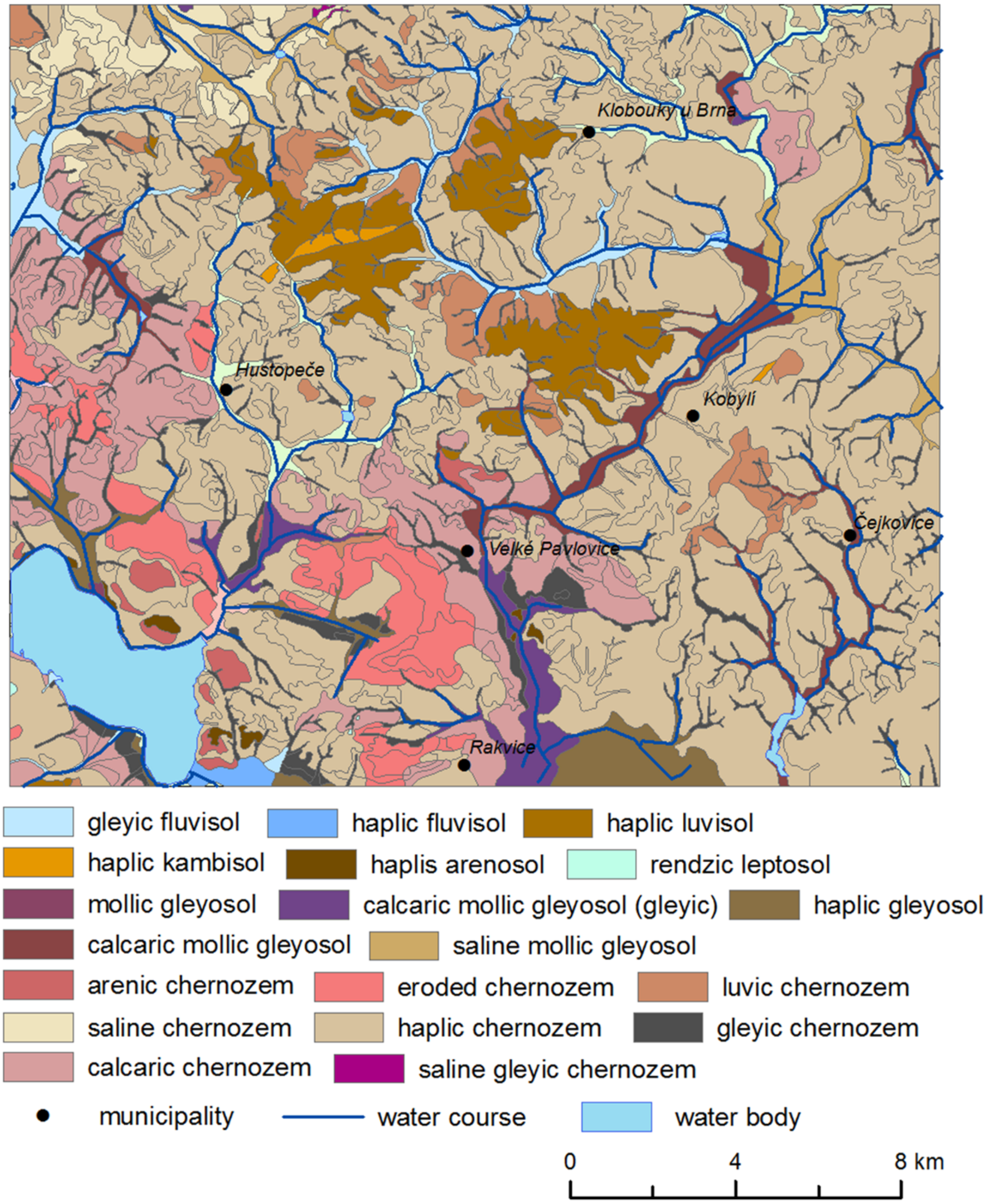

Figure 7
Soil type of the Hustopeče area

adhesion. Soils and rocks with groundwater resources (Fluvisols) have low risk of drought. Wet soils in the lowest parts of alluvial plains represented by Gleysols and Gleyic Fluvisols of all subtypes close to permanent water flow, which is hydraulically connected with groundwater resources, experience practically no drought conditions.

Moisture conditions and their relationship to the formation of surface dryness are determined by the presence or absence of groundwater in a geological environment (aquifer), in other words, by the horizontal movement of the water with vertical variations and vertical movement of water in the pores under gravity and capillary action. Individual types of geological environments, occurring in the studied area, therefore produce different responses to natural rainfall conditions. The speed of water movement is related to the geological material which determines permeability (Benetin 1958). Water permeability in soils is directly related to the risk of drought. The higher the permeability, the faster is the drying that takes place from the surface to the depth of the soil and increases the risk of drought. The speed of permeability was determined by the Research Institute for Soil and Water Conservation—RISWC (2011) for each major unit of soil defined by genetic

Table 3

Classification of risk level of drought for soils according to Benetin (1958)

No.	Soil sub-type	Risk level of drought	Permeability velocity
1	Haplic Gleysol	1	Less than 0.05 mm/min
2	Gleyic Fluvisol	1	Less than 0.05 mm/min
3	Haplic Fluvisol	2	0.05–0.10
4	Gleyic Fluvisol	1	Less than 0.05
5	Calcaric Fluvisol	2	0.05–0.10
6	Gleyic–Calcaric Fluvisol	1	Less than 0.05
7	Haplic Gleyosol	3	0.10–0.15
8	Mollic Gleysol	1	Less than 0.05
9	Saline Mollic Gleysol	1	Less than 0.05
10	Calcaric Mollic Gleysol	3	0.10–0.15
11	Calcaric Mollic Gleysol (Gleyic)	1	Less than 0.05
12	Luvic Chernozem	3	0.10–0.15
13	Gleyic Chernozem	2	0.05–0.10
14	Haplic Luvisol	3	0.10–0.15
15	Saline Gleyic Chernozem	1	Less than 0.05
16	Haplic Chernozem	4	0.15–0.20
17	Calcaric Chernozem	4	0.15–0.20
18	Haplic Cambisol	4	0.15–0.20
19	Saline Chernozem	1	Less than 0.05
20	Eroded Chernozem	4	0.15–0.20
21	Arenic Chernozem	5	More than 0.20 mm/min
22	Haplic Arenosol	5	More than 0.20 mm/min
23	Rendzic Leptosol	5	More than 0.20 mm/min

Table 4

Classification of risk level of drought for rocks according to RISWC (2011)

No.	Parent material	Risk level of drought	Humidity condition
1	Aluvial sandy–loamy deposits	1	Permanently saturated
2	Deluvial sandy–loamy deposits	2	Seasonally saturated
3	Aluvial sandy–loamy fans	2	Seasonally saturated
4	Loamy slope foot deposits	3	Long-term moist
5	Loess	4	Medium water movement—surface drying fast, water kept at great depth
6	Flysh rocks (claystones, marlstones, shales)	3	Limited water movement—surface drying fast, water kept at a depth
7	Neogenic clays	3	Limited water movement—surface drying fast, water kept at a depth
8	Aeolian sands	5	Extremely quick drying surface
9	Sandstones	4	Surface drying fast
10	Upper sandy–gravel terraces	5	Extremely quick drying surface
11	Limestones	5	Extremely quick drying surface

soil taxon and soil type (soil texture). Based on these values, the risk levels of drought were proposed (Tables 3, 4).

4.4. Land Use/Land Cover

Land use susceptibility to desiccation was based on data from the CORINE land cover (LC) 2006 dataset (EEA 2014) at 100 m resolution (Fig. 8). In determining the evapotranspiration characteristics of the vegetation and anthropogenic land covers (Table 5), a value indicating the ability of the cover to retain water in the landscape was assigned to each area (discontinuous urban area—20, industrial and commercial facilities—1, sports and recreation areas—50, non-irrigated arable land—40, vineyards—60, orchards, gardens and plantations—80, meadows and pastures—150, a mixture of fields and

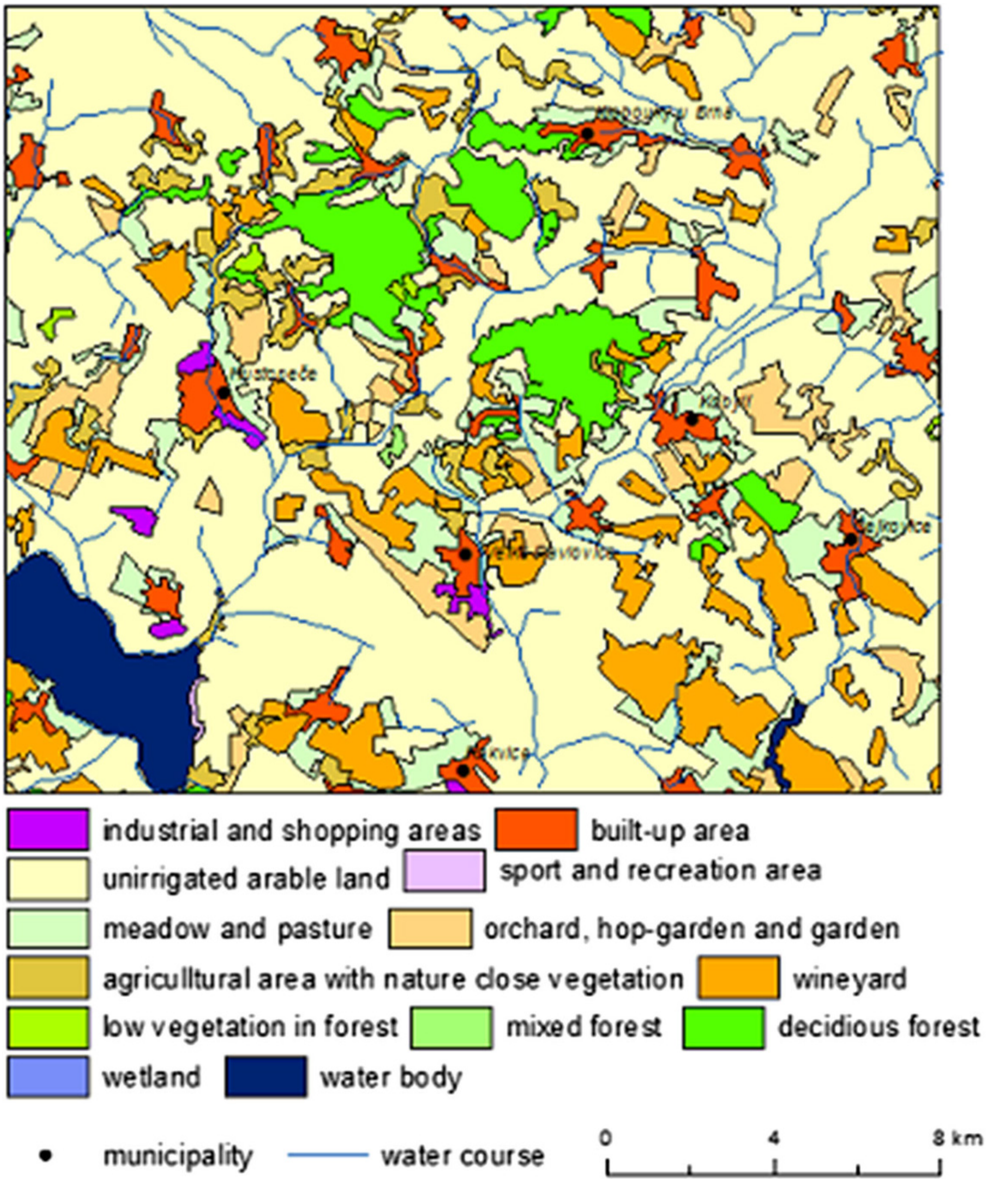

Figure 8
Land cover of the Hustopeče area

Table 5

Evaporation, transpiration and interception of main land cover categories based on Koldovský *(1970),* Vašků *(1971),* Blazejczyk *(1975),* Chapman *(2000) and* Krásný *(2012)*

Land cover category	Evaporation (%)	Transpiration (%)	Interception (%)
Forest	10	60	30
Alluvial forest	10	70	20
Spruce forest	10	40	50
Poor pine forest	20	20	60
Meadow	25	50	25
Arable land	45	40	15
Built-up areas	100	–	–

meadows of long lasting crops—150, agricultural areas with natural vegetation—100, deciduous forests—210, mixed forests—190, natural meadows—150, low vegetation in the forest—170, wetlands and marshes—230, water surface—255) (Koldovský 1970; Vašků 1971; Blazejczyk 1975; Chapman 2000; Krásný 2012). The quantitative scale (0 is no evapotranspiration and 255 is the highest possible evapotranspiration) was chosen on the basis of the recommended numerical variance for fuzzy data standardization. Data were reclassified using a standardized fuzzy method Large in ArcGIS 10.1 and, as in previous factors, reclassified into five risk classes of drought (Fig. 9).

4.5. Spatial Decision Making in GIS for Drought Risk Level Identification

So far, the layers of raster images of individual factors have been described for the entire area of interest. Spatial decision making, however, works with factors and also with constraints that prevent the occurrence of drought (Fig. 6). For our purpose, we considered as constraints features which stop the occurrence of drought (water bodies, areas close to watercourses or affected by hydraulic water connection). In the first case, both natural and anthropogenic water bodies were identified as a constraint raster image. In the second case, a band indicating the extent of the territory from the watercourses within an altitude of 10 m was delineated around watercourses. 10 m elevation difference between water level in the closest water body and neighbouring territory is assumed to represent the maximum vertical water access by plant roots. Both constraint layers were combined and used as a mask to remove pixels from layers representing individual factors. This solution refined the application of a natural breaks method necessary for reclassification. For the final model output, a weighted sum method was applied. WSM sums given point values of factors distinguished by preferential weights. These weights were calculated based on the matrix of Saatýs (1980) pairwise comparisons (Table 6). The resulting image (Fig. 7) was created by the Weighted Sum tool of ArcGIS for Desktop 10.1 software.

5. Results

The procedure for assessing the susceptibility of landscape areas to drought combined aspects of hydrologic regime, based on temperature and precipitation, together with the effects of terrain, soil and geological conditions and of land use. The resulting image (Fig. 10) shows the distribution of areas with different sensitivities to water deficit in the landscape. Both shades of warm colour indicate particularly risky areas. These are especially slopes with south, southeast and southwest orientations, which have lower total precipitation and above-average daily maximum air temperatures. These areas are only partly under drought-resistant agricultural crops (vineyards, orchards, gardens). Vineyards are especially involved in the increased risk of geographic drought during hot, dry periods. High-risk areas include flat areas along the main rivers planted with other annual agricultural crops.

Due to the unfavourable combination of natural conditions and of economic options, these areas

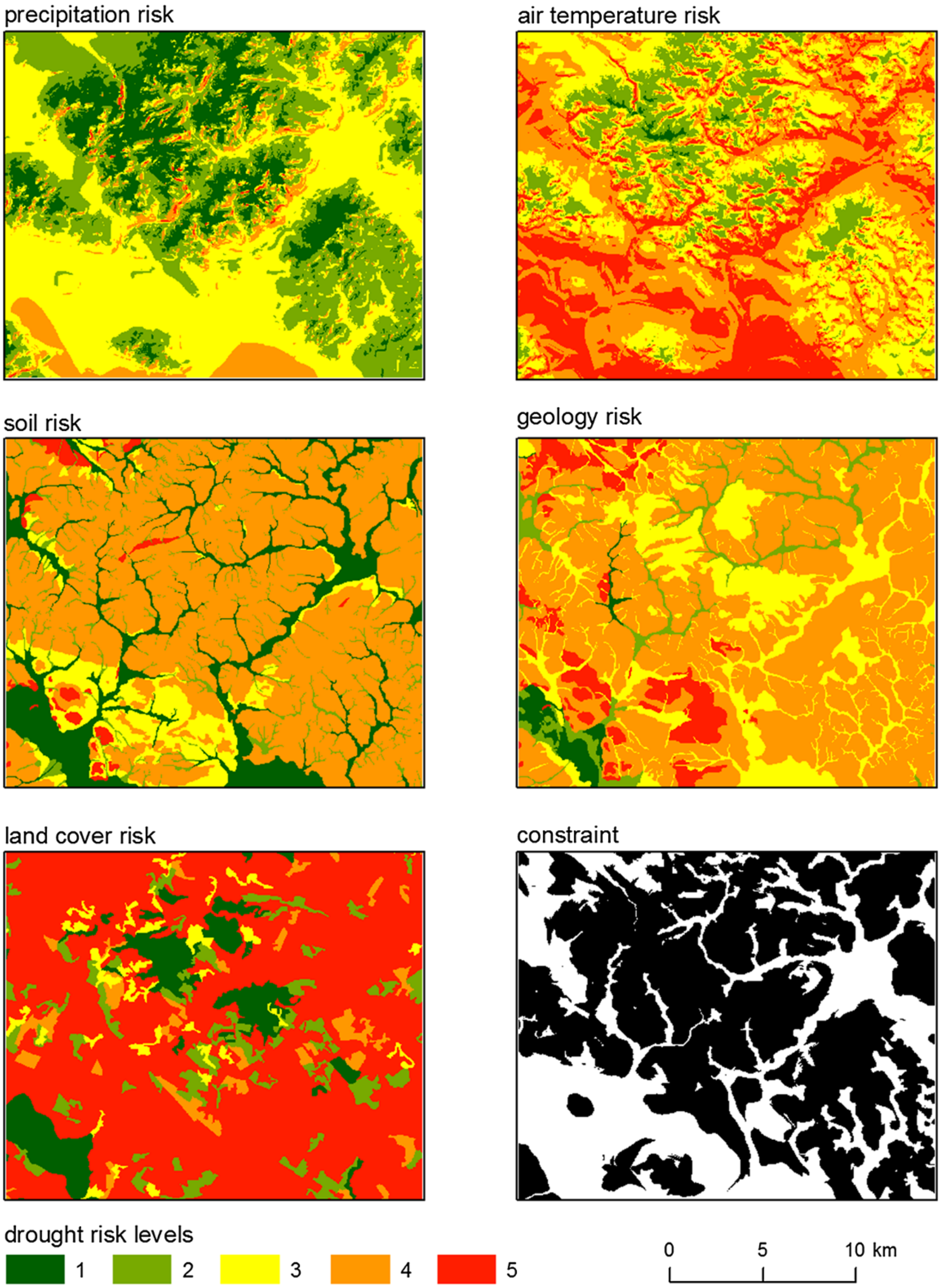

Figure 9
Input data layers (drought risk level layers, constraint layer—*white colour* represents constraint)

require intensive irrigation and more intensive attention on the level of regional offices (Ruda and Musil 2013). Conversely, forests and equivalent cover types in the form of orchards (usually apples, apricots, peaches and cherries) reduce the risk of drought, caused by natural factors. Areas covered with permanent tree cultures (forests and orchards) and elevated areas that are cooler even during

Table 6

Factors' weight according to Saatýs matrix of pairwise comparisons

	Corine LC	Geology	Precipitation	Soil	Temperature	Weight
Corine LC	–	3	1/5	3	1/3	0.1227
Geology	1/3	–	1/7	3	1/5	0.0691
Precipitation	5	7	–	7	3	0.5074
Soil	1/3	1/3	1/7	–	1/5	0.0438
Temperature	3	5	1/3	5	–	0.257

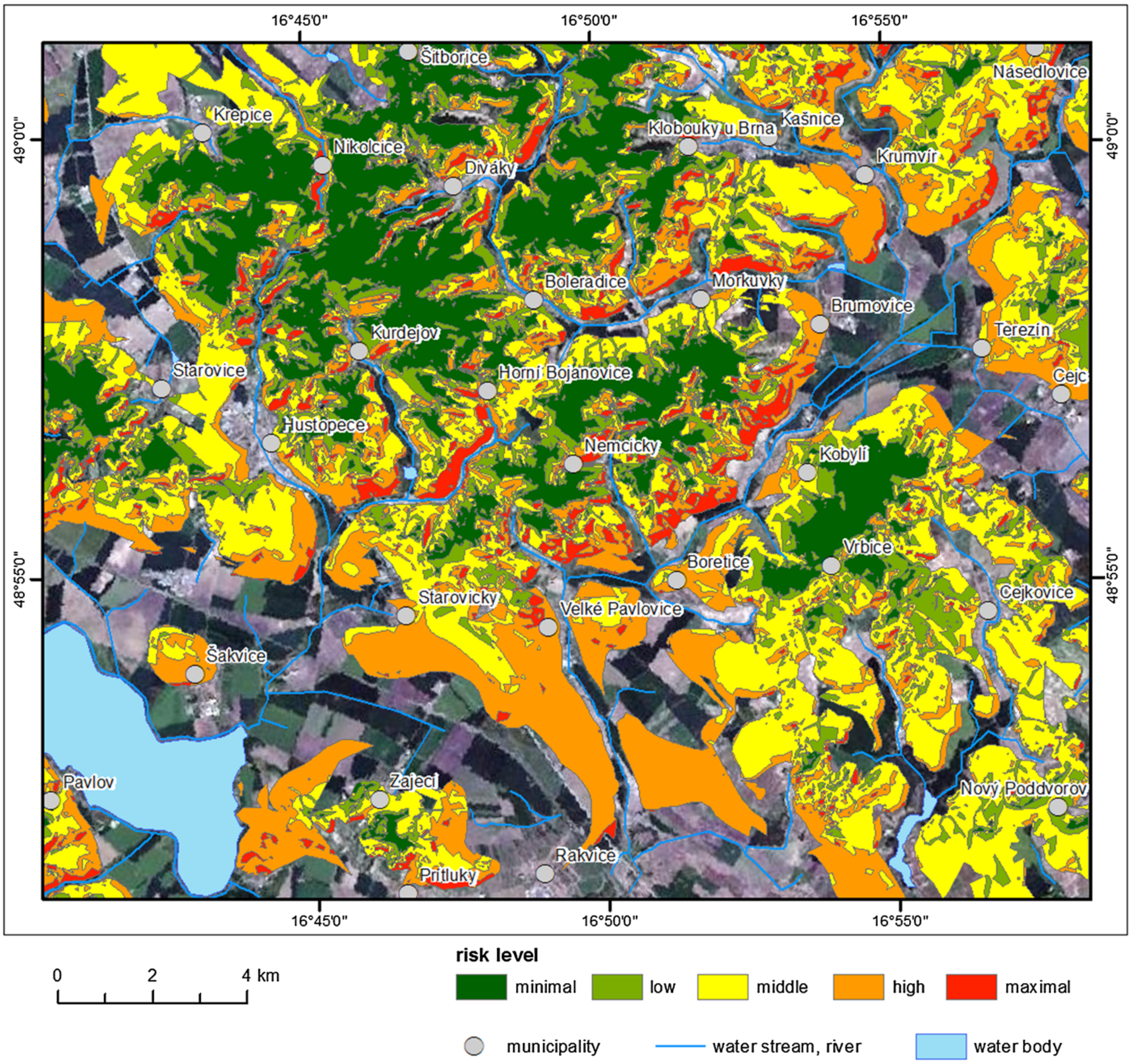

Figure 10
Geographical drought risk categories

extreme heat, and have higher precipitation, have lower drought risk (shades of green colour). Favourable sites are associated with moderate and steep north-facing slopes with lower maximum of daily air temperature and higher precipitation. Yellow areas indicate areas where there is a geographic drought risk, but only at high air temperatures and with long periods without rainfall.

6. *Conclusion*

The results provide the distribution of drought risk in a landscape, as well as knowledge about the relative risks of combinations of territorial components. This modelling, based on controlling factors of drought (high temperatures and prior precipitation), provides one among many possible options of other situations in the same area. The reason for this limitation is the absence of standards that would describe this situation in temperature and precipitation conditions delineating the boundary between "drought" and "drought-free". Pending the establishment of such a standard, a combination of high temperatures (like in the example used above 30 °C) lasting for a minimum period (e.g., 10 days) with a specified minimum of precipitation is assumed to be a valid approach. Attempts to establish standards are being undertaken in many countries and are based on calculations of water deficits in the soil environment (Wilhite *et al*. 2000a, b; RISWC 2011; EEA 2014).

The problem is that every land parcel, every rock and every plant cover have different values of such a critical factor as water deficit. Physical calculations based on measured values are difficult to extrapolate across surrounding heterogeneous environments. Determining the geographical risk of drought bypasses the problem of precise physical calculations and unreliable extrapolation by working with categories of values. But here, it turns out that the critical categories of temperatures, their duration and categories of rainfall are needed for comparison purposes. Any such standard, however, will be always tied to a specific region with the given regional combination of high temperatures and prior precipitation that will represent a required threshold below which the safety level against drought can be graded and above which the degree of "geographic risk of drought" can be determined. This study is an inspiration for further research.

References

Basist, A., Bell, G., Meentemeyer, V. (1994). *Statistical relationships between topography and precipitation patterns*. Journal of Climate, *7*, pp. 1305–1315.

Benetin, J. (1958). Pohyb vody v zemine. Bratislava, Slovenské vydavateľstvo technickej literatúry, 315 p.

Blazejczyk, K. (1975). *Wyznaczanie stopnia przewietrzania dolin*. Przeglad geograficzny, *47*, pp. 153–161.

Blinka, P. (2002). Metoda hodnocení sucha. In Rožnovský, J., Litschmann, T. (ed.): XIV. Česko-slovenská bioklimatologická konference. Lednice na Moravě,pp. 32–44.

Brázdil, R., Kirchner, K. (2007). Vybrané přírodní extrémy a jejich dopady na Moravě a ve Slezsku. Brno, Masarykova univerzita, 432 p.

Bryant, E. A. (1991). Natural Hazards. Cambridge University Press, Cambridge–New York–Melbourne, 294 p.

Chapman, L. (2000). *Assessing topographic exposure*. Meteorological Applications, *7*, pp. 335-340.

Crutchfield, H. J. (1983) General Climatology. Englewood Cliffs, Prentice-Hall, 464 p.

Dezman, L. E., Shafer, B. A., Simpson, H. D., Danielson, J.A. (1983). Development of a Surface Water Supply Index—A Drought Severity Indicator for Colorado. Proc., International Symposium on Hydrometeorology, Bethesda American Water Resources Association, pp. 337–341.

Dracup, J. A., Lee, K. S., Paulson, E. G. (1980). *On the definition of droughts*. Water Res. Res., *16*, pp. 297–302.

Dragota, C. S., Marculet, C., Mic, L. E., Grofu, A. (2012). *Mapping dryness time-scales in the curvature Carpathians and Subcarpathians (Romania) by the standardized precipitation index*. Romanian Journal of Geography, *52*, pp. 137–142.

Earl, H., Davis, R. F. (2003). *Effect of drought stress on leaf and whole canopy radiation use efficiency and yield of maize*. Agronomy Journal, *95*, pp. 688–696.

European Environment Agency (EEA) (2014). Corine Land Cover 2006 seamless vector data [online], accessed [27.8. 2015], available from http://www.eea.europa.eu/data-and-maps/data/clc-2006-vector-data-version-3.

Fraisse, C. W., Breuer, N. E., Zierden, D, Bellow, J. G., Paz, J., Cabrera, V. E., Garcia, A., Ingram, K. T., Hatch, U., Hoogenboom, G., Jones, J. W., O'Brien, J. J. (2006). *A climate forecast information system for agricultural risk management in the southeastern USA*. Computers and Electronics in Agriculture, *53*, pp. 13–27.

Hájek, O., Smékalová, L., Novosák, J. (2014). *Spatial coherence of national and European regional policy: The insights from the Czech Republic and Slovakia*. Politická ekonomie, *62*, pp. 630–644.

Hawkes, J. C. (2004). *A review of European Union funded research into Mediterranean desertification processes*. Advances in Environmental Monitoring and Modelling, *1*, pp. 1–39.

Hayes, M. J. (2003). Drought indices. U.S. National Drought Mitigation Center – NDMC [online], accessed [27.8. 2015], available from http://enso.unl.edu/ndme/enigma/indices.htm#spi

Heathcote, R. L. (1999). Drought, Impacts and Management. In Encyclopaedia of Environmental Science. Dordrecht, Kluwer Academic, pp. 137–139.

Koldovský, M. (1970). Mezní vrstva ovzduší. Praha, Hydrometeorologický ústav, 27 p.

Kolejka, J., Kretek, M. (1997). *Odhad rizika dopadů klimatických změn na vybraná chráněná území přírody Opavska pomocí GIS*. Geografie, *9*, pp. 4–22.

Kolejka, J., Kretek, M. (2001). *Klimatické změny a ochrana přírody. GIS jako účelný nástroj pro hodnocení rizik*. GEOinfo, *1*, pp. 28–31.

Krásný, J. (2012). Podzemní vody České republiky: regionální hydrogeologie prostých a minerálních vod. 1st edition. Praha, Česká geologická služba, 1143 p.

Loucks, D.P., Gladwell, J.S. (1999). Sustainability criteria for water resources systems. Cambridge, UK: Cambridge University Press, International Hydrology Series, 156 p.

Makbul, S., Guler, N., Saruhan, N., Durmus, N., Guven, S. (2011). *Changes in anatomical and physiological parameters of soybean under drought stress*. Turkish Journal of Botany, *35*, pp. 369–377.

Matějka, A., Stráník, Z. (1960a), Geologická mapa ČSR. List M-33-118-A-d šakvice. Měřítko 1: 25 000. Brno Geografický ústav ČSAV.

Matějka, A., Stráník, Z. (1960b), Geologická mapa ČSR. List M-33-118-A-b Hustopeče. Měřítko 1: 25 000. Brno Geografický ústav ČSAV.

McKee, T. B., Doesken, N. J., Kleist, J. (1993). The relationship of drought frequency and duration to time scales. In Preprints, 8th Conference on Applied Climatology, Anaheim, pp. 179–184.

Mo, C. K. (2011). *Drought onset and recovery over the United States*. Journal of Geophysical Research, *116*, pp. 1–7.

Munzar, J. (2004). *Extreme droughts in Central Europe in the preinstrumental period*. Moravian geographical reports. *12*, pp. 13–23.

NDMC. (1996). North American Drought: A Paleo Perspective, [online], accessed [27.8. 2015], available from http://www.drought.unl.edu/monitor/spi.htm.

Oladipo, E. O. (1985). *A comparative performance analysis of three meteorological drought indices*. Int. J. Climatol., *5*, pp. 655–664.

Palát, M., Dvořáková, Š., Kupková, N. (2012). *Consumption of beef in the Czech Republic*. Agricultural Economics. *58*, pp. 308–314.

Palmer, W. C. (1965). Meteorological drought, Research paper No. 45, Washington, D.C, U.S. Weather Bureau, 65 p.

Palmer, W.C. (1968). *Keeping track of crop moisture conditions, nationwide: The new crop moisture index*, Weatherwise, *2*, pp. 156–161.

Palusková, K. (1967). Mapa kvartérních sedimentů. List M-33-118-A-a Pohořelice. Měřítko 1: 25 000. Brno, Geografický ústav ČSAV.

Potts, M. D. (2003). *Drought in a Bornean everwet rain forest*. Journal of Ecology, *91*, pp. 67–474.

Research Institute for Soil and Water Conservation (RISWC). (2011). Nabídka mapových a datových produktů – Hydrologické charakteristiky. Praha, Výzkumný ústav meliorací a ochrany půdy, 23 p.

Reynolds, J. F., Stafford Smith, D. M. (2002). Do humans cause deserts? In: Global Desertification: Do Humans Cause Deserts? (ed. J.F. Reynolds and D.M. Stafford Smith). Berlin, Dahlem Univ. Press, pp. 1–21.

Rhee, J. (2007). A Regional Drought Monitoring System for the Carolina. Dissertation. Department of Geography, Columbia, University of South Carolina, 160 p.

Rožnovský, J. (1998). *Dynamics of occurrence of dry periods in the region of south Moravia and possible reduction of the effect of drought in agriculture*. Acta univ. agric. et silvic. Mendel. Brun, *46*, pp. 63–68.

Ruda, A. (2010). *Contribution to assessment of the tourism impact on landscape*. Acta Universitatis Carolinae Geographica, *1*, pp. 61–74.

Ruda, A., Musil, M. (2013). The organization and administration of GIS in regional offices. In Klimova, V., Zitek, V. (ed.): 16th International Colloquium on Regional Sciences Location: Valtice, JUN 19-21, pp. 444–450.

Saaty, T. L. (1980). The Analytic Hierarchy Process: Planning, Priority Setting, Resource Allocation. New York, McGraw-Hill, 287 p.

Shukla, S., Wood, A. W. (2008). *Use of a standardized runoff index for characterizing hydrologic drought*. Geophysical research letters, *35*, pp. 1–7.

Sima, M., Popovici, E. A., Balteanu, D., Muci, D. M., Kucsicsa, G., Dragota, C., Grigorescu, I. (2015). *A farmer-based analysis of climate change adaptation options of agriculture in the Baragan Plain, Romania*. Earth Perspectives, *2*, pp. 1–21.

Stráník, Z. (red.) (1978). Základní geologická mapa ČSR. List 34-211 Šitbořice. Měřítko 1: 25 000. Ústřední ústav geologický, Brno.

Stráník, Z. (red.) (1982). Základní geologická mapa ČSR. List 34-213 Hustopeče. Měřítko 1: 25 000. Ústřední ústav geologický, Brno

Tomášek, M. (red.). (1994). Půdní mapa ČR. List 34-21 Hustopeče. Mapa měřítka 1:50 000. Český geologický ústav, Praha.

Trnka, M., Kyselý, J., Možný, M., Dubrovský, M. (2009). *Changes in central-european soil-moisture availability and circulation patterns in 1881-2005*. International Journal of Climatology, *29*, pp. 655–672.

Tsakiris, G., Vangelis, H. (2005). *Establishing a drought index incorporating evapotranspiration*. European Water, *9*, pp. 3–11.

Vašků, Z. (1971). Metodika vyhodnocení potřeby odvodnění a závlah. In Ambros Z. (ed.) Praktikum geobiocenologie, Brno, pp. 1–98.

Vitas, A., Erlickytë, R. (2007). *Influence of Droughts to the Radial Growth of Scots Pine (Pinus sylvestris L.) at Different Site Conditions*. Baltic Forestry, *13*, pp. 10–16.

Wilhite, D. A., Glantz, M. H. (1985). *Understanding the drought phenomenon: The role of definitions*. Water International, *10*, pp. 111–120.

Wilhite, D. A., Hayes, M. J., Svoboda, M. D. (2000a). Monitoring drought using the standardized precipitation index. In Drought: A Global Assessment. Edited by D.A. Wilhite. Routledge, London, UK, pp. 168–180.

Wilhite, D. A., Hayes, M., Knutson, C., Smith, K. H. (2000b). *Planning for drought: Moving from crisis to risk management*. Journal of the American Water Resources Association, *36*, pp. 697–710.

(Received September 30, 2014, revised February 22, 2016, accepted April 12, 2016, Published online April 28, 2016)

Pure Appl. Geophys. 174 (2017), 679–700
© 2016 Springer International Publishing
DOI 10.1007/s00024-016-1433-6

Pure and Applied Geophysics

The Use of Geospatial Technologies in Flood Hazard Mapping and Assessment: Case Study from River Evros

Angeliki Mentzafou,[1] Vasiliki Markogianni,[1] and Elias Dimitriou[1]

Abstract—Many scientists link climate change to the increase of the extreme weather phenomena frequency, which combined with land use changes often lead to disasters with severe social and economic effects. Especially floods as a consequence of heavy rainfall can put vulnerable human and natural systems such as transboundary wetlands at risk. In order to meet the European Directive 2007/60/EC requirements for the development of flood risk management plans, the flood hazard map of Evros transboundary watershed was produced after a grid-based GIS modelling method that aggregates the main factors related to the development of floods: topography, land use, geology, slope, flow accumulation and rainfall intensity. The verification of this tool was achieved through the comparison between the produced hazard map and the inundation maps derived from the supervised classification of Landsat 5 and 7 satellite imageries of four flood events that took place at Evros delta proximity, a wetland of international importance. The comparison of the modelled output (high and very high flood hazard areas) with the extent of the inundated areas as mapped from the satellite data indicated the satisfactory performance of the model. Furthermore, the vulnerability of each land use against the flood events was examined. Geographically Weighted Regression has also been applied between the final flood hazard map and the major factors in order to ascertain their contribution to flood events. The results accredited the existence of a strong relationship between land uses and flood hazard indicating the flood susceptibility of the lowlands and agricultural land. A dynamic transboundary flood hazard management plan should be developed in order to meet the Flood Directive requirements for adequate and coordinated mitigation practices to reduce flood risk.

Key words: Flood hazard mapping, land use, GIS techniques, satellite imageries, transboundary river Evros, flood directive.

1. *Introduction*

During the last decades a debate has risen on the link between climate change and global warming and the increase of extreme weather events frequency (e.g. heat or cold waves, high winds, heavy rainfall). Although extreme weather events are integral part of the earth's climate system as a result of large scale atmosphere–ocean circulation patterns and their complex interaction with local weather and climate elements (Khandekar 2013), based on the latest IPCC (2013) "Summary for Policymakers" (SPM), the frequency or intensity of heavy precipitation events has *likely* increased in North America and Europe. Even though the conclusion of climate change contribution in worldwide extreme weather events is premature (Khandekar 2005), based on recent climate models the global warming will affect the hydrological cycle and increase the magnitude and frequency of intense precipitation events in most parts of Europe and especially in Mediterranean area (e.g. Semmler and Jacob 2004). This phenomena is expected to be intensified due to land use changes such as deforestation and urbanization, because although land use types are not directly involved in flood creation, they affect the water holding and infiltration capacities of the soil and therefore influence the flood intensity and propagation. As a result and also due to poor management practices concerning mainly dams operation, the flood risk and vulnerability tend to increase over many areas (Kundzewicz et al. 2010; Feyen et al. 2009). Wetlands are especially vulnerable to such pressures, due to their susceptibility to hydrological changes (Erwin 2009). The European Directive 2007/60/EC aims to the reduction and management of the risks that floods pose to human health, the environment, cultural heritage and economic activity and requires the assessment and management of flood risks. The flood risk management of transboundary water courses raises many challenges due to different approaches to strategic decision making, capacity and resources and

---

[1] Hellenic Centre for Marine Research, Institute of Marine Biological Resources and Inland Waters, 46.7 km Athens-Sounio Ave., 19013 Anavissos Attikis, Greece. E-mail: angment@hcmr.gr

due to the lack of a legal framework for cooperation and the public participation and awareness (UNECE 2009).

Natural hazards, such as floods, are multi-dimensional phenomena which have a spatial component (Meyer et al. 2009; Zerger 2002), and therefor GIS based multi-criteria decision analysis is an appropriate tool for processing spatial data on flood risk (Malczewski 2006; Papaioannou et al. 2015). Under this scope the flood hazard map of Evros transboundary river basin was produced after a grid-based GIS modelling method that aggregates the main factors related to the development of floods: topography, land use, geology, slope, flow accumulation and rainfall intensity (Kourgialas and Karatzas 2011). The verification of this tool was achieved through the comparison between the produced hazard map and the inundation maps derived from the supervised classification of Landsat 5 and 7 satellite imageries of four flood events that took place at Evros delta proximity, a wetland of international importance. Furthermore, the vulnerability of each land use against the flood events was examined. Geographically Weighted Regression has also been applied between the final flood hazard map and the major factors (geological structure, land uses, rainfall intensity, topography) in order to ascertain their contribution to flood events. Scope of this effort was to identify the flood prone areas of Evros transboundary watershed, to examine the effectiveness of the flood hazard mapping methodology proposed by Kourgialas and Karatzas (2011) at the specific case study and to assess the performance and the universality of this approach. Finally, the challenge of flood risk management in the transboundary catchment of Evros river is discussed.

2. *Study Area*

Evros river is the second largest river in Eastern Europe, flowing through Bulgaria, Greece and Turkey and discharging significant quantities of water and sediment in the Aegean Sea (Fig. 1). It emerges at the Rila mountain near the summit of Musala and flows first through a steep glacier valley and then east and southeast fringed by the Balkan and Rhodope mountains before crossing the Thracian plain (Skoulikidis et al. 2009). The total length of the river is about 528 km, 310 km of which belongs to Bulgaria and the remaining 218 km comprise the boundary between Greece and Turkey. The catchment area is about 53,000 km^2 while its annual average discharge fluctuates from 50 to 200 m^3/s. The most important tributaries of Evros river are Tundzha and Ardas in Erdine, Ergene in Ipsala and Erythropotamos near Didimoteicho (Dimitriou et al. 2010). Evros river basin is one of the most intensively cultivated areas in the Balkans and supports a population of 3.6 million people. Major pollution pressures comprise mining activities and untreated effluents from heavy and light industry at the Bulgarian part of the basin, industrial activities at the Turkish part, whilst in Greek part the cultivation activities make it one of the most import agricultural regions of Northern Greece (Dimitriou et al. 2011).

Evros delta, shared by Greece and Turkey, is one of the most important wetland on a national and European level. A major part of the delta in Greece is included in the list of wetlands designated as internationally important under the Ramsar Convention (1971), due to the numerous flora and fauna species hosted. Furthermore, Evros delta is designated as Special Protection Area (SPA) and as Site of Community Importance (SCI) in the Natura 2000 network (Dimitriou et al. 2010). Evros delta is also included in the list of wetlands of international importance of Turkey, while lake Gala in close proximity has been declared a National Park area (Ministry of Forest and Water Management of Turkey 2011).

Many dams and reservoirs are located along Evros river and its tributaries. In the Bulgarian part the total number of large dams and reservoirs is up to 722, mainly for hydropower production and secondarily for irrigation purposes and fish-breeding. In Turkey, seven dams and one regulator are under operation on the Ergene river and its tributaries, serving irrigation, flood control and some drinking water supply purposes, while also 53 small irrigation dams are located on several tributaries (UNECE 2011). In Greece the total number of small dams for irrigation purposes are five (Dimitriou et al. 2010).

The climatic and geomorphological conditions of Evros river basin lead to specific run-off conditions, characterized among others by high inter-annual flow variability (UNECE 2011). During the last decade

Figure 1
Evros river basin

and especially after 1994, the flood frequency and the dikes overtopping especially downstream of Evros river has increased dramatically (Angelidis et al. 2010), sometimes with severe social and economic impacts (Table 1). Among the most disastrous floods were in 2005 (returning period: 1000 years), in 2006 and in 2007 (UNECE 2011). It must be noted that it is not clear if this increase in the appearance of floods (six times greater frequency) is due to extreme climatic changes or a result of the management of the Bulgarian dams (Angelidis et al. 2010).

3. *Methodology*

3.1. *Flood Hazard Mapping*

The estimation of the flood-hazard areas of Evros river basin was accomplished after the methodology developed by Kourgialas and Karatzas (2011). The particular approach incorporates both dynamic and physical spatial properties to describe which areas of a catchment are more prone to floods than others. In this sense, lowland areas with impermeable lithology and high potential flow accumulation have higher flood risk than upstream areas, with higher slopes and permeable geological formations. Therefore, this GIS based multi-criteria decision analysis approach that is widely used, does not aim to present or predict a single flood event but to characterize the flood hazard of the entire catchment based on the protective functions provided by its physical and manmade characteristics.

Based on this approach, the flood-hazard map is produced after the integration of multi-criteria analysis at catchment scale with a grid-based GIS (Table 2). More specifically, six individual maps

Table 1

Major flood event of Evros river during the last decade

a/a	Begin date	End date	Areas affected	Main cause	Magnitude*	References
1	17/01/2003	03/03/2003	Northeastern Greece. Evros Prefecture. Tichero, Ampelakia, Chandra, Megali Doxipara, Mavrokklisi, Mandra, Thourio Southeastern Bulgaria Northwestern Turkey—Ergene River	Heavy rain	6.0	1, 2
2	17/02/2005	24/03/2005	Northeastern Greece—Thrace region. Evros Prefecture, Pytheio area, Sofiko district near Didymotichos. Lavra, Pitia and Poros Bulgaria—Maritsa river Northwestern Turkey—Odrin Tharace region.	Rain and snowmelt	5.6	1, 2, 3
3	02/01/2006	20/01/2006	Greece—Lavara, Kissario, Amorio, Tichero, Thymaria, Psathades in Didymotichos, Pythio, Trigono	Snowmelt	5.5	1, 2, 3
4	09/03/2006	25/03/2006	Northeastern Greece—Evros region. Thrace. Soufli Northwest Turkey—Edirne region. Tychero Southern Bulgaria—Kardzhali region, Haskovo, Plovdiv and Smolyan, Saedinenie	Rain and snowmelt	5.5	1, 2, 3
5	06/08/2007	–	Greece-Alexandroupoli—Makri	Heavy rain	–	3
6	16/11/2007	02/12/2007	Greece—Evros region, Eastern Macedonia and Thrace—Ghodopi, Rodopi, Komotini, Kavala and Drama. Turkey—Thracian and Aegean regions—Tekirdag. Edirne. Marmaris, Bodrum. Muğla province. Bulgaria—Stara Zagora—Radnevo, Galabovo, Tsarevo, Opan and Saedinenie. Sofia, Plovdiv, Burgas, Haskovo.	Heavy rain	6.0	1, 2
7	13/02/2010	20/02/2010	Greece—Evros rivers overflew. Traianoupoli, Ferres, Tichero, Soufli, Orfea, Didimoticho, Orestiada, Kiprinos, Vissa, Metaxades, Trigono Bulgaria—Tundzha River overflew its banks. Elhovo and its surrounding villages	Heavy rain	5.1	1, 2, 3
8	06/02/2012	11/02/2012	Greece—Dikaia, Ormenio, Ptelea, Orestiada—Trigono	Heavy rain	–	3
9	24/01/2013	04/02/2013	Greece—Alexandroupoli, Ferres, Doriskos, Loutro, Didimoticho, Sofiko	Heavy rain	–	3

* Flood magnitude = LOG (duration × severity × affected area)

1. Darmouth Flood Observatory (2014)

2. Ministry of Environment Energy and Climate Change (2012)

3. Ministry of Infrastructure, Transport and Networks—General Secretariat of Public Works—Earthquake Recovery Service (2014)

were produced for each of the main factors that contribute to the development of floods. These factors are: topography, land use, geology, slope, flow accumulation and rainfall intensity of the river basin. The effect of each factor is rated in five different hazard classes: very high, high, moderate, low and very low. In the case of numeric-valued factors (topography, slope, flow accumulation and rainfall intensity) the hazard classes were defined after Jenk's Natural Breaks method. This is dictated by the particular flood hazard methodology (Kourgialas and Karatzas 2011) but is also widely used in other similar modelling techniques for the estimation of flood and other natural disasters prone areas or during risk, hazard or vulnerability mapping (e.g. Mallick et al. 2015; Pasqualini et al. 2011; Stefanidis and

Table 2

Weight evaluation of the factors affecting flood-hazard areas proposed by Kourgialas and Karatzas (2011)

a/a	Factor	Domain of effect	Flood hazard	Weight of effect (w)	Rate (x)	Weighted rating ($w \times x$)	Total weight	Total weight (%)
1	Topography (m)	0–261.7	Very high	10	4.5	45	117	31.5
		261.7–557.4	High	8		36		
		557.4–944.2	Moderate	5		22.5		
		944.2–1,399.3	Low	2		9		
		1,399.3–2,901	Very low	1		4.5		
2	Land use	Zones seaward and artificial surfaces	Very high–high	10	3	30	78	21.0
		Shrub-brush-rangeland	High	8		24		
		Cropland and pasture	Moderate	5		15		
		Other agricultural land	Low	2		6		
		Mixed forest land	Very low	1		3		
3	Geology	Loose, silty porous formations	Very high-High	9	3	27	46.5	12.5
		Cohesive, sandy porous formations	Moderate	5		15		
		Fractured or karstic formations	Low-very low	1.5		4.5		
4	Slope (degrees)	0–3.0	Very high	10	2	20	52	14.0
		3.0–7.6	High	8		16		
		7.6–13.6	Moderate	5		10		
		13.6–21.2	Low	2		4		
		21.2–55.2	Very low	1		2		
5	Flow accumulation	1,198,798–2,333,539	Very high	10	1.5	15	39	10.5
		668,033–1,198,798	High	8		12		
		356,894–668,033	Moderate	5		7.5		
		100,662–356,894	Low	2		3		
		0–100,662	Very low	1		1.5		
6	Rainfall intensity (MFI)	75.3–98.9	Very high	10	1.5	15	39	10.5
		66.2–75.3	High	8		12		
		58.9–66.2	Moderate	5		7.5		
		52.8–58.9	Low	2		3		
		46.1–52.8	Very low	1		1.5		
Total							371.5	100.0

Stathis 2013). In cases of non-numeric valued factors (geology and land use) the hazard classes were defined according to the water infiltration capacity of the geological formations and land use types, after Kourgialas and Karatzas (2011) suggestions. The highly permeable geological formations and land use types were classified as of low and very low flood hazard while the low permeability formations and land use types were characterized as of high and very high flood hazard (Table 2). Afterward, for each factor a weight factor was attributed, depending again on their influence on flood processes. Finally, the flood-hazard map was produced after the aggregation of each weighted factor (Gemitzi et al. 2006) (Formula 1), while again the five flood hazard classes were defined after Jenk's Natural Breaks method.

$$S = \sum_{1}^{i} w_i x_i \qquad (1)$$

where S: the hazard index, w_i: the weight of factor i, and x_i: the rate of factor i.

The flood hazard map concerning the elevation factor was developed in GIS environment using the digital elevation model (DEM) of the river basin of Evros (cell size 150 m). Likewise, the slope map was produced in GIS environment from the digital elevation model (DEM) of the study area. The drainage areas of a river basin can be indirectly determined by flow accumulation (Schäuble et al. 2008). The flow accumulation map was produced using the flow direction map, which was produced from the digital elevation model (DEM) of the river Evros river basin, in the ArcGIS 10.1 software.

The flood hazard map concerning land uses was developed based on CORINE 2000 database (European Environmental Agency 2012). The land uses proposed by European Environmental Agency were

Table 3

Assignment between Corine land use classes and land use classes used in Flood hazard mapping

Corine code	Corine description (level 3)	Land use classes (based on their sensitivity to flooding)	Flood hazard
111	Continuous urban fabric	Zones seaward and artificial surfaces	Very high
112	Discontinuous urban fabric	Zones seaward and artificial surfaces	Very high
121	Industrial or commercial units	Zones seaward and artificial surfaces	Very high
122	Road and rail networks and associated land	Zones seaward and artificial surfaces	Very high
124	Airports	Zones seaward and artificial surfaces	Very high
131	Mineral extraction sites	Zones seaward and artificial surfaces	Very high
132	Dump sites	Zones seaward and artificial surfaces	Very high
133	Construction sites	Zones seaward and artificial surfaces	Very high
141	Green urban areas	Shrub-brush-rangeland	High
142	Sport and leisure facilities	Shrub-brush-rangeland	High
211	Non-irrigated arable land	Cropland and pasture	Moderate
212	Permanently irrigated land	Cropland and pasture	Moderate
213	Rice fields	Cropland and pasture	Moderate
221	Vineyards	Other agricultural land	Low
222	Fruit trees and berry plantations	Other agricultural land	Low
231	Pastures	Cropland and pasture	Moderate
242	Complex cultivation patterns	Cropland and pasture	Moderate
243	Land principally occupied by agriculture, with significant areas of natural vegetation	Cropland and pasture	Moderate
311	Broad-leaved forest	Mixed forest land	Very low
312	Coniferous forest	Mixed forest land	Very low
313	Mixed forest	Mixed forest land	Very low
321	Natural grasslands	Shrub-brush-rangeland	High
322	Moors and heathland	Shrub-brush-rangeland	High
323	Sclerophyllous vegetation	Other agricultural land	Low
324	Transitional woodland-shrub	Other agricultural land	Low
331	Beaches. dunes. sands	Zones seaward and artificial surfaces	Very high
332	Bare rocks	Zones seaward and artificial surfaces	Very high
333	Sparsely vegetated areas	Other agricultural land	Low
411	Inland marshes	Zones seaward and artificial surfaces	Very high
421	Salt marshes	Zones seaward and artificial surfaces	Very high
511	Water courses	Zones seaward and artificial surfaces	Very high
512	Water bodies	Zones seaward and artificial surfaces	Very high
521	Coastal lagoons	Zones seaward and artificial surfaces	Very high
523	Sea and ocean	Zones seaward and artificial surfaces	Very high

categorized in the following five classes based on their sensitivity to flooding: seaward zones and artificial surfaces (very high), shrub-brush-rangeland (high), cropland and pasture (moderate), other agricultural land (low) and mixed forest land (very low), based on the assumption that limited vegetation cover indicates a very high flood hazard (Kourgialas and Karatzas 2011; Table 3; Fig. 2), since there is a nontrivial correlation between natural forest cover/-forest loss and flood frequency (Bradshaw et al. 2007).

The geological map of the study area was retrieved from the Geological Map of Greece, 1:500,000 (Institute of Geology and Mineral Exploration of Greece 1983), the Geological map of Turkey, 1:500,000 (General Directorate of Mineral Research and Exploration of Turkey 1961), and the Generalized Geology of Europe including Turkey (U.S. Geological Survey 2003). Likewise, the flood hazard map concerning the geological structure of Evros basin was developed based on the influence of each lithological formation at the flood processes, e.g. an area dominated by karstic formations is characterized by very low flood hazard potential (Kourgialas and Karatzas 2011). Different approaches for estimating rainfall intensity have been proposed, such as Fournier Index (Fournier 1960), Modified Fournier Index (Arnoldus 1980) and

Figure 2
Land uses of Evros river basin

Precipitation Concentration Index (PCI) (Oliver 1980). In this study, the rainfall intensity was estimated by using the Modified Fournier Index methodology (Arnoldus 1980), which together with Fournier Index, is the most commonly used index of rainfall aggressiveness (Morgan 2005; Formula 2). In order to determine the rainfall intensity, the meteorological data of 32 meteorological stations in Evros river basin were acquired (Table 4).

$$\mathrm{MFI} = \sum_{1}^{12} \frac{p^2}{p} \qquad (2)$$

where MFI: the modified Fournier index, p: the average monthly rainfall, and P: the average annual rainfall

The distribution of the rainfall stations covered quite satisfactorily the entire study catchment with the exception of the high altitudes since only 4 rainfall stations (12.5% of the total) were located above 800 m.a.s.l. In the present study, the spatial distribution of rainfall intensity was estimated based on spline interpolation method, which, comparing to other approaches (e.g. ordinary kriging, co-kriging and IDW—Inverse Distance Weighting), is considered to be the most appropriate for cases with a small number of data points (Kourgialas and Karatzas 2011). The location and altitude of the available stations represented quite well the topography and geographical coverage of the particular catchment (Tables 4, 5; Fig. 3) which therefore is reflected to the interpolated maps. The density of raingauges network is about 1660 km^2/station and can be considered as sufficient, based on WHO (2008) recommended minimum densities of recording precipitation stations. Another limitation is the lack of snowmelt measurements which is a significant source

Table 4

Meteorological stations at Evros river basin

a/a	Meteorological Station	*X* (EGSA)	*Y* (EGSA)	X (°)	*Y* (°)	*z* (m)	Country	MFI
1	Borovets	468,502.94	4,677,319.18	23.62	42.25	1346	BG	80.97
2	Botev	575,178.64	4,729,848.01	24.92	42.72	2376	BG	98.99
3	Cerkezkoy	834,815.86	4,578,386.89	28	41.29	170	TR	55.29
4	Chirpan	609,654.18	4,672,553.68	25.33	42.20	173	BG	52.52
5	Corlu	818,667.05	4,563,863.50	27.80	41.17	183	TR	54.44
6	Didimoteicho	708,998.27	4,580,341.39	26.50	41.35	25	GR	48.90
7	Edirne	712,998.46	4,614,908.40	26.56	41.66	48	TR	53.10
8	Elhovo	712,099.72	4,672,674.19	26.57	42.18	138	BG	47.31
9	Ferres	682,297.01	4,529,628.68	26.17	40.90	26	GR	58.31
10	Haskovo	629,978.66	4,645,131.69	25.57	41.95	230	BG	57.12
11	Hayrabolu	760,328.30	4,566,816.91	27.11	41.21	–	TR	58.34
12	Ihtiman	485,043.92	4,697,251.53	23.82	42.43	636	BG	52.39
13	Kardjali	611,381.40	4,609,534.60	25.34	41.63	–	BG	62.02
14	Karnobat	744,130.74	4,725,970.54	26.98	42.65	198	BG	49.84
15	Kazanluk	614,664.77	4,719,283.32	25.40	42.62	380	BG	53.79
16	Kiprinos	685,741.71	4,605,595.02	26.23	41.58	70	GR	55.44
17	Kırklareli	768,497.76	4,624,556.84	27.23	41.73	232	TR	51.60
18	Koprivshtitsa	529,364.44	4,720,617.09	24.36	42.64	945	BG	68.40
19	Lefkimi	684,797.62	4,544,132.92	26.20	41.03	150	GR	76.52
20	Luleburgaz	779,902.83	4,588,294.16	27.35	41.40	46	TR	56.42
21	Orestiada	711,021.38	4,597,069.06	26.53	41.50	43.5	GR	48.50
22	Panagyurishte	513,807.67	4,710,574.56	24.17	42.55	562	BG	57.83
23	Pazardjik	526,364.29	4,668,406.07	24.32	42.17	205	BG	48.23
24	Peshtera	525,179.76	4,653,197.65	24.31	42.03	436	BG	53.79
25	Plovdiv	561,818.26	4,666,418.09	24.75	42.15	160	BG	46.20
26	Sadovo	578,343.15	4,666,582.61	24.95	42.15	158	BG	48.31
27	Sliven	689,718.75	4,726,488.20	26.32	42.67	226	BG	51.90
28	Smolyan	556,532.94	4,603,450.07	24.68	41.58	1180	BG	79.45
29	Soufli	692,706.47	4,563,223.97	26.30	41.20	15	GR	69.01
30	Stara Zagora	633,954.63	4,697,412.34	25.63	42.42	166	BG	52.43
31	Svilengrad	682,710.43	4,626,294.00	26.20	41.77	54	BG	53.00
32	Yambol	706,982.82	4,705,864.86	26.52	42.48	143	BG	46.95

Table 5

Main statistical values of the study area Rainfall stations

	Bulgaria	Greece	Turkey	Annual Rainfall (mm)		MFI
No of stations	20	6	6	Min	515	46
Mean altitude (m)	512	55	136	Max	1085	99
Min altitude (m)	54	15	46	Range	570	53
Max altitude (m)	2376	150	132	Mean	656	60
Mean Rainfall (mm)	672	665	600	Median	598	55
Max Rainfall (mm)	1085	942	713	StDev	136	13
				25th perc.	564	52
				75th perc.	710	68

of water for the hydrographic network during spring and early summer. In most cases, for the flood hazard estimation, snowmelt is not the crucial factor since the methodology focuses on flash floods which are mostly caused by short in duration, high rainfall intensity events. Therefore, the importance of rainfall and rainfall intensity is apparent in the methodology since it comprises one of the 6 dominant factors for assessing flood risk and affects the output risk map by approximately 11% (total weight of this parameter,

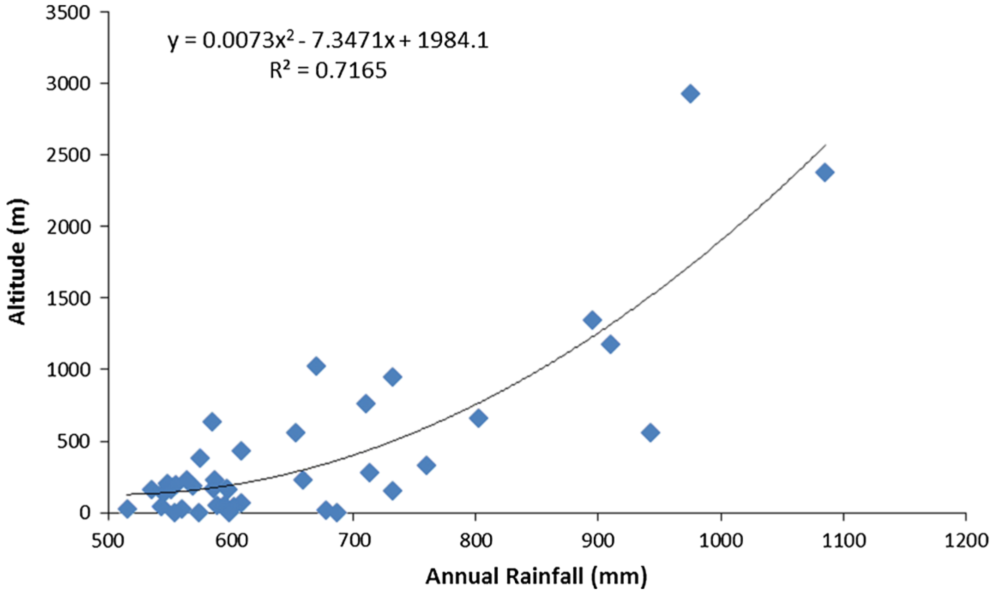

Figure 3
Relationship between Mean Annual Rainfall and Altitude in the study area

Table 2). However, there are many other factors that are taken into account such as slope, land use and topography that also affect the flood risk estimation and amend the effect of high rainfall intensity in areas of relatively low risk (e.g. steep hillslopes, top of mountains, etc.).

3.2. *Validation of Flood Hazard Mapping Methodology—Satellite Images*

The verification of the specific flood hazard mapping methodology was achieved through the comparison between the produced hazard map and the inundation maps derived from the supervised classification of Landsat 5 and 7 satellite imageries of four flood events. The area examined was the riparian zone of the downstream part of the catchment, a 10,000 m buffer zone along the main Evros river thalweg, from Evros delta to the triple point border between Greece, Turkey and Bulgaria. The floods events examined were selected based on their magnitude (Table 1), but also based of the availability of satellite images to cover the specific flood events sufficiently. The flooded event chosen were: a) 17/01-03/03/2003 (date of satellite image retrieved: 03/03/2003), b) 17/02-24/03/2005 (date of satellite image retrieved: 25/03/2005), c) 09-25/03/2006 (date of satellite image retrieved: 13/04/2006), and d) 13-20/02/2010 (date of satellite image retrieved: 19/02/2010).

Six Landsat 5 imageries (two for each date) of 25/03/2005, 13/04/2006 and 19/02/2010 and two Landsat 7-SLC-on of 03/03/2003 with cellsize of 30 m were acquired from the United States Geological Survey (USGS) under a clear sky and windy conditions. The data elaboration and analysis was conducted in ESRI's ArcGIS 10.1 software while for the analysis of the satellite imagery ENVI 4.7 software was used. After selecting the study area scenes and the appropriate dates the digital data were submitted to the following procedures:

1. Georeferencing of the imagery and geographical conversion from WGS'84 to EGSA'87 coordinate system (National Datum) were performed using Beam 4.7 software.
2. Radiometric correction for the conversion of actual radiance values, based on the formula [3] (YCEO 2010).

$$L_\lambda = \{(L_{\mathrm{Max}\lambda} - L_{\mathrm{Min}\lambda}) / (Q_{\mathrm{CALMAX}} - Q_{\mathrm{CALMIN}})\} \times (Q_{\mathrm{CAL}} - Q_{\mathrm{CALMIN}}) + L_{\mathrm{Min}\lambda} \quad (3)$$

where L_λ is the cell value as radiance, Q_{CAL} is the digital number, $L_{\mathrm{MIN}\lambda}$ is spectral radiance scales to Q_{CALMIN}, $L_{\mathrm{MAX}\lambda}$ is spectral radiance scales to Q_{CALMAX},Q_{CALMIN} is the minimum quantized calibrated pixel value (typically $= 1$), Q_{CALMAX} is the maximum quantized calibrated pixel value (typically $= 255$)

3. Atmospheric correction, through the darkest-pixel subtraction technique (Keiner and Yan 1998; Lathrop et al. 1991) via the relevant ENVI 4.7 software tool.
4. Satellite bands of each imagery with the same resolution (m) were joined in a single layer (layer stacking) and stored in image format (Tiff, Geotiff).

Supervised and unsupervised classifications were used to detect the flooded areas. As far as the unsupervised classification is concerned, K-MEANS classification algorithm was used to classify the water-covered from the dry riparian areas for the imageries on 25/03/2005, 13/04/2006 and 19/02/2010. Respectively, supervised classification and particularly Spectral Angle Mapper (SAM) (Becker et al. 2007; Castillejo-González et al. 2009; Debba et al. 2005) was used to detect the aforementioned differentiation of 03/03/2003. K-MEANS classification algorithm has been selected after several test runs and comparison with the results provided by other commonly used algorithms such as Iterative Self-Organizing Data Analysis (ISODATA). With regards to the supervised classification, groups of pixels (ROIs) or individual spectra should be selected as representative areas or materials to be mapped in the output. In this paper the selection of ROIs was selected with great attention even for the different shades of water. Also, SAM has been selected after comparison with the results of other supervised classification techniques, including parallelepiped, minimum distance and maximum likelihood. The classification result was four maps with the inundated areas that were superimposed for comparison purposes to the flood hazard map.

Flooded areas classification was carried out in the riparian zone with medium analysis (spatial resolution 30 m) in order for the wet in the riparian zone to be accurately quantified. Moreover, in order to quantify each classification errors, random points were created inside the inundated areas of each imagery. Creating random points is widely used concerning the classification accuracy assessment (Gass et al. 2013; Turner et al. 2013). The randomness of the selection is achieved by the ArcGIS relevant algorithm (Michigan Technological University 2011) where the user declares the number of points, the minimum distance between them as well as the reference zone (constraining feature class) within which the points will be contained (inundation areas in this case). Taking into consideration the spatial resolution of the satellite imageries (30 m) and the extent of the buffer zone along the main Evros river, it was estimated that 400 points needed to be created in order to have a 30-m minimum distance among them and cover spatially the whole area. This procedure resulted in a satisfactory density of check points (5 points/km^2) and subsequently followed the estimation of the percentage agreement with the actual flooded areas.

3.3. *Geographically Weighted Regression*

There are a number of assumptions underlying the basic regression model, one of which is that the observations should be independent of one another. This is not always the case with data for spatial units and not only might the variables in the model exhibit spatial dependence (that is, nearby locations will have similar values) but also the model's residuals might exhibit spatial dependence. The latter characteristic can be observed if the residuals from the basic regression are plotted on a map where commonly the residuals in neighboring spatial units will have a similar magnitude and sign (Charlton and Fotheringham 2009). The difference between Geographically Weighted (GWR) and multiple linear regression is that GWR incorporates the spatial aspect of the elaborated parameters and thus the produced regression is weighted according to their geographical location. Geographically weighted regression (GWR) is a recent refinement of ordinary regression model, describes relationships among variables that are different concerning their location (Fotheringham et al. 2002) and is used to model spatially varying relationships.

Geographically Weighted Regression (GWR) is a fairly recent contribution to modelling spatially heterogeneous processes (Brunsdon et al. 1996; Fotheringham et al. 1996, 1997, 2002). The underlying idea of GWR is that parameters may be estimated anywhere in the study area given a dependent variable and a set of one or more independent variables which have been measured at places whose location is known. Parameters that were analyzed and correlated in the GWR model with the flood hazard map were the topography, land uses, geology, flow accumulation and rainfall intensity (MFI index) of the Evros river basin. Concerning the geology and the land use parameters, reference numbers have been attributed to each geological and land use type, respectively. Thus, the reference number of each land use or geological formation was correlated with the respective flood hazard index. As far as the input parameters are concerned, the Kernal type (Gaussian) that was selected is the fixed one and it has been determined using the Akaike Information Criterion (AICc; Bandwidth method). AIC serves as an approximately unbiased estimator in instances where the sample size is large and the dimension of the candidate model is relatively small (Davies et al. 2005a). Davies (2002) and Davies et al. (2005b) show that AICc is the minimum variance unbiased estimator of its target discrepancy in a linear regression framework. All the aforementioned parameters were correlated via the relevant ArcGis 10.1 tool, the local coefficient of determination (R^2) was mapped for each one at a catchment scale and the global R^2 was also computed. Statistical report with diagnostic parameters was also generated and a comparative assessment followed to identify the dominant factors that are mostly correlated with the flood hazard map of Evros river basin.

4. Results

4.1. Meteorological Data

The mean annual rainfall of the study area reaches 656 mm while the maximum annual rain (1,085 mm) is observed in a Bulgarian station at an altitude of 2,376 m (Table 5). The minimum rainfall value (515 mm) is observed in a Greek station located at an altitude of 25 m while the correlation between the annual mean rainfall and the stations altitude is well described with a 2nd order polynomial with a R^2 of 0.72 (Fig. 3). The effect of the annual and monthly rainfall values on the MFI index is direct due to the algebraic dependence between these parameters and therefore MFI values illustrate almost identical distribution with the rainfall. Thus, 50% of the stations illustrate a MFI index of up to 55 with a maximum of 99, while 25% of the stations reach a value of 52 (Table 5). The distribution of MFI illustrates a positive skewness and more than 40% of the stations illustrate elevated MFI values that fluctuate above 60. Practically, this means that the study area presents favorable conditions for flood occurrences since it illustrates relatively high rainfall intensities which are counterbalanced though from the relatively low rainfall heights.

4.2. Flood Hazard Mapping

Based on the methodology mentioned above, the following six maps (one for each factor, Fig. 4a–f), which are directly related to flood events, and the final flood hazard map were developed (Fig. 4g).

Although low and very low are the dominant flood hazard classes of Evros river basin, the areas characterized by high and very high flood hazard are significant (19.1 and 6.1%, respectively). Based on the flood hazard map produced, the areas with very high flood hazard potential are (Fig. 4g): (1) the wider Evros delta region, (2) the area located within a zone of few kilometers along the riparian zone of Evros river from delta until Soufli village in Greece, (3) locally along Ardas river in Greece and Bulgaria, (4) the wider area around Edirne city, after the junction of Evros river (Maritsa) from Bulgaria, Ardas river from Greece and Tundzha from Turkey, (5) the wider riparian zone along Ergene river in Turkey, (6) the area around the city Keşan, east of Evros delta at Turkey, where rice field and wetlands are located, (7) along Hayrabolu stream in Turkey, (8) the regions around the cities Plovdiv, Saedinenie and Pazardjik in Bulgaria, and (9) at the coal mines Maritsa Iztok in Bulgaria. Thus, the dominant land uses in the very high flood hazard areas are urban

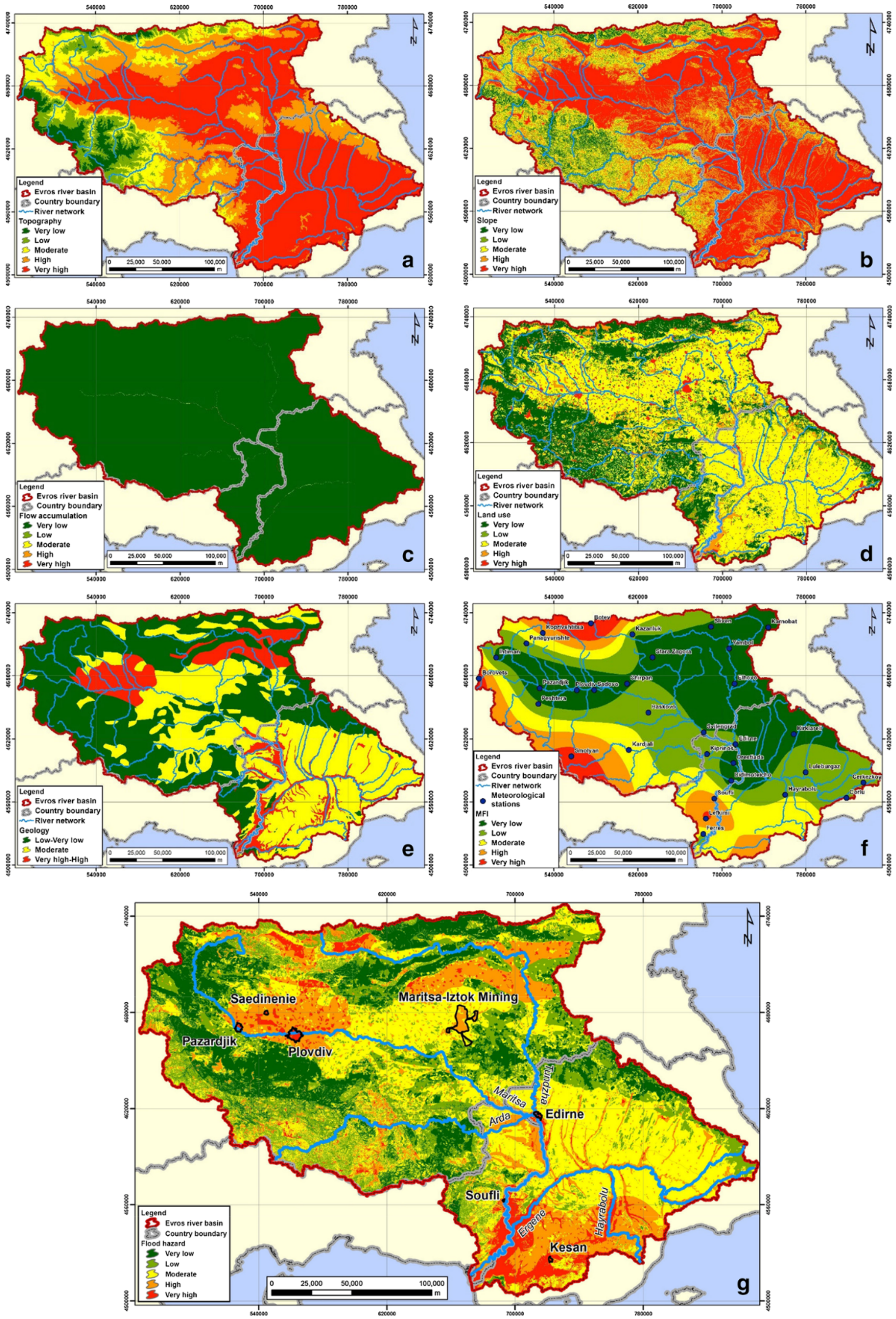

Figure 4
Flood hazard maps of each factor (**a**: topography, **b**: slope, **c**: flow accumulation, **d**: land use, **e**: geology, **f**: rain intensity MFI) and final flood-hazard map for Evros river basin (**g**)

areas followed by agricultural areas and wetlands (Table 8).

4.3. Validation of Flooded Areas Classification

Flooded areas classification was carried out in the riparian zone with medium analysis (spatial resolution 30 m) in order water -covered areas in the riparian zone to be accurately quantified. The elaboration result was quite good and the derived flood maps of each date showed that there were relatively few errors after they were compared carefully with the background of the satellite images. Moreover, in order to quantify the exact estimation errors of each classification, 400 random points were created for each flood map. As far as the flood of 03/03/2003 is concerned, only 19 points from the 400 were located outside flooded areas. Similarly, floods of 13/04/2006, 19/02/2010 and 25/03/2005 presented only 10, 6 and 8 points, respectively that were located away from flooded areas. The percentage estimation errors are 4.75, 2.5, 1.5 and 2% for the classification of flooded areas of March 2003, April 2006, February 2010 and March 2005.

It must be noted that even though the period between the flood's and the satellite image acquisition's date is in some cases fairly long, the remaining remote sensed flooded areas coincide with the flood endangered areas, thus the good performance of the model is verified.

4.4. Geographically Weighted Regression (GWR) Between Flood Hazard Map and Environmental Parameters

The GWR between overall flood hazard map and the numerically transformed, geological map of Evros river basin is positive with local R^2 ranging from 0 to 0.14. Values of R^2 are low, indicating the absence of a strong relationship between the aforementioned parameters (Table 6, Fig. 5a). The highest values though (0.14) are presented at the same areas where porous formations (quaternary, neogene and paleogene sediments) are dominant (western part of Evros river basin) while the lowest ones coincide with Triassic, Paleozoic and metamorphic formations and cretaceous sediments (at northern and central part). Concerning the global regression that GWR tool

Table 6

GWR indices between flood hazard map and environmental parameters

Variable	Geology	Land uses	Rainfall intensity—MFI	Topography	Flow accumulation
Bandwidth	28,701.55	24,969.11	23,115.7	24,131.6	43,358.58
Residual Squares	1,380,538.54	149,422.21	118,783.9	5,454,713,883.3	67,806.18
Effective Number	53.51	73.1	82.1	240.97	11.86
Sigma	16.75	9.31	5.2	240.64	17.24
AICc	42,199.9	13,145.031	27,676.2	1,303,897.98	2055.7
R^2	0.23	0.26	0.79	0.85	0.47
R^2Adjusted	0.22	0.23	0.79	0.85	0.45

Explanation of GWR diagnostics

Bandwidth: is the bandwidth of neighbors used for each local estimation and controls the degree of smoothing in the model

Residual Squares: this is the sum of the squared residuals in the model and the smaller this measure, the closer the fit of the GWR model to the observed data

Effective number: this value reflects a tradoff between the variance of the fitted values and the bias in the coefficient estimates and is related to the choice of bandwidth

Sigma: this value is the square root of the normalized residual sum of squares where the residual sum of squares is divided by the effective degrees of freedom of the residual

AICc: this is a measure of model performance and is helpful for comparing different regression models

R^2: R-squared is a measure of goodness of fit. It may be interpreted as the proportion of dependent variable variance accounted for by the regression model

R^2 Adjusted: calculations for the adjusted R-squared value normalize the numerator and denominator by their degrees of freedom

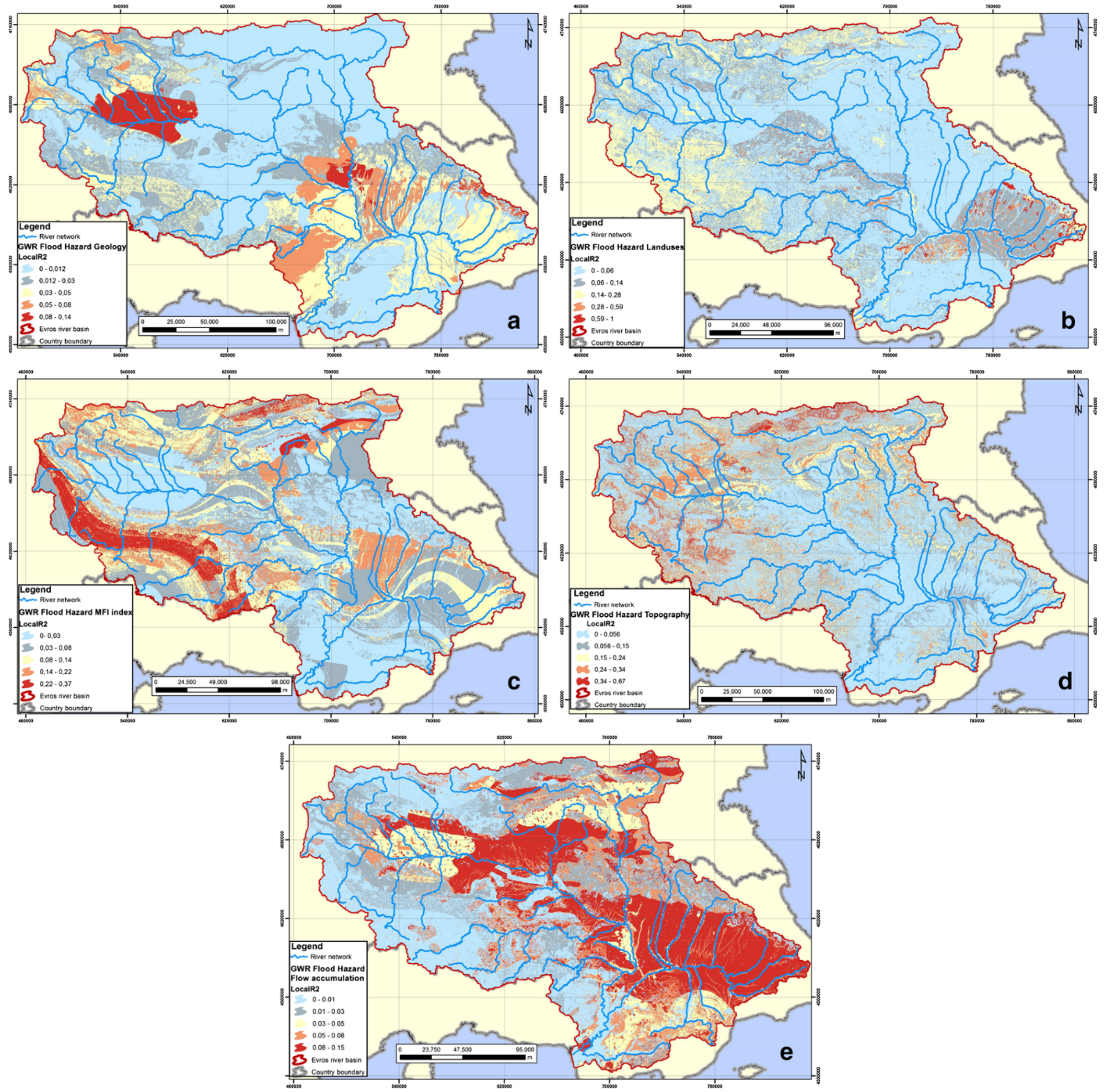

Figure 5

Cartographical representation of determination coefficient (R^2) between flood hazard map of Evros river basin and **a** geological formations, **b** land uses, **c** MFI index, **d** topography and **e** flow accumulation

simultaneously executes, global R^2 is equal to 0.23, value slightly greater than the local one. By means of GWR, having transformed the data in this way it is now possible to investigate local trends in non-stationarity in regression models, something that would not have been obvious from the raw data. Thus, like the Fourier Transform, it is a data transform that may be used to look at a data set from a different viewpoint (Brundson et al. 1996). The technique can also be seen as a response to calls such as Fotheringham (1992), Fotheringham and Rogerson (1993), and Openshaw (1993) for a move away from whole-map statistics to localized statistics which are more informative and which can be mapped.

Regarding GWR between the overall flood hazard map and the numerically transformed land use map of Evros river basin, local R^2 range from 0 to 1, presenting obviously a stronger relationship than the geology parameter (Table 6; Fig. 5b). Areas with the highest correlation (0.59–1) are mainly located where industrial, commercial units and sparsely vegetated areas are detected (eastern part of catchment). Moderate correlation was observed at those areas where permanently irrigated land exists (western part). The global coefficient differs from the local and equals to 0.26, indicating a low-moderate relationship. This difference in local–global R^2 (also regarding the GWR of flow accumulation), exists because GWR expands traditional regression by allowing the assessment of local and not global parameters (Fotheringham and Brunsdon 1999). This regression type controls the existence of spatial nonstationarity in the relationship between independent and dependent variable, enabling spatial change of independent variables' parameters (De Smith et al. 2007).

GWR between the flood hazard map and the rainfall intensity index generated R^2 values ranging from 0 to 0.37, indicating a moderate spatial relationship (Table 6; Fig. 5c). The highest R^2 values (0.22–0.37) are detected at those areas with a moderate rainfall intensity, mainly in the northern and southwestern part of the catchment. The lowest values of coefficient of determination, coincide with the areas that are characterized by the smallest rainfall intensity in the northeastern part of Evros river basin. On the contrary, global regression for the above parameters is higher than the local and equals to 0.79, value revealing a strong interrelationship between the above parameters. GWR focuses on exploring local differentiations and not on the ascertainment of any spatial uniformity. Accepting the fact that each location is characterized by different spatial features, the transition analysis from the global to local scale is enhanced by introducing the spatial parameter (location), hence local regression takes into consideration the location in contrast to the global. Thereby can this difference between local and global R^2 be explained and moreover in this case it indicates that the flooded areas are mostly affected by the cumulative rain of their upstream part of catchment rather than the local rainfall intensity patterns.

The coefficient of determination yielded from the GWR between the flood hazard map and topography ranges from 0 to 0.67, and the areas with the highest values coincident with those of the greatest elevation (2000–2900 m), in the western part of Evros river basin (Table 6; Fig. 5d). The parameter of topography is very important in the assessment process, accompanied by the highest weight, for the generation of the flood hazard map, accredited also by the aforementioned high value of the coefficient of determination. Similar interrelationship is also revealed through the global R^2 which equals to 0.85 and confirms the flood hazard dependence on the topography of the area.

Similar R^2 values (0–0.15) were resulted from the GWR analysis between the flow accumulation and the flood hazard map, indicating a weak relationship in contrast with the global R^2 value (0.47), which reveals a moderate one. The highest values of the correlation coefficient (0.15) appear, as it was expected, at those areas characterized by the greatest flow accumulation values and denser hydrographic network (Fig. 5f).

4.5. Validation of Flood Hazard Mapping Methodology

Based on the inundated areas produced from the satellite images, the flood events with the greatest extent was observed on 19/02/2010 and on 13/04/2006 (area covered 664.6 and 397.8 km^2 respectively), while on 03/03/2003 and on 25/03/2005 the floods were smaller (191.4 and 142.5 km^2 respectively) (Fig. 6). It must be noted that the inundated areas produced from the satellite images do not necessarily coincide with the maximum extent of each flood event, especially in case of the flood event during the period 09-25/03/2006.

The comparison between the flood hazard map produced and the inundated areas indicate the satisfactory performance of the model. More specifically, for each flood event the majority of the inundated area was characterized as areas of high or very high flood hazard (03/03/2003: 98.8%, 5/03/2005: 92.7%, 13/04/2006: 98.9%, 19/02/2010: 98.5%; Table 7), while in the not inundated areas of the riparian zone,

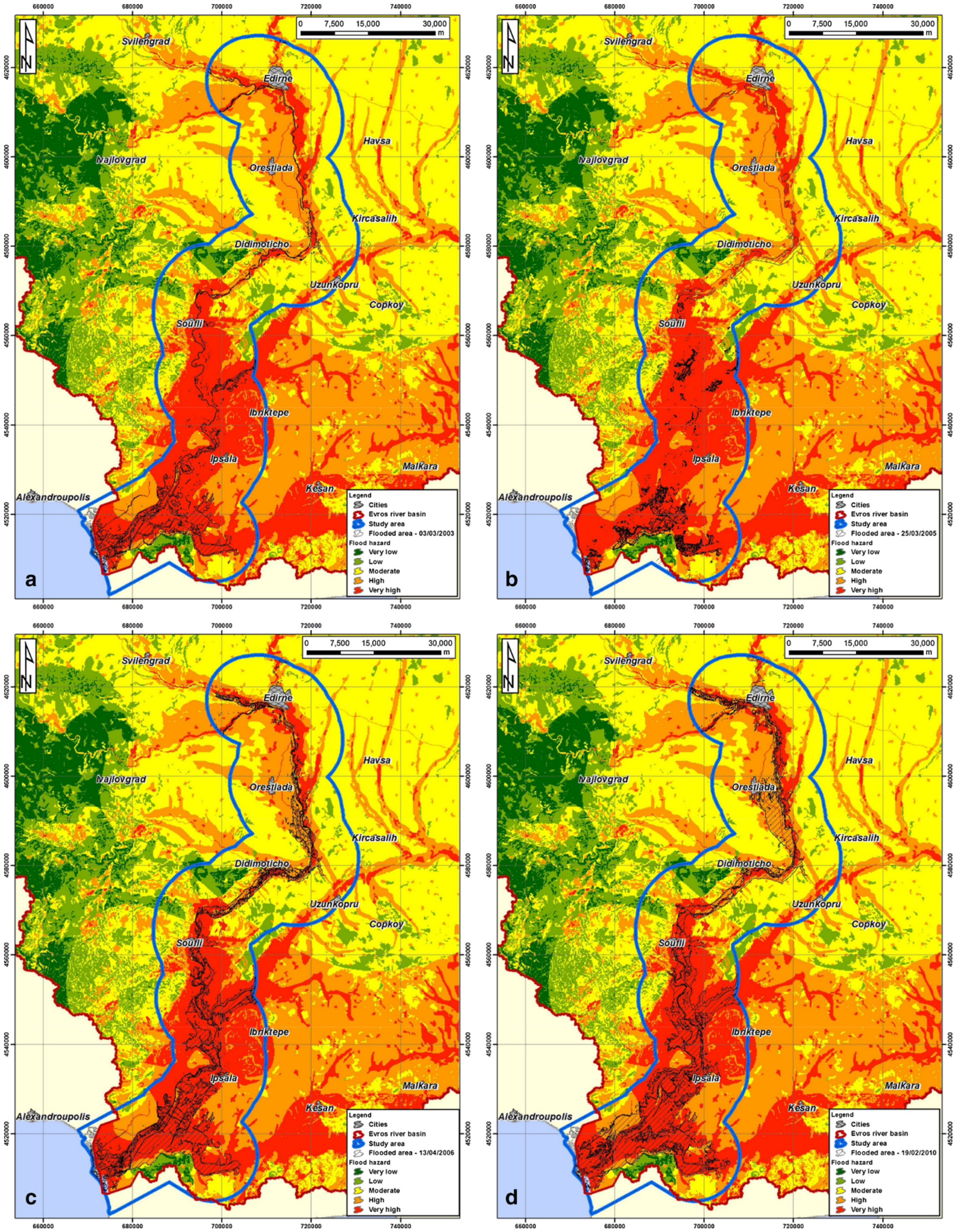

Figure 6
Evros river inundation map for the flood events on **a** 03/03/2003, **b** 25/03/2005, **c** 13/04/2006, **d** 19/02/2010

Table 7

Flood hazard classes and land uses of inundated and not inundated areas of each flood event examined

Flood event	03/03/2003		25/03/2005		13/04/2006		19/02/2010	
	Inundated (%)	Not inundated (%)	Inundated (%)	Not inundated (%)	Inundated (%)	Not inundated (%)	Inundated (%)	Not inundated (%)
Flood hazard classes								
Very low	0.00	1.50	0.10	1.50	0.00	1.60	0.00	1.80
Low	0.20	6.00	0.40	5.90	0.10	6.40	0.10	7.10
Moderate	1.00	29.90	6.80	29.10	1.00	31.90	1.40	35.10
High	9.80	29.40	21.00	28.50	16.00	29.90	22.60	29.60
Very high	89.00	33.30	71.80	35.00	82.90	30.10	75.90	26.50
Land uses								
Agricultural	57.80	80.50	72.30	79.50	76.60	79.50	79.80	79.00
Artificial surfaces	0.00	3.20	0.60	3.10	0.10	3.40	0.30	3.80
Forest and natural vegetation	1.60	13.00	4.50	12.70	1.00	13.90	1.70	15.00
Wetlands	40.50	3.40	22.60	4.70	22.30	3.20	18.30	2.20

Table 8

Flood hazard classes for each land use of the inundated areas of each flood event examined

Flood event	Land use	Flood hazard classes				
		Very low (%)	Low (%)	Moderate (%)	High (%)	Very high (%)
03/03/2003	Agricultural	0.0	0.0	0.7	8.5	90.8
	Artificial surfaces	0.0	0.0	0.0	0.0	100.0
	Forest and natural vegetation	0.0	9.9	16.8	22.1	51.1
	Wetlands	0.0	0.0	0.0	9.4	90.6
25/03/2005	Agricultural	0.0	0.1	7.1	21.8	71.0
	Artificial surfaces	0.0	0.0	2.4	41.5	56.1
	Forest and natural vegetation	1.7	8.7	36.0	12.2	41.3
	Wetlands	0.0	0.0	0.0	19.9	80.1
13/04/2006	Agricultural	0.0	0.0	0.8	17.2	82.0
	Artificial surfaces	0.0	0.0	0.0	0.0	100.0
	Forest and natural vegetation	0.0	5.0	26.5	13.3	55.2
	Wetlands	0.0	0.0	0.1	11.2	88.8
19/02/2010	Agricultural	0.0	0.1	1.1	26.2	72.6
	Artificial surfaces	0.0	0.0	0.0	12.9	87.1
	Forest and natural vegetation	0.4	3.2	28.0	20.8	47.6
	Wetlands	0.0	0.0	0.2	6.6	93.1

the flood hazard potential is lower (area characterized of high or very high flood hazard: 03/03/2003: 62.7%, 5/03/2005: 63.5%, 13/04/2006: 60.0%, 19/02/2010: 56.1%; Table 7). The inundated areas were mainly occupied by agricultural activities and wetlands and the not inundated areas by agricultural activities and at much smaller extent forest and natural vegetation (Table 7). For all flood events examined, the agricultural lands, artificial surfaces and wetlands inundated were characterized as areas of very high or high flood hazard (Table 8).

5. *Conclusion*

During the last decade the flood frequency especially downstream of Evros river has increased dramatically (Angelidis et al. 2010). The climatic and geomorphological conditions of Evros river basin combined with land use changes and poor management practices concerning mainly dams operation and irregular release of river flow, have increased flood risk (Papathanasiou et al. 2013). Especially Evros delta is an extremely vulnerable area concerning flood hazard potential. In order to meet the European Directive 2007/60/EC requirements for the development of flood risk management plans, a GIS based, multi-criteria methodology for flood hazard mapping (Kourgialas and Karatzas 2011) was applied by adapting the method's hazard classes to the examined catchment's environmental conditions while maintaining the hazard weights and weighing rates of the original methodology. The latter have been estimated by a combination of expert judgement and a relevant weighting estimation method (Shaban et al. 2001). The satisfactory performance of this tool was verified, although some adjustments may improve further the model in Evros river basin specifically. The most vulnerable land uses against flood are agricultural lands, artificial surfaces and wetland.

GIS based multi-criteria decision analysis is lately widely used in complex decision problems (Papaioannou et al. 2015) and is quite popular because of its capacity to integrate a large amount of heterogeneous data and the ease in obtaining the weights of a large number of criteria (Chen et al. 2010). Nevertheless, some uncertainties arise due to subjective estimates, such as criteria selection and their thresholds and criteria weights (Chen et al. 2010; Raaijmakers et al. 2008). Based on the GWR results, the primary factors affecting mostly the flood hazard in Evros catchment is topography and land uses, followed by rainfall intensity, geology and flow accumulation. This is not completely in agreement with the weight of factors proposed by Kourgialas and Karatzas (2011), who considered the factor rainfall intensity less important than geology in flood producing. This methodology weakness could be attributed to the different flood producing mechanisms at Evros river basin comparing to the ones in the catchment the methodology was initially developed. More specifically, Evros river basin can be characterized as large-sized limiting the occurrence of flash flood events (Fotopoulos et al. 2010), while the hydrographic network is extensive.

Another important uncertainty issue arises on the choice of the optimal clustering technique, despite the fact that a respective number of GIS based multi-criteria decision analysis applications are using the Jenk's Natural Breaks method for classification of numeric-valued factors (e.g. Mallick et al. 2015; Pasqualini et al. 2011; Stefanidis and Stathis 2013). In order to produce hazard classes that contain data value groups with relatively large differences and to maximize "classing accuracy" (Smith 1986), the use of multiple clustering techniques is often necessary in preliminary analysis of flood hazard mapping (Papaioannou et al. 2015).

GIS based multi-criteria decision analysis lack the ability to comprise the temporal dimension of spatial distributed information and examine phenomena that change over time (Ratsiatou and Stefanakis 2001) comparing to other approaches, such as hydrological and hydraulic modelling. Nevertheless, GIS-based multi-criteria decision analysis can be applied in initial low-cost detection surveys of flood-prone areas (Papaioannou et al. 2015), to support decision-making and help stakeholders develop flood management plans.

The particular approach for estimating the flood-hazard areas of Evros river basin, combines the climatic, geomorphological and land use properties of the catchment to illustrate areas that are more prone to flooding in relation to others. It is a physically based approach and measures the protective function of each part of the basin based on its natural and anthropogenic characteristics. It has certain advantages and disadvantages compared to hydrologic modelling techniques as mentioned above. However, it is very useful in areas where hydrological data are completely absent, inefficient or have low credibility as well as where the hydrological systems are too complex to describe efficiently in a model (large catchments with many different water uses and stakeholders). This is particularly the case in transboundary catchments where all of the aforementioned problems are usually significantly enhanced and the cooperation between the catchment sharing countries is not always ideal.

6. *Discussion*

The flood risk management of transboundary water courses raises many challenges due to different approaches in strategic decision making, capacity and resources and due to the lack of a legal framework for cooperation and the public participation and awareness (UNECE 2009). The European Directive 2007/60/EC, in line with Directive 2000/60/EC and international principles of flood risk management as developed notably under the United Nations Convention on the protection and use of transboundary water courses and international lakes, aims at effective flood prevention and mitigation practices. Especially at Evros river basin, where the countries involved are not all member states of the European Union, the challenges are even more complex. Only bilateral efforts have been made in the past and agreements have been signed related to water environmental cooperation including conservation of protected areas and management issues concerning flood protection at Evros transboundary river basin (Table 9). Important efforts have also be made in scientific level concerning flood risk management

Table 9

Existing agreements related to the management of Evros transboundary river basin

Country	Date	Basins concerned	Comments	References
GR, TR	1934	Maritsa/Evros/Meriç River	Agreement concerning the Control of Hydraulic Works on Both Banks of the Evros/Meriç River	1
GR, TR	1955	Maritsa/Evros/Meriç River	Agreement related to the construction of flood control measures	1
GR, TR	1963	Maritsa/Evros/Meriç River	Protocol on the Rehabilitation of the Meriç River Basin Forming the Significant Part of Turkish-Greek Border in Thrace	1
BG, GR	1964	Maritsa/Evros/Meriç River	Agreement on Cooperation between the People's Republic of Bulgaria and the Kingdom of Greece concerning the utilization of the waters of the rivers crossing the two countries	2
BG, TR	1968	Maritsa/Evros/Meriç, Arda/Ardas and Tundzha/Tundja/Tunca Rivers	The Agreement between the Republic of Turkey and the People's Republic of Bulgaria concerning Cooperation in the Use of the Waters of Rivers Flowing through the Territory of Both Countries established a Joint Commission authorized to settle any disputes which might have arisen	1
BG, GR	1971	Arda/Ardas, Maritsa/Evros/Meriç Rivers	FRESHWATERS AGREEMENTS Title and related joint body Agreement for the Establishment of the Greek-Bulgarian Committee for Cooperation in the Fields of Electric Energy and the Utilization of the Waters of the Rivers Crossing the Two Countries that was assigned to follow up the application of the 1964 agreement	1
GR, TR	1971	Maritsa/Evros/Meriç River	Prevention and means of peaceful settlement of disoute incintents in the cross border land and sea areas of River Evros/Meric	3
BG, TR	1975	Maritsa/Evros/Meriç, Arda/Ardas and Tundzha/Tundja/Tunca Rivers	Agreement between the Government of the Republic of Turkey and the Government of the People's Republic of Bulgaria on Long Term Economic, Technical, Industrial and Scientific Cooperation	1
BG, TR	1993	Tundzha/Tundja/Tunca River	Agreement on Assistance and Cooperation in the Field of Water for Reducing the Negative Effects of the Drought of 1993	1
BG, TR	1998	Maritsa/Evros/Meriç River	Agreement on Cooperation in the Fields of Energy and Infrastructure Between the Government of the Republic of Turkey and the Government of the Republic of Bulgaria	1
GR, TR	2001	Maritsa/Evros/Meriç and Arda/Ardas Rivers	Memorandum of Understanding Concerning Cooperation on Environmental Protection	1
BG, TR	2002	Maritsa/Evros/Meriç River	Protocol signed between the General Directorate of State Hydraulic Works of Turkey and the National Institute of Meteorology and Hydrology of Bulgaria for the installation, operation and maintenance of a flow observation telemetry station on the Maritsa River in Svilengrad, Bulgaria	1
BG, TR	2002	Maritsa/Evros/Meriç River	Agreement between the Ministry for the Environment, Physical Planning and Public Works of the Hellenic Republic and the Ministry of Environment and Water of the Republic of Bulgaria on cooperation in the field of environmental protection	2
GR, TR	2006	Maritsa/Evros/Meriç River	CBC for the prevention and control of floods in the riparian region of Evros/Meric	3

UNECE (2009), Mousmouti (2003), Skias and Kallioras (2007) projects (e.g. INTERREG III A—PHARE CBC program between Bulgaria and Greece that focused on early warning in case of floods and accidental pollution and EC PHARE Cross-Border Cooperation between Turkey and Bulgaria which involved the creation of a hydrometeorological database and the installation of flood warning and water information systems), although none includes all three countries involved. In addition, no agreement exists that would provide a minimum inflow of freshwater into the delta, satisfying the water needs of the ecosystem as well as preventing salt water intrusion and siltation (Kramer and Schellig 2011).

On the other hand, many incidents underline the fact that most agreements, declarations or protocols between the riparian countries have not been fully implemented. Especially during the severe flood events in 2005, recriminations between Turkey, Greece and Bulgaria indicated the lack of a coordinated water management framework and a common flood prevention strategy. Although experts from the three countries agree that the primary cause of major flood events are specific flow patterns and extreme meteorological conditions (Kramer and Schellig 2011), the main argument raised on whether the poor water practices mainly of large Bulgarian reservoirs or whether the inappropriate floodplain management in Greece and Turkey intensify the phenomena and increase flood risk and vulnerability downstream.

The EU legislative framework provides the necessary means for efficient cooperation between the EU member states Greece and Bulgaria. The challenge rises in the cooperation between all the three countries involved. Accession Partnership between the EU and Turkey further provides opportunities for cooperation between Turkey and its European neighbors (Skias and Kallioras 2007). The first step for integrated water management of Evros river basin is the exchange of scientific knowledge and hydrological and water use data in order to develop a common database and the establishment of a common rather than a national flood forecasting and early warning system. These initiatives prerequisite also a common infrastructure establishment and an integrated water management plan for the entire river basin that will also focus on the environmental protection and conservation of natural resources. The political support for this effort and common legislation are preconditions.

REFERENCES

Angelidis, P., Kotsikas, M., & Kotsovinos, N. (2010). Management of upstream dams and flood protection of the Transboundary River Evros/Maritza. *Water Resources Management, 24*, 2467–2484.

Arnoldus, H.M.J. (1980). An approximation of the rainfall factor in the Universal Soil Loss Equation. In M. De Boodt, and Gabriels, D. (Eds.), Assessment of erosion (pp. 127–132). Chichester: Wiley.

Becker, B. L., Lusch, D. P., & Qi, J. (2007). A classification-based assessment of the optimal spectral and spatial resolutions for Great Lakes coastal wetland imagery. *Remote Sensing of Environment, 108*, 111–120.

Bradshaw, C. J. A., Sodhi, N. S., Peh, K. S. H., & Brook, B. W. (2007). Global evidence that deforestation amplifies flood risk and severity in the developing world. *Global Change Biology, 13*, 2379–2395.

Brunsdon, C., Fotheringham, S., & Charlton, M. (1996). Geographically weighted regression: a method for exploring spatial non-stationarity. *Geographical Analysis, 28*, 281–298.

Castillejo-González, I. L., López-Granados, F., García-Ferrer, A., Peña-Barragán, J. M., Jurado-Expósito, M., de la Orden, M. S., et al. (2009). Object- and pixel-based analysis for mapping crops and their agro-environmental associated measures using QuickBird imagery. *Computers and Electronics in Agriculture, 68*, 207–215.

Charlton, M. and Fotheringham, S. (2009). Geographically weighted regression white paper (National Centre for Geocomputation National University of Ireland Maynooth, Maynooth, Co Kildare, Ireland) (http://www.geos.ed.ac.uk/~gisteac/fspat/gwr/arcgis_gwr/GWR_WhitePaper.pdf).

Chen, Y., Yu, J., & Khan, S. (2010). Spatial sensitivity analysis of multi-criteria weights in GIS-based land suitability evaluation. *Environmental Modelling and Software, 25*, 1582–1591.

Darmouth Flood Observatory. (2014). Global Active Archive of Large Flood Events (http://www.dartmouth.edu/~floods/Archives/index.html).

Davies, S.L. (2002). Discrepancy-based model selection criteria using cross-validation. Doctoral dissertation (University of Missouri-Columbia Department of Statistics, Columbia).

Davies, S. L., Neath, A. A., & Cavanaugh, J. E. (2005a). Cross validation model selection criteria for linear regression based on the Kullback-Leibler discrepancy. *Statistical Methodology, 2*, 249–266.

Davies, S. L., Neath, A. A., & Cavanaugh, J. E. (2005b). *On the minimum variance unbiasedness property of AICc and MCp*. Iowa City: Technical report (The University of Iowa Department of Biostatistics.

De Smith, M., Goodchild, M., & Longley, P. (2007). *Geospatial analysis: A comprehensive guide to principles, techniques and software tools*. Winchelsea: Troubador Publishing Ltd.

Debba, P., van Ruitenbeek, F. J. A., van der Meer, F. D., Carranza, E. J. M., & Stein, A. (2005). Optimal field sampling for targeting minerals using hyperspectral data. *Remote Sensing of Environment, 99*, 373–386.

Dimitriou, E., Mentzafou, A., Zogaris, S., Tzortziou, M., Gritzalis, K., Karaouzas, I., et al. (2011). Assessing the environmental status and identifying the dominant pressures of a trans-boundary river catchment, to facilitate efficient management and mitigation practices. *Environmental Earth Sciences, 66*, 1839–1852.

Dimitriou, E., Moussoulis, E., Mentzafou, A., Tzortziou, M., Zeri, C., Colombari, E. and Markogianni, V. (2010). Environmental status assessment for Evros river basin. Final Technical Report (in Greek), (Hellenic Centre for Marine Research, Athens).

Erwin, K. L. (2009). Wetlands and global climate change: the role of wetland restoration in a changing world. *Wetlands Ecology and Management, 17*, 71–84.

European Commission Council. (2000). European Commission Council Directive 2000/60/EC of the European Parliament and of the Council of 23 October 2000 establishing a framework for Community action in the field of water policy. *Official Journal of the European Communities, L327*, 1–72.

European Commission Council. (2007). Directive 2007/60/EC of the European Parliament and of the Council of 23 October 2007 on the assessment and management of flood risks. *Official Journal of the European Union*, *L288*, 27–34.

European Environmental Agency—E.E.A. (2012), Corine Land Cover 2006 (http://www.eea.europa.eu).

Feyen, L., Barredo, J. I. and Dankers, R., Implications of global warming and urban land use change on flooding in Europe. In Water and Urban Development Paradigms—Towards an Integration of Engineering, Design and Management Approaches (ed. Feyen, J., Shannon, K., and Neville, M.) (Taylor and Francis, London 2009), pp. 217–225.

Fotheringham, S. (1992). Exploratory Spatial Data Analysis and GIS. *Environment and Planning A*, *24*, 1675–1678.

Fotheringham, S., & Brunsdon, C. (1999). Local forms of spatial analysis. *Geographical Analysis, 31*, 340–358.

Fotheringham, S., Brunsdon, C., & Charlton, M. (2002). *Geographically weighted regression: The analysis of spatially varying relationships*. Chichester: John Wiley & Sons Ltd.

Fotheringham, S., Charlton, M., & Brunsdon, C. (1996). The geography of parameter space: an investigation of spatial nonstationarity. *International Journal of Geographical Information Systems, 10*, 605–627.

Fotheringham, S., Charlton, M., & Brunsdon, C. (1997). Two techniques for exploring non stationarity in geographical data. *Geographical Systems, 4*, 59–82.

Fotheringham, S., & Rogerson, P. A. (1993). GIS and spatial analytical problems. *International Journal of Geographical Information Science, 7*, 3–19.

Fotopoulos, F., Makropoulos, C., & Mimikou, M. A. (2010). Flood forecasting in transboundary catchments using the open modeling interface. *Environmental Modelling and Software, 25*, 1640–1649.

Fournier, F. (1960). *Climat et érosion: la relation entre l'érosion du sol par l'eau et les précipitations atmosphériques*. Paris: Presses Universitaires de France.

Gass, L., Norman, L.M., Villarreal, M.L., Tolle, C., Coe, M. and Jamwal, P. (2013), A Test of Methods to Measure Vegetation Change Adjacent to Gabions in Sonora, Mexico using Landsat imagery, Presented at the Santa Cruz River Researcher's Day, Tucson Arizona.

Gemitzi, A., Petalas, C., Tsihrintzis, V. A., & Pisinaras, V. (2006). Assessment of groundwater vulnerability to pollution: a combination of GIS, fuzzy logic and decision making techniques. *Environmental Geology, 49*, 653–673.

General Directorate of Mineral Research and Exploration. (1961). Geological Map of Turkey, sheet Istanbul, 1:500,000, Ankara, Turkey.

Institute of Geology and Mineral Exploration—Division of General Geology and Economic Geology (1983), Geological Map of Greece, 1:500,000. Athens, Greece.

IPCC, Climate Change 2013—The Physical Science Basis—Working Group I Contribution to the Fifth Assessment Report of the Intergovernmental Panel on Climate Change - Summary for Policymakers. (Cambridge University Press, United Kingdom and New York 2013).

Keiner, L. E., & Yan, X.-H. (1998). A neural network model for estimating sea surface chlorophyll and sediments from thematic mapper imagery. *Remote Sensing of Environment, 66*, 153–165.

Khandekar, M. L. (2013). *The global warming—extreme weather link: a review of the state of science*. London: The Global Warming Policy Foundation.

Khandekar, M. L., Murty, T. S., & Chittibabu, P. (2005). The global warming debate: a review of the state of science. *Pure and Applied Geophysics, 162*, 1557–1586.

Kourgialas, N. N., & Karatzas, G. P. (2011). Flood management and a GIS modelling method to assess flood-hazard areas—a case study. *Hydrological Sciences Journal, 56*, 212–225.

Kramer, A. and Schellig, A. (2011). Meric River Basin: Transboundary Water Cooperation at the Border between the EU and Turkey, In Turkey's Water Policy National: National Frameworks and International Cooperation (ed. Kramer, A., Kibaroglu, A., and Scheumann, W.) (Springer Berlin Heidelberg, New York) pp. 229–249.

Kundzewicz, Z. W., Lugeri, N., Dankers, R., Hirabayashi, Y., Döll, P., Pińskwar, I., et al. (2010). Assessing river flood risk and adaptation in Europe-review of projections for the future. *Mitigation and Adaptation Strategies for Global Change, 15*, 641–656.

Lathrop, R. G., Lillesand, T. M., & Yandell, B. S. (1991). Testing the utility of simple multi-date thematic mapper calibration algorithms for monitoring turbid inland waters. *International Journal of Remote Sensing*, *12*, 2045–2063.

Malczewski, J. (2006). GIS-based multicriteria decision analysis: a survey of the literature. *International Journal of Geographical Information Science, 20*, 703–726.

Mallick, J., Singh, C. K., Al-Wadi, H., Ahmed, M., Rahman, A., Shashtri, S., et al. (2015). Geospatial and geostatistical approach for ground water potential zone delineation. *Hydrological Processes, 29*, 395–418.

Meyer, V., Scheuer, S., & Haase, D. (2009). A multicriteria approach for flood risk mapping exemplified at the Mulde river, Germany. *Natural Hazards, 48*, 17–39.

Michigan Technological University (2011), Geographic Information Science information and support - How to generate random points in ArcGIS, http://gis.mtu.edu/?p=127 (accessed on 27/02/2015).

Ministry of Environment Energy and Climate Change-Special Secretariat for Water, Flood directive 2007/60/EC: Preliminary Flood Risk Assessment (in Greek) (Athens, 2012).

Ministry of Forest and Water Management (2011), Official statistics (in Turkish) (http://www.milliparklar.gov.tr/Anasayfa/istatistik.aspx?sflang=tr).

Ministry of Infrastructure Transport and Networks—General Secretariat of Public Works—Earthquake Recovery Service (2014), Delimited flooded areas—credit measures (in Greek) (http://www.yas.gr/ApoList.asp?cat_apo_id=106).

Morgan, R. P. C. (2005). *Soil erosion and conservation* (3rd ed.). Oxford: Blackwell Publishing.

Mousmouti, M. (2003). Hellenic-Bulgarian Bilateral Agreements for the Protection and Use of Transboundary Watercourses (http://www.nomosphysis.org.gr/attachments/10/contribution7.mousmouti.doc).

Oliver, J. E. (1980). Monthly precipitation distribution: a comparative index. *Professional Geography, 32*, 300–309.

Openshaw, S. (1993). Exploratory Space-Time-Attribute Pattern Analysers, In Spatial Analysis and CIS (ed. Fotheringham A.S. and Rogerson P.A.) (Taylor and Francis, London), pp. 147–63.

Papaioannou, G., Vasiliades, L., & Loukas, A. (2015). Multi-criteria analysis framework for potential flood prone areas mapping. *Water Resources Management, 29*, 399–418.

Papathanasiou, C., Serbis, D., & Mamassis, N. (2013). Flood mitigation at the downstream areas of a transboundary river. *Water Utility Journal, 3*, 33–42.

Pasqualini, V., Oberti, P., Vigetta, S., Riffard, O., Panaiotis, C., Cannac, M., et al. (2011). A GIS-based multicriteria evaluation for aiding risk management *Pinus pinaster* Ait. Forests: a case study in Corsican Island, Western Mediterranean Region. *Environmental Management, 48*, 38–56.

Raaijmakers, R., Krywkow, J., & van der Veen, A. (2008). Flood risk perceptions and spatial multi-criteria analysis: an exploratory research for hazard mitigation. *Natural Hazards, 46*, 307–322.

Ratsiatou, I. and E. Stefanakis, Spatio-temporal multicriteria decision making under uncertainty, In Proceedings of the First International Symposium on Robust Statistics and Fuzzy Techniques in Geodesy and GIS (ed. Carosio, A. and Kutterer H.) (Zurich, 2001) pp. 169–174.

Schäuble, H., Marinoni, O., & Hinderer, M. (2008). A GIS-based method to calculate flow accumulation by considering dams and their specific operation time. *Computers & Geosciences, 34*, 635–646.

Semmler, T., & Jacob, D. (2004). Modeling extreme precipitation events-a climate change simulation for Europe. *Global and Planetary Change*, *44*, 119–127.

Skias, S. and Kallioras, A., Cross Border Co-operation and the Problem of Flooding in the Evros Delta, In Many Rivers to cross: Cross-border Co-operation in River Management (ed. Verwijmeren, J. and Wiering, M.) (Eburon Academic Publishers, Delft, The Netherlands 2007) pp. 119–143.

Skoulikidis, N. T., Economou, A. N., Gritzalis, K. C. and Zogaris, S., Rivers of the Balkans, In Rivers of Europe (ed. Tockner, K., Uehlinger, U., and Robinson, C. T.) (Academic Press, London 2009) pp. 421–466.

Smith, R. M. (1986). Comparing traditional methods for selecting class Intervals on choropleth maps. *Professional Geographer*, *38*, 62–67.

Stefanidis, S., & Stathis, D. (2013). Assessment of flood hazard based on natural and anthropogenic factors using analytic hierarchy process (AHP). *Natural Hazards, 68*, 569–585.

Turner, A. B., Colby, J. D., Csontos, R. M., & Batten, M. (2013). Flood Modeling Using a Synthesis of Multi-Platform LiDAR Data. *Water, 5*, 1533–1560.

UNECE (United Nations Economic Commission for Europe), Second Assessment of transboundary rivers, lakes and groundwaters (United Nations Publications, Geneva 2011).

UNECE (United Nations Economic Commission for Europe), Transboundary flood risk management: experiences from the UNECE region (United Nations Publications, New York and Geneva 2009).

U.S. Geological Survey (2003), Generalized Geology of Europe including Turkey (https://www.sciencebase.gov/catalog/).

WHO (World Meteorological Organization), Guide to hydrological practices. Volume I: Hydrology - From measurement to hydrological information (World Meteorological Organization, Geneva 2008).

YCEO - Yale Center for Earth Observation, Yale Institute of Biospheric Studies (2010). Index of CEO Documentation (http://www.yale.edu/ceo/Documentation/).

Zerger, A. (2002). Examining GIS decision utility for natural hazard risk modelling. *Environmental Modelling and Software, 17*, 287–294.

(Received June 23, 2014, revised August 30, 2016, accepted November 15, 2016, Published online November 25, 2016)

Pure Appl. Geophys. 174 (2017), 701–721

DOI 10.1007/s00024-016-1298-8

Pure and Applied Geophysics

Regional L-Moment-Based Flood Frequency Analysis in the Upper Vistula River Basin, Poland

A. Rutkowska,[1] M. Żelazny,[2] S. Kohnová,[3] M. Łyp,[4] and K. Banasik[5]

Abstract—The Upper Vistula River basin was divided into pooling groups with similar dimensionless frequency distributions of annual maximum river discharge. The cluster analysis and the Hosking and Wallis (HW) L-moment-based method were used to divide the set of 52 mid-sized catchments into disjoint clusters with similar morphometric, land use, and rainfall variables, and to test the homogeneity within clusters. Finally, three and four pooling groups were obtained alternatively. Two methods for identification of the regional distribution function were used, the HW method and the method of Kjeldsen and Prosdocimi based on a bivariate extension of the HW measure. Subsequently, the flood quantile estimates were calculated using the index flood method. The ordinary least squares (OLS) and the generalised least squares (GLS) regression techniques were used to relate the index flood to catchment characteristics. Predictive performance of the regression scheme for the southern part of the Upper Vistula River basin was improved by using GLS instead of OLS. The results of the study can be recommended for the estimation of flood quantiles at ungauged sites, in flood risk mapping applications, and in engineering hydrology to help design flood protection structures.

Key words: Catchment characteristics, clustering, regional flood frequency, L-moments, multivariate regression, diagnostic measures.

1. *Introduction*

The main objective of regional flood frequency analysis (RFFA) is to provide design flood estimates, which are less uncertain than using local (at-site) flood frequency analysis (FFA), and which can be applied for estimation of design floods at places without observations. The next benefit is the opportunity to introduce series that are shorter than those required by the local approach. The design flood estimates can be applied in designing hydrotechnical constructions: levees, dams, barrages, canals, floodgates, polders and other structures such as bridges.

The RFFA method has been widely tested and applied (Cunnane 1988; Ouarda *et al.* 2001; Merz and Blöschl 2005). Several types of RFFA are discussed in the literature (Taylor *et al.* 2011; Ishak *et al.* 2011; Aziz *et al.* 2014). In the index flood method (IFM), a region is interpreted as a class of catchments for which the quantile functions of design discharge are the same, apart from a site-specific scaling factor, the index flood (Dalrymple 1960; Stedinger *et al.* 1993). The dimensionless factor, a so-called growth curve, is common for an entire homogenous region. The index flood can be estimated, using regression-based techniques with catchment characteristics (CCH) as explanatory variables, and also extrapolated to ungauged catchments. Multivariate regression, rational models, and geomorphoclimatic models are usually applied in the estimation of an index flood (Kohnová *et al.* 2006; Merz and Blöschl 2005; Noto and La Loggia 2009; Brath *et al.* 2001).

Specific geophysical, geomorphological and rainfall conditions, as well as high population density cause higher flood risk of the Upper Vistula River basin (UVB) than of the entire Vistula River basin. The contribution of the surface runoff of the UVB to the total surface runoff of Poland is very high. The diverse hydrological conditions cause exceptionally high variability of maximum discharges in comparison to the rest of Poland (Punzet 1978). A number of researchers have attempted to create hydrological classification systems

---

[1] Department of Applied Mathematics, University of Agriculture in Kraków, Kraków, Poland. E-mail: rmrutkow@cyf-kr.edu.pl

[2] Institute of Geography and Spatial Management, Jagiellonian University in Kraków, Kraków, Poland.

[3] Department of Land and Water Resources Management, Slovak University of Technology in Bratislava, Bratislava, Slovakia.

[4] Center of Flood and Drought Modelling, Institute of Meteorology and Water Management, Kraków, Poland.

[5] Department of River Engineering, Sedimentation Lab, Warsaw University of Life Sciences-SGGW, Warszawa, Poland.

for the UVB. In most cases, boundaries of hydrological regions match those of physical geographic regions (Dębski 1961; Stachý 1966; Soczyńska 1977; Dobija 1981). Dobija (1981), Pociask-Karteczka (1995), also considered to be the influence of climate factors.

A division of Poland into regions using the IFM method with the median as the index flood was completed by Stachý and Fal (1986). All regions were assumed to have Pearson III as the parent distribution function with parameters estimated using the quantile method (Kaczmarek and Trykozko 1964). Regions were defined as sets of catchments with similar quotients $\frac{Q_{p\%}}{Q_{50\%}}$ $(p = 1, p = 10)$. Empirical dimensionless quantiles were calculated for every region as arithmetic means of local quantiles. Punzet (1978), in turn, introduced several regression formulas for the estimation of design floods for three sub-areas of the UVB: Carpathian, upland, and plain non-carpathian.

The purpose of this paper is the estimation of design flood discharge using the regional approach and the IFM. The first step consisted of the division of the UVB into pooling groups based on local hydrological characteristics. This delineation was implemented with the use of cluster analysis, in which similarity is understood as proximity in a multidimensional space, with morphometric, land use, and meteorological at-site characteristics as coordinates. In the second step, the previously identified groups were verified and adjusted; homogeneity within them was tested using statistical methods, and a common regional distribution function (RDF) was estimated for each homogenous region. Two measures of goodness of fit were used to identify the RDF—the HW measure and a bivariate measure introduced by Kjeldsen and Prosdocimi (2015). Next, design discharges were estimated using IFM. In the third step, the multivariate regression function was applied to describe the dependence between the characteristics and the index flood in each region using the ordinary least squares (OLS) and generalised least squares (GLS) methods.

2. Study Area and Data

2.1. Study Area

The UVB is located in southern Poland and covers an area of 50,732 km^2, which is 25 % of the total area of the Vistula basin. The map of physical geographical regions is shown in Fig. 1. The UVB has a very diverse hydrological regime (Dynowska and Pociask-Karteczka 1999) with frequent high-intensity precipitation, poor permeability, limited water-bearing capacity of the area parent material in the northern and southern part, and fairly balanced stream recharge, decent permeability, good water-bearing capacity of the parent material, small differences in relief, few streams in the region, and deep groundwater in the middle part. Such large differences are not found in any other region of Poland. Punzet (1991) states that the Vistula River in the UVB boasts the largest water resources of any river in Poland, but they are unevenly distributed spatially and vary substantially over time.

2.2. Data

52 catchments located in the UVB are shown on the map in Fig. 1. Catchment characteristics with the greatest influence on flood formation in the UVB were used (Bryndal 2011; Dobija 1981; Wałęga 2009; Pociask-Karteczka 1995). They are displayed in Table 1. The morphometric characteristics were analysed using ESRI ArcGIS 10 software. A digital elevation model (triangulated irregular network) was the source of maximum and minimum elevation, mean slope (standard GIS procedure), and the longitude and latitude of the catchment centroids. Data were obtained from the Main Geodesy and Cartographic Documentation Center in Warsaw, Poland, as part of the Land Parcel Identification System (LPIS) project. The data were then converted to raster format with a spatial resolution of 10 m × 10 m. Catchment area, maximum length, and the total length of all rivers were obtained from the Map of Hydrological Division of Poland, scale 1:10,000 (KZGW 2010). Land use data were specified using the Topographic Objects Database (ISOK 2014) at the resolution of 1:10,000. Infiltration parameter IN was obtained from the Institute of Meteorology and Water Management, National Research Institute, Poland (Polish acronym: IMGW-PIB). It was calculated from infiltration characteristics of soils (based on the soil map of Poland), with correction factors due to the surface of the bedrock beneath soil cover,

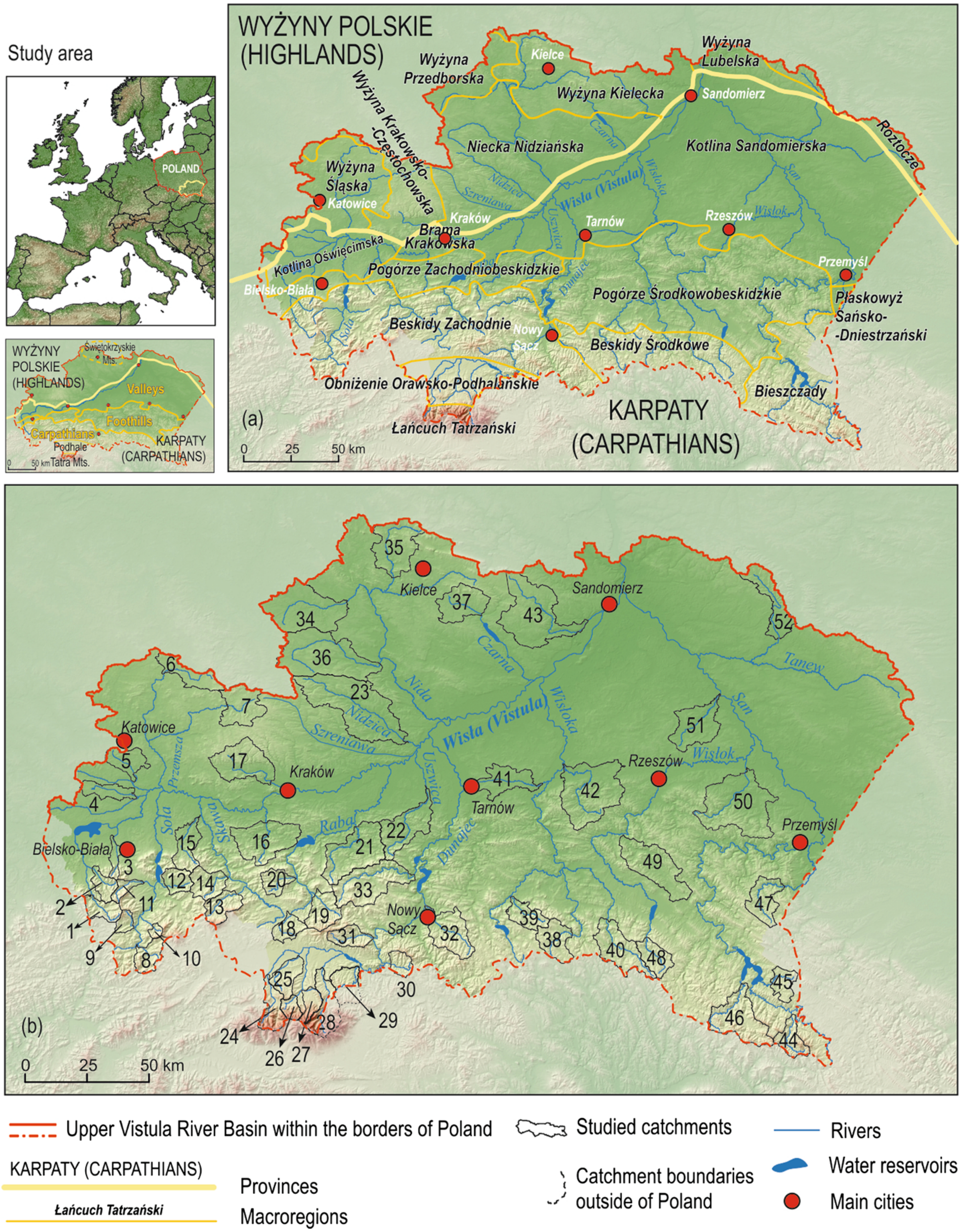

Figure 1

a Physical geographic regions in the Upper Vistula River basin (Kondracki 2014); **b** studied catchments

Table 1

Catchment characteristics and discharge data

No	River/gauging st.	*A* (km^2)	NL (km)	EL (m asl)	SL (°)	DN (m)	SH[a] (–)	RD (km^{-1})	FR[b] (%)	*U*/*N* (–)	*F*/*A* (–)	*IN* (–)	AMrl (years)	$\hat{\mu}_{AM}$ (m^3 s^{-1})
1	Mała Wisła/Ustroń-Obłaziec	107.3	73.3	708.9	13.1	815	0.48	0.68	73.3	0.08	3.69	0.22	62	52.0
2	Brennica/Górki Wielkie	81.5	63.2	605.3	13.3	743	0.38	0.78	70.8	0.10	3.48	0.21	57	48.1
3	Wapienica/Podkępie	50.1	45.1	440.2	6.9	870	0.16	0.9	36.2	0.38	1.00	0.16	58	50.6
4	Korzenica/Międzyrzecze	77.5	43.7	259.9	1.5	68	0.19	0.56	78.1	0.05	4.49	0.57	47	7.0
5	Mleczna/Bieruń Stary	125.2	82.1	268.9	1.7	117	0.46	0.65	47.4	0.22	1.42	0.53	57	10.2
6	Czarna Przemsza/Piwoń	155.0	78.2	351.7	1.7	184	0.23	0.50	43.7	0.11	0.94	0.42	63	18.0
7	Biała Przemsza/Golczowice	216.0	55.7	394.4	3.1	169	0.85	0.26	36.1	0.07	0.63	0.57	57	6.6
8	Ujsoła/Ujsoły	105.6	83.9	828.8	12.9	811	0.69	0.79	72.3	0.03	2.98	0.25	42	33.7
9	Bystra/Kamesznica	49.3	41.4	721.4	11.6	771	0.65	0.84	50.8	0.05	1.14	0.16	41	12.3
10	Żabniczanka/Żabnica	23.3	20.4	879.8	14.5	775	1.24	0.88	73.0	0.02	2.91	0.28	43	15.9
11	Żylica/Łodygowice	52.5	47.5	700.1	13.0	879	0.24	0.91	57.2	0.17	2.02	0.24	42	16.5
12	Łękawka/Łękawica	94.6	81.4	569.5	9.9	555	0.77	0.86	58.8	0.07	1.71	0.19	27	31.7
13	Skawica/Skawica Dolna	135.4	117.8	794.7	13.4	1293	0.48	0.87	71.3	0.04	2.88	0.21	53	58.3
14	Stryszawka/Sucha	140.4	120.2	570.4	10.4	783	0.53	0.86	56.7	0.08	1.58	0.19	43	59.0
15	Wieprzówka/Rudze	152.6	135.6	409.5	6.3	687	0.28	0.89	32.4	0.14	0.59	0.22	51	66.0
16	Skawinka/Radziszów	317.7	266.8	330.3	5.8	512	1.04	0.84	34.3	0.12	0.63	0.18	43	92.0
17	Rudawa/Balice	294.4	147.1	347.3	4.2	287	0.40	0.50	28.8	0.13	0.49	0.37	43	16.8
18	Raba/Rabka 2	91.6	76.8	657.0	8.1	510	0.62	0.84	43.4	0.10	0.92	0.22	29	31.0
19	Mszanka/Mszana Dolna	156.3	119.9	685.8	11.7	875	0.75	0.77	49.2	0.05	1.08	0.19	49	76.9
20	Krzczonówka/Krzczonów	93.2	70.9	576.2	10.4	527	0.45	0.76	49.8	0.06	1.12	0.25	43	50.1
21	Stradomka/Stradomka	363.0	299.5	358.4	6.5	798	0.57	0.82	33.4	0.07	0.56	0.15	52	121.4
22	Uszwica/Borzęcin	260.6	194.5	291.8	4.6	411	0.23	0.75	34.2	0.09	0.59	0.21	58	102.3
23	Nidzica/Dobiesławice	642.4	262.0	262.4	2.9	248	0.23	0.41	10.1	0.05	0.12	0.33	57	9.4
24	Czarny Dunajec/Koniówka	133.0	77.9	1187.2	15.8	1386	0.26	0.58	55.9	0.03	1.52	0.20	43	64.4
25	Wlk. Rogoźnik/Ludźmierz	125.3	78.0	771.5	5.9	576	0.36	0.62	18.4	0.07	0.25	0.14	44	50.4
26	Biały Dunajec/Harenda	58.6	35.6	1160.0	15.8	1301	0.61	0.61	56.1	0.15	2.26	0.23	44	42.5
27	Poroniec/Poronin	78.0	52.2	1140.7	11.6	1514	0.43	0.67	63.4	0.05	2.68	0.16	47	26.7
28	Białka/Trybsz	202.9	85.7	1263.5	17.4	1996	0.26	0.42	20.1	0.06	1.00	0.56	18	94.2
29	Niedziczanka/Niedzica	139.7	61.0	795.6	10.9	756	0.50	0.44	24.4	0.03	0.84	0.50	43	44.7
30	Grajcarek/Szczawnica	73.0	51.1	803.8	14.2	777	0.94	0.70	75.8	0.02	3.34	0.22	48	21.7
31	Ochotnica/Tylmanowa	108.7	74.9	795.6	14.6	901	0.32	0.69	67.5	0.03	2.25	0.21	43	25.4
32	Kamienica/Nowy Sącz	237.6	170.5	594.9	10.6	813	0.32	0.72	58.0	0.09	1.72	0.18	53	137.1
33	Łososina/Jakubkowice	347.0	217.6	538.2	9.6	916	0.30	0.63	42.4	0.09	0.86	0.19	53	157.2
34	Biała Nida/Mniszek	438.0	146.6	257.8	1.3	99	0.36	0.33	36.3	0.05	0.61	0.52	48	13.4
35	Bobrza/Słowik	314.8	149.7	299.4	2.7	237	0.51	0.47	43.8	0.18	1.07	0.48	52	23.9
36	Mierzawa/Michałów	535.7	134.3	268.6	1.8	195	0.30	0.25	17.3	0.09	0.23	0.45	29	6.7
37	Czarna/Raków	307.3	101.3	284.5	2.3	236	0.58	0.46	64.6	0.02	1.96	0.42	44	17.9
38	Wisłoka/Krempna Kotań	165.7	118.0	563.4	8.0	459	0.78	0.71	78.6	0.01	3.80	0.16	11	71.7
39	Sękówka/Gorlice	122.6	65.0	516.2	9.3	564	0.33	0.53	70.1	0.04	2.67	0.16	53	72.7
40	Jasiołka/Zboiska	259.7	189.1	524.9	7.6	541	0.28	0.73	67.6	0.02	2.24	0.13	41	74.8
41	Grabinka/Głowaczowa	187.4	93.3	227.6	1.3	76	0.27	0.50	40.8	0.09	0.81	0.47	14	30.6
42	Brzeźnica/Brzenica	484.4	297.5	272.5	3.7	354	0.62	0.61	27.7	0.08	0.43	0.27	63	78.7
43	Koprzywianka/Koprzywnica	519.6	308.5	248.8	2.1	371	0.34	0.59	29.5	0.05	0.45	0.36	63	33.3
44	Wołosaty/Stuposiany	118.9	68.3	858.4	12.7	793	0.37	0.57	85.6	0.01	6.19	0.13	42	72.1
45	Czarna/Polana	89.3	66.8	613.6	7.4	463	0.72	0.75	72.6	0.02	2.86	0.54	42	35.7
46	Solinka/Terka	314.6	256.5	785.7	12.8	878	0.41	0.81	89.4	0.01	9.65	0.12	53	161.9
47	Wiar/Rybotycze	178.5	110.0	461.4	6.7	416	0.57	0.62	74.6	0.01	3.07	0.14	38	70.4
48	Wisłok/Puławy	130.7	102.0	574.8	7.6	456	0.43	0.78	78.7	0.01	3.80	0.13	30	54.9
49	Stobnica/Godowa	336.0	233.1	336.2	5.8	370	0.26	0.69	42.8	0.06	0.83	0.21	33	80.8
50	Mleczka/Gorliczyna	428.7	271.6	253.0	3.3	266	0.51	0.63	16.6	0.07	0.22	0.33	61	62.4
51	Trzebośnica/Sarzyna	254.8	135.6	211.5	1.6	108	0.33	0.53	39.9	0.07	0.75	0.45	53	21.7
52	Biała Łada/Biłgoraj	225.0	80.2	258.3	2.3	148	0.23	0.35	38.6	0.04	0.66	0.37	42	7.7

Nr number of catchment, *A* area, *NL* network length, *EL* mean elevation, *SL* mean slope, *DN* height difference, *SH* shape coefficient, *RD* river network density, *FR* forest ratio, *F/A* ratio of forested area to arable land area, *U/N* ratio of urbanised (+waters) to non-urbanised area, *IN* infiltration parameter, *AMrl* annual maxima record length, $\hat{\mu}_{AM}$ mean of the AM over the whole period of observation

[a] $\mathrm{SH} = \frac{A}{L_{\max}^2}$ where $L_{\max}$ (km) is the maximum distance from the river mouth

[b] Bushes were included in the forest areas

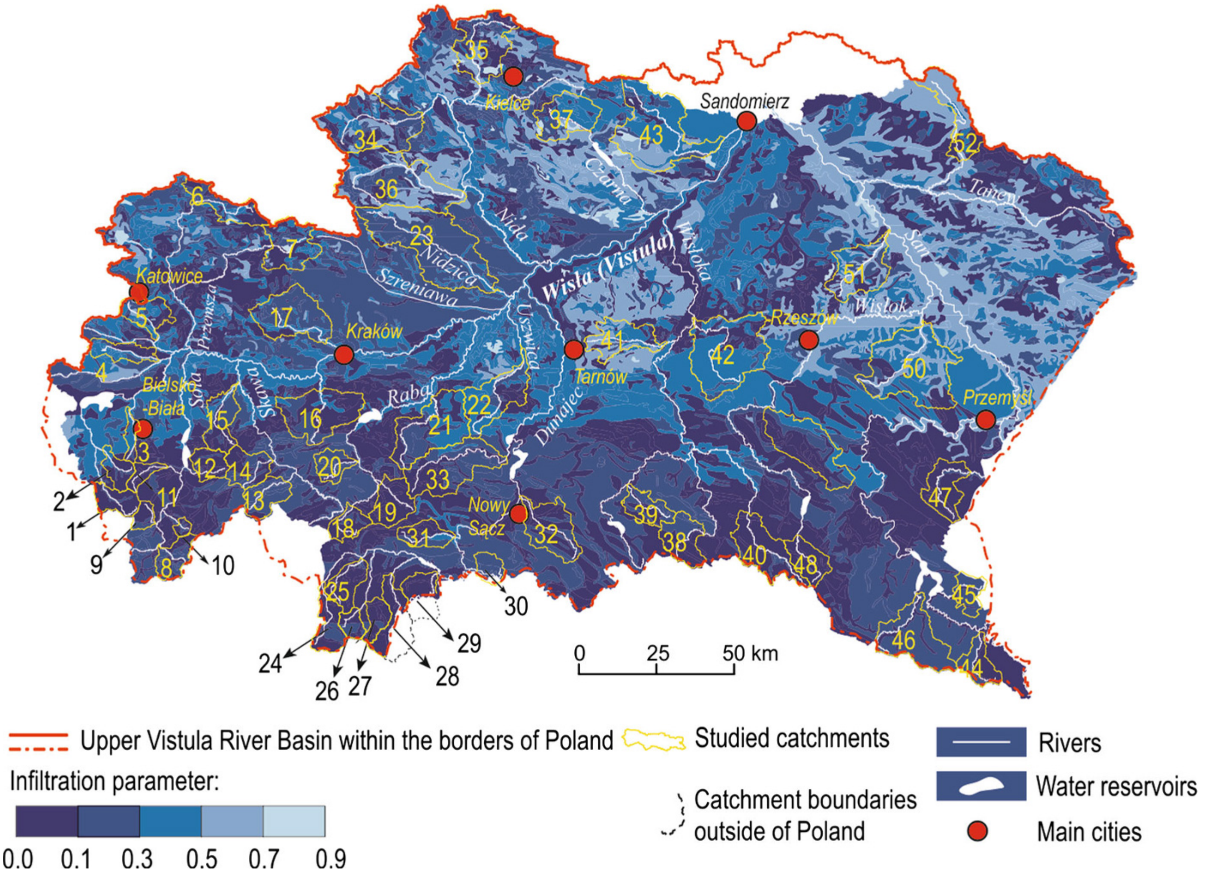

Figure 2
Spatial distribution of the infiltration parameter (Setmajer *et al.* 1971 with minor changes)

land use, and groundwater table depth (Setmajer *et al.* 1971). The infiltration is pictured in Fig. 2. It should be noted that for the estimation of design discharge using the Punzet formulas (Punzet 1978), the method developed for the UVB for catchments $A \geq 50\ \text{km}^2$, the parameter of impermeability N_p, which can be obtained from IN using the formula $N_p = (1 - \text{IN}) \times 100$, is used (Punzet 1978; Setmajer *et al.* 1971).

The estimates of the annual maxima of daily rainfall totals with 50 % probability of exceedance, $P_{50\,\%}$, were obtained from IMGW-PIB. Data were derived from maximum daily rainfall totals for periods of time of at least 50 years using the fit to the Gumbel distribution, the standard procedure at IMGW-PIB. The spatial distribution of $P_{50\,\%}$ can be seen in Fig. 3. Annual maxima (AM) data were also obtained from IMGW-PIB and were screened prior to analysis. More than a dozen gaps were noted due to failures of measuring devices or due to flooding. When a gap was observed in a flood year, it was omitted (Hosking and Wallis 1997). A total of 2367 station-years' discharge data were used in the study.

3. Methods

Since the L-moments were introduced by Greenwood *et al.* (1979), they have been considered as a practical tool in estimating the parameters of probability distribution functions of the hydrological series (Vogel and Fennessey 2001; Lu and Stedinger 1992; Wang 1997; Landwehr *et al.* 1979; Strupczewski *et al.* 2012; Kochanek *et al.* 2012, 2008). The utility of the L-moment estimates is expressed through their higher robustness in terms of outliers and greater

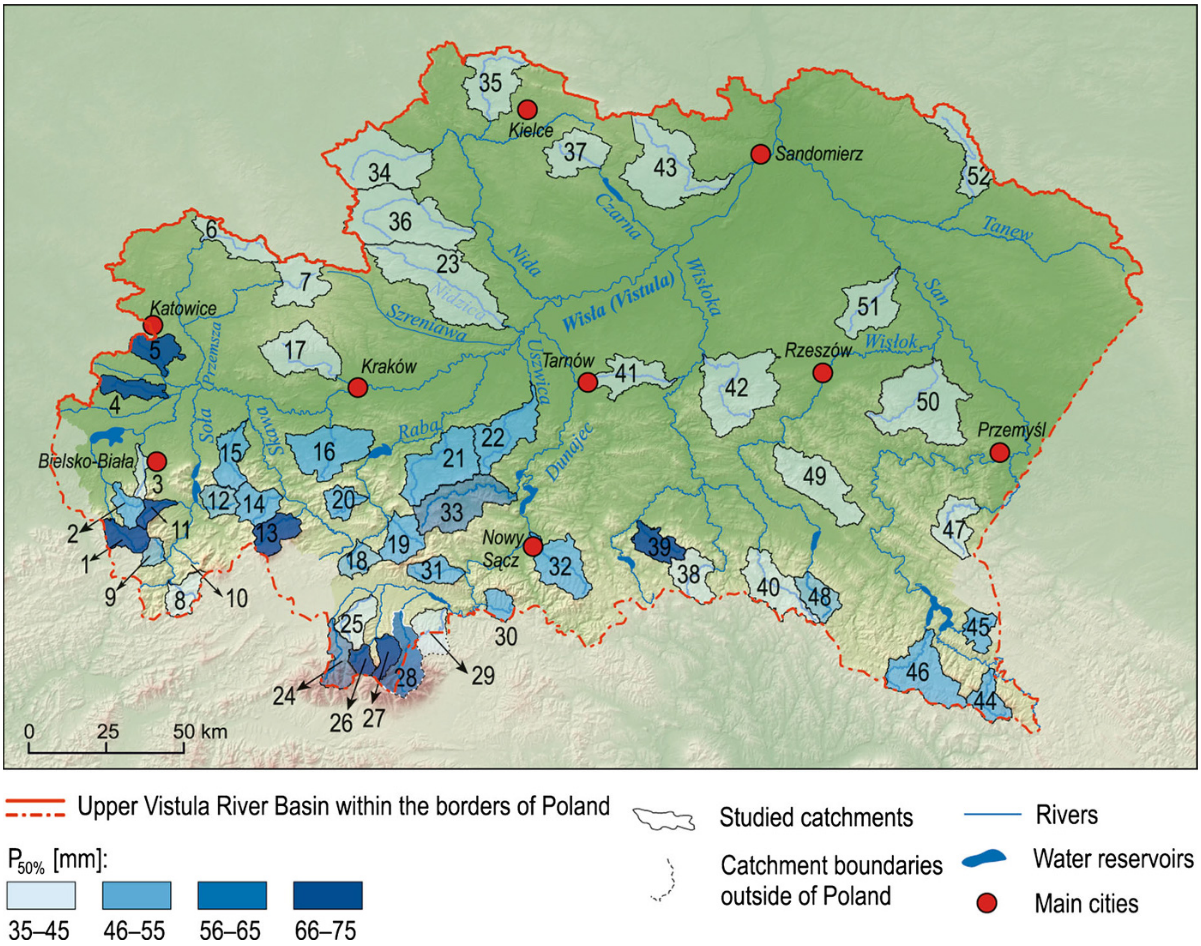

Figure 3
Spatial distribution of rainfall

effectiveness rather than of conventional moments in the case of small samples. In the HW methodology, proposed in the 1990s (Hosking and Wallis 1997), the earlier results were utilised and complemented to yield a more complex tool, which has been applied to RFFA ever since and resulted in its wide application around the world (Burn and Goel 2000; Kohnová *et al.* 2006; Adamowski 2000; Yang *et al.* 2010; Madsen *et al.* 1998; Gaál *et al.* 2009; Castellarin *et al.* 2012; Salinas *et al.* 2014a, b).

In geophysical research, the term region refers to a group of contiguous areas. However, catchments which are hydrologically similar (in the sense of the common q) do not have to be located near each other. To overcome this confusion, the expression pooling group (PG) was introduced in the Flood Estimation Handbook (1999). This term is used by many researchers (Castellarin *et al.* 2001; Kohnová *et al.* 2006; Reed *et al.* 1999).

In the IFM, the quantile function at site $i, i = 1, \ldots, N$ is given as (Stedinger *et al.* 1993):

$$Q_i(F) = \mu_i q(F), \tag{1}$$

where N is the number of sites in a region, F is a distribution function, μ_i is the index flood, and $q(F)$ is the regional, dimensionless quantile of the non-exceedance probability F. It is common to every site in a PG and the term hydrological similarity of catchments refers just to q. The index flood is a location parameter, which is assumed as the mean value of AM in this paper.

The return period T of a quantile Q is the inverse of the probability that discharge X will be at least Q

in any year, $T(Q) = \frac{1}{P(X \geq Q)}$, i.e. when Q has the T-year return period, then discharge X not less than Q occurs once per T years, on average. Hence, average frequencies of flood discharge can be derived using Eq. (1). The required size of each pooling group is advised to be at least $5T$ (Jakob *et al.* 1999; Castellarin *et al.* 2001; Merz and Blöschl 2005) or $3T$ (Gaál *et al.* 2013) station-years where T is the target return period.

3.1. Cluster Analysis

The agglomerative Ward method (Ward 1963) and the deglomerative *k*-means method (Jain and Dubes 1988; Kaufman and Rousseeuw 2005) were used, with Euclidean measure as a distance, wherein the former supplied the initial grouping of catchments for the latter. To avoid the multicollinearity of data, only coordinates with a low value of Pearson correlation coefficient $\hat{r}$ were considered. If data were spatially not autocorrelated then, using t test for significance of correlation coefficient for two samples of 52 elements, $\hat{r}$ not greater than 0.25 would be insignificant. But, due to the presence of spatial autocorrelation which reduced the effective sample size, $\hat{r}$ was enhanced to 0.5. The coordinates were not discharge statistics and were not directly related to each other through a formula, as for example $\mathrm{RD} = \frac{\mathrm{NL}}{A}$. Cluster analysis helped to identify which CCH are responsible to the greatest degree for the demarcation of PG. However, it was merely an initial form of division. Thus, some adjustments were made by moving catchments from one group to another or combining groups to achieve homogeneity (Hosking and Wallis 1997; Kohnová *et al.* 2006).

3.2. Determination of Pooling Groups

The HW L-moment-based methodology (Hosking and Wallis 1997) was used to (1) check for homogeneity within clusters, (2) adjust catchment grouping in case of non-homogeneity, (3) select an appropriate RDF, and (4) estimate flood quantiles. The minimum number of catchments in every pooling group was seven. For each group of interest, the regional L-moment ratios: $\bar{t}$, the average coefficient of L-variation (LCV) and $\bar{t}_3, \bar{t}_4$, the average L-skewness, and L-kurtosis were calculated. Then, three measures of dispersion V_1, V_2, V_3 were derived, namely the weighted standard deviation of the LCV, the weighted average distance of both the LCV and L-skewness from their regional counterparts, and the weighted average distance of both the LCV and L-kurtosis from their regional counterparts, respectively (see Hosking and Wallis 1997, formulas (4.4), (4.6), (4.7)).

It should be noted that in the determination of the final number of pooling groups, expert knowledge as subjective judgment should also be employed, which refers to previous results, known from literature, and local knowledge from the study area. The high diversity of hydrological conditions in the UVB was considered. The number of groups is a trade-off between small groups which provide small bias in flood quantile estimation and large groups which are recommended to meet at least the $3T$ requirement.

3.2.1 Heterogeneity Measures Based on L-Moments

To assess V_j, as they would be expected in a homogenous PG, a kappa distribution was fitted by setting equally the regional average L-moment ratios $1, \bar{t}, \bar{t}_3, \bar{t}_4$ to the theoretical L-moment ratios for a potentially homogenous group. Then, using simulations, the heterogeneity measures $H_j, j = 1, 2, 3$ were evaluated (Hosking and Wallis 1997, Section 4.3.3, formula (4.5)). The group was homogenous if $H_j < 1$, possibly heterogenous if $1 \leq H_j < 2$, and definitely heterogenous if $H_j \geq 2$. Among these three H_js, the statistic H_1 possesses the largest discriminatory power between the homogenous and heterogenous regions (Hosking and Wallis 1997; Kohnová *et al.* 2006).

3.2.2 The Discordancy Measure

The discordancy measure D_i is designed to check if the i-th catchment is discordant from a group as a whole (Hosking and Wallis 1997, formula (3.3)). D_i represents a generalisation of the squared Rosner's test statistic for outliers (Miziński *et al.* 2013; McCuen 2003). Critical values for D_i increase from 1.33 for $N = 5$ to 3 for $N \geq 15$. If a catchment is flagged as being discordant, deeper analysis of discharge data is needed to identify the possible reason of that fact and to make a decision on whether or not the catchment should be removed from further considerations.

3.3. *Choice of a Regional Frequency Distribution*

For each candidate distribution, the generalised logistic (GLO), generalised extreme value (GEV), lognormal (GNO), generalised Pareto (GPA) and Pearson III (PE3), the parameters were estimated by fitting the theoretical ratios $1, \mathrm{LCV}, \tau_3$ to their regional counterparts $1, \bar{t}, \bar{t}_3$. Then, the theoretical L-kurtosis τ_4^{dist} was derived for each candidate distribution. Next, a four-parameter kappa distribution was fitted to the regional ratios $1, \bar{t}, \bar{t}_3, \bar{t}_4$, and $N_{\text{sim}} = 500$ simulations of N catchments were executed, with this kappa distribution at each catchment. The bias and standard deviation of the regional L-moment ratios were equal to $B_r = \frac{1}{N_{\text{sim}}}\sum_{m=1}^{N_{\text{sim}}}(\bar{t}_{r(m)} - \bar{t}_r)$ and $\sigma_r = (\frac{1}{N_{\text{sim}}-1}(\sum_{m=1}^{N_{\text{sim}}}(\bar{t}_{r(m)} - \bar{t}_r)^2 - N_{\text{sim}}B_r^2))^{\frac{1}{2}}$, where $t_{r(m)}$ was the regional L-moment ratio in the m-th simulation ($r = 3, 4$). The L-moment ratio diagram was a helpful tool for identification of the RDF by depicting the location of regional L-moment ratios among theoretical lines representing the relationships between τ_3 and τ_4.

3.3.1 *The HW Method*

The final choice of the RDF was based on z^{dist}, the standard HW measure in which theoretical τ_4^{dist} and bias-corrected regional kurtosis $\bar{t}_4 - B_4$ are compared (Hosking and Wallis 1997, formula (5.6)). The acceptable distribution had to fulfill the condition $|z^{\text{dist}}| < 1.64$ for 90 % confidence level. The best fit was showed by the value z^{dist} closest to zero.

3.3.2 *The Kjeldsen and Prosdocimi Method*

The measure is the minimum value of the Mahalanobis distance between the two vectors: bias-corrected regional L-moment ratios, $\bar{t}_B = (\bar{t}_3 - B_3, \bar{t}_4 - B_4)$ and their theoretical counterparts of a possible candidate distribution, $\tau^{\text{dist}} = (\tau_3^{\text{dist}}, \tau_4^{\text{dist}})$. The formula reads $D^{\text{dist}} = (\tau^{\text{dist}} - \bar{t}_B)^T \Omega^{-1} (\tau^{\text{dist}} - \bar{t}_B)$, where Ω is a covariance matrix between regional L-skewness and L-kurtosis (Kjeldsen and Prosdocimi 2015). An RDF is useful if its theoretical line on the L-moment ratio diagram is intersected by the confidence ellipse. Assuming a bivariate normality of $\bar{t}_B$, D^{dist} should asymptotically follow a Chi-square distribution with 2 *df*, if observations are independent and a region is homogenous. Thus, if $D^{\text{dist}} < 4.605$, then an RDF is accepted with 90 % confidence level. The lowest value shows the best fit. Kjeldsen and Prosdocimi (2015) certified a high performance of the D^{dist} measure, namely its weak sensitivity to correlation between the AM series and more frequent selection of the true distribution by D^{dist} than by z^{dist}.

3.4. *Estimation of Flood Quantiles, Assessment of Uncertainty, and Comparison Between the Regional and Local Approach*

Assuming that $l_{1(i)}$ and $\hat{q}(F)$ are estimates of μ_i and of $q(F)$, respectively, the at-site quantile $\hat{Q}_i(F), i = 1, \ldots, N$ of the given non-exceedance probability F was estimated from Eq. (1) as:

$$\hat{Q}_i(F) = l_{1(i)} \cdot \hat{q}(F). \tag{2}$$

The measure of uncertainty of $\hat{Q}_i(F)$ was the regional average relative root mean square error, evaluated via the Monte Carlo simulations (Hosking and Wallis (1997), Section 6.4):

$$RMSE_R = \frac{1}{N}\sum_{i=1}^{N} RMSE_i, \tag{3}$$

where $RMSE_i = \left(\frac{1}{M}\sum_{m=1}^{M}(\frac{\hat{Q}_{im} - \hat{Q}_i}{\hat{Q}_i})^2\right)^{\frac{1}{2}}$, and $\hat{Q}_{im}(F)$ is calculated from Eq. (2) in the m-th simulation. The relative discordancy between $\hat{Q}_i$ and $\hat{Q}_i^{loc}$ quantiles, estimated using the regional and local approach, was measured using the mean absolute relative error:

$$MAE_R = \frac{1}{N}\sum_{i=1..N} \frac{|\hat{Q}_i - \hat{Q}_i^{loc}|}{\hat{Q}_i^{loc}}. \tag{4}$$

3.5. *Relationship Between Index Flood and Catchment Characteristics*

The relation between catchment variation of the index flood was modelled using a multivariate regression model (Wiesberg 1985). The power–law relationship was assumed between the mean discharge μ_i and catchment characteristics $A_{i1}, ..., A_{iJ}$ as $\mu_i = A_{i0} \cdot A_{i1}^{\beta_1} \cdot ... \cdot A_{iJ}^{\beta_J} \cdot e^{\omega_i}$ for $i = 1, .., N$ which is equivalent to:

$$\mathbf{Y} = \mathbf{X}\beta + \omega, \tag{5}$$

where $\mathbf{Y} = (\ln \mu_1, \ldots, \ln \mu_N)^T$, $\omega = (\omega_1, ..., \omega_N)^T$, $\mathbf{X} = \begin{bmatrix} 1 & \ln A_{11} \\ \vdots & \vdots \\ 1 & \ln A_{N1} \end{bmatrix}$, ω is the residual of the model and $\beta = (\beta_0, ..., \beta_J)$ and $\beta_0 = \ln A_{i0}$ are parameters to be estimated.

In practice, the response variable is never fully explained due to complexity of meteorological, geomorphological, and land use processes, and due to multicollinearity that appears among variables affecting the formation of runoff. Thus, theoretical assumptions for use of (5) are never ideally fulfilled. Various regression methods are used to relate CCH to streamflow characteristics, e.g. ordinary, generalised, and weighted least squares (Stedinger and Tasker 1985; Stedinger *et al.* 1993; Kroll and Stedinger 1998; Kjeldsen and Jones 2009; Tasker and Stedinger 1989). The models are useful when estimating the flow characteristics at ungauged sites. It should be stressed that the regression formula can be applicable at ungauged sites if CCH do not fall outside the range of values used to develop the equations.

3.5.1 OLS

Assumptions for the method are: $E(\omega|\mathbf{X}) = 0$, $\text{rank}(\mathbf{X}) = J$, as well as normality, homoscedasticity, and lack of autocorrelation of ω. The backward stepwise procedure supported by the AIC criterion (Akaike 1974), which favours the smallest value of the log-likehood function, adjusted for the number of parameters, was applied. The final parameter and index flood estimates were $\hat{\beta}_0, \ldots, \hat{\beta}_J$ and $\hat{\mu}_i = e^{\hat{\beta}_0} \cdot A_{i1}^{\hat{\beta}_1} \cdot \cdots \cdot A_{iJ}^{\hat{\beta}_J}$. The procedure enabled the selection of variables from among the CCH listed in Table 1 for every PG. It should be stressed that the final choice of explanatory variables may differ from the choice of CCH responsible to the greatest degree for formation of PG.

3.5.2 GLS

The GLS regression method incorporates the lengths of the data series, differences in the variance between sites, and cross-correlations between stations. Heteroscedasticity and cross-correlation of residuals are assumed. In this model $\omega = \delta + \eta$, where the modeling error δ and the sampling error η are mutually independent. The former represents the inability of the regression model to fully reflect the true value of the index flood and the latter is an index flood estimation error (Stedinger and Tasker 1985; Kjeldsen and Jones 2009; Mediero and Kjeldsen 2014; Griffis and Stedinger 2007). The covariance matrix of the total error is $\Lambda = \sigma_\delta^2 \mathbf{1}_N + \Sigma$, where $\sigma_\delta^2 \mathbf{1}_N$ is the model error matrix and Σ is the sampling error covariance matrix which may have unequal diagonal elements and some of the off-diagonal elements may be nonzero. If Λ is known, then the solution of (5) reads:

$$\hat{\beta}_{GLS} = (\mathbf{X}^T \Lambda^{-1} \mathbf{X})^{-1} \cdot \mathbf{X}^T \Lambda^{-1} \mathbf{Y}, \tag{6}$$

which is the unbiased estimator of β with the minimum variance (Johnston 1984). If Λ is unknown, then its estimator $\hat{\Lambda} = \hat{\sigma}_\delta^2 \mathbf{1}_N + \hat{\Sigma}$ is used. The residual modelling error variance $\hat{\sigma}_\delta^2$ and the solution of (5) can be derived by solving (6) and the equation $(\mathbf{Y} - \mathbf{X}\hat{\beta}_{GLS})^T \hat{\Lambda}^{-1} (\mathbf{Y} - \mathbf{X}\hat{\beta}_{GLS}) = N - J - 1$. The estimator $\hat{\Sigma}$ can be obtained from: $\hat{\Sigma}_{ij} = \sigma_i \sigma_j \frac{n_{ij}}{n_i n_j} \rho_{ij}$ for $i \neq j$, and $\hat{\Sigma}_{ii} = \frac{\sigma_i^2}{n_i}$.

$$\hat{\Sigma}_{ij} = \begin{cases} \frac{\sigma_i^2}{n_i}, & i = j, \\ \sigma_i \sigma_j \frac{n_{ij}}{n_i n_j} \rho_{ij}, & i \neq j \end{cases} \tag{7}$$

where σ_i^2 is the variance of the log-transformed discharge data in the ith catchment, n_{ij} is the number of overlapping years between the ith and jth series, and ρ_{ij} is the inter-site correlation between the sample mean values, which was assumed to be the correlation coefficient between the overlapping series. However, $\hat{\Sigma}$ contains raw estimates; thus it often results in a $\hat{\Lambda}$ that cannot be inverted. Therefore, to adjust $\hat{\Sigma}$, the following two nonlinear regression models were considered for the off-diagonal elements:

$$\rho_{ij}^{\mathrm{TS}} = \Theta^{\frac{d_{ij}}{\mathrm{ad_{ij}}+1}}, \qquad \rho_{ij}^{\mathrm{KJ}} = \phi_1 e^{-\phi_2 d_{ij}} + (1-\phi_1) e^{-\phi_3 d_{ij}}, \tag{8}$$

where d_{ij} is the distance between the catchment centroids. The former formula above was proposed by Tasker and Stedinger (1989) (TS fit leading to matrix $\hat{\Sigma}^{\mathrm{TS}}$) and the latter by Kjeldsen and Jones (2009) (KJ fit leading to matrix $\hat{\Sigma}^{\mathrm{KJ}}$). The adjusted diagonal elements of $\hat{\Sigma}$ were calculated as $\frac{1}{Nn_i}\sum_{i=1}^{N}\sigma_i^2$ (Haddad *et al.* 2010).

3.5.3 *Assessment and Comparison of the OLS and GLS Regression*

The normality of residuals, derived as differences between the logarithms of the observed mean annual discharge, $ln(\mu_{i,\mathrm{obs}})$ and $ln(\hat{\mu}_i)$ (Eq. 5) was tested using the Shapiro–Wilk (SW) test (Shapiro and Wilk 1965). The variance inflation factor tested if at least one of the explanatory variables is highly correlated with others, $\mathrm{VIF}_j = \frac{1}{1-R_j^2}$, where R_j^2 is the coefficient of determination obtained from regressing the jth variable against all others. The model becomes questionable if $\mathrm{VIF} > 5$ (Montgomery and Peck 1992) and unreliable if $\mathrm{VIF} > 10$ (Merz and Blöschl 2005); otherwise, the model is valid. The significance for spatial autocorrelation was tested using the Moran I statistic (Moran 1950) with weights in the form of inverses of Euclidean distances between catchment centroids. The coefficient of determination $R_{OLS}^2 = 1 - \frac{\sum_{i=1}^{N}(\mu_{i,obs}-\hat{\mu}_i)^2}{\sum_{i=1}^{N}(\mu_{i,obs}-\overline{\mu}_{i,obs})^2}$ was used to evaluate the performance of the OLS model. Additionally, the leave-one-out jackknife bootstrapping method (Efron 1993; Sahinler and Topuz 2011; Castellarin *et al.* 2004) was used. To assess the uncertainty, each i-th catchment, in turn, was dropped from a homogenous PG, and the parameter estimates $\hat{\beta}_{ij}, j = 1, \ldots, J$ were derived for smaller samples. The parameter and index flood estimates were produced, $\hat{\beta}_{j-k,j} = \frac{1}{N}\sum_{i=1}^{N}\hat{\beta}_{ij}$, $\hat{\mu}_{j-k} = e^{\hat{\beta}_0} \cdot A_1^{\hat{\beta}_1} \cdot \ldots \cdot A_J^{\hat{\beta}_J}$, where the subscript "$j-k$" refers to the jackknife method. Finally, the root mean square error and mean absolute error were calculated, respectively, as $\mathrm{RMSE}_{j-k} = (\frac{1}{N}\sum_{i=1}^{N}(\frac{\mu_{i,\mathrm{obs}}-\hat{\mu}_{i,j-k}}{\mu_{i,\mathrm{obs}}})^2)^{\frac{1}{2}}$, $MAE_{j-k} = \frac{1}{N}\sum_{i=1}^{N}\frac{|\mu_{i,\mathrm{obs}}-\mu_{i,j-k}|}{\mu_{i,\mathrm{obs}}}$.

To assess the performance of the GLS regression model, the pseudo coefficient of determination was used, $R_{\mathrm{GLS}}^2 = 1 - \frac{\sigma_\delta^2(J)}{\sigma_\delta^2(0)}$ (Griffis and Stedinger 2007), where $\sigma_\delta^2(J)$ and $\sigma_\delta^2(0)$ refer to a model with J and with 0 explanatory variables, respectively. The average variance of prediction AVP measured how well the model predicts the logarithm of the mean discharge, on average, $\mathrm{AVP} = \sigma_\delta^2 + \frac{1}{N}\sum_{i=1}^{N} x_i(X^T\hat{\Lambda}^{-1}X)^{-1}x_i^T$. The mean standard error of prediction SEP (in %) for the true index flood (rather than for the logarithmised value) was computed as $\mathrm{SEP} = 100(e^{\mathrm{AVP}}-1)^{\frac{1}{2}}$ (Griffis and Stedinger 2007).

The question whether a full GLS model is needed or if OLS is sufficient was addressed using the error variance ratio EVR, the relative magnitude of the average sampling variance to the model error variance, $EVR = \frac{\mathrm{tr}\hat{\Sigma}}{N \cdot \sigma_\delta^2}$. Griffis and Stedinger (2007) recommend the use of GLS rather than OLS if $EVR > 0.2$.

All calculations were completed in **R** programme (R 2013; Hosking 2013; Viglione 2014; Chasalow 2012).

4. *Results*

4.1. *Identification of Pooling Groups*

Using data from Table 1, several sets of morphometric and land use CCH were created. The sets were complemented with rainfall $P_{50\%}$, the major factor affecting the flood generating mechanism, and with longitude and latitude (LO, LA). The inclusion of LO and LA was necessary because the index flood is to be regressed against CCH in an area of large morphometric diversity, to obtain geographically contiguous regions (Rossi and Villani 1994). Flood regionalisation methods which incorporate both catchment attributes and spatial nearness have high predictive performance (Merz and Blöschl 2005). The following sets of CCH were designed for further studies: $U_1 = \{A, \mathrm{SH}, \mathrm{IN}, P_{50\%}, \mathrm{LO}, LA\}$, $U_2 = \{\mathrm{SL}, \mathrm{SH}, \mathrm{RD}, P_{50\%}, \mathrm{LO}, \mathrm{LA}\}$, $U_3 = \{\mathrm{NL}, \mathrm{SH}, \mathrm{IN}, P_{50\%}, \mathrm{LO}, \mathrm{LA}\}$, $U_4 = \{\mathrm{EL}, \mathrm{SH}, \mathrm{RD}, P_{50\%}, \mathrm{LO}, \mathrm{LA}\}$, $U_5 = \{\mathrm{EL}, \mathrm{SH}, \mathrm{RD}, \mathrm{IN}, P_{50\%}, \mathrm{LO}, \mathrm{LA}\}$, $U_6 = \{\mathrm{EL}, \mathrm{SH}, \mathrm{RD}, \mathrm{FR}, \mathrm{IN}, P_{50\%}, \mathrm{LO}, \mathrm{LA}\}$, $U_7 = \{\mathrm{EL}, \mathrm{SH}, \mathrm{RD}, F/A, \mathrm{IN}, P_{50\%}, \mathrm{LO}, \mathrm{LA}\}$, $U_8 = \{\mathrm{EL}, \mathrm{SH}, \mathrm{RD}, U/N, \mathrm{IN}, P_{50\%}, \mathrm{LO}, \mathrm{LA}\}$.

Subsequently, cluster analysis was used. First, the number of clusters was stated to be 15 and afterwards it was decreased by 1–3. For each group of catchments, the measures H_1, H_2, H_3, D_i were calculated. The smallest homogenous clusters were identified and their tendency to expand into larger clusters was observed. Sometimes, a cluster was observed to be homogenous in itself but would turn out not to be homogenous following the addition of another catchment. The number of homogenous clusters varied when various U_i were considered, which proved that the power of formation of homogenous regions by sets of characteristics U_i was different. The set U_2 was observed to provide the highest number of homogenous clusters among all $U_i, i = 1, \ldots, 8$. Therefore, the pooling process from that point on was based on clusters identified by CCH from U_2. It should be stressed that even for U_2 only a few clusters turned out to be homogenous. The proportion of homogenous clusters varied from $\frac{1}{4}$ to $\frac{1}{3}$ when the number of clusters changed from 15 to 3. Thus, U_2 could be treated as a set of characteristics with the greatest effect on q.

The analysis also revealed that, using U_2, northern clusters cover larger areas than southern clusters. Additionally, one northern cluster was homogenous, while the others were smaller and rarely homogenous. Therefore, a refinement procedure was introduced in which homogenous clusters were combined and/or catchments were attached to homogenous clusters from adjacent areas. This led to many different possibilities of dividing the study area into homogenous PG. Finally, the division that provided the smallest sum of RMSE values (Eq. 3) for quantiles of $T = 2, 10$ and 100 years was selected. An optimisation algorithm written in **R** code had a supporting role in this step, in which many catchment combinations were considered and their homogeneity was tested.

Three pooling groups were identified as a first variant (variant I) of regionalisation: PG1, PG2, and PG3. It should be stressed that a change of the optimisation condition may result in yet another division. This concerns mainly catchments located along the boundaries, e.g. the inclusion of catchments 20, 21, 22 in PG1 instead of PG2 did not undermine homogeneity, but did cause a slight increase of the sum of RMSE of quantiles of $T = 2, 10, 100$ years. Six catchments numbered 4, 46, 44, 48, 17, and 25 were not assigned to any group, as they had caused heterogeneity after joining a pooling group. The reason for the heterogeneity remains mostly unknown. The second variant (variant II) was introduced by the division of the PG1 into two subregions. This step was taken due to very high diversification of CCH which may reduce the reliability of the regression models. Catchments with the highest elevation and rainfall, located in the west of the study area, were assigned to PG1A, while the eastern catchments were assigned to PG1B. Figure 4 shows the division of the study area in the form of variant I and variant II. The key advantage of introducing of variant II is the opportunity to reflect the wide array of runoff formation processes in PG1. The key disadvantage is the inability to estimate quantiles for very long T in small PG where the condition $3T$ may not be fulfilled.

4.2. *Statistical Characterisation of Pooling Groups*

The results of the statistical analysis are shown in Table 2. The test statistics H_1, H_2, H_3 were less than 1, which confirmed homogeneity within all groups in both variants. The PG3 consisted of far fewer catchments than PG1 and PG2. The discordancy measures were less than critical values everywhere, apart from the catchment 9, both in PG1 and in PG1A. A possible reason for this is a lack of data from 2007, when a high AM discharge was observed in adjacent catchments 1, 8, and 10, positioned approximately as the quantile of order 0.84 in the AM sample which may lead to high t_3 and t_4 values. As no other reason was identified, the catchment was not excluded.

4.3. *Identification of RDF*

The following z^{dist} values and RDF identified via this measure were obtained for PG1, PG1A, PG1B, PG2, PG3: −0.39 (GPA), 0.18 (GNO), −0.03 (PE3), 0.70 (GPA), 0.20 (GNO); however, GNO and PE3 were also accepted for PG1 and PG2, GEV and GPA were accepted for PG1A, GPA for PG1B, and GEV and PE3 were also accepted for PG3. The following D^{dist} values were obtained for PG1, PG1A, PG1B, PG2, PG3: 0.016 (GPA), 0.017 (GNO), 0.0046 (PE3),

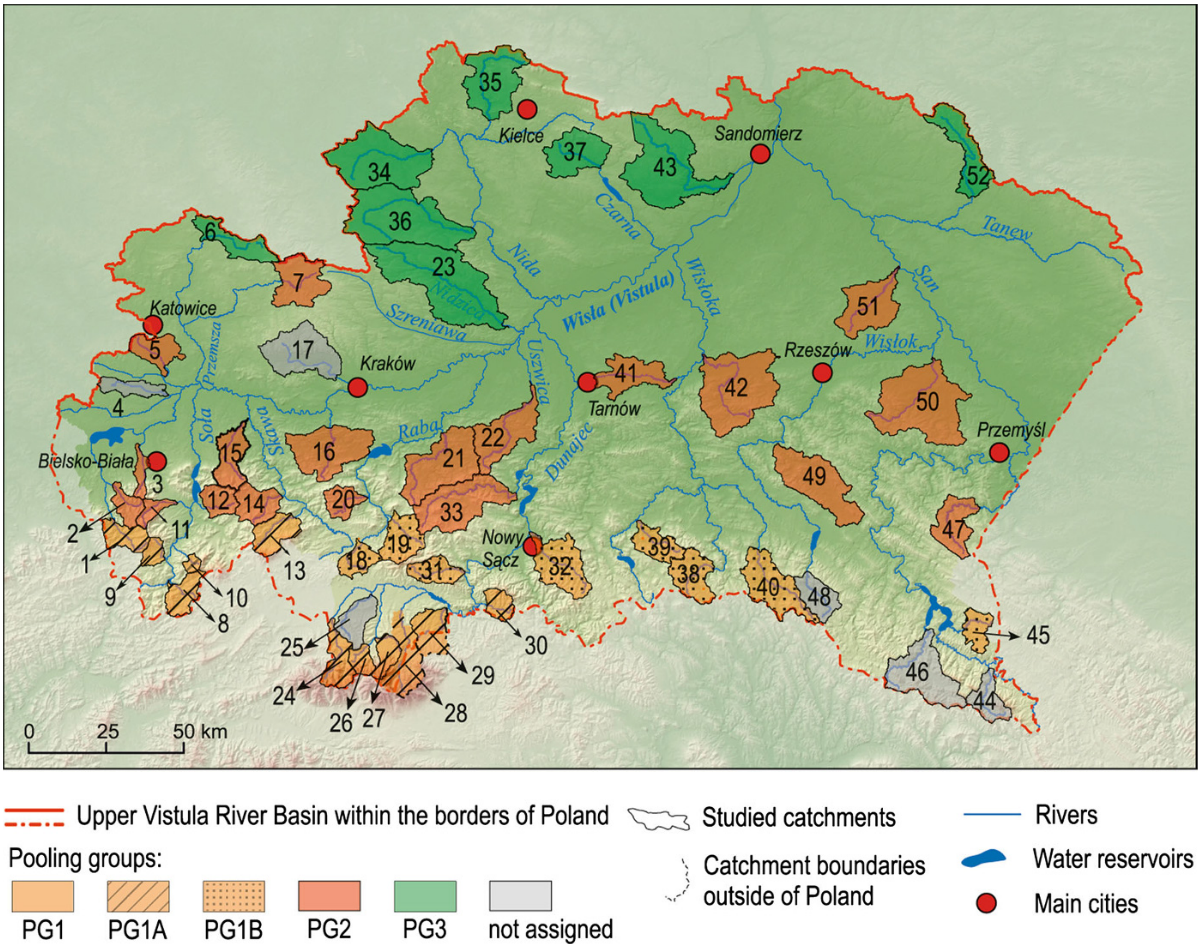

Figure 4
Pooling groups with regard to similarity in factor q (Eq. 1)

Table 2

Results of regionalisation

PG	N	$\bar{t}$	$\bar{t}_3$	$\bar{t}_4$	H_1	H_2	H_3	R_D	RDF	Loc.	Scale	Shape
1	19	0.40	0.39	0.21	0.97	0.73	0.62	0.10–3.49[a]	GPA	0.25	0.66	−0.12
1A	11	0.40	0.40	0.23	0.88	0.93	0.79	0.14–2.63[a]	GNO	0.73	0.52	−0.86
1B	8	0.40	0.36	0.17	0.56	0.04	−0.16	0.49–1.98	PE3	1.00	0.81	2.17
2	19	0.43	0.36	0.20	0.21	0.82	0.53	0.23–2.02	GPA	0.16	0.79	−0.06
3	8	0.36	0.27	0.18	0.47	−0.74	−0.14	0.37–1.29	GNO	0.84	0.52	−0.56

PG pooling group, N number of sites, R_D range of D, loc., scale, shape, parameters of RDF

[a] The discordancy of the Bystra catchment (nr 9) was manifested by $D_1 = 3.49$ for PG1 and $D_{1A} = 2.63$ for PG1A

0.032 (GPA), 0.010 (GNO). The two sets of results fully correspond. The final choice is shown in Table 2. The asymptotic condition $D^{\mathrm{dist}} < 4.605$ was fulfilled by all distributions in all pooling groups; therefore, it had a weak discriminatory power. The possible reason was a sample size that was too small. Negative values of shape parameters suggest that RDFs are heavy tailed, which indicates the possible existence of very large discharge. Figure 5 shows an L-moment ratio diagram where the pairs $(\bar{t}_3, \bar{t}_4)$ are located in the L-skewness L-kurtosis space. An ideal fit of the PG1 and PG3 averages to the GPA and GNO, as well as a close location of PG2 to GPA is observed. The sample L-moment ratios of PG1 and PG2 are scattered among each other and no evident division in disjoint samples is visible, which reflects the high dispersion and diversity of every group. The group PG3 is slightly separated from PG1 and PG2 with L-skewness not exceeding 0.32. The catchment 9 from PG1 has coordinates $t_3 = 0.44, t_4 = 0.36$ and is positioned somewhat above the main data point cloud, which depicts the higher value of its discordancy measure.

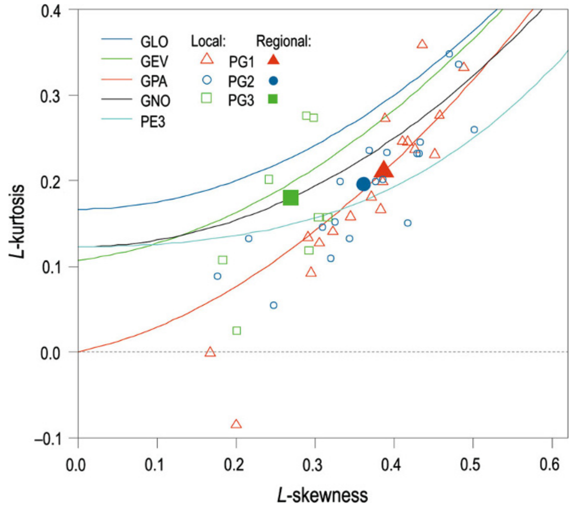

Figure 5

The L-moment ratio diagram. The *continuous lines* depict the theoretical distribution functions, and the graph's symbols are local or regional (*bold symbols*) L-moment ratios

4.4. *Characterisation of Pooling Groups*

The features of each pooling group are shown in Table 3. Substantial differences in topographic, land use, and rainfall characteristics between pooling groups in variant I are observed. Catchments of PG1 are characterised by the smallest areas and by the highest EL, DN, SL, FR, $P_{50\%}$ among the three groups, unlike those of PG3. The catchments of PG1 are more elongated than those of PG2, PG3, which is expressed in larger SH. The RD and IN are similar in PG1 and PG2, while higher IN and lower RD are observed in PG3. The highest rainfall $P_{50\%}$ is observed in PG1, moderate in PG2, and the lowest in PG3. In variant II, the division of PG1 into two subgroups enabled the distinction of PG1A, the group with the highest EL, DN, SL, and $P_{50\%}$.

The three groups of catchments differ in terms of physical geography. The PG1 group consists of high and middle mountain catchments found in the southern Carpathians (Tatra Mountains, part of the Beskidy Zachodnie, Beskidy Środkowe, and part of the the Bieszczady Mountains). The PG2 consists of several lower ranges of the northern Carpathians, the foothills, and the western part of the highlands. The PG3 consists, generally, of catchments in the middle and eastern part of the highlands (see Fig. 1).

Table 3

Key statistics of CCH for PG1, PG1A, PG1B, PG2, and PG3

PG	*N*	*A*	EL	DN	SL	SH	RD	FR	IN	$P_{50\%}$
1	19	23.3–259.7	801.9	911.6	12.0	0.56	0.70	60.2	0.25	50.3
			0.29/0.14	0.45/0.27	0.25/0.19	0.46/0.37	0.19/0.10	0.28/0.14	0.52/0.17	0.1/0.1
1A	11	23.3–202.9	934.9	1108.6	13.8	0.59	0.68	57.9	0.27	51.4
			0.22/0.21	0.38/0.35	0.15/0.11	0.48/0.21	0.23/0.16	0.34/0.15	0.49/0.14	0.11/0.09
1B	8	89.3–259.7	618.9	640.8	9.6	0.51	0.72	63.4	0.22	48.8
			0.15/0.09	0.29/0.30	0.26/0.17	0.43/0.43	0.12/0.03	0.19/0.11	0.59/0.14	0.09/0.06
2	19	50.1–484.4	411.3	503.0	6.5	0.46	0.71	43.8	0.27	46.4
			0.36/0.34	0.56/0.44	0.57/0.49	0.50/0.33	0.24/0.15	0.33/0.23	0.49/0.26	0.18/0.14
3	8	155.0–642.4	278.9	214.8	2.1	0.35	0.42	35.5	0.42	36.6
			0.12/0.06	0.38/0.15	0.25/0.16	0.38/0.26	0.26/0.15	0.48/0.23	0.15/0.11	0.04/0.01

For every characteristic, three values are shown: the mean value and (below) cv/cd where cv is the coefficient of variation and cd $= \frac{d_{0.75}-d_{0.25}}{2d_{0.5}}$, in which d_p is the quantile of order *p*. Abbreviations and units according to Table 1. $P_{50\%}$ is the estimate of the annual maxima of daily rainfall totals with 50 % probability of exceedance

Table 4

Quantile estimates $\hat{q}$ of the RDF for various return periods

PG	Return period T (years)				
	2	10	50	100	200
1	0.73	2.00	3.53	4.28	5.09
1A	0.73	1.94	3.65	4.58	5.65[a]
1B	0.74	2.04	3.40	3.99	4.58[a]
2	0.72	2.11	3.65	4.36	5.10
3	0.84	1.82	2.85	3.36	3.85[a]

[a] The rule 3T not fulfilled

4.5. Estimation of Flood Quantiles

With the use of the 3T rule, only quantiles of return periods not longer than $T = 250$ for PG1, $T = 300$ for PG2, $T = 130$ for PG3, $T = 160$ for PG1A, and $T = 100$ for PG1B, can be estimated. In Table 4, the quantiles $\hat{q}$ of the RDFs are shown that can be used for calculation of the design discharge from Eq. (2). In Table 5 the quantiles $\hat{Q}_i(0.99)$ (Eq. 2) are presented for both variants. A difference of several percentage points in discharge is observed between the estimates for variant I and variant II.

The comparison between the 100-year discharge obtained for regional and local estimation resulted in the following errors (Eq. 4): $\mathrm{MAE}_{\mathrm{PG1}} = 19.7\,\%$, $\mathrm{MAE}_{\mathrm{PG2}} = 16.3\,\%$, $\mathrm{MAE}_{\mathrm{PG3}} = 11.7\,\%$, $\mathrm{MAE}_{\mathrm{PG1A}} = 20.4\,\%$, and $\mathrm{MAE}_{\mathrm{PG1B}} = 14.0\,\%$. Figure 6 shows the regional and local 100-year flood estimates for PG1 (variant I), and PG1A and PG1B (variant II). A high compatibility between both estimators is observed. Note that all red dots are above and all blue dots are below the green dots. Hence, the division of the PG1 caused an increase in regional estimates for catchments from PG1A and a decrease for catchments from PG1B.

The quality of the estimation (Eq. 3) of regional quantiles was high. The RMSE ranged from 2.9 % (PG3) to 7.1 % (PG1A) for $T = 2$, from 4.1 % (PG3) to 7.7 % (PG1A) for $T = 10$, and from 8.3 % (PG3) to 14.0 % (PG1A) for $T = 100$.

4.6. Relationships Between an Index Flood and Catchment Characteristics

The following CCH were selected for regression formulas: $A, P_{50\,\%}$ (PG1), $A, P_{50\,\%}, IN$ (PG1A), $A, P_{50\,\%}, IN, EL$ (PG2). The lack of high collinearity among variables was reflected in VIF values less than 5 (see Table 6). Very low VIF values were obtained for PG1 and PG1A, and higher values for PG2.

Table 5

Flood quantiles $\hat{Q}$ ($m^3\ s^{-1}$) of return period $T = 100$ years estimated using Eq. (2)

River	PG1	PG1A or PG1B	River	PG2	River	PG3
1 Mała Wisła	222.5	238.2	2 Brennica	210.0	6 Czarna Przemsza	60.1
8 Ujsoła	144.1	154.2	3 Wapienica	220.7	23 Nidzica	31.5
9 Bystra	52.8	56.5	5 Mleczna	44.6	34 Biała Nida	44.7
10 Żabniczanka	68.2	73.0	7 Biała Przemsza	28.6	35 Bobrza	79.9
13 Skawica	249.3	266.9	11 Żylica	72.0	36 Mierzawa	22.4
18 Raba	132.8	123.7	12 Łękawka	138.1	37 Czarna 1	57.2
19 Mszanka	329.1	306.6	14 Stryszawka	257.2	43 Koprzywianka	111.0
24 Czarny Dunajec	275.4	294.8	15 Wieprzówka	287.8	52 Biała Łada	25.8
26 Biały Dunajec	182.1	194.9	16 Skawinka	401.2		
27 Poroniec	114.2	122.2	20 Krzczonówka	218.3		
28 Białka	403.3	431.7	21 Stradomka	529.6		
29 Niedziczanka	191.2	204.7	22 Uszwica	446.4		
30 Grajcarek	92.9	99.4	33 Łososina	685.5		
31 Ochotnica	108.7	101.2	41 Grabinka	133.6		
32 Kamienica	586.7	546.5	42 Brzeźnica	343.2		
38 Wisłoka	307.1	286.0	47 Wiar	307.2		
39 Sękówka	311.1	289.8	49 Stobnica	352.4		
40 Jasiołka	320.3	298.4	50 Mleczka	272.3		
45 Czarna 2	152.8	142.3	51 Trzebośnica	94.5		

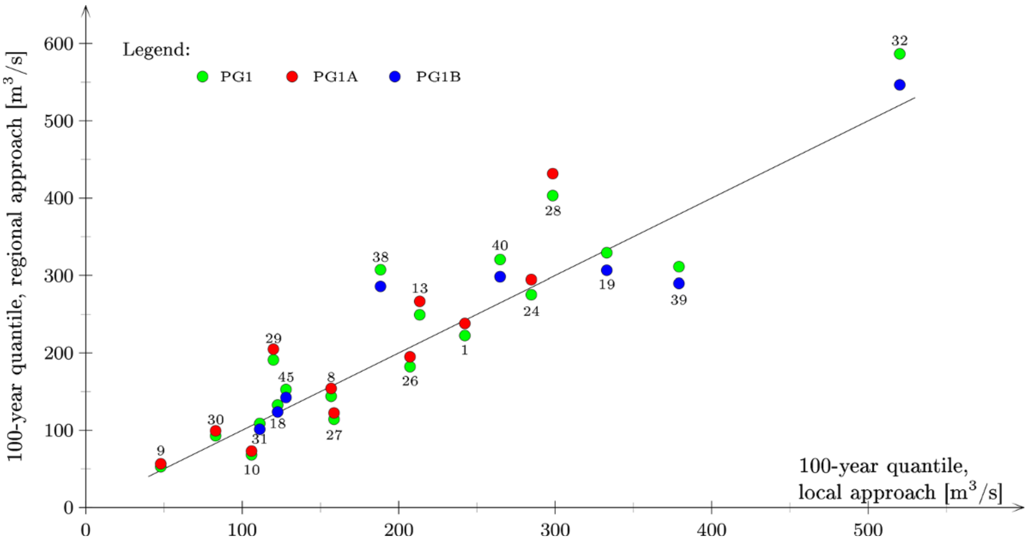

Figure 6

Comparison between 100-year flood estimates obtained via the regional and local approach for pooling groups PG1, PG1A, and PG1B. The y-coordinates of the *green*, *red*, and *blue dots* are regional estimates from PG1, PG1A, and PG1B, respectively, and x-coordinates are local estimates. The diagonal line represents ideal compatibility. The catchments are numbered according to Fig. 1 and Table 1

Table 6

Results of the validation and assessment of uncertainty of the OLS/GLS regression scheme

PG	VIF	$p^{\mathrm{SW}}_{\mathrm{OLS/GLS}}$	$R^2_{\mathrm{OLS/GLS}}$	$I_{\mathrm{OLS/GLS}}$	$\mathrm{AVP}_{\mathrm{OLS/GLS}}$	$\mathrm{SEP}_{\mathrm{OLS/GLS}}$	EVR
1	1.10	0.50	0.87/0.89	−0.15/−0.13	0.06/0.06	25.64/24.52	0.27
1A	1.25	0.55	0.94/0.95	−0.04/−0.03	0.05/0.04	22.11/20.63	0.43
2	4.20	0.55	0.86/0.87	−0.20/−0.20	0.15/0.15	40.82/40.76	0.14

VIF the highest variance inflation factor in the region, p^{SW} the p value of the SW test, R_2 the (pseudo)coefficient of determination, I the Moran statistic, *AVP* the average variance of prediction, *SEP* the standard error of prediction, *EVR* error variance ratio

For OLS, the RMSE_{j-k} (MAE_{j-k}) varied from 22.5 to 45.1 % (18.7–36.3 %), while the lower values were obtained for PG1 and PG1A, and higher for PG2. Therefore, higher predictive performance was represented by the OLS model for PG1 and PG1A, and slightly lower by the OLS model for PG2.

As many as six variables were selected both for PG1B and PG3 for the final regression scheme, A, EL, SL, FR, IN, $P_{50\,\%}$. Such a large number of covariates in comparison with the very small sample size caused immense uncertainty, reaching an RMSE_{j-k} (MAE_{j-k}) of over 700 % (over 450 %) for PG1B, and of over 250 % (200 %) for PG3. Due to low predictive performance, the multivariate regression model is not applicable for PG1B and PG3.

The GLS model was applied to PG1, PG2, and PG1A. The spatial structure of the inter-site correlation in PG1, PG2, and the sample estimates (Eq. 8) are depicted in Fig. 7. A high compatibility between sample correlations and KJ and TS estimates is observed for PG2. However, large sample fluctuations and no clear dependence between correlations and distance is visible in PG1; thus the fit is poorer in this region. The spatial structure of the inter-site correlation is also poor in PG1A, which is similar to PG1.

The diagnostic measures AVP, EVR, SEP were compared for the GLS models based on matrices $\hat{\Sigma}$, $\hat{\Sigma}^{\mathrm{TS}}$, $\hat{\Sigma}^{\mathrm{KJ}}$ of raw and adjusted estimates (8). The GLS model which had the lowest SEP value was finally

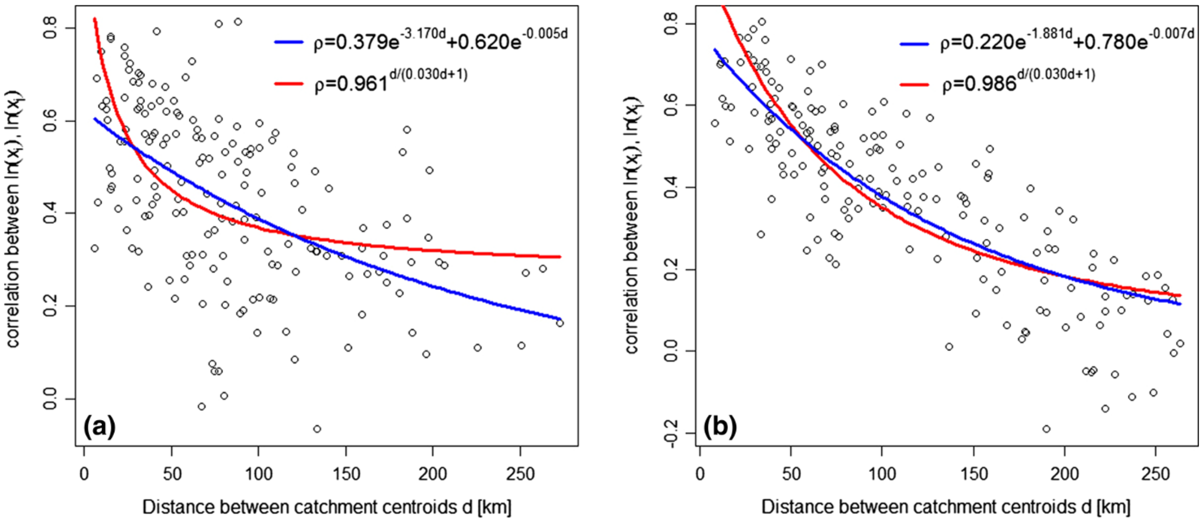

Figure 7
Inter-site correlation structure **a** PG1, **b** PG2

selected. The model based on $\hat{\Sigma}^{\mathrm{TS}}$ was developed for PG1 and PG1A, and the model based on $\hat{\Sigma}^{\mathrm{KJ}}$ was developed for PG2.

The lowest model error variance was obtained for PG1A ($\sigma_\delta^2 = 0.03$) and the highest for PG2 ($\sigma_\delta^2 = 0.12$). The final diagnostic measures, both for OLS and GLS, are shown in Table 6. High p_{SW} and R^2_{GLS} values confirm the good fit. The I statistics are insignificant, thus residuals are spatially uncorrelated. The AVP and SEP values are much lower in PG1 and PG1A than in PG2; hence, the predictive performance of the models is higher in PG1 and PG1A than in PG2. For PG1 and PG1A, the comparisons between $\mathrm{AVP_{OLS}}$, $\mathrm{SEP_{OLS}}$ and $\mathrm{AVP_{GLS}}$, $\mathrm{SEP_{GLS}}$ indicate a moderate improvement of the model when GLS is used instead of OLS which is reflected in a value of EVR higher than 0.2. For PG2, the EVR value less than 0.2 suggests a lack of necessity of the use of GLS instead of OLS; thus, the models seem to be equivalent. Finally, the following GLS regression models were obtained:

$$\hat{\mu}_{\mathrm{PG1}} = e^{-11.02} \cdot A^{1.07} \cdot P^{2.50}_{50\,\%}, \tag{9}$$

$$\hat{\mu}_{\mathrm{PG1A}} = e^{-10.47} \cdot A^{0.91} \cdot P^{2.66}_{50\,\%} \cdot \mathrm{IN}^{0.36}, \tag{10}$$

$$\hat{\mu}_{\mathrm{PG2}} = e^{-5.50} \cdot A^{0.74} \cdot P^{1.72}_{50\,\%} \cdot \mathrm{IN}^{-1.49} \cdot \mathrm{EL}^{-0.52}. \tag{11}$$

The variables selected for use in regression formulas were different from those most closely associated with the formation of homogenous regions in this study.

5. *Discussion*

The region PG2 is seen from Table 2 to have the highest $\bar{t}$ which shows the largest variability of RDF. The next two characteristics, $\bar{t}_3$ and $\bar{t}_4$, were the highest in PG1A which reflects the largest asymmetry and peakedness of the RDF. The region PG3 is observed to have the lowest $\bar{t}$ and $\bar{t}_3$ which reflects the lowest variability and asymmetry of the RFD.

The existing hydrological classifications were depicted in Fig 8 (see also the Sect. 1). Among them, only Stachý and Fal (1986) considered similarity in the regional frequency distributions, while the other authors studied various physical geographic and climatological factors and hydrological regimes. There is some similarity between the contour of the PG3 region and the contours of the northern regions classified by Dębski (1961), Soczyńska (1977), and, partially, of the northern region of Stachý and Fal (1986). Another similarity is visible between the contour of the PG1A and the contour of the south-

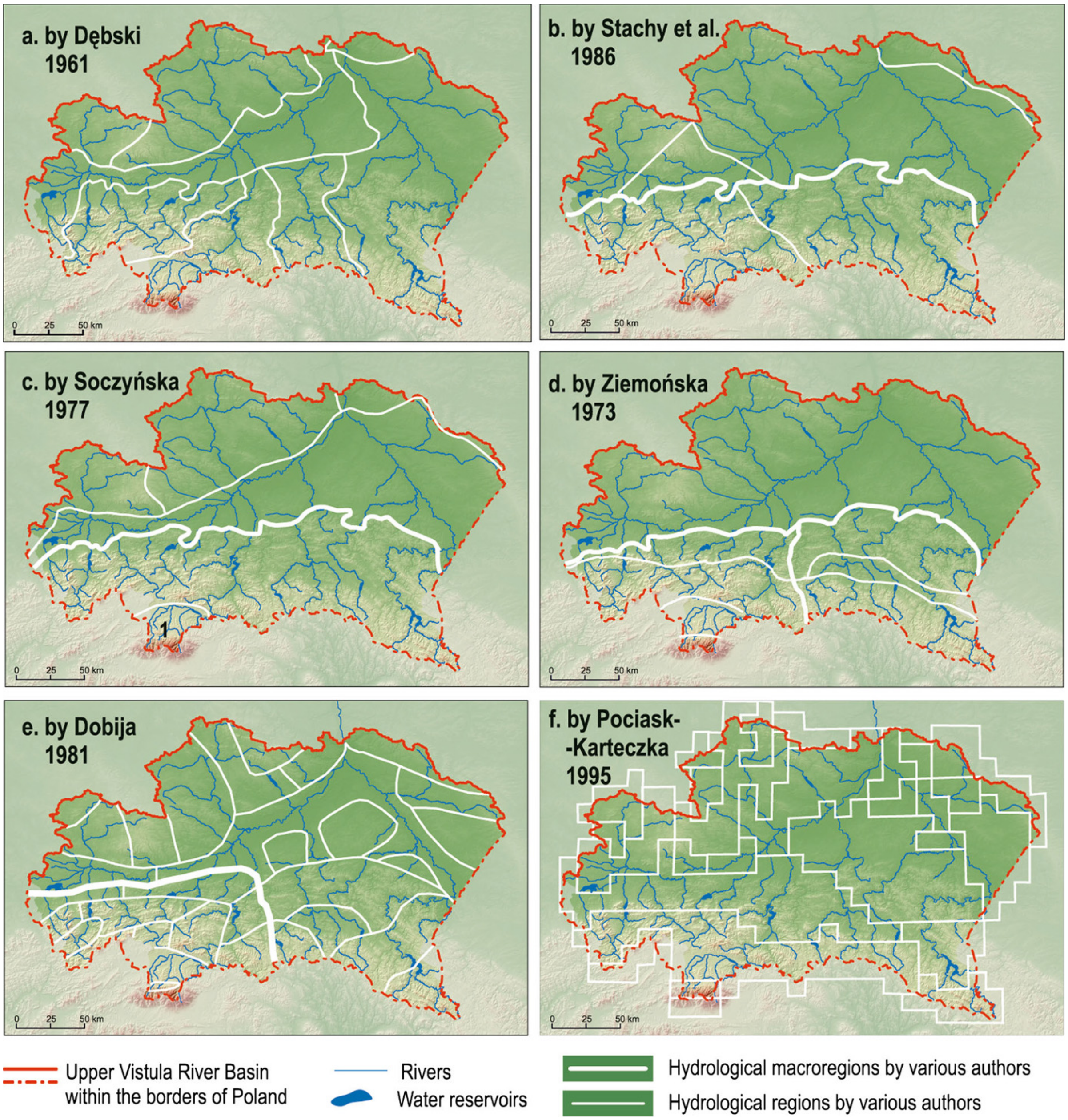

Figure 8
The hydrological classifications of the Upper Vistula River basin

western macroregion classified by Dobija (1981). However, no similarity was found between classifications of Ziemońska (1973); Pociask-Karteczka 1995) and the division obtained using the L-moment-based RFFA.

The comparison between the estimates of design discharges obtained using two regional approaches: the HW method and the method introduced by Stachý and Fal (1986) (SF method) was completed. The absolute relative differences for eight randomly selected catchments (9, 12, 24, 34, 38, 39, 40, 51) were computed as $R_T = \left|\frac{Q_T^{\mathrm{SF}} - Q_T^{\mathrm{HW}}}{Q_T^{\mathrm{HW}}}\right| \cdot 100\,\%$, $T = 10$, $T = 100$. Results show a relatively good agreement between Q_T^{SF} and Q_T^{HW}, because R_T varied from 4.4 % to 40.2 % for $T = 10$ and from 7.7 % to 31.9 % for $T = 100$.

Regarding regression formulas (9, 10, 11), the highest power at $P_{50\,\%}$ is observed in PG1A and the lowest in PG2; thus, rainfall has been shown to affect index flood more in PG1A and PG1 than in PG2. The negative sign of the power at IN in Eq. (11) is easy to interpret, because higher infiltration causes lower discharge. The direct physical explanation for why in Eq. (10) the sign is positive cannot be formulated. However, some calculations allowed us to notice that due to high power at $P_{50\,\%}$, equal to 2.66, and negative correlation between $P_{50\,\%}$ and IN ($\hat{r} = -0.29$), the increase of the index flood with increasing $P_{50\,\%}$ is stronger than the decrease of the index flood with decreasing IN. Thus, finally, only increase of the index flood is observed with decreasing IN in (11), similar to (10).

Among the three pooling groups, the best diagnostic measures, both for OLS and GLS, were obtained for PG1A. Thus, the extraction of PG1A from PG1 was certified.

6. *Conclusions*

The L-moment-based approach to regional flood frequency analysis of the UVB is presented in the paper. The application of the cluster analysis and HW methodology enabled the division of the study area into three (variant I) and four (variant II) pooling groups of catchments with similar frequency distributions. Design discharge was estimated using a regional growth curve and an index flood method for every studied catchment and was compared to discharge obtained via a local approach.

The results allowed the formulation of the conclusion that the HW method was proved as suitable for estimating the design discharges in most of the gauged catchments considered. The size of every pooling group was a trade-off; small groups provided design discharge of a not very long return period and lower uncertainty, and large groups supplied design discharge of a long return period and higher uncertainty. The division of the UVB into homogenous pooling groups was not unique, as the HW method provided many homogenous groups of various sizes and locations; therefore, an optimisation condition was introduced for final division into pooling groups. The slope, shape, river network density, and rainfall were revealed to have the greatest effect on the growth factor q, and rainfall, area, elevation, and infiltration had the greatest effect on index floods.

The multivariate regression model based on the OLS method was featured by a good quality for three major pooling groups. The GLS model improved the quality of the OLS model for the southern pooling groups PG1 and PG1A, while for the central group PG2, no improvement was obtained.

The design discharges obtained both for gauged and ungauged catchments using this RFFA method should be compared to design discharges obtained using other methods such as the SF method and the Punzet formula. This comparison will require a separate study.

The results of the study may be treated as a starting point for the regionalisation of other parts of the Vistula River Basin. In the future, other methods of RFFA will also be recommended, to compare the results produced by various methods of regionalisation.

Acknowledgments

The authors wish to thank the reviewers for their helpful comments, which assisted in the overall improvement of the paper. We also thank the native speakers Mr. Grzegorz Zębik and Ms. Madeline Olszak for linguistic support. This research was partially supported by the Ministry of Science and Higher Education of the Republic of Poland. The investigation described in the contribution was also partially financed by the Slovak Grant Agency under VEGA Projects Nos. 1/0776/13 and 1/0710/15.

REFERENCES

ADAMOWSKI, K. (2000), *Regional analysis of annual maximum and partial duration flood data by nonparametric and L-moment methods*, J. Hydrol. *229*, 219–231.

AKAIKE, H. (1974), *A new look at the statistical model identification*, IEEE T. Automat. Contr. *19*(6), 716–723. doi:10.1109/TAC.1974.1100705.

Aziz, K., Rahman, A., Fang, G., and Shrestha, S. (2014), *Application of artificial neural networks in regional flood frequency analysis : a case study for Australia*, Stoch. Env. Res. Risk A. *28*(3), 541–554. doi:10.1007/s00477-013-0771-5

Brath, A., Castellarin, A., Franchini, M., and Galeati, G. (2001), *Estimating the index flood using indirect methods*, Hydrolog. Sci. J. *46*(3), 399–418.

Bryndal, T. (2011), *The identification of small drainage basins prone to flash-flood creation (as exemplified by the Dynów, Strzyżów and Przemyśl foothill areas*, Przegląd Geograficzny. *83*, 27–49. (In Polish)

Burn, D.H., and Goel, N.K. (2000), *The formation of groups for regional flood frequency analysis*, Hydrolog. Sci. J. *45*, 97–112.

Castellarin, A., Burn, D.H., and Brath A. (2001), *Assessing the effectiveness of hydrological similarity measures for flood frequency analysis*, J. Hydrol. *241*, 270–285.

Castellarin, A., Kohnová, S., Gaál, L. Fleig, A., Salinas, J.L., Toumazis, A., Kjeldsen, T.R., and Macdonald, N. (2012), Review of Applied Statistical Methods For Flood-Frequency Analysis in Europe (Centre for Ecology & Hydrology on behalf of COST, ISBN: 978-1-906698-32-4), 122 pp.

Castellarin, A., Galeati, G. Brandimarte, L., Montanari, A., and Brath, A. (2004), *Regional flow-duration curves: reliability for ungauged basins*, Adv. Water Resour. *27*, 953965.

Chasalow, S. (2012), combinat: combinatorics utilities. R package version 0.0-8. https://CRAN.R-project.org/package=combinat

Cunnane, C. (1988), *Methods and merits of regional flood frequency analysis*, J. Hydrol. *100*(1–3), 269–290.

Dalrymple, T. (1960), Flood Frequency Analyses, Water Supply Paper 1543-A, U.S. Geological Survey, Reston, Va.

Dębski, K., Hydrologic characteristic of Poland (PWN, Warszawa, 1961), 159 pp. (In Polish)

Dobija, A. (1981), *Seasonal variability of the runoff in the Upper Vistula river basin (up to the Zawichost gauging station)*, Zesz. Nauk. UJ, Prace Geogr., *53*: 51–112.

Dynowska I., and Pociask-Karteczka J., (1999) Water circulation, in: L. Starkel (Ed.), Geography of Poland—the natural environment, PWN Scientific Publishing, Warsaw, 343–373. (In Polish)

Efron, B., and Tibshirani, R.J., (1993) An introduction to the bootstrap (New York: Chapman & Hall).

FEH: Flood Estimation Handbook. Vol. 1–5. (Institute of Hydrology, Wallingford, 1999).

Gaál, L., Lapin, M., Szolgay, J., and Faško, P. (2009), *Hybrid approach to delineation of homogeneous regions for regional precipitation frequency analysis*, J. Hydrol. Hydromechan., *57*, 226–249. doi:10.2478/v10098-009-0021-1.

Gaál, L., Kohnová, S., and Szolgay, J. (2013), Regional flood frequency analysis in Slovakia: Which pooling approach suits better? In Comprehensive Flood Risk Management: Research for policy and practice, 27–30.

Greenwood J.A., Landwehr J.M., Matalas N.C., and Wallis J.R. (1979), *Probability Weighted Moments: Definition and Relation to Parameters of Several Distribution Expresible in Inverse Form*, Wat. Resour. Res. *15*(5), 1049–1054.

Griffis, V.W., and Stedinger, J. R. (2007), *The use of GLS regression in regional hydrologic analyses*, Journal of Hydrology (2007) *344*, 82–95. doi:10.1016/j.jhydrol.2007.06.023

Haddad, K., Rahman, A., and Green, J. (2010), *Design rainfall estimation in Australia: A case study using L moments and Generalized Least Squares Regression*, Stoch. Env. Res. Risk A. *25*(6), 815–825.

Hosking, J.R., and Wallis, J.R., Regional Frequency Analysis. An Approach Based on L-moments, (Cambridge University Press, Cambridge, 1997).

Hosking, J.R. (2013), Regional frequency analysis using L-moments. R package, version 2.5. https://CRAN.R-project.org/package=lmomRFA.

Ishak, E. H., Haddad, K., Zaman, M., and Rahman, A. (2011), *Scaling property of regional floods in New South Wales, Australia*, Nat. Hazards *58*(3), 1155–1167. doi:10.1007/s11069-011-9719-6.

ISOK Topographic Object Database, http://www.isok.gov.pl/en/topographic-objects-database-bdot, accessed Feb 20, 2014

Jain, A.K., and Dubes, R.C., Algorithms for Clustering Data. Prentice Hall Advanced Reference Series (Prentice Hall, New Jersey 1988).

Jakob, D., Reed, D.W., and Robson, A.J., Choosing a pooling-group. Flood Estimation Handbook, vol. 3. (Institute of Hydrology, Wallingford, 1999).

Johnston, J., Econometric Methods, (McGraw-Hill, New York,1984).

Kaczmarek, Z., and Trykozko, E. (1964) *Application of the method of quantiles to estimation of the Pearson distribution*. Acta Geoph. Pol. *XII*(1):5–12.

Kaufman, L., and Rousseeuw, P.J., Finding groups in data. An introduction to cluster analysis. (Wiley Series in Probability and Statistics, New York, 2005).

Kjeldsen, T. R., and D. A. Jones (2009), *An exploratory analysis of error components in hydrological regression modeling*, Water Resour. Res., *45*, W02407, doi:10.1029/2007WR006283.

Kjeldsen, T. R., and Prosdocimi, I (2015), *A bivariate extension of the Hosking and Wallis goodness-of-fit measure for regional distributions*, Water Resour. Res., *51*(2), 896–907.

Kochanek, K., Strupczewski, W.G., Singh, V.P., and Węglarczyk S. (2008), *The PWM large quantile estimates of heavy tailed distributions from samples deprived of their largest element, Estimation des grands quantiles de distributions queue dcroissance lente par la mthode des moments pondrs par les probabilits partir d'chantillons amputs de leur plus grande valeur*, Hydrological Sciences Journal, *53*:2, 367–386,doi:10.1623/hysj.53.2.367.

Kochanek, K., Strupczewski, W.G., and Bogdanowicz, E. (2012), *On seasonal approach to flood frequency modelling. Part II: flood frequency analysis of Polish rivers*, Hydrol. Process. *26*, 717–730.

Kohnová, S., Szolgay, J., Solin, L., and Hlavčová, K. (2006), Regional Methods for Prediction in Ungauged Basins. Case Studies. (KEY Publishing, Ostrava-Přívoz, 2006).

Kondracki, J. Regional Geography of Poland (2014), PWN, Warszawa, 444 pp. (In Polish)

Kroll, C.N., and Stedinger, J.R. (1998), *Regional hydrologic analysis: Ordinary and generalized least squares revisited.* Water Resources Research *34*(1), 121–128. doi:10.1029/97WR02685.

Landwehr, J.M., Matalas, N.C., and Wallis, J.R. (1979), *Probability weighted moments compared with some traditional techniques in estimating Gumbel parameters and quantiles*. Wat. Resour. Res. *15*, 1055–1064.

Lu, L.H., and Stedinger, J. R. (1992), *Sampling variance of normalized GEV/PWM quantile estimators and a regional homogeneity test*. J. Hydrol. *138*, 223–245.

Madsen, H., Mikkelsen, P.S., Rosbjerg, D., and Harremos, P. (1998), *Estimation of regional intensity-duration-frequency curves for extreme precipitation*. Water Sci. Technol. *37*(11), 29–36.

KZGW, Map of Hydrological Division of Poland in scale 1:10000. (2010)

McCuen, R.H. Modeling Hydrologic Change. (Lewis Publishers, Boca Raton Florida, 2003).

Mediero, L., and Kjeldsen, T. R. (2014), *Regional flood hydrology in a semi-arid catchment using a GLS regression model*. Journal of Hydrology, *514*, 158–171. doi:10.1016/j.jhydrol.2014.04.007

Merz, R., and Blöschl, G. (2005), *Flood frequency regionalization—spatial proximity vs. catchment attributes*, J. Hydrol. *302*(1–4), 283–306.

Miziński, B., Niedzielski, T., Kryza, M., and Szymanowski, M. (2013), Automatic removal of outliers in hydrologic time series and quality control of rainfall data: processing a real-time database of the Local System for Flood Monitoring in Klodzko County, Poland, EGU General Assembly 2013, held 7–12 April, Vienna, Austria, id. EGU2013-12579.

Montgomery, D. C., and Peck, E. A., Introduction to Linear Regression Analysis, Second Edition, (Wiley, New York, 1992).

Moran, P.A.P. (1950), *Notes on continuous stochastic phenomena*, Biometrika *37*.

Noto, L.V., and La Loggia, G. (2009), *Use of L-moments Approach for Regional Flood Frequency Analysis in Sicily, Italy*, Water Resour. Manag. *23*, 2207–2229.

Ouarda, T.B.M.J., Girard, C., Cavadias, G.S., and Bobée, B. (2001), *Regional flood frequency estimation with canonical correlation analysis*, J. Hydrol. *254*, 157–173.

Pociask-Karteczka J. (1995), Principles of hydrologic regionalization on example of the Upper Vistula Basin, Habilitation Dissertation 291, Jagiellonian University, Kraków), 95 pp. (In Polish)

Punzet, J. (1978), Water resources of the upper Vistula river basin. Maximum water discharge, their spatial variability and occurrence probability. IMGW-PIB, Warszawa, 138 pp. (In Polish)

Punzet, J. (1991), Characteristic flows, In: Upper Vistula River Basin, part I (eds: Dynowska, Maciejewski). PWN, Warszawa-Kraków) 167–215. (In Polish)

R Core Team (2013), R: A language and environment for statistical computing. (R Foundation for Statistical Computing, Vienna, Austria, https://www.r-project.org)

Reed, D. W., Jakob, D., Robinson, A.,J., Faulkner, D. S., and Stewart, E. J. (1999) *Regional frequency analysis: a new vocabulary, Hydrological Extremes: Understanding, Predicting, Mitigating*, Proc. IUGG 99 Symposium, Birmingham, IAHS Publ. *255*, 237–243.

Rossi, F., and Villani, P. (1994), Regional Flood Estimation Methods, University of Salerno, Proc. Coping with Floods, Ed. G. Rossi et al. Kluwer Academic Publishers, pp. 135–169.

Salinas, J.L., Castellarin, A., Viglione, A., Kohnová, S., and Kjeldsen, T.R. (2014) *Regional parent flood frequency distributions in Europe—Part 1: Is the GEV model suitable as a pan-European parent?* Hydrol. and Earth Syst. Sci., *18*, 43814389. doi:10.5194/hess-18-4381-2014

Salinas, J.L., Castellarin, A., Kohnová, S., and Kjeldsen, T.R. (2014) *Regional parent flood frequency distributions in Europe—Part 2: Climate and scale controls*, Hydrol. and Earth Syst. Sci., *18*, 43914401. doi:10.5194/hess-18-4391-2014

Sahinler, S., and Topuz, D. (2007), *Bootstrap and jackknife resampling algorithms for estimation of regression parameters*, J. of Applied Quantitative Methods, *2*(2), 188–199.

Setmajer J., Skarżyńska K., Michalski P., and Burda H. (1971) Mapping study of the coefficient of soil impermeability index of the left bank of the Upper Vistula River Basin, Wyższa Szkoła Rolnicza w Krakowie, Instytut Budownictwa Wodnego i Ziemnego, 15 pp.(In Polish)

Shapiro, S. S., and Wilk, M. B. (1965), *An analysis of variance test for normality (complete samples)*, Biometrika, *52*(34), 591611.

Soczyńska, U. (1977), Methodological principles of a regional catchment model in polish conditions, Materiały Badawcze—Instytut Meteorologii i Gospodarki Wodnej. Seria: Hydrologia, IMiGW, Warszawa, 128 pp. (In Polish)

Stachy, J. (1966), *Distribution of the mean runoff in Poland (Rozmieszczenie odpywu średniego na obszarze Polski)*, Prace PIHM, *88*:3–42. (In Polish)

Stachy J., and Fal B. (1986), *Rules for derivations of Flood Frequency (Zasady obliczania maskymalnych przepyww prawdopodobnych)*, Prace Instytutu Badawczego Dróg i Mostów, *3–4*: 91–147. (In Polish)

Stedinger, J. R., and Tasker, G. D. (1985), *Regional Hydrologic Analysis: 1. Ordinary, Weighted, and Generalized Least Squares Compared*, Water Resour. Res., *21*(9), 1421–1432.

Stedinger, J. R., Vogel, R.M., and Foufoula-Georgiou, E., Frequency analysis of extreme events. In: Handbook of Hydrology, (ed. by D. R. Maidment) (McGraw-Hill, New York, 1993) p. 18.1–18.66.

Strupczewski, W.G., Kochanek, K. Bogdanowicz, E., and Markiewicz, I. (2012), *On seasonal approach to flood frequency modelling. Part I: Two-component distribution revisited*, Hydrol. Process. *26*, 705–716.

Taylor, M., Haddad, M., Zaman, M., and Rahman, A. (2011), Regional flood modelling in Western Australia: Application of regression based methods using ordinary least squares, 19th International Congress on Modelling and Simulation, Perth, Australia, 12–16 December 2011.

Tasker, G. D., and Stedinger, J. R., (1989) *An operational GLS model for hydrologic regression*, J. Hydrol., *111*, 361–375.

Vogel, R.M., and Fennessey, N.M. (1993), *L-Moment diagrams should replace product moment diagrams*, Wat. Resour. Res. *29*(6), 1745–1752.

Waięga, A., Krzanowski, S., and Chmielowski K. (2009), *Method of cluster analysis in identification of homogenous catchments, considering flood indexes and selected physiographic characteristics)*, Infrastruktura i Ekologia Terenów Wiejskich, *6*, 67–81. (In Polish).

Ward, J.H. (1963), *Hierarchical grouping to optimize an objective function*, J. Am. Stat. Assoc. *58*(301), 236–244.

Wang, Q.J. (1997), *LH moments for statistical analysis of extreme events*, Water Resour. Res. *33*, 2841–2848.

Wiesberg, S. (1985), Applied linear regression. 2nd ed.. New York: John Wiley.

Yang T., Xu, C-Y., Shao Q-X., and Chen, X. (2010), *Regional flood frequency and spatial patterns analysis in the Pearl River*

Delta region using L-moments approach, Stoch. Env. Res. Risk A. *24*, 165–182.

Viglione, A. (2014), nsRFA: Non-supervised Regional Frequency Analysis. R package version 0.7-12. http://CRAN.R-project.org/package=nsRFA

Ziemońska Z. (1973), *Hydrographic conditions in the Polish West Carpathians*, Prace Geograficzne—Polska Akademia Nauk, *103*, 126 pp. (In Polish)

(Received December 2, 2014, revised February 9, 2016, accepted April 12, 2016, Published online May 5, 2016)

Pure Appl. Geophys. 174 (2017), 723–736

DOI 10.1007/s00024-016-1309-9

Pure and Applied Geophysics

GNSS Vertical Coordinate Time Series Analysis Using Single-Channel Independent Component Analysis Method

Wei Peng,[1] Wujiao Dai,[1] Rock Santerre,[2] Changsheng Cai,[1] and Cuilin Kuang[1]

Abstract—Daily vertical coordinate time series of Global Navigation Satellite System (GNSS) stations usually contains tectonic and non-tectonic deformation signals, residual atmospheric delay signals, measurement noise, etc. In geophysical studies, it is very important to separate various geophysical signals from the GNSS time series to truthfully reflect the effect of mass loadings on crustal deformation. Based on the independence of mass loadings, we combine the Ensemble Empirical Mode Decomposition (EEMD) with the Phase Space Reconstruction-based Independent Component Analysis (PSR-ICA) method to analyze the vertical time series of GNSS reference stations. In the simulation experiment, the seasonal non-tectonic signal is simulated by the sum of the correction of atmospheric mass loading and soil moisture mass loading. The simulated seasonal non-tectonic signal can be separated into two independent signals using the PSR-ICA method, which strongly correlated with atmospheric mass loading and soil moisture mass loading, respectively. Likewise, in the analysis of the vertical time series of GNSS reference stations of Crustal Movement Observation Network of China (CMONOC), similar results have been obtained using the combined EEMD and PSR-ICA method. All these results indicate that the EEMD and PSR-ICA method can effectively separate the independent atmospheric and soil moisture mass loading signals and illustrate the significant cause of the seasonal variation of GNSS vertical time series in the mainland of China.

Key words: Phase space reconstruction-based independent component analysis, ensemble empirical mode decomposition, mass loading, hurst parameter, GNSS vertical coordinate time series.

1. *Introduction*

GNSS technology has widely been applied in a variety of geophysical studies, and thousands of permanent GNSS stations have been established around the world for this purpose. Analyzing the time series of GNSS stations in the International Terrestrial Reference Frame (ITRF) provides useful information for the study of the global plate motion, crustal deformation, and earthquakes. All these studies are based on the correct interpretation of the coordinate time series as well as on reliable and accurate station coordinates and velocities. The GNSS coordinate time series mainly consists of tectonic deformation (e.g., Dragert *et al.* 2001; Jiang *et al.* 2014), non-tectonic deformation (e.g., Vandam *et al.* 1994; Tiampo *et al.* 2004), and noise (Williams *et al.* 2004). Analyzing the non-tectonic deformation signals by geometric and physical models is crucial in studying the impacts of various geophysical phenomena on GNSS reference stations. Nikolaidis (2002) applied a weighted least-square algorithm to solve the geometric model according to linear trend, annual, and semi-annual variations, and other characteristics of GNSS coordinate time series. Dong *et al.* (2002) investigated the effects of atmosphere, non-tidal ocean, snow, soil moisture, and other environmental factors on GNSS station displacements, and explained the main causes of the annual and semi-annual variations of GNSS time series. However, these geometrical model and physical model cannot directly extract mass loading signals (annual and semi-annual periods) from the GNSS time series. Therefore, a method separating the seasonal non-tectonic deformation signals from the GNSS vertical time series is in really needed.

The Independent Component Analysis (ICA) method is a blind source separation method, which can separate statistically independent source signals from multi-dimensional mixed observation signals (Hyvärinen and Oja 2000). If the geophysical phenomena are independent; then, the independent

---

[1] School of Geosciences and Info-Physics, Central South University, Changsha, China. E-mail: wjdai@csu.edu.cn

[2] Center for Research in Geomatics, Laval University, Quebec City, Canada.

component signals (ICs) decomposed by the ICA method will reflect their physical phenomena. The Phase Space Reconstruction-based Independent Component Analysis (PSR-ICA) method, a single-channel ICA method, can effectively separate the independent source signals, even though they are the same frequency (Dai *et al.* 2014). Therefore, in this study, we use the PSR-ICA method to analyze the seasonal variation of GNSS vertical coordinate time series. However, the vertical time series of a GNSS station is a non-stationary signal, and the PSR-ICA algorithm can only process stationary signal; therefore, we use an adaptive time–frequency decomposition method called Ensemble Empirical Mode Decomposition (EEMD) (Wu and Huang 2009), to process non-stationary GNSS vertical coordinate time series and extract the stationary seasonal signal.

2. *EEMD and PSR-ICA Methods*

The EEMD and PSR-ICA methods are jointly used to analyze the GNSS vertical time series based on their respective advantages. First, GNSS vertical time series is decomposed using the EEMD method, and then, the noise signal and seasonal signal are classified and reconstructed based on the Hurst parameter (Rodriguez *et al.* 2009). After that, the PSR-ICA method is used to decompose the reconstructed one-dimensional seasonal signal into several ICs that are then compared with non-tectonic crustal deformations caused by mass loadings. The data processing flow chart is shown in Fig. 1.

2.1. EEMD Decomposition and Extraction of the Seasonal Non-Tectonic Signal

The EEMD, as a modified EMD algorithm, which can be used to decompose a nonlinear and non-stationary time series $x(t)$ into several Intrinsic Mode Functions (IMFs) and the residual signal (Wu and Huang 2009; Huang *et al.* 1998). Then, the IMFs with different noise contents are classified and reconstructed based on the Hurst parameter. The general equation of the EEMD algorithm is given below:

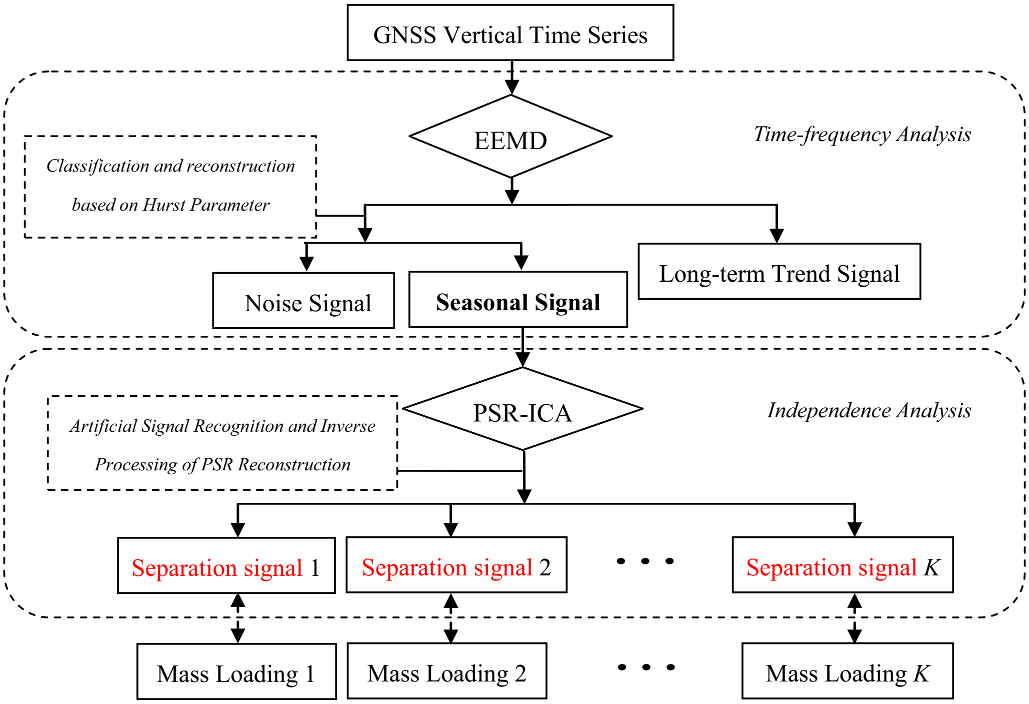

Figure 1
Flow chart of single-channel ICA data processing for the GNSS vertical time series analysis

$$x(t) = \sum_{j=1}^{D} \overline{c_j}(t) + r_D(t), t = 1, 2, \ldots, T \qquad (1)$$

where $\overline{c_j}(t)$ is the IMF component and $r_D(t)$ is the residual signal.

The IMFs of the EEMD algorithm can be divided into stationary and non-stationary parts. The non-stationary IMFs can be reconstructed as a long-term trend signal (Qin *et al.* 2012), and the stationary IMFs need to be analyzed by the Hurst parameter. Hurst parameter has been used to analyze noises in many studies (Montillet *et al.* 2013; Schroeder and Wiesenfeld 1991). The relation between Hurst parameter (H) and noise signal is that the white noise is corresponding to $H = 0.5$, the flick noise is corresponding to $H = 1$ and the random walk is corresponding to $H = 1.5$.

The noise in the GNSS time series can be analyzed usually after removing the linear trend and seasonal variation. However, the EEMD method can decompose the noise, without removing the linear trend and seasonal variation, into a series of IMFs ordered by frequency, and these IMFs can be classified using the Hurst parameter. For example, Montillet *et al.* (2013) used the EMD method and the Hurst parameter to extract the white noise ($H \leq 0.6$) of the GNSS vertical time series. Furthermore, several studies suggest that the best noise model of most GNSS vertical time series is the white plus flicker noise model (WN + FN) (Li *et al.* 2012; Zhang *et al.* 1997; Mao *et al.* 1999; Amiri-Simkooei *et al.* 2007). Therefore, we define the IMFs whose H is within $[0.6, 1.1)$ as colored noise, which can be best characterized by the WN + FN model.

The procedure of the time–frequency analysis can be described as follows.

1. Decompose time series $x(t)$ into IMFs and residual signal.
2. Extract the non-stationary IMFs and the residual signal, and reconstruct them to long-term trend signal.
3. Estimate the Hurst parameter of each stationary IMFs. Sum over the IMFs whose H are within $[0, 1.1]$ as noise signal, and sum over the remaining IMFs as one-dimensional seasonal signal $x'(t)$.

However, the EEMD method cannot decompose components in the same frequency; therefore, the one-dimensional seasonal signal should be analyzed by the single-channel ICA method.

2.2. Seasonal Non-Tectonic Signal Analysis by PSR-ICA Algorithm

PSR-ICA algorithm is a one-dimensional stationary signal processing method (Dai *et al.* 2014, Packard *et al.* 1980; Takens 1981), which does not rely on the time–frequency feature of the components. Therefore, it can separate ICs from the one-dimensional seasonal signals to reflect the effect of the seasonal mass loadings. The procedure of the PSR-ICA algorithm is shown in Fig. 2.

In this flow chart, x' is the one-dimensional seasonal signal; X is the reconstruction phase space; $Y = WX$ is to obtain the ICs from the reconstruction phase space; X^K is the Kth independent subspace; x^K is the reconstructed one-dimensional seasonal signal.

2.2.1 Channel Extension

Phase Space Reconstruction (PSR) is a method of obtaining nonlinear dynamics features through delaying and embedding a one-dimensional signal into a high-dimensional phase space to reflect the characteristics of the signals (Kennel *et al.* 1992). The multi-dimensional phase space contains all signals of physical sources, affecting the seasonal non-tectonic deformation of GNSS stations.

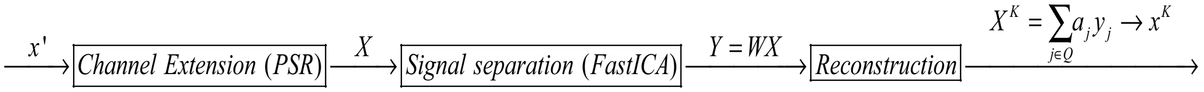

Figure 2
Flow chart of PSR-ICA processing for the seasonal signal analysis

$$X_i = \left\{x_i', x_i'(1+\tau), \cdots, x_i'(1+(m-1)\tau)\right\},\quad i = 1, 2, \cdots, M \tag{2}$$

where $M = T-(m-1)\tau$, m is the embedding dimension, τ is the delay time. m, and τ are the main parameters of the PSR algorithm, whose optimal solution can be obtained using the False Nearest Neighbors method and the Mutual Information method, respectively (Dai *et al.* 2014; Kennel *et al.* 1992; Fraser and Swinney 1986).

2.2.2 Independent Component Signal Separation

Assume a set of independent source signals $S(t')$: $S(t') = [s_1(t'), s_2(t'), \cdots, s_n(t')]^{\mathrm{T}}$ and their corresponding observation signals $X(t')$: $X(t') = [x_1(t'), x_2(t'), \cdots, x_{\mathrm{m}}(t')]^{\mathrm{T}}$, the relationship between $X(t')$ and $S(t')$ can be described as follows (Hyvärinen and Oja 2000):

$$X(t') = AS(t'), t' = 1, 2, \ldots, M \tag{3}$$

where A is $m \times n$-order unknown linear mixed matrix ($n \leq m$).

ICA algorithm is to separate the ICs by solving the mixed matrix W.

$$Y(t') = A^{-1}X(t') = WX(t') \tag{4}$$

ICs $Y(t')$ can be used to estimate $S(t')$ effectively. FastICA algorithm, a widely used ICA algorithm, is used to separate ICs from $WX(t')$ in this study. FastICA algorithm uses the Negentropy, a measure standard of non-Gaussian distribution, to measure the non-Gaussian maximum of $WX(t')$, and it follows the fixed-point iteration theory, which makes the convergence faster and more robust (Hyvärinen 1999).

2.2.3 Independent Component Signals Reconstruction

These ICs $Y(t')$ can reflect the implicit information of the observation signals. However, sometimes, the number of ICs are more than the seasonal mass loadings. Therefore, the ICs should be artificially classified into several clusters. Then, the ICs of the same cluster, corresponding to the same mass loading, are multiplied by their corresponding column of the mixed matrix to construct independent subspaces X^K for reconstructing the source signal x^K (Cardoso 1998). Therefore, the original multi-dimensional phase space is equal to the sum of independent subspaces.

$$X = X^1 + X^2 + \cdots + X^K \tag{5}$$

where X^K is the Kth independent subspace, and it can be described as follows:

$$X^K = \sum_{j \in Q} a_j y_j \tag{6}$$

where Q is the number of ICs in a cluster, and a_j is the corresponding column of the mixed matrix to the y_j, where y_j is the j th IC. The independent subspaces X^K can be reconstructed to a one-dimensional source signal x^K based on the inversion of the PSR method,

$$x_i^K = \begin{cases} \frac{1}{A}\sum\limits_{h=1}^{A} X^K_{j,i-(j-1)\tau} & 1 \leq i \leq 1+(m-1)\tau \\ \frac{1}{m}\sum\limits_{h=1}^{m} X^K_{j,i-(j-1)\tau} & 1+(m-1)\tau \leq i \leq T-(m-1)\tau \\ \frac{1}{B}\sum\limits_{h=m+1-B}^{m} X^K_{j,i-(j-1)\tau} & T-(m-1)\tau \leq i \leq T \end{cases} \tag{7}$$

where $A = ceil(i/\tau)$, $B = ceil((N-i+1)/\tau)$, and $ceil(\cdot)$ denotes the rounding-up function.

3. GNSS Vertical Time Series Analysis

3.1. Analysis of Observation Data and Mass Loadings

The seasonal non-tectonic deformation of GNSS reference station mainly includes the mass loading of atmosphere, soil moisture, non-tidal ocean, snow, etc. However, in most parts of China, the non-tidal ocean mass loading and snow mass loading had a little or no impact on crustal deformation, and they can be neglected. Thus, the effect of atmosphere and soil moisture mass loading are the major factors in the analysis of the seasonal non-tectonic deformation (Wang *et al.* 2005).

To explore the single-channel ICA process and its effect on separating non-tectonic deformation, we use the daily vertical time series of GNSS reference stations collected by the CMONOC. These daily GNSS solutions are generated using the GAMIT/GLOBK software with the double-difference ionosphere-free code and phase observations. Meanwhile, the station receiver antenna phase center, satellite antenna phase center, ocean tides, solid earth pole tides, and solid earth tides are corrected with the absolute phase center model, IGS ANTEX model, FES2004 ocean tide loading model, and IERS2003 model, respectively. The tropospheric delay and satellite coordinates are estimated with the station coordinates during the daily data processing, and then, each daily solutions are transformed into IGS08 using seven-parameter transformations. The data, consisting of 13 GNSS reference stations in the area from 90°E 15°N to 120°E 42°N (see Fig. 3), cover a time span from January 2001 to December 2013.

The vertical time series of those 13 GNSS stations with strong noise is manifested as non-stationary annual variation. To explore the data sets, we randomly choose three GNSS reference stations (BJFS, JIXN, and LUZH) as proxies to demonstrate the process of our methods and its results in detail. Figure 4 shows the vertical displacement time series of BJFS, JIXN, and LUZH sites for a time interval of 13 years.

To illustrate the non-tectonic deformation in the selected area, we calculate the correction values of atmospheric and soil moisture mass loadings of the 13 sites, using the 6-hour sampling atmosphere surface pressure data and the daily sampling National Center for Environmental Prediction (NCEP) reanalysis II soil moisture data from 2001 to 2013. The corrections of mass loadings are calculated using the Quasi-Observation Combination Analysis software (QOCA) (available at http://qoca.jpl.nasa.gov). Results are shown in Fig. 5 for the three selected sites.

After removing the linear trend of GNSS vertical time series using the linear fitting method, the power

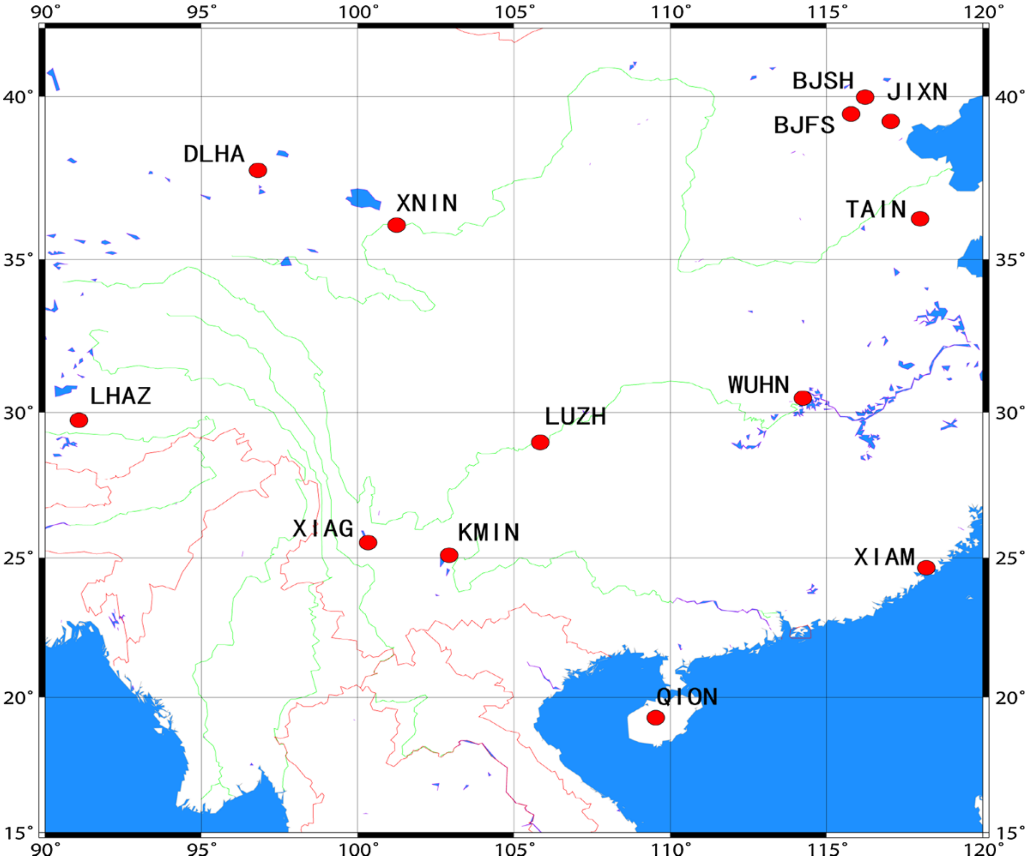

Figure 3
Distribution of the selected CMONOC GNSS stations

spectrum is used to analyze the changes of the seasonal variation of GNSS vertical time series before and after removing the correction values of atmospheric and soil moisture mass loading, as shown in Fig. 6. After the correction, the annual variation of residual time series is significantly weakened, indicating that the correction can effectively reduce the annual variation in the GNSS vertical time series. However, the mass loading corrections cannot completely eliminate the annual variation in the GNSS reference stations. Therefore, decomposing the GNSS vertical time series into several sub-signals (relating to the main mass loadings) is an important way to illustrate the annual variation in the GNSS vertical time series.

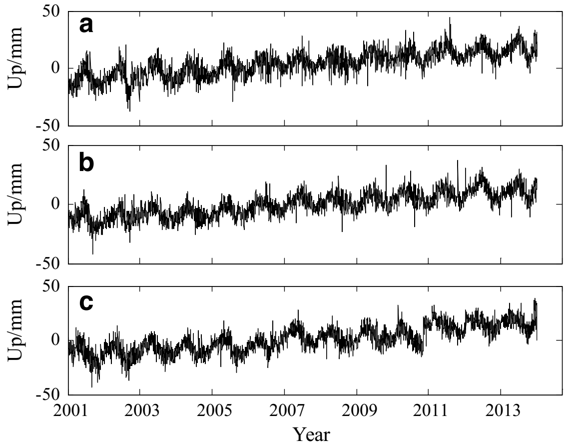

Figure 4
Vertical time series of GNSS reference stations (**a**) BJFS, (**b**) JIXN, and (**c**) LUZH

3.2. *EEMD Decomposition and Reconstruction*

The EEMD method is used to decompose the vertical time series into IMF components and residual signal. The *H* values of IMFs are calculated by the Detrended Fluctuation Analysis method (Grech and Mazur 2013). As the calculation error can be up to 0.1, the IMFs whose *H* values are within [0, 1.1] are reconstructed as noise signal. The noise, the artificial reconstructed seasonal signal, and the long-term trend of BJFS, JIXN, and LUZH sites are shown in Fig. 7.

The EEMD method is also used to de-noise the sum of atmospheric mass loading and soil moisture mass loading. The comparison between the reconstructed seasonal signal and the sum of the de-noised atmospheric and soil moisture mass loadings of the 13 GNSS sites are shown in Fig. 8.

The correlation coefficients, RMS (Root Mean Square) between the seasonal signals, and the sum of the corrections of de-noised seasonal mass loadings (atmospheric mass loading and de-noised soil moisture mass loading) are calculated, and their values for the 13 GNSS stations are shown in Table 1.

The correlation coefficients of the seasonal signals and the de-noised sum of atmospheric mass loading

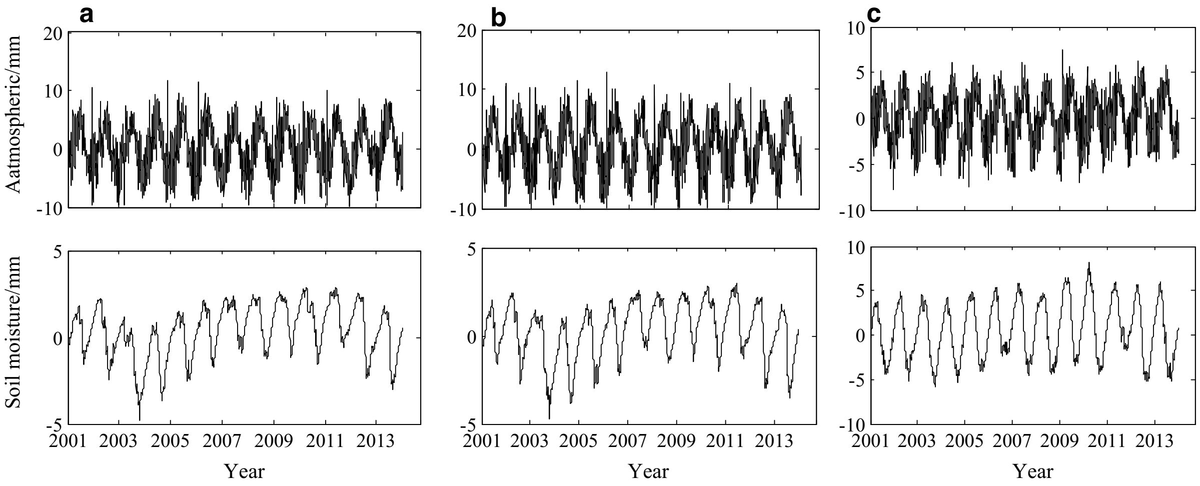

Figure 5
Correction values of atmospheric mass loading and soil moisture mass loading (**a**) BJFS, (**b**) JIXN, and (**c**) LUZH

and soil moisture mass loading are 0.61–0.86, and ΔRMS are 18–48 %. These results are reasonable, including the low correlation of WUHN, XNIN, KMIN, and XIAM sites (in bold), because the mass loading correction cannot completely reflect the seasonal variation of GNSS vertical time series (see Fig. 6).

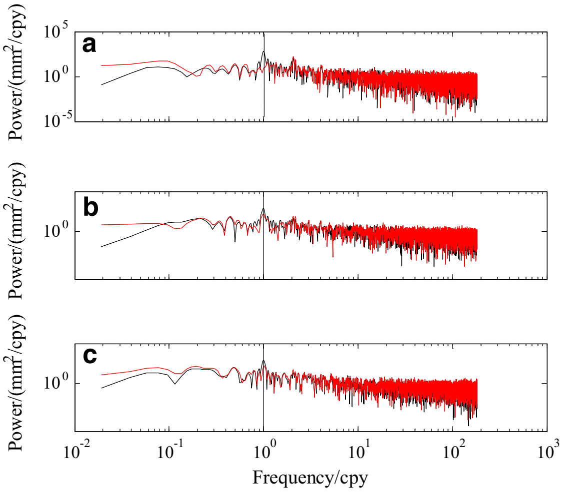

Figure 6
Power spectrum of GNSS vertical time series before (*black line*) and after (*red line*) removing the atmospheric loading and soil moisture loading **a** BJFS, **b** JIXN, and **c** LUZH

From the comparison in Fig. 8 and correlation analysis in Table 1, we can say that there is a strong correlation between the GNSS station annual variation and the two mass loadings in the selected area.

3.3. *Simulation Experiment*

We mixed the de-noised correction of the atmosphere and soil moisture mass loading (red line in Fig. 8) as the simulated non-tectonic deformation signals. First, the PSR method is applied to obtain the multi-dimensional embedding matrix, and the time delay is 8 and the embedding dimension is 2. Then, the FastICA method is used to analyze the multi-dimensional embedding matrix, and the two ICs are obtained. We rename them as Reconstructed signal A (RS-A) and Reconstructed signal B (RS-B) without artificial classification and reconstruction. The comparison of reconstructed signals and its corresponding simulated signals (de-noised atmospheric and soil moisture mass loading) are shown in Figs. 9 and 10, respectively.

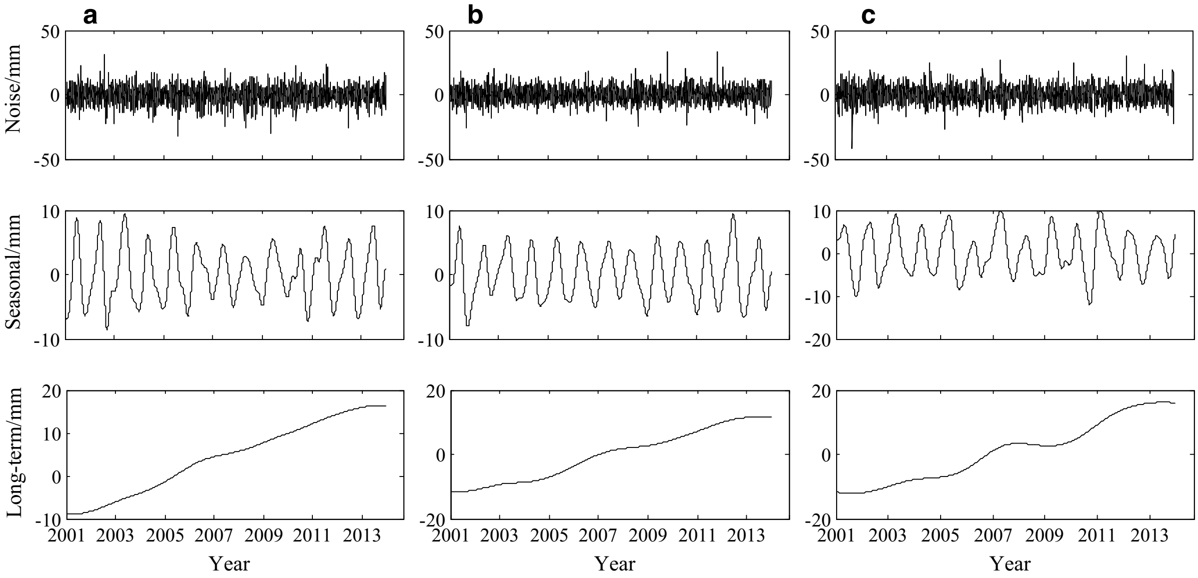

Figure 7
The reconstructed noise, seasonal signal, and long-term trend signal **a** BJFS, **b** JIXN, **c** LUZH

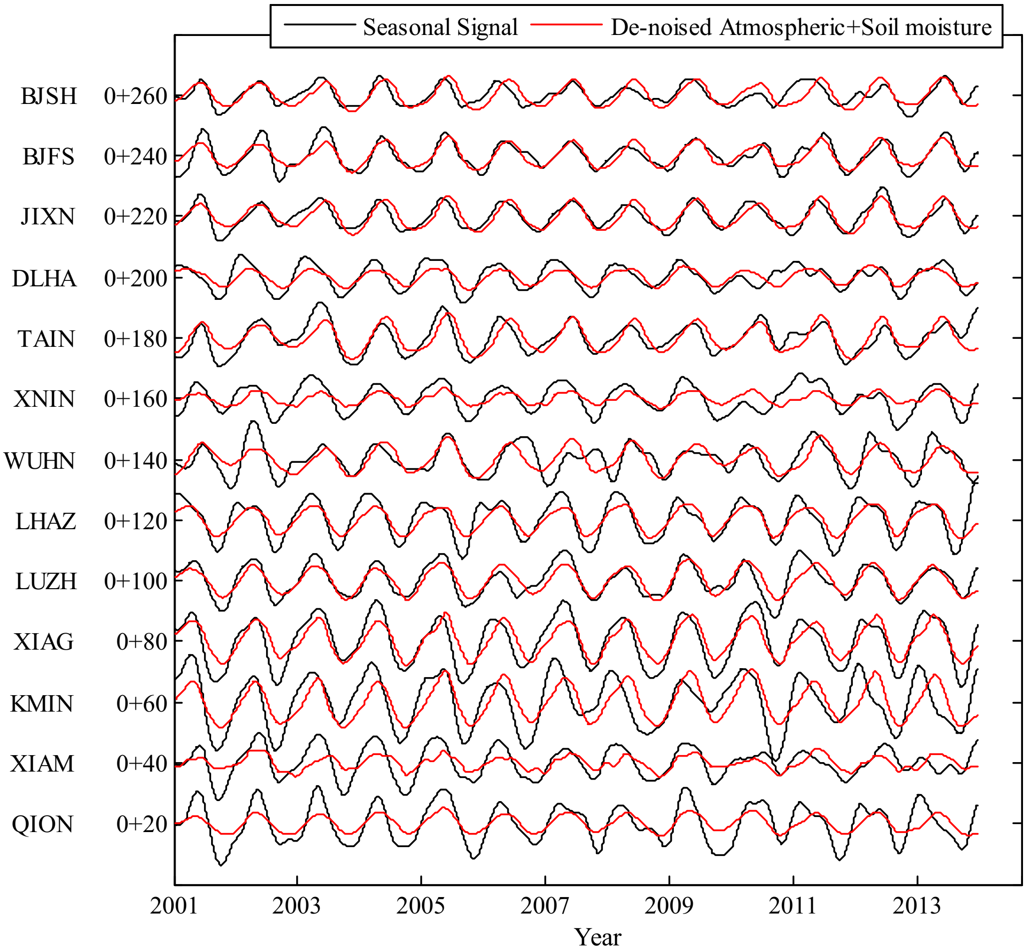

Figure 8
Comparison between the reconstructed seasonal signals decomposed by EEMD and the sum of the de-noised atmosphere and soil moisture mass loading for the 13 GNSS sites (20 mm offset per station)

The correlation coefficients and RMS between reconstructed signals and their corresponding simulation signals are calculated, respectively, and their values are shown in Table 2.

The simulation experiment shows that the signals reconstructed by the PSR-ICA method can effectively reflect the atmospheric and the soil moisture mass loading. The correlation coefficients of the RS-A and the atmospheric mass loading are 0.81–0.96, and the ΔRMS are 11–71 %. In addition, the values of the RS-B and the soil moisture mass loading are 0.71–0.98 and 14–77 %, respectively. These facts suggest that the atmospheric and the soil moisture mass loadings can be separated by single-channel ICA.

3.4. GNSS Vertical Time Series Analysis

The seasonal variation of GNSS vertical time series (black line in Fig. 8) is also used to verify the effectiveness of the PSR-ICA method.

First, the time delay and the embedding dimension are calculated using the mutual information method and the FNN method, respectively. The determined time delay is 51, which is quite different from that of the simulation experiment. A possible explanation could be the difference between seasonal signal and mass loading corrections. The embedding dimension is 2 in most cases, and 3 for the KMIN site, which indicates that the ICs should be reconstructed into two main components.

Table 1

Correlation between seasonal signals and sum of the de-noised atmospheric and soil moisture mass loading

	Latitude N (°)	Longitude E (°)	Correlation coefficients	RMS (mm)	dRMS (mm)	ΔRMS (%)
BJSH	40.25	116.22	0.72	3.1	2.5	19
BJFS	39.61	115.89	0.86	4.2	2.2	48
JIXN	38.58	117.53	0.85	3.8	2.1	45
DLHA	37.38	97.38	0.77	4.0	2.7	33
TAIN	36.22	117.12	0.75	4.7	3.2	32
XNIN	36.60	101.77	**0.61**	4.5	3.7	**18**
WUHN	30.53	114.36	**0.71**	4.9	3.5	**29**
LHAZ	29.66	91.10	0.84	6.1	3.7	39
LUZH	28.87	105.41	0.84	5.1	2.8	45
XIAG	25.61	100.26	0.85	7.6	4.2	45
KMIN	25.03	102.80	**0.64**	8.2	6.2	**24**
XIAM	24.45	118.08	**0.63**	4.9	3.9	**20**
QION	19.03	109.85	0.79	6.3	4.6	27

dRMS RMS after mass loading correction, *ΔRMS* reduction in RMS

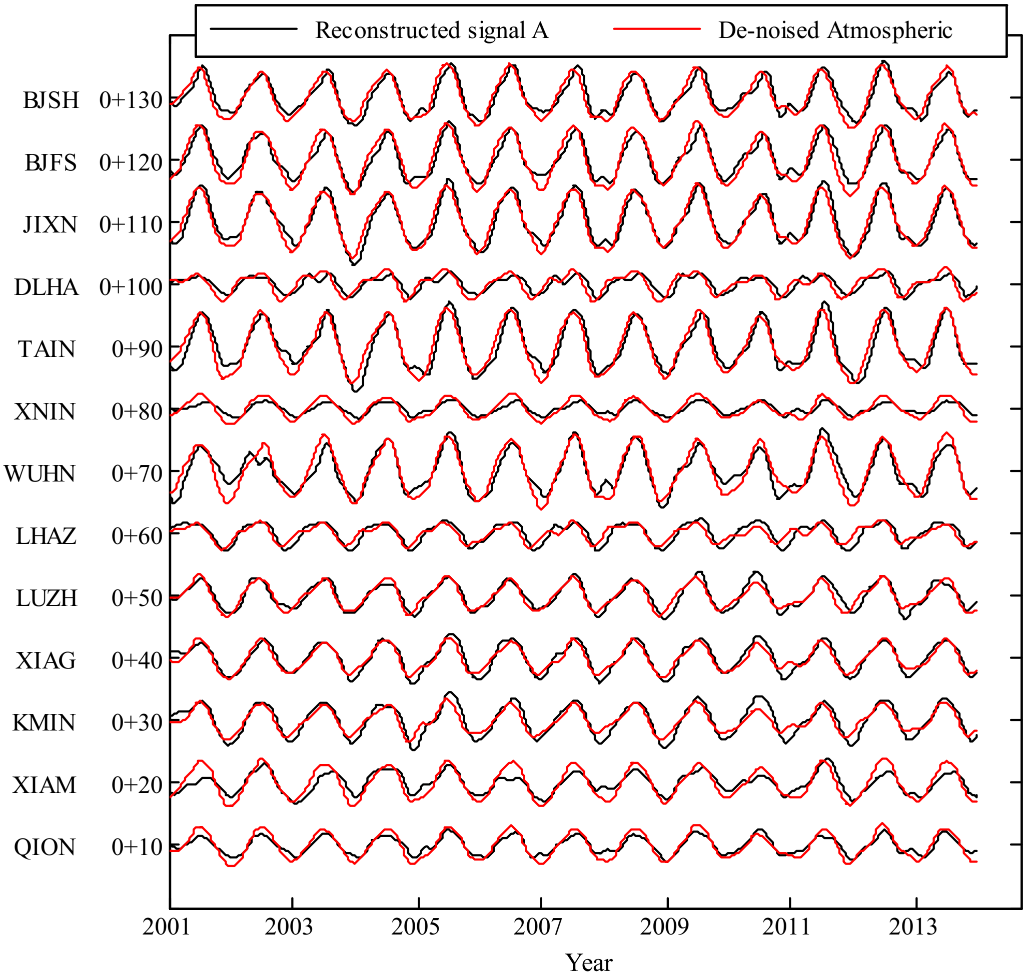

Figure 9
Comparison between the reconstructed signal A separated by PSR-ICA and the simulated signal (de-noised atmospheric mass loading) (10-mm offset per station)

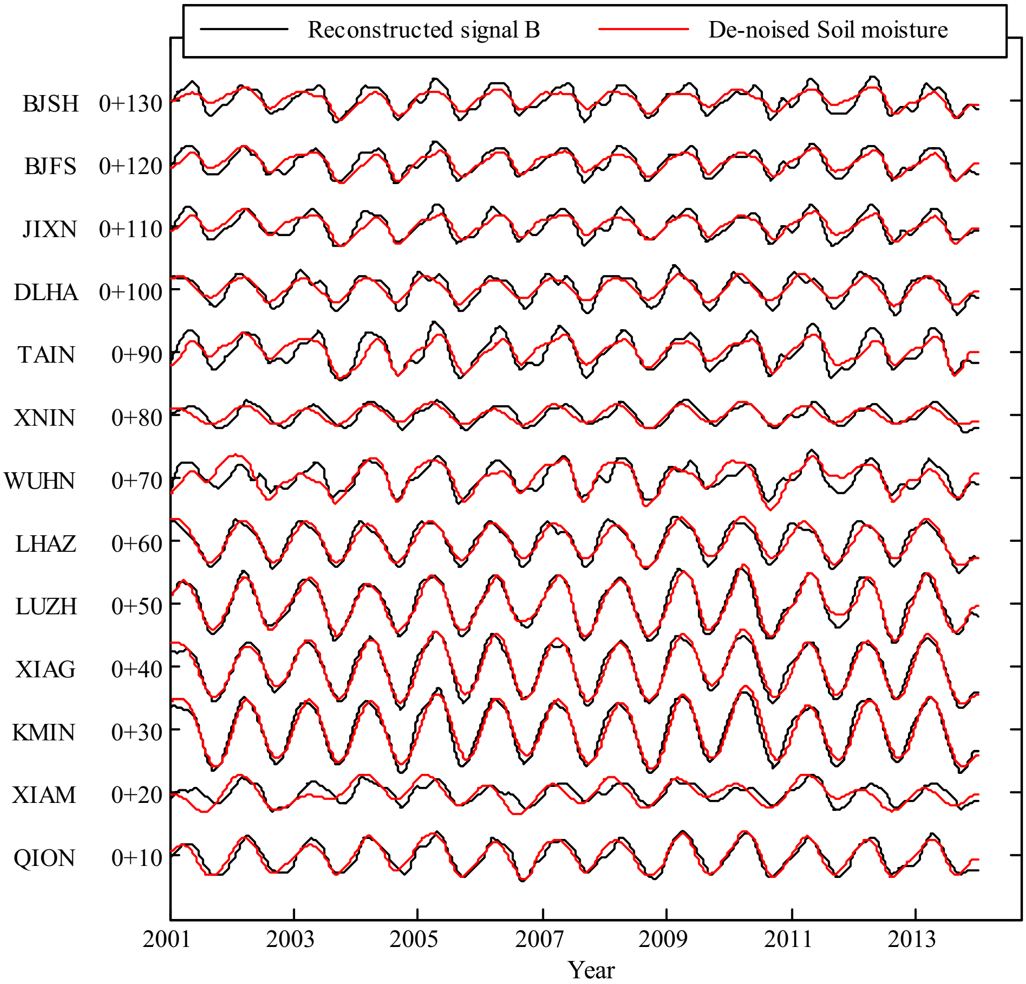

Figure 10
Comparison between the reconstructed signal B separated by PSR-ICA and the simulated signal (de-noised soil moisture mass loading) (10-mm offset per station)

Then, the FastICA method is used to separate the multi-dimensional embedding matrix. A number of ICs are obtained. Three ICs for the KMIN site are artificially reconstructed into two reconstructed signals, Reconstructed signal 1 (RS-1) and Reconstructed signal 2 (RS-2). The comparison of the two reconstructed signals for the 13 GNSS sites and their corresponding mass loadings (de-noised atmospheric and the soil moisture mass loadings) are shown in Figs. 11 and 12, respectively.

The correlation coefficients and RMS between the reconstructed signals (RS-1 and RS-2) and their corresponding mass loading signals (de-noised atmospheric mass loading and de-noised soil moisture mass loading) are calculated, respectively, the results are shown in Table 3.

From the correlation analysis of the reconstructed signals (RS-1 and RS-2) and their corresponding mass loading signals, we can say that some physical sources affect the crustal deformation. (1) The correlation coefficients of the RS-1 and the atmospheric mass loading are between 0.50 and 0.86, and ΔRMS are within the range of 5–47 %, which suggest that the RS-1 can be considered as a seasonal non-tectonic deformation mainly affected by the atmospheric mass loading; and (2) The correlation

Table 2

Correlation coefficients of reconstructed signals (Reconstruction A and Reconstruction B) and their corresponding mass loading signals

	CORR-A	RMS-A (mm)	dRMS-A (mm)	ΔRMS-A (mm)	CORR-B	RMS-B (mm)	dRMS-B (mm)	ΔRMS-B (mm)
BJSH	0.94	2.7	1.0	63	0.84	1.8	1.0	4344
BJFS	0.95	2.9	0.9	69	0.87	1.8	0.9	50
JIXN	0.96	3.4	1.0	71	0.86	1.8	1.0	44
DLHA	0.81	1.2	0.9	25	0.92	2.0	0.9	55
TAIN	0.93	3.5	1.3	63	0.85	2.4	1.3	46
XNIN	0.89	0.9	0.8	11	0.83	1.4	0.8	43
WUHN	0.92	2.9	1.2	59	0.78	2.1	1.3	38
LHAZ	0.86	1.6	0.8	50	0.95	2.5	0.8	68
LUZH	0.93	2.0	0.8	63	0.98	3.3	0.8	76
XIAG	0.94	2.2	0.8	64	0.98	3.5	0.8	77
KMIN	0.93	2.4	1.0	58	0.97	3.8	1.0	74
XIAM	0.87	1.6	1.2	25	0.71	1.4	1.2	14
QION	0.94	1.3	0.8	39	0.93	2.1	0.8	62

Case A RS-A and the de-noised atmospheric mass loading, *Case B* RS-B and the de-noised soil moisture mass loading, *CORR* correlation coefficient, *dRMS* RMS after mass loading correction, *ΔRMS* reduction in RMS

coefficients of the RS-2 and the soil moisture mass loading, except for the WUHN site (in bold), are in the range of 0.50–0.83, and ΔRMS are between 8 and 44 %, which means that the RS-2 can be considered as a seasonal non-tectonic deformation mainly affected by soil moisture mass loading. The vertical time series of WUHN station may be affected by the change of multipath effect and the instability of the station monumentation. The seasonal variation is not obvious and covered by noise and irregular trend variation in some years, which may seriously affect the seasonal signal extraction and the independent signal separation.

According to the analysis of experimental results in Sects. 3.3 and 3.4, the major mass loadings (atmospheric mass loading and the soil moisture mass loading) can be separated effectively by the single-channel ICA.

4. *Discussion and Conclusion*

We have shown that the PSR-ICA method can separate the independent source signals from the mixed mass loading signal in the simulation experiment. However, the correlations are 4–19 % and 2–29 % lower, respectively, between the two separated signals using the PSR-ICA method and atmospheric mass loading and soil moisture mass loading in the simulation experiment. These facts may indicate that the surface mass loadings, such as atmospheric mass loading and soil moisture mass loading, have a weak joint effect on crustal deformation in mainland China.

The PSR-ICA decomposition of the seasonal variation of GNSS vertical time series shows lower correlations with atmospheric and moisture loadings with respect to the simulation experiment. The correlations are systematically 15–20 % lower, which are mainly caused by the difference between simulated signals (simulated by the sum of the de-noised correction of the atmosphere and soil moisture mass loadings) and GNSS time series. Their correlation coefficients are 0.61–0.86, and the PSR-ICA decomposition results of these two experiments are both compared with the de-noised correction of the atmosphere and soil moisture mass loading. However, the mass loading corrections also have errors, such as for the KMIN site, there is no snow in this area during 2001 and 2013, and the snow mass loading corrections have a seasonal variation (up to 1.5 mm). The spatial resolution of mass loading data is 2.5° × 2.5° that mass loading corrections cannot accurately reflect the effect of mass loadings at specified points. Therefore, with the rapid increase of GNSS reference stations worldwide, the separation of mass load signals from GNSS time series is helpful to study the effect of mass loadings on the crustal

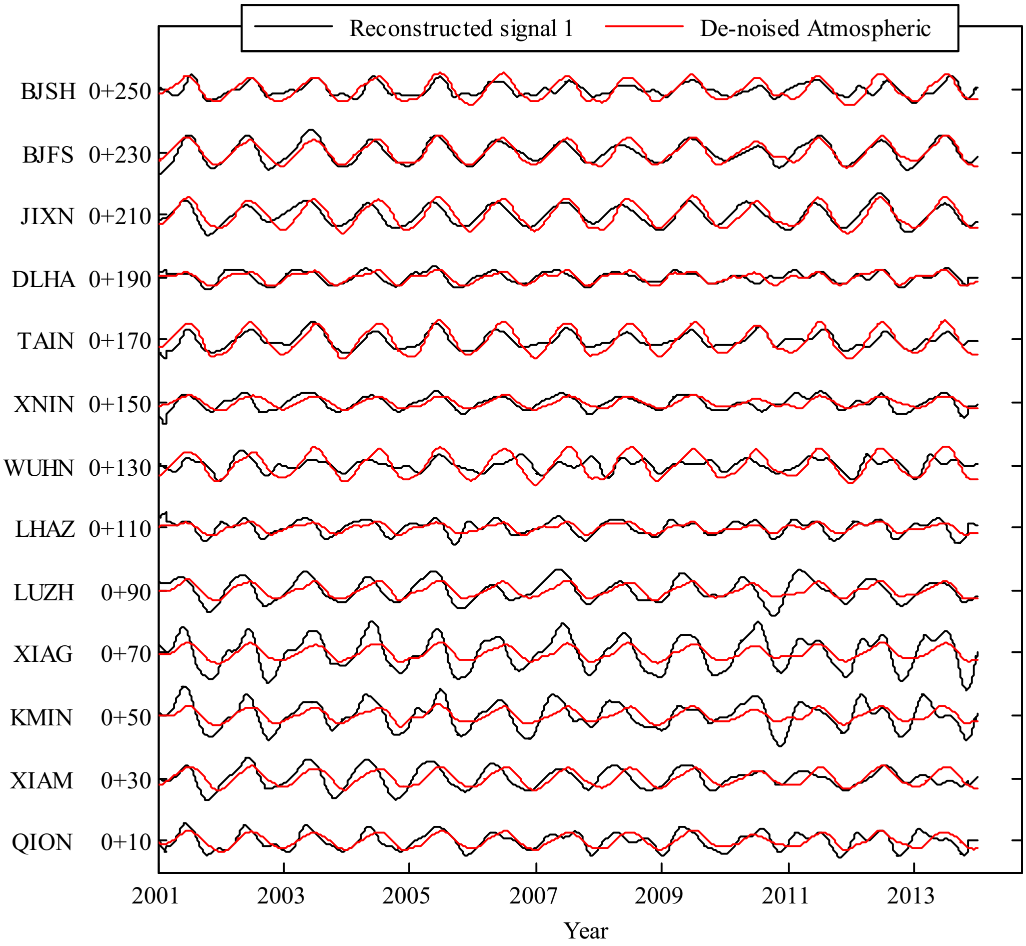

Figure 11
Comparison between the reconstructed signal 1 separated by PSR-ICA and the atmospheric mass loading (20-mm offset per station)

deformation and improve the accuracy of the correction model of mass loadings.

We use the EEMD method to decompose the GNSS vertical time series into noise signal, seasonal signal, and long-term trend signal. The PSR-ICA method is applied to analyze the seasonal signal. We successfully obtain the seasonal non-tectonic deformation signals. Through the case study of the selected GNSS reference stations, the following three conclusions can be drawn: (1) By obtaining noise signal, seasonal non-tectonic deformation signal, and long-term trend signal using the EEMD method, we found that the seasonal signal is strongly correlated with the sum of the major mass loading corrections; (2) In the simulation experiment, the high correlation between the separated signals and mass loadings (correlation coefficients are 0.71–0.98 and ΔRMS are 11–77 %) has proved that the PSR-ICA algorithm can accurately extract the physical source signals from the non-tectonic deformation signals; (3) The high correlation between the signals separated from seasonal signals and mass loadings (correlation coefficients are 0.50–0.86 and ΔRMS are 5–47 %) can effectively illustrate the seasonal variation (mainly annual variation) in the vertical time series of the GNSS reference station, and the separated signals can more accurately reflect the effects of various mass loadings on the crustal deformation.

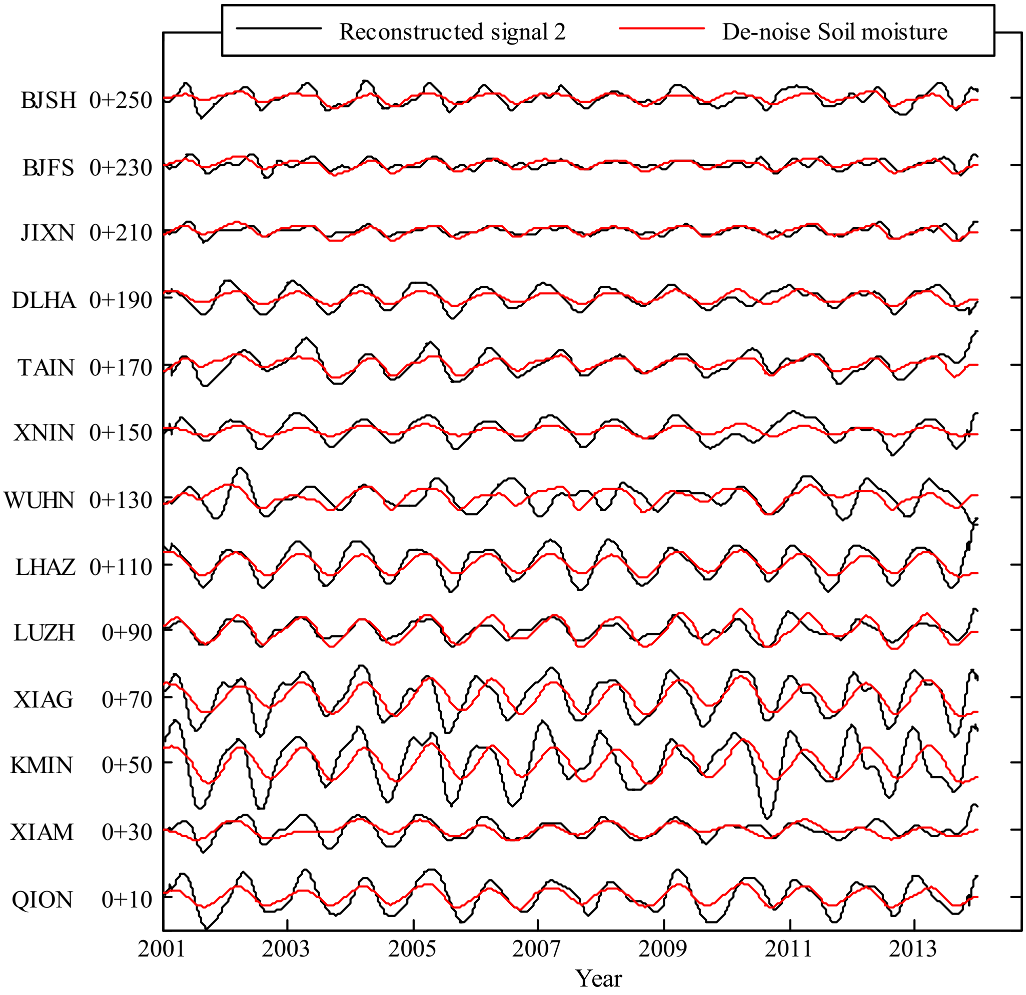

Figure 12
Comparison between the reconstructed signal 2 separated by PSR-ICA and the soil moisture mass loading (20-mm offset per station)

Table 3
Correlation between the reconstructed signals (RS-1 and RS-2) and its corresponding mass loading signals

	CORR	RMS-1 (mm)	dRMS-1 (mm)	ΔRMS-1 (%)	CORR	RMS-2 (mm)	dRMS-2 (mm)	ΔRMS-2 (%)
BJSH	0.75	1.9	1.8	5	0.71	2.4	1.8	25
BJFS	0.86	3.2	1.7	47	0.57	1.3	1.2	8
JIXN	0.79	3.0	2.0	33	0.72	1.1	0.9	18
DLHA	0.76	1.7	1.1	35	0.81	2.8	1.9	32
TAIN	0.80	2.3	2.0	13	0.75	3.2	2.2	31
XNIN	0.57	2.1	1.7	19	0.75	3.1	2.3	26
WUHN	0.61	3.5	3.2	9	**0.35**	1.9	2.9	**−53**
LHAZ	0.64	2.2	1.7	23	0.85	4.5	2.5	44
LUZH	0.62	3.4	2.7	21	0.76	2.4	2.0	17
XIAG	0.73	5.1	4.0	22	0.63	5.5	4.3	22
KMIN	0.63	4.1	3.4	17	0.50	7.0	6.3	10
XIAM	0.50	3.0	2.8	7	0.72	2.6	1.8	31
QION	0.63	2.6	2.1	19	0.83	4.4	2.9	34

Case 1 RS-1 and de-noised atmospheric mass loading, *Case 2* RS-2 and de-noised soil moisture mass loading, *CORR* correlation coefficient, *dRMS* RMS after mass loading correction, *ΔRMS* reduction in RMS

Acknowledgments

We thank the Jet Propulsion Laboratory for providing the QOCA software, and Crustal Movement Observation Network of China for providing the GNSS time series. This work was supported by the State Key Development Program of Basic Research of China (Grant No. 2013CB733303) and the National Natural Science Foundation of China (Grant No. 41074004).

REFERENCES

Amiri-Simkooei, A. R., Tiberius, C. C. J. M., and Teunissen, S. P. (2007). Assessment of noise in GPS coordinate time series: methodology and results. Journal of Geophysical Research: Solid Earth (1978–2012), *112*(B7).

Cardoso, J. (1998). Multidimensional independent component analysis. In Acoustics, Speech and Signal Processing. Proceedings of the 1998 IEEE International Conference, 4, 1941–1944.

Dai, W., Huang, D., and Liu, B. (2014). A phase space reconstruction based single channel ICA algorithm and its application in dam deformation analysis. Survey Review, *47*(345), 387–396.

Dong, D., Fang, P., Bock, Y., Cheng, M. K., and Miyazaki, S. (2002). Anatomy of apparent seasonal variations from GPS-derived site position time series. Journal of Geophysical Research: Solid Earth (1978–2012), *107*(B4), ETG-9.

Dragert, H., Wang, K., and James, T. S. (2001). A silent slip event on the deeper Cascadia subduction interface. Science, *292*(5521), 1525–1528.

Fraser, A. M., and Swinney, H. L. (1986). Independent coordinates for strange attractors from mutual information. Physical review A, *33*(2), 1134.

Grech, D., and Mazur, Z. (2013). On the scaling ranges of detrended fluctuation analysis for long-term memory correlated short series of data. Physica A: Statistical Mechanics and its Applications, 392(10), 2384–2397.

Huang, N. E., Shen, Z., Long, S. R., Wu, M. C., Shih, H. H. *et al.* (1998). The empirical mode decomposition and the Hilbert spectrum for nonlinear and non-stationary time series analysis. In Proceedings of the Royal Society of London A: Mathematical, Physical and Engineering Sciences (Vol. *454*, 1971, 903–995).

Hyvärinen, A., and Oja, E. (2000). Independent component analysis: algorithms and applications. Neural networks, *13*(4), 411–430.

Hyvärinen, A. (1999). Fast and robust fixed-point algorithms for independent component analysis. Neural Networks, IEEE Transactions on, *10*(3), 626–634.

Jiang, Z., Wang, M., Wang, Y., Wu, Y., Che, S. *et al.* (2014). GPS constrained coseismic source and slip distribution of the 2013 mw6.6 Lushan, China, earthquake and its tectonic implications. Geophysical Research Letters, *41*(2), 407–413.

Kennel, M. B., Brown, R., and Abarbanel, H. D. (1992). Determining embedding dimension for phase-space reconstruction using a geometrical construction. Physical Review A, *45*(6), 3403.

Li Z, Jiang. W. P., Liu H. F., and Qu X.C. (2012). Noise model establishment and analysis of IGS reference station coordinate time series inside China. Acta Geodaetica et Cartographica Sinica, *41*(4), 496G503.

Mao, A., Harrison, C. G., and Dixon, T. H. (1999). Noise in GPS coordinate time series. Journal of Geophysical Research: Solid Earth (1978–2012), *104*(B2), 2797–2816.

Montillet, J. P., Tregoning, P., McClusky, S., and Yu, K. (2013). Extracting white noise statistics in GPS coordinate time series. IEEE Geoscience and Remote Sensing Letters, *10*(3), 563–567.

Nikolaidis, R. (2002). Observation of geodetic and seismic deformation with the Global Positioning System. Ph.D. Thesis, University of California, San Diego.

Packard, N. H., Crutchfield, J. P., Farmer, J. D., and Shaw, R. S. (1980). Geometry from a time series. Physical Review Letters, *45*(9), 712.

Qin, Z., Zou, X., and Weng, F. (2012). Comparison between linear and nonlinear trends in NOAA-15 AMSU-A brightness temperatures during 1998–2010. Climate Dynamics, *39*(7–8), 1763–1779.

Rodriguez, E., Echeverria, J. C., and Alvarez-Ramirez, J. (2009). $1/f^{\alpha}$fractal noise generation from Grünwald-Letnikov formula. Chaos, Solitons & Fractals, *39*(2), 882–888.

Schroeder, M., Wiesenfeld, K. (1991). Fractals, chaos, power laws: minutes from an infinite paradise. Physics Today, 44(11), 91-91.

Takens, F. (1981). Detecting strange attractors in turbulence. Dynamical Systems and Turbulence, Warwick1980. Springer, Berlin, Heidelberg, 366–381.

Tiampo, K. F., Rundle, J. B., Klein, W., Ben-Zion, Y., and McGinnis, S. (2004). Using eigenpattern analysis to constrain seasonal signals in Southern California. Pure and Applied Geophysics, *161*(9–10), 1991–2003.

Vandam, T. M., Blewitt, G., and Heflin, M. B. (1994). Atmospheric pressure loading effects on Global Positioning System coordinate determinations.Journal of Geophysical Research: Solid Earth (1978–2012), *99*(B12), 23939–23950.

Wang, M., Shen, Z. K., and Dong, D. N. (2005). Effects of non-tectonic crustal deformation on continuous GPS position time series and correction to them. Diqiu Wuli Xuebao(Chinese Journal of Geophysics), *48*(5), 1045–1052.

Williams, S. D., Bock, Y., Fang, P., Jamason, P., Nikolaidis, R. M., *et al.* (2004). Error analysis of continuous GPS position time series. Journal of Geophysical Research: Solid Earth (1978–2012), *109*(B3).

Wu, Z., and Huang, N. E. (2009). Ensemble empirical mode decomposition: a noise-assisted data analysis method. Advances in Adaptive Data Analysis, *1*(01), 1–41.

Zhang, J., Bock, Y., Johnson, H., Fang, P., Williams, S. *et al.* (1997). Southern California permanent GPS geodetic array: Error analysis of daily position estimates and site velocities. Journal of Geophysical Research: Solid Earth (1978–2012), *102*(B8), 18035–18055.

(Received July 28, 2015, revised March 20, 2016, accepted April 28, 2016, Published online May 14, 2016)